The University Of Sheffield.

Dissolution of UK Vitrified High-Level Radioactive Waste Containing Zinc and Calcium

Adam J. Fisher

A thesis submitted in partial fulfilment of the requirements for the degree of Doctor of Philosophy

Immobilisation Science Laboratory
Department of Materials Science and Engineering
The University of Sheffield, UK.

Sponsored by EPSRC and RWM as part of the Next Generation Nuclear program

May 2020

Abstract

In the UK, vitrified High-Level-Waste (HLW) from the reprocessing of spent nuclear fuel is destined for disposal in a deep geological facility. A new zinc and calcium modified alkali-alumina-borosilicate base glass has been implemented at the Sellafield Ltd. site in anticipation for the immobilisation of post-operational clean-out waste streams alongside standard reprocessed fuel waste. At present, the dissolution behaviour and underlying corrosion mechanisms of zinc and calcium containing HLW glass have not been fully explored, particularly in conditions relevant to geological disposal, which is of importance to assist the development of the disposal safety case.

This body of work comprises fundamental studies to underpin the impact of zinc and calcium addition to the alkali-alumina-borosilicate base glass by assessing the structure-durability relationship. Studies were also developed to investigate the longer-term durability of waste glasses in conditions representative of geological disposal in the UK, incorporating potential groundwater solutions and an alternate corrosion scenario, demonstrated by the introduction of the Cyclic-Vapour-Static (CVS) methodology. The CVS provides, for the first time, a constrained integrated vapour-static groundwater dissolution test that aims to capture the anticipated initial vapour/glass interaction (altering the glass surface) and subsequent groundwater contact in a repository setting. Such a methodology can advance product consistency tests and further inform the safety case for HLW glass formulations destined for geological disposal. Post dissolution characterisation of glass alteration layers from tests were conducted by nuclear magnetic resonance spectroscopy, scanning electron microscopy and X-ray diffraction to identify the role of zinc and calcium on the alteration layer formation, results which are supported by geochemical modelling.

Irrespective of the experimental methodology and compositional complexity of the glasses studied, this work demonstrated the detrimental and positive impact of zinc and calcium additions, respectively, on the chemical durability at later stages of accelerated glass corrosion, the major result being that analogous Stage III ‘rate resumption’ behaviour was observed for all zinc containing glasses, linked to the precipitation of Zn-phyllosilicate clays.

Acknowledgements

This Thesis would not have been accomplished without the help of the following people (in no particular order), no matter how large or small the input, which is duly noted:

Dr Claire L. Corkhill for tremendous, enthusiastic and inspiring academic supervision and guidance. Eternal thanks for offering me the Ph.D position back in 2014. Prof. Neil Hyatt & Prof. Russell Hand for solid scientific guidance. Dr. Coleen Mann, Dr. Daniel J. Backhouse, Dr. Rita W.G. Vasconcelos, Dr. Clare Thorpe, Hannah Smith, Mohammed N. B. Imran and Dr. Florent Tocino for assistance in the field of dissolution. Dr. Dan Bailey for VHT/lab assistance and guidance. Dr. Dale L. Prentice, Dr. James Vigor for computing. Dr. Brant Walkley, Dr. Prashant Rajbhandari, Dr. Laura J. Gardner for NMR guidance. Dr. Lisa Hollands & Dr. Mike T. Harrison for glass fabrication. Dr. Clémance Gausse for geochemical modelling assistance and dissolution discussions. Dr. Luke Boast for designing and developing the 'bean-tins' which are heavily used throughout the department and for sampling. Antonia Yorkshire for sampling. Lucy Mottram for SEM-EDX assistance. Dr. Martin Stennett & Dr. Ben Palmer for general lab assistance. Dr. David Apperley & Dr. Sandra van Meurs for obtaining NMR spectra.
Other colleagues/professionals/academics that didn't specifically assist with the data, but provided good academic and motivating conversations: Dr Sam Walling, Dr Richard Veazey, Prof. Stephane Gin, Dr. Nick Gribble, Dr. Jack Clarke, Dr. Paul Heath, Josh Radford, Dan Geddes, Dr. Ritesh Mohun and the ISL team, past and present - which hopefully covers anyone else who has surely helped in some way.

Many thanks to the staff at The International Atomic Energy Agency who gave great academic and personal advice during my superb six-month placement from May - October 2018 in Vienna: Rebecca Robbins, Michael Ojovan, Ian Gordon, Willie Mayer, Christophe Xerri, Kim Baines and Merle Lust.

And finally a special thanks to Marissa who is the light of my life.

This Thesis is dedicated to Grandad John.

Acknowledgements

-

This Thesis was written on location in the following:

Sheffield, UK.

Vienna, Austria.

Yerevan, Armenia.

Dublin Airport, Republic of Ireland.

Phoenix Sky Harbour International Airport, Arizona, USA.




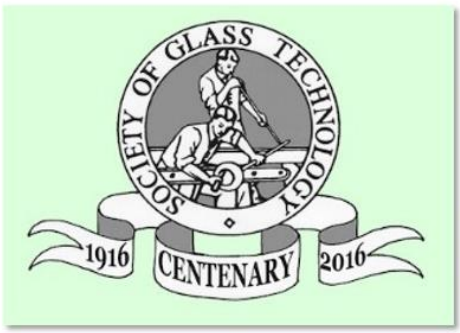


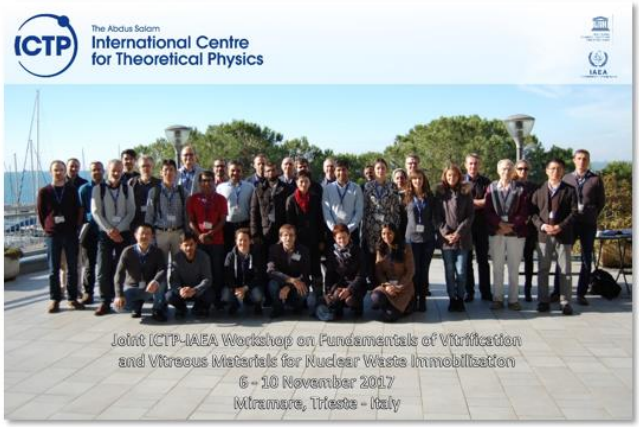

Publications

Academic Journals

The author has contributed to the following publications during the production of this thesis:

1. **Adam J. Fisher**, Mike T. Harrison, Neil C. Hyatt, Russell J. Hand & Claire L. Corkhill. The dissolution of simulant UK Ca/Zn-modified nuclear waste glass: the effect of increased waste loading. *MRS. Advances*. **6**, 95-102 (2021).
2. Sean T. Barlow, **Adam J. Fisher**, Daniel J. Bailey, Lewis R. Blackburn, Martin C. Stennett, Russell J. Hand, Sean P. Morgan, Neil C. Hyatt & Claire L. Corkhill. Thermal treatment of nuclear fuel-containing Magnox sludge radioactive waste. *Journal of Nuclear Materials* **552**, 152965, (2021).
3. **Adam J. Fisher**, Mohammed N. B. Imran, Colleen Mann, Clémence Gausse, Russell J. Hand, Neil C. Hyatt & Claire L. Corkhill. Short communication: The dissolution of UK simulant vitrified high-level-waste in groundwater solutions. *Journal of Nuclear Materials* **538**, 152245, (2020).
4. Sean T. Barlow, Daniel J. Bailey, **Adam J. Fisher**, Martin C. Stennett, Clémence Gausse, Hao Ding, Viktor A. Krasnov, Sergey Yu Sayenko, Neil C. Hyatt & Claire L. Corkhill. Synthesis, characterisation and corrosion behaviour of simulant Chernobyl nuclear meltdown materials. *npj Materials Degradations.* 4:3, (2020).
5. **Adam J. Fisher**, Mike T. Harrison, Neil C. Hyatt, Russell J. Hand & Claire L. Corkhill. The dissolution of simulant Ca/Zn-modified nuclear waste glass: Insight into Stage III behaviour. *MRS Advances*. **5**, [3-4], 103-109, (2020).
6. **Adam J. Fisher**, Neil C. Hyatt, Russell J. Hand & Claire L. Corkhill. The formation of pitted features on the International Simple Glass during dynamic experiments at alkaline pH. *MRS Advances.* **4**, [17-18], 993-999, (2019).
7. Daniel J. Backhouse, **Adam J. Fisher**, James J. Neeway, Claire L. Corkhill, Neil C. Hyatt & Russell J. Hand. Corrosion of the International Simple Glass under acidic to hyperalkaline conditions. *npj Materials Degradations.* 2:29, (2018).
8. Clare L. Thorpe, Colleen Mann, **Adam J. Fisher**, Russell J. Hand, Neil C. Hyatt, Brian J. Riley, Michael J. Schweiger, Jodi Mayer, Christina Arendt, Albert A. Kruger, David Kosson & Claire L. Corkhill. Evaluation of Novel Leaching Assessment for Nuclear Waste Glasses - 18314. WM2018 Conference, March 18-22, 2018, Phoenix, Arizona, USA, *Radwaste Solutions* (2018).
9. Claire L. Corkhill, **Adam J. Fisher**, Dennis M. Strachan, Russell J. Hand & Neil C. Hyatt. PREPUBLICATION: Corrigendum to "The dissolution rates of simulated UK Magnox - ThORP blend nuclear waste glass as a function of pH, temperature and waste loading" [Miner. Mag. 79 (2015) 1529 - 1542] *Mineralogical Magazine*, August 2018, **82** [4], 989-942 (2018).
10. Neil C. Hyatt, Claire L. Corkhill, Daniel J. Bailey, **Adam J. Fisher** & Russell J. Hand. Comment on "Preliminary assessment of modified borosilicate glasses for chromium and ruthenium immobilization", by Farid and Rahman. *Materials Chemistry and Physics*. **192**, 29-32 (2017).

11. Sean T. Barlow, Daniel J. Bailey, **Adam J. Fisher**, Martin C. Stennett, Claire L. Corkhill & Neil C. Hyatt. Synthesis of simulant 'lava-like' fuel contaminating materials (LFCM) from the Chernobyl reactor unit 4. *MRS Advances*. **2**, 1-6 (2016).

Conferences, Symposiums and Workshops Attended

Throughout the duration of this thesis the author has attended the following conferences, seminars, symposiums and workshops which have greatly influenced and inspired much of the work contained within the thesis:

1. Theramin 2020 – Thermal Treatment of Radioactive Waste, Mechanics Institute, Manchester, UK, 4th-5th February 2020.
2. The 43rd Scientific Basis for Nuclear Waste Management, Materials Research Society, Vienna, Austria, 21st-24th October 2019.
3. Glass & Optical Materials Division Meeting, Boston Park Plaza, Boston, Massachusetts, USA, 9th-14th June 2019.
4. Frontiers in Glass: At the interface between Earth Science and Synthetic Materials, University of Bristol, UK, 20th-21st May 2019.
5. Waste Management Symposia, Phoenix Convention Centre, Phoenix, Arizona, USA, 4th-7th March 2019.
6. The 42nd Scientific Basis for Nuclear Waste Management, Materials Research Society, Boston, Massachusetts, USA, 26th-29th November 2018.
7. Joint Nuclear CDTs Winter School, Birmingham, St. John's Hotel, Solihull, UK, 3rd-5th January 2018.
8. Joint ICTP-IAEA Workshop on Fundamentals of Vitrification and Vitreous Materials for Nuclear Waste Immobilization (smr 3159), ICTP, Trieste, Italy, 6th -10th November 2017.
9. Becky Mawhood, Committee Specialist from the House of Commons BEIS Committee, Select Committee Talk, The University of Manchester, UK, 12th July 2017.
10. PETRUS-ANNETEE, PhD and Early-Stage Researchers Conference, Instituto Superior Technico, Lisbon, Portugal, 26th-30th June 2017.
11. 12th Pacific Rim Conference on Ceramic and Glass Technology (PACRIM 12), including Glass & Optical Materials Division Meeting (GOMD 2017), Waikoloa Village Hilton, Hawaii, USA, 22nd-26th May 2017.
12. UK - Ukraine Workshop on Chernobyl Decommissioning, Halifax Hall, Sheffield, UK, 28th February - 1st March 2017.
13. Joint Nuclear CDTs Winter School, Birmingham, St. John's Hotel, Solihull, UK, 4th-6th January 2017.
14. Society of Glass Technology - Centenary Conference & European Society of Glass 2016, The University of Sheffield, UK, 4th-8th September 2016.
15. PETRUS-Opera, PhD and Early-Stage Researchers Conference, Delft University of Technology, Delft, The Netherlands, 27th June - 1st July 2016.
16. International Meeting on Deep Borehole Disposal of High-Level Radioactive Waste, Mercure Hotel, Sheffield, UK 13th-15th June 2016.

17. Mineralogical Society Research in Progress Meeting, Wills Memorial Hall, The University of Bristol, UK, 9th June 2016.
18. Annual Conference, UK Project on Nuclear Issues, Royal United Service Institute, Whitehall, London, UK, 2nd June 2016.
19. In the Wake of Japan's Nuclear Tsunami: Reflections on the Nature of Disaster in the 21st Century Symposium, INOX Dine, The University of Sheffield, UK, 21st April 2016.
20. Geological Disposal, ESRC Nuclear Futures Seminar 2, Leopold Hotel, Sheffield, UK, 6th-7th April 2016.
21. Geological Disposal, ESRC Nuclear Futures Seminar 1, Halifax Hall, Sheffield, UK, 27th-28th January 2016.
22. An Introduction to the Nuclear Industry, National Nuclear Laboratory, Summergrove Hall, Whitehaven, UK, 20th-21st January 2016.
23. Joint Nuclear CDTs Winter School, Royal Angus Hotel, Birmingham, UK, 6th-8th January 2016.
24. EPSRC Fission & Fusion Symposium, The MacDonald Hotel, Manchester, UK, 14th December 2015.
25. Farewell to Magnox Half Day Seminar, Wylfa Sports and Social Club, Cemaes Bay, Anglesey, UK, 28th October 2015.
26. ICO Nuclear CDT Summer School, Imperial College London, UK, 19th June 2015.
27. Thermal Treatment of Nuclear Waste Symposium 2015, Warrington, UK, 15th January 2015.
28. Joint Nuclear CDTs Winter School, NEC Crown Plaza Hotel, Birmingham, UK, 6th-8th January 2015.

Oral Presentations

The work included in this thesis has been disseminated at the following conferences and meetings:

1. The 43rd Scientific Basis for Nuclear Waste Management, Materials Research Society, Vienna, Austria, 21st-24th October 2019.
2. Glass & Optical Materials Division Meeting, Boston Park Plaza, Boston, Massachusetts, USA, 9th-14th June 2019.
3. Frontiers in Glass: At the interface between Earth Science and Synthetic Materials, University of Bristol, UK, 20th-21st May 2019.
4. The 42nd Scientific Basis for Nuclear Waste Management, Materials Research Society, Boston, Massachusetts, USA, 26th-29th November 2018.
5. Joint Nuclear CDTs Winter School, Birmingham, St. John's Hotel, Solihull, UK, 3rd-5th January 2018.
6. Joint ICTP-IAEA Workshop on Fundamentals of Vitrification and Vitreous Materials for Nuclear Waste Immobilization (smr 3159), ICTP, Trieste, Italy, 6th -10th November 2017.
7. PETRUS-ANNETEE, Ph.D and Early-Stage Researchers Conference, Instituto Superior Technico, Lisbon, Portugal, 26th-30th June 2017.
8. 12th Pacific Rim Conference on Ceramic and Glass Technology (PACRIM 12), including Glass & Optical Materials Division Meeting (GOMD 2017), Waikoloa Village Hilton, Hawaii, USA, 22nd-26th May 2017.
9. Joint Nuclear CDTs Winter School, Birmingham, St. John's Hotel, Solihull, UK, 4th-6th January 2017.

10. Society of Glass Technology – Centenary Conference & European Society of Glass 2016, The University of Sheffield, UK, 4th-8th September 2016.

Poster Presentations

The work included in this thesis has been disseminated at the following conferences and meetings;

1. Waste Management Symposia, Phoenix Convention Centre, Phoenix, Arizona, USA, 4th-7th March 2019.
2. 12th Pacific Rim Conference on Ceramic and Glass Technology (PACRIM 12), including Glass & Optical Materials Division Meeting (GOMD 2017), Waikoloa Village Hilton, Hawaii, USA, 22nd-26th May 2017.
3. PETRUS-Opera, PhD and Early-Stage Researchers Conference, Delft University of Technology, Delft, The Netherlands, 27th June - 1st July 2016.
4. Mineralogical Society Research in Progress Meeting, Wills Memorial Hall, The University of Bristol, UK, 9th June 2016.
5. Joint Nuclear CDTs Winter School, Royal Angus Hotel, Birmingham, UK, 6th-8th January 2016.
6. EPSRC Fission & Fusion Symposium, The MacDonald Hotel, Manchester, UK, 14th December 2015.

Site Visits

1. Atomic Weapons Establishment, Aldermaston, UK, 15th-16th January 2018.
2. V.I. Lenin Nuclear Power Station, Chernobyl, Ukraine 13th-14th July 2016.
3. HADES Underground Laboratory, Belgium, 27th June 2016.
4. Centrale Organisatie Voor Radioactief Afval **(**COVRA), Vlissingen, The Netherlands, 27th June 2016.
5. National Nuclear Laboratory, Workington, UK, 20th January 2016.
6. Heysham Nuclear Power Plant, Heyham, UK, 16th October 2014.
7. Sellafield Ltd., Seascale, UK, 15th October 2014.

Outreach Participation

1. Widening participation event - Sixth form student visit. Described the nuclear waste disposal options. The University of Sheffield, 21st September 2017.
2. International Festival of Glass - occupied a stall informing the public of the link between glass and nuclear waste. This was explained through a model nuclear reactor, art-deco uranium glass and the below mentioned nuclear waste island. Stourbridge, UK. 25-26th August 2017.
3. Pi at MOSI' (Pi - short for Platform for Investigation) MOSI's monthly contemporary science programme. Showcased 'Nuclear Waste Island' – a desktop activity introducing the disposal concepts of nuclear waste. Manchester Museum of Science and Industry (MOSI), Manchester, UK. 11th September 2015.

Professional Training

1. Radiation Protection Supervisor Training (Radman Associates) 21st-22nd May 2015.
2. Compressed [Cylinder] Gas Safety Workshop (The Gas Safety Co.) 19th March 2015.

Broader Academic Development

1. International Nuclear Law Module, The University of Manchester, 5th- 10th March 2018.

Submitted Applications

1. White Rose Brussels Office - Climate Change Policy Article Submission, January 2019.
2. Consultation: Working with Communities - Implementing Geological Disposal - Contributed my own opinions towards how communities should be engaged and represented in a siting process for a geological disposal facility for higher activity radioactive waste, January 2018.
3. House of Lords call for evidence - Priorities for Nuclear Research and Technologies - Call for Evidence February 2017.
4. Business, Energy and Industrial Strategy (BEIS) Select Committee - direct communication - suggestions on future energy and climate change policy - submitted through Policy @Manchester, January 2017.

Published response to public consultation

1. Nuclear Decommissioning - Consultation on the Regulation of Nuclear Sites in the Final Stages of Decommissioning and Clean-up. Amending the framework for the final stages of nuclear decommissioning and clean-up, Department for Business, Energy & Industrial Strategy (BEIS), October 2018.
   https://assets.publishing.service.gov.uk/government/uploads/system/uploads/attachment_data/file/749656/government-response-framework-for-nuclear-decomissioning.pdf

Media

1. Inside Yorkshire Podcast – Series 2, Episode 14 - Nuclear Energy with Adam Fisher- 6th April 2020.
2. BBC 6Music - Chernobyl and Material Science - guest on the Steve Lamacq show - 1745-1800 8th August 2017.
3. BBC Radio York – Chernobyl – University work - Interview with Jonathon Cowap - 1000-1100 7th July 2017.
4. The York Press article - 4th August 2016
   http://www.yorkpress.co.uk/news/14658896.York_scientist_working_on_decommissioning_of_Chernobyl_nuclear_power_plant/

Unacknowledged Publication

The author should have been named amongst the published authors on;

1. Sean T. Barlow, Martin C. Stennett, Russell J. Hand, Sean P. Morgan & Neil C. Hyatt. Thermal treatment of UK Magnox Sludge. *Proceedings of the 2nd Petrus-OPERA Conference on Radioactive Waste Management and Geological Disposal, Delft University of Technology*. p19-22 (2016).

Awards

1. Roy G. Post Award ($5,000) Waste Management Symposia 2019, Phoenix Convention Centre, Phoenix, Arizona, USA, 4th-7th March 2019.
2. American Nuclear Society 2018, Waste Management Symposia 2018 - Best oral presentation/paper - contributing author - "Evaluation of Novel Leaching Assessment for Nuclear Waste Glasses" Authors: Claire Corkhill, Clare Thorpe, Colleen Mann, **Adam Fisher**, Russell Hand, Neil Hyatt, University of Sheffield; Brian Riley, Michael Schweiger, Jodi Mayer, Christina Arendt, Pacific Northwest National Laboratory; Albert Kruger, US DOE; David Kosson, Vanderbilt University.
3. Best Poster Nomination - Mineralogical Society Research in Progress Meeting, Wills Memorial Hall, The University of Bristol, UK, 9th June 2016.

Contents

List of Abbreviations

ACT	Activated Complex Theory
AFCI	Advanced Fuel Cycle Initiative (glass)
ASTM	American Society for Testing and Materials
BEIS	Department for Business, Energy and Industrial Strategy
BSE	Back Scattered Electrons
CCD	Charged-Coupled Device
COVRA	Centrale Organisatie Voor Radioactief Afval
CVS	Cyclic Vapour Static
DECC	Department of Energy and Climate Change
DSC	Differential Scanning Calorimetry
DTA	Differential Thermal Analysis
EDS	Energy Dispersive Spectroscopy
EPSRC	Engineering and Physical Sciences Research Council
EXAFS	Extended X-ray Absorption Fine Structure
FIB-TEM/SAED	Fractional Ion Beam Transmission Electron Microscopy/Selected Area Electron Diffraction
FWHM	Full Width Half Maximum
GDF	Geological Disposal Facility
GW	Groundwater
HAW	Highly Active Waste
HF	Hydrofluoric acid
HLW	High-Level-Waste
IAEA	International Atomic Energy Agency
ICDD	International Centre for Diffraction Data
ICDP	Interface-Coupled Dissolution-Precipitation model
ICP-MS	Inductively Coupled Plasma Mass Spectroscopy
ICP-OES	Inductively Coupled Plasma Optical Emission Spectroscopy
ILW	Intermediate Level Waste
LLNL	Lawrence Livermore National Laboratory
LLW	Low-Level-Waste
LMR	Linear Multi-variate Regression
MAS	Magic Angle Spinning
MAS-NMR	Magic Angle Spinning Nuclear Magnetic Resonance Spectroscopy

MCC-1	Material Characterisation Centre 1
MCFT	Micro-Channel-Flow-Through
MIDAS	Materials for Innovative Disposition from Advanced Separations
MW	Mixed Windscale
NanoSIMS	Nanoscale Secondary Ion Mass Spectrometry
NDA	Nuclear Decommissioning Authority
NMR	Nuclear Magnetic Resonance Spectroscopy
NNL	National Nuclear Laboratory (UK)
PCT-A	Product Consistency Test – A
PCT-B	Product Consistency Test – B
PES	Polyethersulphone
PNNL	Pacific Northwest National Laboratory
POCO	Post Operational Clean Out
PPM	Parts Per Million
q/S	Flow rate (q) to sample surface area (S) used in the SPFT methodology
RAF	Royal Air Force
RF	Radio Frequency
RUMGCM	Refined Unified Mechanistic Glass Corrosion Model
SA/V	Surface Area to Volume ratio
SE	Secondary Electrons
SEM	Scanning Electron Microscopy
SNF	Spent Nuclear Fuel
SPFT	Single-Pass-Flow-Through
SRL / SRNL	Savannah River National Laboratory
TEM	Transmission Electron Spectroscopy
TRIS	Hydroxymethyl Aminomethane buffer solution
TST	Transition State Theory
TUoS	The University of Sheffield
UHQ	Ultra-High-Quality water
VHT	Vapour-phase Hydration Test
VLLW	Very-Low-Level-Waste
VTR	Vitrification Test Rig
WRW	Waste calcine
XRD	X-ray Diffraction

Sample Identification Notation

AFCI	Advanced Fuel Cycle Initiative (glass)
ISG	International Simple Glass
ISGI	International Simple Glass Intermediate
ISGO	International Simple Glass Original
MW25	UK HLW glass - Mixed Windscale (MW) with 25 wt.% waste loading
SON68	French inactive HLW glass, analogous to the active R7T7 glass
ZnCa xx:xx	UK HLW simple base glass (xx:xx is the ZnO:CaO molar ratio)
ZnCa xx:xx MW28	UK HLW glass - Mixed Windscale (MW) with 28 wt.% waste loading (xx:xx is the ZnO:CaO molar ratio). Fabricated at TUoS. Waste calcine contains 75o:25m
ZnCa MWXX	UK HLW glass - Mixed Windscale (MW) with XX wt.% waste loading. Fabricated at the VTR. Waste calcine contains 50o:50m
ZnCa MW	Zinc Calcium Mixed Windscale

The University Of Sheffield.

I, the author, confirm that the Thesis is my own work. I am aware of the University's Guidance on the Use of Unfair Means (www.sheffield.ac.uk/ssid/unfair-means). This work has not been previously been presented for an award at this, or any other, university.

Adam J. Fisher

1st May 2020

1. Introduction

The UK government's 2014 White Paper, 'Implementing Geological Disposal' sets out the policy framework for implementing geological disposal for Highly-Active-Waste (HAW), which is defined as the collection of High-Level-Waste (HLW), Intermediate-Level-Waste (ILW) and a small proportion of Low-Level-Waste (LLW) that is destined to be disposed of in a Geological Disposal Facility (GDF) (DECC 2014). At the present time, geological disposal is the safest, the most practical and the internationally agreed solution to the disposal of HAW and unprocessed Spent-Nuclear-Fuel (SNF) (IAEA 2003).

The UK's GDF will incorporate the co-disposal of ILW, HLW and SNF within the same facility, but in separate vaults and galleries. The safety of geological disposal is based on the intensive application of multiple barriers, based on three engineered (wasterform, container and backfill) and one natural (geology) to provide isolation, chemical stability and to prevent the mobility of radionuclides to the geosphere and biosphere for hundreds of thousands of years (Fig. 1.1). The release rate of radionuclides is controlled by wasteform corrosion in surrounding groundwater (Grambow 2006), which may be contaminated with near-field materials such as container corrosion products and alkaline plumes from the corrosion of cementitious backfill material, which may be detrimental to the integrity of vitrified HLW (Frugier *et al.* 2008, Jantzen *et al.* 2010, Burger *et al.* 2013, Mann 2018). A detailed description of the barriers, the UK's waste inventory and the UK's current progress on geological disposal is provided in 1.1 Appendix. Hence, for each wasteform, the long-term hazard that it poses to the geosphere and biosphere requires an accurate description and prediction of the durability performance over geological ages, inferred by accelerated laboratory studies, studies of natural analogues and extended timescale computer modelling (Frugier *et al.* 2008), which, in part, forms the safety case for geological disposal.

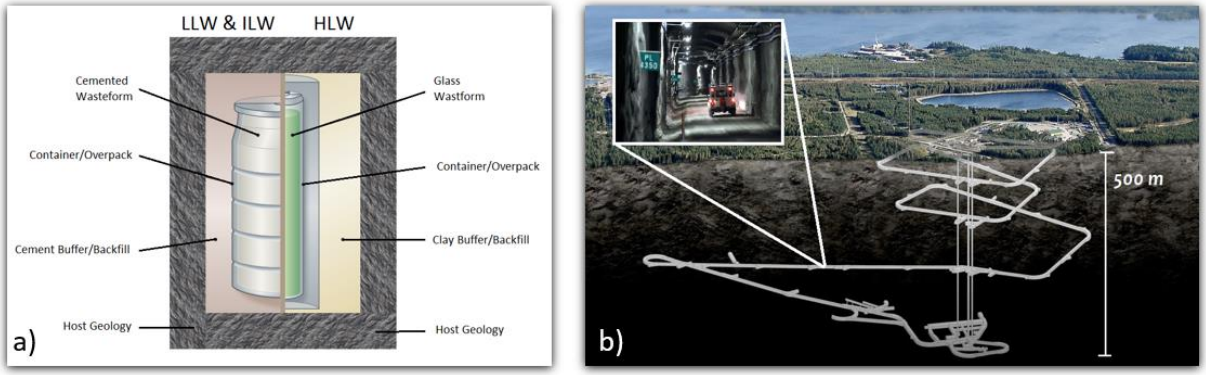

Figure 1.1 a) The multi-barrier concept, adapted from the Nuclear Decommissioning Authority (NDA) (DECC 2014); and b) The GDF concept. Image courtesy of POSIVA (Finland).

During the 1950's, vitrification was established as a safe and secure way to immobilize the radioactive waste generated from the reprocessing of SNF (Magribi *et al.* 1987, Lutze 1988, Vernaz & Brueziere 2014, Harrison 2014). Such waste is categorised as HLW, which the UK has been generating since 1990 at the Sellafield site, using an alkali borosilicate base glass known as Mixed Windscale (MW) ($5.3Li_2O{\cdot}11.1Na_2O{\cdot}21.9B_2O_3{\cdot}61.7SiO_2$ wt.%) to incorporate approximately 25 wt.% reprocessed Magnox and Oxide fuel waste. However, the UK is currently in the process of adopting a modified base glass, containing Al_2O_3, ZnO and CaO additions to MW, which is known as ZnCa MW, which currently incorporates approximately 28 wt.% reprocessed waste. This modification was made to increase the chemical durability of expected future vitrified products, incorporating different wastestreams from the Post-Operational-Clean-Out (POCO) of the Highly-Active-Liquor (HAL) storage tanks prior to their decommissioning (Harrison & Brown 2018). Future vitrified HLW is expected to contain a blend of reprocessed and POCO wastes, whereby a full transition to ZnCa MW is expected (Harrison 2018). At present, MW25 is being produced on two out of three active lines at the Sellafield site and ZnCa MW28 is being produced on the other active line. All active lines are fed with a mixture of reprocessed Magnox (m) and Oxide (o) fuel waste at a 50m:50o ratio.

A wealth of literature attempts to underpin the chemical durability of MW25 from first principles (Abraitis *et al.* 2000, Curti *et al.* 2006, Brookes *et al.* 2011, Harrison 2014, Cassingham *et al.* 2015, Corkhill *et al.* 2018, Goût *et al.* 2019) and in conditions representative of geological disposal (Brookes *et al.* 2011, Serco 2012, Backhouse 2016, Schofield *et al.* 2017, Mann 2018,), however, there is little in the literature to scientifically underpin the dissolution of ZnCa MW-types (Zhang *et al.* 2015, Cassingham *et al.* 2016, Vance *et al.* 2018), despite its current industrial employment, especially at longer timescales and in conditions representative of geological disposal. It has been established that the magnesium content in Mg-containing glass (including MW25 and ZnCa MW) and in groundwater solution is detrimental to the long term stability (Thien *et al.* 2010 & 2012, Fleury *et al.* 2013, Debure *et al.* 2016). This is due to the precipitation of Mg-silicate clays, which reduce the passivating properties of altered glass, manifesting in greater rates of dissolution compared to a glass/dissolving media not containing Mg. Similar behaviour for Zn is expected (Gin *et al.* 2013), whereby a potentially additive detrimental effect on the chemical durability is strongly suggested (Aréna *et al.* 2016) and is in need of investigation.

Hence, the aims of this Thesis are to underpin the impact of ZnO and CaO addition to the modified MW formulation by assessing the structure-durability relationship on base glass-types, and extending this to simulant ZnCa MW-wasteloaded versions in conditions representative of geological disposal in the UK, incorporating potential groundwater solutions and differing corrosion scenarios. Note that the

impact of Al_2O_3 inclusion into the new modified ZnCa MW composition is not directly investigated in this study as there is much greater uncertainty in the long term chemical durability of ZnO and CaO containing waste glass and a pressing need to underpin the impact of such inclusions for the geological disposal safety case (NNL 2014). The inclusions of Al_2O_3 is therefore treated as a constant component in the glass formulations studied.

A breakdown of each chapter describing the development of the Thesis is described as below:

- **Chapter 2 – Literature Review - The impact of ZnO and CaO addition on the structure and durability of borosilicate glass in the context of High-Level-Waste**

A comprehensive review of the literature regarding the impact of ZnO and CaO additions on the stages of borosilicate glass corrosion is provided, with particular emphasis on nuclear waste glass corrosion in geological repository conditions.

- **Chapter 3 – Experimental**

A comprehensive description of the experimental methods employed is provided.

- **Chapter 4 – The initial dissolution rate of the International Simple Glass in acidic and basic media**

An initial study on an international standard glass (the International Simple Glass (ISG)) was undertaken to establish the Single-Pass-Flow-Through (SPFT) experimental methodology (which was employed in Chapters 5 & 9) and to provide a baseline initial dissolution rate comparison, including post dissolution particle characterisation using Scanning Electron Microscopy (SEM). Results from this chapter have been published in *Nature Materials Degradation* and *MRS Advances*.

- **Chapter 5 – Structure-dissolution relationship of simplified High-Level-Waste glass as a function of ZnO:CaO ratio**

Dissolution of ZnCa MW base glasses with different ZnO and CaO content is provided to underpin the structure-dissolution relationship across all stages of glass dissolution, demonstrated by the use of Nuclear Magnetic Resonance Spectroscopy (NMR) and the SPFT, Product-Consistency-Test B (PCT-B) and Materials-Charaterisation-Centre-1 (MCC-1) dissolution methodologies. Post dissolution particle characterisation using Scanning Electron Microscopy (SEM) and X-ray Diffraction (XRD), alongside PHREEQ-C geochemical modelling is provided. This Chapter suggests an optimised ZnCa MW base glass composition in terms of its longer-term chemical durability.

- **Chapter 6 – The dissolution of simulant waste-loaded ZnO/CaO modified base glass for UK High-Level-Waste**

An extension of Chapter 5; dissolution of various ZnCa MW wasteloaded formulations is provided to underpin the dissolution behaviour across later stages of glass dissolution demonstrated by the PCT-B and MCC-1 dissolution methodologies. Post dissolution particle characterisation using Scanning Electron Microscopy (SEM) and X-ray Diffraction (XRD), alongside PHREEQ-C geochemical modelling is provided. The Chapter suggests an optimised waste glass composition, based on its base glass composition and waste loading content in terms of its longer-term chemical durability. Results from this chapter have been published, in part, in *MRS Advances.*

- **Chapter 7 – The dissolution of simulant waste-loaded ZnO/CaO modified base glass for UK High-Level-Waste in groundwater solutions**

A development of Chapter 6 to explore dissolution behaviour in potential repository groundwater solutions. The early stage PCT-B dissolution behaviour of the current industrially produced ZnCa MW28 formulation in groundwater solutions at the expected repository temperature of 50 °C is investigated. Results from this short Chapter have been published in the *Journal of Nuclear Materials.*

- **Chapter 8 – High-Level-Waste glass durability: An alternative experimental methodology for geological disposal**

A hybrid vapour phase - static groundwater dissolution methodology, termed the Cyclic Vapour Static (CVS) is introduced for the first time to investigate the chemical durability of MW25 and ZnCa MW28 under a different, but potentially more representative corrosion scenario compared to standardised (PCT-B & MCC-1) dissolution methodologies. Glass monoliths were initially pre-corroded by vapour at 100 °C for 28 d before the same specimen was subjected to MCC-1 dissolution at 50 °C for 55 d. This Chapter is essentially an extension of Chapters 6 & 7, which attempts to build and strengthen the safety case for geological disposal. Preliminary results from this chapter have been introduced at the *Waste Management Symposia 2019 (Arizona, USA).*

- **Chapter 9 – The effect of transmutation of Sr to Zr on the structure-dissolution relationship of simple glasses**

This final short Chapter expands the relevance of the results presented in Chapter 5, suggesting that the structural-durability relationship can be extended to other elements, particularly those present in HLW, which are susceptible to radioactive decay and transmutation. This work also suggests that the dissolution behaviour of inactive nuclear waste glass compositions used to study nuclear waste glass

corrosion may not be truly representative of the glass compositions at the time of first groundwater contact (or water vapour as alluded to in Chapter 8) in a geological disposal facility.

- **Chapter 10 – Concluding Remarks and Future Work**

An evaluation of the results chapters, which report and reflect on the state-of-the-art of ZnCa MW glass corrosion and suggests future work, not only applicable to ZnCa MW, but for all nuclear waste glass corrosion.

1.1 Appendix

I – Nuclear Power in the UK

The United Kingdom was a significant pioneer of nuclear technology beginning in the late 1940's from Winston Churchill's drive for the UK to become a nuclear weapon state. As a result, the UK became nuclear self-sufficient in all aspects (except commercial mining), which has created a very diverse and complex range of commercial and military nuclear facilities spread throughout the country (Fig. A-1), with the main hub of activity being the Sellafield site in Cumbria, England. Such facilities in the UK encompass, or have historically encompassed all stages of the nuclear fuel cycle to varying degrees, including: mining, uranium enrichment, fuel manufacture, operational and decommissioning power stations, research facilities, spent fuel storage, spent fuel reprocessing, radioactive waste processing, radioactive waste storage and radioactive waste disposal facilities, alongside nuclear weapons manufacture (Corkhill *et al.* 2017, United Kingdom 2018). The UK currently has fifteen operational reactors generating 9.5 GWe, approximately 21 % of the nation's electricity, of which half will be retired by 2025. A new nuclear reactor fleet is expected by 2030 at five sites, which will generate a combined total of 16 GWe.

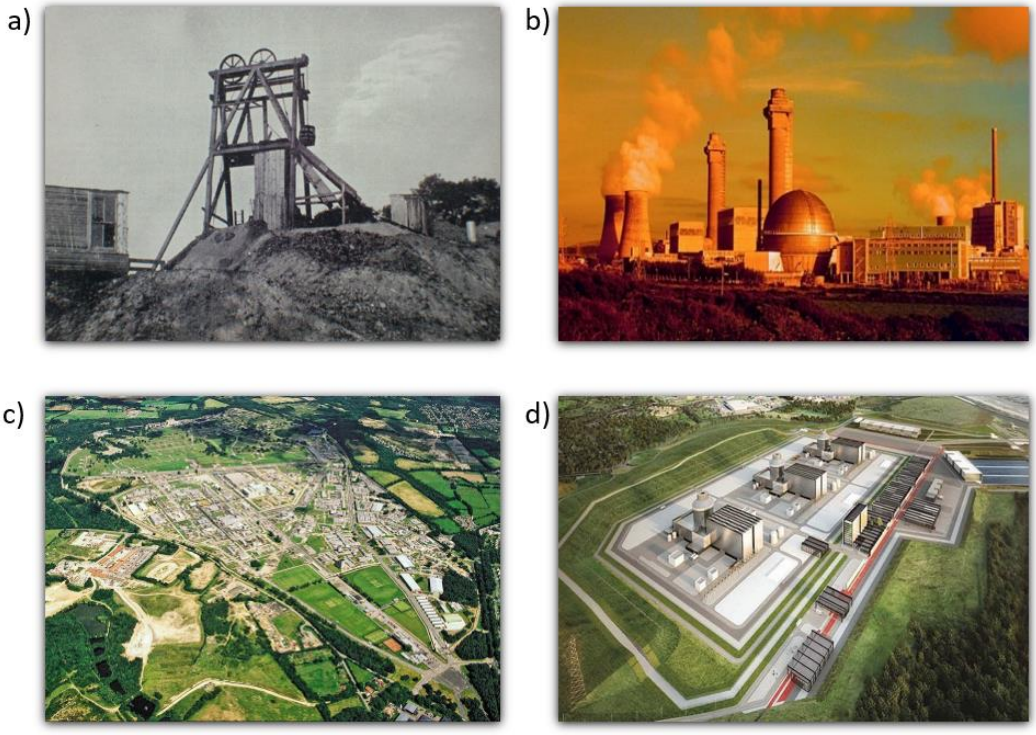

Figure A-1. a) Headgear of South-Terras radium mine 1936 (photo credits H. G. Ordish); b) The Sellafield site, Cumbria, England, UK. The Windscale Piles can be clearly seen with their unique filtering system placed atop of the chimney stacks (photo credit Sellafield Ltd.); c) the Atomic Weapons Establishment site built on the former RAF Aldermaston site (photo credit Basingstoke Observer); d) the planned reactor fleet at the Moorside site (photo credit NuScale).

II – Radioactive Waste in the UK

A consequence of nuclear applications is the generation of hazardous radioactive wastes. These wastes take many forms, from sources used in industrial and medical practices, research and academia, to materials used and contaminated in civil nuclear and defence programs (IAEA 2018). These materials can no longer serve a useful purpose or be decontaminated for free release and follow the standard recycling or landfill disposal routes, so must be managed in a manner that protects the public and environment. In general, most waste is treated and securely stored on licensed nuclear facilities (the majority at the Sellafield site) awaiting final disposal (NDA 2019). The long term strategy for all nuclear waste is immobilisation and ultimate disposal in engineered near-surface facilities and a deep geological repository, for less hazardous and more hazardous waste respectively (IAEA 2018). The majority of the radioactive waste generated in the UK comes from civil nuclear power activities, in particular from the decommissioning of nuclear facilities, the treatment of legacy wastes and from the reprocessing of spent nuclear fuel. At present, the current UK government (United Kingdom 2018) believes that spent nuclear fuel should not be categorised as radioactive waste, so long as the option of reprocessing remains open. The government does not intend to reprocess spent fuel from the proposed new nuclear plants, therefore this spent fuel will be classified as radioactive waste in due course.

The governmental body responsible for the nation's radioactive waste is the Department for Business, Energy and Industrial Strategy (BEIS). Its executive body, the Nuclear Decommissioning Authority (NDA) owns all nuclear licensed sites and is tasked with responsibility for the management of spent fuel and radioactive wastes and the clean-up of radioactive UK legacy sites. A wholly owned subsidiary of the NDA, Radioactive Waste Management (RWM) is the delivery body responsible for the implementation of a deep geological repository. The NDA and RWM attempt to achieve these goals through contracting work to licensed nuclear operators and through the funding of projects conductive at academic institutions, private enterprises and the National Nuclear Laboratory. Considerable sums of money are being spent in the UK to clean-up the 60-year old nuclear legacy, with expenditure for the financial year 2017/18 expected to be £3.24 billion (United Kingdom 2018).

III – Classification and Inventory

The classification system of radioactive waste in the UK is based according to the waste's radioactive content and heat generating capacity (Table A-1), which is broadly in lines with the IAEA's classification

system (IAEA 2009). The wasteform final product is produced in such a way as to meet disposal criteria, such as solidification, embedding and/or encapsulation in cement/glass, examples of which are show in Figs. A-2 - A-4. Current waste volumes are provided in Table A-2.

Table A-1. Overview matrix of the catagories of UK radioactive waste.

Category	Radioactivity	Heat Generating	Equivalent Cs-137 content per 1 m^3 cement	Example	Current Situation	Long-term Solution
High Level Waste (HLW)	>4 GBq/t α or >12 GBq/t β	Yes	>3.125 kg	Vitrified product from the reprocessing of SNF	Long-term interim storage	Deep geological disposal
Intermediate Level Waste (ILW)	>4 GBq/t α or >12 GBq/t β	No	0.003 g - 3.125 kg	From the reprocessing operations of SNF (fuel cladding & materials) or decommissioning of nuclear facilities (sludges, effluents, filter materials, construction materials). Commonly	Long-term interim storage	Deep geological disposal
Low Level Waste (LLW)	<4 GBq/t α or <12 GBq/t β	No	<0.003 g	Decommissioning materials, lab equipment, PPE and hospital refuse. Usually super compacted and cemented into steel containers	Interim storage/disposed of in the LLW repository	Possible new disposal facility
Very Low Level Waste (VLLW)	<100 Bq/g	No	-	From decommissioning of nuclear facilities – concrete, soil, rubble	Interim storage	Unspecified landfill for low-volume, Specified landfill for high-volume

In the UK, Highly-Active-Waste (HAW) is defined as the collection of HLW, ILW and a small proportion of LLW that is destined to be disposed of in a deep engineered geological repository (NDA 2019). Existing LLW is currently disposed of at the LLW Repository (NDA 2019, LLW 2020). Future spent fuel from proposed new nuclear plants will fall under the category of HAW. It should also be noted that some aspects of radioactive waste management policy are devolved to the Scottish, Welsh and Northern Irish administrations, whereby in particular, the Scottish government's ILW policy states that disposal should be in near-surface facilities as near to the site where the waste was produced (Scottish Government 2011). This will require different disposal performance assessments to strengthen the safety case for disposal (Heath *et al.* 2018) as the waste will be closer to the surface than in a GDF (IAEA 2018).

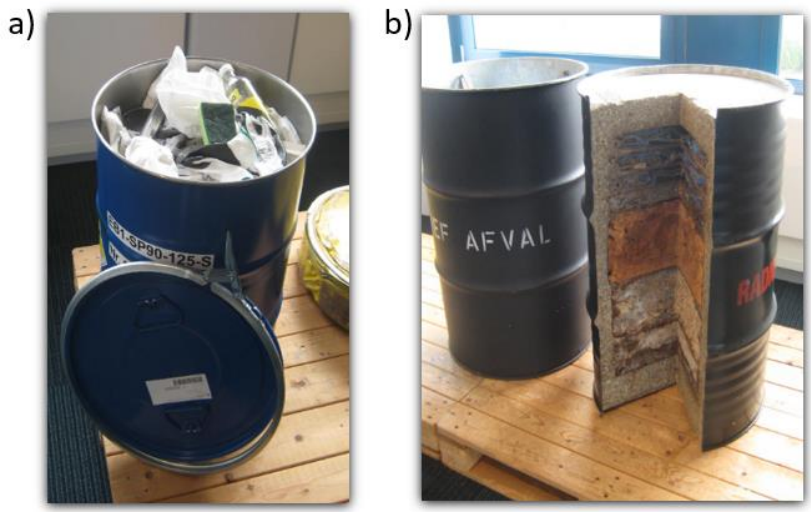

Figure A-2. Examples of a) contaminated materials and b) compaction to form LLW drums. All photo credits A. J. Fisher.

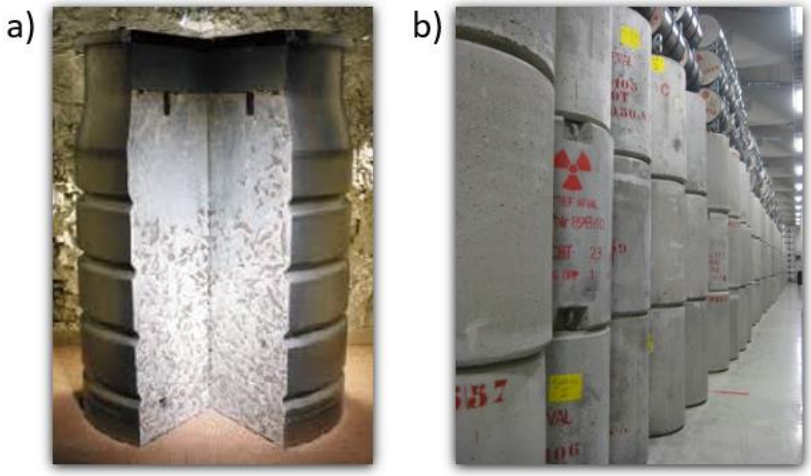

Figure A-3. Examples of ILW drums; a) fuel-cladding encapsulation; b) storage of ILW drums in COVRA facilities – The Netherlands. Similar interim storage is adopted in the UK. (Photo credits: a) NDA; b) A. J. Fisher).

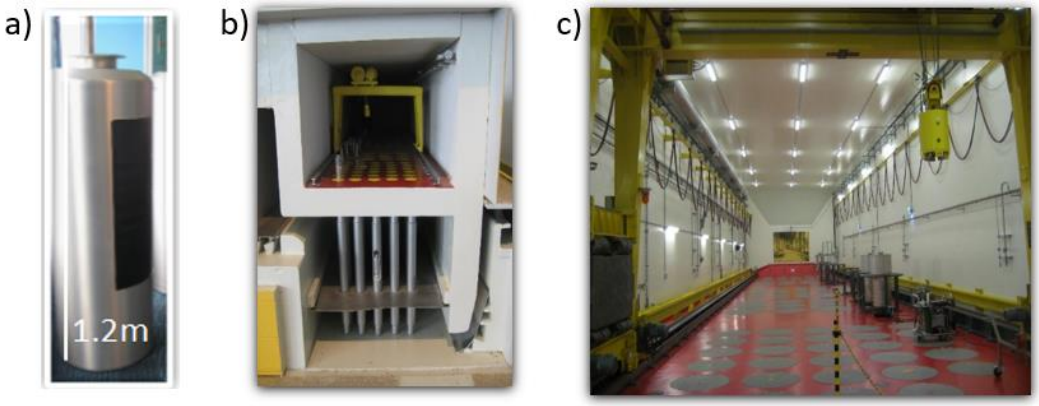

Figure A-4. Examples of HLW interim storage at COVRA – The Netherlands (similar to the UK); (a) vitrified HLW in stainless-steel cannister – glass melt is poured into cannister; (b) cross-section of long-term interim storage of HLW cannisters in COVRA facilities – The Netherlands. Cannisters are stacked in units of five and are air cooled. Similar interim storage is adopted in the UK; (c) view of the interim storage facility. Lead caps can be seen on top of each stack. All photo credits A. J. Fisher.

Table A-2. Radioactive waste – UK inventory as of December 2016 (BEIS 2017).

Category	Volume Disposed (m^3)	Volume Interim Storage (m^3)	Interim Storage Comments	Contribution to total waste inventory by volume (%)	Contribution to total waste inventory by activity (%)
High-Level Waste (HLW)	-	1,960	Vitrified = 867 m^3 Liquid = 1,100 m^3	1.0	95
Intermediate-Level Waste (ILW)	-	99,000	Treated = 31,200 m^3 Untreated = 67,800 m^3	6.1	5
Low-Level Waste (LLW)	227,650	30,100	Most will be disposed of at LLWR	93.9	0.00005
Very-Low-Level Waste (VLLW)	-	935	Awaiting disposal to landfill/ in-situ disposal	N/A	Negligible

IV – Disposal

The UK government's 2014 White Paper, 'Implementing Geological Disposal' sets out the policy framework for implementing geological disposal for HAW (DECC 2014), which is based on a volunteer, bottom-up approach by local communities to host the GDF. Radioactive Waste Management is the governmental body responsible for the delivery of the GDF, from the siting process to the final expected closure of the repository in approximately 2100 (United Kingdom 2018). It proposes the co-disposal of ILW, HLW and SNF within the same facility, but in separate vaults. The safety of geological disposal is based on the intensive application of multiple barriers (Ewing *et al.* 2016), based on three engineered and one natural to provide isolation, chemical stability and to prevent mobility of radionuclides to the geosphere and biosphere for hundreds of thousands of years (IAEA 2018). The series of barriers are described below (Kim *et al.* 2011, Bailey 2015, Marsh *et al.* 2021):

1. **Wasteform** – radionuclides are conditioned into a chemically stable solid material which acts to reduce radionuclide release. UK HLW is immobilized within a vitrified network, UK LLW and ILW is encapsulated within cement. Each material must meet strict waste acceptance criteria before it is disposed. It is desirable for the wasteform to not need conditioning throughout its interim storage period prior to final disposal.
2. **Container/overpack** – the wasteform will be contained within a corrosion resistant stainless steel or copper canister in order to aid handling and transport. The wasteform and canister

are referred to as a waste package and will be disposed of in vaults in the GDF. The container/overpack is envisioned to protect the wasteform from groundwater ingress for approximately 1,000 years. For HLW the canister is the stainless steel can in which the molten glass was poured. Various overpacks exist for LLW and ILW, ranging from standard 200 litre drums to larger 20 m^3 stainless steel packages.

3. **Buffer/backfill** – the vaults will be surrounded by an appropriate material in order to provide physical and chemical protection to the waste packages. Materials are expected to suppress migration of radionuclides (through adsorption of nuclides) and retard groundwater flow. Materials such as bentonite clay are suitable and have the added advantage of being self-healing in the event of ground movements, which have the potential to form cracks in the host rock and allow easy passages for radionuclide migration to the surface. Bentonite is a promising material for HLW backfill, whereas the Nirex reference vault backfill cement is expected for ILW (Vasconcelos *et al.* 2018).
4. **Host Geology** – the rock type hosting the repository (Grambow 2016, Hedin & Olsson 2016, Laverov *et al.* 2016, Von Berlepsch & Haverkamp 2016). The main barrier due to the depth of isolation, 500-1000 m. Not imperative to have the most suitable rock formation.

An interesting point to bear in mind is the current interim HLW storage facility at the Sellafield site. The interim storage of HLW should be closely considered in parallel with all aspects of the geological disposal process. The interim store at Sellafield started receiving HLW in 1990, with the original expectation of an operational GDF by 2027, with all HLW transferred to the GDF before 2040 (Gribble 2018). The current expectation (as of 2018 (United Kingdom 2018)) is that HLW will be sent to a GDF by 2075 at the earliest, which will receive existing and future stockpiles until 2105. The interim HLW store currently has a 50 year lifetime (up to 2040). The key drivers behind safe interim storage are shielding, cooling, the prevention of canister corrosion and to ensure smooth removal of stored canisters after the prolonged storage when the time comes to remove them to a GDF. The inability to safely remove canisters will pose significant problems (the surface dose rate of typical canisters are 4.5×10^3 Svh^{-1} β & γ and 1.5×10^{-2} Svh^{-1} neutron) hence it is imperative to avoid such a situation. A key decision will be made relatively soon (as of May 2021) regarding the future storage of HLW. The current options include:

1. Build an identical new store next to current store
2. Build an identical store elsewhere on site

3. Building an 'Aircraft hangar' type warehouse with HLW packages contained within concrete lined outer packages
4. Extension of the lifetime of the current interim store to 2105

The financial and practical implications of each option need to be fully investigated, but the current plan is to prepare for indefinite interim storage in the eventuality that a GDF doesn't get built (Gribble 2018). This issue highlights the ineffective government strategy towards the disposal of nuclear waste, the financial burden of any one of the four above options seems not to have been considered. It is also worth mentioning that it will take between 10-25 years to transport all of the currently stored HLW containers to their new interim storage, depending on the export strategy (relating to container cleaning) (Gribble 2018).

V – Disposal – the future?

The implementation of geological disposal is an active environment, there is a pressing need to solve, at least in part, the nuclear waste issue (RWM 2017), which has been thwarted on several occasions due to public and political hostility. Current issues are important to consider and need to be communicated effectively to the public (CoRWM 2021). Some issues are listed and addressed below, which should be available in the public domain.

- How pressing is the GDF solution?

No immediate risk, but clear plans should be in place.

- Inventory

The Achilles heel may be the inventory. A fundamental question to address is that of the expected inventory contents and quantity (Tromans 2018). Particularly incorporating the varied amounts of legacy waste and spent fuel from undetermined new build. An indeterminate amount of future waste may be difficult to advise a safety case. This may be the biggest issue to address before the disposal process commences. The expected cost to build a GDF is £ 12 billion for legacy waste only (United Kingdom 2018). The GDF is expected to accept new build fuel from 2130, which will conclude 2190. Hence, it came be predicted that intergenerational interim storage will be required, whereby the management of these sites could be problematic. Military waste will contribute 5-8 % (United Kingdom 2018).

- Volunteerism Vs. Imposed national solution

Arguments can be made against the volunteer approach – a GDF will not solve all nuclear waste issues. Nuclear new build will create interim storage sites in various locations around the coast up until the 2100s, whereby communities may not even be consulted (Tromans 2018), hence, new nuclear build could therefore override public interests. Also if the volunteerism process doesn't work, what will ensue? A fully bottom up approach may not work, however, the government is confident that it will (House of Commons 2018). The government is confident that a GDF will accommodate all waste, legacy and new build. This will be an enormous challenge considering the undetermined waste quantity and specification. How then can it be built or accepted by the regulator? Should the government impose a solution for the national good?

The author of this thesis is of the opinion that an imposed national solution merits the most logical solution for the geological disposal of nuclear waste. A planned top down contingency solution should be considered. This should take the form of a GDF that will be large enough to accommodate all waste, legacy and new build, but should be loose regarding the restrictions of the inventory.

2. Literature Review - The impact of ZnO and CaO addition on the structure and durability of borosilicate glass in the context of High-Level-Waste

2.1 Introduction

This Chapter provides a summary of the existing literature relating to the impact of ZnO and CaO addition (separately and combined) on the structure and durability of borosilicate glass in the context of High-Level-Waste (HLW). The intention is to provide information relevant to this Thesis in support of providing new, fundamental insight into the dissolution behaviour of ZnCa Mixed Windscale (MW), which may ultimately effect the decision on whether to continue (or modify the elemental base glass fractions) the utilisation of ZnCa modified MW frit during vitrification of HLW at the Sellafield site (Harrison 2018).

Firstly, the motivation for the addition of ZnO and CaO to HLW glass frit, from an industrial perspective, will be explained and the Chapter will then explore the effect of the inclusion of each oxide, separately and together, on the structure and durability of borosilicate glass across all stages of glass corrosion. It will conclude with a review of disposal considerations in terms of chemical durability for vitrified HLW compositions, which assisted the development of the experimental methodology applied in this Thesis.

2.2 Industrial Motive

The United Kingdom is currently in the process of adopting a modified base glass for the vitrification of HLW, referred to throughout this Thesis as ZnCa MW ($4.2Li_2O{\cdot}8.6Na_2O{\cdot}6.0CaO{\cdot}6.0ZnO{\cdot}4.2Al_2O_3{\cdot}23.4B_2O_3{\cdot}47.6SiO_2$ wt.%), which contains additional Al_2O_3, CaO and ZnO compared to the nominal four-component MW formulation ($5.3Li_2O{\cdot}11.1Na_2O{\cdot}21.9B_2O_3{\cdot}61.7SiO_2$ wt.%). The molar ratio of ZnO:CaO is 40:60. This modification was made to improve the melt processing and to

increase the chemical durability of expected future vitrified products incorporating waste streams including calcine from spent fuel reprocessing, but particularly wastes rich in caesium phosphomolybdate and zirconium molybdate arising from the Post-Operational-Clean-Out (POCO) (expected Mo content ~ 10wt.% in POCO glass (Harrison 2018)) of the Highly-Active-Liquor (HAL) storage tanks prior to their decommissioning (Harrison & Brown, 2018). Future vitrified products are expected to contain a blend of reprocessed and POCO wastes (Harrison 2018). At present, ZnCa MW is deployed on one of the three operational active vitrification lines at the Sellafield Waste Vitrification Plant (WVP) and standard MW25 remains operational on the two other lines, with a full transition to ZnCa MW on all three lines anticipated in the future (Harrison 2018a). Currently, all active lines are fed with a mixture of reprocessed Oxide (o) and Magnox (m) fuel waste with a 50o:50m ratio.

The addition of Zn and Ca to borosilicate glass is reported to confer beneficial properties for the *processing a*nd *final physical properties* of HLW glass (Musić *et al.* 2019), such as: reducing the melt viscosity; extending the melter lifetime (i.e. reduced refractory lining corrosion); providing greater homogeneity, greater viscosity, and therefore supporting pouring at lower temperatures as demonstrated on the inactive test rig at the Sellafield site (Short *et al*. 2008). The extension of the melter lifetime through the use of this glass is two-fold: the formation of Zn-spinel phases provides protection for the walls of the melter (Pegg 2017), and most importantly, the inclusion of Ca in the glass promotes the formation of $CaMoO_4$ (Dunnett *et al*. 2012). In terms of improving the chemical durability (which will be discussed in detail below), the addition of Zn was shown to reduce Soxhlet leach rates (at the initial rate of dissolution – Stage I) (Matlack *et al*. 1998) and Ca has been reported to stabilize Mo in a chemically durable $CaMoO_4$ phase (Dunnett *et al*. 2012).

Although a full transition from MW to ZnCa MW is anticipated, a decision on the full transition will be made within the next few years (Harrison 2018a) on further evaluation of the data pertaining to the effectiveness of the ZnCa MW in terms of active processing ability, and from laboratory scale experiments of the waste-loading capacity and chemical durability, especially during Stages II and III of dissolution in solutions representative of a disposal environment (i.e. groundwater and near-field contaminants). However, recent evidence suggests that the processing is problematic, due to the readily formed Zn-spinel phases causing blockages around the melter nozzle (Gribble 2018).

2.3 Fundamentals of glass corrosion applied to ZnO and CaO containing glass

At the outset it is worth clarifying the terminology associated with the durability of glass in accordance with the international scientific community: the use of the term *glass corrosion* encompasses all stages of the glass-aqueous solution interaction, whereas glass *dissolution* refers solely and specifically to elemental release and the associated mechanisms. This Section refers to glass corrosion and dissolution of typical alkali/alkaline earth alumina-borosilicate glasses of relevance to nuclear waste glass formulations.

It is well known that in the presence of water glasses corrode (Morey & Bowen 1927, Charles 1958, Cox & Ford 1993). This occurs because glasses are thermodynamically metastable, irreversibly transforming by alteration into more stable, typically crystalline phases. Results from many studies of glass alteration argue that such transformation of pristine glass to stable phases such as clays, apatite etc., involve transient phases, which include metastable (typically amorphous or nanocrystalline) alteration materials such as hydrated glass and gel (Gin *et al*. 2011).

Glass corrosion is far from a simple process since glass alters at various rates due to different mechanisms and environmental conditions. The dissolution kinetics of alkali-borosilicate glass over a given time can be described as a function of glass composition, temperature, pH and solution chemistry. The general mechanisms occur regardless of the glass composition and of the chemical and physical conditions of the solution in contact with the glass surface (Gin *et al*. 2013). Extensive published studies of nuclear waste glass corrosion describe the process in five stages, or more precisely five kinetic rate regimes, each with a different rate-limiting mechanism (Van Iseghem *et al*. 2007, Frugier *et al.* 2008). This approach is based on experimental observations of the corrosion kinetics, simply determined in most cases by measuring the concentration of solubilised elements (particularly boron) from the glass in the surrounding solution. The five stages are listed below:

1. Initial Diffusion (also referred to as Interdiffusion)
2. The Initial Rate (also referred to as the Forward Rate, where the Forward Rate should only represent the dissolution at time t=0)
3. The Rate Drop
4. The Residual Rate
5. Rapid Resumption of Alteration

However, recent consensus considers only three of the five kinetic rate regimes (Fig. 2.1) (Vienna *et al*. 2013, Gin *et al*. 2013, Gin *et al*. 2015) due to the fact that the interdiffusion and rate-drop regimes are not formal kinetic stages. The reason for this is that interdiffusion occurs constantly throughout glass corrosion, no matter the stage of corrosion, but acts alone for only very small time periods, on the scale of $<10^{-15}$ s (Frugier *et al*. 2008). The rate-drop regime is merely a transition between the initial and residual rate, during which time the solution is subject to increasing silica concentration (Grambow 1985), which allows for the glass to begin forming an alteration layer on the surface that could impact continued corrosion (Van Iseghem *et al*. 2009, Gin *et al*. 2013). Hence, for clarity the processes used to describe glass alteration rates will be referred to in three stages, not five specific kinetic rate regimes. All three stages are described in detail below with reference to their associated observable features and underlying mechanics, including the effect of the initial glass structure. Where experimental data exists for Zn and Ca-containing glasses, this is also described. The processes and mechanisms described can be assumed for the general interaction between all alkali/alkaline earth alumina-borosilicate glasses (including nuclear waste glasses) and pure, deionised water. Effects due to other influences, such as temperature, solution pH, solution composition, radiation effects and glass surface area, that will be appropriate for the disposal of vitrified nuclear waste in a GDF are discussed in later sections separately, but are briefly introduced where appropriate.

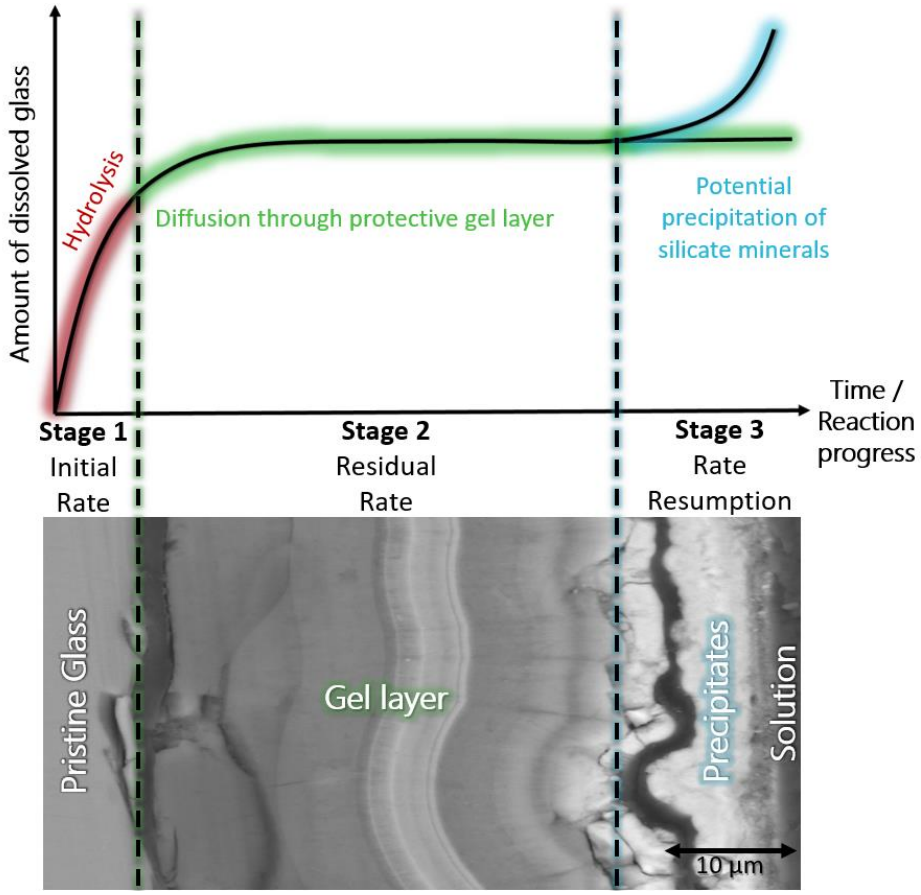

Figure 2.1. The three kinetic regimes/stages of glass corrosion (adapted from Vienna *et al.* 2013) illustrated with a scanning electon microscope image of a cross-sectioned corroded ZnCa alumina-borosilicate glass monolith. The altered layer encompasses both the gel layer and the precipitates. Note that a gel layer is first obseved during Stage II and the thickness of the gel layer will generally increase over time (on the 10-100 micron scale) – thicker gel layers corresponding to faster dissolution rates. The growth in the thickness of the gel layer is less understood during Stage III – it can either: a) grow in thickness, b) reduce in thickness as the gel 'transforms' to precipitates, or c) a combination of a) & b) (Frugier *et al*. 2014, Fournier *et al*. 2014).

2.3.1 Stage I - The Initial Rate

The initial dissolution rate (forward rate at t=0) is controlled by ion-exchange between the glass network modifier cations (alkali and/or alkaline earth) and hydrogenated species (H^+, H_3O^+, H_2O), and subsequently by the hydrolysis of the borosilicate glass network (Boksay *et al*. 1967, Sanders & Hench 1973). Hydrolysis is a direct attack from H_2O molecules on the glass network structure; H_2O penetrates the glass through voids in the structure at very first contact and starts to corrode the network at this instant. However, interdiffusion allows significantly more H_2O species to corrode the network because once H_3O^+ has ion-exchanged into the structure, it dissociates into H_2O and a proton on short timescales, which means that the H_2O molecule is free to participate in hydrolysis and the proton can

ion-exchange (Geneste *et al*. 2006). The hydrolysis attack is initially carried out by three independent mechanisms, which collectively result in the creation of silanol molecules (Si-OH). The first (to be described as opposed to chemically occurring) is the attack from H_2O on the non-bridging-oxygen atoms (NBOs), which results in the creation of a silanol molecule and an OH^- anion (Eqn. 2.1).

$$\equiv Si - O^-_{(s)} + H_2O_{(aq)} \rightarrow \equiv Si - OH_{(s)} + OH^-_{(aq)} \quad [2.1]$$

The second attack is from an OH^- anion directly on to a rigid siloxane bond (≡Si-O-Si≡) (Eqn. 2.2) and results in the formation of a silanol molecule and an NBO in the form of (≡Si-O^-):

$$\equiv Si - O - Si \equiv_{(s)} + OH^-_{(aq)} \rightarrow \equiv Si - OH_{(S)} + \equiv Si - O^-_{(s)} \quad [2.2]$$

The third is a direct attack from a H_2O molecule onto a rigid siloxane bond (≡Si-O-Si≡) (Eqn. 2.3).

$$\equiv Si - O - Si \equiv_{(s)} + H_2O \rightarrow \equiv Si - OH_{(S)} + \equiv Si - OH_{(S)} \quad [2.3]$$

All three initial mechanisms work cotemporally to provide positive feedback, which accelerates glass corrosion (Grambow 1992, 2011). Silicon is finally released into solution after a total of four hydrolysis reactions and is released into solution as orthosilicic acid (H_4SiO_4). The processes set out in Eqns. 2.1-2.3 are, in nearly all cases in the literature, simplified as:

$$SiO_{2\,(s)} + 2H_2O_{(aq)} \rightleftharpoons H_4SiO_{4\,(aq)} \quad [2.4]$$

The initial rate of borosilicate glass dissolution is strongly dependent on the structure of the glass, particularly the extent of network polymerisation of the glass network formers (B & Si), where greater network polymerisation (greater connectivity of the borosilicate glass networks) confers greater durability (Icenhower *et al.* 2013). An increase in the alkali/alkaline earth content has the effect of depolymerising the network by creating excess non-bridging oxygens (NBOs) atoms that develop ‘alkali-rivers’ in the medium range structural order of a glass, as defined by the modified random network model (Warren 1941, Greaves 1985, Shelby 2005), which are more susceptible to hydrolysis (less bonds need to be broken to release B & Si to solution), thus reducing the chemical durability of the glass. Alkali /alkaline earth elements thus take on a network modifying role (Fig. 2.2).

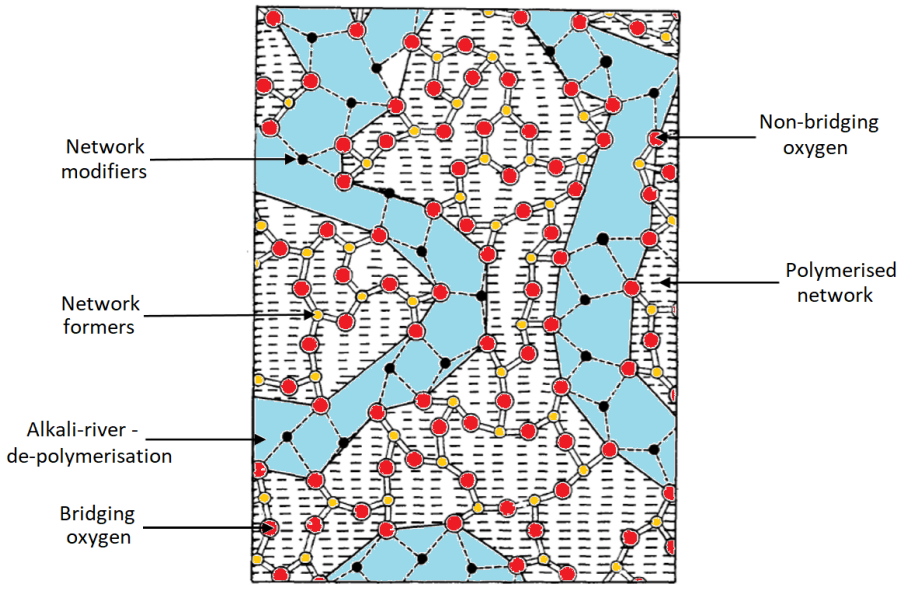

Figure 2.2. Two-dimensional schematic of the modified random network model, adapted from Greaves (1985).

To counteract this behaviour and to increase the durability of the glass, Al_2O_3 can be added, which acts as a network former, forming negative $[AlO_4]^-$ tetrahedral units that slot into the borosilicate network, retaining the network connectivity and, in the process, utilise a cation as charge balance, which negates the formation of a NBO (Fig. 2.3). However, an excess of Al_2O_3 or reduction in the alkali/alkaline earth content results in some Al becoming octahedrally coordinated, thus taking on a network modifying role and depolymerising the glass network, to the detriment of Stage I glass durability (Brawer & White 1977, Shelby 2005). Such reasoning can be directly applied to describe the role of Zn on the glass network (McKeown *et al*. 2000, Le Grand *et al*. 2000, Calas *et al*. 2002, Cassingham *et al*. 2011) as described in detail below.

In borosilicate glass, boron is a network former, which can exist either as trigonal $[BO_3]$ units or as tetrahedral $[BO_4]^-$ units (Scholze 1991, Möncke *et al.* 2015) that are charge compensated by a cation. There is currently no consensus on the form of boron that confers greater durability to borosilicate glasses, but it has been suggested that similar proportions of each form maximises the chemical durability (Schaut 2019). In a multi component borosilicate glass it was reported that Na preferentially charge balances Al > Zn > B units (Cormier *et al.* 2000, Calas *et al*. 2014).

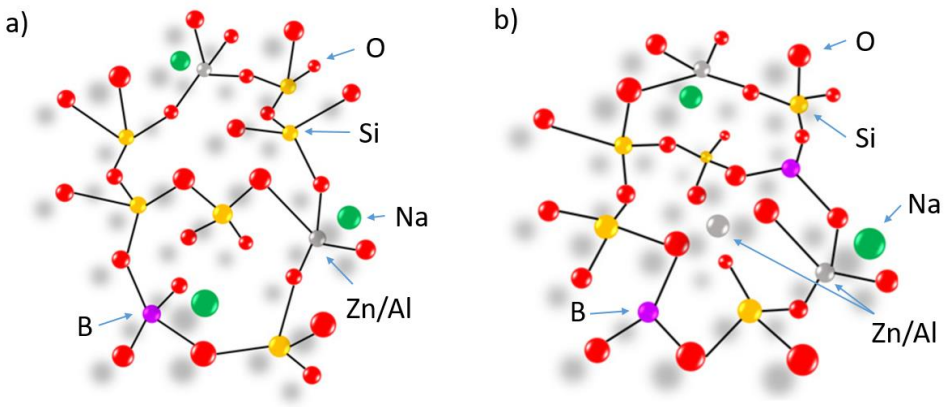

Figure 2.3. Schematic representation of two different zinc-soda-aluminoborosilicate glass networks, where Zn/Al represents either a Zn or Al atom: a) Zn/Al are effectively charge balanced and form network forming tetrahedra; b) an excess of Zn/Al or reduction in the soda content results in an inability to effectively charge balance network forming tetrahedra, hence some of the Zn/Al become octahedrally coordinated and perform a network modifying role. Note that in this example the role of soda can be extended to be representative of all alkali and most alkaline earth elements. Images adapted from Januchta *et al.* (2018).

Effect of ZnO on the glass structure and initial rate: The addition of ZnO at low concentrations (< 5 wt. %) to alkali/alkaline earth borosilicate glasses has been shown to have a preference for four-fold tetrahedral coordination $[ZnO_4]^{-2}$ (McKeown *et al*. 2000, Lusvardi *et al.* 2002, Cassingham *et al.* 2011). Such units are charge compensated by alkali/alkaline earth elements (which would otherwise be playing a network modifying role), therefore reducing the number of non-bridging-oxygen atoms (Le Grand *et al.* 2000, Smedskjaer *et al.* 2013). Such $[ZnO_4]^{-2}$ units polymerise the glass network (similar to $[AlO_4]^{-}$) by corner-sharing oxygen atoms with network forming SiO_4 tetrahedra, forming Si-O-Zn linkages (Holland *et al.* 2007, Cassingham *et al.* 2011), which are hypothesised to increase its resistance to hydrolysis (Della *et al.* 1986). McKeown *et al.* (2000) also suggest that the addition of Zn likely reduces the volume between linked tetrahedral units, which restricts ion diffusion, thus indirectly inferring greater resistance to dissolution. However, with increased ZnO/modifier ratio, a proportion ZnO has been reported to adopt six-fold coordination and play a network-modifying role (Le Grand *et al.* 2000, Calas *et al.* 2002, Petrescu *et al*. 2012), in a similar way to octahedral Al. This could impart some consequence to Stage I chemical durability; since the ZnCa MW formulation contains approximately 5 wt. % ZnO (Zhang *et al.* 2015), this requires investigation. In terms of improving the chemical durability, the addition of Zn was shown to reduce Soxhlet leach rates (Soxhlet tests probe glass dissolution at the initial rate (Stage I) only, under dilute dissolution conditions) (Matlack *et al.* 1998), which justified its addition to the MW formulation. The early stage chemical durability, when compared with other MW-waste glass types, was also shown to be improved (Zhang *et al*. 2015).

Effect of Ca on the glass structure and initial rate: The addition of Ca to the glass network is considered to be detrimental to *Stage I dissolution* due to its network modifying role (Shelby 2005), thus creating NBOs and depolymerizing the glass network. In Ca-rich glasses, Na^+ has a higher ratio of bridging to NBO in its coordination shell. Therefore, Na^+ is more prone to charge compensation than Ca^{2+}, hence, Ca^{2+} is a stronger modifier, creating more NBOs (Wu & Stebbins 2009).

During the initial stage of glass corrosion, glass dissolves at its maximum rate (strictly the forward rate at t=0) until chemical affinity effects (due to the solubility of silicon and, to a lesser extent, aluminium (Gin 1996, Advocat *et al*. 1997, Abraitis *et al*. 2000a, Rajmohan *et al*. 2010, Icenhower & Steefel 2013) reduce the thermodynamic drive for dissolution, and the rate of hydrolysis drops. This process has been described by a range of authors through the application of Transition State Theory (TST) (Eyring 1935). The modified version of this kinetic rate equation for glass, originally applied to aluminosilicate minerals by Aagaard & Helgeson (1982), assumes that the rate-limiting dissolution reaction is the corrosion of the silicate network to form orthosilicic acid (H_4SiO_4) (Grambow 1985) and is given by:

$$r = k_0 v_i a_{H^+}^{\eta} \exp\left(\frac{-E_a}{RT}\right)\left[1 - \left(\frac{Q}{K_g}\right)^{\sigma}\right] \qquad [2.5]$$

where *r* is the dissolution rate (g m^{-2} d^{-1}), k_0 (g m^{-2} d^{-1}) the forward rate constant, which is the intrinsic rate at which the surface of the glass hydrolyses, v_i the stoichiometric coefficient for element *i*, E_a the activation energy (kJ mol^{-1}), RT the product of the gas constant (kJ mol^{-1}) and the absolute temperature (K), a_{H+} the proton activity, η the pH power-law coefficient, Q the ion activity product (unitless), K_g the pseudo-equilibrium constant (solubility constant) for the rate-controlling reaction and σ the Temkin coefficient/rate of decomposition of the activated complex (unitless, and assumed to be unity for borosilicate glass (Lasaga 1995)). Equation 2.5 was developed to express the dissolution of glass across the full pH range by Strachan (2011) by the inclusion of the hydronium activity (a_{OH-}):

$$r = k_0 v_i (a_{H^+}^{\eta_{acid}} + a_{OH^-}^{\eta_{alkaline}}) \exp\left(\frac{-E_a}{RT}\right)\left[1 - \left(\frac{Q}{K_g}\right)^{\sigma}\right] \qquad [2.6]$$

Hence, the saturation state of the system is described by the terms in square brackets in Equations 2.5 & 2.6. When glass dissolves at the initial rate in dilute media, thus negating chemical affinity effects and the formation of alteration layers (obtained by employing the Single-Pass-Flow-Through (SPFT) methodology (ASTM 2010), described in Chapter 3) the saturation term becomes unity, because the ion activity (Q) is negligible in comparison the pseudo-equilibrium constant (K_g). This then enables the determination of the rate law parameters k_0, E_a and η, providing that initial dissolution rates are

obtained from experiments performed over a range of temperature and pH values. Such parameters are useful for input in modelling and computer simulations (PNNL 2014, Neeway *et al*. 2018), such as the developing post-closure performance assessment for sub-surface disposal of vitrified radioactive wastes (e.g. at the Hanford Integrated Disposal Facility in the USA (Lee 2017)).

2.3.2 Stage II - The Residual Rate

Chemical affinity effects and the onset of the transition to the residual rate are observed when dissolved silica in solution (H_4SiO_4) reaches a sufficient concentration, approximately 1 mg L^{-1} (1 ppm) at 90 °C (Frugier *et al*. 2008). Under these conditions, fractional amounts of H_4SiO_4, as well as sparingly soluble constituent glass elements such as aluminium and zirconium, re-condense, releasing molecular water (leaving voids), which form a re-polymerised porous silica-rich gel layer (Fig. 2.1) on the surface of the hydrated glass, incorporating elements of relic part-hydrolysed glass structure (Grambow 1987, Bunker 1994, Jégou *et al*. 2000, Grambow & Müller 2001, Frugier *et al*. 2008, Gin *et al*. 2011, Ma *et al*. 2017). The gel layer is a hydrated, porous, amorphous and reorganized material independent of the pristine glass; the gel is not part of the glass phase because it is entirely a reaction product (Grambow 2006), evidenced by the ease at which it detaches itself from the pristine glass post corrosion (Fig. 2.4a), commonly referred to as flaking in the archaeological literature (Pearson 1988). Such gel layers vary in thickness (dependent upon the reaction progress) from nanometres to micrometres for most glasses (Gin *et al*. 2011). However, a recently proposed dissolution-re-precipitation model (Geisler *et al*. 2010), referred to as the Interface-Coupled Dissolution-Precipitation model (ICDP), may more accurately describe the gel formation and explain most observations of banding (Fig. 2.4b-c) on naturally and experimentally altered glass, including the atomically sharp interface that must be present suggested by the flaking phenomena (Geisler *et al*. 2015). Such a model suggests that the gel is formed due to the congruent dissolution (total hydrolysis) of the glass and subsequent precipitation of amorphous silica directly from solution (Geisler *et al*. 2010, 2015, Hellman *et al*. 2015, Putnis *et al*. 2015), which proceeds as an inwardly moving front into the pristine glass. The driving force simply being the solubility difference between the glass and amorphous silica.

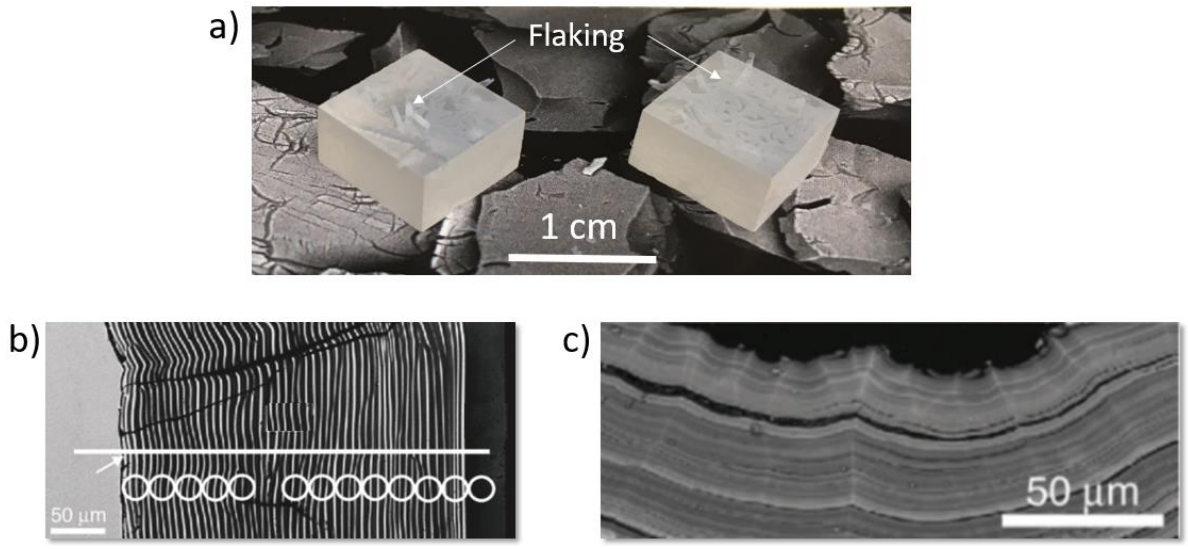

Figure 2.4. a) Flaking phenomena of the gel layer observed on a ZnCa alkali/alkaline earth alumina-borosilicate glass dissolved in UHQ water for 540 d at 50 °C (from experiments performed in Chapter 5). The background images display dehydrate sufaces of glass particles corresponding to a scale bar equalling 50 µm; b) BSE-SEM images of corrosion zone banding of a nuclear waste glass (Geisler *et al.* 2010) & c) BSE image of a 2,500 year old naturally altered archaeological glass (Dülük Baba Tepesi near Doliche, Turkey) also showing non-equilibrium banding patterns inside the corrosion zone (Geisler *et al.* 2010).

When concentrations and activities of the gel-forming elements (silicon, aluminium, zirconium) tend towards steady-state conditions in solution, the glass network hydrolysis rate diminishes rapidly and a gel layer can be said to have formed. Hence, dissolution enters a slowly decreasing or constant residual rate regime due to the passivating effect of the gel. Here, the rate can drop by up to 10^{-4} times the initial rate (Frugier *et al*. 2005); yet it does not drop to zero, meaning that the glass is *still* dissolving, alluding to other mechanisms at work.

If one leans towards the *ICDP model*, debate reigns over the cause of the passivating effect of the gel layer. Some authors suggest pore closure is responsible, by the dynamic re-condensation and restructuring of the hydrated glass with relic glass structures to form a Passivating Reactive Interphase (PRI) (Rebiscoul *et al*. 2004, 2005, Frugier *et al*. 2008, Ma *et al*. 2017, Ohkubo *et al*. 2018), whereas others suggest a limiting diffusion barrier for water and dissolved glass species through the gel layer (Grambow & Müller 2001, Rebiscoul *et al*. 2004, Frugier *et al*. 2008, Verney-Carron *et al*. 2010). Some suggest chemical affinity (Cailleteau *et al*. 2008) and others still a combination of both (Gin *et al*. 2017, Ma *et al*. 2017). In an attempt to reconcile the opposing models, the study by Lenting *et al*. (2018) – *Towards a unifying mechanistic model for silicate glass corrosion* – suggests that the dissolution-re-precipitation model is the main gel forming process, but that a diffusion controlled ion exchange front may evolve at the pristine glass interface, if the gel-forming process is slowed down by transport limitations of the reactive species through the gel layer. Such a unified model is referred to in this Thesis as *the Refined Unified Mechanistic Glass Corrosion Model* (RUMGCM).

Regardless of the processes responsible for gel formation and the resulting passivating effect, depending on the glass composition and dissolving media, the precipitation of secondary phases can also sustain the residual rate, particularly phyllosilicate clays (Fig. 2.5) (Jantzen *et al*. 2010, 2013, Vienna *et al*. 2013). These clays sustain glass corrosion by consuming key elements from the gel, thus weakening its passivating properties by taking it out equilibrium with the solution (Frugier *et al*. 2008). This phenomenon is particularly important for nuclear waste glasses destined for geological disposal (Curti *et al*. 2006) because of the long timescales in which the glass will be subjected to dissolution (releasing radioactive elements), in media containing elements that can enhance the precipitation of phyllosilicate clays (such as Fe and Mg (Jollivet *et al.* 2012, Schofield *et al.* 2017)). The precipitation of secondary phases is a key process that can trigger the next stage of glass corrosion, 'rate resumption' (Stage III).

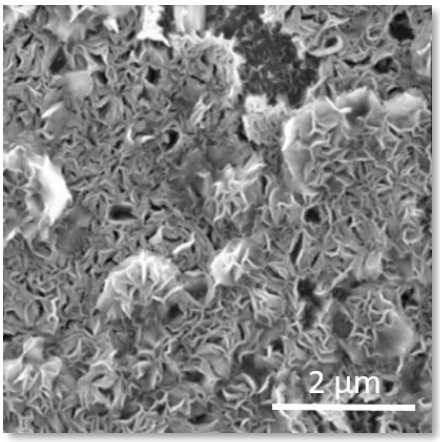

Figure 2.5. Phyllosilicate clay formed on surface of SON68 glass during vapor hydration studies (Ait Chaou *et al*. 2017).

Effect of Zn on the residual rate: The effect of ZnO addition on the residual rate (Stage II) dissolution of borosilicate glass is contested; it has been reported to both improve the durability (Stechert *et al.* 2013, Zhang *et al.* 2015) by improving the passivating properties of the gel layer, without any conclusive mechanism identified (Lewis *et al.* 1982, Tait *et al.* 1982, Calestani *et al.* 1986, Ennas *et al.* 1990, Vance *et al.* 2017) and worsen the durability, due to the formation of clay phases (Aréna *et al*. 2016), which are suggested to cause aggressive Stage II dissolution (Gin *et al.* 2013). Note that the Stage II dissolution behaviour encompasses a wide range of dissolution rates, whereby some glasses/environments encourage aggressive, faster rates (Ribet *et al.* 2004) (Figs. 2.1, 2.7). Interpretation of the literature from vapour phase tests (not necessarily representing residual rate (Stage II) dissolution) on waste-loaded ZnCa MW-type glasses indicate that Zn may worsen the chemical durability (Zhang *et al*. 2015, Cassingham *et al*. 2016) by participating in secondary phase

precipitation. However, in Si saturated static dissolution experiments, which captured Stage II dissolution, the addition of ZnO and CaO in ZnCa MW28 was found to be beneficial, reducing the leach rates in comparison to MW25, however, the mechanisms responsible were unidentified (Harrison and Brown 2018).

Effect of Ca on the residual rate: Durability studies have shown that the addition of Ca to sodium aluminoborosilicate glasses significantly improves residual rate (Stage II) glass durability, at least in the short term and on laboratory experimental timescales by forming a Ca-silica gel layer (Chave *et al*. 2011, Utton *et al*. 2012, Zhang *et al*. 2015, Maraghechi *et al*. 2016, Arena *et al*. 2018). However, it has also been postulated to cause rate resumption (Stage III) at longer timescales due to the precipitation of calcium silicate hydrate (C-S-H) phases (Muller *et al*. 2006, Jantzen *et al*. 2010, 2013). The improvement in Stage II durability is thought to be conferred when Ca integrates into the silica gel layer, acting as a charge compensator to SiO_2 (Mann *et al.* 2019), $[AlO_4]^-$ and $[ZrO_6]^{-2}$ (Rajmohan *et al*. 2010, Rebiscoul *et al*. 2012, Gin *et al*. 2015, Collin & Fournier 2018). Such reasoning could be extended to other alkali/alkaline earth elements and $[ZnO_4]^{-2}$ tetrahedra (which may indirectly explain the beneficial passivating effect of Zn in the gel layer as left inconclusive from the studies reported above). Calcium charge compensation has the effect of decreasing pores sizes and densifying the gel, thus limiting the transport of elements and water through the gel layer (Utton *et al.* 2012, Corkhill *et al.* 2013, Zhang *et al.* 2015, Maraghechi *et al.* 2016, Aréna *et al.* 2018, Mann 2018).

Other studies have shown that Ca can act as a catalyst in the condensation reaction of silica to form the gel (Nieto *et al.* 1995, Chave *et al.* 2011), where the presence of Ca encourages condensation of polysilicate anions and links silicate species together (Iler 1979). Once incorporated into the silica gel, Ca could not be dissolved unless subjected to acidic solution, demonstrating the durability of such a gel layer (Nieto *et al.* 1997). One study of the ISG showed, by application of solid state ^{29}Si NMR, that the silica gel network (containing Ca) was more polymerised than the initial glass structure (Gin *et al.* 2015). However, further work is needed to investigate if Ca directly causes the repolymerisation – such is suggested/interpreted but not as yet conclusive. Studies involving Ca in the dissolving media suggest that a Ca incorporation (in the gel layer) threshold exists, beyond which Ca precipitates with Si dissolved from the glass to form C-S-H or other Ca- and Si-containing precipitates (Chave *et al*. 2011, Mercado-Depierre *et al*. 2013, Corkhill *et al*. 2013, Utton *et al*. 2013, Ferrand *et al*. 2013).

In terms of improving the chemical durability, unrelated to the effects on the gel layer, Ca was reported to stabilize Mo in a chemically durable crystalline $CaMoO_4$ phase (Dunnett *et al.* 2012) for ZnCa MW wasted loaded glasses compared to standard MW25, therefore allowing increased Mo

incorporation, particularly important for POCO waste, which will be Mo-rich. Figure 2.6 illustrates the undesirable formation of yellow-phase (a mixture of alkali molybdates, chromates and sulphates that can be water soluble in the solid state) with increased Mo waste loading > 3 wt.% in MW38 glass (Schofield *et al*. 2017).

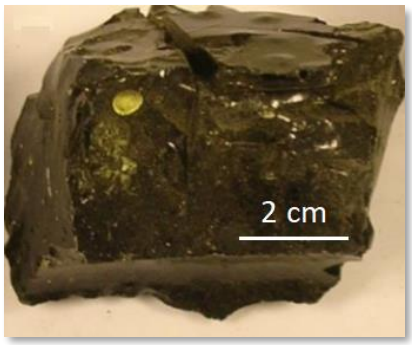

Figure 2.6. Examples of undesirable yelow-phase formation in MW38 waste glass (Schofield *et al*. 2017). The use of ZnCa MW base glass negates such formation.

2.3.3 Stage III - The Rapid Resumption of Alteration

The large precipitation of crystalline silicate minerals including zeolites, particularly analcime ($NaAlSi_2O_6{\cdot}H_2O$) (Strachen & Croak 2000, Burger *et al*. 2013, Strachan & Neeway 2014, Fournier *et al*. 2014), rare earth phosphates (Caurel 1990) and C-S-H (Jantzen *et al*. 2013, Fournier *et al*. 2014), on top of the gel layer, are thought to be responsible for Stage III rate resumption (Fig. 2.7). In some cases these precipitates are embedded within the gel layer (Gin *et al*. 2011). These precipitated minerals are formed from silicon and other elements (particularly Al) present in solution and those present within, and on, the surface of the gel layer, which means that the concentration of silicon in solution is reduced. The glass-solution system is taken away from pseudo-equilibrium conditions and silica (and alumina) from the protective gel barrier is consumed, which leads to an increase in the alteration rate. Precipitation of such phases leads to a thin depleted gel layer on the outer edge of the familiar gel layer. The depleted gel layer is of lower density, depleted in Si and Al, which means that its passivating role is severely diminished (Valle *et al*. 2001). Precipitation can occur suddenly after an extended time period on many nuclear waste glass types, yet this process is not sufficiently well understood to be predicted, nor the subsequent increase in the dissolution rate quantified. It has been suggested that such behaviour must be kinetically limited or highly activated by an increase in temperature and/or pH (such a pH threshold has been suggested (> 10.5 pH) by Ribet & Gin 2004 and Fournier *et al*. 2014),

possibly caused by the influence of near-field materials (Frugier *et al*. 2008). If conditions stabilize, another residual rate can resume, therefore cycles of rapid alteration followed by residual rate regimes cannot be ruled out for the duration of the waste glass in residence in a GDF. The study by Ribet *et al*. (2004) showed that 20 out of 100 different nuclear waste glasses demonstrated Stage III rate resumption when dissolving in UHQ water at 90 °C. Such glasses contained high alkali and low boron content, and Stage III was only observed with pH values at, or in excess of, pH 9.7 at 90 °C. The study showed that Stage III behaviour *can* be associated with the initial glass composition, with no reliance on external influences. The French inactive SON68 glass has been shown to display Stage III rate resumption in high pH environments (pH > 10.5 at 90 °C) (Gin & Mestre 2001) and in moderate pH environments (pH 8.4 – 9.5 but with increased temperature, 150 °C) (Caurel 1990). To the best of current knowledge, Stage III behaviour has not been observed on studies of MW25 in experiments conducted in UHQ water at 90 °C (Curti *et al*. 2006, Brookes *et al*. 2011, Harrison 2014, Gout *et al*. 2019) and in $Ca(OH)_2$ solutions (which suggests that the excess Ca inhibits Stage III – despite the high pH of the associated systems) (Schofield *et al*. 2017) and ZnCa MW-type glasses (Zhang *et al*. 2015, Vance *et al*. 2017, Harrison & Brown 2018), although it should be noted that no long-term tests on ZnCa MW-types have been conducted.

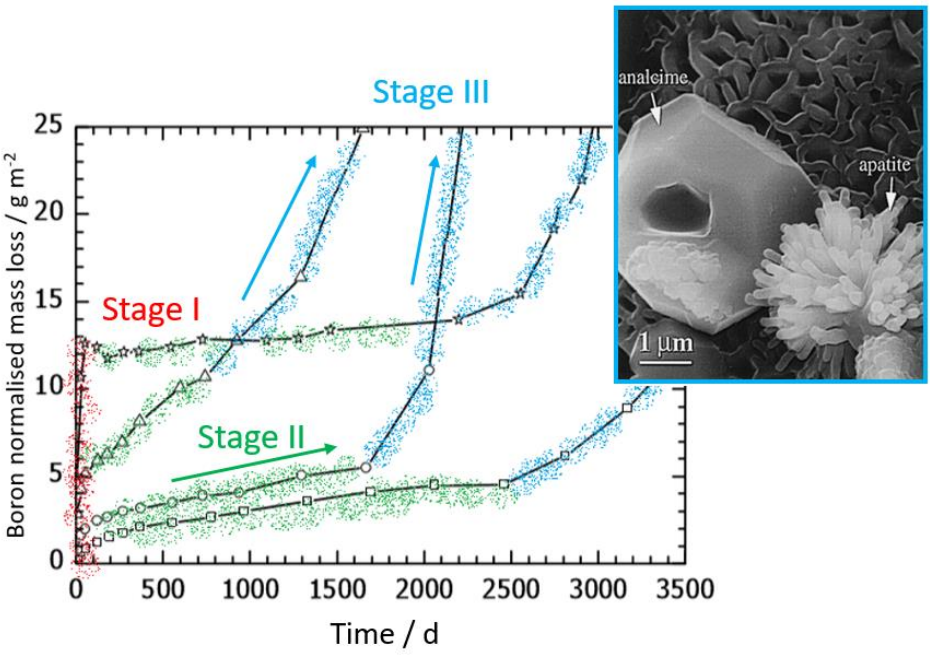

Figure 2.7. Examples of nuclear waste glass dissolution exhibiting Stage III rate resumption (blue) (Ribet *et al*. 2004) triggered by the precipitation of analcime – image taken from Gong *et al*. (1997).

Effect of Zn on the rate resumption: The literature does not suggest a causal effect of Zn on Stage III rate resumption. Zinc has been shown to cause aggressive Stage II dissolution in simple 4-component

zinc soda borosilicate glass containing 2.7 - 13 wt.% Zn (Gin *et al.* 2013) due to the precipitation of the zinc phyllosilicate clay sauconite ($Na_{0.3}Zn_3(SiAl)_4O_{10}(OH)_2 \cdot 4H_2O$). Zinc in synthetic sauconite minerals was found to exist in octahedral coordination (Yokoyama *et al*. 2006).

Effect of Ca on the rate resumption: The addition of Ca has been postulated to cause rate resumption and the transition into Stage III dissolution at longer timescales due to the formation of C-S-H phases (Muller *et al.* 2006, Jantzen *et al*. 2013, Fournier *et al*. 2014). Mann *et al*. (2019) predicted such C-S-H phase formation from geochemical modelling on the ISG during high-pH synthetic cement water dissolution experiments at 30 & 70 °C, however, C-S-H phases were not observed from SEM, due to the low Ca abundance in the leachate solution and the preference for Ca incorporation into the gel layer. Hence, the potentially observed rate resumption was attributed to the precipitation of Al-containing zeolite and phyllosilicate phases. However, in higher Ca-containing leachate such as $Ca(OH)_2$ (not a realistic GDF solution), dissolution experiments conducted at 50 °C on the ISG showed that C-S-H phases were readily observed (without zeolites), without Stage III rate resumption (Backhouse *et al.* 2018). Such comparisons illustrate the varied nature of Ca on the dissolution, which, in part, is dictated by the dissolution media. Experiments simulating expected geological disposal solutions (Mann *et al.* 2019) are more applicable in supporting the safety case for geological disposal, whereby Ca may not induce Stage III rate resumption.

2.4 Other factors influencing glass corrosion

As a result of the interaction between nuclear waste glass and groundwater solution, the radionuclides contained within the wasteform will either: remain within the gel layer, precipitate into stable crystalline phases or will persist as aqueous dissolved species, capable of being transported to the geosphere (Grambow 2006). The presence of gel-forming elements generally favours a reduction in the dissolution rate but, conversely, the same elements may form secondary phases, sustaining alteration (or promoting rate resumption). From the discussion above, it is apparent that it is not possible to identify a single reaction that is responsible for controlling the overall glass dissolution rate; rather the coupling between chemical reactions and the transport of aqueous species within the gel layer determining the overall rate.

In terms of the safety assessment for a geological disposal facility (GDF), a key requirement should be an understanding of the mechanisms governing vitrified HLW dissolution over the long-term (i.e.,

Stage II residual rate and the potential for Stage III rate resumption) and to be confident in extending and validating these mechanisms over geological timescales. For this, realistic values of residual rates and clarity on Stage III rate resumption need to be determined for MW25 and ZnCa MW28 in the presence of near-field materials and in conditions representative of geological disposal environments. Such materials and environments may induce the following processes: sorption reactions, dissolution/precipitation of new phases, local changes in pH, local changes in solution/groundwater composition, local porosity clogging, hence changing the transport properties of aqueous species, and redox reactions. Considerations for the long-term stability of UK vitrified HLW include following factors:

1. Groundwater (granite or clay, depending on the location of the GDF)
2. Canister corrosion products
3. In a hard-rock (granite scenario), the potential for a high pH plume from the co-location of cemented intermediate level waste and cementitiosus backfill contaminating the groundwater
4. Expected temperature of 40-50 °C
5. The presence of magnesium within the wasteform, arising from the reprocessing of Mg-alloy clad Magnox reactor fuel.

Alongside this there are other considerations, relevant for all vitrified HLW:

6. Radiation
7. Mechanism of water contact with glass surface - different corrosion scenarios – such as the potential for water vapour corrosion to proceed before contact with groundwater and near-field solution (ANRDA 2005, Abdelouas 2017, Bouakkaz *et al.* 2019).

A detailed review of the studies that address how these factors influence MW25 is beyond the scope of the present Thesis, however it can be stated that, when compared to the French HLW composition (R7T7 and its inactive surrogate SON68), and the International Simple Glass (ISG, a simplified 6-component glass based on the SON68 composition), relatively little is understood about UK HLW dissolution (including ZnCa MW) beyond standard corrosion tests.

For some of the seven considerations listed above, a brief description of the literature is provided in the following Section. A brief description of the use of natural analogues and computer modelling for predicting the behaviour of vitrified HLW in a GDF is provided in 2.6 Appendix.

2.4.1 Geological disposal - corrosion influencing factors

pH

Solution pH is considered to be the most important parameter affecting glass corrosion (Wicks *et al*. 1981, Werme *et al*. 1983). For many waste glass compositions dissolving in dilute and saturated conditions, a parabolic/V-shape relationship exists between glass dissolution rate and solution pH (Fig. 2.8) (Bourcier 1998, Oelkers 2001, Ojovan & Lee 2017). Acidic solutions are corrosive to nuclear waste glass due to the exchange of hydrogen ions from solution with cations in the glass. Surface layers become rarer with decreasing pH to the point where they do not form, as found from experiments on Savannah River Waste glass (Wicks *et al*. 1986). The increase in dissolution in basic solutions results from the attack of hydroxide ions on Si-O bonds of the glass network and also from the increased solubility of silica in high pH solutions.

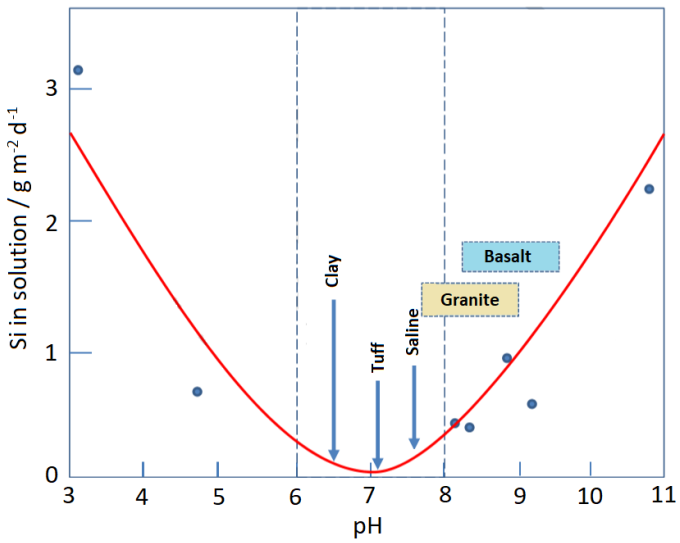

Figure 2.8. The pH dependance of borosilicate glass durability, with typical groundwater pH values from candidate rock types superimposed: clay (Vinsot 2008, Thien *et al.* 2012), saline (Gascoyne 2002), granite (Wicks *et al.* 1987, Gascoyne 2002), tuff and basalt (Wicks *et al.* 1987). Data points taken from Wicks *et al*. (1987). Figure adapted from Ojovan & Lee (2017).

In the pH range 5-9 the dissolution rate of borosilicate glass is relatively consistent, and a solution with a pH in excess of 10.5 pH may trigger Stage III rate resumption (Gin & Mestre 2001, Fournier *et al*. 2014). However, Ojovan & Lee 2017 state that the pH dependence of glass dissolution evolves for solution ostensibly kept at constant pH due to the formation of elemental concentration profiles of elements in the near surface layers. An increase in temperature tightens the parabolic shape of the pH-dissolution rate dependence, thus increasing the dissolution rate at corresponding pH values. Groundwater pH values are expected to be approximately pH 8 for granitic GDF host rock, pH 7 for evaporite (saline) host rock and pH 6.5 for a clay GDF (Vasconcelos 2018), although these values may be influenced by a number of factors specific to the local geology of any specified GDF site. The pH will rise and evolve with subsequent glass corrosion due to alkali release, and it is expected that a pH plume > pH 12 resulting from groundwater contact and subsequent dissolution of cementitious backfill material of ILW waste packages will occur (Mann 2018). Considerations of pH evolution should be accounted for when assessing the performance of waste glass in a repository environment (Ojovan & Lee 2017).

Groundwater

Initial simulations and predictions of the dissolution of nuclear waste glass in groundwater (at 90 °C), focussing on the American Defence Waste Processing Facilty (ADWPF) glass, were conducted in 1987. Results showed that the precipitation of smectite-clays and magnesium silicates (enhanced by elements contained within the groundwater) increased the quantity of altered glass compared with dissolution in pure water (Bruton 1987). Ebert *et al*. (1996) showed that an increase in the dissolution rate of the ADWPF glass at 90 °C was also associated with the precipitation of secondary hydrated aluminosilicate phases. Since then, these results have been experimentally confirmed, albeit using different glass samples. An early study which reported an increase in the long-term residual dissolution rate (Stage II) was made by Grambow and Strachen (1984) who investigated two HLW glasses, leached at 90 °C in a 0.001M $MgCl_2$ solution (groundwater analogue). The explanation for an enhanced dissolution rate in the presence of groundwater was due the precipitation of sepiolite ($Mg_4Si_6O_{15}(OH)_2{:}6H_2O$), consequentially driving the initial rate and increasing the glass alteration. An early study that countered this finding was by Sang *et al.* (1993) who observed a decrease in the early stage dissolution rate for the simulated HLW glass PNL 76-86 (containing U-238 and Pu-239 (Coles *et al.* 1982)) in groundwater solutions (0.04M $MgCl_2$ at 90 °C) compared to UHQ water. They attributed the decrease to a change in glass dissolution mechanism caused by the presence of Mg, whereby such a mechanism was unspecified. However, consensus has been overwhelming passed, which concludes that the presence of Mg in groundwater solution is detrimental to the long-term chemical durability

of HLW-type glasses (Maeda et al. 2011, Thien *et al*. 2012, Fleury *et al*. 2013). Particularly, Jollivet *et al*. (2012) showed that the influence of clayey groundwater increased the dissolution rate of SON68 glass. This effect was explained by the presence of Mg, which precipitated with Si in secondary phases, whilst no other elements in the groundwater had any effect on the glass alteration kinetics. They concluded that if Mg was in solution, it would consume Si and thus sustain the dissolution of the silica gel layer. When all of the Mg in solution had been consumed, the long-term (residual rate) glass dissolution rate returned to levels observed in experiments using pure water.

Studies on the UK's MW25 glass have shown that when dissolved in clay groundwater, MW25 facilitated the precipitation of Mg-smectite clays due to the high Mg content in the waste and groundwater solution (Serco 2012, Schofield *et al*. 2017), which was to the detriment of the chemical durability for the same reason as explained above. However, as previously mentioned, when dissolved in UHQ water at 90 °C, Stage III rate resumption was not observed in a 12.2 year dissolution test on MW25 and SON68 (Fig. 2.9) (Curti *et al.* 2006).

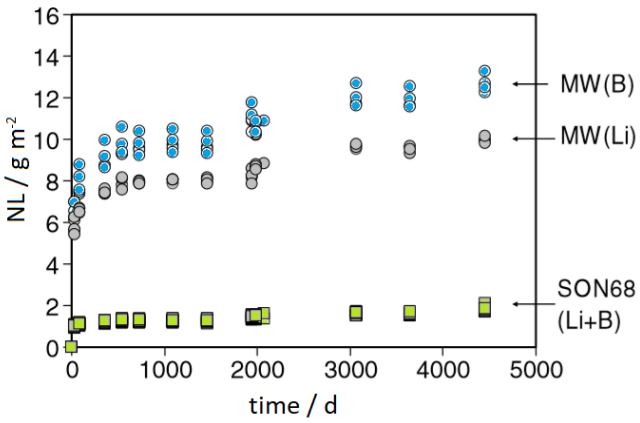

Figure 2.9. Normalised mass losses of B and Li as a function of time for MW-type (MW) and SON68 glass from Curti *et al.* (2006). Note that Stage III dissolution was not observed for both compositions after a 12.2 year PCT-B type experiment at 90 °C, SA/V = 1,200 m^{-1}, in UHQ water.

Studies by Utton *et al.* (2013), Backhouse (2016) and Mann (2018) suggested that dissolution of MW25 was reduced in cementitious leachates when compared to UHQ water due, in part, to the Ca content of the cementitious leachate and the formation of protective alteration layers. Schofield *et al*. (2017) suggested that dissolution in clay, granite and saline groundwater conferred greater durability for MW25 when compared to UHQ water, despite the precipitation of smectite clays, whereby the underlining mechanisms were unspecified, but it is speculated that the beneficial effect of Ca gel-

incorporation was responsible, in line with Utton *et al.* (2013), Backhouse (2016) and Mann (2018). Thien *et al*. 2012 reported a similar conclusion from dissolution studies of the French HLW glass, AVM (loosely similar to MW25) which contains Mg and increased Al content compared to SON68, alluding to the beneficial effect of Ca gel-incorporation from the clayey groundwater solution, despite the precipitation of Mg-smectite clays. Thien *et al.* (2012) concluded that under such experimental conditions, the dissolution in clayey groundwater would improve the long-term behaviour of AVM glasses compared to UHQ water.

A study was undertaken by Utton *et al*. (2012) who studied the effects of different groundwater types representative of potential UK GDF sites on MW25. They found that the initial rate of glass dissolution appeared similar in all cases, regardless of the ionic strength or elemental composition of the groundwater. The dissolution rate after 89 days in a demineralized solution appeared to decrease towards the residual rate, whereas in the groundwater solutions the dissolution rate appeared to be continuing close to the initial dissolution rate, which was presumably due to the precipitation of Mg-silicates sustaining a greater rate of dissolution.

In summary, recent work has established the overriding view that the presence of Mg in groundwater (and as a glass component) favours a residual rate (Stage II) increase due to precipitation of Mg-phyllosilicates (Curti *et al*. 2006, Maeda *et al*. 2011, Thien *et al*. 2012, Jollivert *et al*. 2012, Fleury *et al*. 2013, Debure *et al*. 2016). Literature also suggests that Ca from groundwater solutions is removed from solution to aid the protective properties of the altered gel layer (Sang *et al*. 1996, Utton *et al.* 2013, Backhouse 2016 and Mann 2018). In the situation whereby both Mg and Ca are present in solution, Ca has a preference for gel-incorporation over Mg, which preferentially forms secondary Mg-silicates. Such a conclusion was drawn from mass balance calculations of the chemical composition of the gel layer, from 279 d PCT-B dissolution tests at 50 °C, SA/V = 200 m^{-1} in synthetic clayey groundwater (7.9 < pH < 8.7) (Thien *et al.* 2012) on the French AVM borosilicate HLW glass. Mann (2018) also report similar conclusions, albeit from experiments using synthetic dissolved cement solutions at elevated pH values > 12.

Canister corrosion products

The general consensus is that the effect of Fe from canister corrosion products on the dissolution of vitrified HLW is detrimental (Jollivet *et al*. 2013, Burger *et al*. 2013, Godon *et al.* 2013, Michelin *et al.* 2013, Bouakkaz *et al*. 2016, De Echave *et al*. 2019, Debure *et al*. 2019). To the best of current knowledge, no systematic studies have been performed on UK HLW, instead most studies have focus

on the French SON68 glass at expected GDF temperatures (40-50 °C). For example, a study of the impact of Fe on SON68 corrosion in clay GDF conditions was made by Burger *et al*. (2013). It demonstrated that Fe/Si interactions occurred, which resulted in an increase in the glass alteration rate compared to Fe-free tests. Two types of such interaction affected the glass alteration kinetics, both due to the strong affinity of Fe-rich phases (generally iron corrosion products) with silica: (1) the formation of Fe-silicates precipitates at the surface of the gel layer; and (2) retention of Fe within the gel layer, which caused Fe to penetrate the gel porosity as precipitates in the form of iron-oxyhydroxide or iron-silicates. A key assumption was made when considering the impact of Fe, which proposed that the local precipitation of Fe-silicates within the gel porosity played the same role as the external iron-silicate precipitates, impacting the chemical durability, i.e. driving the dissolution. Recent studies by Jollivet *et al*. (2013), Debure *et al*. (2019) and De Echave *et al*. (2019) confirmed the detrimental effect of Fe-silicate precipitation on SON68 durability. De Echave *et al*. (2019) expanded on such a study by noting that the presence pre-corroded iron and pristine iron resulted in the same detrimental effect on the durability compared to Fe-free tests.

No studies on UK HLW glass have investigated the effect of canister corrosion products, whereby studies from other waste glass compositions generally suggest the formation of Fe-silicate precipitates, which drives silica dissolution and thus enhances dissolution rates (Burger *et al*. 2013). For UK HLW glasses, which contain 1.15 - 3.76 wt.% Mg, the competition between Fe and Mg for dissolved silica from the glass, and the subsequent precipitation of Fe- *and* Mg-silicates will likely result in even greater dissolution rates (including the Mg from potential groundwater), a so-called “additive” effect, demonstrated by Aréna *et al*. (2018) using the ISG dissolving in solutions rich in Fe and Mg (50 °C and SA/V = 20,000 m^{-1}). Hence, it is imperative that further investigations are conducted to predict the long term fate of UK HLW glasses in realistic geological disposal conditions.

Furthermore, very few studies have been published on ZnCa MW-type glasses; the majority of the research has contrasted the dissolution behaviour of ZnCa MW-types (of slightly differing compositions) to MW-types (also of slightly differing compositions, e.g. different waste loadings). These experiments include short term (< 28 d) dissolution tests in UHQ water at 90 °C (Zhang *et al*. 2015, Harrison and Brown 2018) and vapour dissolution tests (Cassingham *et al*. 2015), which generally reported greater durability for ZnCa MW-types. However, longer term dissolution tests on simple Zn-containing borosilicate glass compositions, under the same experimental conditions (90 °C, UHQ water, 4,500 d), suggested that the addition of Zn resulted in the precipitation of Zn-silicates, particularly sauconite ($Na_{0.3}Zn_3(SiAl)_4O_{10}(OH)_2 \cdot 4H_2O$) during dissolution (Gin *et al.* 2013). This point is

of significance, since there may be a triple additive effect of Mg-, Zn- *and* Fe-silicate mineral precipitation for ZnCa MW glass dissolved in a GDF (Aréna *et al*. 2016, 2018). Noting again that Aréna *et al*. (2016) used the ISG dissolving in solutions rich in Zn and Mg (2 mmol/L in separate investigation and 0.5 mmol/L of each in combined elemental dissolution studies at 50 °C and SA/V = 20,000 m^{-1}) (Fig. 2.10)). The Mg-concentration of the solution used in Aréna *et al*. (2016) was below that expected from clayey groundwater (5.7 mmol/L, but greater than granitic groundwater (0.2 mmol/L) (Vinsot 2008)), hence, the quantity of Mg-silicate precipitation expected from ZnCa MW dissolution in clay groundwater may be substantial, factoring in the Mg-content of the glass, resulting in an additive effect (Mg provided both from solution and from the glass). Ultimately, the relative influence of each of these elements, and combinations thereof, on the dissolution rate may be an important contributing factor during the long-term dissolution of ZnCa MW28. Hence, the UK's ZnCa MW glasses are in need of much greater study to understand the long-term durability.

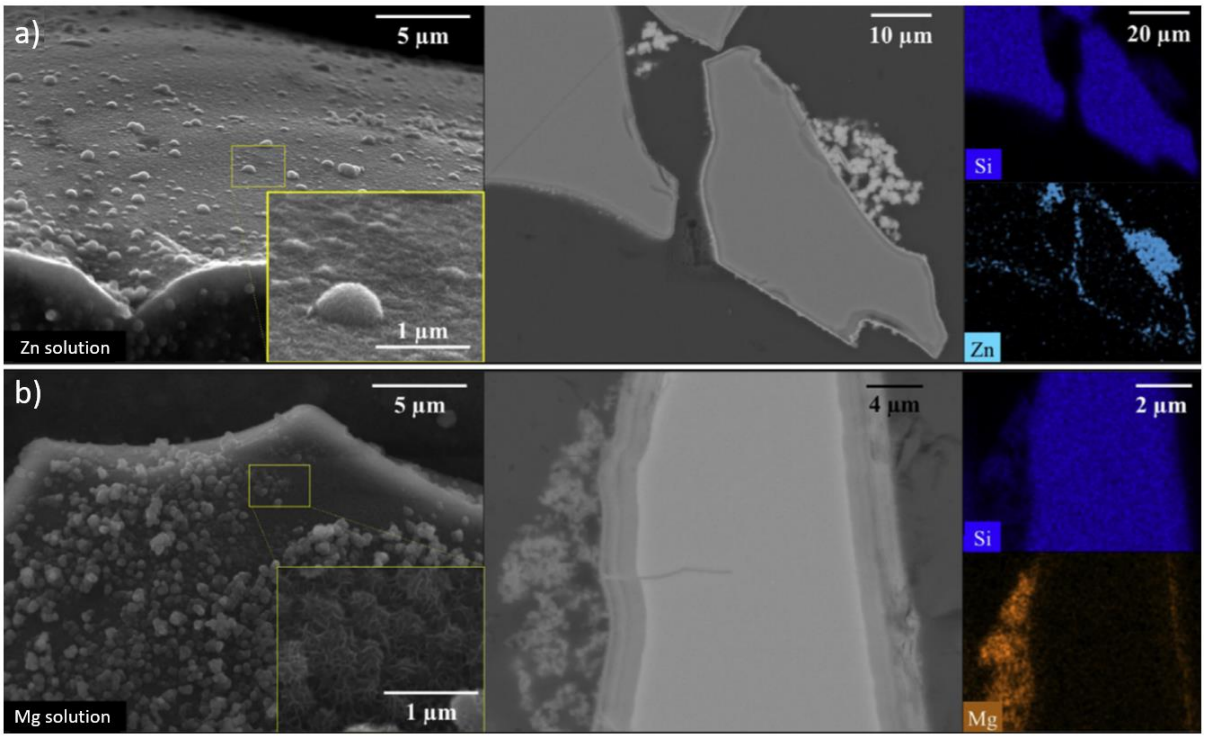

Figure 2.10. SEM images and EDS mapping of ISG powders altered for 511 d in: a) Zn-rich solution (2 mmol/L, 50 °C) showing the precipitation of Zn-silicates and; b) Mg-rich solution (2 mmol/L, 50 °C) showing the precipitaion of Mg-silicates. Images adapted from Aréna *et al*. (2016).

Radiation

Research in the literature on the effects of structural damage caused to glass by radiation, such as ballistic effects from recoiling nuclei, α, β, γ (Delaye *et al*. 2011, Jan *et al*. 2019), and their influence on chemical durability has contrasting conclusions. Such effects are thought to be inconsequential (Advocat *et al*. 2001, Wellman *et al*. 2004, Ojovan *et al*. 2004, 2004a, Peuget *et al*. 2007, Barinov *et al*. 2008, Mougnaud *et al*. 2016, - note that Barinov *et al*. and Ojovan *et al.* conducted tests on an active LLW glass (Fig 2.11)) and, alternatively, detrimental (Mougnaud *et al*. 2018, Peuget *et al*. 2018). The effects of beta and gamma radiation have been suggested to only have an effect on glass corrosion through changing the solution composition through radiolysis (i.e., changing the pH, Eh and dissolved specie concentration) and from ballistic collisions that de-polymerise the glass network (Peuget *et al*. 2006). However, it remains unclear to what extent radiation has on the structure of the altered layer. Mougnaud *et al*. (2018) observed a significant increase in the dissolution rate and the thickness of the alteration layer obtained from the dissolution of irradiated glasses compared to non-irradiated glasses and unpublished studies of the dissolution of active R7T7 (the active version of SON68) are greater than SON68 (Gin 2019). A detailed review of the effects of radiation on glass structure and corrosion is currently in press (Peuget IN PRESS), therefore is not repeated in this Thesis.

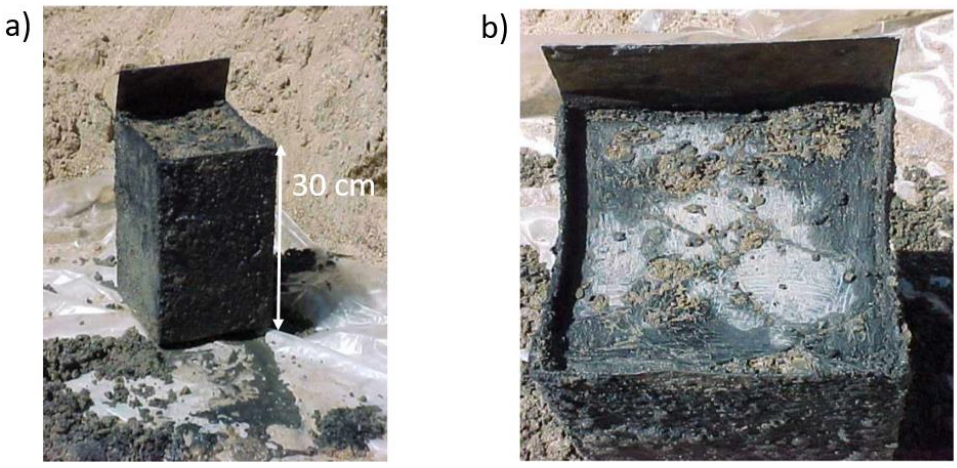

Figure 2.11. A view of degraded LLW borosilicate waste glass 'K-26' contained within a steel container after 12 years dissolution in groundwater in earthern trenches at a depth of 1.7 m (average temperature 4.5 °C). From the research program SIA Radon. Samples taken from this block were subjected to PCT-A tests, which displayed similar leaching behaviour to its pristine non-radioactive version. Image taken from Ojovan *et al*. (2004a).

An understanding of the behaviour of the dissolution of active glasses, as opposed to artificially induced radiation damage from ion irradiation on inactive glasses (Mougnaud *et al*. 2018) is a key challenge and a potential priority for the disposal safety case. Also, to the best of current knowledge, there are no published studies that aim to understand how the chemical changes induced by the

radioactive decay and subsequent transmutation (from the fission products Sr and Cs, to Zr and Ba respectively) influence the structure-dissolution relationship. This has an extended consideration, which suggests that inactive glass compositions may not be truly relevant for comparison with the active versions that will be disposed of, in terms of their fabricated compositions, and in terms of their chemical composition after an extended disposal time-period, relevant to the expected first water vapour/groundwater solution contact. This topic will be address in this Thesis, in Chapter 9.

Mechanism of water contact with glass surface

The study of HLW glass dissolution has developed over the years to provide safety assessments for geological disposal (Ojovan & Lee 2014). Despite the literature referenced above, a gap exists relating glass corrosion to realistic geological disposal environments and the form in which water (or groundwater) comes into contact with the glass surface (Neeway *et al*. 2012, Debure *et al*. 2019, Bouakkaz *et al*. 2019, De Echave *et al*. 2019). Vitrified HLW in a geological repository may initially come into contact with water vapour before encountering groundwater solution in the fully aqueous phase. This is a result of hydrogen gas generation from the corrosion of stainless-steel over-packs under anoxic conditions (Andra 2005), which results in the formation of void spaces inside and outside the canister that will remain open and filled with hydrogen gas. This prevents a fast saturation of the glass with surrounding groundwater solution (Bouakkaz *et al*. 2019). Such conditions may be expected to last up to a maximum of 10,000 years (Abdelouas 2017), during which time, water vapour is expected to alter a portion of the glass before the hydrogen reduces sufficiently for liquid groundwater to contact the glass (Neeway *et al*. 2012). As such, glass vapour hydration corrosion is likely to dominate for a period of time, leading to the development of secondary alteration phases, which may impact the later dissolution process. Literature suggests that pre-vapour corroded nuclear waste glass may be detrimental to the durability in subsequent static aqueous solution dissolution, when compared with glass that was not pre-vapour corroded (Neeway *et al*. 2012). Such results were attributed, in part, to the dissolution, and instantaneous release, of elements from the secondary phases that formed in the vapour stage, which raised the pH of the surrounding solution, thus increasing the rate of dissolution, as evidenced from studies of SON68 (Fig. 2.12) (Neeway *et al.* 2012). Such literature has focussed solely on dissolution in water vapour/solution and, to the author's knowledge, the dissolution in groundwater vapour/solution samples and high pH equivalents has not been undertaken. Such a corrosion scenario has not been investigated for UK HLW, hence, has been addressed, in part, in Chapter 8 of this Thesis.

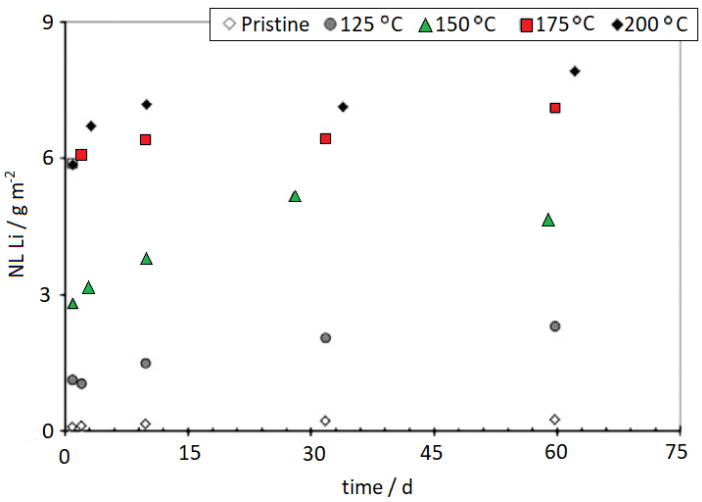

Figure 2.12. Normalised mass loss of the Li tracer as a function of time for SON68 monoliths pre-corroded using the VHT methodology at different temperatures (125-200 °C) then leached in aqueous D_2O at 50 °C. Note the contrast with the pristine (non pre-corroded sample). Adapted from Neeway *et al*. (2012).

2.5 Concluding remarks

Acknowledging the fact that glass dissolution is remarkably complex, with a plethora of variables contributing to the mechanisms and kinetics, it is understandable that the fundamental mechanisms are still not agreed upon. Different approaches to understand the effect of particular variables have been thoroughly conducted, progressing fundamental science, but these results cannot simply be pieced together to provide a holistic description in terms of the practical disposal of vitrified HLW. The dissolution behaviour of the UK's recently implemented ZnCa MW HLW waste glass has not been thoroughly investigated, particularly at longer timescales, in which the literature suggests that the inclusion of Zn could confer detrimental or positive effects, both considered to be due to the precipitation of Zn-silicates. Likewise, literature suggests that the addition of Ca may play a positive role in lowering dissolution rates due to a strengthening the silica gel layer, but the precipitation of Ca-silicate phases carries a risk of promoting Stage III behaviour. The influence of these elements, so clearly contested, needs to be understood, not only at the fundamental level, but in holistic studies aimed to simulate geological disposal environments.

This Thesis aims to expand the knowledge base regarding the dissolution of ZnCa MW-type glasses and how the dissolution kinetics are influenced by systematic changes in the ZnO/CaO ratio, using simplified base glasses in addition to fully (simulant) waste-loaded glasses. Importantly, all stages of glass corrosion will be investigated. For the first time it aims to elucidate potential Stage III behaviour

of vitrified UK HLW, which is important to understand for the long-term disposal safety case. Furthermore, it will enhance the understanding of the behaviour of ZnCa MW waste glasses in different envisioned GDF scenarios, including different groundwater compositions and different modes of groundwater contact. Such studies should provide information of relevance to fundamentally underpin the use of ZnCa MW glass at the WVP in terms of its chemical durability, with the aim to suggest an optimised ZnCa MW base glass formulation (optimised ZnO:CaO ratio).

2.6 Appendix

I – Geological disposal – natural analogues

Validation of laboratory based experiments can come from turning to altered natural glass (Parruzot *et al*. 2015), archaeological glass (Verney-Carron *et al*. 2008, 2010, 2010a) and glass found in meteorites (Morlok & Libourel 2013), which can be used as nuclear waste glass analogues representing various stages of corrosion. These glasses have been subjected to dissolution from thousands to millions of years. The study of these analogues helps to bridge the gap between the short-term laboratory studies and long-term processes in natural environments, particularly evident in the study of altered archaeological Roman glass recovered from the bottom of the Mediterranean Sea after 1,800 years by Verney-Carron *et al*. (2010), which addressed the issue of the effects of cracks on altered glass. It is well known that nuclear glass intrinsically contains cracks due cooling (Minet & Gordon 2003), which means that a larger surface area is exposed to the solution and will contribute to a greater alteration rate. However, the use of this altered Roman glass analogue showed that the effects of the cracks had a relatively minor role in glass alteration over this time period, because the cracks were sealed by alteration products, slowing down the diffusive transport (Verney-Carron *et al*. 2008 & 2010a). In the study by Verney-Carron *et al*. (2010), they also mechanistically modelled the glass alteration (whose kinetic parameters were determined by short-term experiments) over extended time periods, whereby the results were consistent with the archaeological Roman glass, in other words the model for the alteration thickness agreed with the alteration thickness of the 1,800 year old glass sample in similar environmental conditions. This was significant because it validated the predictive capacity of the mechanistic model, thus bridging short-term laboratory experiments with long-term observations, boding well for future modelling and predictions. The same study also calculated the lifetime of a fractured nuclear glass package confined in a GDF in many scenarios, taking into consideration all appropriate physical, chemical and environmental factors. The most realistic conservative result revealed that after 100,000 years, only 5% of the total glass had been altered, the rest of the glass was still in pristine condition. Note, that this was a conservative result, derived from the safety calculations demanded by a rigid safety assessment. In reality the quantity of altered glass is expected to much lower than 5% in all realistic scenarios.

II – Geological disposal - kinetic models

Kinetic modelling can also be used to predict the long-term fate of disposed HLW in a GDF. Generally, these models are based on identifying a predominant alteration mechanism with a few simplified hypotheses, which may not be truly representative to the behaviour of disposed HLW glass. Five of the most common models are discussed very briefly below:

- **The Aagaard-Helgeson Law** – not so much a model, but a law, which does not take into account formation of an alteration layer. This law is based on diffusion kinetics and chemical affinity (Aagaard & Helgeson 1982).

- **The Grambow Model** – the rate limiting step of glass dissolution is the build-up of H_4SiO_4; as the concentration increases, the dissolution rate slows. But as H_4SiO_4 reaches saturation, the model predicts that the rate drops to zero, therefore a final constant rate term was added related to the diffusion of water into the glass matrix (Grambow 1984).

- **The r(t) Model** – considers Si diffusion through an amorphous alteration layer to be the rate-limiting step. The forward and long-term rate are fixed parameters (Ribet *et al*. 2001).

- **The GRAAL Model** – based on water diffusion through a passivating reactive interphase (PRI). The model relies on the reactivity, i.e. the formation and dissolution of the transport limiting PRI layer. Only water diffusion through the PRI is considered to be rate-limiting. This model has proved successful by its ability to account for experimental data and predict results (Vienna *et al*. 2013). A further model that progresses on the GRAAL model is the GM2001 model which takes into account two diffusion processes, water through the glass and silica through the alteration layer. This model considers the diffusion of silica as the rate-limiting step.

- **The STORM Model** – is similar to The Grambow Model but highlights the role of ion exchange in the dissolution process. Here, a constant ion exchange serves to prohibit equilibrium conditions, hence, the dissolution rate does not decrease to zero, but is maintained at some constant rate (Feng & Pegg 1994, McGrail *et al*. 2001).

It should also be noted that computer programs have been developed that model the glass/water reaction; notably PHREEQ-C, GLASSOL and EQ3/6. These programs take input values such as glass and solution compositions, time, temperature, glass surface area, solution volume and flow rate. However, the rate and stability constants are required from experimental results.

Coupled modelling was performed using geochemical/transport codes and radiolysis models to describe the chemical evolution of HLW glass together with its waste package and engineered barrier surroundings by Grambow & Giffaut (2006). Such a study predicted the amount of radionuclide release from a generic nuclear waste glass in a generic near-field environment in a GDF in a clay formation. The release rate as a fraction of total radionuclide content released from the glass per year, was predicted to be (for the following elements): Am 10^{-14} y^{-1}, Pu 10^{-10} y^{-1}, Cs and I $5x10^{-6}$ y^{-1}. The study concluded that the release of Cs and of the potentially vitrified I, posed a problem for the GDF safety assessment because they are soluble species. The actinides, however, are very insoluble under the reducing conditions in the GDF and because of their strong retention on clayey materials. Hence, the actinides are expected to decay in close proximity to the glass, without ever migrating to the biosphere within their lifetime.

3. Experimental

3.1 Materials

3.1.1 Vitrification

A variety of glass compositions were fabricated at The University of Sheffield (TUoS) or acquired from the Vitrification Test Rig (VTR) at the National Nuclear Laboratory (NNL) throughout the course of this work. A description of each glass is provided below, alongside the synthesis conditions (Table 3.1), the analysed compositions (by hydrofluoric (HF) acid digest and inductively coupled plasma optical emission spectroscopy (ICP-OES)), measured densities, and a reference to the chapters of relevance within this Thesis (Tables 3.2 & 3.3).

TUoS Glasses: All glasses developed at TUoS were: 1) made from a selection of the oxide precursors ($Al(OH)_3$ (>99.9 % Acros), H_3BO_3 (>99.9 % Merck), $CaCO_3$ (96 % Fluka), $LiCO_3$ (99.5 % Analar), Na_2CO_3 (98 % Alfa Aesar), SiO_2 (99 %), $SrCO_3$ (99.9 % Sigma), ZnO (99 % Aldrich) and ZrO_2 (99 % Aldrich)) and simulant nuclear waste calcine (where applicable); 2) weighed and then mixed by hand in a bag for five minutes and, 3) after stirred melting, were poured and cast into ingots in a pre-heated iron mould (~100 x 30 x 30 mm). Approximately 200 g of each glass was fabricated in a single melt.

International Simple Glass (ISG): This glass was fabricated in 2012 by the MoSci Corporation in several batches (Rolla, MO, USA), as described in Gin *et al.* (2015). The ISG was developed for international researchers as a standard reference glass for dissolution experiments (Fig. 3.1) (Gin *et al.* 2013). It is a six-component, non-radioactive mixed-alkali alumina-borosilicate reference glass, with a composition simplified from the French inactive surrogate of the R7T7 nuclear waste, SON68. ISG has been studied extensively, with the drive to understand glass corrosion at the fundamental level and to set the foundations for predicting the long term fate of nuclear waste glass over geological timescales in a nuclear waste repository. One batch of the ISG was used in this Thesis, which belonged to the lot number L1201 2601-M1205 0803.

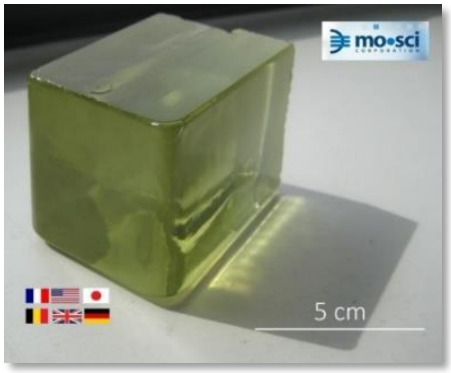

Figure 3.1. The ISG, with flags depicting the members of the international glass corrosion community.

Modified TUoS International Simple Glasses (ISGx): Two glasses, identified as ISG-original (ISGO) and ISG-Intermediate (ISGI) were designed and synthesised at TUoS as variants of ISG, representing the stages of glass composition as a function of time, i.e. capturing the compositional dependence of the radioactive decay of ^{90}Sr to ^{90}Zr (see Table 3.1. for compositions). In Chapter 9, ISG is used as an analogue of a waste glass composition at a time in excess of 300 years after disposal, ISGO represented the glass composition at the time of production, and ISGI at an intermediate stage. Further details are given in Chapter 9.

ZnCa-UK HLW simple glasses (ZnCa xx:xx): As detailed in Chapter 2, the UK recently modified its HLW base glass to include a proportion of Zn and Ca. In Chapter 5, a suite of simplified versions of the ZnCa-containing base glass are investigated, as a function of varying ZnO/CaO molar ratios. These glasses are referred to as ZnCa xx:xx, where xx denotes the percentage of the molar ratio between the two oxides. These glasses were designed around the four-component alkali-borosilicate Mixed Windscale (MW) base glass used at the Sellafield vitrification plant. The ZnCa 40:60 composition has recently been adopted, in part, on one of the three active processing lines at the Sellafield site (Harrison 2018a, Gribble 2018).

Mixed Windscale with 25 wt.% simulant waste loading (MW25): The active version of this glass comprises the largest fraction of UK's vitrified HLW. It is composed of the MW base glass (described above), loaded with 25 wt.% HLW calcine from the reprocessing of Advanced Gas cooled Reactor Oxide (o) and Magnox (m) spent nuclear fuel at a ratio of (75o:25m). An inactive surrogate of MW25, fabricated by Dr. Nate Cassingham (Cassingham *et al.* 2015), using MW frit and a blended nuclear waste simulant calcine, (waste ratio (75o:25m)), provided by NNL, was used in Chapter 8.

ZnCa-modified MW base glass with 28 wt.% waste (ZnCa xx:xx MW28) glasses: As noted above, the ZnCa 40:60 modified MW base glass is been used at the Sellafield site, where it is been prepared with

28 wt.% of waste calcine at a ratio of (75o:25m). In an effort to understand how varying the ZnO/CaO molar ratio influences the dissolution behaviour of *waste loaded* glasses, Chapter 6 investigates three inactive surrogate ZnCa xx:xx MW28 compositions, with varying ZnO:CaO molar ratios (100:0, 40:60 and 0:100). Prepared at TUoS, these glasses were synthesised from raw base glass oxide precursors and an inactive waste calcine (WRW17, containing Ru and Li) (Fig. 3.2), kindly provided by NNL. Chapter 7 investigates the chemical durability of ZnCa 40:60 MW28 in various groundwater solutions.

Figure 3.2. Raw oxide base glass precursors and inactive waste calcine prior to mixing for the ZnCa 40:60 MW28 composition.

ZnCa waste MW-type (ZnCa MWXX): three variants of the inactive surrogate ZnCa MWXX glass with different waste loadings (20, 25 and 35 ± 3 wt.%, incorporating a 50o:50m waste ratio) were provided by NNL, fabricated on the VTR at the Sellafield site. The adopted ZnO/CaO molar ratio is 40:60. Chapter 6 investigates the chemical durability of ZnCa MWXX.

Table 3.1. Melt conditions for the fabricated and acquired simple and complex glasses and featured chapter.

	Simple			Complex		
Glass	ISG*	ISG - type (ISGx)	ZnCa base MW-type (ZnCa xx:xx)	ZnCa waste MW-type (ZnCa xx:xx MW28)	ZnCa waste MW-type (ZnCa MWXX)†	MW25‡
Melt Temp / °C	1300	1400	1200	1060	1028**	1060
Melt Duration /h	4	5	5	5	2-8	5
Cooling rate / °C min^{-1}	50 / °C h^{-1}	1	1	1	Cool naturally in containter	1
Anneal Temp / °C	569	575	450±	500	-	500
Anneal Duration /h	6	1	1	1	-	3
Furnace Type	Electric	Electric	Electric	Electric	VTR (Sellafield Ltd.)	Electric
Stirred	Once	Yes (4 h)	Yes (4 h)	Yes (4 h)	Sparged	Yes (4 h)
Crucible	Platinum-Rhodium	Platinum	Platinum	Platinum	Nicrofer 6025 HT alloy	Mullite
Featured Chapter	4&9	9	5	6&7	6&8	8

*Fabricated by MoSci Corporation (2012)

†Fabricated on the inactive test rig (VTR) at Sellafield Ltd. Information provided by Harrison (2018a)

‡Fabricated by Cassingham *et al.* (2015)

±DTA was initially performed on NNL supplied glass frit (ZnCa 40:60) to obtain the glass parameters in which to fabricate the glass (Tg ~ 510 °C T_{anneal} ~ 450 °C)

**Average internal temperature at the time of pouring was 1028 °C

Table 3.2. Analysed simple glass compositions from HF digest and ICP-OES (relative uncertainty ± 3 %). Associated density uncertainty ± 0.005 g /cm^3.

Glass																							
			ISG-type								ZnCa base MW-type (ZnCa xx:xx)												
Glass Network Role	Oxide		ISGO		ISGI		ISG		ZnCa 0:100		ZnCa 20:80		ZnCa 40:60		ZnCa 60:40		ZnCa 80:20		ZnCa 100:0				
			wt. %	mol. %	wt. %	mol. %	wt. %	mol. %	wt. %	mol. %	wt. %	mol. %	wt. %	mol. %	wt. %	mol. %	wt. %	mol. %	wt. %	mol. %			
Formers	SiO_2		56.50	60.10	56.30	60.10	56.20	60.10	53.20	53.60	51.00	51.90	51.20	52.50	45.40	47.10	46.00	48.10	43.90	46.40			
	B_2O_3		17.40	16.00	17.40	16.00	17.30	15.97	22.30	19.40	23.30	20.50	22.50	19.90	25.30	22.70	23.80	21.50	24.40	22.30			
	Al_2O_3		6.00	3.80	6.00	3.80	6.10	3.84	3.70	2.20	3.70	2.20	3.70	2.20	4.00	2.50	4.00	2.50	3.90	2.40			
Int.	ZnO		-	-	-	-	-	-	-	-	3.00	2.30	5.80	4.40	9.40	7.20	12.50	9.70	15.90	12.40			
	ZrO_2		-	-	1.60	0.85	3.30	1.72	-	-	-	-	-	-	-	-	-	-	-	-			
Modifiers	Na_2O		12.30	12.70	12.30	12.70	12.20	12.65	7.80	7.60	7.90	7.80	7.70	7.70	8.00	8.10	7.90	8.00	7.90	8.10			
	Li_2O		-	-	-	-	-	-	3.50	7.10	3.50	7.20	3.50	7.20	3.80	7.90	3.80	8.00	3.90	8.30			
	CaO		5.00	5.70	5.00	5.70	5.00	5.73	9.40	10.10	7.60	8.30	5.50	6.10	4.10	4.60	2.00	2.20	0.10	0.10			
	SrO		2.80	1.70	1.40	0.85	-	-	-	-	-	-	-	-	-	-	-	-	-	-			
Density / g cm^3			2.50		2.52		2.53		2.58		2.60		2.63		2.64		2.69		2.71				

Table 3.3. Analysed complex glass compositions from HF digest and ICP-OES (relative uncertainty ± 3 %). Density uncertainty ± 0.005 g /cm^3. Total glass compositions for ZnCa MW-types (75o:25m) and MW25 (75o:25m) were normalized. Total glass compositions for ZnCa (50o:50m) were provided by NNL and were not normalized. Note the larger relative uncertainty of ± 5 % attributed to ZnCa MW35 due to less control on the wastestream feed on the VTR.

Glass	ZnCa waste MW-type (75o:25m)			ZnCa waste MW-type (50o:50m)			MW25 (75o:25m)
	ZnCa 0:100 MW28	ZnCa 40:60 MW28	ZnCa 100:0 MW28	ZnCa MW20	ZnCa MW28	ZnCa MW35	
Oxide	wt. %	wt. %	wt. %	wt. %	wt. %	wt. %	wt. %
Al_2O_3	3.26	3.17	3.15	5.10	5.59	6.20	1.41
B_2O_3	20.86	20.51	20.06	18.37	16.27	14.54	18.35
BaO	0.76	0.75	0.74	0.34	0.96	0.70	0.32
CaO	8.21	4.93	0.08	5.00	4.58	3.86	0.01
CeO_2	1.21	1.20	1.17	1.12	1.53	2.13	0.96
Cr_2O_3	0.41	0.44	0.34	0.51	0.73	4.27	0.36
Cs_2O	1.42	1.40	1.40	1.12	1.73	2.13	1.17
Fe_2O_3	1.77	1.78	1.70	2.14	3.15	4.27	1.56
Gd_2O_3	3.22	3.26	3.15	1.33	1.93	2.64	2.63
HfO_2	0.05	0.05	0.05	-	-	-	0.03
K_2O	-	-	-	-	-	-	0.01
La_2O_3	0.63	0.64	0.60	0.60	0.87	1.22	0.53
Li_2O	2.68	2.59	2.57	3.16	2.95	2.74	3.50
MgO	1.50	1.45	1.40	1.94	2.85	3.76	1.15
MnO_2	0.00	0.00	0.00	-	-	-	0.01
MoO_3	1.87	1.86	1.82	1.53	2.34	3.05	1.65
Na_2O	7.04	6.86	6.68	7.55	6.91	5.90	9.03
Nd_2O_3	1.88	1.85	1.79	1.63	2.44	3.35	1.50
NiO	0.29	0.29	0.28	0.33	0.47	0.61	0.27
P_2O_5	0.40	0.40	0.40	-	-	-	0.38
Pr_2O_3	0.60	0.60	0.58	0.51	0.74	1.02	0.52
RuO_2	0.33	0.34	0.32	0.49	0.61	0.86	0.31
SO_3	0.03	0.03	0.03	-	-	-	0.02
SiO_2	38.29	37.66	36.95	39.00	34.37	30.29	51.73
Sm_2O_3	0.40	0.39	0.39	0.40	0.59	0.80	0.31
SrO	0.33	0.33	0.32	0.34	0.49	0.65	0.29
TeO_3	0.28	0.28	0.27	0.16	0.26	0.35	0.01
TiO_2	0.02	0.02	0.01	-	-	-	0.02
Y_2O_3	0.24	0.23	0.23	0.21	0.32	0.44	0.21
ZnO	0.01	4.72	11.59	4.80	4.37	3.66	0.01
ZrO_2	1.99	1.98	1.94	1.84	2.64	3.56	1.74
Total	100.00	100.00	100.00	99.52	99.70	103.00	100.00
Density / g cm^3	2.86	2.89	2.94	2.86	2.89	2.94	2.77

3.2 Analytical Methods

3.2.1 X-Ray Diffraction

X-ray diffraction (XRD) uses X-rays to allow the characterisation of crystalline structures in materials. It can provide information including crystalline lattice parameters, phase identification, phase purity, crystallinity, crystal structure and the percent phase composition. It can also be used to determine if a material has an amorphous nature, such as glass. However, XRD cannot provide elemental analysis, such as elemental composition and elemental quantities.

XRD is physically underpinned by the inter-planar spacing of all crystal structures. Planar X-rays scatter when they strike a crystal lattice of atoms, hence the detection of the scattered X-rays can provide information on the scattering material. X-rays can scatter coherently and incoherently. Coherent elastic scatter is caused by bound electrons of atoms belonging to the crystal lattice. Here, a definite phase relationship can exist between incident and scattered X-rays. Incoherent inelastic scatter is caused by loosely bound or free electrons, whereby no such phase relationship exists.

XRD takes advantage of coherent scattering which is described by Wulff-Bragg's equation (Wulff 1913):

$$n\lambda = 2d\sin\Theta \qquad [3.1]$$

where n is an integer, λ is the wavelength of the X-ray (m), d is the inter-planar spacing (m) and Θ is the angle of the incident beam. This equation describes the condition for constructive interference for two scattered X-rays, which results in peaks of scattered intensity upon detection, as shown in Figure 3.3.

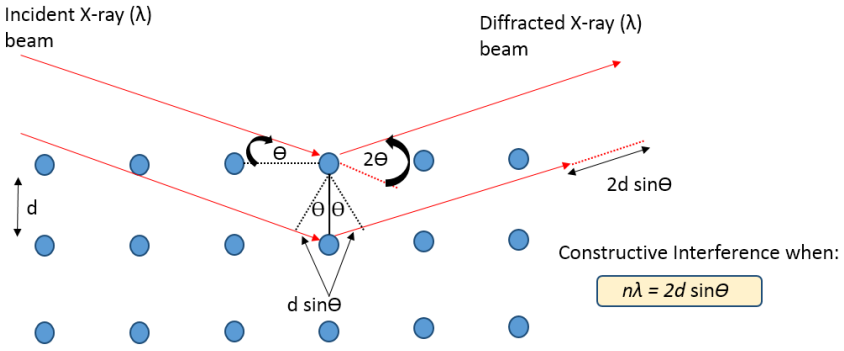

Figure 3.3. Wulff-Bragg's Law and their equation for the condition for constructive interference, hence the condition for diffraction.

Wulff-Bragg's equation can be used to predict the position of diffracted X-ray beams from different sets of lattice planes. The angles from diffracted X-rays are simply determined by the distance (d) between parallel planes of atoms (Fig. 3.3). A moving detector (Fig. 3.4) scanning through a range of angles can measure the angles at which diffracted X-ray peaks (from multiple planes as describe by the Miller Indices) are observed. Each crystalline material will produce characteristic peaks (patterns of position and relative intensity), providing a fingerprint of the crystal structure that can readily be identified against a database of known materials. The database in use is maintained by the International Centre for Diffraction Data (ICDD) (Fawcett *et al.* 2005) and is accessed and applied using various software such as PDF-4, Sieve4+ or WinXPow.

XRD is usually performed on mounted powdered samples in which an X-ray beam is focussed. The sample rotates to provide random sampling. A detector moves through a range of angles (5-35^{o}) and thus receives scattered X-rays. This range of angles is needed because the crystals in the powdered sample are randomly orientated, which scatter X-rays at all angles. Note that all planar orientations are simultaneously presented to the X-ray beam, hence only some planes will be orientated in such a way as to fulfil the Wulff-Bragg condition (Fig. 3.4), which causes the constructed interference. This constructive interference is manifest in a series of conical diffraction shells, where each shell represents diffraction from a specific plane as described by Miller Indices (Fig. 3.4).

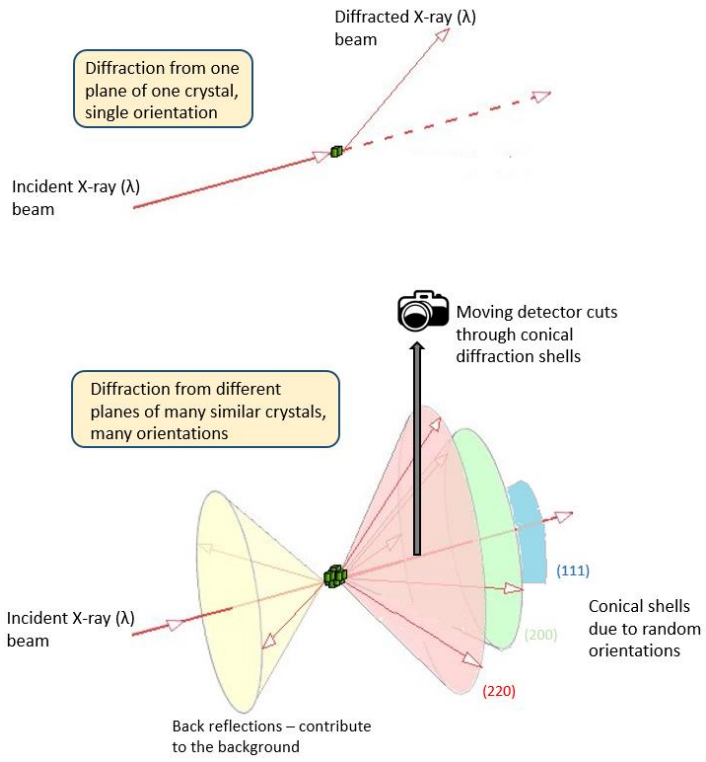

Figure 3.4. Diffraction from a single crystal and from many crystals. Note that the bracketed numbers represent the Miller Indices. Note the moving detector cutting through the conical diffraction shells.

Moving the detector through the angles 5-35 ° (essentially allows scattering measurements to be made between 10-70 °, hence 2Θ degrees (Fig. 3.3)) enables the detection of the diffraction from many planes, i.e. the moving detector provides a cut through 2D snap-shot of the conical diffraction shells (Fig. 3.4). A line scan across this diffraction pattern produces an XY plot which displays intensity against the 2Θ angle; which is how data from XRD is routinely reported (Fig. 3.5). Each plane is represented by one cone/ring depicted in Figure 3.5, hence one can begin to see the complexity in an XRD trace of a multi-phase sample. The scattering intensity drops as $1/2(1 + \cos^2 2\Theta)$ hence, past 70 ° 2θ, the intensity drops substantially.

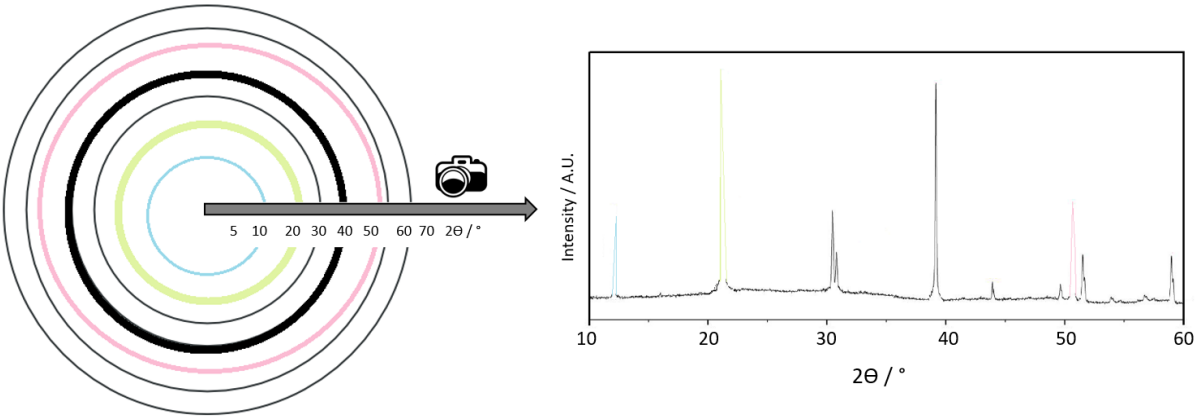

Figure 3.5. A line scan through 2D represented conical shells is depicted as a plot of intensity Vs. 2Θ / °.

XRD can be applied to materials to determine if they possess an amorphous nature. Because glass contains no long-range structure, coherent diffraction does not occur. However, diffraction from a range of short interatomic distances between the atoms in glass is manifest in XRD traces. This can be seen as diffuse scattering across a wide range of 2Θ angles, mainly seen and described as an amorphous hump between 10-40 ° 2Θ, reflective of short interatomic distances.

XRD was routinely applied to all glass samples that were fabricated as part of this thesis to: 1) assess their material properties after fabrication and 2) to assess their material properties after being subjected to dissolution experiments to characterise secondary products that may have formed. The experimental parameters are described below.

Experimental Parameters applied: XRD was performed on compressed and smoothed pristine (<75 µm diameter) and altered glass particles (originally 75-150 µm diameter), in addition to altered monolithic surfaces, all mounted in a zero background sample holder. XRD data was acquired on a Bruker D2 Phaser X-ray Diffractometer, using Kα (λ = 1.541 A) radiation generated from a Cu target at

a working voltage of 30 kV and 10 mA. A Ni filter and a Lynx-Eye position sensitive detector were used. An angular range of 10 < 2Θ < 70, with a 0.02° step size progressing at 0.17 °/min were applied, with a total scan time of 180 minutes. The samples were rotated at a frequency of 60 Hz. All diffraction patterns were analysed using the PDF4+ database (Fawcett *et al.* 2005).

3.2.2 Scanning Electron Microscopy and Energy Dispersive Spectroscopy

Scanning electron microscopy (SEM) works on the principle of using a focussed beam of electrons to generate magnified images of a sample. An electron gun produces a beam of electrons, which are accelerated towards an anode through a voltage difference between 0.1 and 50 kV. This beam is then electromagnetically focussed onto the sample. The beam can be controlled by the user to scan across the surface of the sample using scan coils. A schematic diagram of an SEM is shown in Figure 3.6. As the beam scans the sample, three interactions occur, which are detected and provide useful information:

1. Inelastic Scattering – some of the electrons from the focussed beam are inelastically scattered by k-orbital electrons of the atoms in the sample. These electrons are known as secondary electrons (SE), which directly reflect the topology of the sample.

2. Elastic Scattering – some of the electrons from the focussed beam are elastically back scattered through 180^{o} by the atomic nuclei of the sample's atoms, hence the name Back Scattered Electrons (BSEs). The intensity of BSEs generated correlates with the atomic number (Z) of the elemental sample composition, whereby higher Z atoms generate more BSEs than lower Z atoms. Hence, Z contrast can be ascertained.

3. X-ray generation – some of the electrons from the focussed beam enter the sample at just the correct energy to eject electrons from the 1 s shell of an atom. Both electrons involved in the collision may become secondary electrons. The resulting hole in the 1 s shell is filled by an electron cascading down from the higher 2 p shell, which in the process releases an X-ray photon with an energy identical to the difference between the two electron shells (Russ 1984). The X-ray energy is characteristic of the element of the atom from which it was released. Thus, identification of the sample's elemental composition can be undertaken. This technique is known as Energy Dispersive Spectroscopy (EDS).

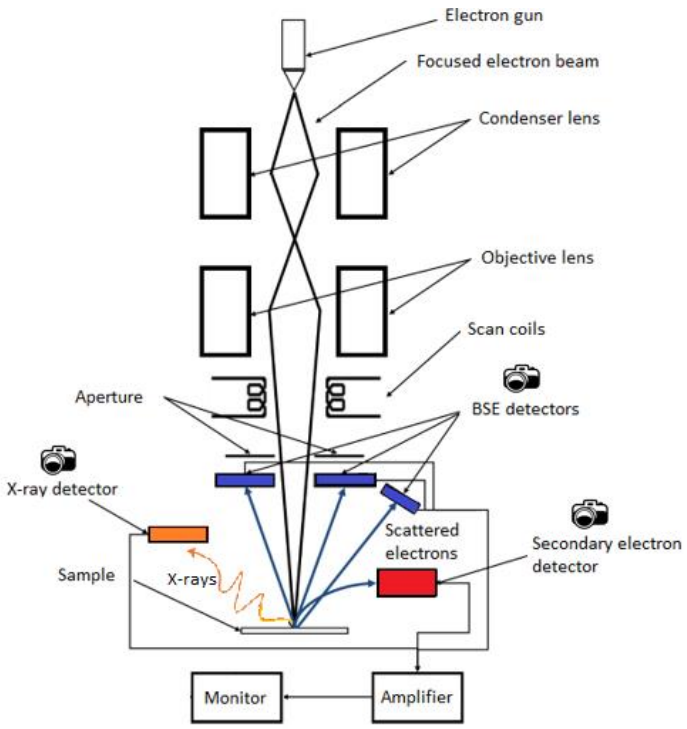

Figure 3.6. Scanning electron microscope schematic. Adapted from Goodhew *et al.* (2001).

SEM/EDS was routinely applied to all glass samples pre- and post-alteration to gain microstructural information on the pristine glass and altered glass, respectively, in addition to identification of the chemical composition of alteration products and measurements of alteration layer thicknesses on monolithic samples. Samples were prepared in three styles, which were appropriate for both pristine and altered glass: 1) monolithic epoxy-mounted, 2) particle epoxy-mounted and 3) particle adhesion to carbon stubs. All are shown in Figure 3.7.

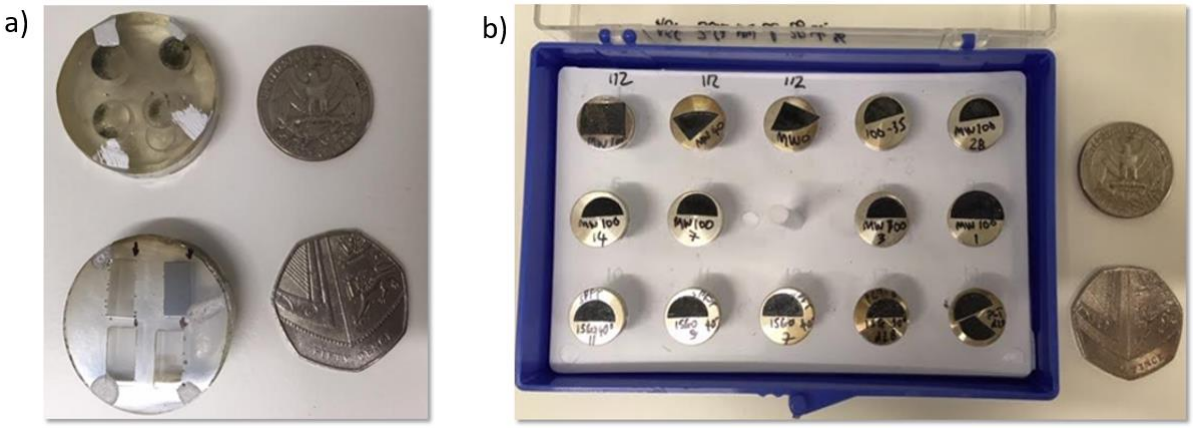

Figure 3.7. Samples used for SEM/EDS analysis: a) polished epoxy mounted cross-sectional glass particles and monoliths; and b) carbon pads with sprinkled whole glass particles (pre- and post-dissolution experimentation). A quarter from the USA (top coin) and a 50 pence piece from the UK (bottom coin) are included as a size comparison.

The epoxy mounted samples were ground using SiC abrasive paper and isopropanol lubricant (in the order 400, 800 and 1200 grit) and subsequently polished using diamond suspension (in the order 6, 3 and 1 µm) to reveal clear cross-sectional images. Polished samples were carbon-coated using an Agar Auto Carbon Coater and conductive silver paint was applied (including the bottom of the sample (Fig. 3.7)) to reduce electron charge build-up during SEM on the sample surface, which is detrimental to the acquisition of images. Particles adhered to carbon stubs were also carbon coated.

Experimental techniques/parameters applied: SEM was performed using two microscopes for imaging (BSE and SE) and the acquisition of elemental composition (EDS): 1) a Hitachi TM3030 desktop and 2) an FEI Inspect F50. The applied voltage and working distance for both microscopes was 15 kV and 10 mm respectively. EDS was obtained in conjunction with SEM on the Hitachi TM3030 / FEI Inspect F50 using a Bruker Quantax 70/ Oxford Instruments spectrometer respectively, whereby spectra were obtained for between 3-10 minutes.

The thickness of altered layers on monolithic samples was measured using the computer software ImageJ. Ten BSE images were taken along the length of a 10 mm monolith, and five thickness measurements were taken on each. Hence, the average thickness for each monolith consisted of taking the mean value from 50 measurements in the ideal case. Some samples had a disrupted layer, due to sample preparation issues and, therefore, a somewhat lower number of measurements were taken. Alteration layer thicknesses were not ascertained from particle samples (both mounted in epoxy resin and adhered to carbon pads) due to their random orientations. The altered layers examined were those from the top side of the monolith. The sides and bottom were also examined and these were found to display approximately the same features, with the same alteration thickness within experimental error. The only difference was that more secondary precipitates were noted to form on the top-side, which was noticeable, but not substantial.

3.2.3 Solid-State Nuclear Magnetic Resonance Spectroscopy

Solid-state nuclear magnetic resonance spectroscopy (NMR) is used to obtain information on the structural environment of certain materials by exploiting the electromagnetic properties of nuclei. In the case of alkali aluminoborosilicate glasses it is possible to identify the fractions of different silicate Q_n species (silicate tetrahedra with different numbers of bridging and non-bridging oxygen atoms, therefore gleaning information on the network connectivity), the proportions of B_3 and B_4 structural

units and the coordination environment of Al from ^{29}Si, ^{11}B and ^{27}Al NMR respectively. Silicon-29 NMR is also sensitive to next nearest neighbours, therefore it is possible to identify nearest-neighbour species bonded to the silicate tetrahedra thorough bridging oxygen atoms, such as Si-O-Si, Si-O-B and Si-O-Al.

Most nuclei possess a quantized property called spin, which is a purely quantum effect (a consequence of relativity and quantum mechanics) with no direct classical counterpart (Cohen-Tannoudji *et al.* 2019). Quantum spin is loosely analogous to the spin of macroscopic bodies, and can be interpreted as the spinning of an individual nucleus around an axis, which gives the nucleus some angular momentum (J). Quantized spin is a quantum mechanical property which permits nuclei to exist with only integer or half-integer spin values (I), which is due, in part, to the mass and charge of the nucleus. Nuclei possessing an even mass number and even charge, such as ^{12}C and ^{16}O have zero spin, hence zero angular momentum and are thus unable to be probed by NMR. Only nuclei with an odd mass number, which possess half-integer spin can be probed; examples of which are ^{27}Al, ^{29}Si (I = 1/2) and ^{11}B (I = 3/2). Note that even mass numbered nuclei with odd charge can have integer spins, but are difficult to examine and are excluded from most NMR investigations. The combined effect of the electromagnetic properties of a nucleus (γ) and the angular momentum (J) (due to the intrinsic spin) gives rise to a magnetic moment (μ) which is fundamental to the NMR spectroscopic technique:

$$\mu = \gamma J \qquad [3.2]$$

where:

$$\gamma = \frac{ge}{2m_p} \qquad [3.3]$$

where g a dimensionless factor, e is the electron/proton charge and m_p is the proton mass. Each nuclide possessing a magnetic moment (μ) has an associated energy. In the absence of a magnetic field, random orientation of μ is observed and each nuclide of the same element possesses the same energy, hence, the energy levels are said to be degenerate. On the application of an external magnetic field (B_o) this degeneracy is lifted due to the interaction of B_o and μ (the Zeeman interaction). Here, the spinning nuclides align parallel and anti-parallel to B_o. Each nuclide has associated with it [2I + 1] quantized energy levels. These energy states are described by the quantum number m, where m ranges from –I to +I in integer steps. In the case of ^{29}Si, with spin value I = 1/2, only two quantized energy levels exist. The energy (E) of each level is given by:

$$E = -\mu \cdot B_o \qquad [3.4]$$

where μ can now be represented as μ = mℏ, (ℏ is the reduced Planck's constant). This is clearly illustrated in Figure 3.8. The energy difference between the levels, due to the Zeeman interaction is equal to ℏγB$_o$, which, is only dependent on B$_o$.

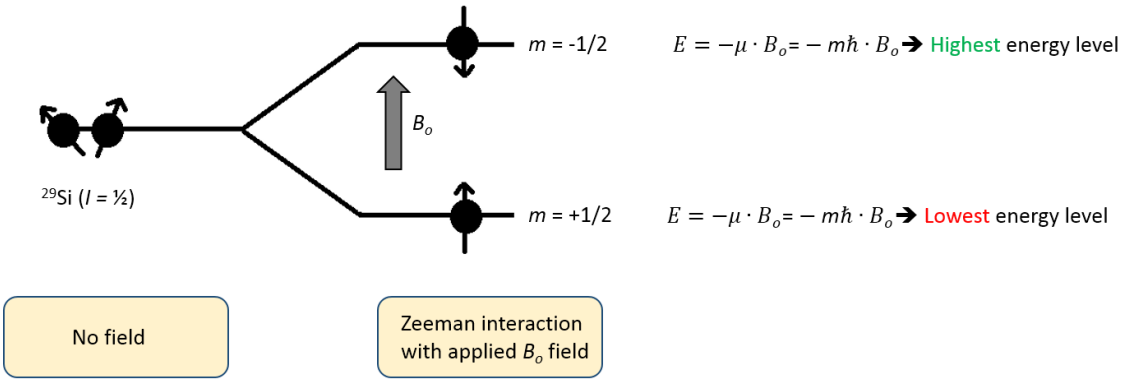

Figure 3.8. Depiction of the alignment of ^{29}Si nuclei on the application of an external magnetic field. Associated energy levels are also illustrated.

The relative population of the higher and lower energy levels is given by the Boltzmann distribution, which is dependent upon the temperature. Note that the population difference between energy levels is miniscule, hence the populations are near identical at room temperature (the temperature at which NMR experiments are conducted) and the associated spins in each level can be thought of as cancelling each other out. However, there is a slight preponderance for nuclei to exist in the lower energy level and it is this miniscule visible spin excess that makes NMR spectroscopy possible.

Due to the intrinsic spin of nuclei, the generated magnetic moment precesses around the externally applied magnetic field (conventionally applied along the Z-axis), however it is not possible to detect this precession in this situation. The frequency of the precession is known as the Larmor frequency (ν) (where ν = γB$_o$). An NMR signal is produced by irradiating the nuclei with a burst of radio-frequency radiation at exactly the Larmor frequency. This small transfer of energy has the effect of tipping the precessing nuclei through ninety degrees away from B$_o$ to lie along the y-axis. After this tipping action, the nuclei then relax, precessing around the Z-axis to realign with B$_o$ after a period of time. This realignment causes the nuclei to release their excess energy in the form of radio-frequency radiation which is detected by an antenna (the same antenna used for the original irradiation). This finger-print precessional radiation is recorded as a function of time and is subsequently Fourier-transformed into the frequency domain from which information on the structural properties of a material can be gleaned. It is beyond the scope of this Chapter to describe in greater detail the processes and operational techniques of acquiring an NMR spectra, such as the employment of the Car Purcell spin-

echo, but thorough accounts can be found in the text-books by Engelhardt (1987), Kirkpatrick (1988) and Apperley *et al.* (2012). However, it is important to discuss the interpretation of NMR spectra in terms of the spectral parameters and the properties of material that produce such spectra.

It is important to state that the total energy of a system probed by NMR (E_{NMR}) contains multiple energy terms and is thus more complex than outlined above and displayed in Figure 3.8 (Apperley *et al.* 2012):

$$E_{NMR} = E_z + E_{RF} + E_S + E_J + E_D + E_Q \qquad [3.5]$$

where E_Z is the contribution from the Zeeman interaction, E_{RF} is the contribution due to the interaction of the spins with the applied radio-frequency burst, E_S is the shielding effect, E_J is the contribution from indirect spin coupling, E_D is the contribution from dipolar spin couplings and E_Q is the quadrupolar spin coupling. All contributing terms cause a range of magnetic field strengths at individual nuclei of the same nuclide, thus causing a broadening of solid-state NMR spectra. The most important term when probing the structure of a material is the shielding effect (E_S). This effect is caused by the electrons of the atom shielding the nucleus from the applied magnetic field B_o. Hence, nuclei in different structural environments (with different numbers of electrons) experience different magnetic fields which, when subjected to NMR investigations, translates to a characteristic finger-print resonance frequency associated to particular structural environments of the nuclei under investigation. This frequency is reported as a chemical shift (in ppm) relative to a recognised standard.

However, to obtain structural information, such as the identification of nearest neighbour species, proportionalities of certain structural units and coordination environments, it is essential to isolate the shielding effect (E_S) in Equation 3.5. Conventional NMR produces a broad spectrum from which little structural information is available. Employing an experimental technique called Magic-Angle-Spinning (MAS) produces spectra with enhanced surface to noise ratios and resolution, thus elucidating narrow identifiable peaks (see ^{29}Si MAS spectra in Figure 3.9, which shows four different Si-site environments). MAS works by tipping and spinning the sample at a 'magic angle' of 54 ° 44' to B_o (as opposed to tipping the nuclei through 90 ° as mentioned above), corresponding to tipping radio-frequencies between 2 and 10 kHz. The last four terms in Equation. 3.5 are dependent upon the orientation of the precessing spins subjected to B_o and the 'tipping' frequency. At the magic angle the terms E_J, E_D and E_Q are zero. Hence, the resulting spectra can be interpreted solely in terms of E_S. A full explanation of MAS requires a good understanding of quantum-mechanical time-dependent Hamiltonians and a good introduction can be found in Kirkpatrick (1988).

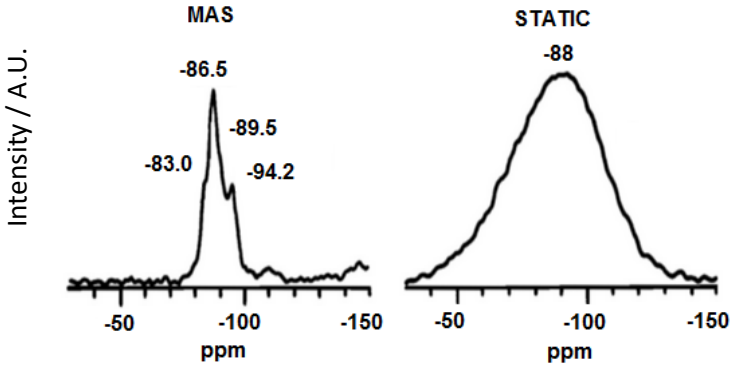

Figure 3.9. Comparison of MAS and static ^{29}Si NMR spectra on an illite crystalline clay sample. Note the four identifiable peaks (from different Si sites in the material) in the MAS spectra, which are unresolved in the static spectra. Spectra adapted from Kirkpatrick (1988).

3.2.3.1 Experimental Parameters Applied

All solid-state MAS-NMR spectra were obtained from 0.5 g of powdered pristine glass sample (< 75 µm diameter) at the EPSRC UK National solid-state NMR Service at Durham University. The nuclei of interest were ^{11}B, ^{29}Si and ^{27}Al. The full range of ZnCa MW base glass compositions discussed in Chapter 5 and from the ISG-type glasses discussed in Chapter 8 were analysed by ^{27}Al, ^{11}B and ^{29}Si MAS-NMR. Spectra from all nuclei were obtained from a *Varien* VNMRS spectrometer with optimised experimental parameters listed in Table 3.4.

All post-dissolution solid-state MAS-NMR spectra were obtained from 0.33 g of ZnCa xx:xx particles (Chapter 5) with a diameter < 0.20 µm, altered for 303 d, in 25 mL of UHQ water and at 90 °C at The Sheffield Analytical and Scientific Services (Department of Chemistry (TUoS)) using a Bruker AVIIIHD 500 MHz spectrometer (Fig 3.10). Experimental parameters are provided in Table 3.4. Such alteration conditions were assumed to provide sufficient time to develop alteration layers/secondary phases to analyse with MAS-NMR, without totally altering the particles. Particles exposed to 35 d PCT-B dissolution tests were assumed unsuitable for MAS-NMR analysis due to the short test duration and subsequent under-developed alteration layers. Comparisons of the MAS-NMR data pre- and post-dissolution from ZnCa xx:xx particles is discussed in Chapter 5.

Despite the use of different instruments for MAS-NMR data collection, chemical shift data and resonance positions are comparable since the same external standard was applied for both measurements, hence 'global' differences to the extent of network polymerisation can be ascertained. However, the difference in magnetic field strength between the two instruments results in different resonance widths (FWHM) (the greater magnetic field on TUoS instrument results in greater

resolution/narrower resonance widths), which are not directly comparable, rendering spectral deconvolution comparisons between the pristine and altered glasses incompatible.

Table 3.4. Solid-state NMR experimental parameters.

Pristine glass – measured at the EPSRC UK National solid-state NMR Service at Durham University								
Nuclei	Frequency (MHz)	Mean spin-rate (Hz)	Pulse delay (s)	Pulse length (μs)	Acquisition time (ms)	Mean number of acquisitions	Probe - outer diameter (mm)	Reference material
^{11}B	128.30	13000	0.2	1	10	6000	4	BF_3/OEt_2
^{27}Al	104.20	13000	0.2	1	10	7000	4	1M aq. $Al(NO_3)_3$
^{29}Si	79.44	6000	240	4	20	200	6	Tetramethylsilane (TMS)

Altered glass - measured at TUoS								
Nuclei	Frequency (MHz)	Mean spin-rate (Hz)	Pulse delay (s)	Pulse length (μs)	Acquisition time (ms)	Mean number of acquisitions	Probe - outer diameter (mm)	Reference material
^{11}B	160.40	12500	60	2.25	200	32	4	BF_3/OEt_2
^{27}Al	130.28	12500	9	2.75	200	128	4	1M aq. $Al(NO_3)_3$
^{29}Si	99.34	12500	120	4	200	256	4	Tetramethylsilane (TMS)

Figure 3.10. The NMR facility at TUoS: sample loading into the Bruker AVIIIHD 500 MHz spectrometer.

Raw spectra obtained from different glass samples can be compared at the outset, offering an initial 'global' overview, and in some cases, offering the most credible insight into the structural differences between glass samples. However, deconvolution interprets the spectra in far greater detail, but is somewhat subjective. The nature of spectral deconvolution is credible if grounded by good predictions of the type of structures expected within the glass (such as the Dell-Bray model for borosilicate glass) and from data provided in the literature of similar glass compositions.

3.2.3.2 Spectral Deconvolution

As described in Chapter 2 (Section 2.3.1), glasses are disordered amorphous materials, which possess varying bond angles, bond lengths and nearest and next-nearest neighbour environments. These characteristics result in a large distribution of ^{29}Si chemical shifts in NMR spectra. Hence, a good theoretical structural basis can aid deconvolution. Spectral deconvolution was performed on the ^{11}B and ^{29}Si data. All elements of interest are discussed in greater detail below, in an attempt to underpin the theoretical structural considerations/calculations (based on a modified Dell-Bray model (Dell *et al.* 1983)) to the NMR spectral deconvolution:

^{27}Al: No spectral deconvolution was performed as there was no variation between spectra from all samples discussed in Chapters 5 and 8. All aluminium was observed to be four-fold coordination.

^{11}B Theoretical calculations: The calculations to ascertain BO_3 and BO_4 percentage contributions for the ZnCa MW base glass series discussed in Chapter 5 are presented through Equations 3.6-3.15 (whereby the oxides represent their mole fraction), which correspond to the equations and parameters for each base ZnCa MW composition listed in Table 5.5 in Chapter 5. The calculations performed were modified from the model for alkali aluminoborosilicate glass by Du & Stebbins (2005) (applied by Januchta *et al.* 2019) to include the addition of Zn and Ca (Calas *et al.* 2014). All of these models were refinements of the original model proposed by Dell *et al.* (1983).

$$R_{eff} = \frac{[(Na_2O) + (Li_2O) + (CaO)] - [(Al_2O_3) + (ZnO)]}{(B_2O_3)} \quad [3.6]$$

$$K = \frac{(SiO_2)}{(B_2O_3)} \quad [3.7]$$

$$R_{max} = \frac{1}{2} + \frac{1}{16}K \quad [3.8]$$

$$R_{d1} = \frac{1}{2} + \frac{1}{4}K \quad [3.9]$$

$$R_{dl2} = 2 + K \quad [3.10]$$

Where the fraction of B4:

$$B4 = \frac{8+K}{12}\left(1 - \frac{R_{eff}}{2+K}\right) \quad \text{if } R_{d1} < R_{eff} < R_{d2}, \quad [3.11]$$

$$B4 = R_{max} \quad \text{if } R_{max} < R_{eff} < R_{d1}, \quad [3.12]$$

$$B4 = R_{eff} \quad \text{if } R_{eff} < R_{max.} \quad [3.13]$$

The predicted B3 fraction is therefore:

$$B3 = 1 - B4 \quad [3.14]$$

A comparison between the predicated B4/B3 contributions and measured contribution was given by the ratio:

$$B_{Accuracy} = \frac{B\ Measured}{B\ Predicted} \quad [3.15]$$

^{11}B Spectral fitting: The ^{11}B spectra discussed in Chapter 5 were fitted from four peak assignments as shown in Table 3.5. These assignments were based on those used by Parkinson *et al.* (2007) and Backhouse *et al.* (2019), who studied similar simple glass compositions. An example of these fits is shown in Figure. 3.11. Spectral fitting was performed by Dr. Prashant Rajbhandari. Quantification of B speciation was provided by the integral of each fit, whereby values were corrected for the loss of intensity from the BO_3 contributions to the spinning sidebands.

Table 3.5. Peak assignments and fitting shapes for ^{11}B MAS-NMR spectra on the ZnCa MW base glass types discussed in Chapter 5.

Coordination	Peak	Fitting shape	Comments
BO3	(a) ring	Q_{mas} 1/2	Amplitude, width and position were refinable.
	(b) non-ring	Q_{mas} 1/2	
BO4	(a) (1B, 3Si)	Gaussian	Amplitude, position, apodisation of theroretical lineshape, quadrupolar frequency were refinable.
	(b) (0B, 4Si)	Gaussian	Asymmetry parameter (η_q) were fixed.

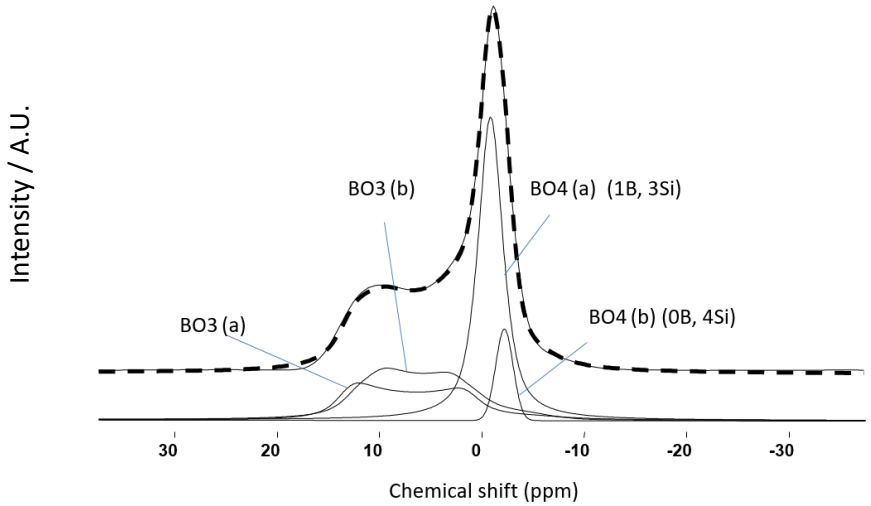

Figure 3.11. ^{11}B MAS-NMR example fits.

^{29}Si Theoretical calculations: Accurate spectral deconvolution of the ZnCa MW base glass series discussed in Chapter 5 required an a-priori prediction of the expected Q_n specie percentage contribution. These predictions were aided by the pre-acquisition of the B specie contribution from ^{11}B spectral deconvolution. The amount of alkali oxide (mole fraction) associated with the silicate network (R_2O (Si)) was determined by a modification of the equation from El-Damrawi *et al.* (1993), where all terms relate to the molar fraction:

$$R_2O(Si) = R_2O - \{R_2O[BO_4(B_2O_3)] + R_2O[Al_2O_3]\} \quad [3.16]$$

where R_2O is the total alkali content of the glass, $R_2O[BO_4(B_2O_3)]$ is the amount of alkali associated with the borate network and $R_2O[Al_2O_3]$ is the amount of alkali associated with Al_2O_3.

Accounting for the charge neutrality of the tetrahedral coordinated Zn content, gives Equation 3.17:

$$R_2O + CaO\ (Si\ /\ Zn) = (R_2O + CaO) - \{R_2O[BO_4(B_2O_3)] + R_2O[Al_2O_3]\} \quad [3.17]$$

Where R_2O + CaO (Si / Zn) is the amount of alkali/Ca associated with the Si/Zn network forming tetrahedral. Note the assumption that one mole of Al_2O_3 /B_2O_3/ ZnO is associated with one mole of alkali (R_2O)/CaO. The amount of network forming Zn tetrahedra left uncharged, and therefore representing Zn octrahedra (ZnO_6) performing a network modifying role, is:

$$ZnO_6 = ZnO - [3.17] \quad [3.18]$$

The fraction of Q3 is given by:

$$Q3 = [3.17] - SiO_2 \quad [3.19]$$

Therefore, the fraction of Q4[X] predicted (where X= network forming Al, B or Zn), inclusive of the dual network forming/modifying role or Zn, is:

$$Q4[X] = \frac{SiO_2 - [3.19]}{SiO_2} \qquad [3.20]$$

All predictions are noted in Table. 5.5 (Chapter 5) alongside the experimental results for an effective comparison.

^{29}Si Spectral fitting: Normalized, background-subtracted spectra were fitted with a combination of Gaussian line profiles as shown in Figure 3.12, alongside the maximum boundary conditions (Table 3.6). The boundary conditions for the peak position and FWHM were imposed based on the literature (Table 3.7), however, particular attention was paid to Engelhardt (1985 & 1987), Bunker *et al.* (1990), Holland *et al.* (2007), Goswami *et al.* (2008) and Angeli *et al.* (2012) due to the similarities in glass compositions. No conditions were placed on the amplitude, as this was compared to the theoretical predictions, which allowed for the omission of outliers. A total of ten fits were applied with different boundary conditions (within the bounding maximum), with the most reasonable fit, based on comparisons with the theoretical predictions, selected as being the most representative. Quantification of Q speciation was provided from the integral of each Gaussian, calculated using the DMFit software. Experimental uncertainties for each fit and for each Gaussian line profile were calculated from the standard deviation of the ten fits (excluding outliers).

Due to the nature of ^{29}Si spectra obtained from the seven-component ZnCa MW base glasses discussed in Chapter 5, which were relatively complex compositions in comparison to those from the literature listed in Table 3.9, it was difficult to identify pure Q_4 contributions, and in some cases, pure Q_3 contributions. Hence, the combined Q_4 & $Q_4(BO_3)$ and $Q_4(X)$ & Q_3 Gaussians line profiles were applied (where X = Al, B & Zn network formers/intermediates) (Fig 3.12). Section 3.4 - Appendix II describes the ^{29}Si NMR spectral deconvolution parameters in detail.

Table 3.6. Gaussian line profiles and maximum boundary conditions used to deconvolute the ^{29}Si spectra.

	Maximum boundary conditions	
Gaussian	Chemical shift peak position (ppm)	FWHM (ppm)
Q_4 & $Q_4(BO_3)$	-105 > p > -110	10.5 < FWHM < 17
$Q_4(X^*)$ & Q_3	-85.5 > p > -105	10.5 < FWHM < 17
Q_3	-85 > p > -95	10.5 < FWHM < 17
Q_2	-80 > p > -90	10.5 < FWHM < 17

* X = Al/B/Zn

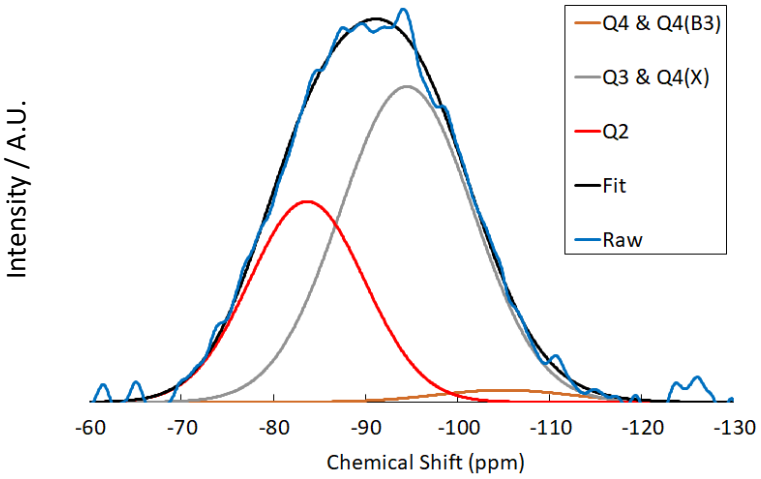

Figure 3.12. ^{29}Si MAS-NMR raw spectra including example fit and spectral de-convolution.

Table 3.9. Table of NMR literature line fits for deconvolution of ^{29}Si spectra. Grey shading represents the most appropriate to this study.

Reference	Glass Oxide mol. %	Q4(Si)		Q4(X) (X = B, Al)		Q3 (Si) & Q3(B)*		Q3	Q2	Combined peak Chemical shift (ppm)	Comments
		Chemical shift (ppm)	FWHM (ppm)	Chemical Shift (ppm)	FWHM (ppm)	Chemical Shift (ppm)	FWHM (ppm)	Chemical Shift (ppm)	Chemical Shift (ppm)		
Angeli et al. (2012)	63Si-17B-17Na-3Cs	-	-	-100 Q4 & Q4-BO3	-	-90 Q3 & Q4-BO4	-	-	-	-	-
Backhouse et al. (2019)	Aluminoborosilicate	-100	-	-	-	-90 Q3 & Q4(X)	-	-	-	-	X = B, Al
Bunker et al. (1990)	-	-	-	same as Angeli et al. (2012)	-	same as Angeli et al. (2012)	-	-	-	-	-
Dhara et al. (2016)	50Si-30B-20Na	-	-	-	-	-	-	-100 (35%)	-91 (65%)	-97	Insufficient Na to charge balance large Q3 & Q2 contributions
	45Si-27B-18Na-10Ba	-	-	-	-	-	-	-96 (28%)	-86 (72%)	-	Insufficient Na to charge balance large Q3 & Q2 contributions
Duddridge et al. (2003)	MW 2.4-11.98 Al/Bi/La	-	-	-98 → -104 Q4(B) (-100 fixed mainly) -94 → -96 Q4(Al)	-	-	-	-77 → -89 (La & Bi content)	-	-	Al/Bi/La investigated individually
Engelhardt (1985)†	30.3Ca-3Al-66.7Si	-	-	Q4(2Al) (18%)	-	Q3(Si) (82%)	-	-	-	-87	Vaguely similar ratios to ZnCa 0:100, Just % contribution to the Q speciation
	26.3Ca-7Al-66.7Si	-	-	Q4(2Al) (40%)	-	Q3(Si) (60%)	-	-	-	-94	Just % contribution to the Q speciation
Engelhardt (1987a)	Aluminosilicate	-	-	-97 → -107 Q4(1Al)	≤ 20	-	-	-	-	-	-
	Aluminosilicate	-	-	-93 → -99 Q4(2Al)	≤ 20	-	-	-	-	-	-
Mägi et al. (1984)	60+ silicates	-105 → -120	-	-	-	-91 → -101	-	-90 → -101	-74 → -94	-	-
Goswami et al. (2008)	Li-Zn-silicates	-110	-	-	-	-91	-	-	-80	-	-
Kirkpatrick et al. (1985)†	Aluminosilicate	-	-	-97 → -107 Q4(1Al)	≤ 20	-	-	-	-	-	-
	Aluminosilicate	-	-	-93 → -102 Q4(2Al)	≤ 20	-	-	-	-	-	-
Holland et al. (2007)	MW 12 Zn	-111	17	-97 Q4(B)	15	-	-	-	-	-	Self extrated data
	MW 12 Al	-	-	-95 Q4(Al/B)	15	-88	5	-	-	-	Self extrated data
Parkinson et al. (2007)	MW 10 Cs/10 Mg	-	-	-93 Q4(B)	20	-80	20	-	-	-	-
	MW 9.66 mol. % Cs	-	-	-	-	-	-	-	-	-90	No deconvolution
Soleilhavoup et al. (2010)	x=0.28-0.73 in xB-(1-x)Si	-	-	~-110 Q4(BO3)	24	-	-	-	-	-	-
	Pure Silica	-112	-	-	-	-	-	-	-	-	-

*Cannot resolve Q3(Si) & Q3(B)

†The poor resolution allowed no clear decision as to whether the contribution of a third component is significant

3.2.4 Inductively-Coupled Plasma Optical Emission Spectroscopy (ICP-OES)

ICP-OES is an elemental analysis technique, which can measure the concentration of elements in aqueous solution down to approximately 0.01 ppm. This spectroscopic technique uses inductively coupled plasma (argon source) to produce excited atoms that can be identified by their characteristic radiative emission. Atoms are excited through two interactions: inelastic scattering of an electron off an atom (M) (Equ. 3.21) and the radiative recombination of an ion (M^+), with an electron, which leads to the emission of photons (hv) (Equ. 3.22) characteristic of each element, where the intensity of the total measured emission is proportional to the elemental concentration in solution (Hieftje 2007).

$$e + M \rightarrow M^* + e \qquad [3.21]$$

$$M^+ + e \rightarrow M^{+*} + h\nu \qquad [3.22]$$

The photons pass though axial and radial windows to broaden the wavelength envelope, which then pass through the spectrometer and are finally received upon charge-coupled devices (CCDs). Using a computer, the photons are essentially converted to the elemental concentration in solution by measuring the intensity of the characteristic emission peaks against a set of known calibration standards. A schematic of an ICP-OES is shown in Figure 3.13.

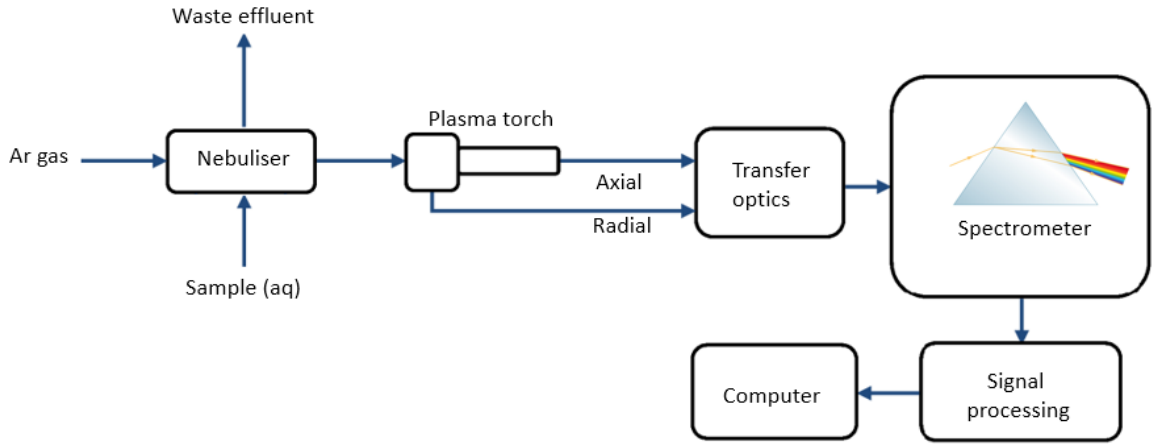

Figure 3.13. Schematic of an ICP-OES, adapted from Thermo Fisher Scientific (2012).

ICP-OES analysis was performed by the author at the MIDAS centre at TUoS using a ThermoFisher iCAPDuo 6300 instrument.

ICP-OES was used throughout Chapters 4 – 9. Multi-element calibration standards were prepared using high quality Fluka elemental standards, diluted in 1% HNO_3 solution. Standards were made

according to the dissolved elements of interests, alongside elements present in the original leaching solution, such as groundwater compositions.

3.2.5 Geochemical modelling

The geochemical modelling package PHREEQC version 3 was used to calculate the saturation indices of various secondary phases in leachates during glass dissolution. This technique probed the possible formation of such secondary phases and aided phase identification from SEM, EDS and XRD analysis. The concentration of elements from ICP-OES analysis were used as input, alongside the pH and experimental conditions to calculate a range of possible phases saturated in solution according to the Lawrence Livermore National Laboratory (LLNL) database. Geochemical modelling was performed in Chapters 5 and 6.

3.2.6 Differential Thermal Analysis (DTA)

Differential thermal analysis can be used to determine important thermal properties of glass, such as the glass transition temperature (T_g), fictive temperatures, the bulk crystallisation temperature, liquidus temperature of crystals and temperatures of minor crystalline phase development. DTA works by linearly heating a small amount of powdered glass sample (5-50 mg) and an inert reference material in the same furnace. Two identical thermocouples are used, one for measuring the temperature of the sample and the other for the reference material. The differential temperature between the two materials is plotted against the increasing temperature. A difference in the measured temperatures, in the form of exothermic or endothermic peaks signify events taking place within the sample under investigation, on the premise of an inert reference material. Exothermic peaks display the heat released upon crystallisation and endothermic peaks are, in the majority of cases, the result of the change in specific heat at the glass transition temperature. Other endothermic peaks at higher temperatures can be attributed to the melting of crystals formed during heating. It should also be noted that multiple peaks can be seen which can imply multiple crystal phase assemblages and, in rarer cases, multiple glass transition temperatures if the glass is non-homogenous.

It should be noted that the value of T_g obtained by Differential Scanning Calorimetry (DSC) or DTA is not as exact value, but is a function of the heating rate. T_g shifts to higher temperatures with increasing heating rate, therefore to maintain consistency with different glass samples the same heating profile should be adhered to in all DTA.

Experimental Parameters applied: DTA was performed on a TA SDT Instrument Q600 v20.9 to determine the glass transition (T_g) temperatures of the ZnCa MW base glasses discussed in Chapter 5. Data was collected over the temperature range 22 to 1300 °C at a rate of 10 °C /min. A single ramping profile was deployed. The glass transition temperature was determined by the extrapolation of the tangents at the points of interest.

3.2.7 Glass density measurements

Glass densities were ascertained using helium pycnometry, which works by the principle of inert gas displacement. Changes in the volume of glass powder (< 75 µm, < 1 g), calculated by the pressure of a filled and discharged sample chamber, was divided by the sample mass to obtain the density. Measured densities of all glass compositions are provided in Tables 3.2 & 3.3.

3.3 Glass dissolution methodology

3.3.1 Glass sample preparation

Three types of sample were prepared to meet the requirements of the dissolution investigations:

1. **Powders** were produced by manually crushing pre-cut glass ingots in an impact mortar and pestle. The crushed glass was sieved to obtain 75-150 µm diameter particles. Ultrasonic washing in isopropanol (six repetitions of three minute bursts) was performed to remove fine fragments of glass (typically <5 µm diameter, as shown in Figure 3.14) from the particles. Note that glass was spread evenly (a thin layer 2-3 mm deep) on the bottom of a large beaker and covered to a depth of 5-7 mm of isopropanol from the surface of the glass powders. It should be noted that even with repeated washing, it was not possible to remove all fine fragments, however a significant proportion were successfully removed, as shown in Figure 3.15. After washing, particles were dried in an oven at 90 °C for one hour, which was determined to be sufficient to remove all isopropanol from the glass. Note that initial surface roughness, cracks and pitted features were observed on the surface of glass particles (Fig. 3.15).

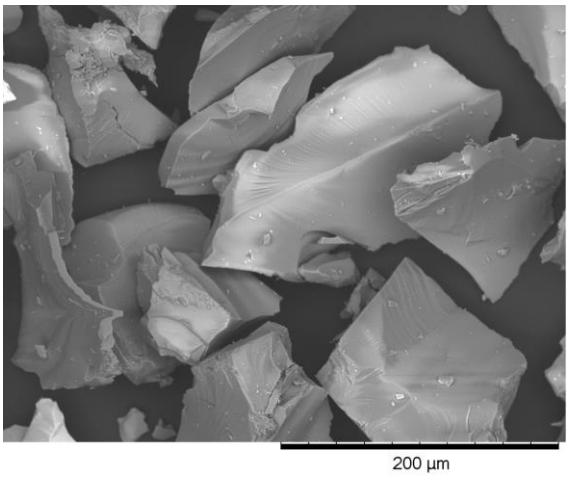

Figure 3.14. Fine-fragments (<5 µm diameter) adhered to crushed glass particles pre-washing (75 – 149 µm diameter).

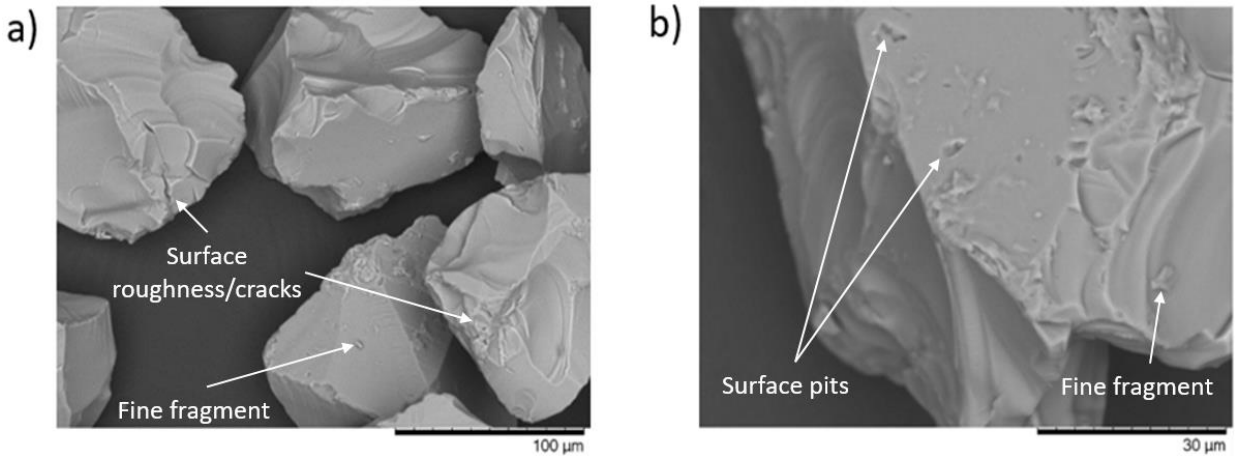

Figure. 3.15. A significant reduction in the quantity of fine-fragments (<5 µm diameter) adhered to crushed glass particles post-washing (75 – 149 µm diameter); a) overview displaying surface roughness/cracks and remaining fine fragments; and b) examples of surfaces pits and remaining fine fragments.

2. **Monoliths** were produced from as cast glass ingots. Individual MCC-1 monolith samples were sectioned and cut to the required dimensions (10 x 10 x 5 mm) using a Buehler IsoMet low-speed saw with a petroleum lubricated Buehler Series 15 diamond wafering blade. Monoliths were carefully prepared to avoid 'corner snagging', the loss of a perfect corner due to tearing caused by the combined weight of the ingot and saw arm (essentially gravity). A corner-snagged monolith (shown on the right in Figure 3.16) has the potential to introduce minor inaccuracies in the geometric measurement of the surface area of a monolith, important for dissolution rate determination, and can provide sites for preferential dissolution. After cutting, all six surfaces of the monoliths were ground using SiC abrasive paper and isopropanol lubricant using 400, 800 and 1200 grit papers, and subsequently polished using diamond suspension with 6, 3 and then 1 µm. Finally, the monoliths were ultrasonically washed in isopropanol (three repetitions of three

minute bursts) and stored in a desiccator until use. Monoliths for VHT and VHT-MCC-1 hybrid tests were prepared in an identical fashion, but with the dimensions 10 x 10 x 1.5 mm.

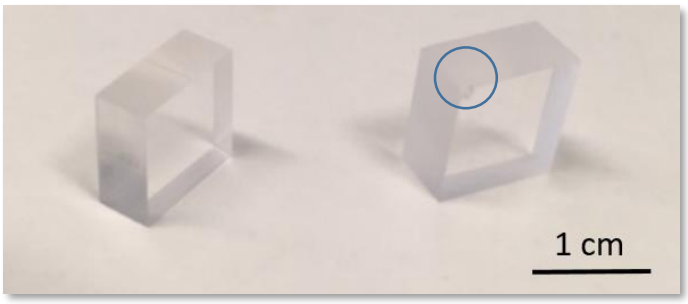

Figure 3.16. Left: Example of a fully prepared MCC-1 glass monolith (ground and polished). Right: example of a corner-snagged MCC-1 monolith, with the corner snag highlighted in the blue circle.

3.3.2 Single Pass Flow Through (SPFT) Methodology

The Single Pass Flow Through (SPFT) method (ASTM 2014, C1662-10) is a dynamic dissolution test in which a number of variables are well constrained, which allow for precise and consistent measurements of dissolution rates in dilute conditions. Such a methodology is useful for the measurement of initial dissolution rates, which in turn can be used to determine rate parameters such as those described in Chapter 2 (Equs. 2.6 & 2.7). Ascertaining rate parameters is essential for predictive models of glass corrosion behaviour (Neeway *et al.* 2017).

The SPFT method is described as follows; fresh solution flows at a constant rate and temperature (controlled by a syringe pump and oven, respectively) through a reaction vessel containing a sample (in this Thesis, powdered glass with a size fraction 75-150 µm diameter), as shown in Figure 3.17. The attainment of dilute conditions prevents the saturation of aqueous species in solution, which enables the sample to dissolve at its initial rate. The key experimental parameter in SPFT investigations is the ratio between the pump flow-rate (q) and the total crushed glass sample surface area (S), often referred to as $\log_{10}[(q/S) / \text{m s}^{-1}]$. Where S, the surface area, is calculated from:

$$S = \frac{3m}{\rho r_0} \qquad [3.23]$$

where m is the mass of the glass sample (g), ρ is the measured glass density (g m^3) and r_0 is the average particle radius (m) based on the geometric surface area (assuming glass spheres with an average radius of 56.25 µm). Investigations, known as a 'q/S sweep', performed at various $\log_{10}[(q/S)]$ values, are used to determine when dilute conditions are achieved, enabling the accurate measurement of

the intrinsic dissolution rate. Further information regarding the development and utilisation of the SPFT method can be found in 3.4 Appendix I and the following key literature references: McGrail and Peeler (1995), McGrail *et al.* (1997), Abraitis *et al.* (2000), Pierce *et al.* (2008), Icenhower and Steefel (2013), PNNL-23503 (2014) and Cassingham *et al.* (2015).

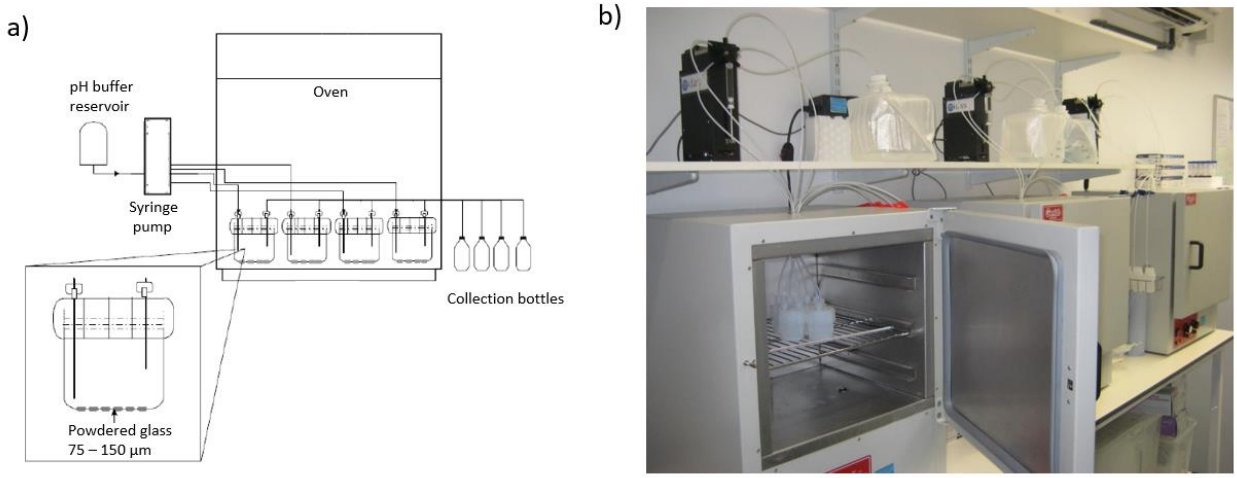

Figure 3.17. The SPFT set-up: a) Schematic of the apparatus, adapted from Pierce *et al.* (2010); and b) the laboratory SPFT bank at TUoS (2015-2017) (See also 3.4 Appendix I - SPFT).

In Chapter 4 of this Thesis, pump flow-rates used in SPFT experiments were varied from 10-80 ml d^{-1} and the mass of the ISG was varied between 0.29-1 g to investigate ten q/S ratios. All tests were performed on duplicate samples in 60 ml Teflon vessels, and quoted results correspond to the average of the duplicate data sets. It should be noted that Teflon vessels are permeable to carbon dioxide which can affect the pH and reaction path for some glass compositions (Xing & Pegg 1994), however the pH effect is assumed negligible in these SPFT tests as the buffered solution should negate such effects. The 'q/S sweep' was performed at 40 °C and pH(RT) 9 only (Chapter 4), which was sufficient to establish suitable q/S ratios to determine dilute conditions and hence ascertain forward rate measurements under different experimental conditions. Experiments were conducted at 40, 50 and 70 °C and pH(RT) 4.5, 5.5, 7.0, 9.0 and 11.0 (a description of the buffered solutions used to maintain these conditions is provided in Section 3.3.7) to ascertain the rate law parameters described by the Transition State Theory (TST) Equation (Equ. 2.6 & 2.7, Chapter 2).

Effluent samples were collected at regular intervals and the flow-rates were determined gravimetrically. The leachate solution was acidified with 1 vol. % ultrapure concentrated HNO_3 to avoid precipitation of secondary phases prior to elemental concentration analysis. The elemental release to solution reported in Chapter 4 was measured by analysing effluent solution for Si, B, Na, Ca and Al

concentrations using ICP-OES (ThermoScientific iCAPDuo6300, as described in Section 3.2.4). Boron is typically used to track the corrosion progress in most dynamic and static glass dissolution tests because it is highly soluble and is not usually retained in any alteration layer/product (Scheetz *et al.* 1984). However, in SPFT experiments, where dilute conditions are met at high flow-rates, Si can also be assumed to be an indicator of glass dissolution (Jollivet *et al.* 2012, Inagaki *et al.* 2013). The use of alkali metals to track dissolution progress is not recommended in SPFT investigations (ASTM 2018) because they may be released faster (due to the interdiffusion of water molecules and alkali) than the rate at which the connected glass network (composed of the network forming elements – Si & B) is congruently dissolving, under certain test conditions (See section 2.3.1). The Na data, therefore, is included in Chapter 4 for completeness.

All experiments were performed until the release of elements, and subsequent normalised B, Si, Na, Ca and Al dissolution rates, had attained steady-state conditions. Steady-state conditions were defined, in accordance with the ASTM standard and Neeway *et al.* (2018), as having at least three dissolution rate measurements near the end of the test (to eliminate the influence of dissolving fine fragments attached to the glass particles at early stages) that did not deviate by more than 15 % from their mean value, and where the sample had lost no more than 30 % of its original surface area calculated from the surface area correction model developed by McGrail *et al.* (1997) (explained shortly (Equ. 3.26)). The mean dissolution rate from ≥ 3 measurements at steady-state for each test was then recorded.

Some experiments were purposely set up for a longer test duration of > 100 days to provide insight into the maintenance of steady-state dissolution conditions over longer time periods and the surface morphology/features of corroded glass particles.

Dissolution rates were calculated according to Equation 3.24, where r_i represents the normalised dissolution rate of element *i* (g m^2 d^{-1}), where *i* is Si, B, Na, Al, Zn, Ca or Sr, C_i the concentration of element *i* in the effluent solution (mg L^{-1}), $C_{i,o}$ the background concentration of element *i* from the input buffer solution (mg L^{-1}), *q* the solution flow-rate (m s^{-1}), f_i the mass fraction of element *i* in the glass (unitless) and S the effective surface area of the powdered glass sample (m^2). Note that S changes throughout the duration of the experiment as the glass dissolves.

$$r_i = \frac{(C_i - C_{i,o}) \bullet q}{f_i \bullet S} \qquad [3.24]$$

The parameter f_i was calculated by:

$$f_i = mass_i\% \bullet \left(\frac{mol_i}{mol_{oxide}}\right) \bullet \left(\frac{MW_i}{MW_{oxide}}\right) \qquad [3.25]$$

Where $mass_i\%$ is the mass% of element *i* oxide in the glass, mol_i is the molar quantity of element *i* in the oxide, mol_{oxide} of the number of moles of oxide, MW_i is the molecular mass of element *i* (g mol^{-1}) and MW_{oxide} is the molecular mass of the oxide (g mol^{-1}).

A surface area correction model developed by McGrail *et al.* (1997) was applied to calculate the change in S throughout the experiment. This correction determined the mass of glass m_j (g) that remained at each time interval (*j*):

$$m_j = m_0 - \frac{1}{f_i}\left[\sum_{k=1}^{j-1} q_k C_{k,i} \Delta t_k + q_j C_{j,i} \frac{\Delta t_j}{2}\right] j \geq 1 \qquad [3.26]$$

where m_0 is the initial mass of the glass (g) and the summation term represents the accumulated mass loss from time step *k*=1 to time step *j*-1, calculated from the concentration of B (C_B). The second term (in square brackets) represents the average total mass loss from time step *j*-1 to *j*. Hence, the surface area at time point *j*, S_j (m^2), can be calculated by the following (applied in Equation 3.24 to calculate dissolution rates):

$$S_j = \frac{3}{\rho r_0} m_0^{1/3} m_j^{2/3} \qquad [3.27]$$

Modifications to the rate data due to the application of the surface area correction model (also known as the shrinking core model) is demonstrated in Chapter 4, 4.5 Appendix II & III.

Determination of the experimental uncertainty of the dissolution rates accounts for the uncertainty associated with each parameter described in Equation 3.24. For these uncorrelated random errors, the standard deviation of a function $f(x_i)$ is given by:

$$\sigma_f = \sqrt{\sum_{i=1}^{n} \left(\frac{\partial f}{\partial x_i}\right)^2 \sigma_i^2} \qquad [3.28]$$

where σ_f is the standard deviation of $f(x_i)$, x_i is the parameter pertaining to element *i* and σ_i is is the standard deviation of parameter σ_i. Substituting Equation 3.24 into Equation 3.28, and using a relative error, $\hat{\sigma}_{r_i} = \frac{\sigma_{r_i}}{r_i}$ gives:

$$\hat{\sigma}_{r_i} = \sqrt{\frac{\left(\hat{\sigma}_{C_{i,S}} C_{i,S}\right)^2 + \left(\hat{\sigma}_{C_{i,b}} C_{i,0}\right)^2}{\left(C_{i,S} - C_{i,0}\right)^2} + \hat{\sigma}_q^2 + \hat{\sigma}_{f_i}^2 + \hat{\sigma}_S^2} \qquad [3.29]$$

from which the experimental uncertainty on r_i can be derived. Relative errors of 10%, 10%, 3% and 15% were ascribed to C_i, $C_{i,o}$, f_i and S respectively and errors between 3-5 % were ascribed to q values based on gravimetric measurements.

In Chapter 5, no *q*/S sweep was performed, thus the SPFT experiments were performed at pH(RT) 9 and 40 °C (buffered by TRIS) at a flow-rate to surface area ratio of $\log_{10}[(q/S) / m\ s^{-1}] = -6.78$ only. Such a decision was deemed feasible as a 'q/S ratio' (of -6.78 m s^{-1}) is suggested to be sufficiently fast to maintain dilute conditions based on the SPFT investigation of the International Simple Glass reported in Chapter 4 (making the assumption that the dissolution behaviour of the simple ZnCa glasses investigated in Chapter 5 would be similar) and from the literature from similar simple glass compositions (McGrail *et al.* 1997 & 2000, Pierce *et al.* 2010, Backhouse *et al.* 2018, Neeway *et al.* 2018). The SPFT results reported in Chapter 5 are *largely* based on the Si release, which under Stage I dissolution is most likely to represent the initial dissolution rate. The normalised dissolution rates of element *i* (g m^2 d^{-1}), where *i* is Si, B, Na, Al, Zn and Ca were also obtained and analysed.

In Chapter 8, experiments were performed at pH(RT) 7, 9 (buffered by TRIS) & 11 (set by LiCl-LiOH) at 40 °C on ISGI and ISGO at a flow-rate to surface area ratio of $\log_{10}[(q/S) / m\ s^{-1}] > -7.0$. The flow-rate to surface area ratio was selected based on the same reasoning described above. The normalised dissolution rates of element *i* (g m^2 d^{-1}), where *i* is Si, B, Na, Al, Sr and Ca were obtained.

3.3.3 Product Consistency Test B (PCT-B)

The Product Consistency Test (PCT) is a static, internationally defined (ASTM C1285-14 (ASTM, 2010)) powdered leaching test to assess the chemical durability of hazardous and nuclear glass/glass ceramic wasteforms. The basic set-up is shown in Figure 3.18. The powdered nature of these tests was developed to probe greater reaction progress, due to the greater exposed surface area, thus

accelerating the onset of saturated aqueous systems. The ASTM standard defines two methods: the PCT-A has tightly constrained experimental parameters (7 days, 90 °C , UHQ water only), whereas the PCT-B allows for much greater flexibility in the experimental parameters and is much more commonly applied in the literature.

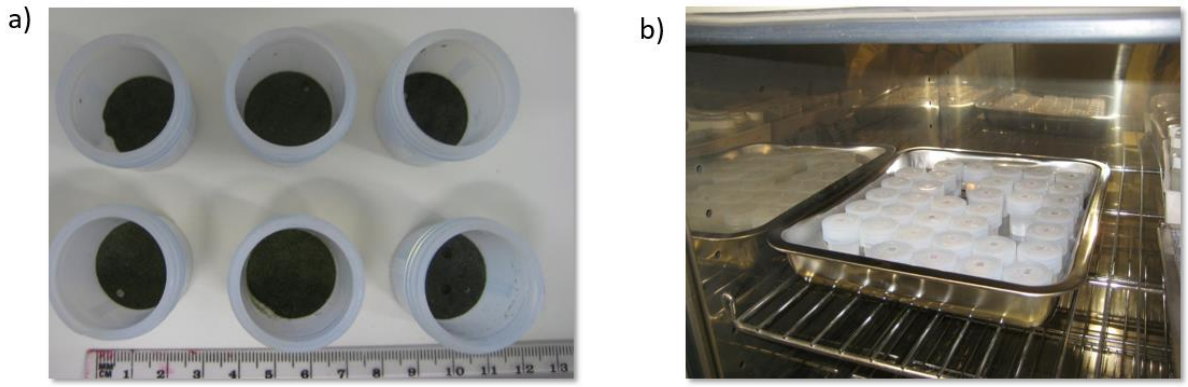

Figure 3.18. The PCT-B set-up: a) glass powders in their vessels post experimentation; and b) a set of PCT-B experiments within an oven.

The PCT-B experiments described in Chapters 5, 6 and 8 were all performed in duplicate in UHQ water at 90 ± 2 °C (50 ± 2 °C for Chapter 7, in groundwater solutions) with a surface area of total particles to solution volume ratio (SA/V) = 2,000 m^{-1}, in 15 ml flat-bottomed Teflon vessels. It should be noted that Teflon vessels are permeable to carbon dioxide which can affect the pH and reaction path for some glass compositions (Xing & Pegg 1994). Experiments were prepared on a laboratory bench-top and were conducted in an oven. Approximately 1 g of crushed glass particles (75-150 µm diameter) were used, although the exact mass varied based on the measured density of each glass composition to satisfy the required SA/V ratio. 10 ml of UHQ was used. Throughout the experimental duration, the vessel lids were tightened by hand at regular intervals to negate the effects of solution loss. Duplicate samples were removed from the oven (i.e. sacrificed) at 1, 3, 7, 14, 28 and 35 days, where ~8 ml of leachate solution was taken for elemental analysis by ICP-OES (see Section 3.2.4) and 1 ml of leachate was used to ascertain the pH. These timepoints were sufficient to probe the transition and residual rates (Stage II) for most glass compositions (see Chapters 5 and 8), although some experiments were extended to 112 days to provide comparisons with specific literature (see Chapter 6).

The leachate solutions for ICP-OES analysis were filtered through 0.22 µm polyethersulphone (PES) syringe filters and then acidified with 1 vol. % HNO_3 acid to avoid precipitation of secondary phases prior to elemental concentration analysis. Vessels were weighed at each time point to determine the amount of solution evaporated during experimentation, so that an accurate SA/V ratio could be extracted, to calculate the normalised mass loss of element, *i*, (NL_i) in g m^{-2}:

$$NL_i = \frac{(C_i - C_{i,b})}{f_i \cdot (SA/V)} \qquad [3.30]$$

where C_i is the average concentration of *i* in solution in the, in mg L^{-1}; $C_{i,b}$ is the average concentration of *i* in the blank tests, in mg L^{-1}; f_i is the mass fraction of *i* in the glass monolith and SA/V is the surface area to volume ratio of the glass monolith, in m^{-1}, where SA is based on the geometric surface area (assuming glass spheres with an average radius of 56.25 µm). Experimental uncertainties were calculated in a similar manner to Equations 3.28 & 3.29. Dissolution rates were calculated from appropriate linear regressions, whereby uncertainty in the rate was calculated from a chi-squared fit.

Post experimentation, the remaining glass powders were dried at 90 °C for one hour and stored in small centrifuge tubes for analysis by XRD and SEM-EDS to detect alteration products.

3.3.4 Materials Characterisation Centre Test-1 (MCC-1)

The MCC-1 test is a static, internationally defined (ASTM C1220-98 (ASTM, 2014)) monolithic leaching test developed to assess the chemical durability of hazardous and nuclear glass / glass-ceramic wasteforms. The monolithic nature of these tests constrains the SA/V ratios to 10 m^{-1} and enables detailed investigations of the altered sample post-experimentation. Longer experimental durations are required to explore the different dissolution rate regimes compared to the accelerated PCT-B protocol.

The experiments performed in Chapters 5 & 6 were conducted with monoliths 10 x 10 x 5 mm in size, placed in UHQ water at 50 ± 2 °C at a SA/V of 10 m^{-1}. The monolithic SA was 400 ± 20 mm^2 and approximately 40 ml of UHQ was used; in most cases this was varied slightly according to the exact SA of the prepared monoliths. Each monolith was placed onto a PTFE Teflon basket in a 60 ml Savillex Teflon vessel. It should be noted that Teflon vessels are permeable to carbon dioxide which can affect the pH and reaction path for some glass compositions (Xing & Pegg 1994). Aliquots (~10 mL) of the leachate were taken from sacrificial duplicate samples for elemental concentration and pH analysis at 7, 14, 21, 31, 52, 95, 175, 360 and 540 days. The leachate solution was acidified with 1 vol. % ultrapure concentrated HNO_3 (after pH measurement) to avoid the precipitation of secondary phases prior to elemental analysis. The normalized mass loss, which represents the amount of glass dissolved, is also given by Equation 3.30. Experimental uncertainties and rates were calculated in a similar manner to the PCT and SPFT experiments, using Equations 3.28 and 3.29.

3.3.5 Vapour hydration test (VHT)

The Vapour-phase Hydration Test (VHT) method, defined by ASTM International (ASTM C1663-09, ASTM 2009), is used to study the corrosion of glass/glass ceramic wasteforms exposed to water vapour at elevated temperatures, with particular emphasis on secondary phase formation, alteration layer thickness and composition, elucidated from SEM/EDS and XRD analysis. Corrosion commences through a limited amount of condensed solution on the glass surface. Monolithic samples are suspended inside stainless steel test vessels with a pre-determined amount of solution placed at the bottom of the vessel, prior to placement in the oven at a temperature of over 100°C (to allow steam formation), as shown in Figure 3.19.

In Chapter 8 of this Thesis, VHT experiments were conducted at 100 ± 2 °C for 28 d with 0.06 mL (corresponding pressure 0.085 MPa) of granitic groundwater (used for consistency and prepared as described in Section 3.3.8). Monoliths 10 x 10 x 1.5 mm in size were used.

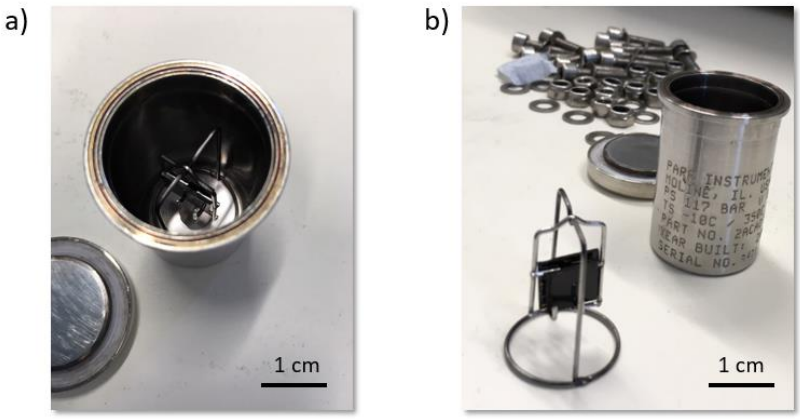

Figure 3.19. The VHT set-up: a) A glass monolith emplaced within the vessel with 0.06 ml of granitic groundwater; and b) a monolith suspended from stainless steel hangers, ensuring contact of the sample with water vapour on all sides.

3.3.6 VHT/MCC-1 Hybrid - The Cyclic Vapour Static (CVS) Test

In Chapter 8, it was decided to undertake a hybrid VHT/MCC-1 experiment, termed the Cyclic Vapour Static (CVS) test. This is a non-standard dissolution test based on similar approaches in the literature (Bates *et al.* 1982, 1984, Ait Chaou *et al.* 2010, Neeway *et al.* 2012). In this experiment, pre-VHT corroded samples (as described in Section 3.3.4) were exposed to MCC-1 dissolution for 55 d at 50 ± 2 °C in granitic groundwater. The monolithic SA was 200 ± 20 mm^2 and approximately 20 ml of granitic groundwater was used; in most cases this was varied slightly according to the exact SA of the prepared monoliths. These parameters were chosen to reflect what might be expected to occur in the event of a HLW glass container breach in a UK geological disposal facility; corrosion of a portion of the exposed

glass wasteform will likely initially proceed through interaction with water vapour, before full liquid granitic groundwater contact occurs (Andra 2005, Neeway *et al.* 2012) as described in Section 2.4.1 Chapter 2.

The experiments were prepared and performed anaerobically: preparation of solutions and sampling was performed in an anaerobic glove box (<2 ppm O_2), and the test vessels were placed in a container (Boast 2018) within the oven, with flowing $N_{2(g)}$ at all times, as shown in Figure 3.20. Some vessels also contained iron pieces to mimic the presence of stainless steel containers for HLW glass, however, these samples will not form part of this Thesis but were set up in an attempt to address future work in a parallel 720 d CVS investigation.

The time period between the termination of the VHT and commencement of the MCC-1 stage was limited by experimental preparation, hence, it can be assumed that no significant drying of the monoliths occurred between the VHT and MCC-1 stage. The significance of such a fusion of VHT and MCC-1 was to capture the expected temporal corrosion sequence in granitic geological disposal environments.

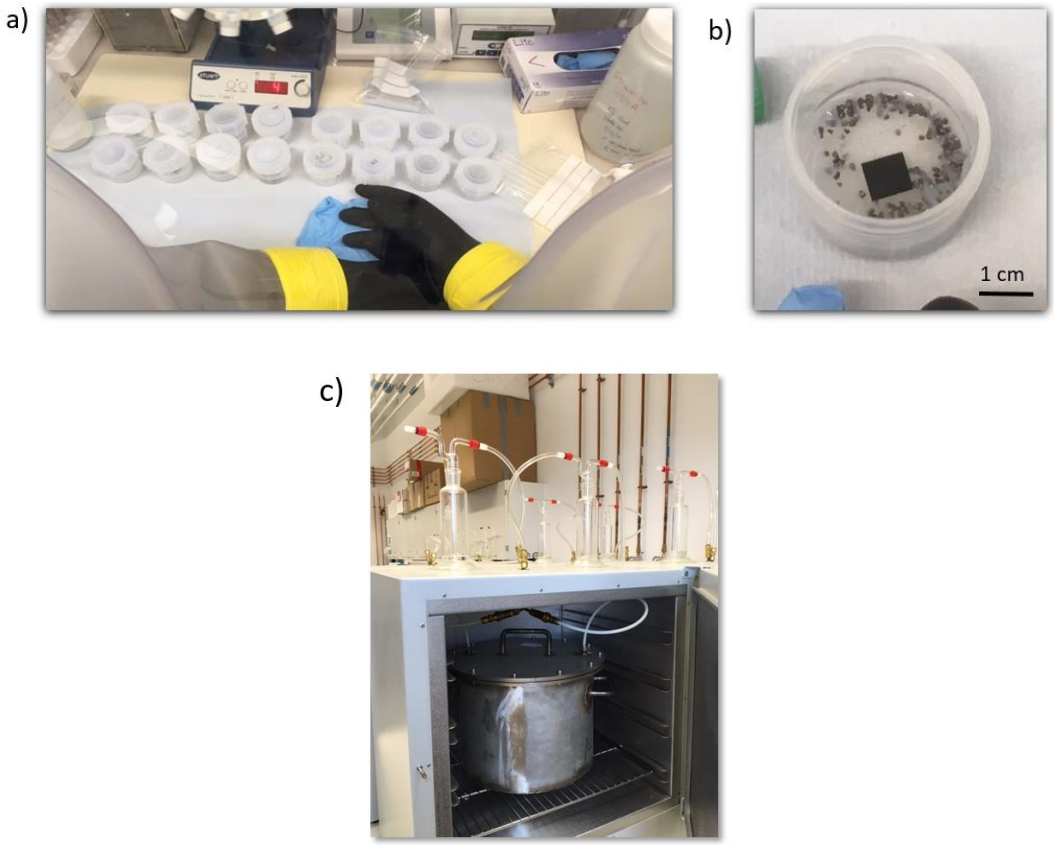

Figure 3.20. The VHT-MCC-1 hybrid (CVS) set-up. (a) preparation of the MCC-1 stage of the experiment under anoxic conditions within an anaerobic chamber; (b) MCC-1 stage preparation – note the iron turnings; c) the nitrogen flushed containers (known colloquially as 'bean-tins' (Boast 2018)) containing the MCC-1 vessels under experimentation.

3.3.7 Buffered leaching solutions

Acidic buffer solutions: In Chapter 4, acidic buffer solutions for pH(RT) 4.5 and 5.5 were prepared from 0.01 M HNO_3 added to ultra-high-quality (UHQ) water (18.2 $M\Omega cm^{-1}$), adjusted to the desired pH with 9.9×10^{-3} M and 1×10^{-2} M ammonium hydroxide (NH_4OH), respectively (Wellman *et al.* 2007). The UHQ water was produced by a Millipore Direct-Q (UV) 3 water purification system. Solutions were magnetically stirred throughout preparation (Fig. 3.21).

Alkaline buffer solutions: In Chapters 4, 5 and 8, alkaline buffer solutions for pH(RT) 7 and 9 were prepared from measured amounts of the organic tris hydroxymethyl aminomethane buffer (TRIS) (0.01 and 0.05M, respectively) added to UHQ water, and adjusted to the desired pH values with 15 M HNO_3. Solutions for pH 11(RT) were prepared from 0.01 M LiCl and UHQ water and were adjusted to the desired pH values with 1 M LiOH. Solutions were magnetically stirred throughout preparation (Fig. 3.21).

In Chapters 4, 5 & 9, the modelled pH(T) were calculated using the Nernst Equation, which were in agreement with the values reported in Pierce *et al.* (2008).

Figure 3.21. Preparation of acidic and alkaline buffer solutions.

3.3.8 Synthetic Groundwater Compositions

Three groundwater (GW) types, representative of three different generic geological disposal environments (granite, clay and saline) were prepared for the leaching experiments conducted in Chapters 7 & 8. Table 3.8 contains the targeted and analysed (by ICP-OES) compositions. The granitic solution was based on the anticipated groundwater at the Finnish geological disposal site (Gascoyne

2002) and was adopted in this Thesis to maintain consistency, noting that the chemical composition of expected UK granitic groundwater is similar. The clay solution was based on the anticipated Callovo-Oxfordian pore water (Vinsot 2008) at the French and Belgium geological disposal site and was adopted in this Thesis to maintain consistency. A generic saline solution was also used in accordance with Gascoyne (2002).

Table 3.8. Composition of the three groundwater-types to simulate generic geological disposal conditions. Parentheses denote analysed composition from ICP-OES (± 3 %) / measured pH values upon fabrication of groundwater solution (± 0.15).

Element	Granitic GW (mmol/L) (Gascoyne 2002)	Saline GW (mmol/L) (Gascoyne 2002)	Clay GW (mmol/L) (Vinsot 2008)
Na	2.8 (2.7)	140 (157.0)	55 (61.2)
K	0.1	2.1	1.1
Ca	0.5 (0.31)	19.9 (18.9)	7.5 (6.7)
Mg	0.2 (0.19)	0.4 (0.41)	5.7 (5.3)
Cl	2	180	50
HCO_3	2	2	-
SO_4	0.1	4	15
SiO_2	0.2 (0.00)	-	-
pH(RT)	8.2 (8.2)	7.7 (7.7)	6.5 (7.0)

Each of the groundwaters in Table 3.9 were prepared from specific amounts of reagents added to 1 L of UHQ at a maximum of three days before the commencement of an experiment to avoid carbonation. Each groundwater was mixed with a magnetic stirrer for approximately 30 minutes after preparation.

Table 3.9. Reagents used in the preparation for 1 L of each of the three groundwater-types.

Reagents	Granitic GW (g)	Saline GW (g)	Clay GW (g)
KCl	0.0074	0.16	0.082
Na_2SO_4	0.014	0.57	2.13
$MgCl_2.6H_2O$	0.041	0.081	1.16
$CaCl_2$	0.055	2.21	0.83
NaCl	0.035	7.59	1.46
$NaHCO_3$	0.17	0.17	-

3.3.9 pH measurements

All pH measurements were conducted at room temperature (~ 20 °C) using a Mettler Toledo LE422 probe with a Mettler Toledo Five Easy Plus reader, which was calibrated using Lovibond Water Testing (Tintometer Group) buffers at pH 4, 7 and 11. The pH measurements from anoxic experiments were measured within a nitrogen filled glovebox. Average pH values from duplicate samples were reported.

3.4 Appendix

I – SPFT

SPFT Pump set-up

This section provides in-house instructions for users operating the system deployable at The University of Sheffield. It attempts to; 1) aid the ASTM (2010) SPFT standard, which should be followed, particular for the cleaning pre- and post-experimentation and 2) simplify the Kloehn instruction manual.

SPFT experiments are based around an accurate pumping system. The pump in use is a Kloehn VersaPump 6 (V6); a programmable liquid metering device. It operates at a 48,000 step resolution over changeable mounted syringes with a volume capacity of 1, 5 and 10ml. Four or more pumps can be controlled and participate in two-way serial communication with a single computer. Each pump is connected to a six-way valve, in which two of these valve ports are connected to the syringe and the input solution. Therefore, there are four valves that can be used to pump solution into reaction vessels. Each pump has a signature address (/1, /2, /3 and /4, see back of pump), meaning that multiple different SPFT experiments can operate simultaneously and independently.

The pumps are controlled and communication between them and the computer is mediated through the terminal emulator and serial console PuTTY. The pumps accept command strings which are used to set the desired operation/constraints of the SPFT experiments, i.e. the appropriate flow-rates assigned to the four reaction vessels. The commands are inputted only once at the start of the experiment and control the desired flow-rates indefinitely until a command is manually entered to terminate the experiment upon completion.

To illustrate the control of the pumps, commands are given in the following sections: Initialisation start-up of SPFT pumps and Pump program commands. In essence, communication is via call and response between the inputted commands and the computer.

The Kloehn pumps are very accurate within < 1%, based on gravimetric measurements of collected solution. Inaccuracies usually arise from air bubbles in the system, which can arise from a number factors such as: 1) loose feedline connections; 2) loose syringe connection to the valve port; 3) loose vessel lids; 4) too long feedlines, whereby solution could flow (due to gravity) back into the solution reservoir or collection vessels. In all instances, feedlines should be as short as possible.

Note each valve letter has an associated computer command number (where o = the letter ‘o’ and not zero):

A = o1, B = o2, C = o3, D = o4, E = o5 and F = o6

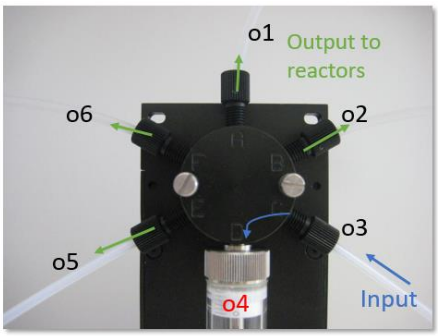

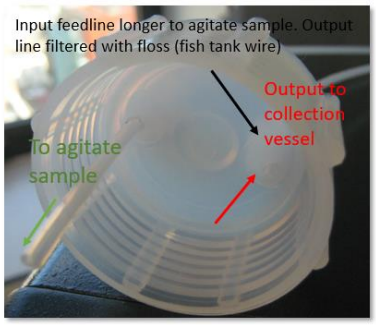

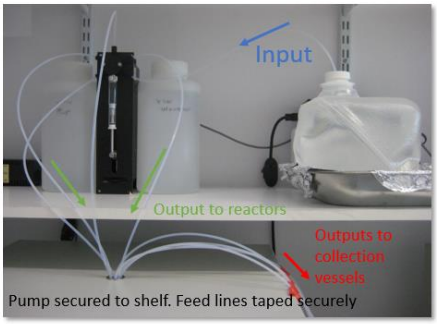

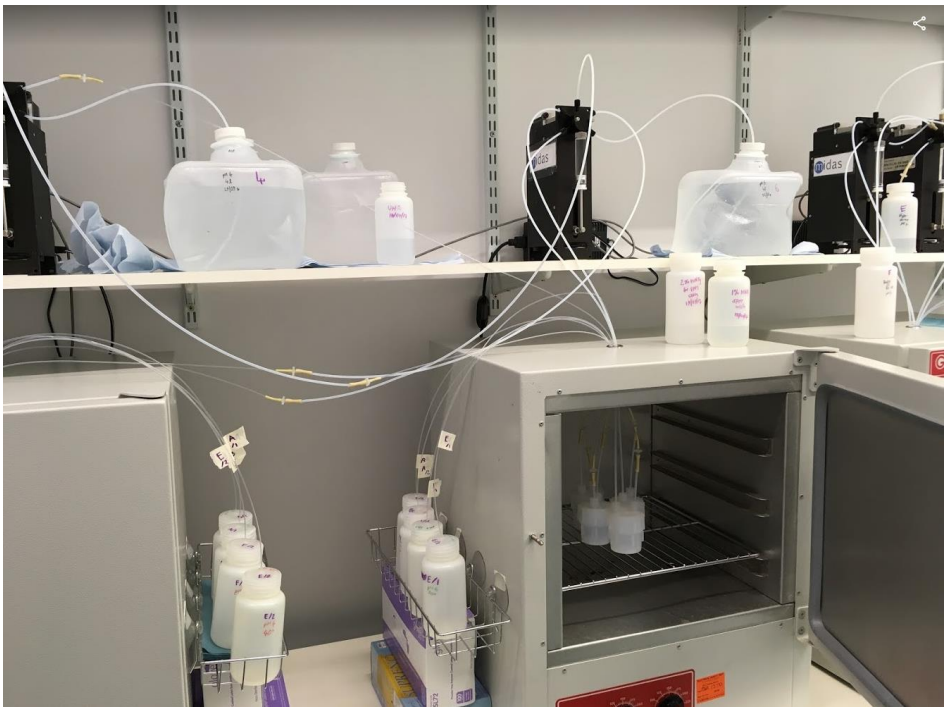

Initialisation of SPFT pumps

The blank PuTTY screen appears. Input the following black text followed by the return key. The green text is the immediate computer response. The red text are notes for the operator.

/1? Ascertaining syringe position for pump number 1. Change number accordingly for other pumps.

/0'0 Responds by saying that the syringe is at position 0 out of a possible 48,000 steps.

/1~v8 Command telling the pump that it is connected to a 6-way valve.
/0'8 Pump acknowledgement.

/1W4R Sets the syringe to initialization position.
/0 Pump acknowledgement.

/1? Ascertaining syringe position for pump number 1.
/0'553 Responds by saying that the syringe is at position 553 out of a possible 48,000 steps, i.e. initialization position. Note that the initialisation position is set by the first user. To change please consult the Kloen instruction manual. However, if below 1,000 steps, it is recommended to leave as set by the first user.

/input one of the commands listed below (including the ml/d commands) followed by the return key.

Pump program commands – experimental

Key

/2 – pump unit selection
:p - return position
o5 – moves valve clockwise to port o5
o-1– moves valve anti-clockwise to port o1
Axxxxx – aspirates xxxxx steps of solution from input reservoir (recommended connection port o3)
Mxxx – wait for xxx mill-seconds
Dxxx – dispsense xxx out of 48,000 steps of solution
Jp – jump to return position (after designated number of loops)
g – start loop
G351 – loop for 351 repetitions
R – ends the code

This will loop indefinitely until the user terminated the experiment by entering:

/2TR – terminates experiment

Note the order in which solution is aspirated and dispensed is to avoid 'sweeping' over the syringe attached to valve port o4. This is to avoid the introduction of air bubbles into the system. It is recommended that the users follows the below command 'order', such as o5 ➔ o6 ➔ o1 ➔ o2 then back through o-1 ➔ o-6 ➔ o-5.

5ml/d (5ml syringe) for /2

/2:p o-3 A48000 g o5D17M7501 o6D17M7501 o1D17M7501 o2D34M15001 o-1D17M7500 o-6D17M7500 o-5D17M7500 G351JpR

10ml/d (10ml syringe) for /1 and /3

/1:p o-3 A48000 g o5D17M7501 o6D17M7501 o1D17M7501 o2D34M15001 o-1D17M7500 o-6D17M7500 o-5D17M7500 G351JpR

10ml/d (5ml syringe) for /2

/2:p o-3 A48000 g o5D33M7458 o6D33M7458 o1D33M7458 o2D67M14917 o-1D34M7459 o-6D34M7459 o-5D34M7459 G176JpR

20ml/d (10ml syringe) for /1

/1:p o-3 A48000 g o5D34M7457 o6D34M7457 o1D34M7457 o2D67M14914 o-1D33M7457 o-6D33M7457 o-5D33M7457 G175JpR

40ml/d (10ml syringe) for /1 and /3

/1:p o-3 A48000 g o5D67M7443 o6D67M7443 o1D67M7443 o2D134M14885 o-1D67M7442 o-6D67M7442 o-5D67M7442 G88JpR

80ml/d (10ml syringe) for /1 and /3

/1:p o-3 A48000 g o5D134M7414 o6D134M7414 o1D134M7414 o2D268M14827 o-1D134M7413 o-6D134M7413 o-5D134M7413 G44JpR

120ml/d (10ml syringe) for /1

/1:p o-3 A48000 g o5D201M7384 o6D201M7384 o1D201M7384 o2D402M14767 o-1D201M7383 o-6D201M7383 o-5D201M7383 G29JpR

120ml/d (10ml syringe) for /3

/3:p o-3 A48000 g o5D201M7384 o6D201M7384 o1D201M7384 o2D401M14767 o-1D200M7383 o-6D200M7383 o-5D200M7383 G29JpR

240ml/d (10ml syringe) for /1

/1:p o-3 A48000 g o5D402M7296 o6D402M7296 o1D402M7296 o2D804M14591 o-1D402M7295 o-6D402M7295 o-5D402M7295 G15JpR

240ml/d (10ml syringe) for /3

/1:p o-3 A48000 g o5D402M7296 o6D402M7296 o1D402M7296 o2D803M14591 o-1D401M7295 o-6D401M7295 o-5D401M7295 G15JpR

Flush

/1go3A48000o5D11500o6D11500o1D11500o2D11500G31 - this code flushes ~70ml through, enough to flush/fill a 60 ml vessel.

II – ^{29}Si NMR spectral deconvolution parameters

Some authors have noted that the with the exception of Q4, the Q_n/Q_n(X) (where X = Al, B, Zn and/or Zr) species overlap significantly and a simple correlation of chemical shift and Q_n/Q_n(X) type for a silicate sample of unknown structure is likely to be risky. Hence, the chemical shift is a guide only. Several authors do not attempt structural deconvolution due to this ambiguity. However, as described in this thesis, a good theoretical structural basis and a good understanding of the ^{29}Si spectral parameters, alongside similar literature, can aid deconvolution and make it a valuable structural probe for more complex simple glasses such as the ISG and the ZnCa MW base glasses.

^{29}Si spectral parameters

Structural silicate units, represented by Gaussian peaks in the deconvolution of ^{29}Si specta are characterized by three main parameters: 1) **Chemical Shift** (line position), 2) **Intensity** (integrated peak area) and 3) **Linewidth** (FWHM). Each is closely related to the chemical structure of sample. Relationships between these parameters have been derived mainly from empirical correlations of experimental NMR data with known structural properties of selected silicates and aluminosilicates.

1. Chemical Shift (line position)

ISOTROPIC (*all Si atoms aligned with field, uniform*) – is the most important parameter. This reflects very sensitively the immediate structural surroundings of a silicon atom. What determines the shift is the number of Si atoms attached to silica tetrahedral via bridging oxygen atoms. Characteristic high-field shifts (more –ve ppm) are observed in solid silicates with increasing polymerization (larger Q_n) i.e. the shielding of the central Si atom increase along the sequence Q_0 ➔ Q_4.

More shielding of central atom ➔ higher chemical shift. More –ve ppm values.

Less shielding of central atom ➔ high chemical shift, but more +ve ppm values.

In glasses with Al, B, Zn and/or Zr the shifts are further influenced by the replacement of Si with Al, B, Zn and/or Zr in the Si tetrahedra framework. Low-field shifts are observed with an increasing number of attached Al, B, Zn and/or Zr atoms, compared to Si. Hence, not as –ve as pure Si Q_4 contributions. It is unclear as to which of the Al, B, Zn and Zr additions has a greater influence on the chemical shift. Therefore, at present, the effect on the chemical shift from these atoms is collective/additive, as denoted by the Q_4(X) contribution applied in this thesis and Angeli *et al.* (2012).

In addition to the degree of SiO_4 polymerization and Al, B, Zn and/or Zr substitution, cation effects and peculiarities in the geometry of the Si tetrahedra framework may also exert considerable influences on the

chemical shifts. Empirical correlations between isotropic chemical shifts and total cation-oxygen, mean Si-O distances and mean Si-O-Si bond angles have been found to be useful in characterizing such shift effects. These correlations predict high-field (more –ve ppm) on the ^{29}Si peaks with increasing cation-O bond strength, decreasing Si-O distances and widening of the Si-O-Si and Si-O-Al/B/Zn/Zr bond angle.

ANISOTROPIC (*orientation dependence of 3D shielding*) – if ^{29}Si atoms are not aligned with field there may be some variation of the chemical shift.

2. Intensity (integrated peak area)

Directly related to the number of corresponding silicon atoms present in the sample being investigated. Therefore, from the relative peak intensities the quantitative proportions of the various Si sites can be determined from the sample directly. For structural considerations, the relative number of Si atoms present in the distinct structural sites is mostly sufficient, which can be obtained directly from the normalized intensity ratios of the different signals of the spectrum. The intensity of partially overlapping peaks may be separated by deconvolution into individual Gaussian component peaks. If spinning sidebands occur in the MAS spectrum, their intensities have to be added to the intensity of the central peak. Absolute Si concentrations may be determined by comparing the intensities with those of a standard sample of known Si concentration.

3. Linewidth (FWHM)

Provided that instrumental factors can be ignored, such as inhomogeneity of B_o, mis-setting of magic angle or rotor instabilities, the most likely factors include:

1. Dispersion of isotropic chemical shifts due to structural disorder of Al, B, Zn and/or Zr substitution for Si. Line broadening by chemical shift dispersion is a very common occurrence and is the most limiting factor. Due to a large number of different environments around nominally equivalent $Q_n(X)$ type Si atoms, many lines overlap with slightly equivalent chemical shifts. Different environments are created by a distortion of bond angles, bond length and by local distribution of atoms within the second nearest and further tetrahedral neighbours. Hence, broad lines 10-20 ppm are observed for disordered systems such as glass and 0.2-3 ppm for perfectly ordered systems.
2. Non-averaged dipolar interactions of the ^{29}Si nucleus with ^{1}H, ^{27}Al or other NMR active nuclei.
3. The presence of paramagnetic impurities in the sample (such as Fe).

4. The initial dissolution rate of the International Simple Glass in acidic and basic media

Summary

Prior to undertaking experiments to understand the influence of the ZnO/CaO ratio on the initial dissolution rate of borosilicate glass (Chapter 5), it was necessary to set up the apparatus for performing Single-Pass-Flow-Through (SPFT) experiments. In establishing the set-up and methodology, new initial dissolution rate (Stage I) data of the International Simple Glass (ISG) in acidic and basic media, from which the rate law parameters (K_o, η, and E_a as described in Chapter 2, Equs. 2.6 & 2.7) were obtained. These data were combined with those performed in a parallel study at Pacific Northwest National Laboratory U.S.A. (PNNL) (Neeway *et al.* 2018), and were published as part of Backhouse *et al.* (2018). For the first time, evidence for preferential localised dissolution was observed on the ISG under the dynamic experimental conditions of the SPFT protocol, which may be related to the fundamental glass structure or the experimental methodology. This data was published in Fisher *et al.* (2019). In their entirety, the data presented in this Chapter highlight some areas of the SPFT protocol that would benefit from further review, with the possibility of improving the methodology.

As noted above, this Chapter has been published, in part, in the following publications:

Adam J. Fisher, Neil C. Hyatt, Russell J. Hand & Claire L. Corkhill. The formation of pitted features on the International Simple Glass during dynamic experiments at alkaline pH. *MRS Advances.* **4**, [17-18], 993-999 (2019).

Daniel J. Backhouse, **Adam J. Fisher**, James J. Neeway, Claire L. Corkhill, Neil C. Hyatt & Russell J. Hand. Corrosion of the International Simple Glass (ISG) under acidic to hyperalkaline conditions. *npJ Materials Degradations.* 2:29 (2018).

4.1 Introduction

Obtaining accurate initial dissolution rates and rate law parameters is important since these can be used as input to kinetic models of glass dissolution for safety and performance assessments for the geological disposal of vitrified nuclear waste. As a basis to fully understand the dissolution kinetics and mechanisms of borosilicate glass dissolution, so that scientists, geological disposal implementers, the public and regulators can have confidence in the aforementioned models, the International Simple Glass (ISG) is being widely studied (Gin *et al.* 2012, 2015, Kasper *et al.* 2019). As such, this glass composition has been chosen as a reference material to set-up SPFT experiments, so that validation of the methodology can be made against the wealth of literature pertaining to ISG.

Experiments to determine initial dissolution rates and to ascertain the rate law parameters described in Chapter 2, Equs. 2.5 & 2.6 were conducted at 40, 50 and 70 °C and pH(RT) 4.5, 5.5, 7, 9 and 11. Acidic pH values were buffered by 0.01M HNO_3 adjusted by 1x10 $^{-2}$M NH_4OH and the alkaline pH values were buffered by TRIS (pH 7 & 9) and LiOH (pH 11). A full description of the buffers is presented in Section 3.3.7. The q/S sweep (described in Chapter 3) was undertaken at pH(RT) 9 at 40 °C only, justified as follows: 1) these conditions are most representative of those of disposal in a conceptual UK hard rock GDF; and 2) they maintain consistency with those chosen to conduct SPFT experiments in Chapter 5 of this Thesis. Some experiments, particularly those in the basic regime, were set up for a long test duration (> 100 d) to provide insight into the maintenance of steady-state dissolution conditions over extended time periods and to scrutinize the standard SPFT methodology, which advises that experiments be conducted over a 14 d period. Scanning Electron Microscopy (SEM) was performed on glass particles after the q/S sweep at pH(RT) 9 at 40 °C to assess surface features, such as the formation of altered layers, which could be indicative of non-dilute experimental conditions. SEM was also performed on glass particles after the extended duration experiments at pH(RT) 7 at 40 °C and pH(RT) 11 at 40 °C to allow for a broader investigation of the surface features across the basic pH regime at 40 °C and after extended experimental duration.

4.2 Results

4.2.1 Characterisation

The ISG was observed to be X-ray amorphous and single phase (Kasper *et al.* 2018), possessing a density of 2.50 g cm^3 (Gin *et al.* 2012). SEM analysis of the ISG particles prior to dissolution experiments showed extensive cracking and surface roughness and the presence of a small quantity of adhered glass fines (<5 µm diameter) (Fig. 4.1), arising from mechanical crushing, despite thorough washing according to the ASTM standard method (ASTM 2010, 2018).

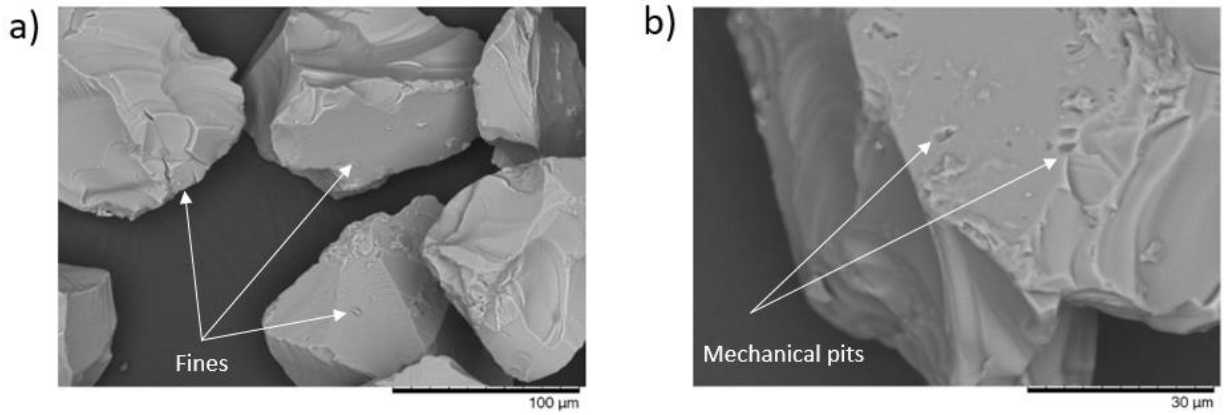

Figure 4.1. Pristine ISG glass particles, 75-150 µm in diameter, after washing according to ASTM protocol (ASTM 2010, 2018). Surface features resulted from sample preparation; a) evident cracks, surface roughness and adhered fine fragments; b) surface roughness and mechanical pitted features.

4.2.2 Experimental parameters

The pH(RT) and the calculated pH at the experimental temperatures pH(T), alongside the SPFT experimental parameters are shown in Table 4.1.

Table 4.1. List of experimental parameters and pH(T). The q/S sweep noted in the comments column identifies the experimental parameters used for the q/S sweep.

Temp / °C	pH (RT)	pH (T)	Test duration /d	Target flow-rate (q) /ml d^{-1}	ISG Mass /g	Target log [(q/S) /m s^{-1}]	Comments
40	4.5	4.5	32	80	0.29	-6.82	
	5.5	5.5	32	80	0.29	-6.82	
	7	6.57	100	80	0.44	-7	
	9	8.67	43	10	1.00	-8.26	q/S sweep
	9	8.67	34	10	0.80	-8.16	q/S sweep
	9	8.67	43	10	0.55	-8	q/S sweep
	9	8.67	34	10	0.37	-7.83	q/S sweep
	9	8.67	37	20	0.50	-7.6	q/S sweep
	9	8.67	39	20	0.25	-7.36	q/S sweep
	9	8.67	34	80	0.65	-7.17	q/S sweep
	9	8.67	35	80	0.50	-7.06	q/S sweep
	9	8.67	35	80	0.30	-6.83	q/S sweep
	11	10.89	100	80	0.29	-7	
50	4.5	4.5	32	80	0.30	-6.83	
	5.5	5.5	32	80	0.30	-6.83	
	7	6.39	120	80	0.44	-7	
	9	8.40	57	80	0.44	-7	
	11	10.67	35	80	0.29	-7	
70	4.5	4.5	32	80	0.30	-6.74	
	5.5	5.5	32	80	0.30	-6.82	
	7	5.91	120	80	0.44	-7	
	9	8.08	57	80	0.44	-7	
	11	10.43	35	80	0.29	-7	

4.2.3 Determination of dilute conditions – q/S sweep and glass particle analysis

Data showing the determination of steady-state (SS) dissolution rates from the experiment pH(RT) 9 at 40 °C, and at $\log_{10}$[(q/S) /m s^{-1}] = -7.36, are shown in Figure 4.2. Steady-state dissolution conditions were met after 16 d, when the dissolution rates (calculated from Equ. 3.24) based on the release of boron, silicon and sodium (R_B, R_{Si} and R_{Na}), and calculated from the mean value of the rates obtained between 16-29 d inclusive, were: R_B = 0.018 ± 0.005, R_{Si} = 0.019 ± 0.006 and R_{Na} = 0.0137 ± 0.005 g m^{-2} d^{-1}. The same approach was applied to all q/S sweep values listed in Table. 4.1, with results listed in

Table. 4.2. Corresponding plots of the dissolution rates as a function of q/S are provided in 4.5 Appendix - I.

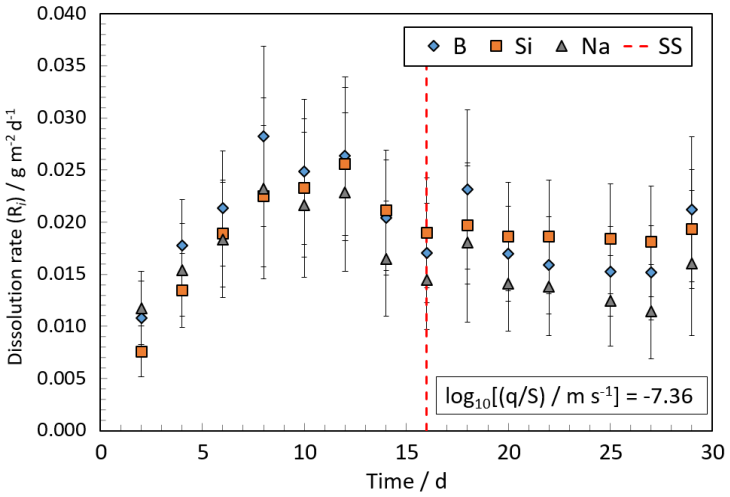

Figure 4.2. Example of the attainment of steady-state (SS) conditions - pH (RT) 9 at 40 °C at a flow-rate (q) to sample-surface-area (S) ratio of $\log_{10}[(q/S)\ m\ s^{-1}] = -7.36$. Calculated B, Si and Na dissolution rates (g m^{-2} d^{-1}) versus sampling day. Note that steady-state dissolution was determined after 16 d.

The q/S sweep displayed in Figure 4.3 shows that the obtained dissolution rates had little dependence on q/S, instead being scattered around mean dissolution rates of $R_B = 0.016 \pm 0.006$, $R_{Si} = 0.013 \pm 0.007$ and $R_{Na} = 0.015 \pm 0.007$ g m^{-2} d^{-1}. This is consistent with the 40 °C data of Neeway *et al.* (2018), who also reported an invariant response of elemental dissolution rate of ISG at 90 °C using the same buffer solutions as those utilised here.

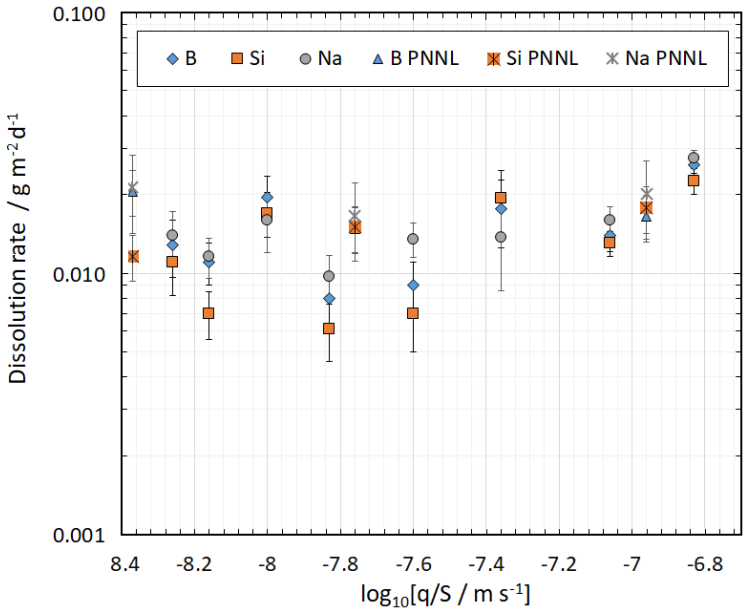

Figure 4.3. The 'q/S sweep' for ISG, showing the normalised dissolution rates of B and Si (g m^{-2} d^{-1}) as a function of the flow-rate (q) to sample-surface-area (S) ratio $\log_{10}[(q/S)\ /\ m\ s^{-1}]$ at pH(RT) 9 at 40 °C. Analogues data from Neeway *et al.* (2018) is labelled as PNNL (Pacific Northwest National Laboratory, USA).

Inspection of glass particles by SEM, shown in Figure 4.4, from almost all q/S experiments after the termination of the experiment, showed no evidence for alteration layer formation, indicating that dissolution was maintained under dilute conditions as prescribed by the SPFT standard method. However, there was some evidence for glass dehydration cracking / alteration layer formation from the $\log_{10}[(q/S)\ /m\ s^{-1}]$ = -8.26 experiment only, indicative of feedback effects from saturated, non-dilute conditions, which may be expected at this low flow-rate (Fig. 4.4a). There was also evidence for localised preferential attack at the surface of the glass particles, in the form of small, dark pits < 20 µm in size (Fig. 4.4b).

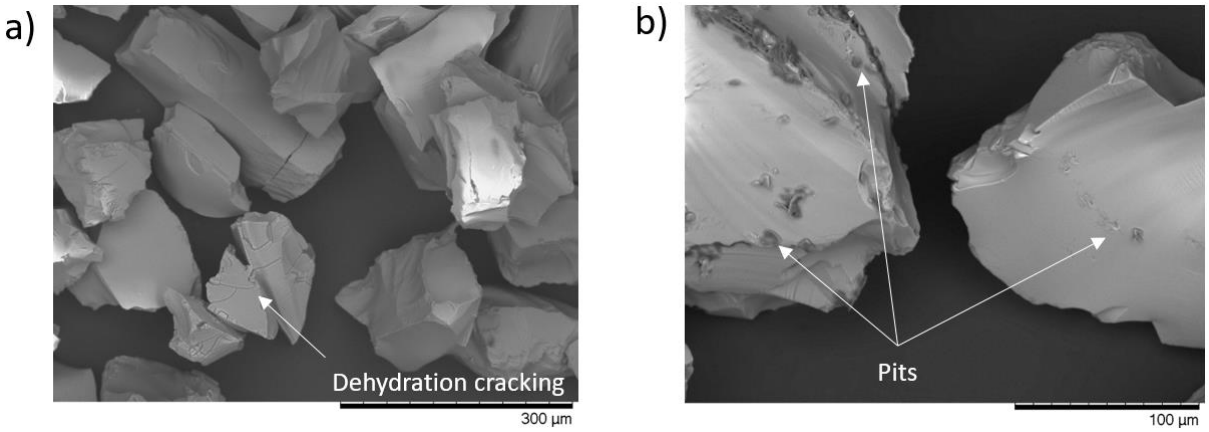

Figure 4.4. SEM images of glass particles after the termination of SPFT experimentation at $\log_{10}[(q/S)\ /\ m\ s^{-1}]$ = -8.26 - pH(RT) 9 at 40 °C, showing: a) glass dehydration cracking on particles to the lower left; and b) localised corrosion pitting.

4.2.4 Initial dissolution rates and glass particle analysis

Initial rates: The initial dissolution rates (Stage I) (R_B, R_{Si} and R_{Na}) at pH(RT) 9 at 40 °C were obtained from the mean value of the dissolution rates measured at $\log_{10}[(q/S)\ m\ s^{-1}]$ values larger than -7.4 (Fig. 4.3). This value (or in excess) has been used in numerous other SPFT studies of alkali-borosilicate glass (McGrail *et al.* 1997, McGrail *et al.* 2000, Pierce *et al.* 2010, Cassingham *et al.* 2015). $Log_{10}[(q/S)\ m\ s^{-1}]$ values ranging from -7.0 to -6.74 were chosen to conduct the rate law determination experiments, with confidence that dilute conditions, enabling the accurate measurement of initial dissolution rates, would be maintained over all temperatures and pH values studied. Neeway *et al.* (2018) indicated that a $\log_{10}[(q/S)\ m\ s^{-1}]$ value of -7.0 was sufficient to achieve initial rate conditions at pH(RT) 9 at 90 °C, which is more aggressive than the conditions studied here. Initial rates (R_B, R_{Si} and R_{Na}) from all experiments performed in the current study are provided in Table 4.2, which also details the experimental conditions and average steady-state concentrations of B, Si and Na (ppm).

The initial dissolution rates of B (R_B), as a function of pH and temperature are shown in Figure 4.5 together with the same data obtained by Neeway *et al.* (2018). There was a good correlation between the two data sets, indicating that SPFT data were reproduced well across different laboratories. The solid lines in Figure 4.5 were obtained from a multiple linear regression fit to the data in the basic regime according to Equation 2.7 (a full derivation can be seen in 4.5 Appendix - IV). The dashed lines in the acidic regime are a guide to the eye to illustrate a possibly expected linear dependence (Knauss *et al.* 1989) (a linear regression was applied to the acidic regime, however, due to the limited data points, the regression failed to produce insightful data). Despite the basic data points collected in the present study being in agreement with the published SPFT data of Neeway *et al.* (2018), the dissolution rate data are somewhat different to those obtained using different dissolution methodologies. This will be discussed in Section 4.3.2.

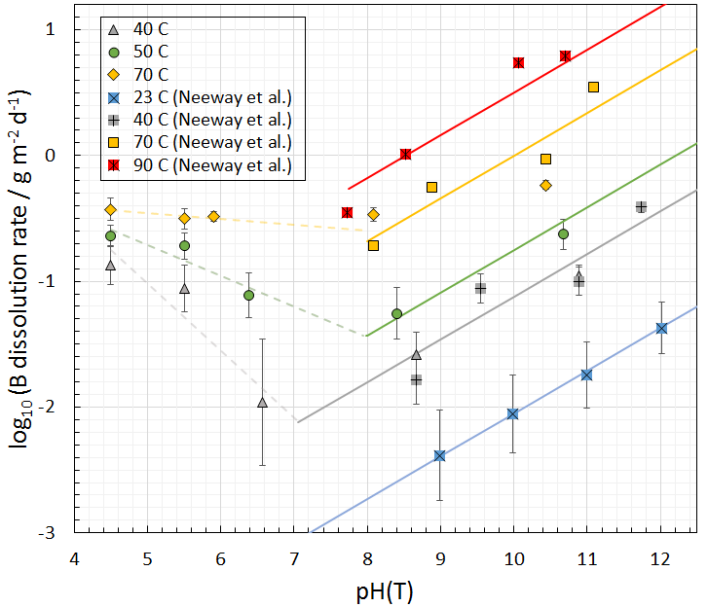

Figure 4.5. Compiled initial dissolution rates from this study and from Neeway *et al.* (2018) showing the $\log_{10}$ [R_B/ g m^2 d^{-1}] normalised initial rates versus pH (T) from all experiments. The solid lines were obtained from a multiple linear regression fit to the data in the basic regime, whereas the dashed lines in the acidic regime are a guide to the eye to illustrate the expected linear dependence (Knauss *et al.* 1989).

Table 4.2. Steady-state normalised dissolution rates (g m^2 d^{-1}) from all experiments. Steady-state ppm values have had background concentrations subtracted where applicable. Note that the Na q/S data has been ommited due to experimental issues with ICP-OES measurements. Log [(q/S*)* /m s^{-1}] values from all experiments are reported in Table 4.1.

Temp / °C	pH (RT)	pH (T)	Test duration /d	Time to attain steady-state /d	Initial sample mass /g	Steady-State			Steady-State concentrations/ppm			Steady-State rates / 10^{-2} g m^{-2} d^{-1}		
						Average surface area† (S) /10^{-3} m^2	Surface area % of original‡	$\log_{10}$[(q/S) /m s^{-1}]	B	Si	Na	B	Si	Na
40	4.5	4.50	32	9	0.29	6.04	98	-6.81	0.49	0.01	0.35	13.41 ± 2.40	0.08 ± 0.02	14.34 ± 2.40
40	5.5	5.50	32	25	0.29	6.05	97	-6.81	0.32	0.03	0.87	8.75 ± 1.60	0.13 ± 0.02	13.11 ± 1.60
40	7	6.57	100	25	0.44	9.17	100	-7.00	0.06	0.01	-	1.10 ± 0.28	0.01 ± 0.007	-
40 (log(q/S) = -8.26)	9	8.67	43	21	1.00	21.1	100	-8.26	1.4	6.05	-	1.30 ± 0.26	1.10 ± 0.22	-
40 (log(q/S) = -8.16)	9	8.67	34	20	0.80	16.9	100	-8.16	0.9	3.12	-	1.10 ± 0.22	0.70 ± 0.14	-
40 (log(q/S) = -8.00)	9	8.67	43	30	0.55	11.6	100	-8.00	1.08	5.11	-	1.90 ± 0.38	1.70 ± 0.34	-
40 (log(q/S) = -7.83)	9	8.67	34	26	0.37	7.8	100	-7.83	0.29	1.2	-	0.80 ± 0.16	0.60 ± 0.12	-
40 (log(q/S) = -7.60)	9	8.67	37	32	0.50	10.5	100	-7.60	0.14	0.6	-	0.90 ± 0.18	0.70 ± 0.14	-
40 (log(q/S) = -7.36)	9	8.67	39	16	0.25	5.27	100	-7.36	0.25	1.4	-	1.80 ± 0.36	1.90 ± 0.38	-
40 (log(q/S) = -7.06)	9	8.67	35	21	0.50	10.5	100	-7.06	0.11	0.47	-	1.40 ± 0.28	1.30 ± 0.26	-
40 (log(q/S) = -6.83)	9	8.67	35	31	0.30	9.26	98	-6.83	0.1	0.46	-	2.60 ± 0.52	2.6 ± 0.52	-
40	11	10.89	100	35	0.29	5.98	98	-6.81	0.41	1.81	0.76	11.02 ± 1.00	16.06 ± 2.30	16.64 ± 1.00
50	4.5	4.5	32	21	0.30	5.94	94	-6.72	0.69	0.07	0.32	22.93 ± 3.10	0.43 ± 0.06	15.69 ± 3.10
50	5.5	5.5	32	21	0.30	5.91	94	-6.73	0.58	0.09	0.32	19.10 ± 2.80	0.57 ± 0.08	15.74 ± 2.80
50	7	6.39	120	87	0.44	8.16	89	-6.95	0.39	0.02	0.7	7.74 ± 1.30	0.08 ± 0.01	7.78 ± 2.80
50	9	8.4	57	26	0.44	8.99	98	-6.99	0.31	1.42	0.5	5.52 ± 0.90	4.91 ± 0.90	3.40 ± 0.51
50	11	10.67	35	8	0.29	5.99	98	-6.81	0.87	4.06	1.55	23.63 ± 4.50	21.10 ± 4.00	23.29 ± 3.50
70	4.5	4.5	32	25	0.30	5.22	85	-6.67	0.98	0.27	0.73	37.16 ± 7.70	2.00 ± 5.00	41.77 ± 7.70
70	5.5	5.5	32	25	0.30	5.37	88	-6.76	1.04	0.35	0.83	31.30 ± 5.20	2.02 ± 0.34	37.65 ± 0.52
70	7	6.39	120	13	0.44	8.62	94	-6.97	1.73	0.28	3.2	32.66 ± 2.70	1.01 ± 0.10	33.58 ± 0.70
70	9	8.4	57	36	0.44	7.61	83	-6.91	1.53	6.56	2.65	33.99 ± 4.00	28.02 ± 4.00	32.72 ± 4.00
70	11	10.67	35	10	0.29	5.74	94	-6.79	1.73	7.89	3.11	58.32 ± 8.80	51.06 ± 7.70	58.11 ± 8.80

† At the onset of steady-state and on application of the shrinking core model

‡ Indicates the need for the application of the shrinking core model if <100%

Glass particle analysis: Inspection of dissolved glass particles from experiments conducted for an extended duration of 100 d at 40 °C, pH(RT) 7 and a $\log_{10}[(q/S)\ m\ s^{-1}] = -7$, and at pH(RT) 11 and at $\log_{10}[(q/S)\ m\ s^{-1}]$ -6.81, revealed the presence of three distinct surface phenomena. The numbers below correlate to the features identified in Figures 4.6 and 4.7:

1. Glass dehydration cracking
2. Troughs of preferential dissolution along stress lines/intitial surface roughness/cracks on the pristine glass (such features are highted, prior to dissolution in Figure 4.1).
3. Two types of pitted features: a) oval and dark troughs and b) pits thought to initiate around mechanically-induced sample preparation artefacts.

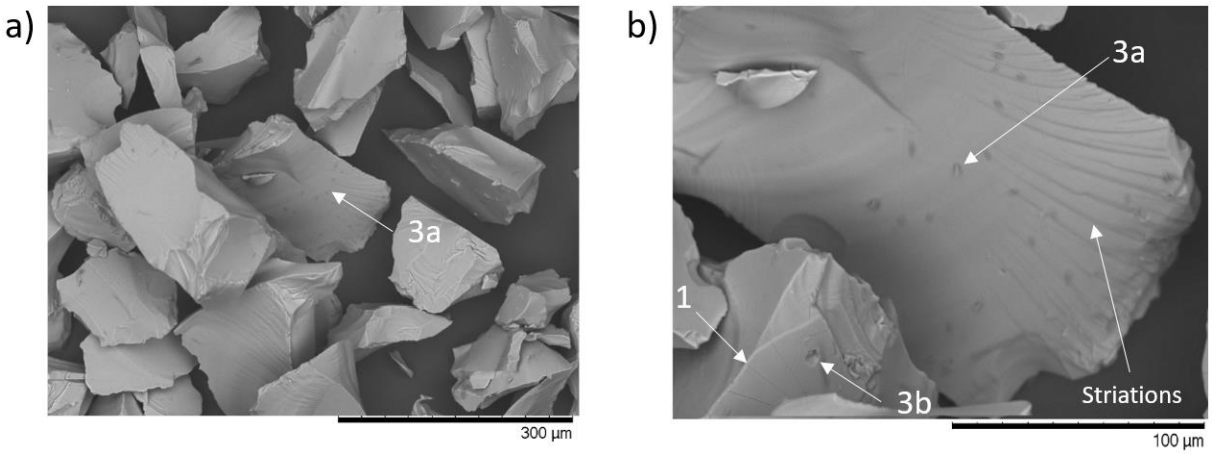

Figure. 4.6. Particles of ISG post-100 d SPFT experimentation at 40 °C and pH(RT) 7 at $\log[(q/S)\ m\ s^{-1}] = -7$; a) evidence for localised preferential attack pitting (3a); b) evidence for localised preferential attack pitting (3a & b) and glass dehydration cracking (1). The striated features are thought to originate from mechanical sample preparation.

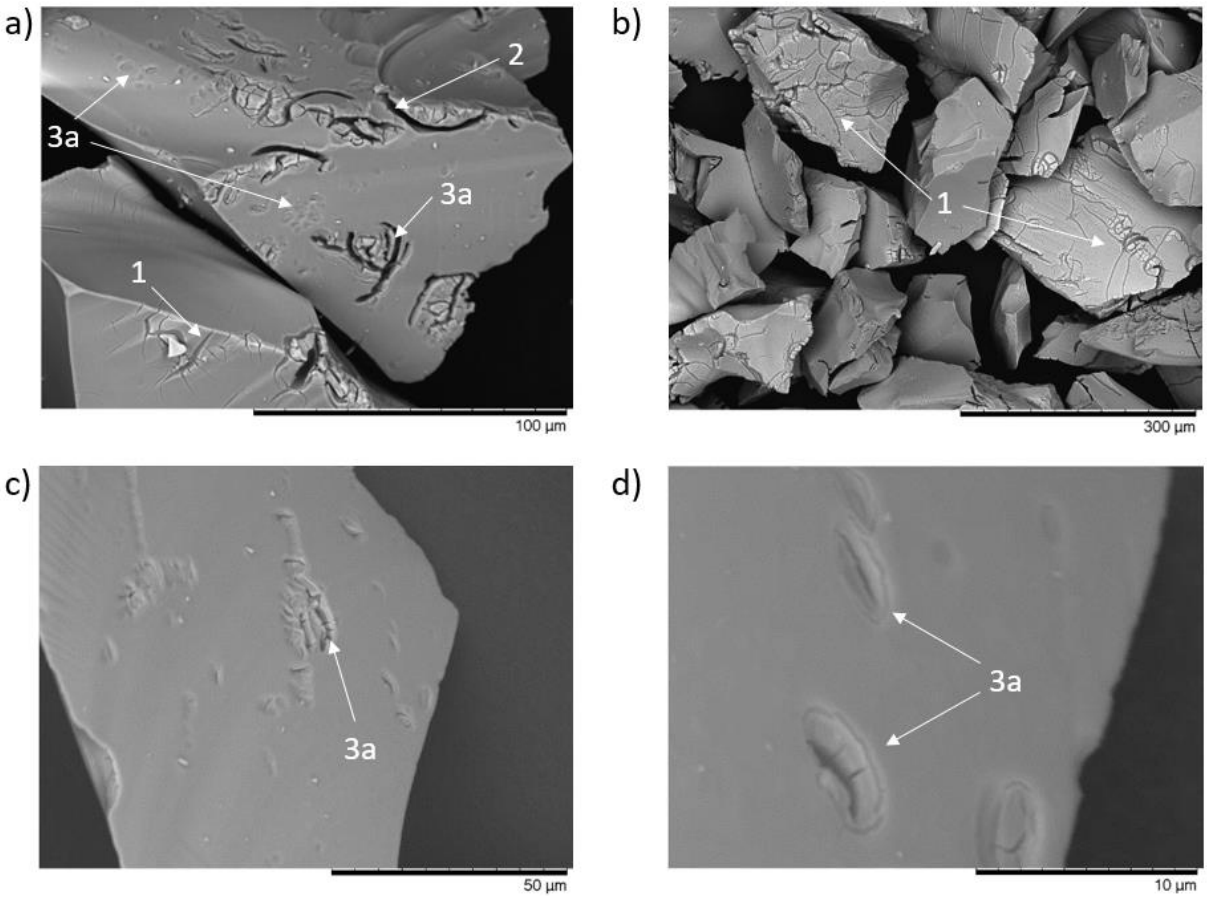

Figure 4.7. Particles of ISG post-100 d SPFT experimentation at pH(RT) 11 and 40 °C at log[(q/S) m s^{-1}] = -6.81; a) evidence for localized preferential attack (pits and troughs (3a), and dehydration cracking (1); b) dehydration cracking (1) on most particles; c) evidence for trough formation from the growth and coalescence of individual pits (3a); and d) high magnification image of depressed pits (3a) with collapred dehydrated altered layer overlaid.

Dehydration cracking could be formed from a dehydrated altered gel layer (discussed in more detail in Section 4.3.4). The pitted features are hypothesised to represent localized preferential corrosion of the surface. Such features were most prevalent at pH(RT) 11, as shown in Figure 4.7, which could be expected due to the higher solubility of silica at elevated pH, and the resulting higher dissolution rates (Strachan 2011). Under these high alkalinity conditions, it is possible that the growth and coalescence of the oval shaped pits formed deeper curved trough-like features with greater reaction progress (Fig. 4.7c-d). The pits shown in Figure 4.7d appear to be overlaid by a collapsed dehydrated altered layer (possibly from the compromised structural integrity of the altered layer upon drying of the sample). In contrast, at pH(RT) 7, there was only minor evidence for glass dehydration cracking (Fig. 4.6b). Striations visible on the right hand side in the images in Figure 4.6b originate from mechanical fractures induced during sample preparation, and are thus not believed to be a product of the dissolution process.

4.2.5 Rate law parameter determination

The initial dissolution rate (R_B, R_{Si} and R_{Na}) data from the basic pH regime, combined with the dataset from Neeway *et al.* (2018), were used to perform a linear multi-variate regression (LMR) using Equation 4.1 (derived from Equation 2.6 (derivation provided in Appendix - IV)) to extract the rate law parameters (k_0, η and E_a):

$$log_{10}(R_i) = log_{10}(k_0) - \eta log_{10}(a_{OH^-}) - \frac{1}{2.303}\frac{E_a}{RT} \qquad [4.1]$$

where R_i is the measured dissolution rate, k_0 (g m^{-2} d^{-1}) the initial rate constant, which is the intrinsic rate at which the surface of the glass hydrolyses, η the pH power-law coefficient, a_{OH^-} the hydronium activity, E_a the activation energy (kJ mol^{-1}) and RT is the product of the gas constant (kJ mol^{-1}) and the absolute temperature (K).

The parameters determined for all three elements are shown in Table. 4.3 and the *η* value for boron is displayed as solid lines in Figure 4.5. The values reported for each element were consistent, indicating that the ISG was dissolving congruently (on average). Activation energies (E_a) for B, Si and Na fell within the commonly observed range for borosilicate glass compositions relevant to nuclear waste (42 to 84 kJ mol^{-1}), indicating that the dissolution of the ISG at the initial rate is controlled by a surface controlled mechanism (Lasaga 1981) (hydrolysis), as opposed to a diffusion controlled mechanism (where E_a < 40 kJ mol^{-1}). The activation energy for Si reported here (77.4 ± 4.7 kJ mol^{-1}) is: 1) identical to the value obtained for the ISG by Inagaki *et al.* (2013) (77.4 ± 1.9 kJ mol^{-1}, obtained at pH 10 using an Arrhenius plot), who used the micro channel flow through (MCFT) methodology ; 2) similar to the value reported for SON68 glass (77.7 ± 2.7 kJ mol^{-1}, obtained at pH 7 using an Arrhenius plot) by Jollivet *et al.* (2012), and; 3) close to the value reported for pure silica (74.5 kJ mol^{-1}) by Dove (1994) and Icenhower & Dove (2000). Values obtained for the pH power law coefficient (*η*) (0.34 for B and Na, and 0.38 for Si) were similar to literature values for other glasses: basaltic glass and pure silica glass (η_{Si} = 0.40) (Brady & House 1996); and aluminoborosilicate glass (η_{Si} = 0.40 ± 0.03) (McGrail *et al.* 1997), (η_B = 0.40 ± 0.04) (Pierce *et al.* 2008) and (η_B=0.39) (Vernaz & Dussossoy 1992). Values of $log_{10}(k_0)$ (7.95-8.62 g m^{-2} d^{-1}), the intrinsic rate at which borosilicate glass hydrolyses, are near identical to the values of 8.52 g m^{-2} d^{-1} for SON68 and 8.33 g m^{-2} d^{-1} for AFCI glass (Vienna *et al.* 2018) and are similar, within experimental error, to those reported for UK HLW simulant glasses, 7.4 ± 0.9 g m^{-2} d^{-1} for MW25 and 9.0 ± 0.9 g m^{-2} d^{-1} MW30 (Corkhill *et al.* 2018). Previous literature values for k_0 have been reported erroneously as the intercept of the pH power law coefficient regression (Pierce *et al.* 2008, Cassingham *et al.* 2015), hence, there is limited literature to draw relative comparisons.

Table 4.3. Rate law parameters for B, Na and Si obtained by analysis of SPFT in the basic regime.

	$\log_{10}(K_0$ / g m^{-2} d$^{-1})$	η	E_a (kJ mol^{-1})
B	8.62 ± 0.54	0.34 ± 0.03	79.5 ± 3.5
Na	8.79 ± 0.75	0.34 ± 0.04	80.3 ± 4.8
Si	7.95 ± 0.73	0.38 ± 0.04	77.4 ± 4.7

4.2.6 Initial dissolution rate determination as a function of Si / Al concentration

Figure 4.8 shows the B dissolution rates as a function of Si, Al and Si + Al concentration in solution (leached from the glass in the q/S sweep experiments), at pH(RT) 9 and 40 °C alongside data from Neeway *et al.* (2018). A scattered response was observed for the boron dissolution rate dependence on dissolved silicon (Fig. 4.8a), which may suggest a non-linear dependence; a power regression gave the best fit, with a R^2 value of 0.21. The non-linear dependence is inconsistent with the model proposed by Grambow (1985), who stated that the concentration of dissolved Si in solution was the dissolution rate determining factor. This suggests that the rate drop (the observed transition from the initial rate to the residual rate) for the ISG and other alumina-borosilicate glasses (Gin 1996, Advocat *et al.* 1997, Abraitis *et al.* 2000a, Rajmohan *et al.* 2010, Icenhower & Steefel 2013) may not solely be due to increasing Si concentration in solution, but may also depend on another element. A scattered response in R_B as a function of Al concentration was also observed (Fig. 4.8b). However, the combined effect of Si + Al concentrations on R_B, shown in Figure 4.10c, may tentatively suggest a negative linear correlation; an R^2 value of 0.20 was obtained and the plot is arguably less scattered compared to the independent effects of Si and Al in solution on R_B (Figs. 4.10a and b, respectively). This may indicate that a mixed Si/Al affinity rate law is applicable to the ISG, which has been well reported in the literature for a range of glass compositions (Gin 1996, Advocat *et al.* 1997, Abraitis *et al.* 2000a, Rajmohan *et al.* 2010, Icenhower & Steefel 2013). Unfortunately, the data presented here is not robust enough to support such a claim, nevertheless, it would be interesting to consider the possibility of a combined effect of Si and Al on ISG dissolution in future experiments. This could be facilitated by the addition of an a_{Al} term, and/or the effects of Al should be included in the activity product term (Q/K) within the Transition State Theory equation (Equ. 2.6), as previously argued by Gin (1996) and Abraitis *et al.* (2000).

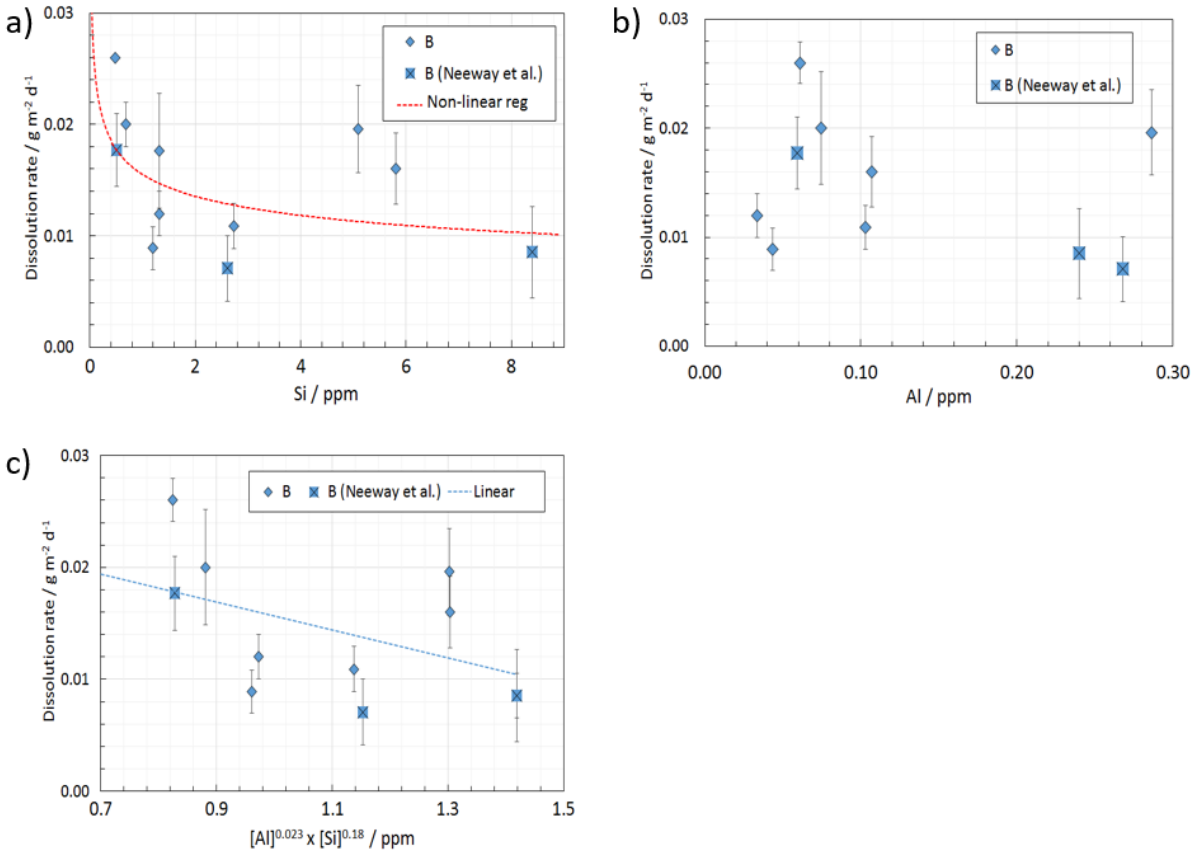

Figure 4.8 a) Effect of Si concentration in solution (ppm) on R_B (g m^{-2} d^{-1}) at pH(RT) 9 & 40 °C, where the dashed red curve is a guide to illustrate the non-linear dependence of R_B; (b) Effect of Al concentration in solution (ppm) on R_B (g m^{-2} d^{-1}); and (c) Effect of [Si + Al] normalized (to compositional elemental fraction) concentration in solution (ppm) on R_B (g m^{-2} d^{-1}), where the dashed line is a guide to illustrate the possible linear dependence of R_B. Note; points running from left to right in all plots correlate with high log_{10}[q/S] values (dilute) running to low log_{10}[(q/S) m/s^{-1}] values (possibly saturated), which is consistent with increasing Si, Al or [Si + Al] concentration.

4.3 Discussion

4.3.1 Invariant dissolution as a function of q/S

Before comparing the obtained data with dissolution rates and kinetic dissolution parameters reported in the literature, it is important to consider the irregular behaviour observed for the dissolution rate as a function of flow-rate (q) to surface-area (S). The scattered (or arguably invariant) nature of the 'q/S sweep' of this data-set (Fig. 4.3), is not typically observed for borosilicate glasses, but was previously observed for the ISG (Neeway *et al.* 2018).

The literature contains data from q/S sweeps from many glass compositions, which demonstrate a clearly defined plateau in the dissolution rate at high q/S values, where the dissolution rate becomes

independent of q/S. This is considered to represent dilute conditions, where the solution is far from equilibrium with respect to silica. The dissolution rate at the plateau (but not before) is invariant and typically an order of magnitude greater than the dissolution rates reported at lower q/S ratios. The majority of glass compositions for which this behaviour has been observed (McGrail *et al.* 1997, McGrail *et al.* 2000, Abraitis *et al.* 2000, Pierce *et al.* 2008, Icenhower & Steefel, 2013, Cassingham *et al.* 2015) were multi-component HLW simulants, not simple compositions like the ISG investigated here.

An invariant 'q/S sweep', like that reported for ISG, was reported in one instance for a simple quaternary high soda, alumina-borosilicate simple glass formulation (Icenhower *et al.* 2008), without any clear explanation. However, this glass was determined to be phase separated, containing a highly soluble sodium metaborate phase ($Na_2B_4O_7$). It was concluded that this phase preferentially dissolved out of the glass matrix, leaving pitted features in the residual Si-Al matrix (no images of these features were published), which could manifest itself in an invariant 'q/S sweep'. This behaviour was evidenced by faster Na dissolution rates compared to B and Si. In the present study, pitted features were observed in glass particles post-SPFT experimentation (Figs. 4.4, 4.6 & 4.7), with a preponderance for pits in more aggressive environments (higher pH). The ISG was observed to dissolve congruently in the basic regime, making it unlikely that a distinct dissolved secondary phase (such as the sodium metaborate observed by Icenhower *et al.* 2008) was the origin of the surface pits and the unusual dissolution behaviour as a function of q/S.

Therefore, other possibilities should be considered to account for the observed scattered/invariant 'q/S sweep', also observed by Neeway *et al.* (2018). Firstly, the glass network structure should be contemplated. It is speculated that most alkali-borosilicate glasses are composed of distinct borosilicate ($^{[3]}$B-O-Si) and alkali-borosilicate networks ($^{[4]}$B-O-Si) (Shelby 2005), where alkali elements charge compensate the $^{[4]}$B units. Based on the modified network model, percolation channels (described in Section 2.3.1) are created under this scenario (Zachariasen 1932, Wright *et al.* 1980, Greaves *et al.* 1985). Percolation channels in dissolved nuclear waste simulant glass samples from static experiments have been described by Jantzen *et al.* (2010), who proposed that they were associated with alkali channels within the glass network; the dissolution of the alkali-borosilicate network in such a scenario may be preferred. The initial rate of dissolution, therefore, may not be congruent, but dependent on distinct local networks, with some been more durable than others. Thus, it is possible that very subtle phase separation at the molecular level, arising from the presence of different glass networks, could potentially result in both the scattered/invarient dissolution response

as a function of q/S and the formation of localised corrosion pits observed in the present study. Since the elemental fraction (f_i) is used in the calculation of the dissolution rate (Equ. 3.24), the overall rate may not accurately reflect *local* B and Si dissolution rates, but instead, capture a global average. In such a scenario, the observed dissolution rates may be incomparable between different samples/sections of the same sample, giving rise to invariant/random behaviour. This behaviour may be more pronounced in simple glass formulations compared to multi-oxide component nuclear waste glass, which can be assumed to contain less pronounced percolation channels due to their complex network structure and reduced Si, B and alkali content.

While this could be considered a plausible explanation, it should be noted that there is no published evidence for the phase separation, at any scale, of the ISG. Indeed, the ISG was reported as being homogenous by Kasper *et al.* (2019), as determined by transmission electron spectroscopy (TEM) and XRD. Further dissolution work on grossly phase separated glass could provide greater insight and test this hypothesis.

4.3.2 Comparison of initial rate data obtained by SPFT with published data

As noted above, the initial dissolution rates of the ISG (R_B, R_{Si} and R_{Na}) obtained at different pH(RT) and temperatures are in general agreement with those obtained by Neeway *et al.* (2018), who employed similar q/S values. This demonstrates the high reproducibility of the SPFT methodology across different laboratories. The initial rates of the ISG based on silicon (R_{Si}), obtained at different pH(RT) and temperatures were not in agreement with those of Inagaki *et al.* (2013), who used the micro-channel-flow through (MCFT) methodology to ascertain R_{Si} (Fig. 4.9). Using MCFT, with a log[(q/S) /m s^{-1}] = -5.1, the initial rates obtained by Inagaki *et al.* (2013) for ISG were greater, by factors varying between 2 to 7, than data presented here and independently in Neeway *et al.* (2018) (Table 4.4). Furthermore, the bottom of the conventional "U/V" shape (Section 2.4.1 - Chapter 2) formed when graphically representing R_{Si} as a function of pH (Bourcier 1998, Oelkers 2001, Ojovan & Lee 2017), appeared at pH 4 in the study of Inagaki *et al.* (2013), while data presented in this Chapter place the bottom of the "U/V" at pH(RT) 5.8-6.4 (Fig. 4.9), which is consistent with literature values for other simulant HLW glasses, including: pH(RT) 7 at 90 °C for SON68 (Gin & Mestre 2001); pH(RT) 6 at 90 °C for SRL165 and the five component simple glass counterpart, CSG (Bourcier, 1994); and pH(RT) 7 at 18, 60 and 90 °C for UK Magnox (Abraitis *et al.* 2000c). Knauss *et al.* (1989) also give values of pH 6 at 70 °C, and pH 6.5 at 25 and 50 °C for a simple analogue nuclear waste glass.

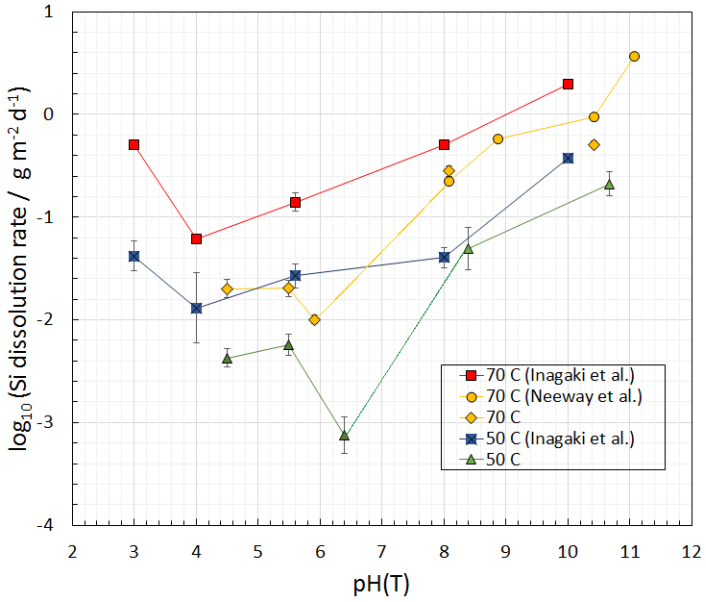

Figure 4.9. Comparison of the normalised initial dissolution rates of Si, $\log_{10}(R_{Si}$ / g m^2 d^{-1}) versus pH(T) obtained in the current study and those of Inagaki *et al.* (2013) obtained by the MCFT method. The errors presented in the above plots are relative errors, where: $2\sigma_{rel} = (2\sigma/R_i)/\log_{10}[R_i]$. Note that the 70 °C data from this study and Neeway *et al.* (2018) has been connected as a visual aid to illulstrate the U/V-shape dissolution trend.

The discrepancies in R_{Si} could be the result of intrinsic differences in the two methodologies. In the SPFT method glass particles and a flow-rate on the order of mL d^{-1} are employed, while in MCFT, a glass monolith and a significantly lower flow rate (approximately µL d^{-1}) are used. It has been postulated that under MCFT conditions, the solution may become appreciably concentrated over the short distance that it travels across the surface of the glass (Neeway *et al.* 2018), leading to the potential overestimation of the initial rate. Furthermore, the solution pH buffer utilised by Inagaki *et al.* (2013) in all experiments contained KCl and HCl, thus it is possible that K from this buffer participated in ion-exchange reactions with alkali elements (i.e., Li and Na) in the glass, enhancing the dissolution rate. Additionally, chloride salts have also been shown to increase the dissolution rate of amorphous silica (Icenhower & Dove, 2000). In contrast, TRIS buffer, used to stabilise the solution in the range pH(RT) 7 to 9 in this investigation, has been used in a wide range of studies (McGrail *et al.* 1997, Icenhower *et al.* 2008, Pierce *et al.* 2010, Icenhower & Steefel, 2013, Cassingham *et al.* 2015, Hopf *et al.* 2016). However, literature suggests that the use of TRIS may have an impact on the increased dissolution of borosilcate glass, due to boron-TRIS complexation (Tournie *et al.* 2013 , Stone-Weiss *et al.* 2019).

The R_{Si} for the ISG reported in the literature (Table 4.4) show contrasting results. Comparison of the two MCFT investigations, performed at pH 10 (90 °C), reveal a disagreement in the initial rates (Inagaki

et al. 2013, Fournier *et al.* 2016), despite being performed under the same conditions. Fournier *et al.* (2016), using a log[(q/S) /m s^{-1}]= -4.8, reported a SPFT dissolution rate of 16.7 g m^{-2} d^{-1}, which is significantly faster than 5.13 ± 0.77 g m^{-2} d^{-1} reported separately in Neeway *et al.* (2018). However, taking the data from that study and applying a linear multivariate regression, it is possible to predict an initial rate of $4.15^{+44.9}_{-3.80}$ g m^{-2} d^{-1} under similar conditions. The large errors associated with this predicted initial rate are due to the fact that a normally distributed error band for $\log_{10}(R_i)$ becomes a log normally distributed error band for R_i with a significant asymmetry in the positive and negative error bars. Wider investigations (not detailed here (Hand 2018)) indicate that similarly large errors in the predicted initial rates, R_i, (as distinct from $\log_{10}(R_i)$ values) arise with all dissolution data sets reported in the literature, especially for higher temperatures and pH values (Corkhill *et al.* 2018). Thus, while the initial rate measured by Fournier *et al.* (2016) (Table 4.4) (16.7 g m^{-2} d^{-1}) is significantly faster than the rates obtained here, the intial rate measured by Fournier *et al.* (2016) actually lies within the error band given by the rate parameters obtained in this work ($4.15^{+44.9}_{-3.80}$ g m^{-2} d^{-1}). Reduction of the errors in the predicted rates requires significantly larger data sets to enable a reduction in the individual error terms for the rate parameters.

Table 4.4. Compilation of normalised R_{Si} of the ISG reported in the literature (MCFT & SPFT investigations) alongside data from this study.

Method	Temp / °C	pH(T)	Buffer	log[(q/S) /m s^{-1}]	Initial rate R_{Si} /g m^{-2} d^{-1}	Reference
MCFT	23	10.00	KOH	-5.10	0.029 ± 0.002	Inagaki *et al*. (2013)
SPFT	23	10.00	TRIS	-7.41	0.009 ± 0.003	Neeway *et al.* (2018)
MCFT	50	5.60	KOH	-5.10	0.027 ± 0.002	Inagaki *et al.* (2013)
SPFT	50	5.50	TRIS	-6.73	0.006 ± 0.001	This study
MCFT	70	5.60	KOH	-5.10	0.14 ± 0.02	Inagaki *et al.* (2013)
SPFT	70	5.50	TRIS	-6.76	0.020 ± 0.003	This study
MCFT	70	8.00	KOH	-5.10	0.51 ± 0.03	Inagaki *et al*. (2013)
SPFT	70	8.08	TRIS	-6.91	0.25 ± 0.04	This study
MCFT	90	10.00	KOH	not available	5.58 - 13.03	Fournier *et al*. (2016)
SPFT	90	10.00	KOH	-4.80	16.7	Fournier *et al.* (2016)
MCFT	90	10.00	KOH	-5.10	7.65 ± 0.17	Inagaki *et al.* (2013)
SPFT	90	10.06	TRIS	-5.84	5.13 ± 0.77	Neeway *et al.* (2018)

Despite all initial rate measurements listed in Table 4.4 being within the large error bands given by the rate parameters in Table 4.3, a description of why these discrepancies arise is warranted. Possible insufficient flow-rates used in this study may contribute to the wide variety of R_{Si} for the ISG. These flow-rates were selected based on results from the 'q/S sweep' (Figure 4.3) to provide the initial rate data. Manifestation of insufficient flow-rates may be in the form of dehydrated altered gel layers and pitted features such as those in Figures 4.6 and 4.7.

Previously, when glass dehydration cracking has been observed, it is proposed to result from preferential local attack rather than being indicative of dehydration cracking of an altered layer (McGrail *et al.* 1997). However, the features in Figures 4.4b and 4.7 (a, c-d) from experiments at pH(RT) 9, 40 °C and pH(RT) 11, 40 °C respectively, which clearly *do* reflect localised chemical attack, are quite different from those in Figures 4.4a and 4.7b, the latter being strongly reminiscent of dehydration cracking of a formed alteration layer. The presence of an alteration layer from these high pH samples could indicate that the SPFT method was not always yielding true initial rate conditions, physically attributed to insufficient low flow-rates, especially for the highest pH values, where Si solubility is significantly greater. However, altered gel layers have been seen in experiments with flow rates in excess of 200 mL d^{-1} (Icenhower 2018), which is significant if elements are released congruently because this suggest that some precipitate in a saturated boundary layer as per the hypothesis of Putnis *et al.* (2007), Geisler *et al.* (2010) and Hellmann *et al.* (2012). Hence, the presence of an altered gel layer doesn't necessarily mean that dissolution was not at the initial rate. It should be noted that glass dehydration cracking/alteration layer formation cannot be strictly avoided in the SPFT methodology as there will always be some feedback effects – infinitely dilute conditions can never be maintained, there will always be some silica in solution (ASTM 2010).

4.3.3 Attainment of steady-state dissolution

The attainment of steady-state dissolution conditions, across all experiments listed in Table 4.2 were observed between 8-87 d, with 18/22 experiments reaching steady-state after 14 days, which is the advised experimental duration according to the SPFT ASTM (2010, 2018). Most SPFT experiments in the literature were conducted in excess of 14 days, which suggests that the ASTM standard should be updated to reflect contemporary experimentation (Icenhower *et al.* 2008, Pierce *et al.* 2010, Icenhower & Steefel, 2013, Cassingham *et al.* 2015, Hopf *et al.* 2016).

4.3.4 Pit Formation

The formation of the pitted features (Figs. 4.4, 4.6 & 4.7) has been mentioned in previous sections of this Chapter where applicable, however, this phenomenon merits further discussion. The appearance of such features could be attributed to the following:

1. Features may arise from preferential dissolution at sites of high-energy formed within the pristine glass, such as cracks and crevices and mechanically-formed pits (formed during sample preparation) (Sessegolo *et al.* 2019).

2. A local pH increase in the solution at the interface between an altered layer and the pristine glass (Mendel *et al.* 1984, Hench *et al.* 1986, Chinnam *et al.* 2018, Lenting *et al.* 2018).

3. The dissolution of a separate soluble phase (Icenhower *et al.* 2008), however, as discussed in Section 4.2.1, this will not be considered further since the ISG has been proven to be single phase.

The first possible explanation, relating to the presence of high-energy surface sites, is deemed to be quite likely. However, since the pitted features present on the glass after dissolution are not always located at these sites, i.e., the quantity of dissolved pits does not equate with the quantity of high-energy surface sites observed on the pristine particles (e.g. compare Figures 4.4, 4.6 and 4.7 with the pristine glass in Figure 4.1a), another mechanism might also be responsible.

A local pH increase at the surface of the glass has been hypothesised to occur in static dissolution experiments. While the present study describes results from dynamic investigations (with relatively rapid replacement of solution), the same mechanism could be operating at a very localised scale, especially when one considers that the glass particles themselves remain static during the experiments; and the solution, while encouraged to be replenished at the bottom of the vessel near the glass and removed from the upper part of the vessel (away from the glass), is not constantly stirred (Chapter 3 – 3.4 Appendix I). A localised increase in pH (i.e., not over the whole surface of the glass, but at distinct regions of the surface) could arise from the presence of alkali-concentrated regions, such as those occurring from the presence of distinct glass networks and/or from alkali channels consistent with the modified random network model, as described in Section 4.3.1 (Zachariasen 1932, Wright *et al.* 1980, Greaves *et al.* 1985). Because the first stage of glass dissolution is interdiffusion (Section 2.3 – Chapter 2), the local solution pH will be increased in those high alkali concentrated regions and, because the solubility of Si is greater at higher pH values, this could result in aggravated attack at those regions, forming pits. The growth of pits into troughs could naturally follow the alkali rivers and/or be due to the aggressive dissolution in the vicinity of the pH rise.

Jantzen *et al.* (2010) observed extensive pitted features (Fig. 4.10a & b) and suggested they were experimental evidence of existing percolation channels and hence, the medium range order structure of a glass as defined by the modified random network model. Similar features were recently observed by Chinnam *et al.* (2018) on the ISG in static monolithic dissolution experiments after the gel layer had been peeled back with carbon tape, as shown in Figure 4.10c & d. Results from the present investigation are consistent with this hypothesis, despite showing a lesser quantity of pits; due to the dynamic experimentation, the quantity of pits should be expected to be lower and that faster flow-rates and less aggressive solutions will produce fewer pitted features. The fact that a small number of

pits were observed in Figures 4.6a and b, for samples where initial rates were attained, indicates that pit formation could be a key mechanism in the glass dissolution process. If such features were noted from other published flow-through investigations, it would have been of benefit to the understanding of glass corrosion, however, since the standard updated protocol does not require the inspection of particles after dissolution (ASTM 2018), one can assume they were not observed. In only one instance a small number of pits were observed in MW25 at $\log_{10}[(q/S)\ /m\ s^{-1}] = -7.78$ at 90 °C in deionized water (Iwalewa *et al.* 2017).

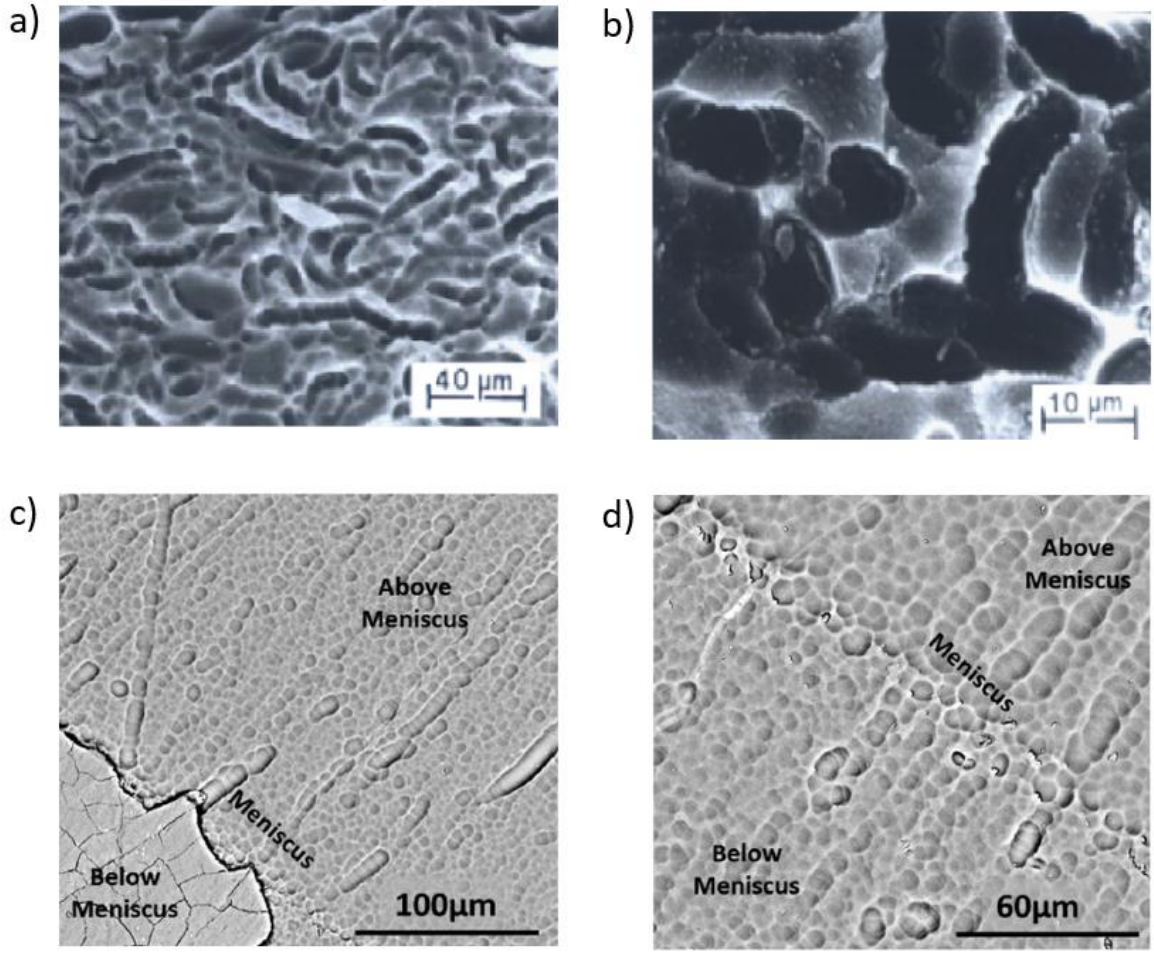

Figure 4.10. Glass surface morphology after the removal of the altered layer showing pitted features on: a) & b) simulated HLW glass SRL 131 after 28 d MCC-1 experiments in deionized water (Jantzen *et al.* 2010); c) & d) the ISG after 70 d in a partial immersion experiment (MCC-1 & vapour), whereby the meniscus idicates the water level. Not that c) shows the unremoved gel layer to the bottom left (Chinnam *et al.* 2018).

4.3.5 Suggested improvements to the SPFT experimental methodology ASTM (2010)

This study has highlighted some areas of the ASTM (2010) SPFT methodology that would benefit from review. Some suggestions based on the findings of the present study have been listed below, with the

aim of advancing the understanding of glass dissolution, by maintaining experimental consistency and undertaking additional analyses. Note that during the time period of the Thesis the ASTM SPFT standard (ASTM 2010) was updated in 2018 (ASTM 2018). The suggestions listed below are still applicable to ASTM 2018, unless otherwise stated.

1. **A clear definition of steady state conditions is required.**

   The ASTM (2018) standard states that; "*Repeat 8.3.3 – 8.3.14 at a pre-determined time interval, preferably every two days, for a 14-day period. Initial tests with a glass require frequent analyses of the effluent solution to assure that the steady state solution concentration is determined. Collection intervals and overall test duration can be modified in subsequent tests as insight into the dissolution rate is gained*". The supposition here is that steady-state will be reached after 14 days. However, it is clear from the work performed in the present work, and that of others (Pierce *et al*. 2008, Icenhower & Steefel 2013, and whereby steady-state was reached just before 14 days – Icenhower *et al*. 2008, Pierce *et al.* 2010), that it can take considerably longer for this to be achieved. Therefore, it is suggested that a minimum experimental duration of 40 days in aggressive conditions (acidic and alkali pH and high temperature), and 60 days in neutral conditions, at all temperatures, should be used to elucidate steady-state conditions, and that there should be a restriction that very early sampling time points (< 5 days) should not be used to calculate steady state conditions, to negate the effect of the dissolution of high energy fine fragments and high energy sites, such as sharp corners and needle like features.

2. **Application of the shrinking core model should be formally adopted.**

   Most SPFT literature includes the application of the shrinking core model, which accounts for the decreasing glass surface area with reaction progress, developed by McGrail *et al.* (1997) as described in Chapter 3, Equations 3.26-3.27 . However, a number of publications do not include the shrinking core model, which de-value the obtained data. See Figure 4.11, Table 4.2 and Appendix II-III for a comparison of results obtained with and without the application of the shrinking core model.

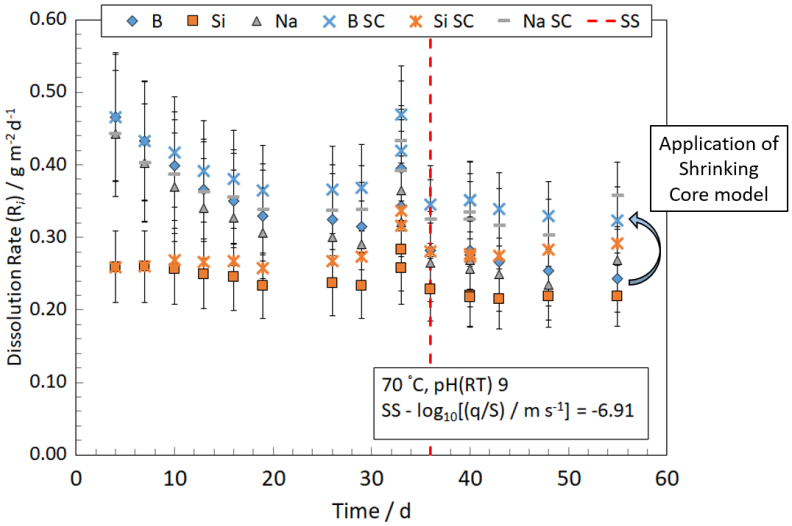

Figure 4.11. Illustration of the increase/correction in dissolution rate of the ISG with the application of the shrinking core (SC) model (McGrail et al. 1997). SS = steady-state attainment.

3. **Appropriate buffer solutions should be suggested.**

   This will maintain consistency with datasets. However, the updated ASTM (2018) standard now suggests a range of buffer solutions (including 0.005 M potassium hydrogen phthalate, TRIS and LiCl + LiOH (as used in this Thesis – Section 3.3)) stating; "*Buffers should be selected to avoid strong complexants and solutes known to affect the dissolution rate. Glass components that are also components of the buffer in concentrations that are significant with respect to the concentrations generated due to release from the glass should not be used to determine the dissolution rate of the glass".*

4. **Analysis/characterisation, such as SEM, TEM, XRD of samples post-dissolution should be a requirement.**

   This will allow for a better understanding of surface changes throughout experimentation. A suggestion for future work would be to conduct extended SPFT experiments (120 d), with sacrificial samples taken at various time points to investigate surface changes. Such work could provide greater insight into the pit formation and alteration layer development as observed in this study.

4.4 Conclusion

Dissolution of the ISG has been investigated using the SPFT methodology and the initial rates and rate law parameters (according to TST) determined. Dilute experiments were performed under a range of temperatures (40-70 °C) and pH(RT) (pH 4.5 to 11), and a linear-multivariate-regression was applied to the Transition State Theory kinetic rate law to obtain the fundamental rate law parameters necessary to model the dissolution kinetics, including: the activation energy (E_a); pH power-law coefficient (η); and the intrinsic rate constant (k_0). Initial dissolution rates were found to be scattered/invariant with respect to different flow-rates (q) to sample surface area (S) (q/S sweep), which could be related to the glass structure. The initial rate of Si was found to be 2 to 7 times lower (hence, more accurate) than determined by other methodologies published in the literature, for example, the micro-channel-flow-through method that is often thought to be analogous to SPFT. Basic initial rates reported here are in good agreement with recent SPFT studies, which gives confidence in their accuracy, which is of significance to the glass community whom often report and use initial rates of the ISG as input data to feed kinetic rate modelling. Also, for the first time, evidence for preferential localised dissolution has been observed for the ISG under extended dynamic experimental conditions of the SPFT protocol; which may be related to the fundamental glass structure. Additionally, q/S ratios were established representative of dilute conditions to apply to other simple glass compositions investigated in later Chapters 5 & 9, to negate having to perform a ‘q/S sweep’ on each composition. The data presented highlight some areas of the SPFT protocol that would benefit from review.

4.5 Appendix

I – Determination of steady-state dissolution – q/S sweep at pH(RT) 9 and 40 °C

Steady-state (SS) normalised dissolution rates are denoted by the red dashed line. Note that in the cases of: c) SS selected at 30 d in order to omit outliers at 17 & 27 d; h) $\log_{10}[(q/S) / m\ s^{-1}] = -6.83$, an approach to steady-state (ASS) dissolution was observed, denoted by the yellow dashed line.

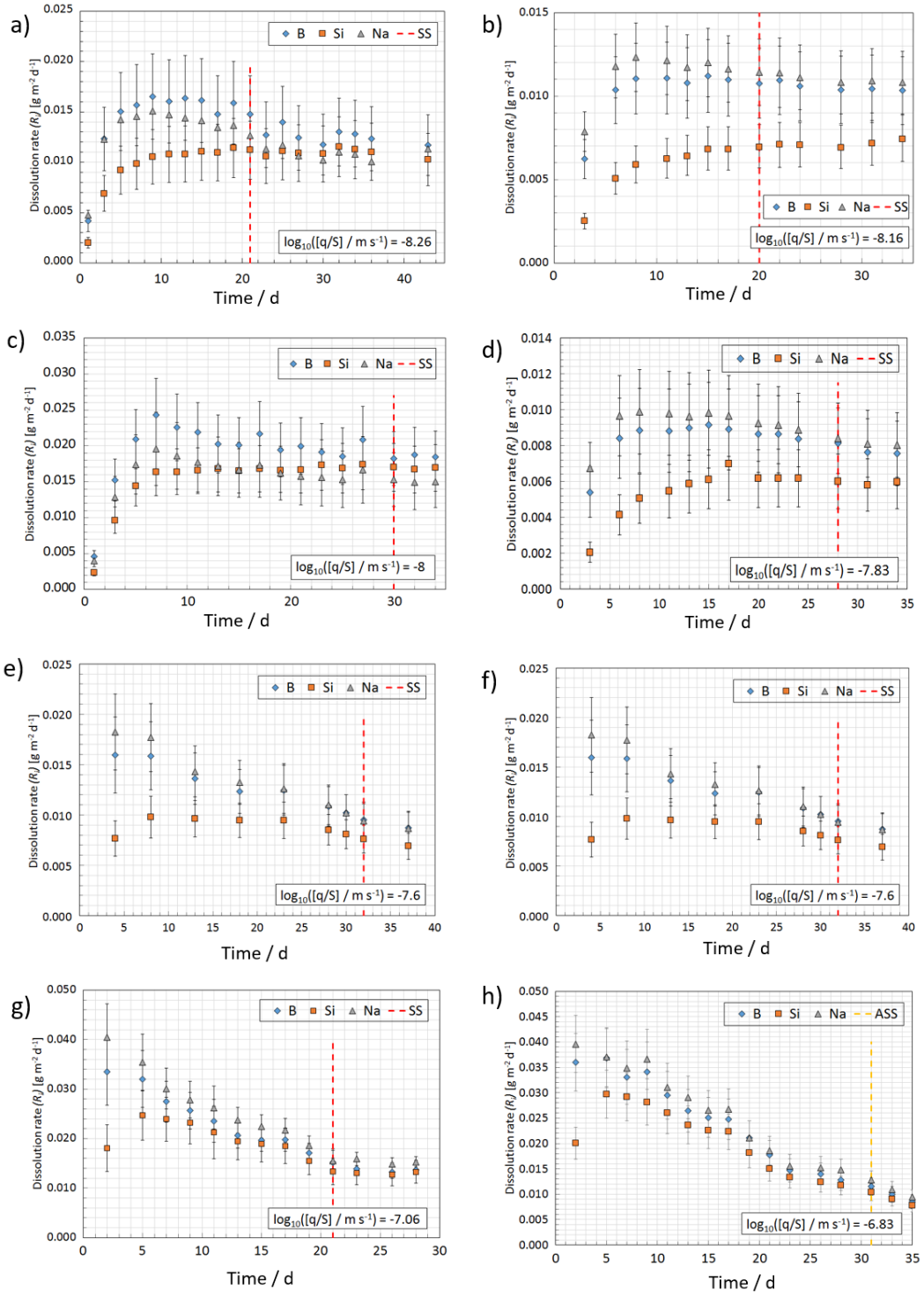

II – Determination of steady-state dissolution – Basic regime

Note – data from shrinking core model (SC) only shown if the SS surface area decreased < 99 % of original surface area. In cases otherwise, data points overlap. b) The input buffer drited below desired pH value at approximately 79 d, which resulted in a discontinuous drop in the normalised dissolution rate. Hence, SS dissolution was reached at approximately 43 d.

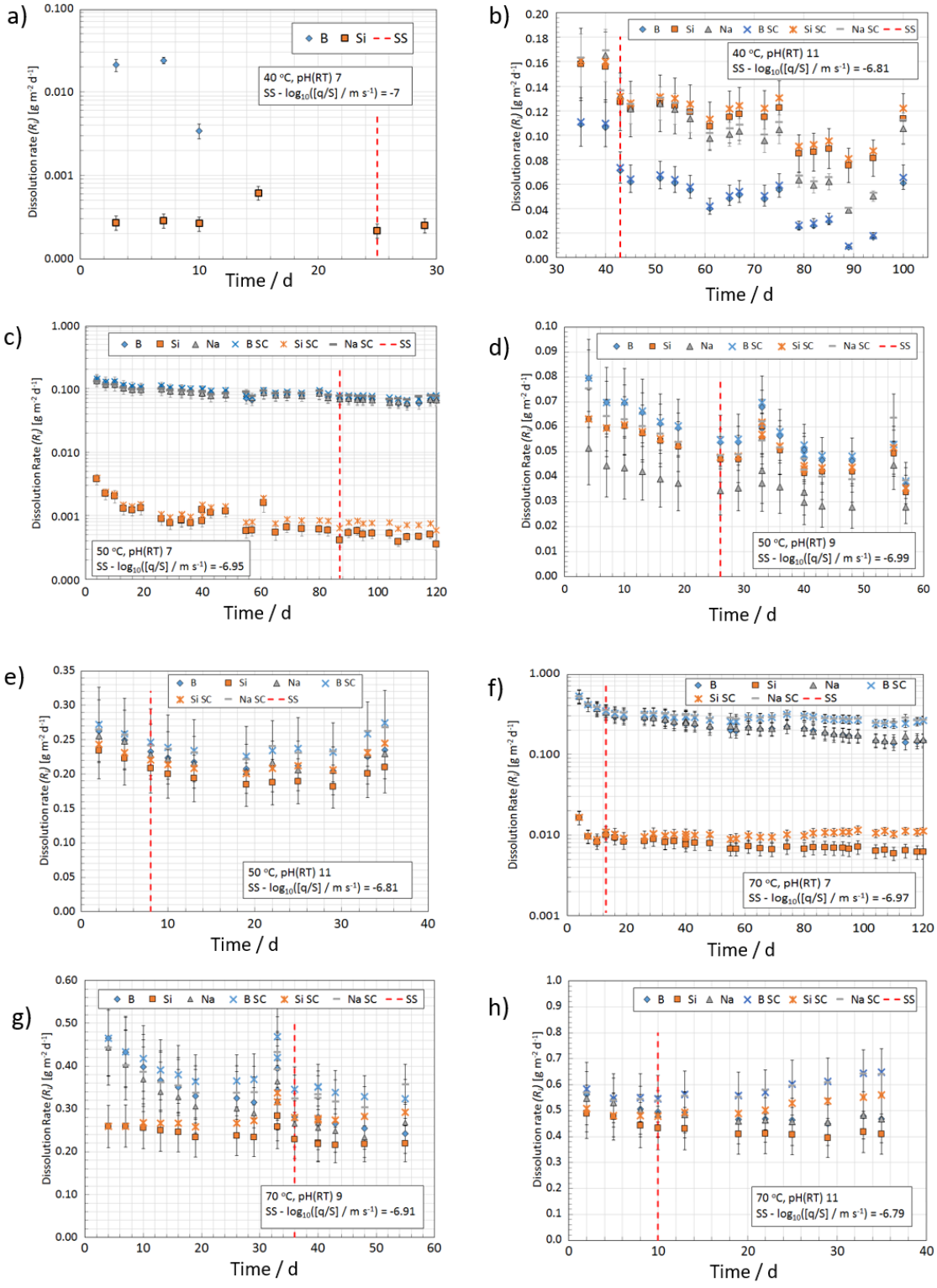

III – Determination of steady-state dissolution – Acidic regime

Note – shrinking core model (SC) only shown if the SS surface area decreased < 95 % of original surface area.

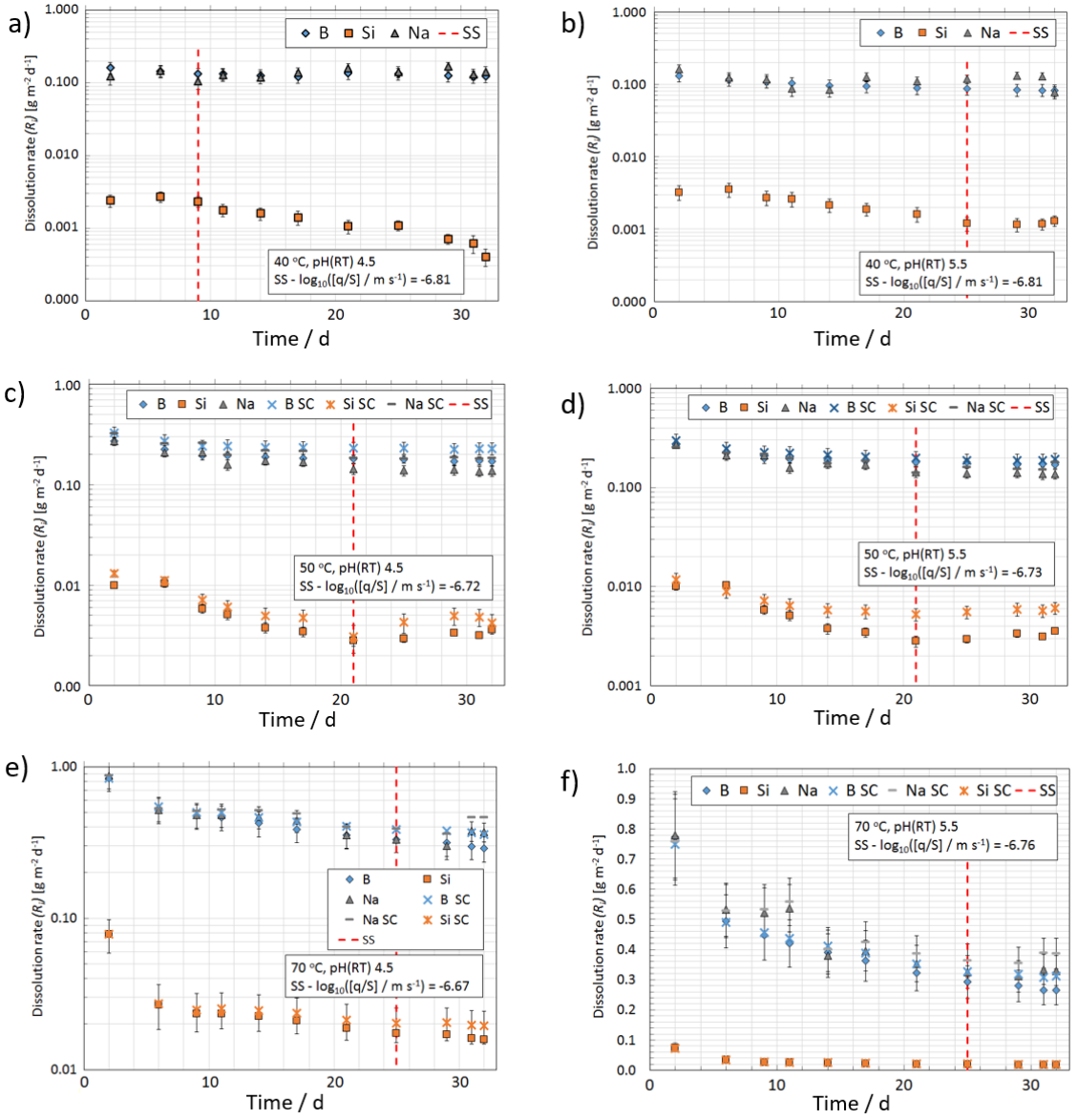

IV – Derivation

$$r = k_0 v_i (a_{H^+}^{\eta_{acid}} + a_{OH^-}^{\eta_{alkaline}}) \exp\left(\frac{-E_a}{RT}\right)\left[1 - \left(\frac{Q}{K_g}\right)^{\sigma}\right]$$

Where a_{H^+} and a_{OH^-} are simplified to pH for brevity

$$\log r = \log k_0 + \log v_i + \eta pH + log \exp\left(\frac{-E_a}{RT}\right) + \sigma log\left[1 - \left(\frac{Q}{K_g}\right)\right]$$

Simplifying log terms

$$\log r = \log k_0 + \log v_i + \eta pH - \left(\frac{E_a}{2.303RT}\right) + \sigma log\left[1 - \left(\frac{Q}{K_g}\right)\right]$$

Now noting that $\log \mathrm{NR} = \log \mathrm{r} - \log v_i$, i.e. $\mathrm{NR} = \mathrm{r}/v_i$ and $\sigma log\left[1 - \left(\frac{Q}{K_g}\right)\right] = 0$ when dilute conditions are sustained at the forward rates as $1 - \left(\frac{Q}{K_g}\right) = 1$

$$\log \mathrm{NR} = \log k_0 + \eta pH - \left(\frac{E_a}{2.303RT}\right)$$

Which corresponds to the parameters in the linear multi-variate regression (LMR):

$$\mathrm{Z} = \mathrm{Z}_0 + \mathrm{ax} + \mathrm{by}$$

Therefore $\mathrm{a} = \eta$, $\mathrm{x} = \mathrm{pH}$, $\mathrm{b} = -\mathrm{E_a}$ and $\mathrm{y} = \frac{1}{2.303\mathrm{RT}}$

where *r* is the dissolution rate (g m^{-2} d^{-1}), k_0 (g m^{-2} d^{-1}) the forward rate constant, which is the intrinsic rate at which the surface of the glass hydrolyses, v_i the stoichiometric coefficient for element *i*, E_a the activation energy (kJ mol^{-1}), RT the product of the gas constant (kJ mol^{-1}) and the absolute temperature (K), a_{H+} and a_{OH-} the proton and hydronium activity, η the pH power-law coefficient, Q the ion activity product (dimensionless), K_g the pseudo-equilibrium constant (solubility constant) for the rate-controlling reaction and σ the Temkin coefficient/rate of decomposition of the activated complex (dimensionless, and assumed to be unity for borosilicate glass (Lasaga 1995)).

5. Structure-dissolution relationship of simplified High-Level-Waste glass as a function of ZnO:CaO ratio

Summary

This Chapter presents data relating to the structure and dissolution of a series of simplified ZnCa-containing alkali-aluminaborosilicate MW base glass. It demonstrates the effects of Zn and Ca incorporation on the structure of the glass and the subsequent influence on the chemical durability at the initial, residual and resumed rates of dissolution. A significant decrease in the chemical durability was observed for the Zn-containing glasses in long-term MCC-1 UHQ water dissolution tests (pH(RT) < 9 at 50 °C), which was attributed to the abundant precipitation of Zn-silicates (particularly Zn-bearing phyllosilicate clays). It is hypothesised that the precipitation of Zn-silicate clays are associated with early Stage III 'rate resumption'. This hypothesis, upon suggested further confirmatory work, recommends that the classical definition of 'Stage III' behaviour (Frugier *et al.* 2008, Vienna *et al.* 2013) could be expanded to incorporate the precipitation of Zn-silicate clays, which were formed in a dissolution-re-precipitation process.

5.1 Introduction

The UK is currently in the process of adopting a modified base glass, containing ZnO and CaO, for the vitrification of HLW at a molar ratio of 40:60 ZnO:CaO in the nominal four-component Mixed Windscale (MW) formulation (Table 5.1). The addition of ZnO and CaO is known to provide many beneficial properties for the processing and final physical properties such as: reducing the melt viscosity; extending the melter lifetime (i.e. reduced refractory lining corrosion); supporting pouring at lower temperatures (Short *et al.* 2008) and providing greater homogeneity and improved chemical durability (Matlack *et al.* 1998).

Table 5.1. The original MW and new ZnCa MW base glass formulations deployed on two and one active lines, respectively, at the Sellafield vitrification plant. Note that the impact of Al_2O_3 inclusion into the new modified ZnCa MW composition is not directly investigated in this study and is therefore treated as a constant component in the glass formulations studied (NNL 2014).

Oxide Component	MW	ZnCa MW
	wt. %	
SiO_2	61.7	47.6
B_2O_3	21.9	23.4
Al_2O_3	-	4.2
Na_2O	11.1	8.6
Li_2O	5.3	4.2
ZnO	-	5.9
CaO	-	6.1

Currently, ZnCa MW is deployed on one of the three operational active vitrification lines at the Waste Vitrification Plant (WVP) at the Sellafield site. A decision to extend ZnCa MW to the other two lines, or to return to the original MW formulation, will be made within the next few years (Harrison 2018a) on further evaluation of data pertaining to the effectiveness of the ZnCa MW in terms of active processing ability (on the one active line), and from laboratory scale experiments of the waste-loading capacity and chemical durability, especially Stages II and III in solutions more representative of a geological disposal environment. However, recent evidence suggests that the processing is problematic, due to the readily formed Zn-spinel phases causing blockages around the melter nozzle (Gribble, *pers. Comm*).

In terms of improving the chemical durability of the glass, the addition of Zn was shown to reduce Soxhlet leach rates (at the initial rate) (Matlack *et al.* 1998) and Ca was reported to stabilize Mo in a chemically durable $CaMoO_4$ phase (Dunnett *et al.* 2012) for ZnCa MW wasted loaded glasses compared to standard MW25. Fundamental durability studies have also shown that the addition of Ca to sodium aluminaborosilicate glasses significantly improves Stage II glass durability, at least in the short term (Chave *et al.* 2011, Utton *et al.* 2012, Zhang *et al.* 2015, Maraghechi *et al.* 2016, Aréna *et al.* 2018), but Ca has been postulated to cause rate resumption and the transition into Stage III dissolution at longer timescales (Muller *et al.* 2006). The effect of Zn addition to glass on the durability behaviour is contested; it has been reported to both increase (Lewis *et al.* 1982, Calestani *et al.* 1986, Della *et al.* 1986, Ennas *et al.* 1990, Stechert *et al.* 2013) and decrease (Gin *et al.* 2013) the durability. Interpretation of the literature from vapour phase tests on waste-loaded ZnCa MW-type glasses indicate that Zn may worsen the chemical durability (Zhang *et al.* 2015, Cassingham *et al.* 2016) by participating in secondary phase precipitation.

Due to uncertainties surrounding the effect of ZnO and CaO addition on the chemical durability of alkali-aluminaborosilicate glass, this Chapter aims to systematically account for the compositional effects of Zn and Ca on the structure-durability relationship across all stages of glass corrosion, using a series of six simplified glass compositions, based on the UK HLW base glass formulation (Table 3.2, Chapter 3 and Table 5.2), that vary in respect to their ZnO:CaO content (referred to hereon as ZnCa xx:xx where xx denotes the molar ratio percentage of each oxide). This will provide information of relevance to fundamentally underpin the use of ZnCa MW glass at the WVP in terms of its chemical durability, in addition to providing information required for the developing safety case for the geological disposal of vitrified HLW. Such a study also reduces the complexities associated with studying multi-oxide component waste-loaded glasses (discussed in Chapters 6-8).

Table 5.2 Analysed ZnCa xx:xx glass compositions from HF digest and ICP-OES (relative uncertainty ± 3 %). Density uncertainty ± 0.005 g /cm^3.

Glass Network Role	Oxide	ZnCa base MW-type (ZnCa xx:xx)											
		ZnCa 0:100		ZnCa 20:80		ZnCa 40:60		ZnCa 60:40		ZnCa 80:20		ZnCa 100:0	
		wt. %	mol. %	wt. %	mol. %	wt. %	mol. %	wt. %	mol. %	wt. %	mol. %	wt. %	mol. %
Formers	SiO_2	53.20	53.60	51.00	51.90	51.20	52.50	45.40	47.10	46.00	48.10	43.90	46.40
	B_2O_3	22.30	19.40	23.30	20.50	22.50	19.90	25.30	22.70	23.80	21.50	24.40	22.30
	Al_2O_3	3.70	2.20	3.70	2.20	3.70	2.20	4.00	2.50	4.00	2.50	3.90	2.40
Int	**ZnO**	-	-	**3.00**	**2.30**	**5.80**	**4.40**	**9.40**	**7.20**	**12.50**	**9.70**	**15.90**	**12.40**
Modifiers	**CaO**	**9.40**	**10.10**	**7.60**	**8.30**	**5.50**	**6.10**	**4.10**	**4.60**	**2.00**	**2.20**	**0.10**	**0.10**
	Li_2O	3.50	7.10	3.50	7.20	3.50	7.20	3.80	7.90	3.80	8.00	3.90	8.30
	Na_2O	7.80	7.60	7.90	7.80	7.70	7.70	8.00	8.10	7.90	8.00	7.90	8.10
Density / g cm^3		2.58		2.60		2.63		2.64		2.69		2.71	

This Chapter describes the following experiments, which include solid state (XRD, SEM) and geochemical (ICP-OES and PHREEQ-C) analysis:

1) Flow-through dissolution (SPFT – pH(RT) 9 and 40 °C) investigations with complementary ^{27}Al, ^{11}B and ^{29}Si MAS-NMR reveal how the glass structure is related to the initial rate of dissolution (Stage I).
2) PCT-B investigations (UHQ, 90 °C, 35 d) reveal how the residual rate of dissolution (Stage II) varies between glass compositions and how it compares with Stage I dissolution behaviour.
3) MCC-1 investigations (UHQ, 50 °C, 540 d) probe how the structure and composition of the altered layers relate to Stage II & III dissolution, suggesting rate-limiting and rate-increasing steps in the dissolution mechanism.

5.2 Results

5.2.1 Glass Characterisation – SEM, XRD and DTA

SEM showed that each sample was transparent, homogenous and free of inclusions or crystals (images omitted for brevity). XRD displayed diffuse scattered peaks, which confirmed the amorphous nature of all samples (Figure 5.1). Thermal analysis appeared to indicate the presence of two glass transition (T_g), crystallization (T_c) and liquidus (T_l) temperatures for the compositions ZnCa 100:0 and ZnCa 80:20, indicative of a two-phase glass (Table 5.3), where phase separation is commonly reported for similar Zn-rich glass compositions (Taylor & Owen 1981, Taylor 1990, Goswami *et al.* 2008, Petrescu *et al.* 2012, Soleimanzade *et al.* 2014, Kullberg *et al*. 2016, Vance *et al.* 2017). Hence it is strongly assumed that ZnCa 100:0 and 80:20 are phase separated. A plot of the glass transition region is displayed in Figure 5.2. The glass transition temperature was greatest for ZnCa 0:100, whereby the following T_{g1} (°C) sequence was observed: ZnCa 0:100 > 20:80 > 40:60 > 60:40 > 80:20 > 100:0.

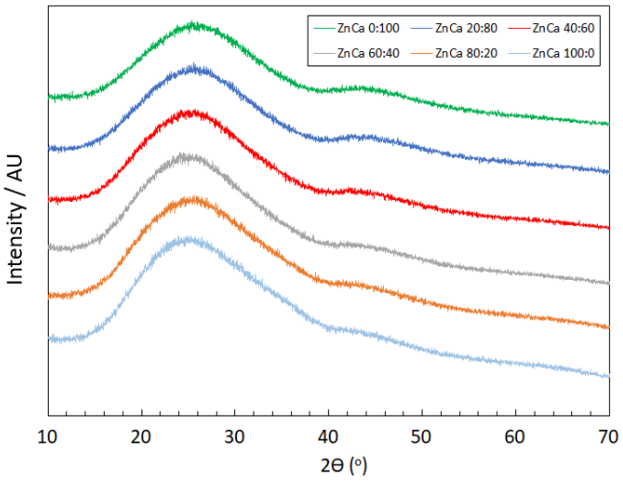

Figure 5.1. XRD traces of the ZnCa xx:xx series.

Table 5.3 Thermal analysis highlighting T_g, T_c and T_l for the full range of the ZnCa xx:xx series.

		ZnCa 100:0	ZnCa 80:20	ZnCa 60:40	ZnCa 40:60	ZnCa 20:80	ZnCa 0:100
Temperature / °C	T_{g1}	464.5	480	514	520	527.5	534
	T_{g2}	499.5	498	-	-	-	-
	T_{c1}	588	600	610	623	629	634
	T_{c2}	675	715	-	-	-	-
	T_{l1}	620	625	641	643	650	655
	T_{l2}	719	750	-	-	-	-

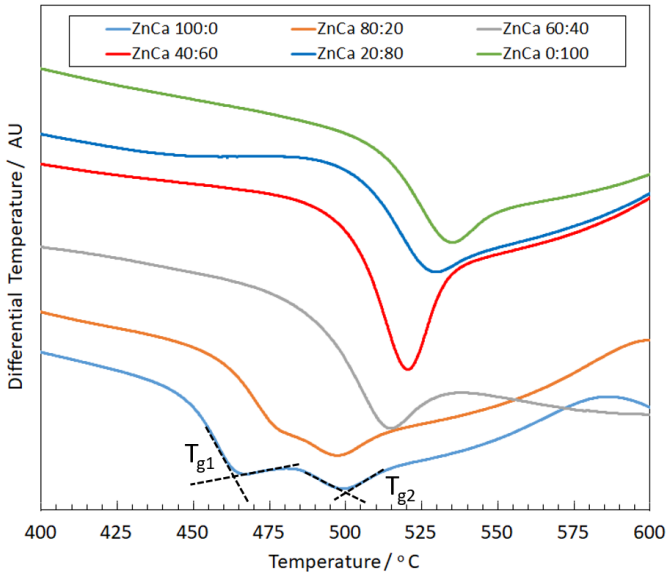

Figure 5.2. DTA traces for the full range of the ZnCa xx:xx series focussing on the glass transition range. The acquisition of T_{g1} and T_{g2} (Shelby 2015, Kaky *et al*. 2017) from linear extrapolation of the tangent points for ZnCa 100:0 is illustrated.

5.2.2 Glass Structure - MAS-NMR

5.2.2.1 ^{27}Al MAS-NMR

Aluminium was found to be entirely in four-fold tetrahedral coordination ($^{[4]}$Al) across the the ZnCa xx:xx series, indicated by the ^{27}Al peak maximum falling between 50-80 ppm (Fig. 5.3) (Engelhardt & Michel 1987b). This confirmed that Al was entirely in a network forming role in all glass compositions. Comparable spectra have been observed for similar alkali-aluminoborosilicate glasses (Darab *et al.*, 1997, 1999, Du & Stebbins 2005, Pierce *et al.* 2010).

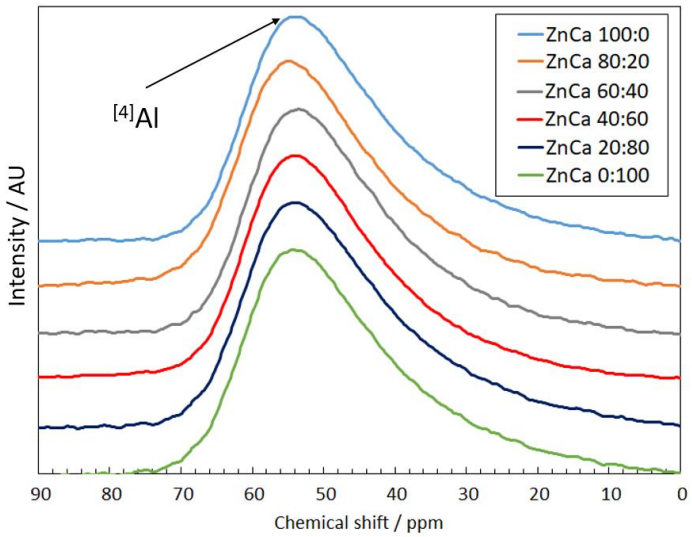

Figure 5.3. ^{27}Al MAS-NMR spectra for the ZnCa xx:xx series.

5.2.2.2 ^{11}B MAS-NMR

The ^{11}B MAS-NMR spectra, their deconvolution fitting parameters and the fraction of BO_3 ($^{[3]}$B) and BO_4 ($^{[4]}$B) contributions for each of the ZnCa xx:xx compositions are shown in Figure 5.4 and Table 5.4. Detailed plots of the spectral deconvolution giving rise to data in Table 5.4 are provided in Appendix I. The total integrated spectral deconvolution of the $^{[3]}$B and $^{[4]}$B regions showed that as the Zn:Ca ratio increased there was a general trend towards increasing $^{[3]}$B units and decreasing $^{[4]}$B units (Fig. 5.5a). The increase in $^{[3]}$B may be due to the requirement of charge compensation on the $[ZnO_4]^{-2}$ tetrahedra, which may result in less alkali available to convert $^{[3]}$B to $^{[4]}$B (Dell *et al*. 1983). Concurrently, a reduction in the Ca content may result in less charge available to charge compensate $^{[4]}$B units, on the assumption that Ca^{2+} can contribute towards the charge compensation of $^{[4]}$B (Shelby 2005, Wu and Stebbins 2009), hence $^{[3]}$B units are preferentially formed.

Deconvolution of the $^{[3]}$B and $^{[4]}$B regions revealed the presence of different B co-ordination environments throughout all compositions (Fig. 5.5b). The $^{[4]}$B (0B, 4Si) contribution was invariant with respect to the Zn:Ca ratio, however, the $^{[4]}$B (1B, 3Si) contribution was observed to decrease. This may suggest that the $^{[4]}$B (0B, 4Si) units are not affected by the presence of Zn and Ca, which may imply inherent phase separation throughout the compositional series, where borosilicate (associated with $^{[3]}$B) and alkali/alkaline earth borosilicate (associated with $^{[4]}$B) networks co-exist.

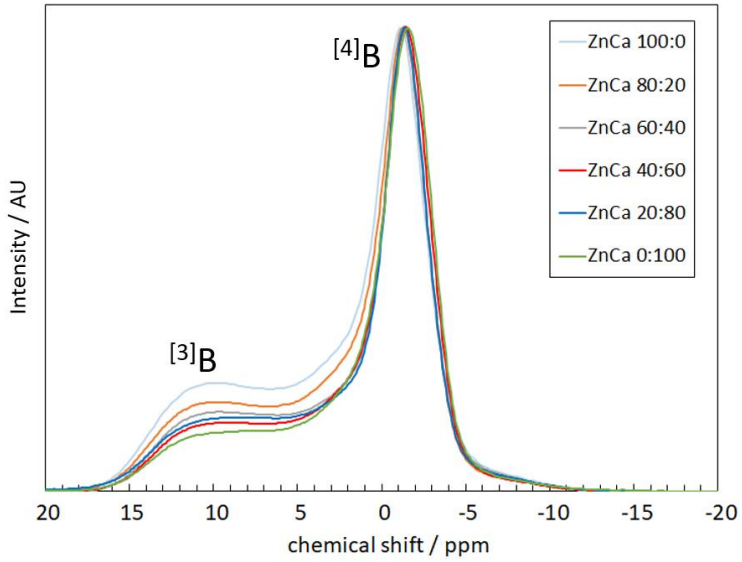

Figure 5.4. ^{11}B MAS-NMR spectra for the ZnCa xx:xx series. Spectral deconvolution is provided in 5.5 Appendix I.

Table 5.4 ^{11}B MAS-NMR spectral fitting parameters and BO_3 and BO_4 contributions for the ZnCa xx:xx series.

Composition	B Species	Chem shift (ppm) (± 1)	C_Q MHz (± 0.2)	Rel .% (± 2)	Rel .% Error	Total .% BO_3/BO_4	Total ± .%	η_Q (± 0.1)
ZnCa100:0	BO_3 (a) ring	16.8	2.7	20.49	0.2	48.1	9.6	0.4
	BO_3 (b) non-ring	14.5	2.7	27.58	0.2			0.3
	BO_4 (a) (1B, 3Si)	-0.8	-	44.83	-	51.9	10.4	-
	BO_4 (b) (0B, 4Si)	-2.2	-	7.09	-		1.4	-
ZnCa80:20	BO_3 (a) ring	16.8	2.7	20.42	0.4	44.1	8.8	0.4
	BO_3 (b) non-ring	14.5	2.7	23.64	0.3			0.3
	BO_4 (a) (1B, 3Si)	-1	-	48.17	-	56.0	11.2	-
	BO_4 (b) (0B, 4Si)	-2.2	-	7.78	-		1.6	-
ZnCa60:40	BO_3 (a) ring	16.8	2.7	18.4	0.4	41.0	8.2	0.4
	BO_3 (b) non-ring	14.6	2.7	22.59	0.3			0.3
	BO_4 (a) (1B, 3Si)	-1.1	-	50.32	-	59.0	11.8	-
	BO_4 (b) (0B, 4Si)	-2.25	-	8.69	-		1.7	-
ZnCa40:60	BO_3 (a) ring	16.8	2.7	15.16	0.4	36.6	7.3	0.4
	BO_3 (b) non-ring	14.6	2.7	21.43	0.3			0.3
	BO_4 (a) (1B, 3Si)	-1.2	-	54.74	-	63.4	12.7	-
	BO_4 (b) (0B, 4Si)	-2.3	-	8.66	-		1.7	-
ZnCa20:80	BO_3 (a) ring	16.9	2.7	15.42	0.4	37.1	7.4	0.4
	BO_3 (b) non-ring	14.6	2.7	21.7	0.3			0.3
	BO_4 (a) (1B, 3Si)	-1.15	-	55.03	-	62.9	12.6	-
	BO_4 (b) (0B, 4Si)	-2.3	-	7.86	-		1.6	-
ZnCa0:100	BO_3 (a) ring	16.9	2.7	13.89	0.4	32.3	6.5	0.4
	BO_3 (b) non-ring	14.4	2.7	18.39	0.3			0.3
	BO_4 (a) (1B, 3Si)	-1.3	-	59.49	-	67.7	13.5	-
	BO_4 (b) (0B, 4Si)	-2.3	-	8.23	-		1.6	-

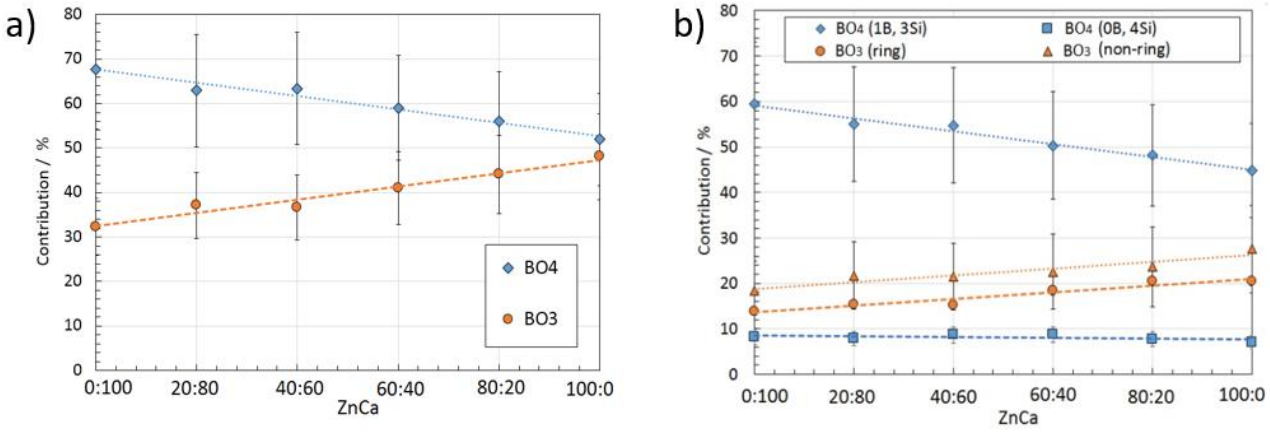

Figure 5.5. ^{11}B MAS-NMR spectra for the ZnCa xx:xx series: a) Total $^{[3]}$B and $^{[4]}$B contribution; b) proportion of individual $^{[3]}$B and $^{[4]}$B contributions. Spectral deconvolution is provided in 5.5 Appendix I.

5.2.2.3 ^{29}Si MAS-NMR

Background subtracted ^{29}Si MAS-NMR spectra are shown alongside corresponding spectral deconvolution results in Figure 5.6, whereby individual spectral deconvolution plots (Q_n specie quantification) are available in Figure 5.7. With increasing Zn:Ca ratio there was a tendency towards a more negative chemical shift (Table 5.5) and a greater proportion of Q_4(X) species (where X = $^{[4]}$Al, $^{[3\ \&\ 4]}$B and/or $^{[4]}$Zn), indicative of a more polymerised network (Fig. 5.6b). This trend was observed up to, and including, the ZnCa 60:40 composition, after which a decrease in the Q_4(X) species and an increase in the Q_2 species were observed. Due to the limits of the applied spectral deconvolution, it was difficult to isolate pure Q_3 contributions from Q_4(X) for some compositions, hence the distinction: Q_3(Un) and Q_3(R), where Un = unresolved and R = resolved (Fig. 5.6b). The spectra from the Zn-rich glasses (ZnCa 100:0, 80:20 & 60:40) revealed a broadening of the overall spectral width, where more Q_4 and Q_2 species were observed when compared to the Ca-rich (ZnCa 40:60, 20:80 & 0:100) compositions. This may be an artifact of the large distribution of chemical shifts induced by a wide range of Si environments resulting from the substituiton of the elements B, Al and four-fold Zn into the silicate network, thus, changes in next nearest neighbour and the type of NBO sites. It may be possible that Zn in the Zn-rich glasses (ZnCa 100:0, 80:20 & 60:40) is also performing a network modifier role (six-fold coordination), which would result in lower Q_n species due to the creation of NBOs. Therefore, it is plausible that both a combination of chemical shift dispersion and a fraction of modifying Zn contributed to the overall broadening of the spectral widths for the Zn-rich glasses.

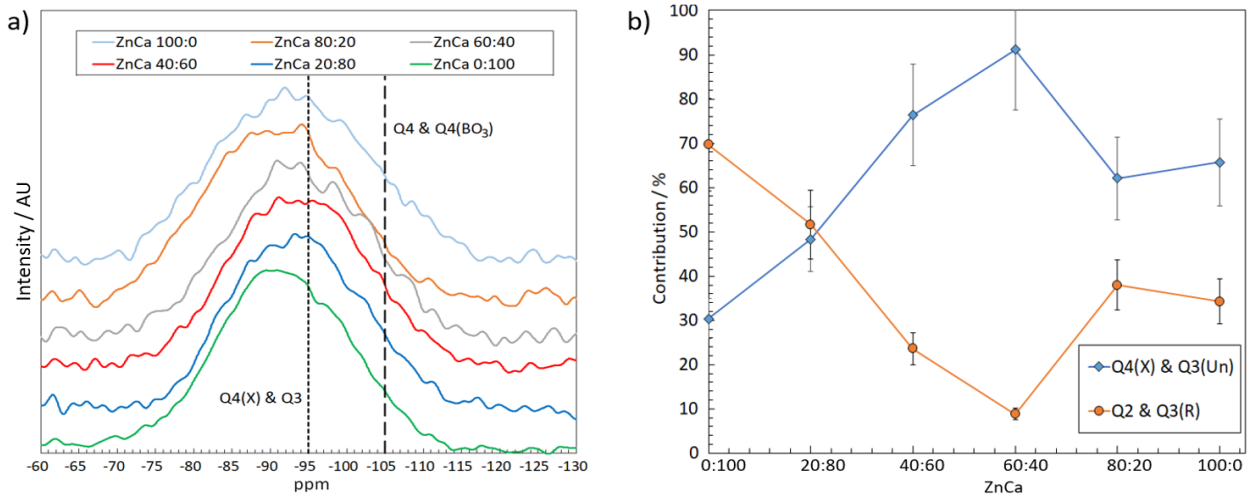

Figure 5.6. a) ^{29}Si MAS-NMR spectra for the ZnCa xx:xx series. The dashed lines represent the approximate chemical shift of the Q4(X) & Q3 and Q4 & Q4(BO_3) contributions; b) Q_n contributions for the ZnCa xx:xx series.

Table 5.5 Data from the ^{29}Si MAS-NMR spectral deconvolution for the ZnCa xx:xx series.

		ZnCa 100:0	ZnCa 80:20	ZnCa 60:40	ZnCa 40:60	ZnCa 20:80	ZnCa 0:100
Speciation	Fit peak (ppm)	-93 ± 0.5	-91.6 ± 0.5	-92.15 ± 0.5	-92.9 ± 0.5	-92.6 ± 0.5	-90.5 ± 0.5
Q4 & Q4(BO_3)	peak (ppm)	-106	-105	-105	-105	-	-
	FWHM (ppm)	17	17	11	16	15	-
	cont. %	17.5 ± 2.6	2.3 ± 0.3	18.4 ± 2.8	15 ± 2.3	-	-
Q4(X) & Q3	peak (ppm)	-95	-94.5	-92.8	-94.5	-98.5	-99.8
	FWHM (ppm)	17	17	17	17	17	13
	cont. %	48.2 ± 7.2	59.8 ± 9.0	72.8 ± 10.9	61.4 ± 9.2	48.36 ± 7.3	30.4 ± 4.6
Q3	peak (ppm)	-	-	-	-	-88.7	-89.5
	FWHM (ppm)	-	-	-	-	17	15
	cont. %	-	-	-	-	51.64 ± 7.7	63 ± 9.5
Q2	peak (ppm)	-85	83.7	-80	-85.5	-	-80.4
	FWHM (ppm)	17	15	13	17	-	17
	cont. %	34.3 ± 5.1	38 ± 5.7	8.8 ± 1.3	23.6 ± 3.5	-	6.7 ± 1.0

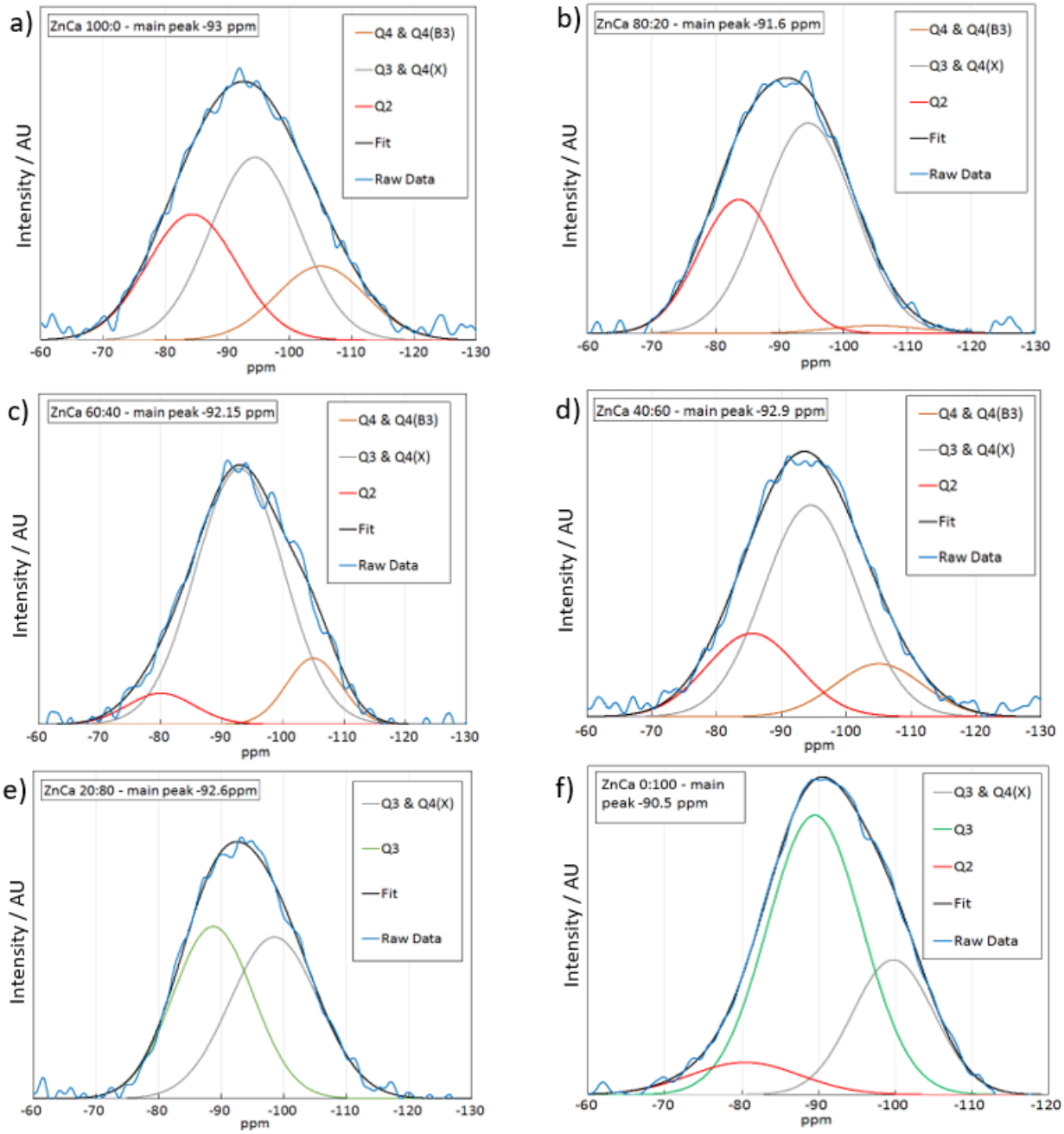

Figure 5.7. a-f) ^{29}Si MAS-NMR spectral deconvolution from each composition within the ZnCa xx:xx series.

5.2.2.4 MAS-NMR comparison with predictions and modified Dell-Bray model

The $^{[X]}$B and Q_n speciation predictions and measured MAS-NMR data (Table 5.6), suggests that Zn plays a dual (intermediate) role in the Zn-rich compositions (Le Grand *et al.* 2000, Calas *et al.* 2002, Petrescu *et al.* 2012). Table 5.6 can be complemented by referring to Equations 5.1-5.15 below (originally introduced as Equations 3.6-3.20 in Chapter 3)), which account for the comparisons between structural predictions and observed measurements.

$$R_{eff} = \frac{[(Na_2O)+(Li_2O)+(CaO)]-[(Al_2O_3)+(ZnO)]}{(B_2O_3)} \quad [5.1]$$

$$K = \frac{(SiO_2)}{(B_2O_3)} \quad [5.2]$$

$$R_{max} = \frac{1}{2} + \frac{1}{16}K \quad [5.3]$$

$$R_{d1} = \frac{1}{2} + \frac{1}{4}K \quad [5.4]$$

$$R_{dl2} = 2 + K \quad [5.5]$$

Where the fraction of B4:

$$B4 = \frac{8+K}{12}\left(1 - \frac{R_{eff}}{2+K}\right) \quad \text{if } R_{d1} < R_{eff} < R_{d2}, \quad [5.6]$$

$$B4 = R_{max} \quad \text{if } R_{max} < R_{eff} < R_{d1}, \quad [5.7]$$

$$B4 = R_{eff} \quad \text{if } R_{eff} < R_{max.} \quad [5.8]$$

The predicted B3 fraction is therefore:

$$B3 = 1 - B4 \quad [5.9]$$

A comparison between the predicated B4/B3 contributions and measured contribution is given by the ratio:

$$B_{Accuracy} = \frac{\text{B Measured}}{\text{B Predicted}} \quad [5.10]$$

The amount of alkali oxide (mole fraction) associated with the silicate network (R_2O (Si)) was determined by a modification of the equation from El-Damrawi *et al.* (1993), where all terms relate to the molar fraction:

$$R_2O(Si) = R_2O - \{R_2O[BO_4(B_2O_3)] + R_2O[Al_2O_3]\} \quad [5.11]$$

where R_2O is the total alkali content of the glass, $R_2O[BO_4(B_2O_3)]$ is the amount of alkali associated with the borate network and $R_2O[Al_2O_3]$ is the amount of alkali associated with Al_2O_3.

Accounting for the charge neutrality of the tetrahedral coordinated Zn content, gives Equation 3.17:

$$R_2O + CaO\ (Si\ /\ Zn) = (R_2O + CaO) - \{R_2O[BO_4(B_2O_3)] + R_2O[Al_2O_3]\} \quad [5.12]$$

Where R_2O + CaO (Si/Zn) is the amount of alkali/Ca associated with the Si/Zn network forming tetrahedral. Note the assumption that one mole of Al_2O_3 /B_2O_3/ ZnO is associated with one mole of

alkali (R_2O) / CaO. The amount of network forming Zn tetrahedra left uncharged, and therefore representing Zn octrahedra (ZnO_6) performing a network modifying role, is:

$$ZnO_6 = ZnO - [5.12] \quad [5.13]$$

The fraction of Q3 is given by:

$$Q3 = [5.12] - SiO_2 \quad [5.14]$$

Therefore, the fraction of Q4[X] predicted (where X= network forming Al, B or Zn), inclusive of the dual network forming/modifying role or Zn, is:

$$Q4[X] = \frac{SiO_2 - [5.14]}{SiO_2} \quad [5.15]$$

The dual role of Zn is evidenced from Equation 5.13 (results displayed in Table 5.6); hence predictions indicate that a significant quantity of tetrahedral network forming $[ZnO_4]^{-2}$ would be unable to form due to a deficit in charge compensating cations in the Zn-rich compositions. This indirectly infers that the remaining Zn should take on a network modifying ZnO_6 configuration, which leads to network depolymerisation (lower Q_n speciation) in the Zn-rich compositions. The comparisons between the rows $Q_4(X)$ predicted (plotted in Fig. 5.8) and [Q_4 & $Q_4(^{[3]}B)$] + [$Q_4(X)$ & Q_3] (which are shaded in grey in Table 5.6) tentatively agree with this inference, which also illustrates the relative agreement between structural predictions and measurements (Fig. 5.8).

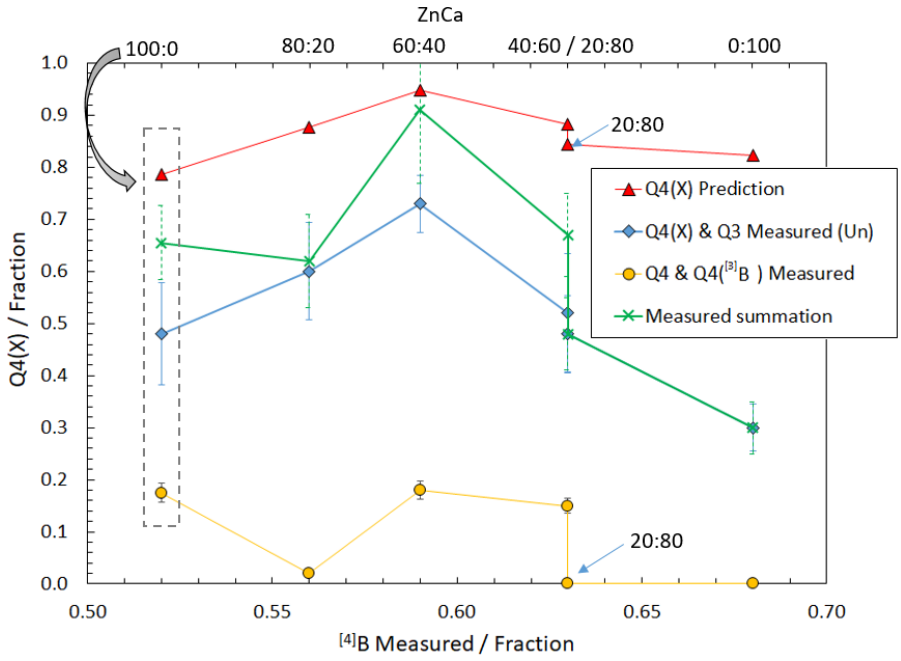

Figure 5.8. $Q_4(X)$ fraction (predicted and measured) from ^{29}Si MAS-NMR deconvolution versus $^{[4]}B$ measured fraction from ^{11}B MAS-NMR for the ZnCa xx:xx series. Note: that the grey dashed box shows the data points associated with ZnCa 100:0; the data points for ZnCa 40:60 correspond to greater $Q_4(X)$ contributions despite having the same measured $^{[4]}B$ fraction as ZnCa 20:80 (noting that the ZnCa 20:80 data has been explicitly identified within the plot). The measured summation is the total sum of the $Q_4(X)$ & Q_3 Measured (Un) and the Q_4 & $Q_4(^{[3]}B)$ fractions.

Table 5.6 $^{[X]}B$ and Q_n speciation: predictions and measurements. Parenthesised numbers correspond to the equations in this Chapter. Associated compositional relative uncertainty ± 3 %.

	Oxide Component	Composition					
		ZnCa 100:0	ZnCa 80:20	ZnCa 60:40	ZnCa 40:60	ZnCa 20:80	ZnCa 0:100
		mol. %	mol. %	mol. %	mol. %	mol. %	mol. %
	SiO_2	46.4	48.1	47.1	52.5	51.9	53.6
	B_2O_3	22.3	21.5	22.7	19.9	20.5	19.4
	Al_2O_3	2.4	2.5	2.5	2.2	2.2	2.2
	Na_2O	8.1	8.0	8.1	7.7	7.8	7.6
	Li_2O	8.3	8.0	7.9	7.2	7.2	7.1
	ZnO	12.4	9.7	7.2	4.4	2.3	0.0
	CaO	0.1	2.2	4.6	6.1	8.3	10.1
Compositional Boundaries	R_{eff} [5.1]	0.08	0.29	0.48	0.72	0.92	1.17
	K [5.2]	2.08	2.24	2.08	2.64	2.54	2.76
	R_{max} [5.3]	0.63	0.64	0.63	0.66	0.66	0.67
	R_{dl} [5.4]	1.02	1.06	1.02	1.16	1.13	1.19
	R_{dl2} [5.5]	4.08	4.24	4.08	4.64	4.54	4.76
BO_x / Fraction	BO_3 Predicted [5.9]	0.92	0.71	0.52	0.34	0.34	0.10
	BO_3 Measured	0.48	0.44	0.41	0.37	0.37	0.32
	BO_4 Predicted [5.6-5.8]	0.08	0.29	0.48	0.66	0.66	0.90
	BO_4 Measured	0.52	0.56	0.59	0.63	0.63	0.68
	BO_4 Prediction accuracy [5.10]	0.15	0.52	0.81	0.95	0.95	0.76
Predicted / Mol. %	R_2O + CaO	16.5	18.3	20.5	20.9	23.2	24.8
	R_2O + CaO available for $[ZnO_4]^{-2}$ & $Si(Q_3)$ [5.12]	2.49	3.75	4.71	6.14	8.13	9.46
	$[ZnO_4]^{-2}$ left uncharged (ZnO_6) [5.13]	9.91	5.90	2.49	-	-	-
	Q_3* [5.14]	0.00	0.00	0.00	1.75	5.88	9.46
$Q_n(X)$ / Fraction	$Q_4(X)$ Predicted - Zn duel role [5.15]	0.79	0.88	0.95	0.88	0.84	0.82
	Q_4 & $Q_4(B3)$ - Measured	0.175 ± 0.03	0.02 ± 0.003	0.18 ± 0.03	0.15 ± 0.02	0.00	0.00
	$Q_4(X)$ & Q_3 - Measured	0.48 ± 0.07	0.60 ± 0.09	0.73 ± 0.11	0.52 ± 0.08	0.48 ± 0.07	0.30 ± 0.05
	[Q_4 & $Q_4(B3)$] + [$Q_4(X)$ & Q_3]	0.66 ± 0.07	0.62 ± 0.09	0.91 ± 0.14	0.67 ± 0.08	0.48 ± 0.07	0.30 ± 0.05

*Formed after all $[ZnO_4]^{-2}$ is charge compensated - no Q3 predicted in Zn-rich glasses if it is assumed that Zn is playing a fully network-former role.

It should be noted that the network former elements are preferentially charged balanced in the order Al, Zn, B (Cormier *et al.* 2000). Therefore, assuming Al and most of the Zn tetrahedral units are charge balanced, it would suggest that the majority of B is trigonal coordinated ($^{[3]}$B prediction in Table 5.6) for the Zn-rich compositions, which is in contrast to what the ^{11}B MAS-NMR spectra suggest (Fig. 5.8 and BO_3 measured (Table 5.6)). This may indirectly indicate some form of phase separation into distinct micro-domains, most likely influenced by the Zn content, noting that the measured and predicted $^{[3]}$B fractions are in relatively good agreement for the Ca-rich compositions, apart from ZnCa 0:100. In the case of ZnCa 0:100, the discrepancy between the predicted and measured Q_4(X) fraction could be attributed to the predication that Ca^{2+} charge balances $^{[4]}$B preferentially (hence a greater predicted Q_4(X) contribution), but in reality Ca^{2+} contributes to creating Q_3 species (Wu and Stebbins 2009).

The key result was the observation of an inflection point in Figure 5.8 in both the Q_4(X) fraction and the $^{[4]}$B measured fraction at the ZnCa 60:40 composition, beyond which (in terms of greater Zn content), Zn takes on a dual network former/modifier (intermediate) role (Petrescu *et al.* 2012), as predicted by the Dell-Bray model calculations and qualitatively suggested by ^{27}Al, ^{11}B and ^{29}Si MAS-NMR measurements. Note that accurately quantifying the MAS-NMR measurements is particularly difficult due to the ambiguity in isolating pure Q_3 contributions from ^{29}Si MAS-NMR spectra. The spectral deconvolution applied in this study was the most complex attempted with respect to the literature (due to the six/seven oxide ZnCa xx:xx series compositions) compared to the wealth of literature available on two- to five-component glass compositions (Mägi *et al.* 1984, Kirkpatrick *et al.* 1985, Engelhardt 1985 & 1987a, Bunker *et al.* 1990, Angeli *et al.* 2012, Duddridge *et al.* 2003, Holland *et al.* 2007, Parkinson *et al.* 2007, Goswami *et al.* 2008, Soleilhavoup *et al.* 2010, Dhara *et al.* 2016, Backhouse *et al.* 2019). Such deconvolution on this semi-complex compositional series is at the limits of this methodology, highlighting the ambiguity and difficulty in probing structural contributions from ^{29}Si spectral deconvolution. Yet, despite this, this work demonstrates that good theoretical structural predictions can be used to inform spectral deconvolution on more complex glass compositions, which can be strengthened through the use of independent complementary techniques such as Raman spectroscopy and Extended X-ray Absorption Fine Structure (EXAFS). Such work can be beneficial to aid future ^{29}Si spectral deconvolution on more complex glass compositions, which in turn, can also be used to provide insight into structure-dissolution relationships and provide input data for computer simulations.

5.2.3 Chemical Durability

5.2.3.1 Relationship between glass composition and dissolution rate I: The Initial Rate (Stage I)

The initial rate of dissolution (Stage I) of ZnCa 0:100 was approximately a factor of 14 times greater than that of ZnCa 100:0, based on the release of Si as determined by SPFT (Fig. 5.9d and Table 5.7). The initial rate of the intermediate composition, ZnCa 40:60, was 7.5 times greater than the ZnCa 100:0. Steady state conditions were met after 22 d for ZnCa 100:0 and 40:60 and approached steady-state after 31 d for ZnCa 0:100 (Fig. 5.9 and Table 5.7). These results suggest there is a correlation between the extent of network polymerisation and the initial dissolution rate. Glasses possessing greater network polymerisation, as indicated by larger $Q_4(X)$ contribution and δ^{29}Si peak shift, i.e. ZnCa 100:0 and 40:60, showed greater chemical resistance at the initial rate of dissolution, where Si release is directly related to the of hydrolysis of Si-O-X bonds (where X = network former). Such a claim is supported by comparison with the International Simple Glass (ISG), which possesses a greater (in terms of greater negativity) δ^{29}Si peak shift of -97 ppm (Gin *et al.* 2015, Angeli *et al.* 2018) than the ZnCa 100:0 and ZnCa 40:60 compositions, at -93 and -92.15 ppm, respectively; the dissolution behaviour of ISG (Fig. 5.9d), accordingly, shows greater chemical resistance than the ZnCa xx:xx series.

Unlike the other compositions, incongruent dissolution was observed for ZnCa 100:0 (Fig. 5.9a); the initial dissolution rate of Zn was greater than that of B and Si by a factor of 1.8 and 3.3, respectively. Similarly, the initial rate of Na was lower than the other elements detected. Incongruent dissolution is a manifestation of phase separation: heterogeneous glasses are postulated to display incongruent dissolution behaviour at the initial rate (Icenhower *et al.* 2008). This observation suggests that Zn acts partially as a network modifier, as hypothesised from structural analysis (MAS-NMR). In such a scenario, a six-fold coordinated Zn modifier may be released more readily to solution than the remainder of the glass network composed of the network forming elements (Al, B, Si and four-fold Zn).

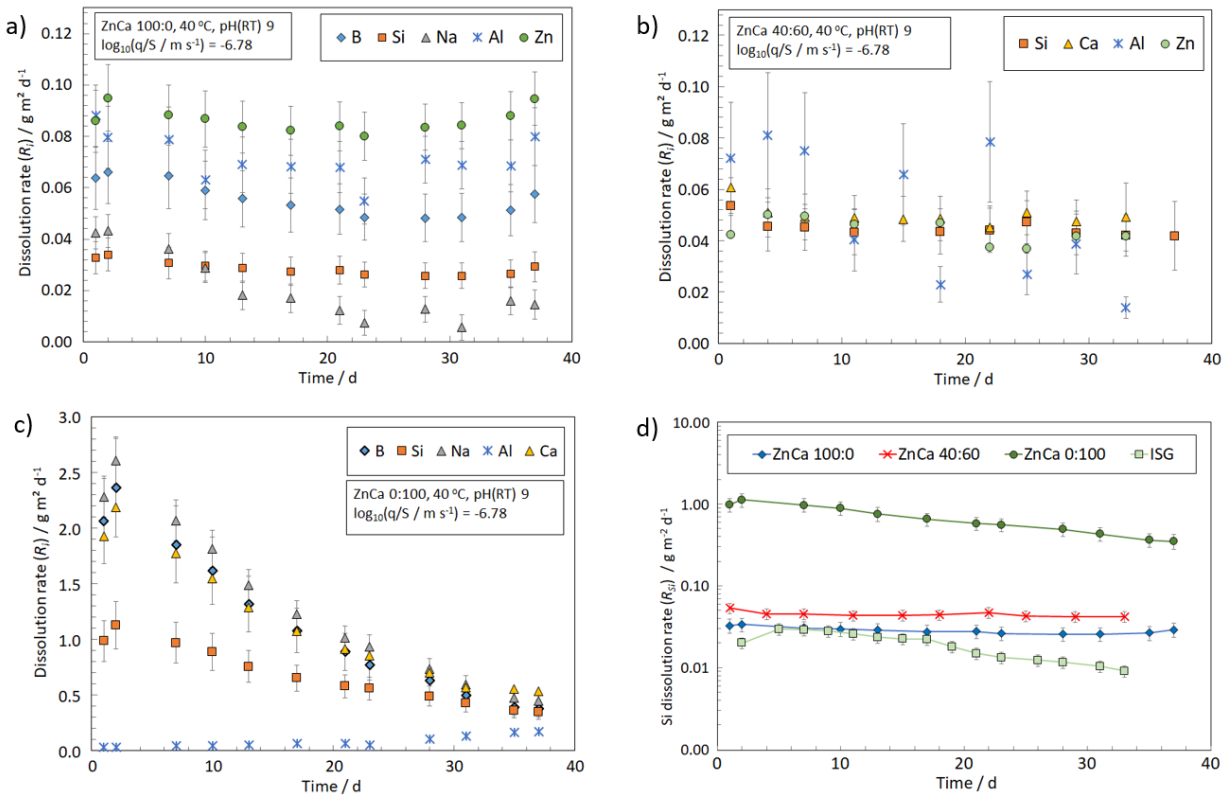

Figure 5.9. Dissolution rate (R_i) of elements from the 37 d SPFT experiments at 40 °C, pH(RT) 9 of glass compositions: (a) ZnCa 100:0, (b) ZnCa 40:60; and (c) ZnCa 0:100; and (d) comparison of the Si dissolution rate for ZnCa 100:0, 40:60 and 0:100 with that of the International Simple Glass (Chapter 4).

Table 5.7 SPFT experimental parameters and steady-state dissolution rate data. Steady-state ppm values (± 10 %) have had background concentrations subtracted where applicable. n/a = not applicable.

Glass		ZnCa 100:0	ZnCa 40:60	ZnCa 0:100
Temp /°C		40	40	40
pH(RT)		9	9	9
pH(T)		8.67	8.67	8.67
Test duration /d		37	37	37
Time to attain steady-state /d		22	22	31*
Initial sample mass /g		0.280	0.275	0.270
Steady-State	Average surface area† (S)/10^{-3} m^2	5.53	5.53	5.53
	Surface area % of original‡	100	100	100
	$\log_{10}[(q/S)/m\ s^{-1}]$	-6.78	-6.78	-6.78
Steady-state concentrations / ppm	B	0.24	-	1.85
	Si	0.40	0.78	5.67
	Na	-	-	0.72
	Al	0.14	-	0.23
	Zn	0.72	0.14	n/a
	Ca	n/a	0.14	2.62
Steady-state rates / g m^{-2} d^{-1}	B	0.049 ± 0.009	-	0.38 ± 0.07
	Si	0.026 ± 0.005	0.048 ± 0.01	0.36 ± 0.07
	Na	-	-	0.46 ± 0.07
	Al	0.066 ± 0.011	-	0.17 ± 0.10
	Zn	0.086 ± 0.015	0.039 ± 0.01	n/a
	Ca	n/a	0.048 ± 0.01	0.54 ± 0.08

* On approach to steady-state

† On application of the shrinking core model

‡ Indicates the need for the application of the shrinking core model if < 100%

Surface features post SPFT dissolution: Inspection of the particles post-SPFT revealed the presence of four distinct phenomena (Figs. 5.10-5.13, whereby overlaid numbers correspond to the following definitions), which are similar, but more varied than those described in Chapter 4:

1. Glass dehydration cracking (ZnCa 0:100)
2. Troughs of preferential dissolution along stress lines/initial surface roughness/cracks/ fractures on the pristine glass (all samples)
3. Two types of pitted features: a) Pits/pitted troughs (ZnCa 100:0), b) mechanical pits, thought to be intial surface imperfections from mechanical sample preparation, which developed into dissolution pits. The reason for this distinction is that they are also observed on pristine glass particles, for example, Fig. 3.4 - Chapter 3 (ZnCa 0:100)

4. Secondary precipitation/beginning of alteration layer formation (ZnCa 0:100)

A distinction is made between Features 2 and 3a. The troughs in 2 are narrower, thin, deep, long, well connected and densely concentrated (Fig. 5.10c & 5.11). The pits and pitted trough features in 3a are smooth, unconnected, randomly distributed and appear to be less deep (Fig. 5.10). The fact they were not evident in ZnCa 40:60 (Fig. 5.11) and ZnCa 0:100 (Fig. 5.12) glasses, but present in the potential two-phase (ZnCa 100:0) glass, which dissolved incongruently, suggests that they may result from the preferential dissolution of one of the two glass phases. It is possible that the trough features could merge with greater reaction progress, e.g. through the coalescence of features 2 & 3 (e.g. Fig. 5.10b) and/or the transformation of features 2 into 3a.

The ZnCa 0:100 composition showed evidence for the presence of Ca-containing precipitates (Fig. 5.12 & 5.13) on the surface of approximately 10 % of particles post-SPFT. These precipitates were observed in regions of high energy sites for dissolution, i.e. glass particle edges and areas of initial surface roughness/asperities on the glass caused by sample preparation. These phases were unidentifiable by XRD due to their low abundance, however, EDS mapping showed the precipitates were rich in Ca (Fig. 5.13) and PHREEQ-C geochemical modelling of the solutions predicted that the zeolite phase, scolecite ($CaAl_2Si_3O_{10}{\cdot}3H_2O$ – saturation index 2.08), was saturated in solution and could, therefore, precipitate during the SPFT experiment. The presence of such Ca-rich precipitates may indicate that the SFPT experiment did not confer dilute conditions and the dissolution did not occur at the initial rate, in which case the initial rate reported herein has been underestimated. However, if this were the case, the trend in the initial rates of the ZnCa xx:xx series (Fig. 5.9) would not be altered – ZnCa 0:100 would still be the least durable. Note that the convergence of congruent dissolution for all elements in this glass composition signifies the close approach to initial rate conditions. It is also possible that the Ca-precipitates could have formed post-SPFT during the drying process, through the presence and drying of saturated residual solution on the surface of glass particles.

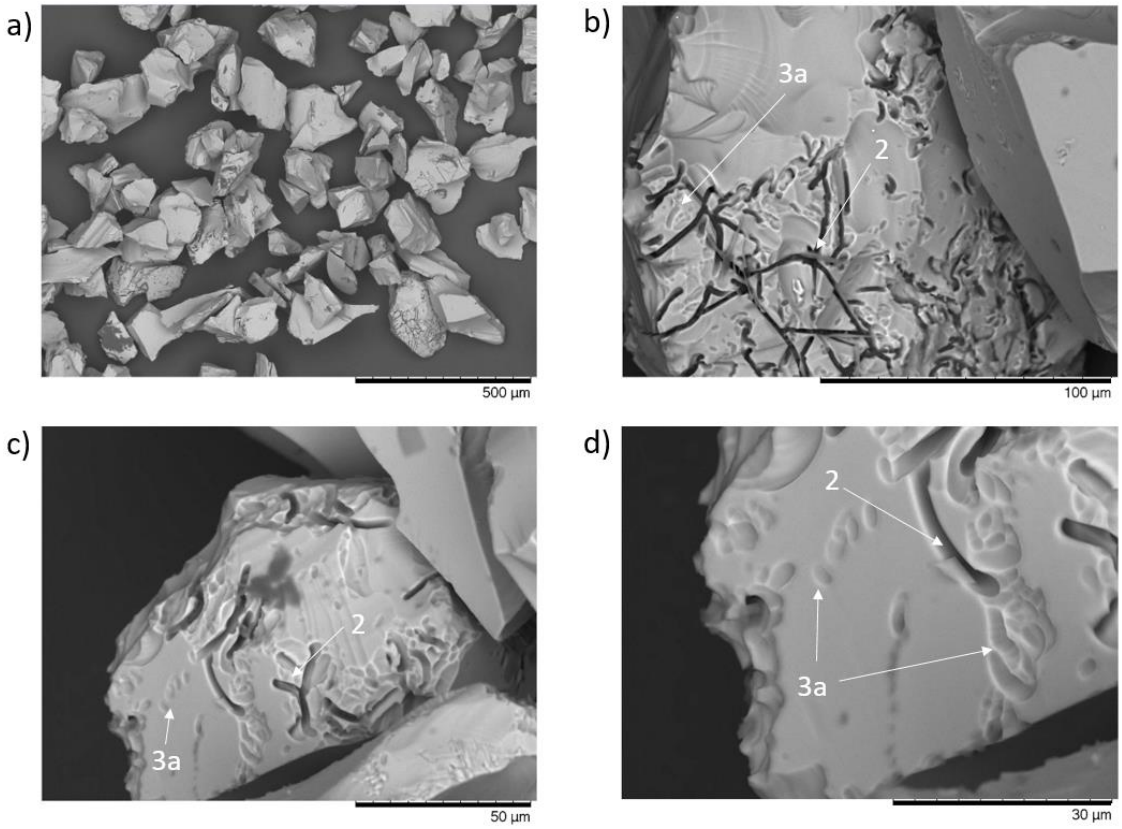

Figure 5.10. Post-SPFT ZnCa 100:0 particles: a) Overview; b, c & d) Troughs of preferential dissolution along stress lines/initial surface roughness/cracks (2) and pitted/pitted trough features (3a).

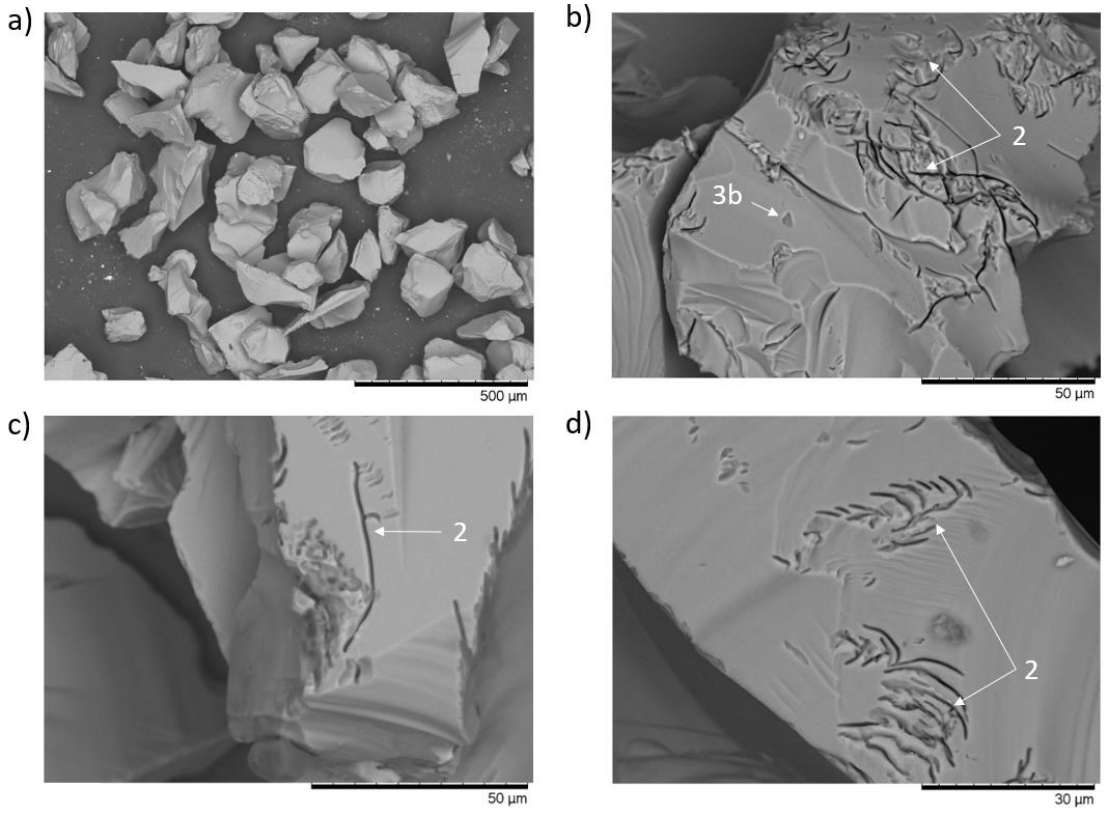

Figure 5.11. Post-SPFT ZnCa 40:60 particles: a) Overview; b, c & d) Troughs of preferential dissolution along stress lines/initial surface roughness/cracks (2) and mechanical pits (3b).

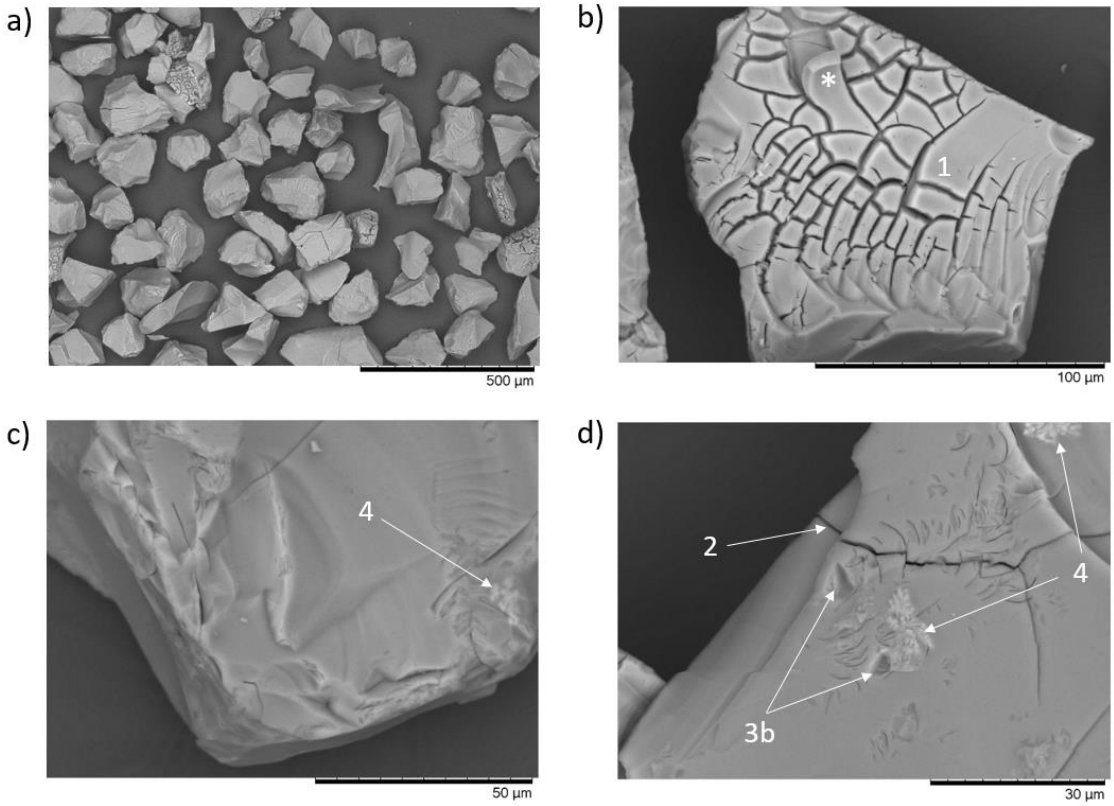

Figure 5.12. Post-SPFT ZnCa 0:100 particles a) Overview; b) glass dehydration cracking (1), note the peeled layer (*); c & d) Troughs of preferential dissolution along stress line/initial surface roughness/cracks (2) and secondary precipitation (4).

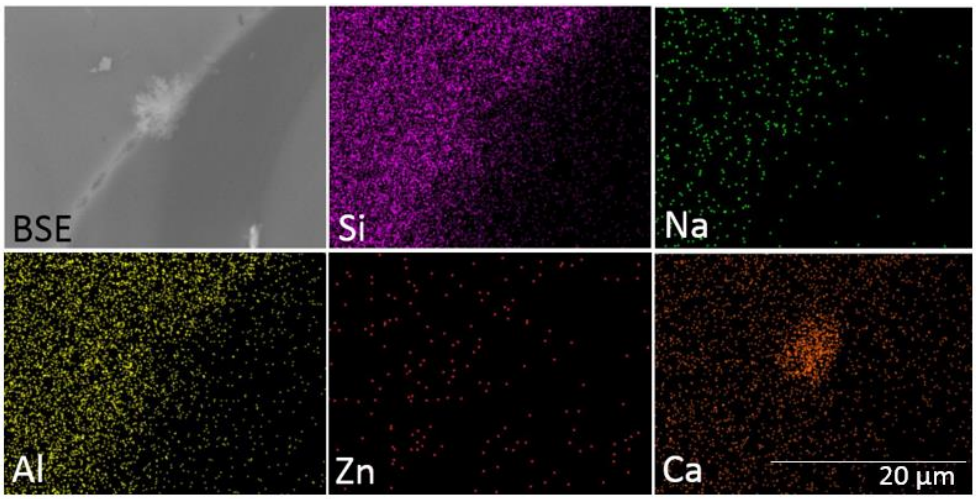

		Element At. %			
Section	Spot #	Si	Al	Na	Ca
Altered surface	1	71.2 ± 3.5	20.3 ± 1.0	0.56 ± 0.01	7.3 ± 0.3
Precipitate	2	51.3 ± 2.5	32.5 ± 1.6	0.20 ± 0.01	15.5 ± 0.8
Precipitate	3	44.7 ± 2.2	42.2 ± 2.1	-	12.8 ± 0.6
Precipitate	4	50.8 ± 2.5	34.8 ± 1.7	-	14.2 ± 0.7
Altered surface	5	71.7 ± 3.6	21.1 ± 1.1	-	7.0 ± 0.4
Altered surface	6	71.6 ± 3.6	19.6 ± 1.0	-	8.7 ± 0.4

Figure 5.13. Post-SPFT ZnCa 0:100. Evidence for Ca secondary phase – predicted by geochemical modelling to be scolecite ($CaAl_2Si_3O_{10}{\cdot}3H_2O$) – at a high energy cracked edge.

5.2.3.2 Relationship between glass composition and dissolution rate II: The Residual Rate (Stage II)

Product Consistency Test-B experiments were performed over a duration of 35 d to determine Stage II dissolution behaviour. The variation in the pH at each timepoint is shown in Figure 5.14a. Measurements recorded for the whole ZnCa xx:xx series indicated similar readings within instrumental uncertainty, however, some subtle changes in the pH were observed for the different glass compositions. At early reaction progress, < 3 d, the leachate of the Ca-rich glasses exhibited the highest pH, whereas at later reaction progress, > 28 d, the leachate from the Zn-rich glasses exhibited the highest pH values, partly correlating to the magnitude of the NL_B (Fig. 5.14b). The normalized mass loss of B, Si and Na (NL_i, where *i* = element of interest (B, Si, Na, Ca and Zn)), showed that the residual rate of dissolution was observed after approximately 14 d, at which point the durability followed the sequence, based on NL_i (from the most to least durable), of ZnCa 0:100 > 20:80 > 40:60 > 60:40 > 80:20 > 100>0 (Figs. 5.14b-d). Note that this is the opposite trend to that observed in SPFT experiments (discussed further in Section 5.3).

The NL_{Ca} showed two distinct trends (Fig. 5.14e). In the Zn-rich glasses (ZnCa 80:20 and ZnCa 60:40), the NL_{Ca} dissolution trend was similar in behaviour to $NL_{B,\ Si\ \&\ Na}$, reaching the residual rate of dissolution after approximately 14 d within experimental uncertainty. The Ca-rich glasses (ZnCa 40:60, 20:80 and 0:100), showed a slight reduction in NL_{Ca} after 7 d, which may be indicative of the early incorporation of Ca within the silica gel layer (Chave *et al.* 2011, Utton *et al.* 2013, Mercado-Depierre *et al.* 2013, Mann 2018, Aréna *et al.* 2019). The two dissolution trends between the Zn- and Ca-rich compositions suggest that Ca was not effectively incorporated into an alteration layers (gel and/or secondary precipitates, to be discussed below) for the Zn-rich glasses compared to the Ca-rich glasses.

For all compositions, the NL_{Al} (Fig. 5.14g) decreased throughout the full experimental duration (1-35d). However, two distinct trends were observed. The rate of decrease was fast for the Zn-rich compositions over the time period 1-7 d, after which the rate of decrease became slower through the time period 7-35 d. For the Ca-rich glasses, a gradual rate of decrease was observed throughout the duration of the experiment (1-35 d). Such difference may lie in the formed alteration products; the alteration products identified in the Zn-rich glasses suggest the potential early (< 7 d, further elucidated and supported from the MCC-1 studies, particularly the geochemical modelling Section 5.2.3.5) formation of Al-containing clays (Fig. 5.15-5.19), whereas the alteration products formed on the Ca-rich glasses suggests Al incorporation into the silica gel layer (Chave *et al.* 2007, Frugier *et al.* 2008) (again, supported by MCC-1 studies reported in Section 5.2.3.4.2).

For the Zn-rich glass compositions, the NL_{Zn} was initially high, which was followed by a fast reduction until 7 d, and then a gradual reduction until 35 d. It should be noted that NL_{Zn} values < 0.001 g m^{-2} are at the limits of detection of the ICP-OES analysis, whereby results (particularly for the Ca-rich glasses) may not be representative (Fig. 5.14f). However, a reasonable explanation for the reduction NL_{Zn} for the Zn-rich glasses could be the incorporation of Zn into a hydrated silica-rich gel layer or into silicate secondary phases (clays) on the surface of the glass, which is in agreement with XRD and EDS mapping of these glasses after the termination of the dissolution experiment (Figs. 5.15-5.24).

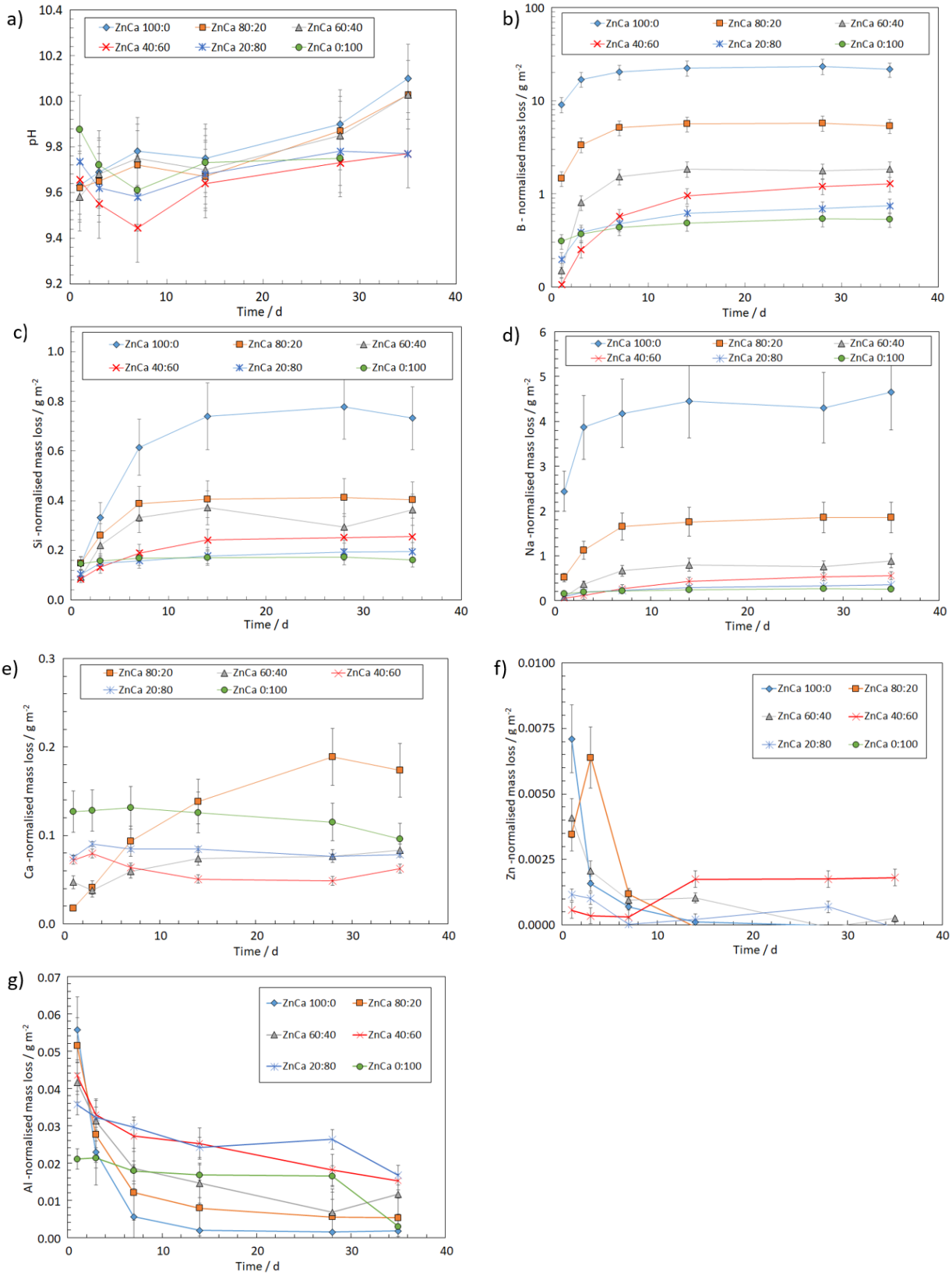

Figure 5.14. The (a) pH(RT) measurements of the leachate and (b-g) normalised mass loss of elements for the ZnCa xx:xx series from the 90°C, 35 day PCT-B experiments in UHQ.

Combined XRD traces and SEM post-35 d PCT-B (Figs. 5.15 and 5.16-5.24 respectively), indicate the possible formation of one or a combination of the following two smectite clays on the surface of the ZnCa 100:0 and ZnCa 80:20 samples: Na-beidellite ($Na_{0.61}Al_{4.7}Si_{7.32}O_{20}$ $(OH)_4$) [PDF 47-0197] (Jantzen *et al.* 2010) and sauconite - 15 Å ($Na_{0.3}Zn_3(Si,Al)_4O_{10}(OH)_2{\cdot}4H_2O$) [PDF 29-1500] (Gin *et al.* 2013, noting Yu *et al.* 2020 attributed similar/almost identical XRD traces to Zn-saponite). Noting that beidellite clays are commonly formed on most alkali alumina borosilicate glasses during dissolution (Jantzen et al. 2010), hence the formation of Na-beidellite cannot be discounted, especially as its formation was predicted in the geochemical models (p 147). Note that sauconite is a naturally occuring Zn-containing saponite (Ross 1946, Güven 1988), which synthesized Zn-smectites usually resemble (Yokoyama *et al.* 2006, Pascua *et al.* 2010). These phases were consistent with PHREEQ-C geochemical modelling of the elemental leachate concentrations, which predicted that Na-beidellite and the zeolite, analcime ($Na_{0.96}Al_{0.96}Si_{2.04}O_6{\cdot}H_2O$) were saturated in solution for both samples and at all time points. When modelling the elemental concentrations from solutions collected after 1 d of dissolution, where Zn concentrations were at their greatest, the formation of Zn_2SiO_4 was predicted for all of the Zn-containing glasses. Thermodynamic data for hydrated Zn-bearing silicate phases were not available in the database employed (nor, to the author's knowledge, other databases available). The reduction in the NL_{Zn} after 3 day PCT-B tests support the XRD, SEM and modelling data which suggests the formation of Zn-silicates for all the Zn-containing glasses.

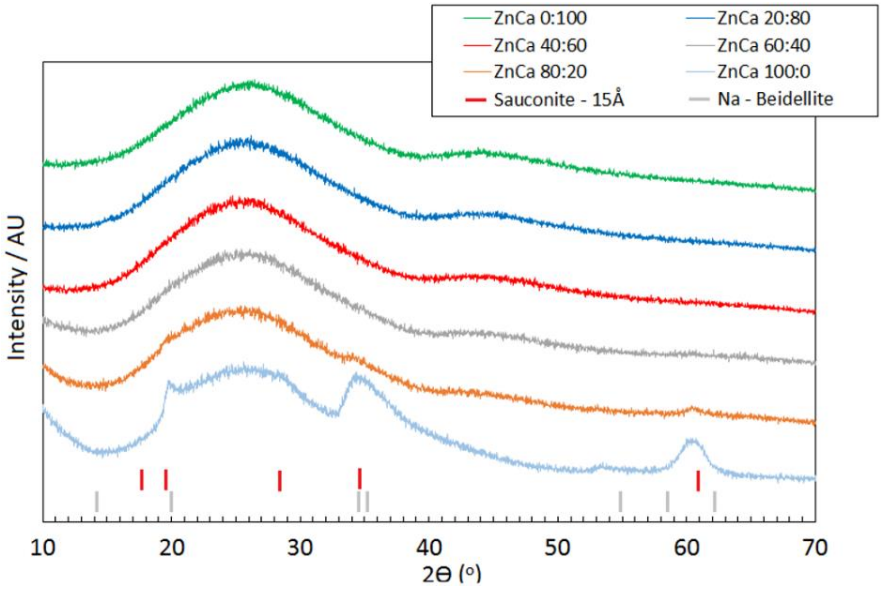

Figure 5.15. XRD traces of the ZnCa MW series post 35-day PCT-B dissolution at 90 °C in UHQ.

Cross-sectional BSE SEM images after the 35 d PCT-B experiments revealed the presence of alteration layers on the ZnCa 100:0, 80:20 and 60:40 glass compositions (Fig. 5.16). For the Ca-rich glasses (ZnCa

40:60, 20:80 and 0:100), no alteration layers were observed at the SEM resolution employed. However, this cannot discount the presence of these phenomena. A cross-sectional view of the alteration layer of the ZnCa 100:0 composition (highlighted by the BSE contrast) (Fig. 5.16d) illustrates the complexity of the altered layer.

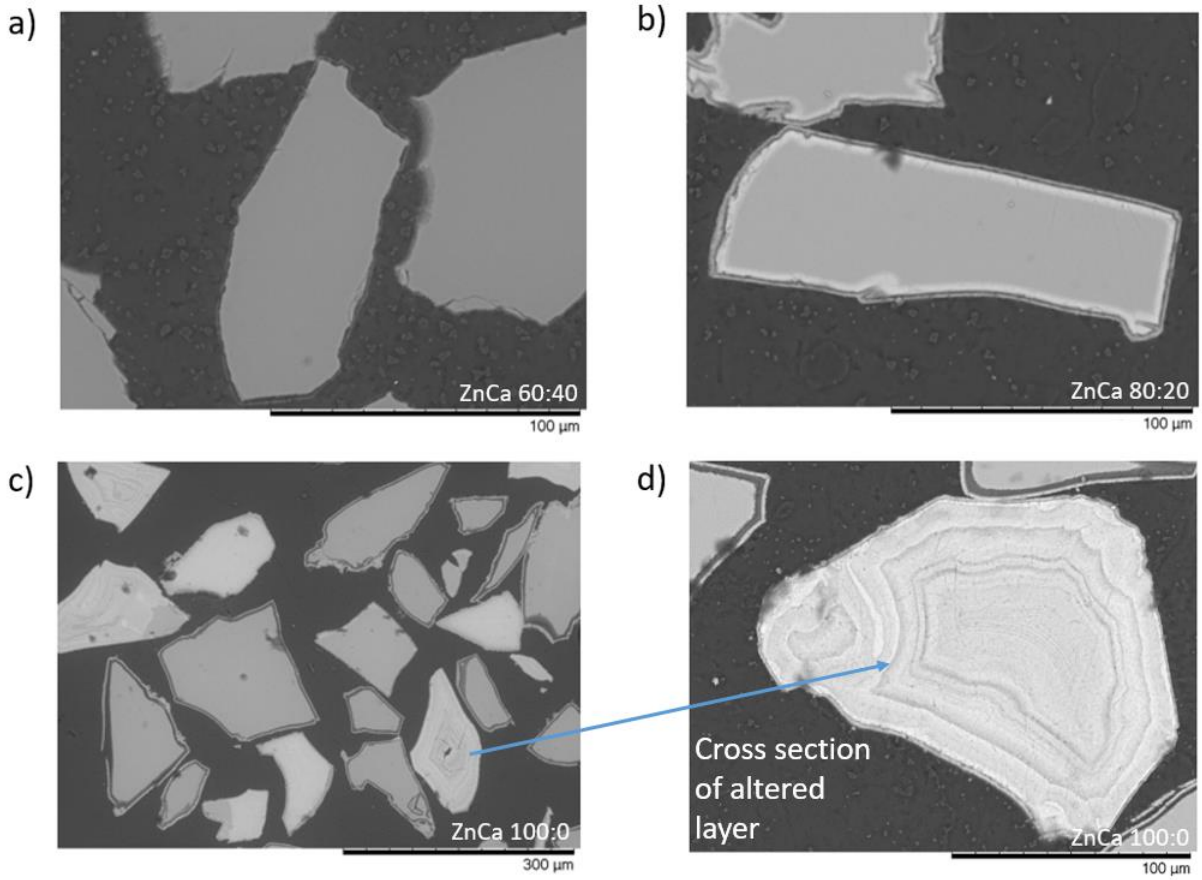

Figure 5.16. BSE-SEM image of glass particles post 35 day PCT-B dissolution at 90 °C in UHQ surrounded by attached and detached alteration layers: (a) ZnCa 60:40; (b) ZnCa 80:20; (c & d) ZnCa 100:0 – BSE contrast indicates a cross section through the underlying pristine glass (darker) and the altered layer (lighter), which was an effect of random particle orientation inherent within the sample preparation (Section 3.2.2 – Chapter 3).

The altered layer formed on the outer surface of ZnCa 100:0 particles (Fig. 5.17 & 5.18) was comprised of two distinct regions: an inner gel layer adjacent to the pristine glass, which was depleted in Na and Zn, and an outer layer, which was concentrated in all elements. The presence of Zn in the outer layer, combined with negligible Zn detection in the leachate and within the inner layer suggests that Zn has been incorporated into crystalline or amorphous phases (Lewis *et al.* 1982, Gin *et al.* 2013), as predicted by geochemical modelling and confirmed by XRD (Fig. 5.15).

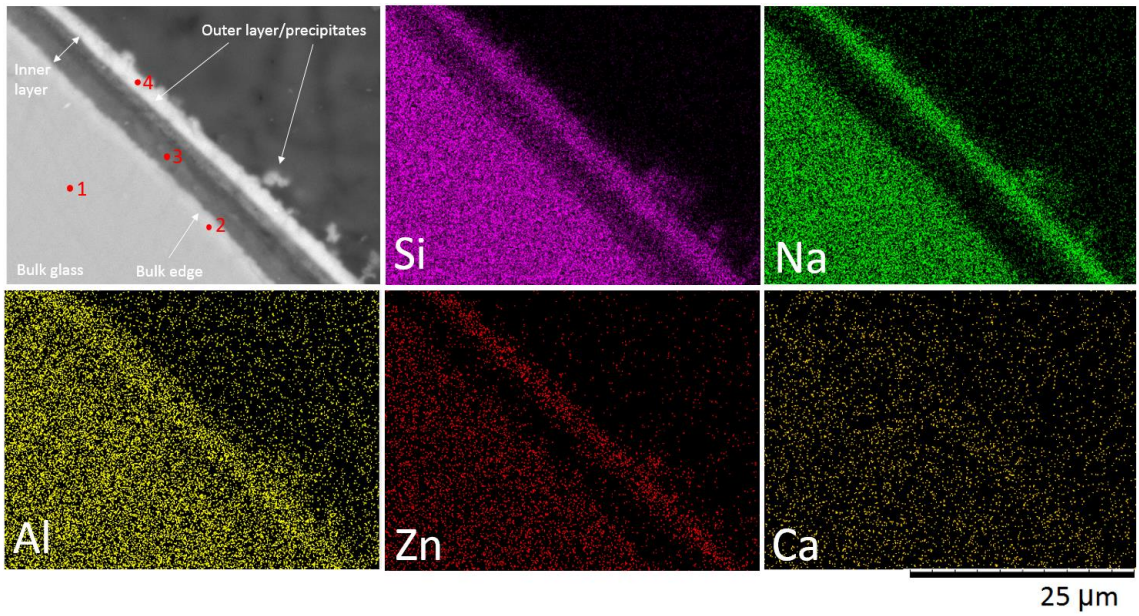

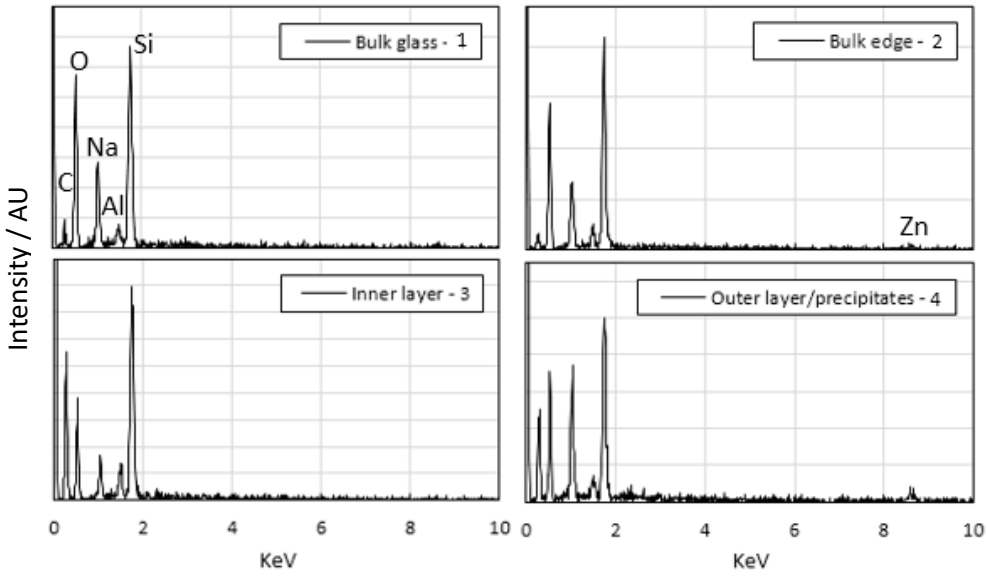

		Element At. %			
Section	Spot #	Si	Al	Na	Zn
Bulk glass	1	57.6 ± 1.3	5.3 ± 0.2	28.7 ± 4.2	8.4 ± 0.6
Bulk edge	2	60.3 ± 5.0	6.1 ± 1.4	25.3 ± 2.9	8.3 ± 0.6
Inner layer	3	71.6 ± 4.4	2.4 ± 0.05	14.4 ± 0.3	11.4 ± 0.1
Outer layer/ precipitates	4	52.3 ± 4.3	5.9 ± 0.8	15.6 ± 0.4	26.2 ± 2.1

Figure 5.17. BSE-SEM image, elemental map and elemental At. % of a cross-section particle from ZnCa 100:0 post 35 day PCT-B dissolution (UHQ, 90 °C).

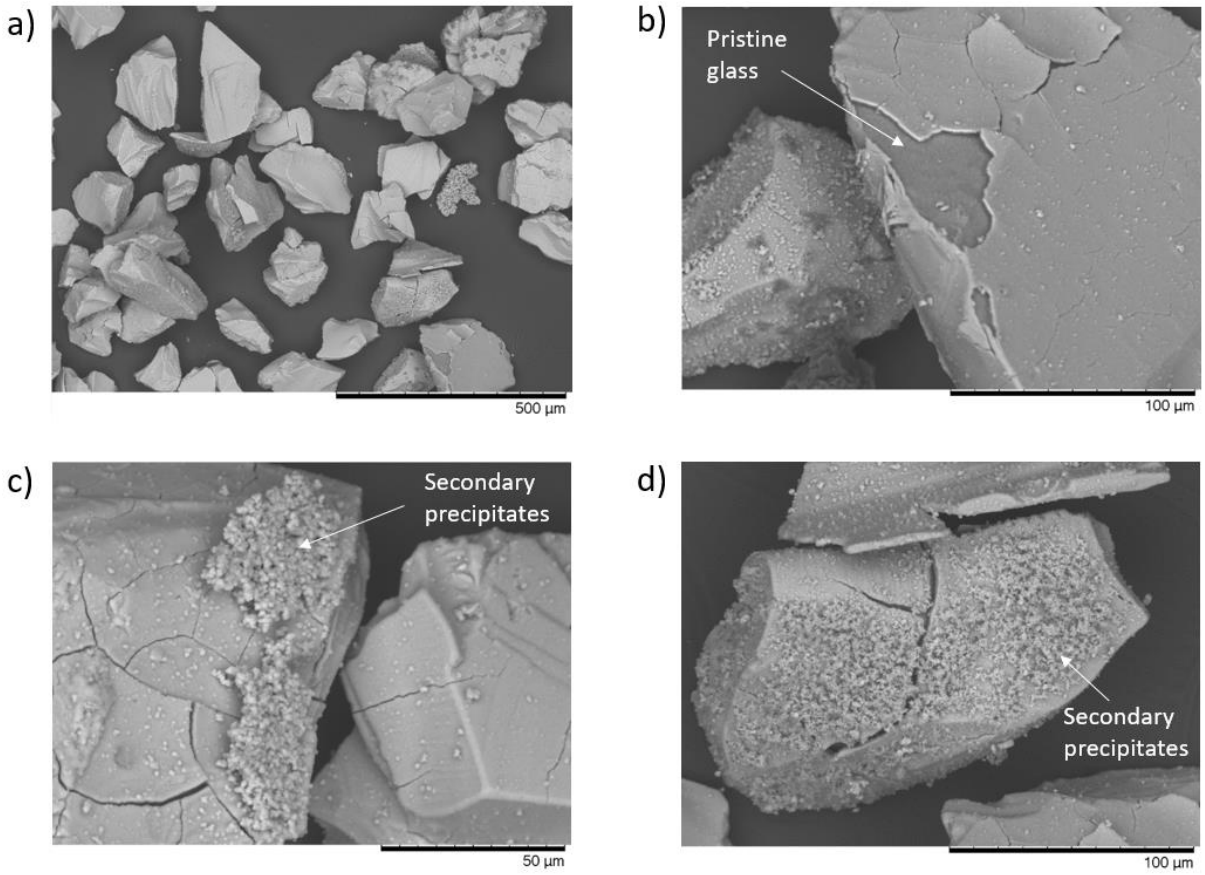

Figure 5.18. BSE SEM images of ZnCa 100:0 post 35-day PCT-B (UHQ, 90 °C): a) overview; b, c & d) evidence for secondary phase precipitation and cracked altered layers revealing pristine glass.

The alteration layer formed on ZnCa 80:20 particles (Fig. 5.19) comprised of two regions, which were slightly different to those observed on ZnCa 100:0. Both formulations exhibited an outer layer of precipitates, but the 'bulk edge' – the area at the interface between the glass matrix and the alteration layer (see Fig. 5.19) – of ZnCa 80:20 was depleted in Na. This suggests that this region reflects the portion of the glass surface that is dissolving to form the alteration layer. It was also enriched in Zn, Ca and Si, with respect to the bulk glass, but depleted in Al. A thin alteration layer was detected on the ZnCa 60:40 sample (Fig. 5.16a), but was too small to gain any compositional information from EDS at the employed resolution.

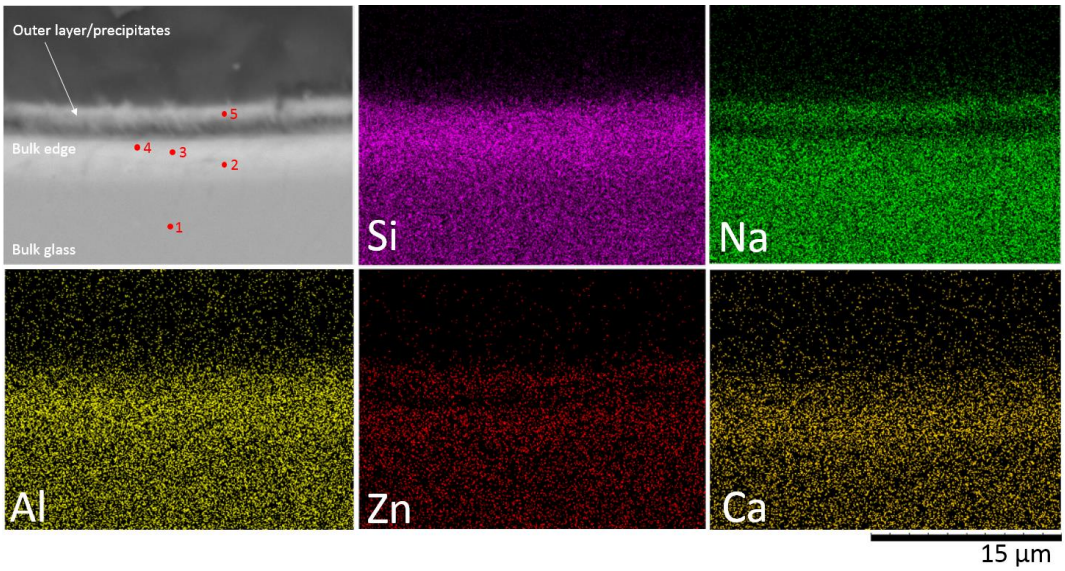

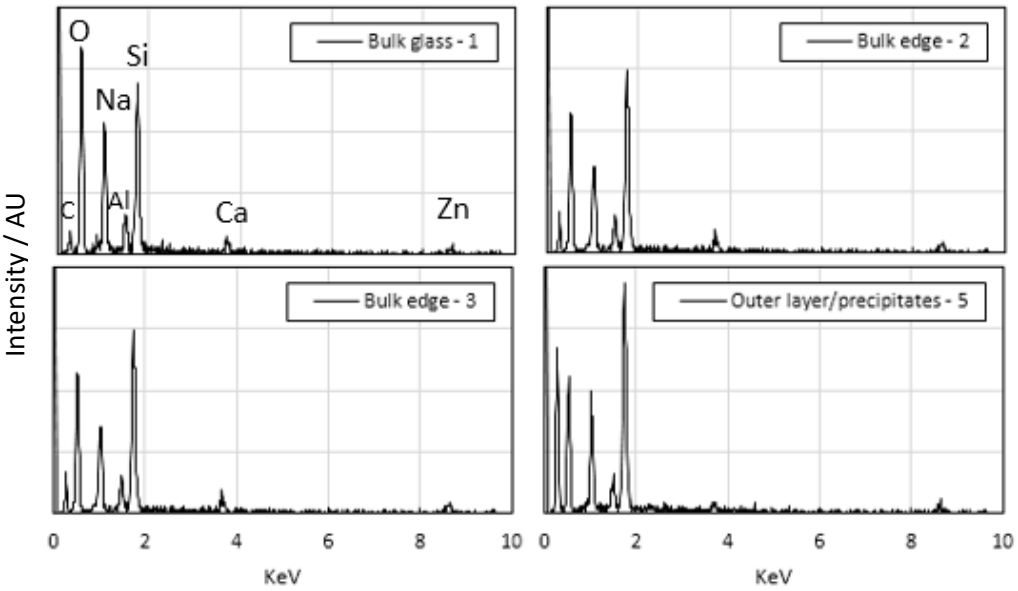

		Element At. %				
Section	Spot #	Si	Al	Na	Zn	Ca
Bulk glass	1	41.7 ± 5.7	10.4 ± 1.1	32.3 ± 4.5	10.9 ± 0.5	4.7 ± 0.5
Bulk edge	2	47.1 ± 9.2	9.5 ± 0.5	18.8 ± 1.8	18.4 ± 2.7	6.2 ± 0.2
	3	49.2 ± 6.4	9.1 ± 0.4	20.1 ± 2.0	16.4 ± 2.0	5.2 ± 0.1
	4	50.0 ± 9.4	10.2 ± 1.8	18.5 ± 1.9	16.0 ± 0.5	5.4 ± 0.1
Outer layer/ precipitates	5	53.2 ± 1.8	7.3 ± 0.1	20.3 ± 2.3	16.8 ± 1.4	2.3 ± 0.1

Figure 5.19. BSE SEM image., elemental map and elemental At. % of a cross-section particle of ZnCa 80:20 post 35-day PCT-B (UHQ, 90 °C).

BSE Images of ZnCa 80:20, 60:40, 40:60, 20:80 and 0:100 particles post 35 d PCT-B investigations are shown in Figures 5.20-5.24. With a decrease in the ZnO:CaO ratio it is clear that secondary phase formation and alteration layer formation is suppressed. The ZnCa 80:20 composition displayed a de-hydrated altered layer covering all particles, overlaid with unidentified secondary precipitates (Fig. 5.20). The ZnCa 60:40 composition had a de-hydrated layer (Fig. 5.21b) on some particles and pitted features on others. Pitted surfaces with a low number of secondary phases were observed on the ZnCa 40:60 composition (Fig. 5.22), whilst the ZnCa 20:80 and 0:100 particles appeared unaltered, but with numerous precipitated secondary phases (Figs. 5.23 and 5.24, respectively).

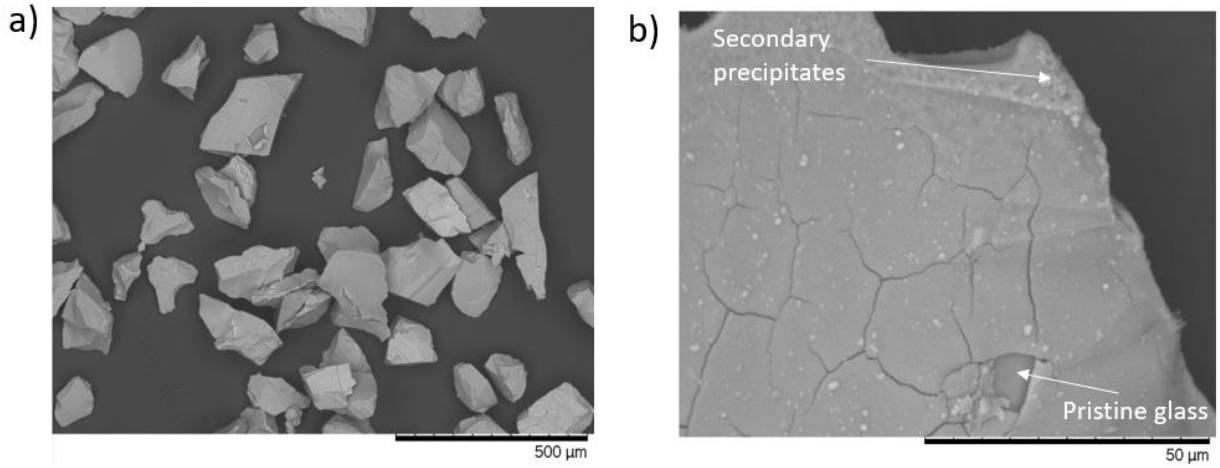

Figure 5.20. BSE SEM images of ZnCa 80:20 post 35-day PCT-B (UHQ, 90 °C).

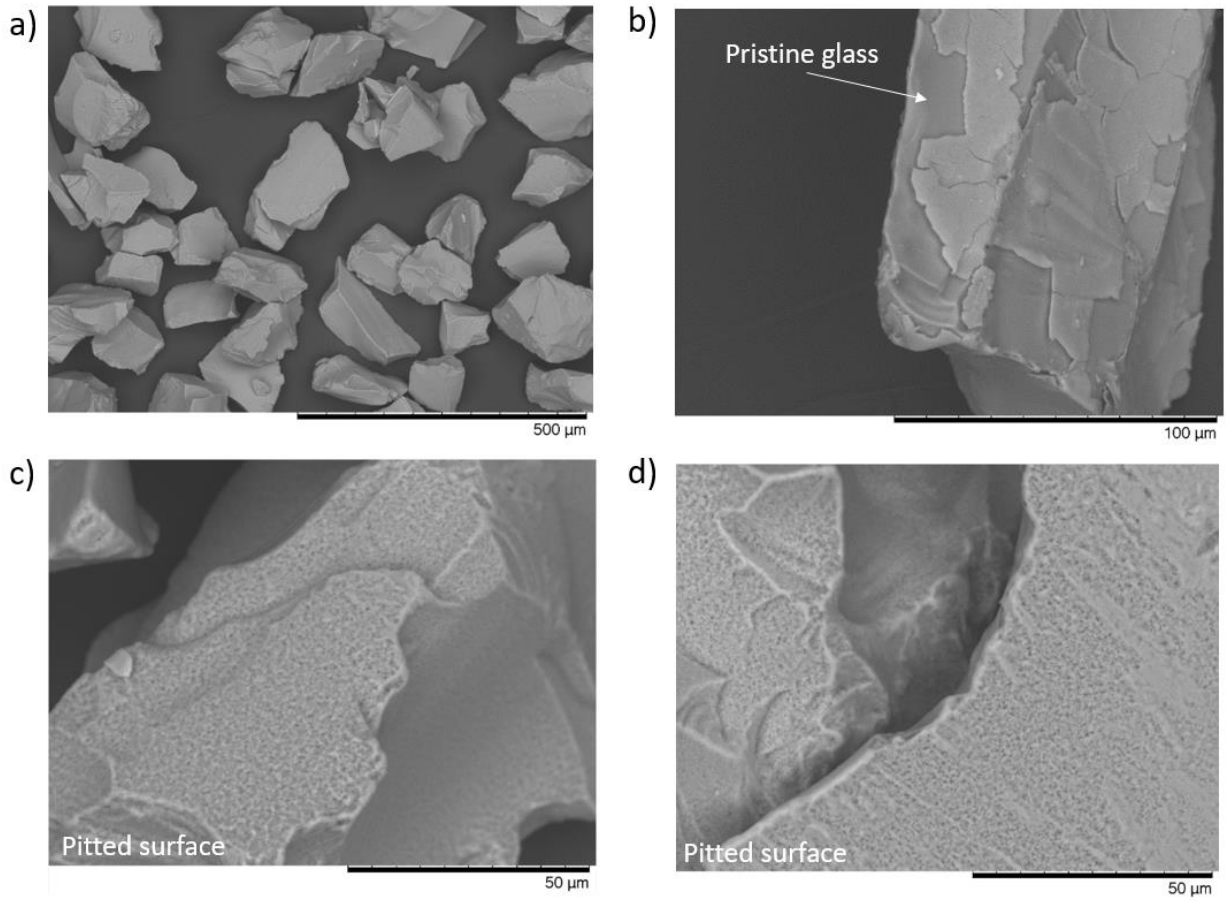

Figure 5.21. BSE SEM images of ZnCa 60:40 post 35-day PCT-B (UHQ, 90 °C).

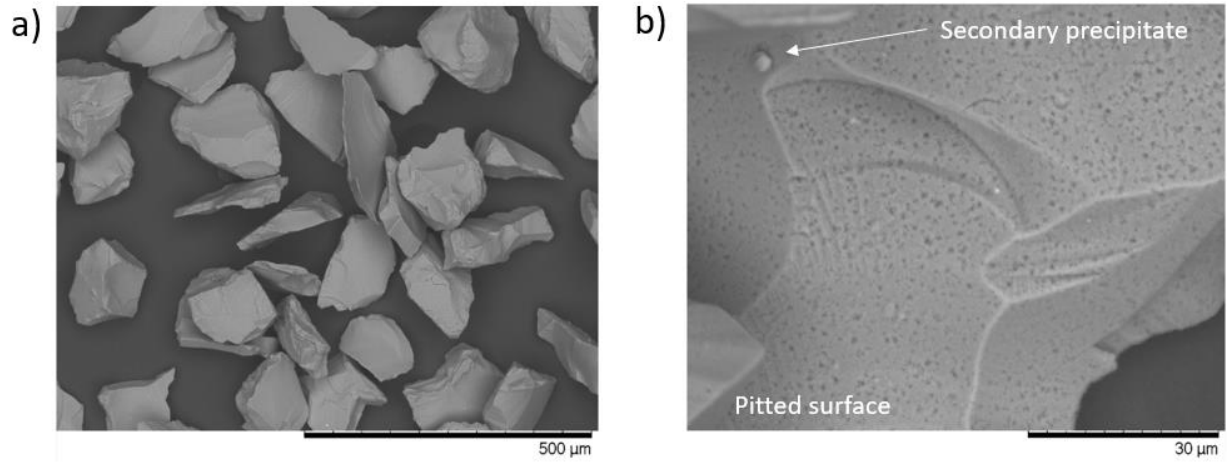

Figure 5.22. BSE SEM images of ZnCa 40:60 post 35-day PCT-B (UHQ, 90 °C).

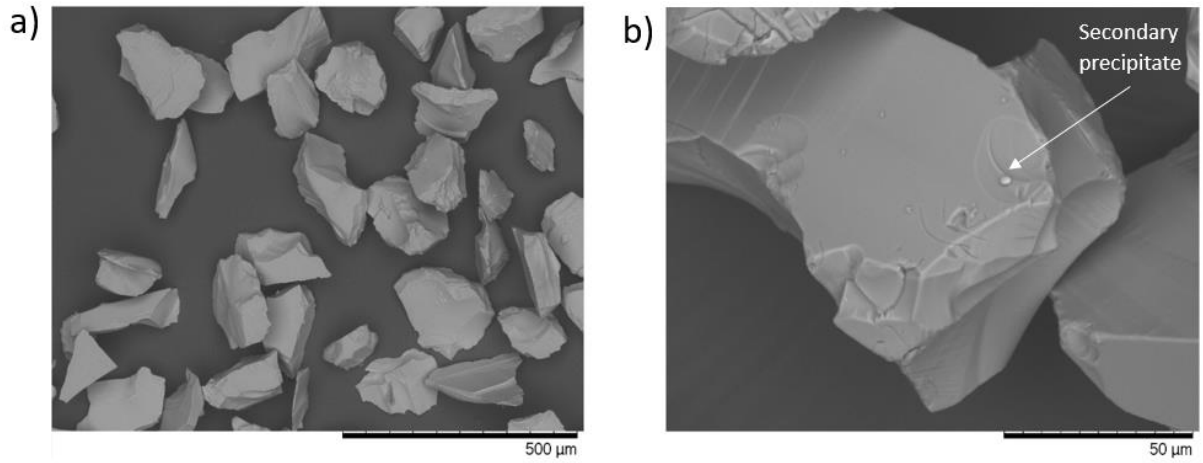

Figure. 5.23. BSE SEM images of ZnCa 20:80 post 35-day PCT-B (UHQ, 90 °C).

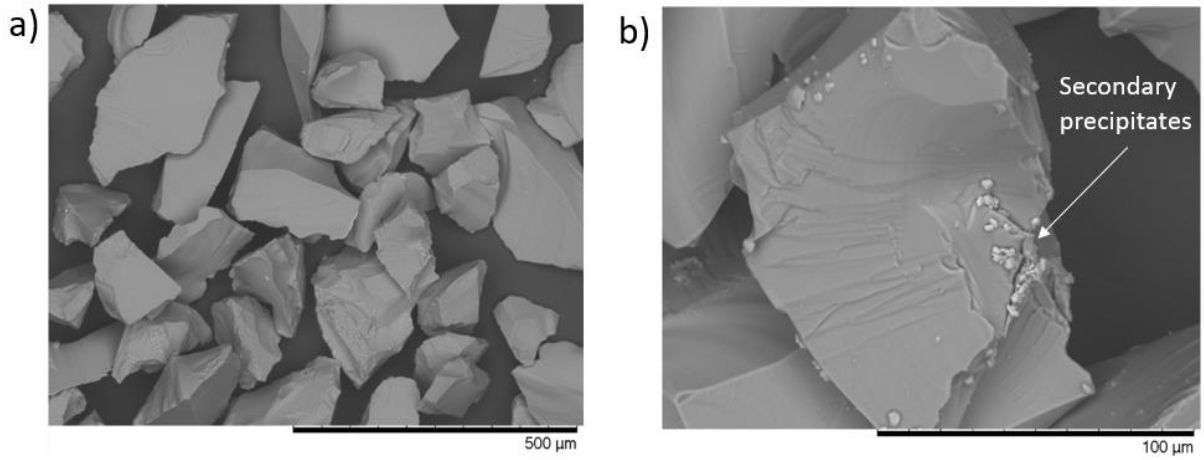

Figure 5.24. BSE SEM images of ZnCa 0:100 post 35-day PCT-B (UHQ, 90 °C).

PHREEQ-C geochemical modelling from the leachate obtained from the 35 d time point from the PCT-B test indicated that a range of phases were saturated in solution. These include:

- The phyllosilicate clay, Na-bediellite $Na_{0.33}Al_{2.33}Si_{3.67}O_{10}(OH)_2$, which was predicted to form in solution from all glass compositions.
- Predicted zeolites phases were analcime, $Na_{0.96}Al_{0.96}Si_{2.04}O_6{:}H_2O$ (predicted for all glass compositions), mesolite ($Na_2Ca_2(Al_2Si_3O_{10}{\cdot}8H_2O$) and scolecite ($Na_{0.33}Al_{2.33}Si_{3.67}O_{10}(OH)_2$, predicted to form in solution for the Ca-rich glass compositions.
- Tobermorite ($Ca_5Si_6H_{11}O_{22.5}$) was predicted to form in solution of the ZnCa 0:100 composition.
- $ZnSiO_4$, although unlikely in a hydrated form, was predicted to form in the solutions for all of the Zn-containing glasses.

More detailed analysis of geochemical modelling was preformed from the leachate from the MCC-1 investigations detailed in Section 5.2.3.5 of this Chapter, which allowed for comparison with SEM and XRD results. It should be noted that the geochemical modelling results from the MCC-1 tests and PCT-B tests were largely consistent.

5.2.3.3 Alteration Layer - MAS-NMR analysis

The ^{29}Si MAS-NMR spectra obtained from the altered Ca-rich glasses (altered gel layer and the underlying pristine glass) showed a negative chemical shift, indicative of greater network polymerisation compared to their pristine counterparts (Fig. 5.25). Such shifts have been observed for the Ca-containing International Simple Glass (Gin *et al.* 2015, Angeli *et al.* 2019), which was described as being direct evidence of the reorganization of the silicate network/gel formation at high reaction progress, due to the re-condensation of Si-OH to reform Si-O-Si bonds. This process is likely to be more energetically efficient than the complete hydrolysis of the glass species and their precipitation into more stable crystalline phases.

The ^{29}Si MAS-NMR spectra from the Zn-rich altered glasses, show sharp peaks, indicative of the presence of the Si- and Al-containing secondary precipitates identified by XRD (sauconite and potentially Na-beidellite) and as suggested by geochemical modelling. In particular, the peaks observed at -95.2 ppm (Figs. 5.25a-c) were consistent with the most intense peak of Zn-saponite, reported in the literature to occur at -95.9 ppm, noting that sauconite is a naturally occurring Zn-saponite (Güven 1988) observed in the saponite synthesis study by Vogels *et al.* (2005). The study also observed peaks of lesser intensity at -91.5 and -86.7 ppm, which do not appear in the present analysis. This may be due to the additional contribution from the underlying pristine glass underneath the alteration layer, which may mask the signal. The Si:Al ratios of some the Zn-saponites in the study by Vogels *et al.* (2005) were 5.67 & 12.3, which are loosely similar to the ratios of 8.86 ± 1.40 and 7.29 ± 0.27 obtained in the present study for ZnCa 100:0 and ZnCa 80:20, respectively, whereby the Si:Al ratios were calculated from the EDS quantification analysis of the outer precipitate layer reported in Figures 5.17 & 5.19 from the PCT-B tests. The tenuous observation of a shoulder at -87.8 ppm (Fig. 5.25a-c (denoted by the arrow)), in addition to the most intense peak at -95.2 ppm are potentially consistent with the ^{29}Si MAS-NMR spectra from Na-beidellite (Altaner *et al.* 1990, Bouna *et al.* 2012).

^{29}Si MAS-NMR spectra from the hydrated Zn-silicate mineral hemimorphite ($Zn_2SiO_4 \cdot H_2O$), which has been observed to form in vapour corrosion experiments on similar simple Zn-containing borosilicate glass formulations (Cassingham *et al.* 2016) was obtained as part of this investigation. However, the

spectra from hemimorphite was inconsistent with that observed from the dissolved glass particles in this study, therefore it is suggested that hemimorphite was not formed in these experiments (data shown in 5.5 Appendix II).

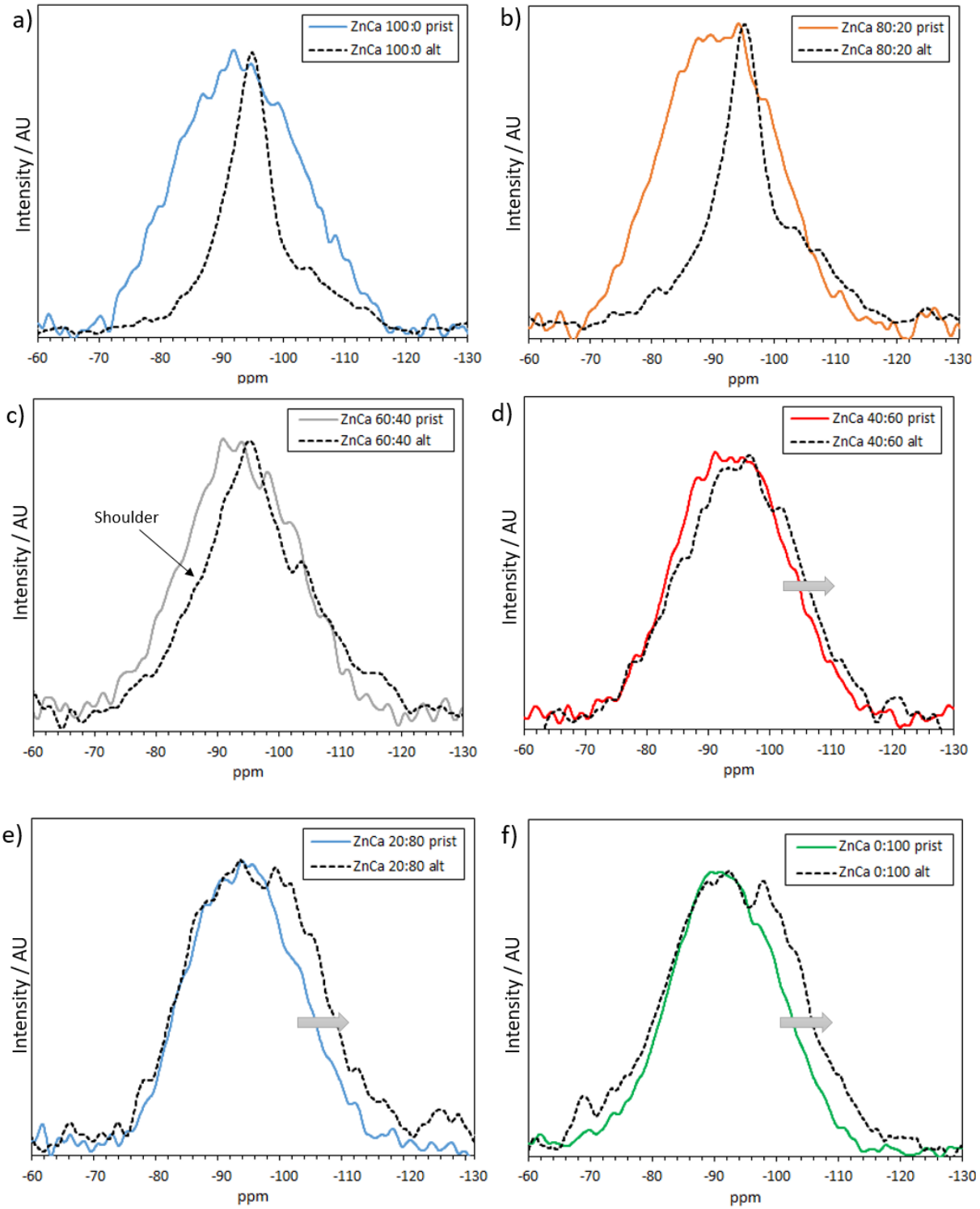

Figure 5.25. ^{29}Si MAS-NMR comparison between pristine (prist) and altered (alt) glass from the ZnCa xx:xx series. Alteration conditions - 303 d, UHQ, 90 °C, 0.33 g of glass with particle size < 0.20 µm diameter: a-c) altered signal from suggested secondary precipitates; d-f) signal from altered gel layer and underlying pristine glass, where a shift towards more negative ppm (indicated by the arrow) is observed for the Ca-rich compositions, representing greater polymerisation of the gel network compared to the pristine glass.

The ^{27}Al MAS-NMR spectra (Fig. 5.26a) from the altered particles indicated the emergence of $^{[6]}$Al at approximately -8 ppm, (compared to the pristine glass spectra Fig. 5.3, which contained only $^{[4]}$Al) alongside the familiar $^{[4]}$Al environment at approximately -55 ppm in the Zn-rich glasses (both environments have been observed in similar pristine glasses by Duddridge *et al.* (2003) and Holland *et al.* (2007), but not the Ca-rich compositions (Fig. 5.26a). Such observations for the dissolved glasses are partially consistent with the Zn-saponite spectra in the study by Vogels *et al.* (2005), except for the shoulder at approximately 65 ppm, which was not observed in Vogels *et al.* (2005). However, the shoulder at approximately 65 ppm is consistent with the Na-beidellite spectra (Bouna *et al.* 2012) and/or other undetermined crystalline phase/s associated with $^{[4]}$Al environments as suggested by Diallo (*et al.* 2019).

The ^{11}B MAS-NMR spectra from the altered particles showed a subtle reduction in the $^{[3]}$B contribution for ZnCa 100:0 only (Fig. 5.26b), indicating that $^{[3]}$B units were more susceptible to dissolution than $^{[4]}$B units. However, this remains largely speculative as a direct comparison between the altered glass ^{11}B spectra and the pristine glass ^{11}B spectra is not possible due to the different instruments used, as explained in Section 3.2.3.1 – Chapter 3.

For all analysed spectra, spectral deconvolution of the altered glass was not undertaken due to the inability to discriminate between the underlying pristine glass and the altered gel layer and secondary phases, particularly for the Ca-rich glasses. Future work, including micro-focus XRD may further elucidate/identify the nature of the secondary phases.

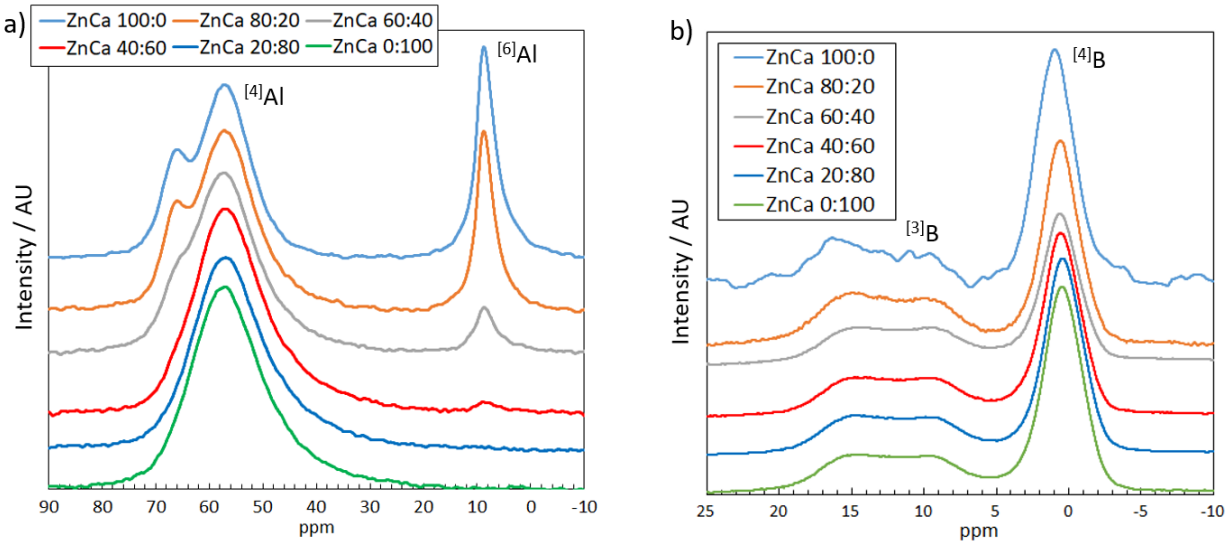

Figure 5.26. MAS-NMR altered glass spectra from the ZnCa MW series. Alteration conditions - 303 d, UHQ, 90 °C, 0.33 g of glass with particle size < 0.20 µm diameter: a) ^{27}Al and b) ^{11}B.

5.2.3.4 Relationship between glass composition and dissolution rate III: From the Residual Rate (Stage II) to Rate Resumption (Stage III)

5.2.3.4.1 Normalised Mass Loss

The relationship between glass composition and dissolution rate at low reaction progress was determined by MCC-1 experiments. The normalised mass loss of elements over the 540 d duration of the experiment showed two distinct dissolution behaviours: (i) attainment of steady residual rate (Stage II) for the Ca-containing end member (ZnCa 0:100) and; (ii) rate resumption for the Zn-containing glasses (ZnCa 100:0 & ZnCa 40:60). Figure 5.27 shows the NL for B, Si, Al, Ca and Zn, in addition to the leachate pH. Data from ZnCa MW28 (the waste loaded version of the Zn:Ca 40:60 composition) is overlaid for comparison, which will be discussed in more detail in Chapters 6 & 10. Figure 5.28 shows the same data, but for the early timescales (0-100 d) only.

The results can be summarised as follows:

- ZnCa 0:100 followed the 'classical' behaviour of glass dissolution (Fig. 2.1 - Chapter 2) and reached a steady residual rate of dissolution after 175 d based on the $NL_{B, Si, Na}$ (Figs. 5.27b - d). Only for this glass did the NL_{Al} decrease throughout the experiment (Fig. 5.27g), indicating uptake into an altered gel layer or secondary phases.
- The ZnCa 40:60 and 100:0 compositions demonstrated an initially low rate of dissolution, up to 31 d (ZnCa 100:0) and 95 d (ZnCa 40:60) when the dissolution rate rapidly resumed, based on the $NL_{B, Si, Na}$ (Fig. 5.28a-c). After this time point, the dissolution rate of ZnCa 100:0 proceeded much more rapidly than all of the other compositions and, at 360 d, there was potentially a second rate resumption, which coincided with a significant decrease in the NL_{Zn}.

The sequence of durability, based on the normalised mass loss of all elements at each timepoint (from the most to the least durable) was: ZnCa 100:0 > ZnCa 40:60 > ZnCa 0:100. The NL_B for ZnCa 0:100 after 540 d was approximately a factor of 1.4 greater than the Zn-containing glasses (Fig. 5.27a). However, the sequence is reversed when considering dissolution *rates* over the time period 175-540 d (which was selected to coincide with the residual rate (Stage II) dissolution time period of ZnCa 0:100 for an appropriate comparison between glass compositions) (Table. 5.8). The B dissolution *rate* over the period 175-540 d was approximately 10 times greater for ZnCa 100:0 than for ZnCa 0:100.

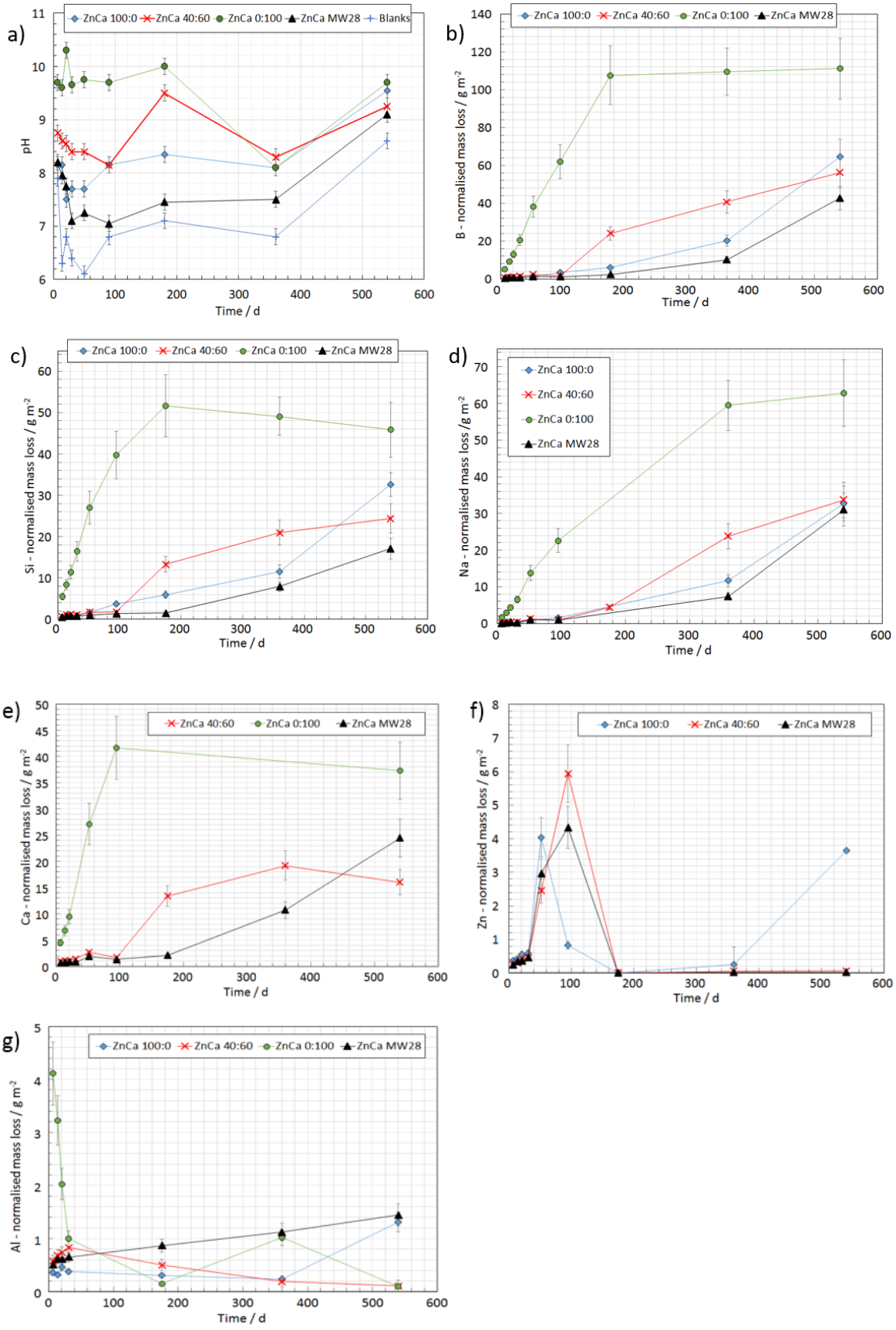

Figure 5.27. Leachate pH(RT) (a) and normalised mass loss of elements (b-g) for ZnCa 0:100, 40:60, 100:0 & 40:60 MW28 at various time points over the course of 540 d MCC-1 investigations at 50 °C in UHQ. Note (b-d) the negative impact of Zn addition on the chemical durability at longer timescales (> 100 d) for the Zn-containing glasses.

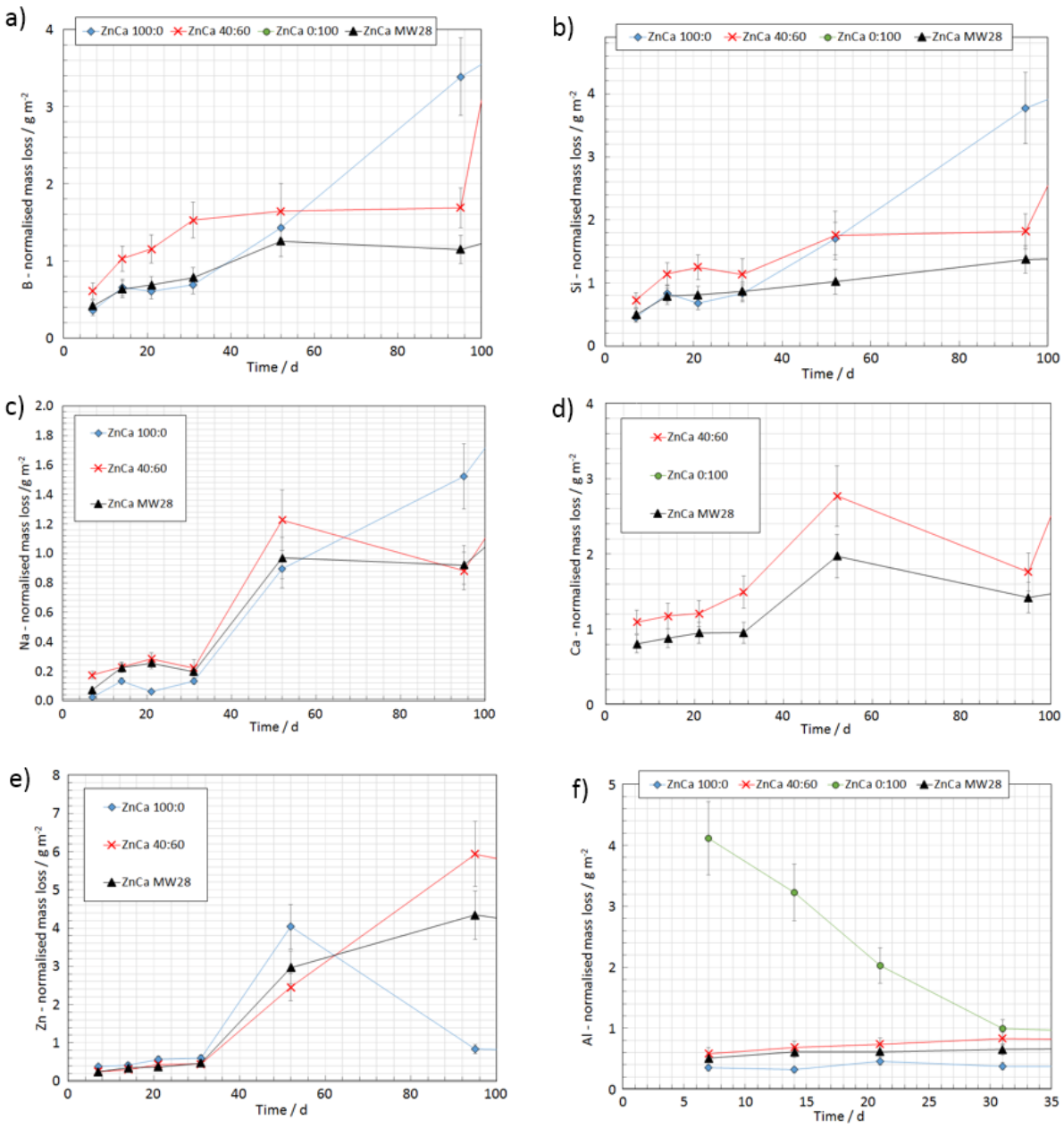

Figure 5.28. Normalised mass loss of elements at early time points (a-f) for ZnCa 0:100, 40:60, 100:0 & 40:60 MW28 in MCC-1 investigation at 50 °C and in UHQ. Note that ZnCa 0:100 is off the scale (a-e) for the benefit of clarity for the other glass compositions.

Table 5.8 Dissolution rates for ZnCa 0:100, 40:60, 100:0 & 40:60 MW28 in MCC-1 investigation at 50 °C and in UHQ over the time period 175-540 d. Rates obtained from a chi-square fit

Glass	Dissolution Rate 175-540 d (NR_B / g m^{-2} d^{-1})	R^2
ZnCa 100:0	0.101 ± 0.014	0.915
ZnCa 40:60	0.088 ± 0.022	0.999
ZnCa 0:100	0.010 ± 0.060	0.999
ZnCa MW28	0.056 ± 0.010	0.884

As noted above, the drop in the NL_{Zn} (Fig. 5.27f & 5.28e) may coincide with the rapid increase of dissolution of all other elements between 95-175 d for ZnCa 40:60 and between 31-175 d for ZnCa 100:0. This may indicate that the formation of Zn-silicate secondary minerals (Gin *et al.* 2013, Aréna *et al.* 2016), which remove Zn and silica from solution and/or the gel layer, provides a thermodynamic driver for accelerated dissolution. This might be described as a form of 'rate resumption' or Stage III dissolution behaviour, although it does not follow all of the same behaviour as reported previously in the literature for this phenomenon. This is discussed more fully in Section 5.3.4.2 of this Chapter.

The difference in the measured pH at initial stages (<52 d) between each composition may reflect the initial durability of each composition (Strachan 2011), whereby the lower the NL_B, the lower the associated leachate pH value (Fig. 5.27a). The drop in the initial pH values (1-52 d) for each Zn-containing glass correlated with the low rate of dissolution and the increase in pH values >52 d, this coincided with the increase in glass dissolution. This is discussed in more detail in Section 5.3.4.2. The leachate pH readings at 360 d may have been subjected to carbonation due to pH leachate measurements in excess of six months post experimental termination (vessels with leachate only stored in a cupboard), thus underestimating the pH value at the time of leachate sampling. All other time point pH measurements were made directly when leachate was sampled, hence, likely subjected less to the effects of carbonation.

5.2.3.4.2 Alteration Layer Formation

The monoliths exposed to dissolution media for 540 d (including ZnCa MW28 for comparison and completeness (to be discussed separately in Chapter 6)) were entirely covered in alteration layers, as shown in Figure 5.29. After approximately 30 minutes of benchtop drying in air, the altered layers on the Zn-containing compositions became cracked and flaked, induced by the drying and dehydration

process. This has been proposed to be the result of a sharp physiochemical interface between the alteration layer and pristine glass (Geisler *et al.* 2015, Lenting *et al.* 2019). The extent of flaking, subjectively, followed the sequence (from the most aggressive to least aggressive) ZnCa 100:0 > ZnCa 40:60 > ZnCa MW28, noting that the ZnCa 0:100 formulation exhibited no sign of flaking. Such behaviour may be of consideration for the disposal of vitrified waste in a GDF, i.e. this form of weathering in Zn-containing glasses may expose sections of pristine glass to solution for further dissolution (Ojovan 2019) and may grant mobility to flaked sections of alteration layers (Ojovan 2018). Stratified alteration layers were evident by eye on the ZnCa 40:60 & 100:0 compositions (see Alteration layer 1 (white) and Alteration layer 2 (grey) Fig. 5.29). The presence of white spots on ZnCa 40:60 MW28 indicate alteration products formed within air bubbles produced upon glass casting.

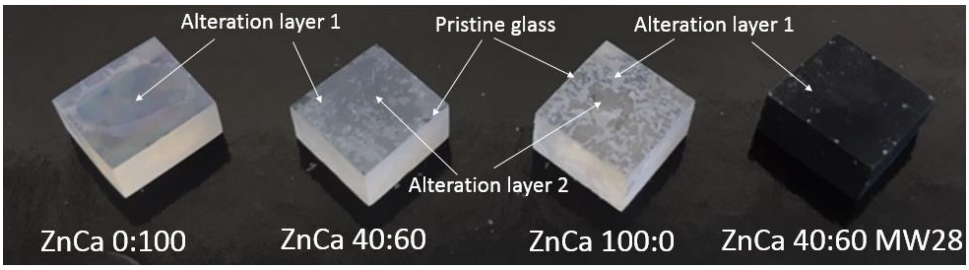

Figure 5.29. ZnCa monoliths removed from dissolution media after 540 d displaying fragile, cracked and flaking alteration layers. The dimensions of the monoliths are 10 x 10 x 5 mm. For a comparison with the pristine ZnCa xx:xx glass series, please refer to Fig. 3.16, Chapter 3. Prior to dissolution, the ZnCa xx:xx series are transparent and MW28 is an opaque, black glass.

Measured alteration layer thicknesses (details of the thickness measurement methodology are provided in Section 3.2.2 – Chapter 3) are displayed in Figure 5.30 (also including ZnCa MW28 for comparison), whereby the earliest time points signify the first observation of such features (< 30 d for ZnCa 0:100). Results showed that ZnCa 0:100 possessed a greater total average thickness at all time points when compared with the other compositions. This is consistent with the normalised mass loss data, whereby ZnCa 0:100 was the least durable. All compositions displayed different alteration layer structures and compositions (Fig. 5.30 and Figs. 5.31-5.34). Particularly, all compositions had an outer layer (attributed to secondary precipitates, except for ZnCa 0:100 which, can be attributed to an outer gel layer) and an inner layer (gel layer). Both of these features were depleted in Na and Ca (for the Ca containing glasses) and enhanced in Al relative to the bulk glass (Figs. 5.31-5.34). The Zn-rich glasses had an additional feature: inner bright bands in the inner (gel) layer contained enhanced Zn concentrations (Fig. 5.30b & c). The outer layer of the Zn-rich glasses were also rich in Zn relative to the bulk glass; when combined with XRD observations (Figs. 5.32-5.34), this suggests that the outer layer is composed of Zn-containing silicate precipitates. When comparing glass monoliths from

different time points, it is apparent that in the Zn-containing glass compositions, the outer (secondary precipitate) layer was formed before the inner layer (gel layer) (Fig. 5.30).

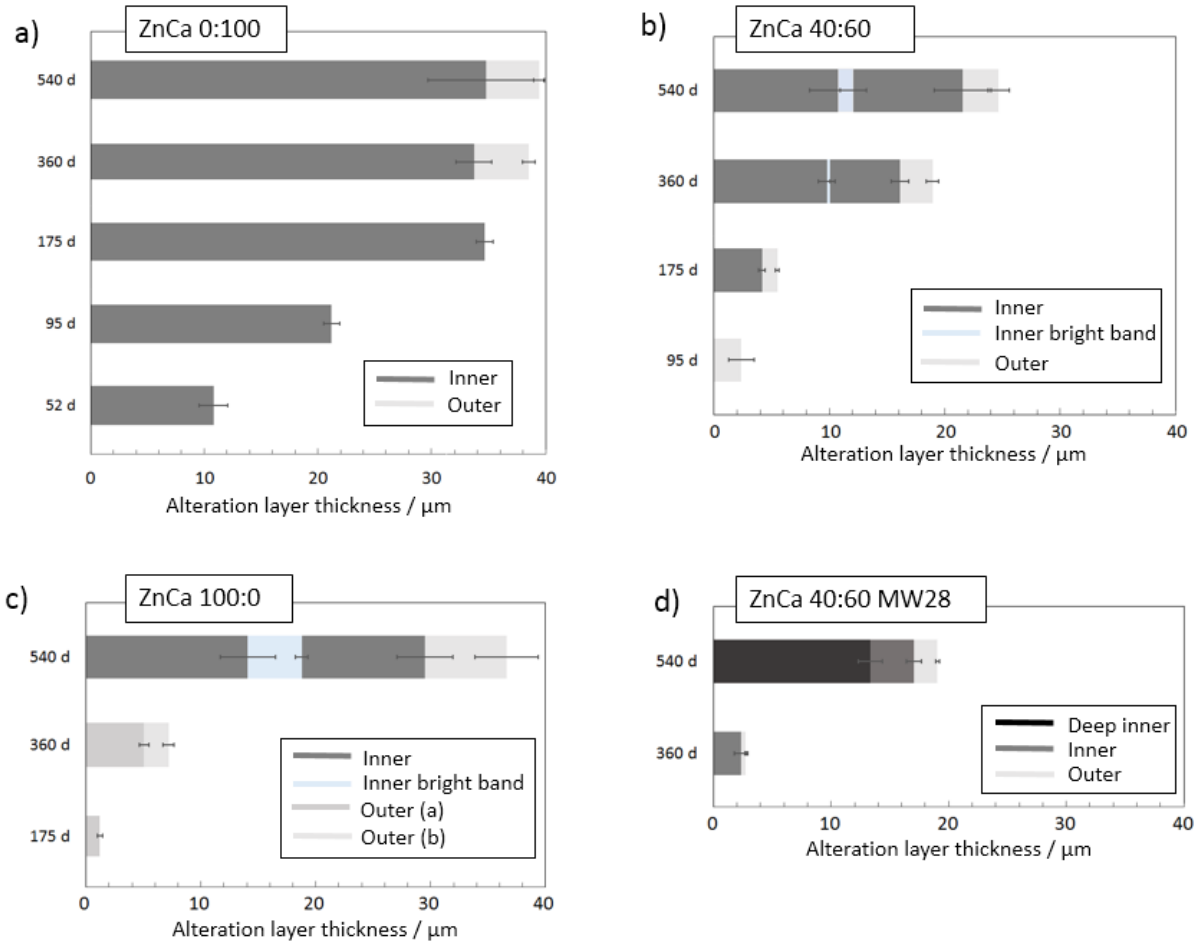

Figure 5.30. Alteration layer thicknesses and composition from MCC-1 investigations post-dissolution at 50 °C in UHQ: (a) ZnCa 0:100; (b) ZnCa 40:60; (c) ZnCa 100:0 and for completeness; (d) ZnCa 40:60 MW28. Note < 0 µm represents bulk glass. Reported errors represent the standard deviation from 15 measurements along the length of the monolith.

Alteration layers observed on ZnCa 0:100, 40:60 and 100:0, particularly the inner (gel) layers, displayed oscillatory zoning (Figs. 5.31-5.34) (Wang *et al.* 2016). The following details the nature of the alteration layers specific to each glass composition in the ZnCa xx:xx series:

ZnCa 0:100

Cross sectional BSE images of ZnCa 0:100 exposed to UHQ at 50 °C for 540 d displayed two distinct alteration layers: an inner and outer layer, which are both presumed to be gel layers (Fig. 5.31a-c). The inner layer had reduced Na and Ca concentrations and an enhanced Al concentration compared to the bulk glass, as evidenced by EDS spot mapping (Table 5.9). The outer layer was depleted in Na, had a similar Ca fraction to the inner layer, and had a significantly greater Al concentration compared to the bulk glass and inner layer. The XRD trace from the top surface of the monolith indicted the characteristic main reflection of tobermorite xCaO·SiO$_2$·zH$_2$O [PDF 06-0013] (Jantzen *et al.* 2010) (Fig. 5.31d) at 29.2 ° 2Θ and a slight edge at 30 ° 2Θ, similar to that observed by Backhouse *et al.* (2019) who investigated the dissolution behaviour of a similar simple Ca-alkali-aluminoborosilicate glass.

Table 5.9 Averaged elemental composition of each distinct alteration layer of ZnCa 0:100 post 540 d MCC-1 dissolution at 50 °C in UHQ associated with Figure 5.31.

		Element At. %			
Section	Spot #	Si	Al	Na	Ca
Bulk glass	7-8	65.1 ± 0.2	6.0 ± 0.0	13.4 ± 0.1	15.5 ± 0.3
Outer bulk	5-6	65.0 ± 0.2	6.1 ± 0.0	13.5 ± 0.0	15.5 ± 0.3
Inner layer	3-4	69.5 ± 0.6	10.4 ± 0.6	7.1 ± 0.9	13.0 ± 2.8
Outer layer	1-2	72.5 ± 0.1	16.4 ± 0.1	-	11.1 ± 0.2

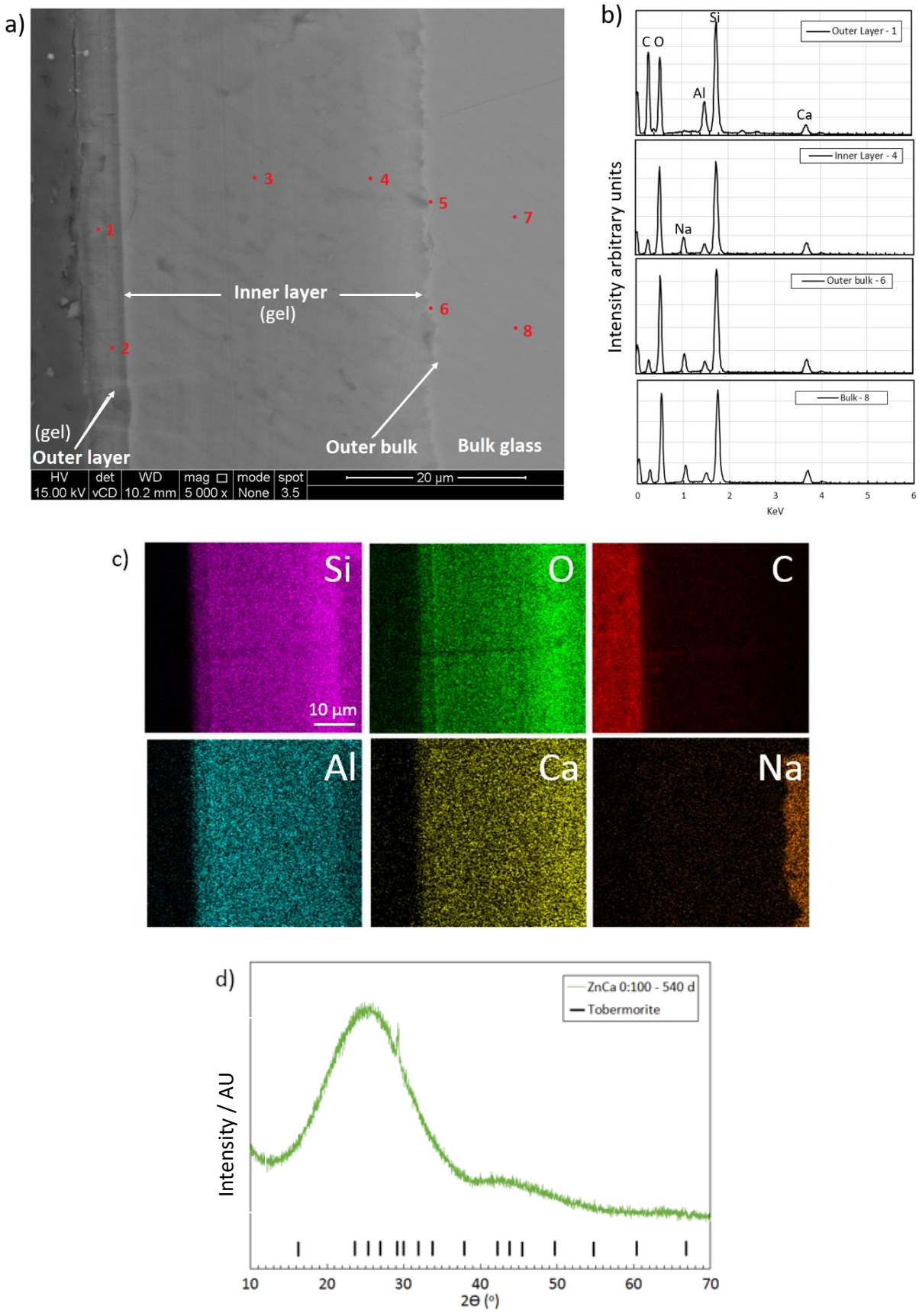

Figure 5.31. SEM and XRD analysis on ZnCa 0:100 post 540 d MCC-1 experimentation at 50 °C in UHQ: a) BSE image, note the oscillatory banding structure of the inner layer, red spots correspond to EDS spot analysis (3 µm diameter spot size) in b); c) elemental mapping; d) XRD trace.

ZnCa 40:60

Cross sectional BSE images of ZnCa 40:60 exposed to UHQ at 50 °C for 540 d displayed a complex oscillatory alteration layer with specific Ca and Al enhanced inner layer bands (inner bands 1 & 2), a Zn-rich inner bright band, and a Zn-rich and Ca- and Al-deficient outer layer (Table 5.10 and Fig. 5.32a -c). The Al concentration of the inner layer was enhanced in comparison to the bulk glass. It is assumed that all the inner layers are gel layers and that the outer layer is composed of secondary precipitates resembling a continuous layer of phyllosilicate clays (sauconite and potentially Na-beidellite), as evidenced by the XRD trace obtained from the top surface of the monolith and from the Na-rich content in the outer layer. (Figs. 5.32d).

Table 5.10. Averaged elemental composition of each distinct alteration layer on the surface of ZnCa 40:60 post 540 d MCC-1 experimentation at 50 °C in UHQ.

		Element At. %				
Section	Spot #	Si	Al	Na	Ca	Zn
Bulk glass	9-9a	63.91 ± 0.64	6.66 ± 0.07	16.64 ± 0.17	8.23 ± 0.08	4.56 ± 0.05
Inner layer	8-8a	75.32 ± 0.75	12.32 ± 0.12	4.19 ± 0.04	5.69 ± 0.06	2.49 ± 0.02
Inner layer - band 2	7-7a	74.28 ± 0.74	14.6 ± 0.15	2.13 ± 0.02	6.17 ± 0.06	2.83 ± 0.03
Inner bright band	5-6	66.78 ± 0.14	11.84 ± 0.08	5.30 ± 0.23	4.91 ± 0.06	11.15 ± 0.23
Inner layer	4-4a	75.17 ± 0.75	14.11 ± 0.14	1.87 ± 0.02	7.54 ± 0.08	1.30 ± 0.01
Inner layer - band 1	3-3a	74.61 ± 0.75	14.70 ± 0.15	2.00 ± 0.02	7.02 ± 0.07	1.67 ± 0.02
Outer Layer	1-2	62.66 ± 0.93	6.50 ± 0.75	6.55 ± 0.93	3.3 ± 1.1	21.0 ± 1.5

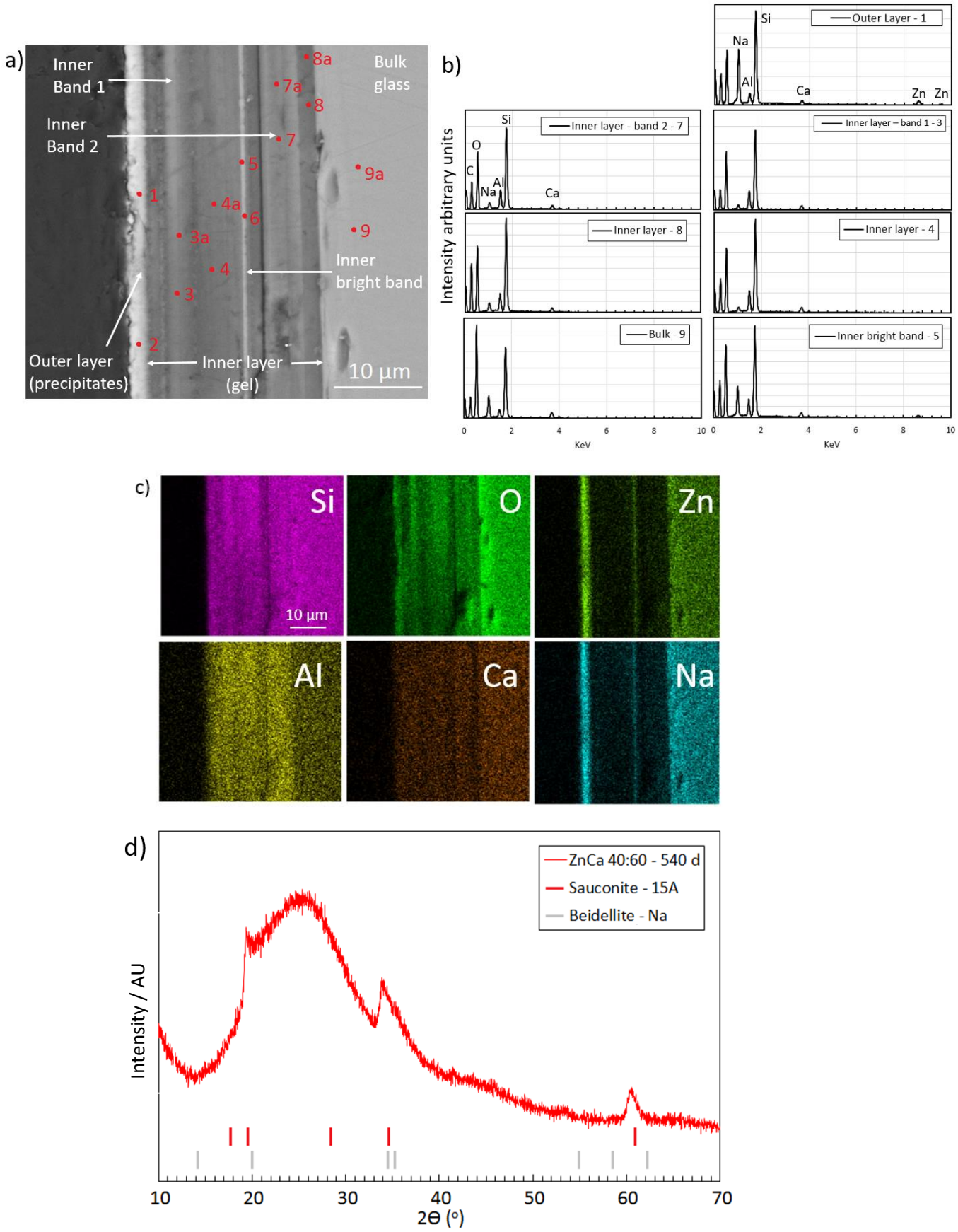

Figure 5.32. SEM and XRD analysis of ZnCa 40:60 post 540 d MCC-1 experimentation at 50 °C in UHQ: a) BSE image, red spots (3 µm diameter spot size) correspond to EDS spot analysis in b); c) elemental mapping; d) XRD trace.

ZnCa 100:0

Cross sectional BSE images of ZnCa 100:0 exposed to UHQ at 50 °C for 540 d displayed a complex oscillatory alteration layer with Zn-enhanced layers (inner bright band, band 1), a Zn-rich outer layer, and a Zn-deficient edge layer (Fig. 5.34). The Al concentration in the inner layers was enhanced in comparison to the bulk glass (Table 5.11 and Fig. 5.34 (a-c). It is assumed that all of the inner layers are gel layers. The XRD trace obtained from the top surface of the altered monolith indicted the presence of the phyllosilicate clays (sauconite and potentially Na-beidellite) (Fig. 5.34d), consistent with similar observations for the ZnCa 40:60 composition.

Table 5.11 Averaged elemental composition of each distinct alteration layer on the surface of ZnCa 100:0 post 540 d MCC-1 experimentation at 50 °C in UHQ.

		Element At. %			
Section	Spot #	Si	Al	Na	Zn
Bulk glass	1	68.3 ± 0.7	5.8 ± 0.1	16.5 ± 0.2	9.4 ± 0.1
	2	67.9 ± 0.7	6.0 ± 0.1	16.5 ± 0.2	9.5 ± 0.1
Inner layer (gel)	3	78.7 ± 0.8	12.9 ± 0.1	6.5 ± 0.1	1.8 ± 0.1
	4	79.2 ± 0.8	12.9 ± 0.1	6.6 ± 0.1	1.4 ± 0.0
	10	64.6 ± 0.7	9.3 ± 0.1	11.0 ± 0.1	15.0 ± 0.2
	19	64.7 ± 0.7	9.8 ± 0.1	10.3 ± 0.1	15.0 ± 0.2
Inner bright band	5	65.1 ± 0.7	9.4 ± 0.1	11.1 ± 0.1	14.2 ± 0.1
	6	65.9 ± 0.7	9.1 ± 0.1	10.2 ± 0.1	14.7 ± 0.1
	7	68.7 ± 0.7	10.3 ± 0.1	10.6 ± 0.1	10.4 ± 0.1
	8	73.2 ± 0.7	10.3 ± 0.1	8.0 ± 0.1	8.4 ± 0.1
Inner layer - band 1	9	55.1 ± 0.6	5.8 ± 0.1	11.9 ± 0.1	26.9 ± 0.3
	18	58.4 ± 0.6	0.2 ± 0.1	11.1 ± 0.1	30.3 ± 0.3
Outer layer (precipitates)	11	56.3 ± 0.6	5.6 ± 0.1	8.2 ± 0.1	29.9 ± 0.3
	12	46.9 ± 0.6	9.4 ± 0.1	13.4 ± 0.1	30.4 ± 0.3
	13	48.8 ± 0.5	10.4 ± 0.1	10.5 ± 0.1	30.6 ± 0.3
	14	65.8 ± 0.7	6.4 ± 0.1	6.1 ± 0.1	21.4 ± 0.2
	15	62.2 ± 0.6	6.8 ± 0.1	9.5 ± 0.1	21.1 ± 0.2
Edge layer (precipitates)	16	70.8 ± 0.7	10.4 ± 0.1	9.0 ± 0.1	9.7 ± 0.1
	17	75.3 ± 0.8	11.1 ± 0.1	8.4 ± 0.1	5.0 ± 0.0

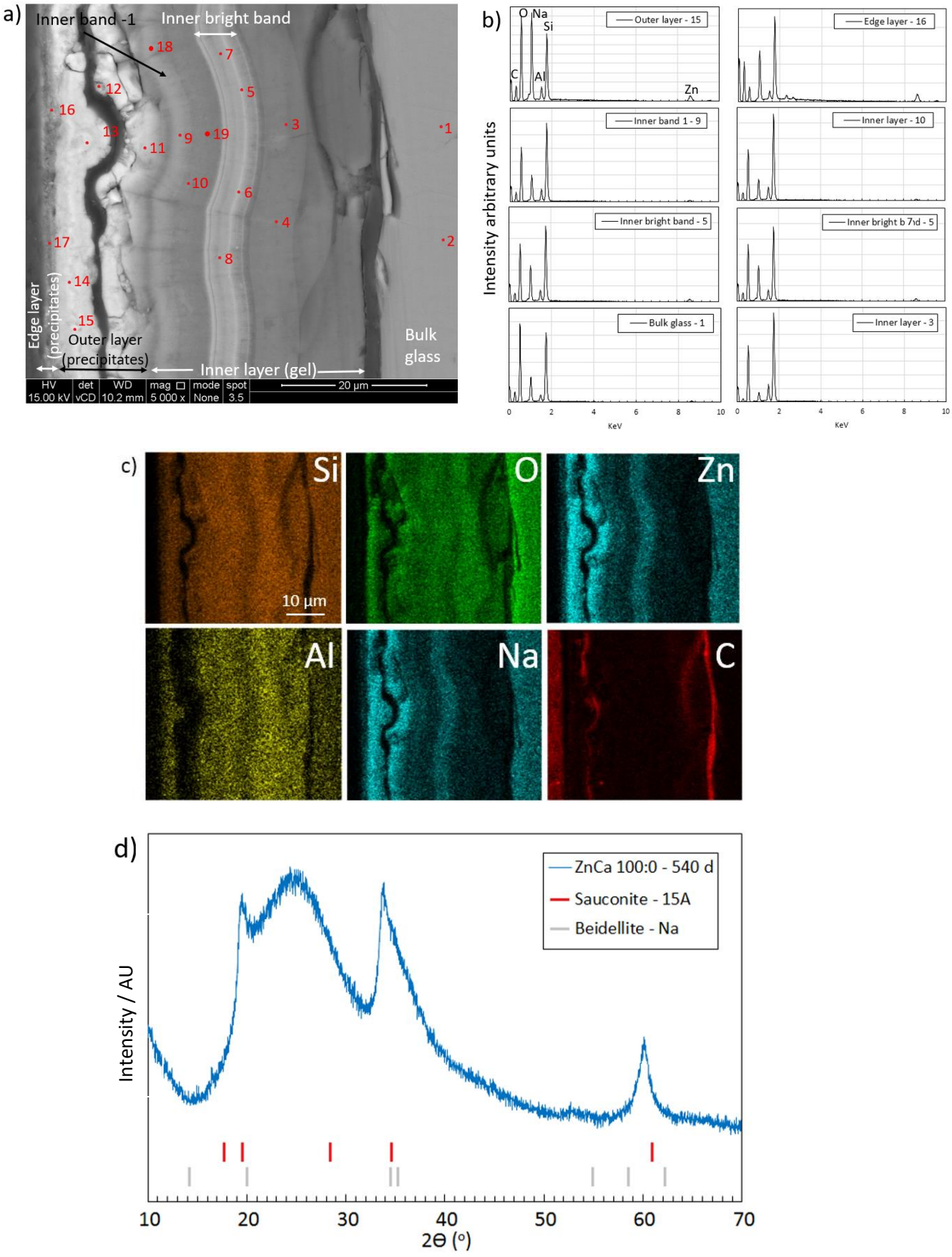

Figure 5.33. SEM and XRD analysis on ZnCa 100:0 post 540 d MCC-1 experimentation at 50 °C in UHQ: a) BSE image, red spots correspond to EDS spot analysis (3 µm diameter spot size) in b); c) elemental mapping; d) XRD trace.

5.2.3.5 Geochemical Modelling

Geochemical modelling by the software PHREEQ-C using the LLNL database identified that the phases listed in Table 5.12 and Fig. 5.34 were saturated in solution, throughout the course of, or at specific time points during the MCC-1 dissolution investigation. These phases may represent some of the secondary precipitates observed in SEM and XRD. Note that saturation indices > 1 represent saturation (Fig. 5.34). The initial pH of the UHQ water was 7.1 for the 7-21 d time points and 6.4 for the 31-720 d time points. This difference was due to the different starting dates for each experiment. The beidellite and $ZnSiO_4$ phases were potentially consistent with SEM and XRD observations. Note that the phase zincsilite ($Zn_3Si_4O_{10}(OH)_2 \cdot 4(H_2O)$) has been suggested to form during SON68 dissolution in the study by Debure *et al.* (2019), but zincsilite, alongside sauconite, were not available as phases in the thermodynamic database utilised (LLNL) and in other databases, therefore were not predicted to form. Future work directed at expanding such databases would greatly benefit the field of vitrified HLW corrosion since, as well as being incorporated in UK HLW glass formulations, Zn in also a component in the French R7T7 HLW glass and the inactive SON68 simulant HLW glass.

A key finding was that Zn_2SiO_4 was saturated in solution for ZnCa 40:60 and 100:0 at 50 °C at pH values between 8.3-9.5 and 7.5-9.55, respectively, over approximately the full experimental duration, except for 175 d when Zn was not detected in solution. The saturation index of Zn_2SiO_4 increased in the time period 360-540 d (Fig. 5.34c) by a factor of 1.75, which corresponded with the 'rate resumption' (Stage III) based on the normalised mass loss of B displayed in Figure 5.27b. Also, throughout this time period, the total alteration layer thickness increased by an approximate factor of four (Fig. 5.30c). Together, these data and the XRD and SEM analysis suggest that the precipitation of a Zn silicate phase increases the dissolution rate.

The Ca-containing zeolite, mesolite, was calculated to be saturated in solution for ZnCa 40:60 and 0:100 at 50 °C at pH values between 8.3-9.5 and 7.5-9.55, respectively, over approximately the full experimental duration. The modelled formation of Zn_2SiO_4, tobermorite and Na-beidellite were partly consistent with the XRD, SEM (Figs. 5.31-5.33) and potentially the MAS-NMR (inferred for Na-beidellite only Fig. 5.25) results.

Table 5.12 Mineral phases identified by PHREEQ-C geochemical modelling to be saturated in solution for all or some of the ZnCa xx:xx glass compositions in the MCC-1 investigations at 50 °C in UHQ after 540 d.

Phases Identified from Lawrence Livermore National Laboratory database			
Phase	Chemical formula	Comments	Associated composition ZnCa xx:xx
Beidellite-Ca	$Ca_{.165}Al_{2.33}Si_{3.67}O_{10}(OH)_2$	Phyllosilicate - Smectite	100:0 & 40:60
Beidellite-H	$H_{.33}Al_{2.33}Si_{3.67}O_{10}(OH)_2$	Phyllosilicate - Smectite	100:0, 40:60 & 0:100
Beidellite-Na	$Na_{.33}Al_{2.33}Si_{3.67}O_{10}(OH)_2$	Phyllosilicate - Smectite	100:0, 40:60 & 0:100
Gibbsite	$Al(OH)_3$	-	40:60 & 0:100
Kaolinite	$Al_2Si_2O_5(OH)_4$	Kaolinite Subgroup - Kaolinite-Serpentine Group	100:0, 40:60 & 0:100
Laumontite	$CaAl_2Si_4O_{12}.4H_2O$	Zeolite	40:60 & 0:100
Mesolite	$Na_{.676}Ca_{.657}Al_{1.99}Si_{3.01}O_{10}.2.647H_2O$	Zeolite - Nantrolite subgroup	40:60 & 0:100
Mordenite	$Ca_{.2895}Na_{.361}Al_{.94}Si_{5.06}O_{12}.3.468H_2O$	Zeolite	0:100
Prehnite	$Ca_2Al_2Si_3O_{10}(OH)_2$	-	40:60 & 0:100
Scolecite	$CaAl_2Si_3O_{10}.3H_2O$	Zeolite - Nantrolite subgroup	100:0 & 40:60
Tobermorite-11Å	$Ca_5Si_6H_{11}O_{22.5}$	CSH	0:100
Zn_2SiO_4	Zn_2SiO_4	Zn_2SiO_4	100:0, 40:60 & 0:100

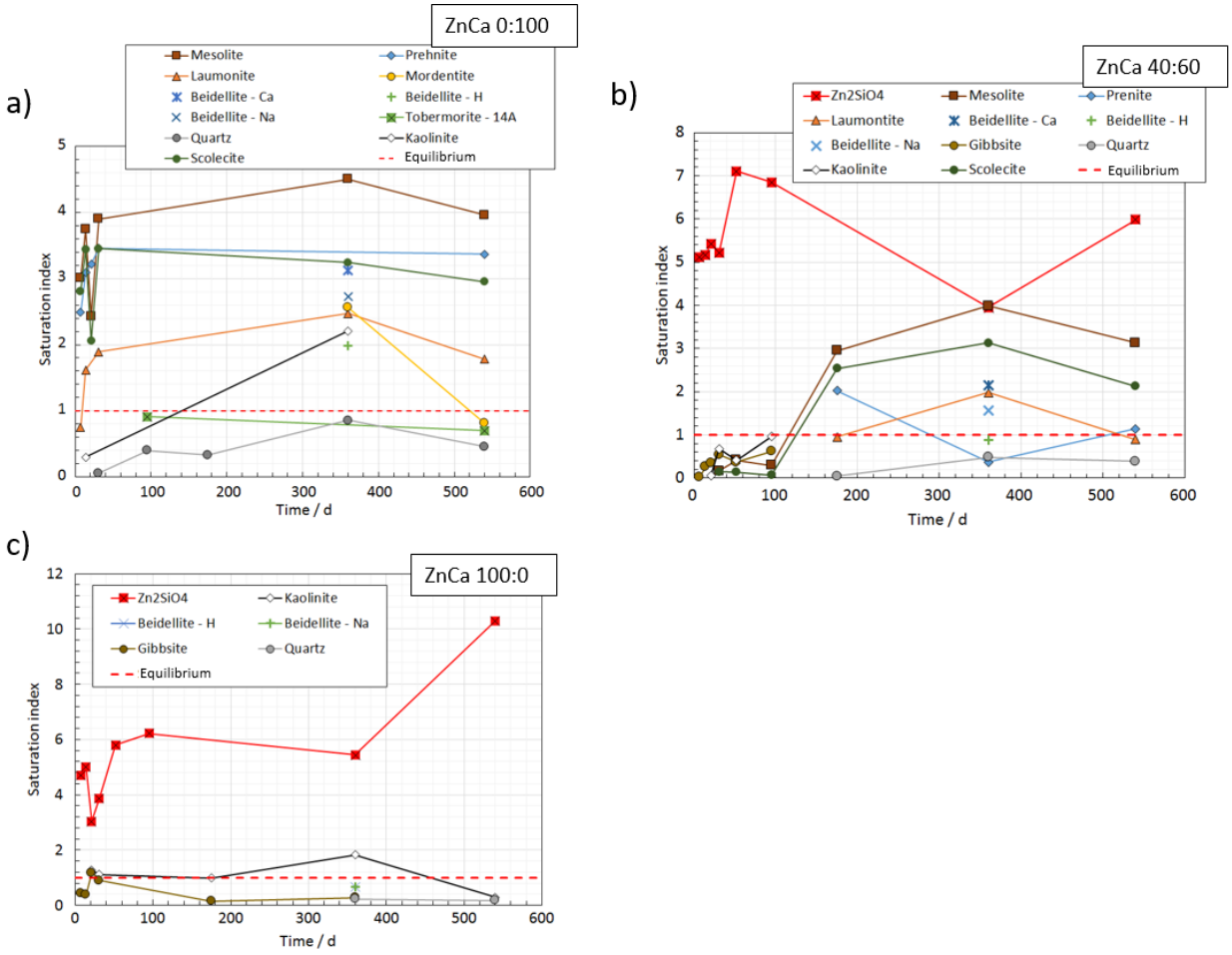

Figure 5.34. Geochemical modelling of the solution chemistry from the leachate of the MCC-1 dissolution investigations of the ZnCa xx:xx compositions at 50 °C in UHQ after 540 d: a) ZnCa 0:100; b) ZnCa 40:60 & c) ZnCa 100:0.

5.3 Discussion

The aim of this study was to investigate the effect of ZnCa addition to the MW base glass formulation at a fundamental level, paying particular attention to the structure-durability relationship. A detailed discussion of how ZnCa addition influenced the glass structure, and thus the dissolution kinetics and mechanisms, are detailed below.

5.3.1 Structure – Pristine glass

The ^{29}Si MAS-NMR spectra obtained from the pristine Zn-rich glasses revealed a broadening of the overall MAS-NMR spectra, whereby more Q_4 and Q_2 species were observed compared to the Ca-rich glasses (Fig. 5.6 & Table 5.5).

The first explanation for this behaviour may be due to the large distribution of chemical shifts caused by the environments of the multi-network forming elements (Si, B, Al & Zn - assuming Zn is playing a network-forming role). The large number of different environments and strongly assumed phase separation, suggested by the thermal data (Fig. 5.2), is likely to result in line broadening by chemical shift dispersion around nominally equivalent Q_n(X) type Si tetrahedra (where X = B, Al, Zn), in which the spectral fit Q_3 & Q_4(X) (Fig. 5.6) would be the dominant feature. This scenario would lead to many overlapping lines with slightly different chemical shifts caused by variation in bond angle and bond length, which manifest in an overall broadening of the spectra, especially for the Zn-rich glasses. Such line overlap would prove difficult to deconvolute into individual components.

The second explanation may be that Zn takes on both a network former *and* modifier role in the Zn-rich glasses, hence is an intermediate specie (Petrescu *et al.* 2012). It has been reported that Zn can take on both roles (Dumas & Petiau 1986, Lusvardi *et al.* 2004, Smedskjaer *et al.* 2013), preferentially as a modifier in glasses with low alkali concentration or substantial Zn content, which is consistent with the Zn-rich formulations used in this study. The strongly assumed phase separated Zn-rich glasses, suggested by the thermal data, alongside literature for similar glass compositions which report phase separation (Taylor 1990, Taylor & Owen 1981, Goswami *et al.* 2008, Soleimanzade *et al.* 2014, Kullberg et al. 2016, Petrescu *et al.* 2012, Vance *et al.* 2017), could support the claim that Zn is acting as both a network former and modifier, hence an intermediate. In this scenario, Zn must be playing a dual structural role to explain the observed phenomena; increasing Q_3 & Q_4(X) contributions as a network-former and also increasing the Q_2 contributions as a modifier. However, the same issue

regarding the large distribution of chemical shifts exists, which make any real justification for such explanations difficult. If Zn is performing a dual (intermediate) role, a global smearing and broadening of the spectra should be expected in the multi-oxide network forming Zn-rich glasses.

The ^{11}B spectra were consistent with the literature for similar glass compositions (Angeli *et al.* 2012, Vance *et al* 2017), which have shown that there is an increase in $^{[4]}B$ units with the addition of alkali/alkaline earth (Ca in this study). However, the deconvolution of the $^{[3]}B$ and $^{[4]}B$ regions revealed the presence of different co-ordination environments (Fig. 5.5). Here, the $^{[4]}B$ (0B, 4Si) contribution was invariant with respect to the ZnCa ratio, but the $^{[4]}B$ (1B, 4Si) contribution was reduced. The fact that $^{[4]}B$ (1B, 4Si) units (assuming that the 1B is predominantly a tetrahedral boron unit in need of charge compensation (Gupta 1986, Möncke *et al.* 2015)) are associated with charge compensating cations compared to $^{[4]}B$ (0B, 4Si) units, means it could be possible for Ca to be drawn to the former, thus inducing a heterogeneous distribution of modifier cations (Wu & Stebbins 2009). Such results indicate potential indirect evidence for micro-domain phase separation, whereby borosilicate (associated with BO_3) and alkali/alkaline earth borosilicate (associated with BO_4) networks co-exist.

The DTA data, which displays two glass transition temperatures for ZnCa 100:0 and ZnCa 80:20, provides evidence to suggest that the Zn-rich glasses were phase separated, with speculated regions comprising of 4- and 6-fold Zn, which was indirectly inferred by ^{29}Si MAS-NMR and predicted based on an extended modified Dell-Bray model (Table 5.6). It should be noted that glass networks with more connected structural units require higher onset temperatures for structural relaxation, hence an increase in T_g is usually associated with a strengthening of the glass network. In this study, T_{g1} followed the clear sequence, from Ca-rich to Zn-rich: ZnCa 0:100 (505 °C) > ZnCa 100:0 (445 °C). However, the fact that some Zn may be playing a network modifying role, thus reduced the extent of network polymerisation and potentially encouraged phase separation, a reduction in T_g may be expected as well as the creation of a second T_g (T_{g2}) respectively.

The key point is that complementary structural experimental techniques and structural predictions strongly suggest that increasing the Zn content, at the expense of Ca in this glass series, induced phase separation due to the predominant intermediate role of Zn. Whereas the Ca addition in the counterpart Ca-rich compositions likely induced network depolymerisation within a single phase glass, with the potential for inducing a heterogeneous distribution of modifier cations (Wu & Stebbins 2009).

5.3.2 Relationship between glass composition and dissolution rate I: The Initial Rate (Stage I)

Measurements of Stage I initial dissolution rates from this study are consistent with those reported in Bourcier *et al.* (1992), Bakel *et al.* (1996), Oelkers & Gislason (2001), Wellman *et al.* (2005) and Icenhower (2008) for similar simple glass compositions. It has recently been suggested that the impact of glass composition on the initial rate of dissolution has a relatively small effect (Icenhower *et al.* 2008, Vienna *et al.* 2018), but results from this study, which showed that there was factor of 14 difference between the least durable ZnCa 0:100 and most durable ZnCa 100:0 (Fig. 5.9d), potentially challenge this hypothesis.

The pitted and troughed surface features observed on the suggested two-phase ZnCa 100:0 glass (labelled as 3a in Fig. 5.10) were not observed on the nominally single-phase ZnCa 40:60 and 0:100 compositions, which tentatively suggests that their formation was a result of the presence of less-durable micro-domains that preferentially dissolved. This hypothesis is strengthened by the observed incongruent dissolution for this composition at the initial rate (Fig. 5.9a), which showed that Zn was most readily released from the glass, potentially from domains that were rich in network modifying Zn. The same pitted and trough features were observed on the ISG (Figs. 4.6 & 4.7 - Chapter 4) under identical experimental conditions. The fact that these pitted and trough features were only observed on ZnCa 100:0 in this chapter suggests that initial surface roughness and cracks on the pristine glass cannot be used to explain all post-dissolution features (noting that such initial surface roughness and cracks can explain features observed on ZnCa 40:60 and 0:100 (Figs. 5.11 & 5.12)). Wu & Stebbins (2009) reported that in alkali and alkaline earth aluminoborosilicates, the distribution of modifier cations was heterogeneous, which manifested in micro-domain phase separation, which could be interpreted and extended to affect the dissolution behaviour. Such reasoning could be applied to this study concerning the Zn-rich glasses: ZnCa 100:0 and 80:20. This consideration is important for accurate empirical and theoretical models, particularly relating to initial dissolution behaviour.

The identification of Ca-rich secondary phase formation on ZnCa 0:100 shows the relative rapidity and ease of the potential formation in flow-through conditions (note the flow-rate: 80 ml/d), noting also that such phases could have been formed post experimentation during the drying process, where residual solution on the surface of particles may become saturated and allow for secondary phase precipitation. In-situ Raman observations, recently implemented by Geisler *et al.* (2019), would have the potential to elucidate the kinetics of such in-situ secondary phase precipitation.

5.3.3 Relationship between glass composition and dissolution rate II: The Residual Rate (Stage II)

All of the glass compositions were observed to transition to residual rate dissolution (Stage II) after approximately 14 d from PCT-B dissolution tests. Residual rates based on the NL_B from 14-35 d were approximately equal (exhibiting a very low rate of dissolution) for all compositions except ZnCa 100:0, which showed a slightly faster rate (14-28 d), thought to be due to the precipitation of the phyllosilicate clays sauconite and potentially Na-beidellite (Fig. 5.14b). The dissolution behaviour of ZnCa 100:0 was similar to the Zn-rich glasses in the study by Gin *et al.* (2013), who observed constant aggressive Stage II dissolution (and the precipitation of the Zn-phyllosilicate sauconite) throughout 1,700 d tests on two simple four-component formulations ($13.8Na_2O{\cdot}2.7ZnO{\cdot}13.8B_2O_3{\cdot}65.9SiO_2$ wt. % and $12.4Na_2O{\cdot}13ZnO{\cdot}15.7B_2O_3{\cdot}58.9SiO_2$) under similar experimental conditions. Quantification of residual rates from the study of Gin *et al.* were not provided, however, the results showed that a transition to Stage III rate resumption was not observed (or potentially missed at early timescales due to the accelerated nature of PCT-B tests).

In the present PCT-B study, there was arguably no real change in the NL_{Ca} (within experimental error) with reaction progress in any of the glass compositions, except for the Zn-rich ZnCa 80:20 and 60:40 compositions, which showed an increase (Fig. 5.14e). These observations suggest that the formation of a Ca-silicate gel layer, which is widely reported in the literature to passivate glass dissolution, was not formed for any of the glass compositions, or below the limits of SEM resolution (a reduction in NL_{Ca} would indicate Ca uptake in a gel layer/secondary precipitates). It is possible that a Ca-silicate gel layer was not observed due to the short time scale of the experiment (35 d) (or again beyond the limits of SEM resolution), however, in the case of the Zn-containing glasses, which also showed the greatest decrease in NL_{Al} (Fig. 5.14f) and a concurrent decrease in NL_{Zn}, it can be hypothesised that the formation of a passivating gel layer may have been hindered by the preferential formation of Zn-silicates, which also contain Al (corroborated by results from MCC-1 experiments, discussed below). Such an effect could be interpreted as a pseudo-competition between the detrimental and positive effects of Zn and Ca respectively on the chemical durability during residual rate dissolution (Stage II).

The observed cracking and spalling of altered layers post-dissolution may lead to questions on the behaviour of disposed HLW glass in geological disposal environments, especially considering semi-dynamic (over geological timescales) conditions, whereby such behaviour could be detrimental to the long-term performance by exposing the underlying pristine glass (Ojovan 2018 & 2019), hence tests

of wasteloaded glasses are investigated in Chapter 6. Such considerations could be considered in future long-term modelling and performance assessments.

Stage III rate resumption was not observed in the 35 d PCT-B tests (or potentially missed at early timescales due to the accelerated nature of PCT-B tests). Longer term and more delicate tests are needed to probe such behaviour, which are provided by the MCC-1 investigations. Note the study by Gin *et al.* (2013) reported a correlation between the SA/V and the onset of residual rate Stage II dissolution for SON68 glass (UHQ, 90 °C), whereby Stage II dissolution was observed after 365, 100 and 10 d for SA/V = 12, 80 and 2,000 m^{-1} respectively.

5.3.4 Relationship between glass composition and dissolution rate III: From the Residual Rate (Stage II) to Rate Resumption (Stage III)

5.3.4.1 Ca-rich glass behaviour

In the composition ZnCa 0:100, the appearance of the outer (gel) layer between 175-360 d from the MCC-1 tests (Fig. 5.30a & Fig 5.31a) coincided with the onset of residual rate dissolution (Stage II) (Fig. 5.27). The outer (gel) layer was fully depleted in Na, had lower Ca content and had an increased Si and Al concentration compared to the inner (gel) layer. Such a finding is consistent with the theory of the formation of a dense outer silica gel layer that passivates a dissolving surface, which results in a dramatic drop in the dissolution rate (Cailleteau *et al.* 2008, Gin *et al.* 2015). The outer layer in such a situation may continuously be subject to in-situ silicate network re-polymerisation and re-organisation, whereby the removal of Na could be playing a key role, which may potentially trigger network re-polymerisation. In such a layer, Ca is the only charge balancing cation in the gel (charge balancing Al) (Gin *et al.* 2015), noting that ^{29}Si MAS-NMR from same altered glass suggested the re-polymerisation of the gel layer (Fig. 5.25f). This reasoning may also be indirectly implied by the reduction in NL_{Si} and NL_{Ca} (Figs. 5.27c & e) and sustained residual rate dissolution based on NL_B over the period 175-540 d.

The inner (gel) layer displayed oscillatory zoning, similar in nature to those expected in a direct dissolution-precipitation mechanism (Geisler *et al.* 2010, Putnis *et al.* 2015, Hellman *et al.* 2015). Despite the formation of this layer, there was no passivation of dissolution until 175 d when a threshold was potentially crossed, whereby the initial rate transitioned to the residual rate; these observations are in line with the Refined Unified Mechanistic Glass Corrosion Model (RUMGCM) as suggested by Lenting *et al.* (2018). (Note that the RUMGCM attempts to unify the Interface-Coupled

Dissolution-Precipitation model (ICDP) model (Geisler *et al.* 2010, 2015, Hellman *et al.* 2015, Putnis *et al.* 2015) with the re-polymerisation model (Grambow 1987, Bunker 1994, Jégou *et al.* 2000, Gin *et al.* 2000, Grambow & Müller 2001, Frugier *et al.* 2008, Gin *et al.* 2011, Me *et al.* 2017) (Section 2.3.2 - Chapter 2). Applying the RUMGCM to the dissolution of the ZnCa 0:100 composition, the onset of the residual rate of dissolution is controlled by the solid-state diffusion (of H^+) into the pristine glass and outward diffusive transport of elements through the outer (and possibly inner) gel layers. This diffusive aspect only starts when the ICDP process stops, or slows to a velocity < diffusion of H^+ into the glass. However, the termination of the ICDP process is related to a build-up of alkali at the bulk glass/gel interface and the saturation of aqueous silica in the interfacial solution, the location labelled as the bulk edge (more specifically the glass/gel interface) in Figure 5.31a due to an increasing transport distance between the interfacial solution, through the gel layer to the leaching media with increasing time, which may have occurred after approximately 175 d. Here, a critical time point/gel layer thickness may have been exceeded, which consequently slowed down the dissolution (hydrolysis of Si-O bonds) to the point that the diffusion process started and dominated the dissolution process in place of the ICDP (Section 2.3.2 in Chapter 2). Thus, to reconcile the appearance of the outer gel layer, it is speculated that the switch in mechanisms potentially enabled the alteration layer to chemically and structurally reorganise, which may have been most evident in the outer gel layer.

The key finding is that observations from dissolved ZnCa 0:100 glass monoliths potentially correspond directly with the proposed RUMGCM, whereby the replacement of the ICDP by interdiffusion at a critical time point, associated with a critical alteration (gel) layer thickness was observed, which may have led to the structural reorganisation as evidenced by the appearance of the outer layer and suggested greater network polymerisation from ^{29}Si MAS-NMR. In this scenario, the long-term fate of the glass depends on the diffusion properties and growth of the gel layer, which, in terms of geological disposal, will be influenced by external factors.

5.3.4.2 Mixed Zn and Ca glass behaviour

In the ZnCa 40:60 glass, clear oscillatory gel banding and an outer precipitate layer was observed (Figs. 5.32 & 5.35) after 540 d. A significant increase in the dissolution rate was also observed after 95 d (Fig. 5.35), similar to the Stage III 'rate resumption' dissolution previously observed for other glass compositions (Strachen & Croak 2000, Ribet *et al.* 2004, Frugier *et al.* 2008, Burger *et al.* 2013, Strachan & Neeway 2014, Fournier *et al.* 2014). However, the suggested mechanistic cause of the 'rate resumption', i.e. the precipitation of Zn-silicate phases, does not conform with the *classically* reported

mechanism of 'rate resumption', which is associated with the following behaviour, irrespective of the type of borosilicate glass (Vienna *et al.* 2013):

1. A reduction in the Si concentration in solution prior to the 'rate resumption', which may take the solution away from equilibrium and/or destabilise the protective gel layer, thus increasing the driving force for dissolution (Pierce *et al.* 2006, Vienna *et al.* 2013). However, conflicting data shows that the NL_{Si} can increase at the same time as the rate resumption (Gin *et al.* 2001, Ribet & Gin 2004, Ebert *et al.* 2011); the reason for this discrepancy, may lie in the pristine glass composition.
2. A reduction in the Al concentration in solution prior to the 'rate resumption' (Frugier *et al.* 2008, Fournier *et al.* 2014).
3. An increase in pH – it is suggested that pH > 10.5 is when rate resumption occurs (Ribet & Gin 2004 and Fournier *et al.* 2014) – which *initiates* the secondary mineral precipitation, and the pH *continues to increase* during the 'rate resumption' (Frugier *et al.* 2008).

These characteristics are only partially consistent with those observed in the present study where 'rate resumption' occurs, e.g. after 95 d for ZnCa 40:60:

1. A reduction in the NL_{Si} was not observed prior (< 95 d) to the 'rate resumption' (based on NL_B (Fig. 5.28a - b)), however, it could be argued that a constant, very low steady state dissolution rate was observed from 55-95 d, based on the NL_B & NL_{Si}. Such evidence remains largely inconclusive regarding its relation with 'Classical Stage III'.
2. A reduction in NL_{Al} was observed after 31 d, consistent with the 'Classical Stage III' description.
3. The pH increased from 8.2 to 9.4 throughout the time period 95-175 d, in line with the 'Classical Stage III' description. However, these pH measurements were significantly lower than the pH 10.5 threshold for zeolite precipitation (Ribet & Gin 2004, Fournier *et al.* 2014).

Given the clear increase in dissolution rate after a period of steady state, despite the non-conformance with all aspects of the classical description of Stage III, this data suggests that Stage III might be expanded to incorporate the rapid precipitation of silicate clays formed in a dissolution-re-precipitation process. It is hypothesised, therefore, that for borosilicate glasses containing Zn, the precipitation of Zn-silicate clays (Fig 5.35) cause *early* Stage III 'rate resumption'. This appears to be intrinsic to Zn-containing borosilicate glass compositions containing > 4.7 wt.% ZnO.

Before 31 d of dissolution, the NL_{Zn}, NL_{Na}, NL_B and NL_{Si} were equal, displaying a very low rate of dissolution. An increase in NL_{Na} between 31-55 d and an increase in NL_{Zn} from 31-95 d (Fig. 5.28c & e) indicates that a threshold for the greater release of Na and Zn was crossed after 31 d. Since Na and Zn

were released at a greater rate than B and Si at this time point, it is speculated that Zn in the glass network was more readily hydrolysed than Si and B (recalling that all of the Zn in this glass composition was in a network-forming role – see Section 5.2.2). The increase in NL_{Zn} (and NL_{Na}, which may have been charge balancing $[ZnO_4]^{-2}$ tetrahedra in the pristine glass) is suggested to facilitate further corrosion, indirectly increasing the NL_{Si} and therefore also the NL_B. It is important to note that the increase in NL_{Na} and NL_{Zn} had no apparent effect on the measured leachate pH (within uncertainty), therefore the increased dissolution may be considered not to be a result of increasing pH, as in the classical 'rate resumption' definition.

Subsequently, Zn-silicate clays formed over the course of the experimental duration (noting a drastic reduction in NL_{Zn} > 95 d (Fig. 5.27f)), which were first directly observed by BSE-SEM from 95 d (Fig. 5.30). Zn-silicate clay formation supported a sustained fast dissolution rate from 95-540 d. With greater reaction progress, a gel layer was observed to form, first observed after 175 d, in contrast to traditional glass corrosion behaviour in which the gel typically forms much earlier (Frugier *et al.* 2008, Vienna *et al.* 2013). Again, this is suggested to be largely compositional dependent, based on the Zn behaviour, noting that robust studies on Zn-containing borosilicate glass corrosion in low SA/V experiments are relatively limited.

These observations allow two combined mechanisms to be hypothesised that lead to the onset of Stage III 'rate resumption': (1) the large increase in NL_{Zn} (more readily hydrolysed) essentially triggered/facilitated the increase in NL_B and NL_{Si}, which subsequently (2) allowed for the large precipitation of Zn-silicate clays (sauconite (Fig. 5.32)), which sustained the 'rate resumption'. Such a hypothesis needs to explain the later gel formation process, which, as noted above, was first observed after 175 d (Fig. 5.30b & 5.35). At this time point, the appearance of a banded structure suggests gel formation via the RUMGCM (Lenting *et al.* 2018), which points to changes in the solution saturation of Si and Zn. Such changes may allow the build-up of significant concentrations of Si, in excess of those required to form Zn-silicates, allowing for Si-recondensation into a gel layer. However, this gel layer does not seem to be of a strongly passivating nature based on the maintenance of 'rate resumption' from 175-540 d (Fig. 5.35). This is interesting since the gel layer contained Ca, which generally plays a passivating role (Chave *et al.* (2011), Utton *et al.* (2013), Corkhill *et al.* (2013), Aréna *et al.* (2018) and Mann (2018)).

An interesting observation for ZnCa 40:60 at 360 and 540 d was that the inner bright bands (Figs. 5.30b & 5.32a) were measured at approximately the same distance from the bulk glass (~ 10.5 µm). This may be indicative of temporal dependence on the formation of such a band, whereby a threshold (pH, concentration of a particular element in solution, reaction progress) may have been exceeded. The

nature and structure of the bright inner band was difficult to ascertain, but this threshold could indicate the precipitation of Zn-phases w*ithin* the gel layer or a build-up of diffusing Zn species at this particular location, possibly marking the transition between a dense and less dense zone within the whole gel layer. This is evidenced by Zn concentrations either side of the inner bright band, whereby there are differences in the Zn concentration (Table 5.10 & Fig. 5.32), with greater Zn concentration towards the bulk glass side, and lower Zn concentration on the solution side (see A and B, respectively, in Figure 5.35). Hence, it could be assumed that the outer zone (B) was denser (consistent with the outer dense gel layer in ZnCa 0:100), thus Zn^{2+} may have been unable to diffuse sufficiently. Lenting *et al.* (2018) made a similar observation of a denser inner band in a quaternary Ca-borosilicate glass, which coincided exactly at the position where Nanoscale Secondary Ion Mass Spectrometry (NanoSIMS) measurements indicated a transport barrier for aqueous Ca^{2+} (which may be applicable for Ca^{2+} in this study (Table 5.10)). Here, the authors reported differences in the alteration structures either side of the band, whereby the inner side (closest to the glass) had a greater porosity. A similar phenomenon in this study for the behaviour of Zn^{2+} is thus speculatively proposed.

The pH readings < 95 d could be assumed to be approximately equal within instrumental uncertainty (Fig. 5.27a), however, the drop in pH could reflect the precipitation of silicate clays (Aréna *et al.* 2018) (predicted to form at very early stages ~ 7 d from PHREEQ-C geochemical modelling (Fig. 5.34)), which may counter the pH rise from cation release from glass dissolution due to the H^+ produced (Wang *et al.* 2016) from the formation of Zn-silicates. Also note that the predicted and potentially evidenced (from PHREEQ-C geochemical modelling and XRD respectively) Na-beidellite formation (Fig. 5.34b and 5.32d) may also have countered the pH rise due to the consumption of Na from solution.

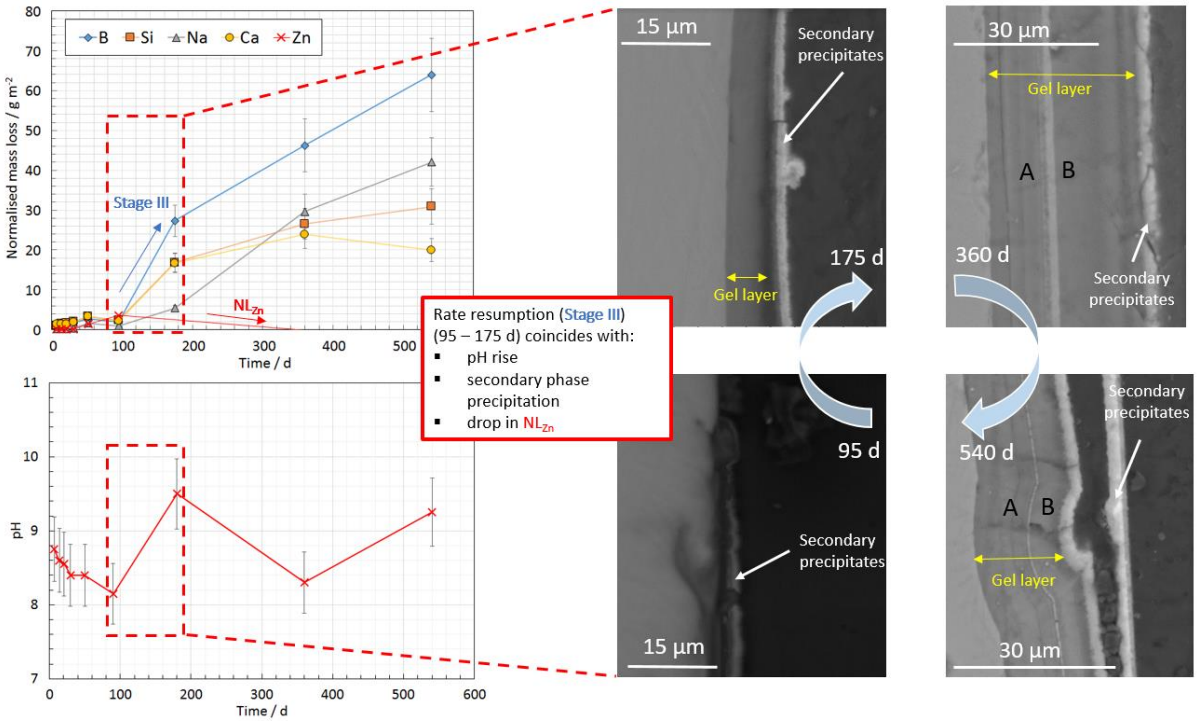

Figure 5.35. Schematic overview of ZnCa 40:60 subjected to MCC-1 dissolution (UHQ, 50 °C) illustrating the evolving relationship between normalized mass loss, leachate pH and secondary phase precipitation. Note that the BSE images are included to illustrate the temporal evolution of the alteration layer. A = high Zn concentration and B = low Zn concentration in the gel layer. Note the pH(RT) measurement at 360 d may be underestimated due to measurement of the leachate six months post-experimental termination.

5.3.4.3 Zn-rich glass behaviour

For the ZnCa 100:0 composition, similar alteration features as ZnCa 40:60 were observed, but without the Ca content. The significant increase in the dissolution rate (similar to Stage III behaviour, as described above) may have occurred at an earlier time point, after 31 d compared with 95 d for ZnCa 40:60 (Fig. 5.28a). A possible second rate resumption was also observed after 360 d, suggesting cyclical periods of the dissolution-re-precipitation of Zn-silicates, as identified by SEM (Fig. 5.30c & 5.33a) and XRD (Fig. 5.33d).

The nature and structure of the inner bright band was difficult to ascertain, but its presence could indicate the precipitation of Zn-phases within the altered layer or there could have been a build-up of diffusing Zn species at this particular location, possibly marking the transition between a dense and less dense zone within the labelled inner layer. This was evidenced by Zn concentrations either side of the inner bright band, where there were stark differences in the Zn concentration (Table 5.11 - see inner layer row), with greater Zn concentration towards the solution side, and lower Zn concentration

on the bulk glass side, which was the reverse of ZnCa 40:60. The difference may be explained by the passivating effects of Ca in the alteration layer (such as gel densification) (Chave *et al.* 2011, Aréna *et al.* 2018) of ZnCa 40:60, which may have limited the diffusion of Zn. Note that the thickness of the inner band varied across the length of the monolithic sample, a result of potential inherent localised variations in the initial glass surface condition (Fig. 5.30).

It should be noted that in the absence of Ca in ZnCa 100:0, there may have been limited charge compensation for Al and Zn in the gel layer. Hence, in the early stages of dissolution, it is speculated that there was a greater likelihood for Al to form secondary phases (such as sauconite – 15 Å ($Na_{0.3}Zn_3(Si,Al)_4O_{10}(OH)_2 \cdot 4H_2O$) (Fig 5.33d and Gin *et al.* 2013). It is also possible that Zn^{2+} could charge compensate (Aréna *et al.* 2016) Al in the gel layer, potentially limiting the sauconite formation rate indirectly observed from the period prior (in which a gel layer potentially developed Fig. 5.30c) to the second rate resumption after 360 d (Fig. 5.27b)). Such insight may collectively infer a diffusion controlled process (particularly for Zn) within the gel (360-540 d), which controls the rate of Zn-silicate formation, thus controlling the dissolution rate. Such reasoning speculatively infers a pseudo-competition between a Zn charge compensatory role in the gel and Zn-silicate formation.

The edge layer (the outer precipitate layer in contact with solution) (Fig. 5.33a) possessed lower Zn concentration compared to the outer layer (precipitates (Table. 5.11)), which could be indicative of Si re-precipitating on top of the Zn-silicate layer and/or that the secondary Zn-silicates partly dissolved, supported by the increase in $NL_{Si\ \&\ Zn}$ after 540 d. However, this may also have manifested/promoted the second rate resumption between 360-540 d (Fig. 5.27).

For all compositions, future work on samples corroded in excess of 1,370 d will further elucidate the dissolution behaviour (samples terminated after 1,373 d and currently subjected to post dissolution characterisation). Such a timepoint is beyond the scope of this Thesis, but will be reported in a future publication.

Oscillatory banding - the current explanation for the formation of the oscillating band gel structure, which must be a self-organisational phenomena, comes from the proposed ICDP model suggested by Geisler *et al.* (2010), which allows for the development of layered structures. The formation of complex banded alteration layers observed on all ZnCa xx:xx compositions (Figs. 5.31-5.33) is hard to reconcile with the re-polymerisation/re-condensation gel formation concept (Grambow 1987, Bunker 1994, Gin *et al.* 2000, Jégou *et al.* 2000, Grambow & Müller 2001, Frugier *et al.* 2008, Gin *et al.* 2011, Me *et al.* 2017), which cannot effectively account for the oscillatory banding, particularly the

observation of several layers with different porosity (indirectly observed by the difference in Zn, Ca and Al concentration either side of the bright band in Figures. 5.32 & 5.33 and Tables 5.8 & 5.9. Thus, the structure and texture of these layers are potentially consistent with the ICDP model (Geisler *et al.* 2010, 2015, Hellman *et al.* 2015, Putnis *et al.* 2015), which proposes that the alteration layers (including gel and secondary precipitates) are formed by amorphous silica precipitating directly from solution. The observation of the altered gel layer from ZnCa 0:100 (Fig. 5.31a & 5.36) is also potentially consistent with the RUMGCM theory (Lenting *et al.* 2018).

Oscillatory banding has also been observed in static monolithic dissolution experiments (Barkatt *et al.* 1993, Falmon 1996, Leturcq *et al.* 1999, Anaf 2010, Dohmen *et al.* 2013, Geisler *et al.* 2015, Schalm & Anaf 2016, Backhouse *et al.* 2018), which is believed to emerge at later stages of the dissolution process. However, as shown in Figure 5.36, such banding was observed for ZnCa 0:100 after 52 d, which was observed to fall *within* the initial or at the very latest, early transitional dissolution rate (Fig. 5.27), noting that the onset of clear residual rate dissolution (Stage II) was observed after 175 d based on NL_B (Fig. 5.27b). This may provide evidence that alteration layers do form at early stages of dissolution, whereby initial dissolution rate conditions are maintained and observed (Icenhower 2018). These results are consistent with the altered particles from the SPFT tests, which show potential altered layers on ZnCa 0:100 (Fig. 5.12) and with real-time in-situ observations of silicate glass corrosion in which a 25 µm thick alteration layer developed without any drop in the dissolution rate (Geisler *et al.* 2019). It should also be noted that gel layers were recently observed on the ISG in stirred coupon dissolution tests, which are hypothesised to allow the most dilute conditions with a SA/V ~ 0.1 m^{-1}) (Ryan *pers. Comm*). Such works is ongoing (as of March 2021) but is at the forefront of the glass corrosion community.

The presence of complicated bands could have arisen from changes in local compositional variations of the pristine glass, such as alkali-rich regions as alluded to from the results from the ISG in Chapter 4 and from the SPFT investigations in this Chapter (particularity the observation of pitted features illustrated in Figures 5.10 & 5.11) and resultant pH variations. However, local solution chemistry in non-stirred media could be consistent with the observed features. The heterogeneity in the thickness in these bands over the full length of the monolith (Fig. 5.30) potentially reflected the localised variations in dissolution conditions, consistent with both of the above explanations.

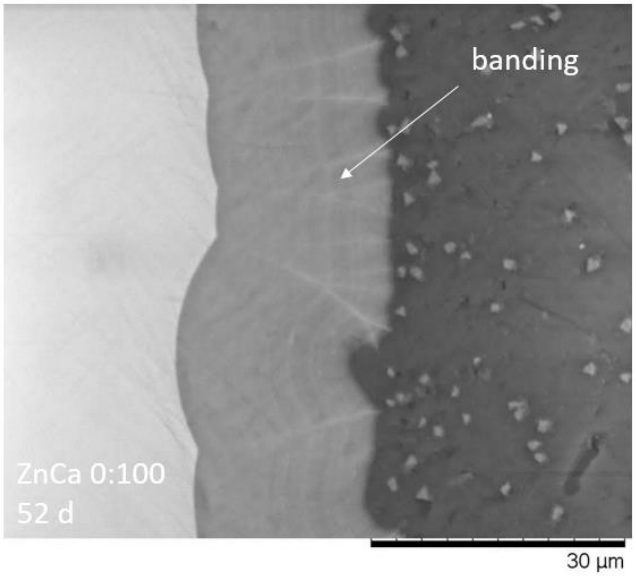

Figure 5.36 ZnCa 0:100 after 52 d MCC-1 alteration in UHQ at 50 °C. Dissolution was potentially sustained at the initial rate (Stage I), despite the observation of a clear oscillating band gel layer. Only after 175 d, with the appearance of an outer gel layer, did the dissolution rate drop and transition to the residual rate (Stage II).

5.4 Conclusion

The objective of this investigation was to systematically account for the compositional effects of Zn and Ca on the structure-durability relationship across all stages of glass corrosion on a suite of simple ZnCa borosilicate glass formulations. Results from ^{27}Al, ^{11}B and ^{29}Si MAS-NMR structural analysis and the SPFT dissolution experiments suggested that there was a correlation between the network connectivity and initial rate of dissolution (Stage I), hence, a clear structure-durability relationship, consistent with the study by Icenhower *et al.* (2008), who hypothesised that there was a correlation between glass structure (as evidenced by chemical shifts in NMR) and initial dissolution rates. In the current study, the more polymerised Zn-rich glasses were more chemically resistant to dissolution at the initial rate (Stage I) than the Ca-rich glasses. The ZnCa 60:40 composition was the most polymerised, while compositions containing larger ZnCa ratios indicated that Zn was in tetrahedral and potentially octahedral coordination, thus the glass network was less polymerised (which calculations predicted based on an extended modified version of the Dell-Bray model for borosilicate glass (Dell *et al.* 1983)) and strongly suspected to be phase separated (Taylor 1990, Taylor & Owen 1981). The phase separation (of indeterminate size) in the Zn-rich glasses (ZnCa 100:0 & ZnCa 80:20) observed by differential thermal analysis, manifested in incongruent dissolution behaviour (which showed that Zn was most readily released from the glass, likely from domains that were rich in

network modifying Zn as suggested by the structural analysis) resulted in preferential sites for dissolution on the surface of glass particles post SPFT experimentation.

However, the PCT-B dissolution data suggest an inverse relationship between the initial and residual rate (Stage II), whereby the Ca-rich glasses became more chemically resistant to dissolution than the Zn-rich glasses after transitioning into the residual rate of dissolution (Stage II). This may be due to the positive passivating effect that Ca has on the structure of the alteration layer as also suggested by Chave *et al.* (2011), Utton *et al.* (2013), Corkhill *et al.* (2013), Aréna *et al.* (2018) and Mann (2018), advanced in this study by post-dissolution ^{29}Si MAS-NMR, suggesting greater gel-network polymerisation. The presence of Zn resulted in the precipitation of Zn-silicates (sauconite) (Ledieu *et al.* 2004, Cailleteau *et al.* 2011, Gin *et al.* 2013) to the detriment of the longer-term durability. Hence, PCT-B results indirectly suggested that there was a pseudo-competition between Zn and Ca during residual rate dissolution (Stage II), whereby Ca cannot play an effective passivating role in the gel layer due to the affinity for the precipitation of Zn-silicates, which hindered the formation of the protective gel layer, thus driving the dissolution.

Results from the MCC-1 investigations (a refinement of PCT-B tests which are not sensitive enough to capture delicate evolutionary dissolution behaviour) were in conflict with the PCT-B results: the Zn-containing glasses were more chemically resistance than the Ca-containing glasses based on the NL_i, but importantly *not* on dissolution rates at greater reaction progress (175-540 d), which were limited to 540 d tests. It is thus expected that continued 'rate resumption' will be observed for the Zn-containing glasses (Gin *et al.* 2013) over greater time periods, leading to the conclusion and consistency with the PCT-B tests that the Ca-containing glasses will be the most durable in the long-term (> 540 d). Results from the MCC-1 tests also alluded to an indeterminate threshold controlled by the concentration of Zn in solution, which resulted in the precipitation of the Zn-silicates (most likely sauconite), causing a 'rate resumption' in relatively mild dissolving media (pH < 9 and at 50 °C). Such findings lead to the hypothesis that the precipitation of Zn-silicate clays cause *early* Stage III 'rate resumption', which is intrinsic to Zn-containing borosilicate glass compositions containing > 4.7 wt.% ZnO, without the effect of external influences (which may be exacerbated in Zn-containing dissolving media (Aréna *et al.* 2016)). This hypothesis (upon suggested further confirmatory work) suggests that the classical definition of Stage III 'rate resumption' could be expanded to incorporate the precipitation of Zn-silicate clays, which were formed via a suggested dissolution-re-precipitation process.

Such conclusions are applicable to SPFT, PCT-B and MCC-1 dissolution tests performed in Teflon vessels, which are permeable to CO_2, which can thus suppress the pH and reaction pathway for *some*

glass compositions (Xing and Pegg 1994). It therefore remains inconclusive if such effects are applicable to the series of ZnCa MW glasses studied here. For a fully descriptive and robust performance assessment (Ewing 2020) of the dissolution behaviour it is recommended to conduct all future experiments under an inert N_2 atmosphere. However, recent investigations show that the reaction pathway under anoxic and oxic conditions, based on the $NL_{B,\ Si\ \&\ Na}$ for similar ZnCa MW waste glass compositions are near identical based on 40 °C, UHQ PCT-B tests (Fisher & Corkhill 2021).

Such structure-dissolution investigations highlighted the fact that initially durable glasses (dissolving at the initial rate, Stage I), based on the connectivity of the glass network, such as the more polymerised Zn-containing glasses, did not translate to long-term durable glasses. Hence, the selection of a glass composition based on greater chemical resistance during Stage I dissolution can be misleading, and in the case of geologically disposed nuclear waste glass, undesirable.

Overall, this investigation highlighted that small changes to a series of glass formulations produce markedly different behaviour in terms of the structure-durability relationship at different dissolution reaction progress, which should be considered carefully when selecting base glass compositions for the immobilization of HLW (and ILW) in terms of geological disposal durability. Therefore, on the basis of this investigation, the optimal base glass composition in terms of longer timescale chemical durability, which is more representative of geological disposal conditions, was ZnCa 0:100 ($3.5Li_2O{\cdot}7.8Na_2O{\cdot}9.4CaO{\cdot}3.7Al_2O_3{\cdot}22.3B_2O_3{\cdot}\ 53.2SiO_2$ wt.%). The next challenge to address is how this fundamental knowledge translates to simulant waste loaded ZnCa MW formulations, especially in terms of ‘rate resumption’ Stage III, detailed in Chapter 6.

5.5 Appendix

I - ^{11}B MAS-NMR - Spectral Deconvolution

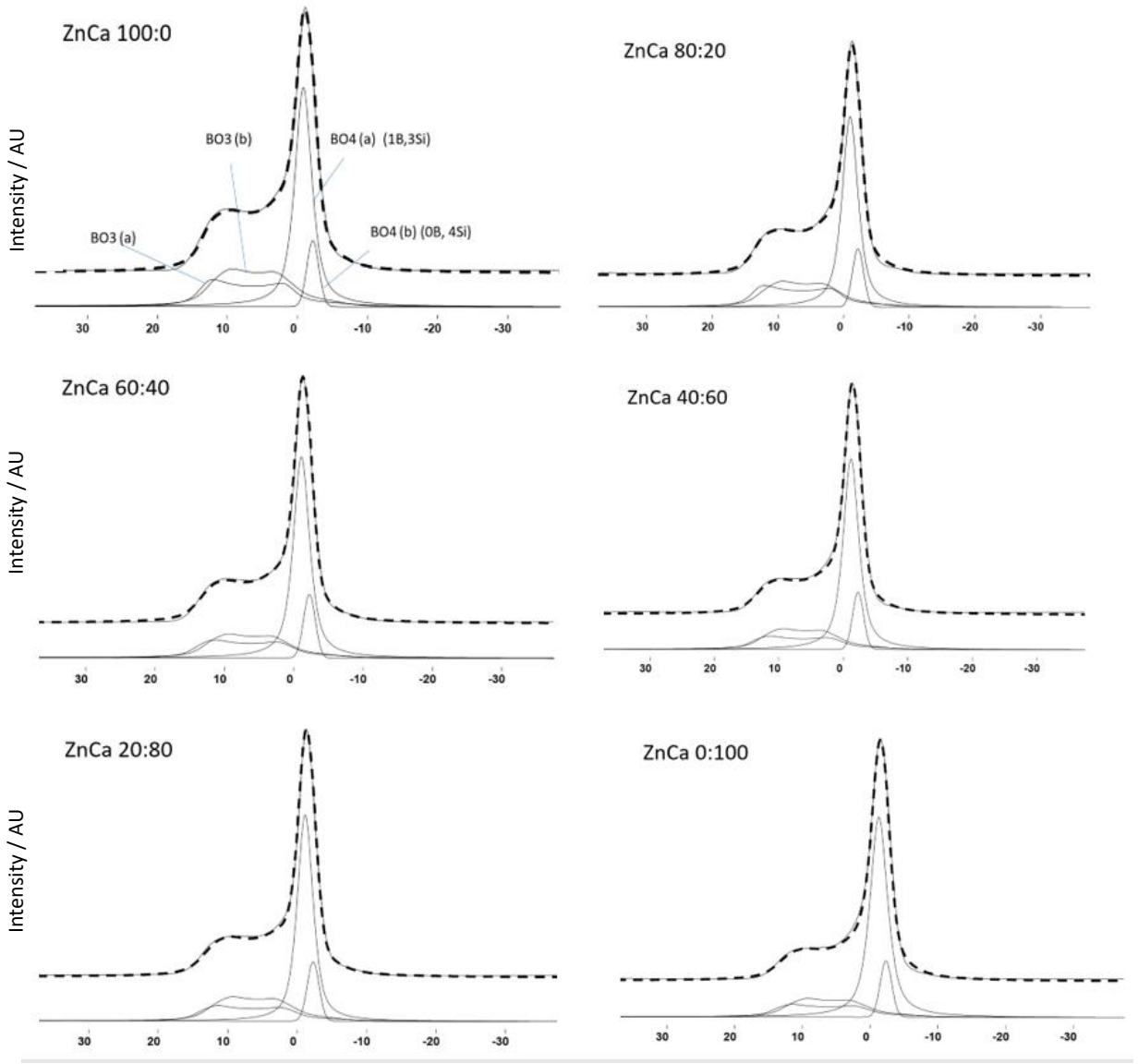

II - ^{29}Si MAS-NMR

A comparison of the ^{29}Si MAS-NMR spectra from the mineral hemimorphite ($Zn_2SiO_4 \cdot H_2O$), ZnCa 100:0 pristine glass and ZnCa 100:0 altered glass (303 d, UHQ, 90 °C, 0.33 g of glass with particle size < 0.20 µm diameter). The secondary precipitates formed on the altered glass do not represent hemimorphite.

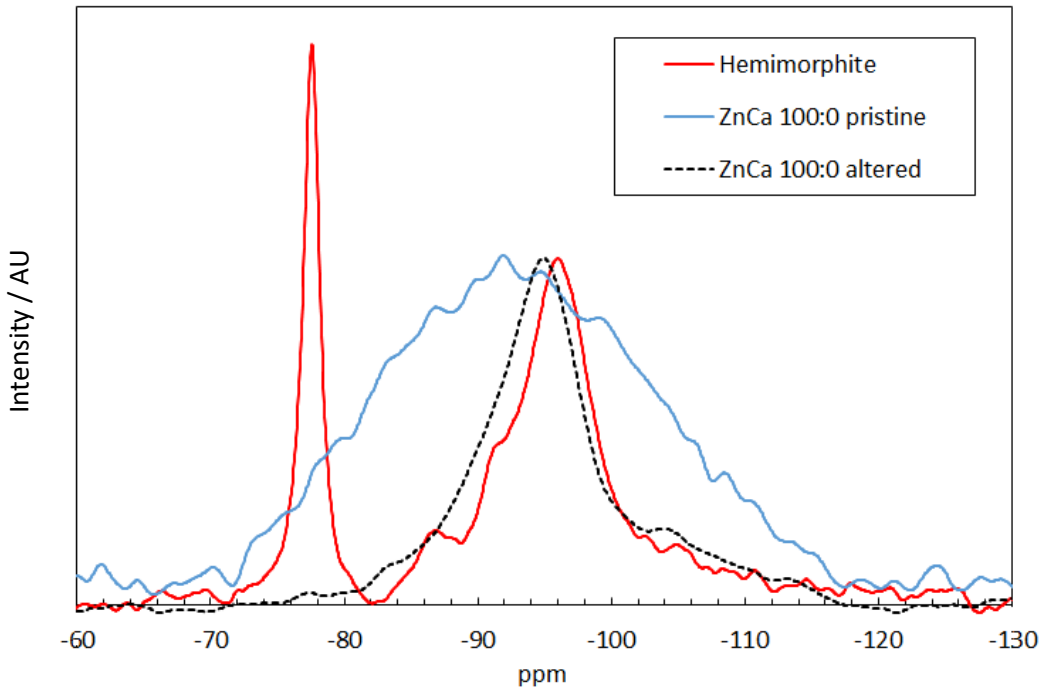

6. The dissolution of simulant waste-loaded ZnO/CaO modified base glass for UK High-Level-Waste

Summary

This Chapter presents data relating to the dissolution of a series of waste-loaded ZnCa MW glass types over each stage of glass corrosion, demonstrating how Zn and Ca influence the long-term chemical durability of waste-loaded ZnCa MW glass. As observed for the simple base glasses in Chapter 5, the dissolution behaviour of waste-loaded glass was significantly influenced by the ZnO:CaO ratio, whereby lower chemical durability was observed for the Zn-rich glasses. Behaviour analogous to Stage III 'rate resumption' was observed and it is hypothesised that this is related to the consumption of Al and Si from the gel, and Zn and Mg from the solution, and associated Zn-silicate (phyllosilicate clays) (consistent with the Stage III hypothesis suggested in Chapter 5) and Mg-silicate (phyllosilicate clays) precipitation. Results confirm previous findings for MW (ZnCa-free) glasses that increasing the waste loading from 28 to 35 wt.% improves the chemical durability.

This Chapter has been published, in part, in the following publications:

Adam J. Fisher, Mike T. Harrison, Neil C. Hyatt, Russell J. Hand & Claire L. Corkhill. The dissolution of simulant UK Ca/Zn-modified nuclear waste glass: the effect of increased waste loading. *MRS. Advances*. **6**, 95-102 (2021).

Adam J. Fisher, Mike T. Harrison, Neil C. Hyatt, Russell J. Hand & Claire L. Corkhill. The dissolution of simulant Ca/Zn-modified nuclear waste glass: Insight into Stage III behaviour. *MRS Advances.* **5**, [3-4], 103-109, (2020).

6.1 Introduction

From an industrial perspective, it is important to acknowledge that there will be variability in the waste loading of vitrified HLW waste at the Sellafield site (Gribble 2018). To date, approximately 7,000 HLW canisters have been fabricated including MW and ZnCa MW types, as shown in Table 6.1, where ZnCa MW is listed as POCO-type waste. Waste loading ranges from low loadings of < 6 wt.% waste calcine (0.19 % total inventory, produced during the initial commissioning of the vitrification plant) to medium loadings of ~18 wt.% (approx. 200 canisters, arising from various operational procedures, such as clearing blockages in the melter), to more ideal values of 28 to 35 wt.% (contributing the largest share). Since waste incorporation has been shown to effect the chemical durability of MW glass, with greater waste incorporation resulting in enhanced durability (Brookes *et al.* 2011, Harrison 2014), it is important to understand these effects in the ZnCa-modified MW glass. As of August 2018, thirty canisters of ZnCa MW28 containing Oxide:Magnox (50:50) waste have been produced (0.43 % total inventory) (Gribble 2018). It is expected that this will rise to approximately 1,340 canisters containing a variety of waste streams, including Post Operation Clean-Out (POCO) waste at as yet unknown waste loading, by 2040 (Harrison 2018, 2020).

Table 6.1. Comprehensive list of vitrified product held in the UK (Schofield *et al.* 2017). Tech waste is described in 6.5 Appendix I.

		Estimated number of HLW containers			
	Waste Glass	**Current (as of 2015)**	**To be made (2015-2034)**	**To repository >2040**	**Sent/to send overseas**
Magnox -type MW	**Magnox**				
	< 18 wt.%	100	-	>3010	-
	25 wt.% baseline	2700	Expected		-
	28 wt.%	209	Expected		-
Oxide-type MW	**Blend (Oxide:Magnox 75:25)**				
	<17 wt.%	100	-	1487	1780
	25 wt.% baseline	2400	-		
	28 wt.%	767	-		
	Blend (Oxide:Magnox 50:50)				
	28 - 35 wt.%	-	1574	1574	-
	Butex type				
	<35 wt.%	-	120	120	-
POCO-type (inc ZnCa MW)	**Poco research phase**				
	waste loading to be defined	-	1340	1340	-
	Tech waste research phase				
	waste loading to be defined	-	Expected	Expected	-
	Melter heels	-	70	70	-
	Filters and swarf	-	70	70	-
Sub Totals		6276	>3174	**>7671**	1780

Building on the results of Chapter 5, which showed that the ZnO:CaO ratio exerted a significant influence on the durability of simplified 6-component ZnCa-sodium aluminoborosilicate glasses, this Chapter aims to understand if these effects are also observed in simulant waste-loaded glasses. It further aims to understand how the level of waste-loading influences ZnCa MW glass. Using a series of high (PCT-B – accelerated dissolution progress) and low (MCC-1 – steady dissolution progress) surface area to volume ratio experiments, this Chapter sets out to understand the kinetics and mechanisms of dissolution with a particular emphasis on Stage II and III dissolution. This will include the studies (A-C) listed in the experimental matrix (Table 6.2), where (A) refers to glasses made at Sheffield, with varying ZnO:CaO ratio, (B) is the same as the middle composition used in (A) (representative of the currently implemented formulation at the Sellafield site), but the testing parameters were varied, and (C) comprises glasses made on the Vitrification Test Rig (VTR) at Sellafield, with different waste loadings and using a different waste calcine. The Sheffield-synthesised ZnCa 40:60 MW28 contained Oxide:Magnox (75o:25m) calcine, while the VTR-synthesised ZnCa MW28 contained Oxide:Magnox (50o:50m) calcine. Thus, the composition in (B) is nominally the same as the middle (C) composition (ZnCa MW28), except for minor variations due to the waste calcine. Please see Chapter 3, Table 3.3 for ICP HF-digest compositional analysis of each glass.

Table 6.2. Experimental matrix for Chapter 6. The list of glass compositions is provided in Chapter 3, Table 3.3.

Experimental Matrix						
Study	Glass*†	Experiment	Experimental Aim	Temp / °C	Solution	Duration / d
(A)	ZnCa 100:0 MW28 ZnCa 40:60 MW28 ZnCa 0:100 MW28	PCT-B 2,000 m^{-1}	Explore influence of ZnO:CaO ratio on accelerated dissolution progress, alteration layer composition/morphology and geochemical modelling of secondary precipitates.	90	UHQ	112
(B)	ZnCa 40:60 MW28	MCC-1 10 m^{-1}	Explore dissolution progress in finer detail on the currently adopted formulation at the Sellafield Ltd. site, including alteration layer composition and morphology and geochemical modelling of secondary precipitates.	50	UHQ	540
(C)	ZnCa MW20 ZnCa MW28 ZnCa MW35	PCT-B 2,000 m^{-1}	Explore influence of wasteloading on accelerated dissolution progress, alteration layer composition/morphology and geochemical modelling of secondary precipitates.	90	UHQ	112

*ZnCa xx:xx MW28 - (75o:25m blend waste) - fabricated at TUoS.

†ZnCa MWXX - (50o:50m blend waste - ZnCa ratio 40:60) - fabricated at the VTR, Sellafield Ltd. Kindly contributed by Dr. Mike Harrison, NNL.

6.2 Results

6.2.1 Characterisation of pristine glass compositions

ZnCa xx:xx MW28 Series

All glass compositions in the ZnCa xx:xx MW28 suite – where xx:xx refers to the Zn:Ca ratio, and 28 refers to the wt.% wasteloading with simulant calcine – were observed to be single phase, containing

dispersed crystalline inclusions. In all compositions Ru was detected by SEM EDS (Fig. 6.1 & 6.5 Appendix II) and RuO_2 was identified by XRD [PDF 21-1172] (Fig 6.2), which was an expected feature of the waste glass being studied. Ruthenium oxide was well distributed throughout the matrices of all compositions, with one large Ru- and Mo-enriched formation observed approximately every 16 mm^2 (Fig. 6.1d & 6.5 Appendix II), potentially an artefact of the melting conditions at The University of Sheffield (Chapter 3). Such a phase is not typically observed, to our knowledge, in vitrified products from the VTR at the Sellafield site. The composition ZnCa 100:0 MW28 also contained the spinel phase magnetite (Fe_3O_4) [PDF 75-0449] (Fig. 6.2). Note that Na/Ca-molybdate phases were not detected due to low MoO_3 content (1.87, 1.86 & 1.82 wt. % in ZnCa 0:100, 40:60 & 100:0 MW28 respectively, Chapter 3). These phases are expected to precipitate in MW glass compositions with a MoO_3 content in excess of 6 wt. % (Dunnett *et al.* 2012).

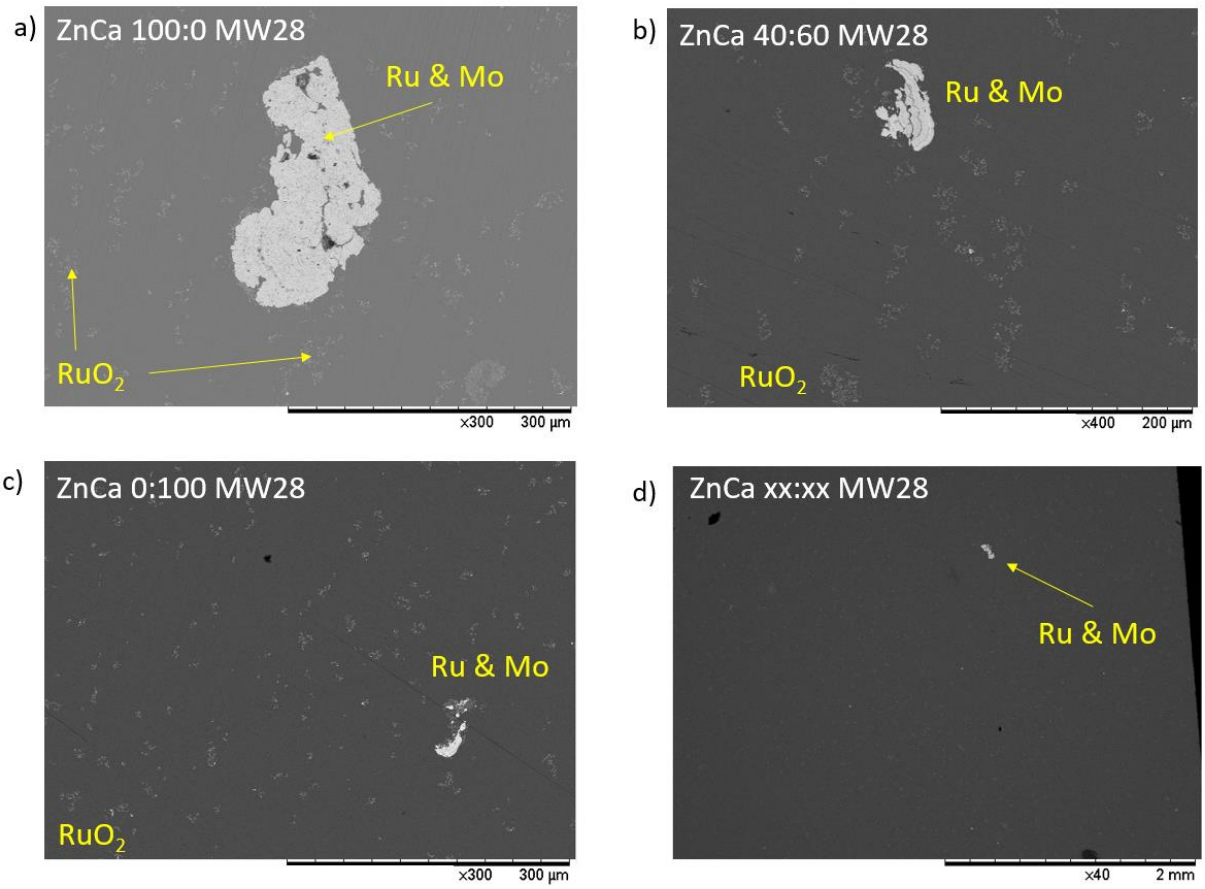

Figure 6.1 a-d) Phase assemblage from cross sections of monolithic samples for the ZnCa xx:xx MW28 compositions. Note that d) was representative of all compositions.

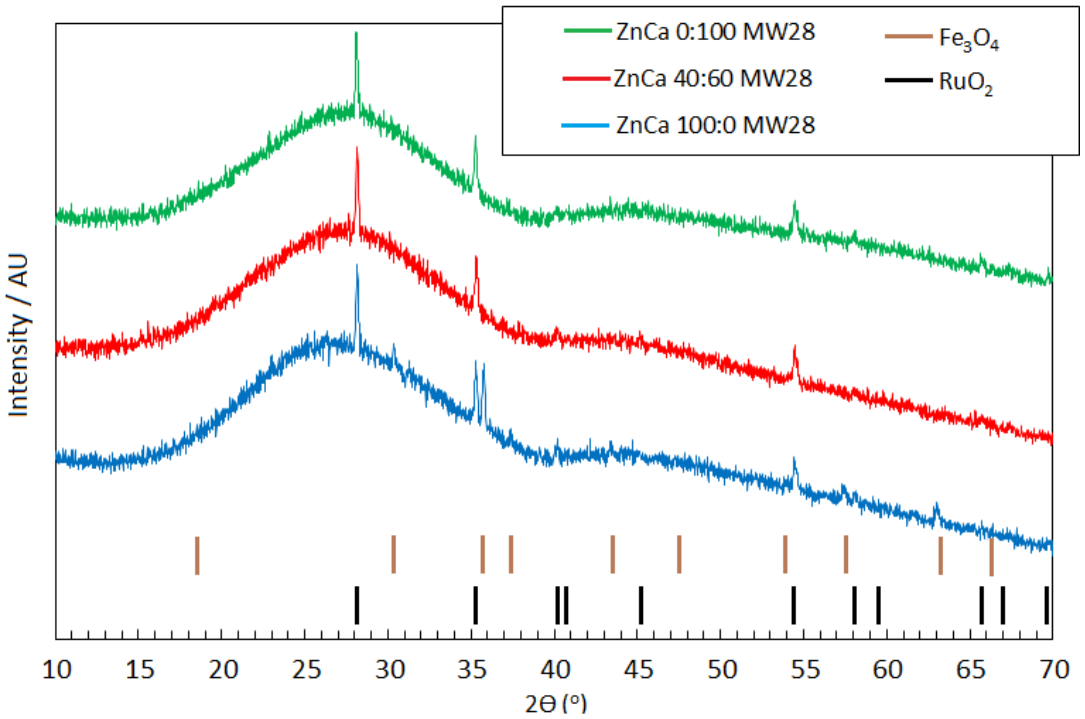

Figure 6.2. XRD from the pristine ZnCa xx:xx MW28 compositions fabricated at TUoS.

ZnCa MWXX Series

The ZnCa MWXX compositions, obtained from the VTR at the Sellafield site, had a Zn:Ca ratio of 40:60. When the waste loading of ZnCa MWXX was varied, each composition exhibited distinct characteristics, with larger crystallite contributions corresponding to greater waste content. In all compositions RuO_2 and Fe_3O_4 were detected by XRD (Figs. 6.3) [PDF 21-1172 & PDF 89-0688 respectively] and inferred by SEM EDS (in order to avoid duplication of data, such inclusions can be observed in Figs. 6.26-6.28 in the pristine glass from cross sectional samples post PCT-B dissolution). In addition, XRD traces from ZnCa MW28 & MW35 potentially identified CeO_2 [PDF 44-1001] and $Nd_2Zr_2O_7$ [PDF 78-1618] in the ZnCa MW35 trace only. The difference in the type of crystallites observed within the ZnCa 40:60 MW28 (Fig. 6.2) and ZnCa MW28 (Fig. 6.3) compositions was attributed to greater Fe, Ce and Nd content in ZnCa MW28 associated with the different waste calcines used in the synthesis of these glasses: the Sheffield-synthesised ZnCa 40:60 MW28 contained Oxide:Magnox (75o:25m) calcine, while the VTR-synthesised ZnCa MW28 contained Oxide:Magnox (50o:50m). As a result, the ZnCa 40:60 MW28 contained 1.78 wt.% Fe_2O_3 and 1.20 wt.% CeO_2, while the ZnCa MW28 contained 3.15 wt.% Fe_2O_3 and 1.53 wt.% CeO_2 (Table 3.3 - Chapter 3).

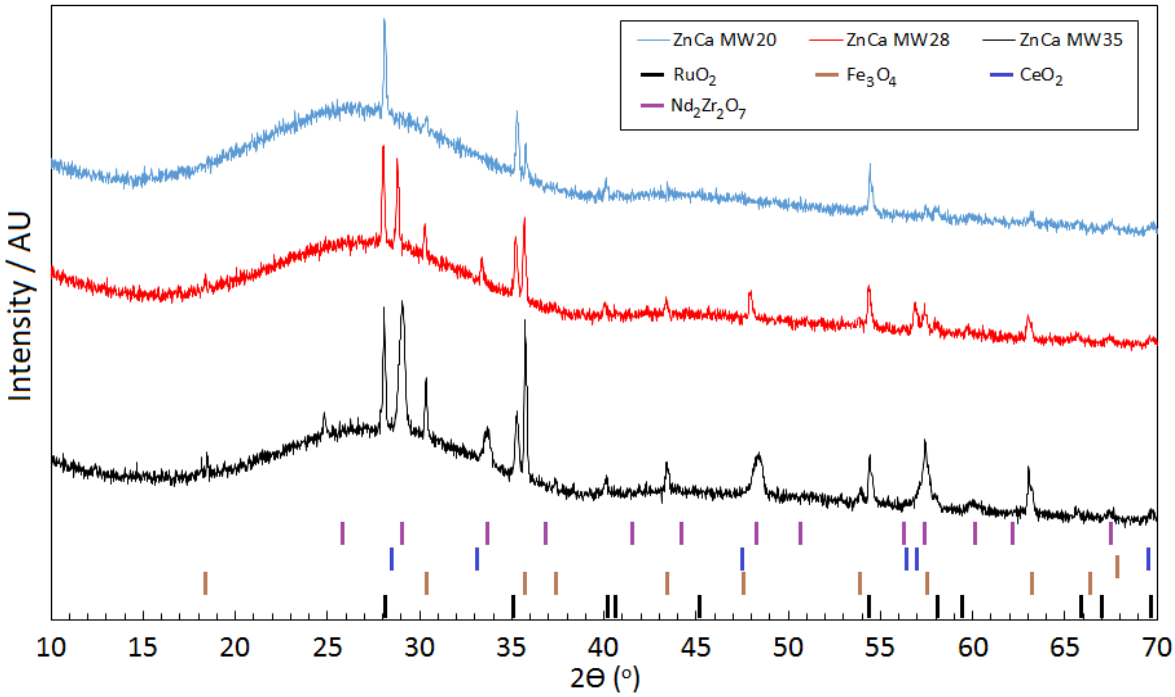

Figure 6.3. XRD from the pristine ZnCa MWXX compositions fabricated at the Sellafield VTR.

6.2.2. Durability

6.2.2.1 PCT-B - ZnO:CaO ratio variation in ZnCa xx:xx MW28, UHQ, 90 °C (Study A)

The results of the PCT-B experiments are displayed in Figs. 6.4-6.5 and Table 6.3. The chemical durability, based on the NL_B and NR_B, over the course of the 112 d experiments followed the trend (from the most durable to the least durable) ZnCa 0:100 > 40:60 > 100:0. The NR_B taken between 28-112 d was approximately a factor of two greater for ZnCa 100:0 MW28 than for ZnCa 40:60 MW28. The NL_B and NL_{Mo} increased throughout the duration of the experiment for the two Zn-containing glasses (Figs. 6.4a-c). Also a decrease in the NL_{Zn} and NL_{Mg} (Figs. 6.4f & h) from 3 d and 1 d respectively was observed alongside a reduction in the NL_{Si} between 7-35 d. As discussed in Chapter 5, collectively this could be attributed to the precipitation of Zn- and Mg-silicates throughout the duration of the experiment. An increase in $NL_{B\ \&\ Na}$ for ZnCa 100:0 MW28 after just 7 d could be interpreted as early Stage III 'rate resumption' (applying the extended definition of Stage III as hypothesised in Chapter 5).

In contrast, characteristic rate drop (Frugier *et al.* 2008, Vienna *et al.* 2013) and a subsequent slower residual rate (Stage II) of dissolution was attained and sustained, between 7-112 d based on the NL of

all elements (excluding Mg), for ZnCa 0:100 MW28 (Figure. 6.5d and Table 6.3). This indicates that the Ca-rich composition was the most durable glass throughout the experimental duration. A reversal of this durability trend was observed at early time points ≤ 3 d (Fig. 6.4, Table 6.3), whereby the Zn-rich glass was observed to be the most durable. In accordance with results presented in Chapter 5, this can be inferred by the network forming role of Zn and its resulting greater resistance to hydrolysis.

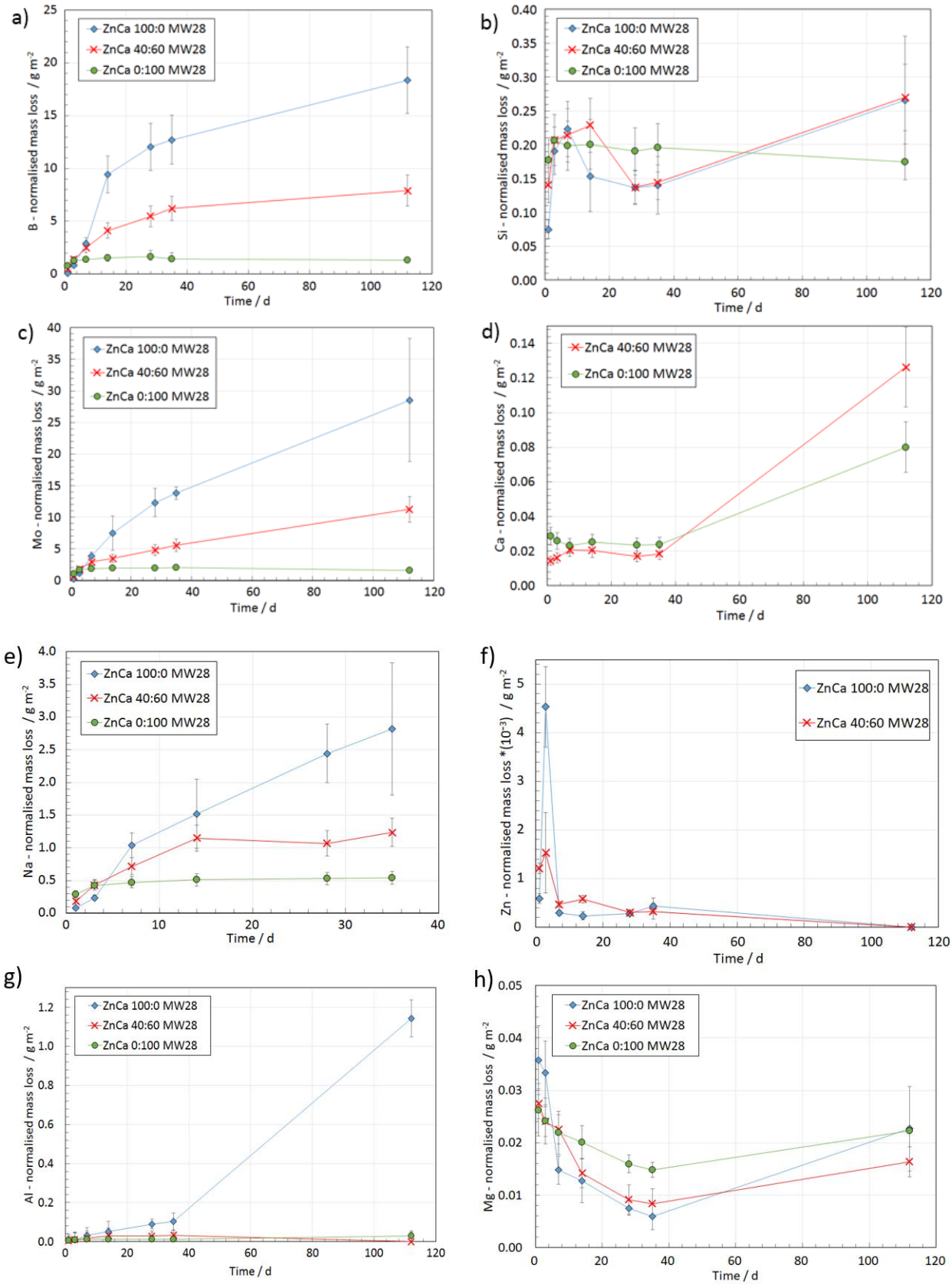

Figure 6.4. A comparison of the normalised mass loss of elements for the ZnCa xx:xx MW28 series from the 2,000 m^{-1}, 90 °C, 112 d PCT-B experiments in UHQ water.

Table 6.3. Early stage dissolution rates and residual rates from PCT-B tests at 2,000 m^{-1}, 90 °C, 112 d and in UHQ for the ZnCa MW-type and MW25 (Harrison *et al.* 2014) glasses, calculated from a chi-square fit. Negative rates are effectively zero within experimental uncertainty.

Glass	Dissolution rate 0 - 3 d		Residual rate 28 - 112 d	
	(NR_B / g m^{-2} d^{-1})	(NR_{Si} / g m^{-2} d^{-1})	(NR_B / g m^{-2} d^{-1})	(NR_{Si} / g m^{-2} d^{-1})
ZnCa 100:0 MW28	0.19 ± 0.03	0.068 ± 0.009	0.046 ± 0.044	0.0014 ± 0.0012
ZnCa 40:60 MW28	0.52 ± 0.07	0.083 ± 0.011	0.027 ± 0.021	0.0016 ± 0.0010
ZnCa 0:100 MW28	0.54 ± 0.07	0.018 ± 0.002	-0.0040 ± 0.0042	-0.0006 ± 0.0004
ZnCa MW20	0.40 ± 0.05	0.078 ± 0.010	0.089 ± 0.039	-0.0001 ± 0.001
ZnCa MW28	0.27 ± 0.04	0.052 ± 0.007	0.099 ± 0.026	-0.0002 ± 0.001
ZnCa MW35	0.15 ± 0.02	0.034 ± 0.004	0.071 ± 0.023	-0.0001 ± 0.0004
MW25	0.82 ± 0.02	0.057 ± 0.006	0.0073 ± 0.003	0.0011 ± 0.001

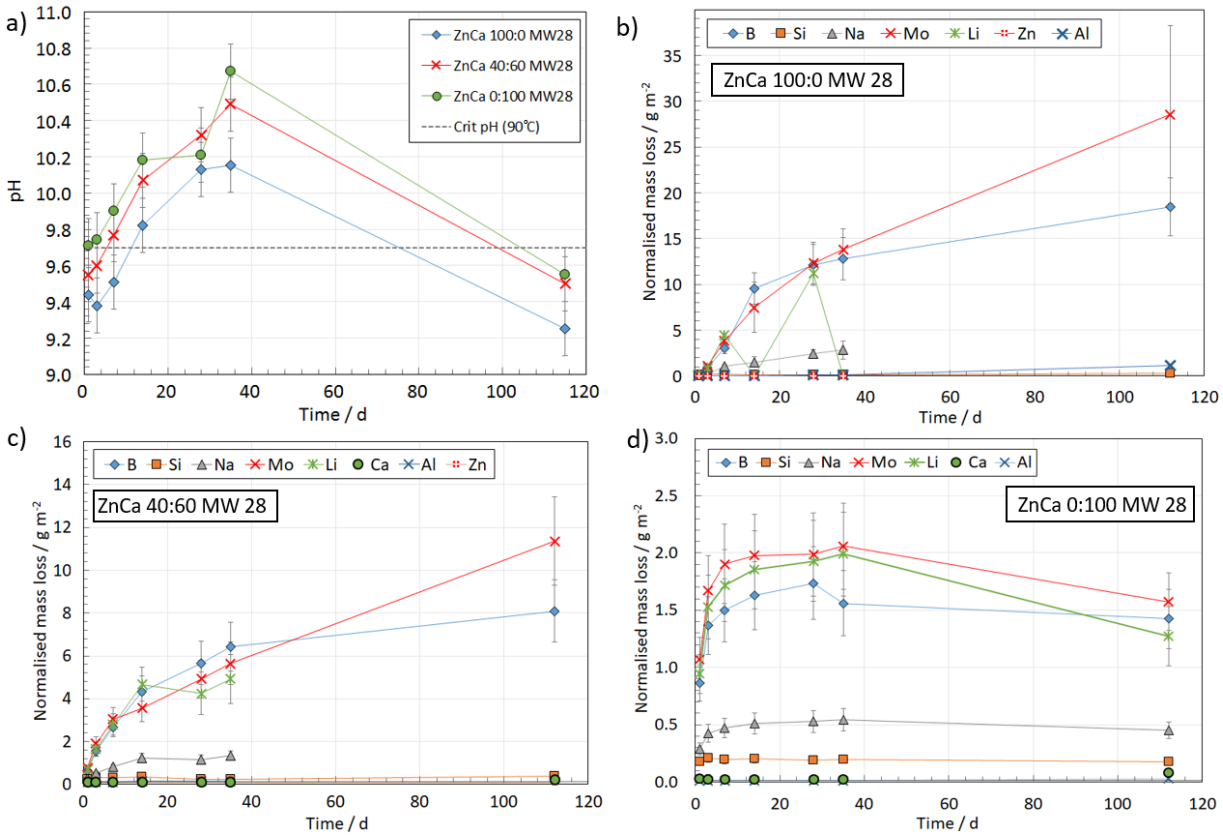

Figure 6.5. a) pH(RT) measurements of the leachate; (b-d) normalised mass loss of elements for the ZnCa xx:xx MW28 series from the 2,000 m^{-1}, 90 °C, 112 d PCT-B experiments in UHQ. Note that the Zn data points in (c) are obstructed from view by the Ca and Si data points.

A spike in the NL_{Ca} after 112 d for the Ca-containing glasses (Fig. 6.4d) may reflect the dissolution of a secondary phase/s. The same reasoning could be applied for the Al spike for ZnCa 100:0 MW28 (Fig. 6.4g). The initially high NL_{Zn} (Fig. 6.4f) (1-3 d) and subsequent rapid reduction in NL_{Zn} for the Zn-rich glasses, may represent the formation of secondary precipitates, consistent with the temporal XRD and SEM sequence (Section 6.2.2.2) which, when combined, provide evidence for the formation of Zn-containing secondary precipitates. Such reasoning can also be applied to the NL_{Mg} and the Mg-containing secondary precipitates (Section 6.2.2.2). The initially high NL_{Zn} (3 d) from ZnCa 100:0 MW28 (Fig. 6.4f) could represent the release of Zn network-modifiers, assuming a dual role of Zn (network former and modifier) for the Zn-end member, inferred from the structural results of the MW base glasses presented in Chapter 5.

An increase in the pH by approximately one pH unit was observed from 1-35 d across all compositions (Fig. 6.5a) (e.g. increasing from pH 9.52 ± 0.15 to 10.50 ± 0.15 for ZnCa 40:60 MW28). This may be consistent with the normalised mass loss plots; the correlation possibly being indicative of the reaction progress. The pH values for each composition could loosely be interpreted to reach steady-state between approximately 14-35 d (within instrumental error), correlating with steady-state dissolution conditions. A significant decrease in pH (approximately one pH unit) occurred between 35-112 d, which may have been associated with the precipitation of secondary silicate minerals between these time points (consistent with the SEM images, Section 6.2.2.2), which consume hydroxyl from solution. However, although pH measurements between 35 and 112 d (inaccessible with the PCT-B dissolution methodology employed) would substantiate the observed pH drop, it cannot be ruled out that 112 d measurements were influenced by carbonation effects (Xing and Pegg 1994). The most conservative interpretation of the pH readings may be that at all time points the pH values, from highest to lowest followed the trend: ZnCa 0:100 > ZnCa 40:60 > ZnCa 100:0, which is consistent with the results from the MCC-1 tests from the simple glass series reported in Chapter 5 (Fig. 5.27a), or that they are approximately equal within experimental error, consistent with the results from the PCT-B tests from the simple glass series reported Chapter 5 (Fig. 5.14a).

6.2.2.2 Alteration layer formation

Alteration layer thicknesses cannot be accurately measured from particles dissolved in PCT-B experiments due to the uncertatiny in particle orientation. Within this section, alteration layer thicknesses are mentioned (in brief) to provide an indicative indication, assuming that the layer concerned represents a 90° cross-section, approximating the most accurate analysis.

ZnCa 100:0 MW28

The temporal evolution of particle surfaces throughout the time duration 14-112 d is provided by SEM in Figure 6.6 (1-7 d analysis did not reveal any significant phases), which shows the development of alteration layers, which ultimately covered all particles, to varying degrees. Agglomeration of particles (noticed upon immediate inspection after the vessel lid was removed) was a common feature (Fig. 6.7) after experiments of duration in excess of 28 d. This has the potential to reduce the surface area of particles in contact with solution and, hence, result in an underestimatation of the NL_i. In conjunction with XRD analysis (Fig. 6.8) it is apparent that after 7 d, the phyllosilicate smectite clays saponite 15-Å ($Ca_{0.2}Mg_3(Si,Al)_4O_{10}(OH)_2{\cdot}4H_2O$) [PDF 29-1491] (based on the peaks at 19.5, 29.0, 34.3 and 60.3 °2Θ) and sauconite 15-Å ($Na_{0.3}$ $Zn_3(Si, Al)_4O_{10}(OH)_2{\cdot}4H_2O$) [PDF 29-1500] (based on the peaks at 19.6, 28.4, 34.6 and 60.9 °2Θ)) were formed. As noted in Chapter 5, sauconite is a Zn containing saponite phase, which is essentially a Zn-phyllosilicate smectite clay. Nontronite ($Na_{0.3}(Mg,Fe^{2+})_3(Si,Al)_4O_{10}(OH)_2{\cdot}nH_2O$)) [PDF 34-0842] is tentatively assigned based on the high angle peaks at 53.4 and 72.0 °2Θ as there is signficant overlap with the peaks from the other phases at low angles, therefore these have not been used for phase assignment. Phyllosilicate phases have been observed on similar waste glass compositions in the literature (Muller *et al.* 2006, Curti *et al.* 2006, Gin *et al.* 2013). It was not possible to identify any zeolite minerals in the XRD traces or SEM; this is not surprising since zeolites are generally understood to form at pH values > 10.5 and/or temperatures > 90 ° C (Ribet & Gin 2004, Fournier *et al.* 2014), which is higher than the moderately high alkalinity (9.2 < pH < 10.2) observed here.

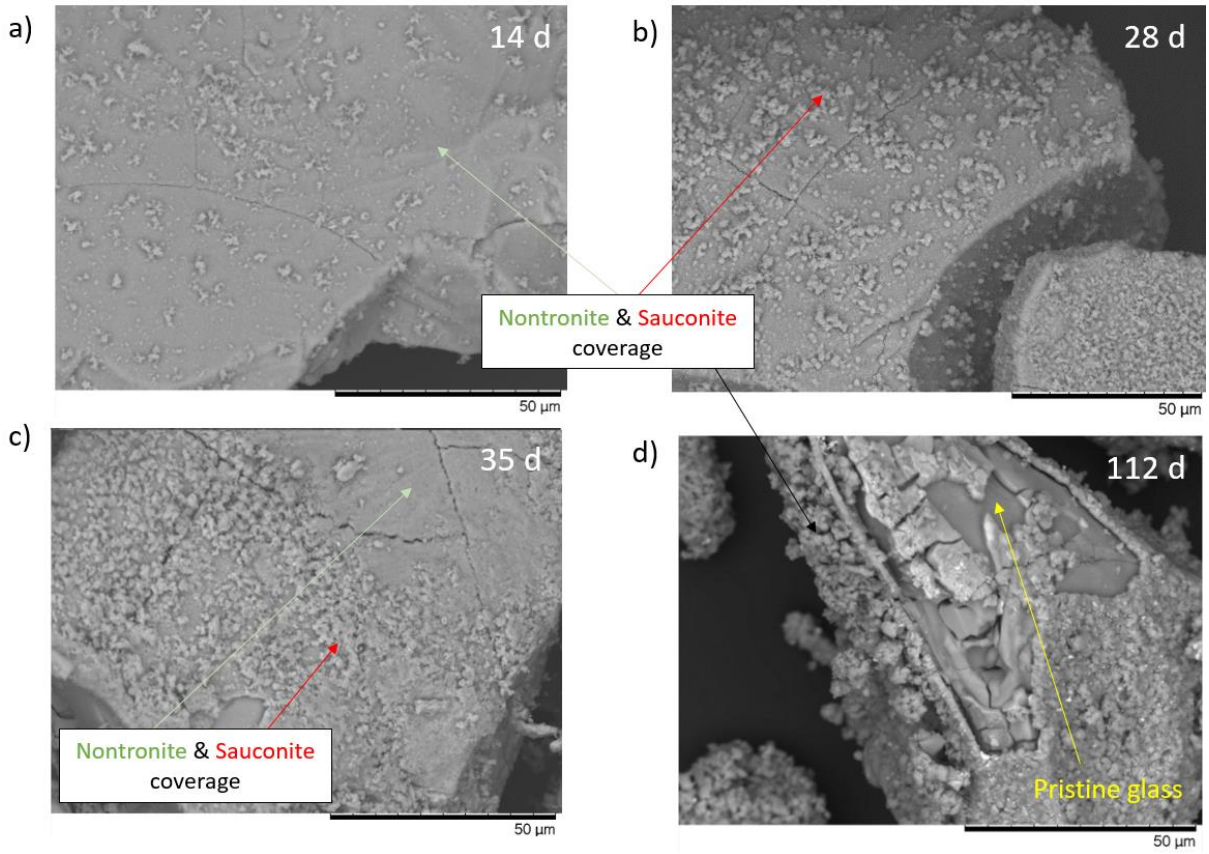

Figure 6.6. BSE SEM images of ZnCa 100:0 MW28 post 112 d PCT-B (UHQ, 90 °C): (a-d) temporal evolution of the glass particles post PCT-B experimentation. Note that the distinction between the nontronite and sauconite phases is tentatively suggested based on BSE images published by Muller *et al.* (2006), Ait Chaou *et al.* (2017) and De Echave *et al.* (2019) of nontronite and by Gin *et al.* (2013) of sauconite, alongside date presented in Chapter 5.

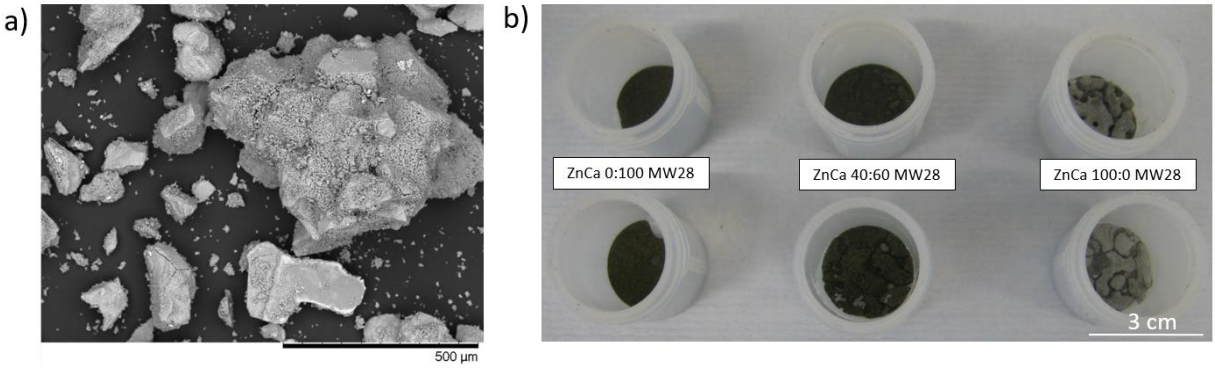

Figure 6.7. a) BSE SEM image of ZnCa 100:0 MW28 clumped particles post 112 d PCT-B (UHQ, 90 °C). Other images of identical dimensions contained at least one agglomeration of particles ranging in size 200-550 µm diameter and b) photograph of test vessels post 35 d PCT-B experimentation. Note the clumped nature of ZnCa 40:60 MW28 and ZnCa 100:0 MW28 was not an artefact of the drying process as the agglomerated particles were observed immediately after the vessel lid was removed, still submerged in UHQ.

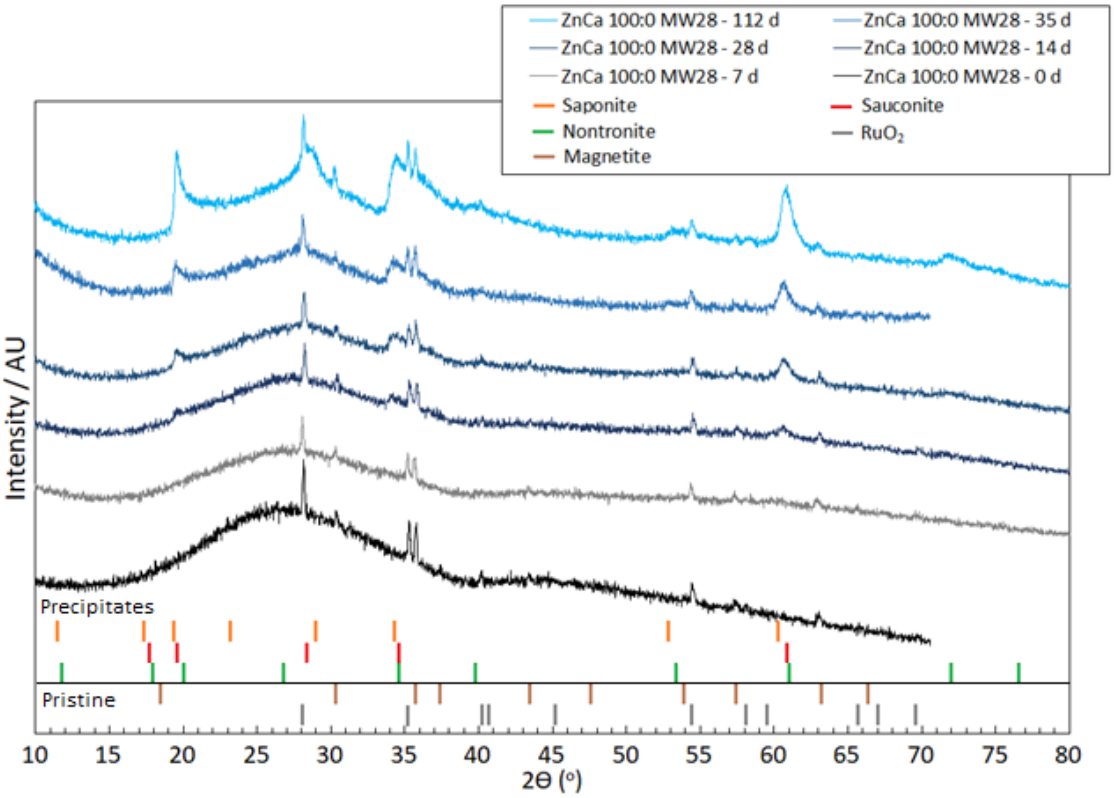

Figure 6.8. XRD temporal evolution of ZnCa 100:0 MW28 particles post PCT-B dissolution at 90 °C in UHQ.

Alteration product stratification on ZnCa 100:0 MW28 was observed after 112 d, as shown in Figure 6.9. The alteration products followed the sequence, from the surface of the pristine glass outwards: pristine glass, gel layer (assumed but beyond the resolution employed here), phyllosilicate smectite clays (nontronite, saponite and sauconite), and rare earth/Zr phosphates (Hyatt *et al.* 2004). The latter assignment is based on observations from MCC-1 tests presented in Section 6.2.2.4. The potential stratification of the secondary phases can be explained by Ostwald's Law which states that any system leaving a metastable phase (glass) evolves towards the *nearest* metastable state under given conditions of pressure and temperatures and not towards the *most* stable (Bauer *et al.* 1998). The trend hypothesised for glass corrosion follows the formation sequence: gels/clays; disordered zeolites; ordered zeolites (analcime) and; finally, feldspars/micas/rare earth phosphates (Dibble & Tiller 1981, Ebert *et al.* 1991, Jantzen *et al.* 2010, Frugier *et al.* 2014).

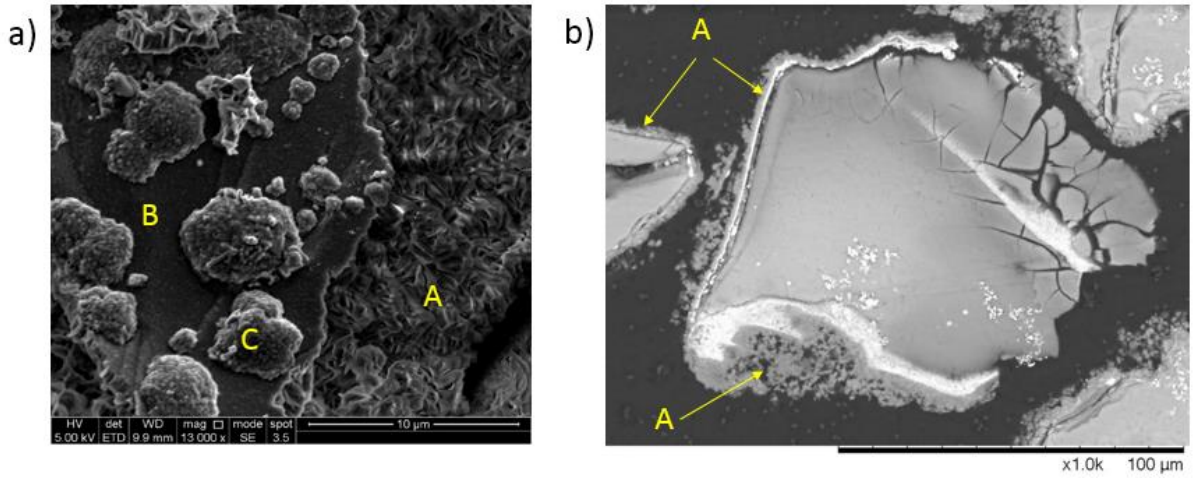

Figure 6.9. a) Secondary electron SEM image of ZnCa 100:0 MW28 post 112 d PCT-B (UHQ, 90 °C). Three distinct phases are suggested: A - smectite clays; B – Zn-silicate (sauconite) and C - rare earth/Zr phosphates/silicates; b) Cross sectional BSE image showing the surrounding alteration layer/secondary precipitates around a glass particle. Note the absence of a conventional gel layer. The bright fringe is potentially nontronite and/or rare earth/Zr phosphates/silicates, which is discussed in the MCC-1 results in section 6.2.2.4. EDS was unobtainable at the resolution employed.

EDS spot analysis was used to obtain semi-quantitative elemental compositions of each of the layers shown in Figure 6.9. Detailed SEM EDS data for two representative areas of this composition dissolved for 112 d are shown in Figures 6.10 and 6.11 and the corresponding semi-quantitative data are given Tables 6.4 and 6.5 respectively. The compositions of each layer were consistent with XRD peak assignment: A = nontronite, similar in morphology to the phyllosilicate layer observed in studies by Van Iseghem *et al.* (2006), Frugier *et al.* (2009) and Ait Chaou *et al.* (2017); B = Zn-silicate (sauconite), similar in morphology to that observed by Gin *et al.* (2013)) and; C = rare earth/Zr-phosphates/silicates (Vienna *et al.* 2001, Hyatt *et al.* 2004). The distinction between nontronite and sauconite (Fig. 6.6) was based very tentatively on BSE images of nontronite provided by Muller *et al.* (2006), Ait Chaou *et al.* (2017) and De Echave *et al.* (2019), and of sauconite by Gin *et al.* (2013), alongside results presented in Chapter 5. The rare earth/Zr phosphates were not observed in XRD traces, likely due to their low abundance in comparison to the smectite clays.

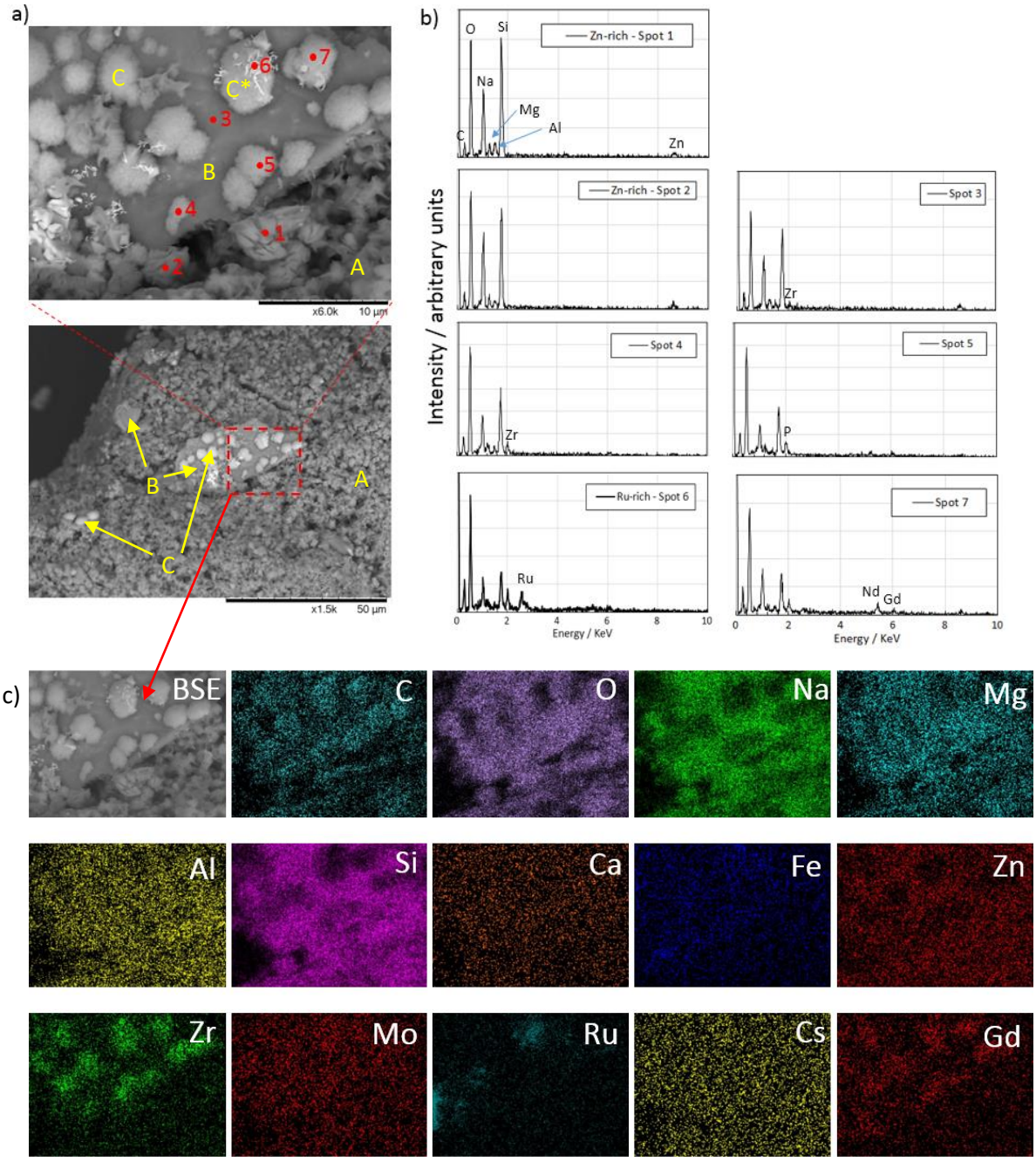

Figure 6.10. SEM and EDS mapping of ZnCa100:0 MW28 after 112 d PCT-B dissolution in UHQ at 90 °C: a) BSE images of secondary phases; b) EDS counts and c) EDS mapping.

Table 6.4. Elemental At.% of the EDS spot mapping associated with Figure 6.10 for ZnCa 100:0 MW28 after 112 d PCT-B dissolution in UHQ at 90 °C.

		Element At. %									
Spot #	Layer	Si	Al	Na	Zn	Mg	Zr	Gd	Nd	P	Ru
1	A	55.4 ± 0.9	6.9 ± 0.1	16.1 ± 0.3	14.8 ± 0.5	6.9 ± 0.1	-	-	-	-	-
2	A	50.3 ± 0.7	3.6 ± 0.1	14.6 ± 0.3	23.3 ± 0.6	7.9 ± 0.1	0.3 ± 0.0	-	-	-	-
3	B	50.2 ± 0.7	4.3 ± 0.1	20.2 ± 0.4	16.4 ± 0.4	7.4 ± 0.1	0.4 ± 0.0	0.1 ± 0.0	0.1 ± 0.0	-	-
4	C	41.6 ± 0.4	4.1 ± 0.1	27.9 ± 0.3	7.3 ± 0.1	6.6 ± 0.1	2.1 ± 0.1	1.8 ± 0.1	0.7 ± 0.1	8.0 ± 0.1	-
5	C	40.6 ± 0.3	2.3 ± 0.1	26.2 ± 0.3	8.0 ± 0.1	4.8 ± 0.1	1.8 ± 0.1	2.8 ± 0.1	3.9 ± 0.1	9.7 ± 0.1	-
6	C*	31.5 ± 0.2	0.4 ± 0.0	27.4 ± 0.2	9.8 ± 0.1	0.7 ± 0.0	-	4.8 ± 0.1	3.7 ± 0.1	11.9 ± 0.1	9.8 ± 0.2
7	C*	37.9 ± 0.3	5.5 ± 0.1	19.8 ± 0.2	16.5 ± 0.2	3.9 ± 0.1	2.4 ± 0.1	3.6 ± 0.1	1.4 ± 0.1	6.8 ± 0.1	2.4 ± 0.1

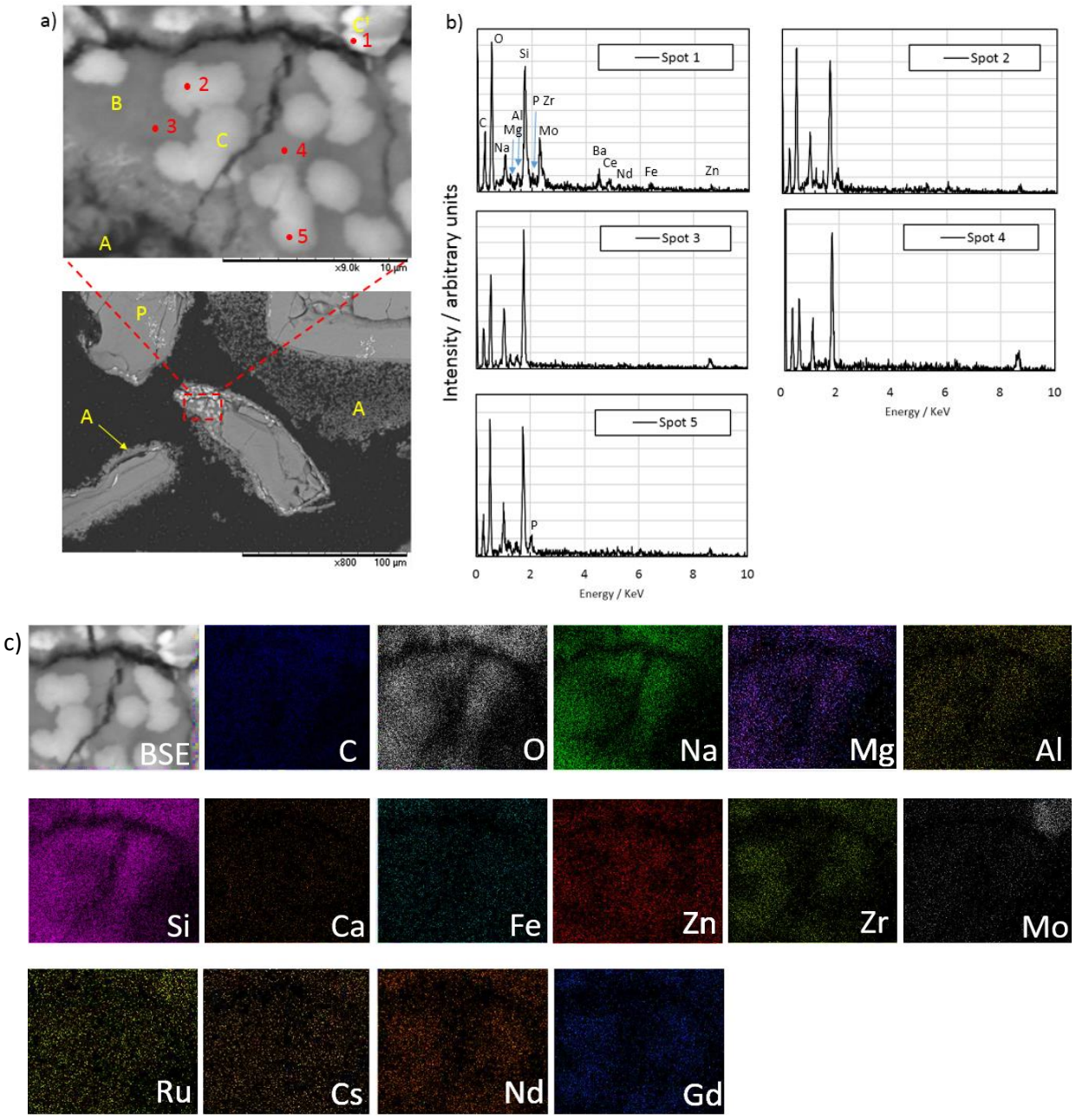

Figure 6.11. SEM and EDS mapping of ZnCa100:0 MW28 after 112 d PCT-B dissolution in UHQ at 90 °C: a) BSE images of secondary phases; b) EDS counts and c) EDS mapping. Note that C† represented a Mo-rich secondary precipitate, which was not observed on any other particle, despite intensive scans.

Table 6.5. Elemental At.% of the EDS spot mapping associated with Figure 6.11 for ZnCa 100:0 MW28 after 112 d PCT-B dissolution in UHQ at 90 °C.

		Element At. %															
Spot #	Layer	Si	Al	Na	Zn	Mg	Zr	Gd	Nd	P	Ru	Ba	Ce	Fe	Ti	Ca	Mo
1	C†	52.0 ± 2.6	3.5 ± 0.2	10.2 ± 0.5	5.1 ± 0.3	0.75 ± 0.04	2.3 ± 0.1	0.56 ± 0.03	0.19 ± 0.01	2.1 ± 0.1	-	5.6 ± 0.3	1.2 ± 0.1	1.9 ± 0.1	0.10 ± 0.01	-	14.5 ± 0.7
2	C	58.5 ± 2.9	4.5 ± 0.2	5.7 ± 0.3	12.5 ± 0.6	5.7 ± 0.3	2.0 ± 0.1	1.7 ± 0.1	1.1 ± 0.1	5.8 ± 0.3	-	-	0.58 ± 0.03	-	0.93 ± 0.05	-	-
3	B	53.8 ± 3.0	4.4 ± 0.2	12.9 ± 0.7	20.7 ± 1.0	5.8 ± 0.3	-	0.15 ± 0.01	-	1.1 ± 0.1	-	-	-	-	0.15 ± 0.01	0.10 ± 0.01	-
4	B	49.6 ± 2.5	0.61 ± 0.03	10.8 ± 0.5	33.4 ± 1.7	1.8 ± 0.1	-	1.1 ± 0.1	-	-	-	0.61 ± 0.03	0.22 ± 0.01	1.9 ± 0.1	-	-	-
5	C	56.5 ± 2.8	3.2 ± 0.2	6.1 ± 0.3	16.6 ± 0.8	1.7 ± 0.1	2.0 ± 0.1	3.1 ± 0.2	1.2 ± 0.1	7.2 ± 0.4	-	0.28 ± 0.01	0.47 ± 0.02	1.27 ± 0.1	0.14 ± 0.01	-	-

ZnCa 40:60 MW28

The temporal evolution of the secondary phases precipitated throughout duration of the PCT-B investigation of ZnCa 40:60 MW28, from 0-112 d, is provided by XRD in Fig. 6.12. The same secondary phases as ZnCa 100:0 MW28 were tentatively identified from their most intense X-ray reflections (nontronite, saponite and sauconite), and SEM/EDX observations were consistent with the formation of these smectite clay phases with compositions corresponding to those indexed (Figs. 6.13 & 6.14). Agglomoration of particles post-dissolution was observed after 35 d (Fig. 6.7b). The smectite clay coverage was approximately the same in appearance after 112 d as it was after 35 d, and was similar in appearance to the surface of the particles observed by Muller *et al.* (2006). The secondary phases were located on the surface of a gel layer (Fig. 6.14), in contrast to ZnCa 100:0 MW28, which did not show a gel layer at the SEM resolution employed (yet a gel layer is assumed). The gel layer for this sample was enhanced in Ca compared to the pristine glass (Fig. 6.14 and Table 6.6). No secondary rare earth/Zr-phosphate precipitates were observed.

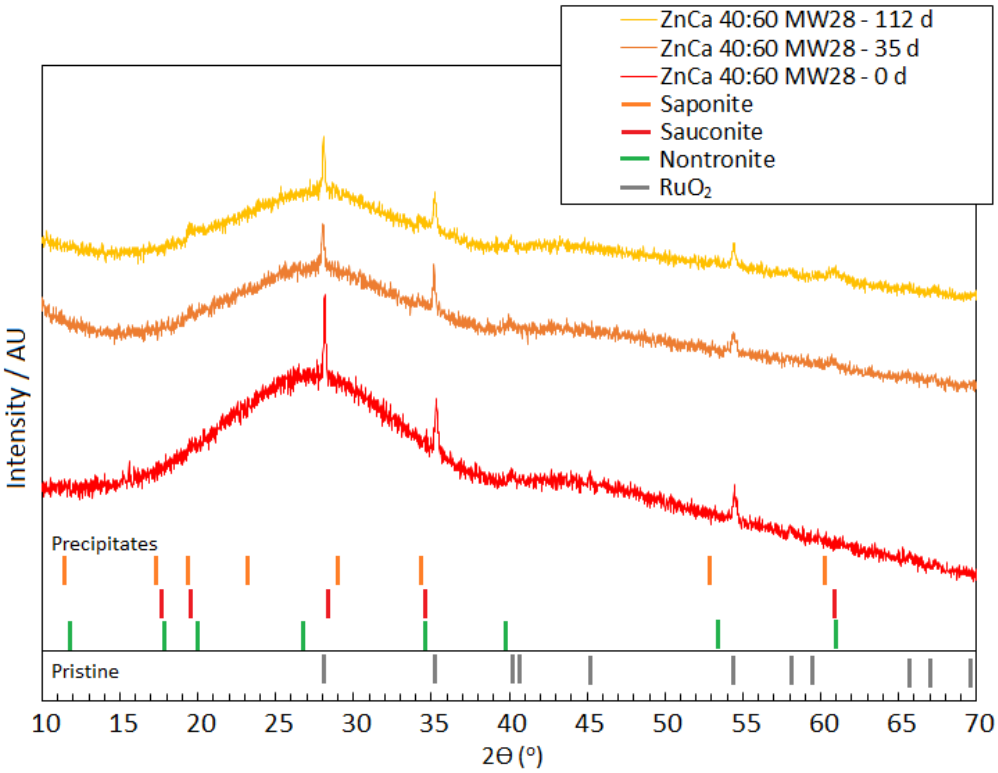

Figure 6.12. XRD temporal evolution of ZnCa 40:60 MW28 particulates post PCT-B dissolution at 90 °C in UHQ.

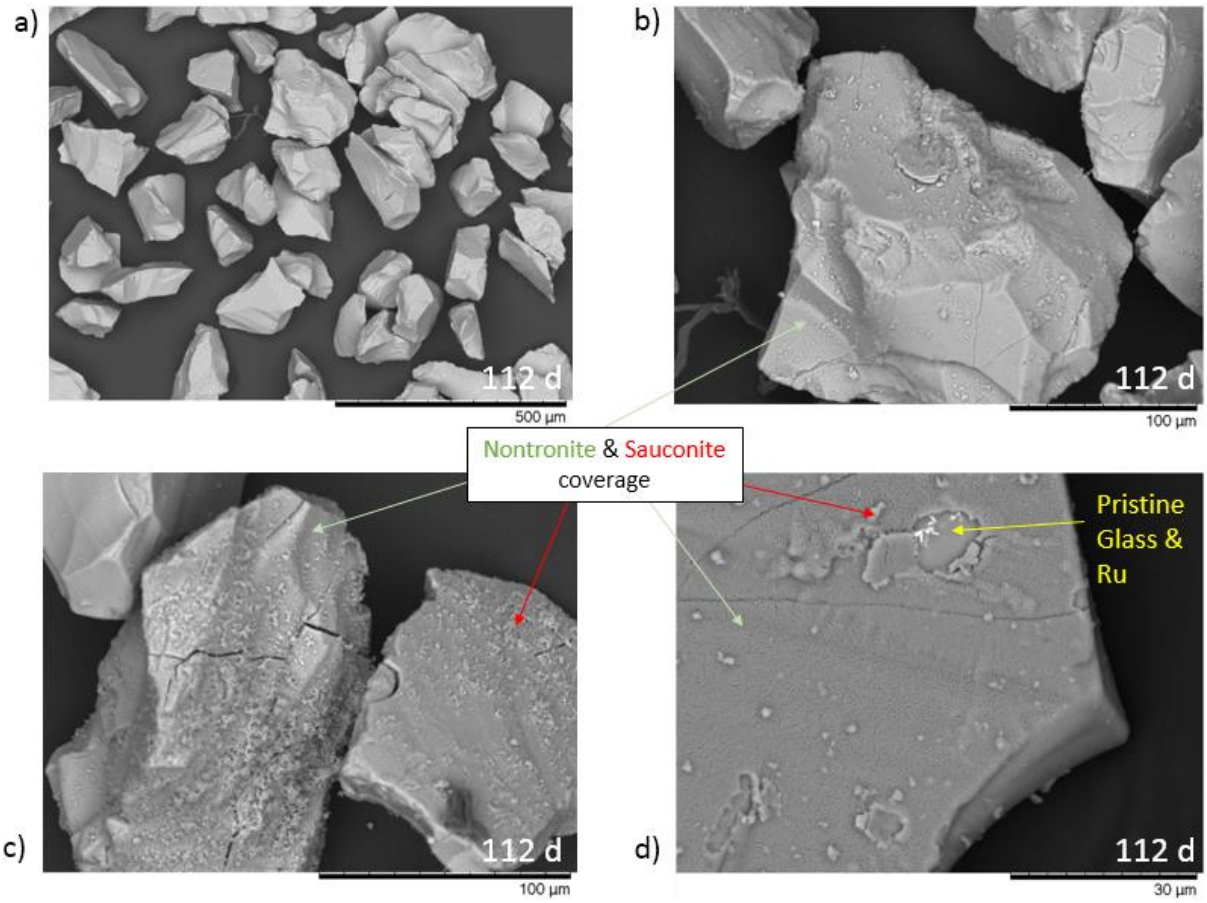

Figure 6.13. BSE SEM images of ZnCa 40:60 MW28 post 112 d PCT-B (UHQ, 90 °C); note in (d), that the pristine glass was revealed after the exfoliation of the secondary smectite layer upon drying.

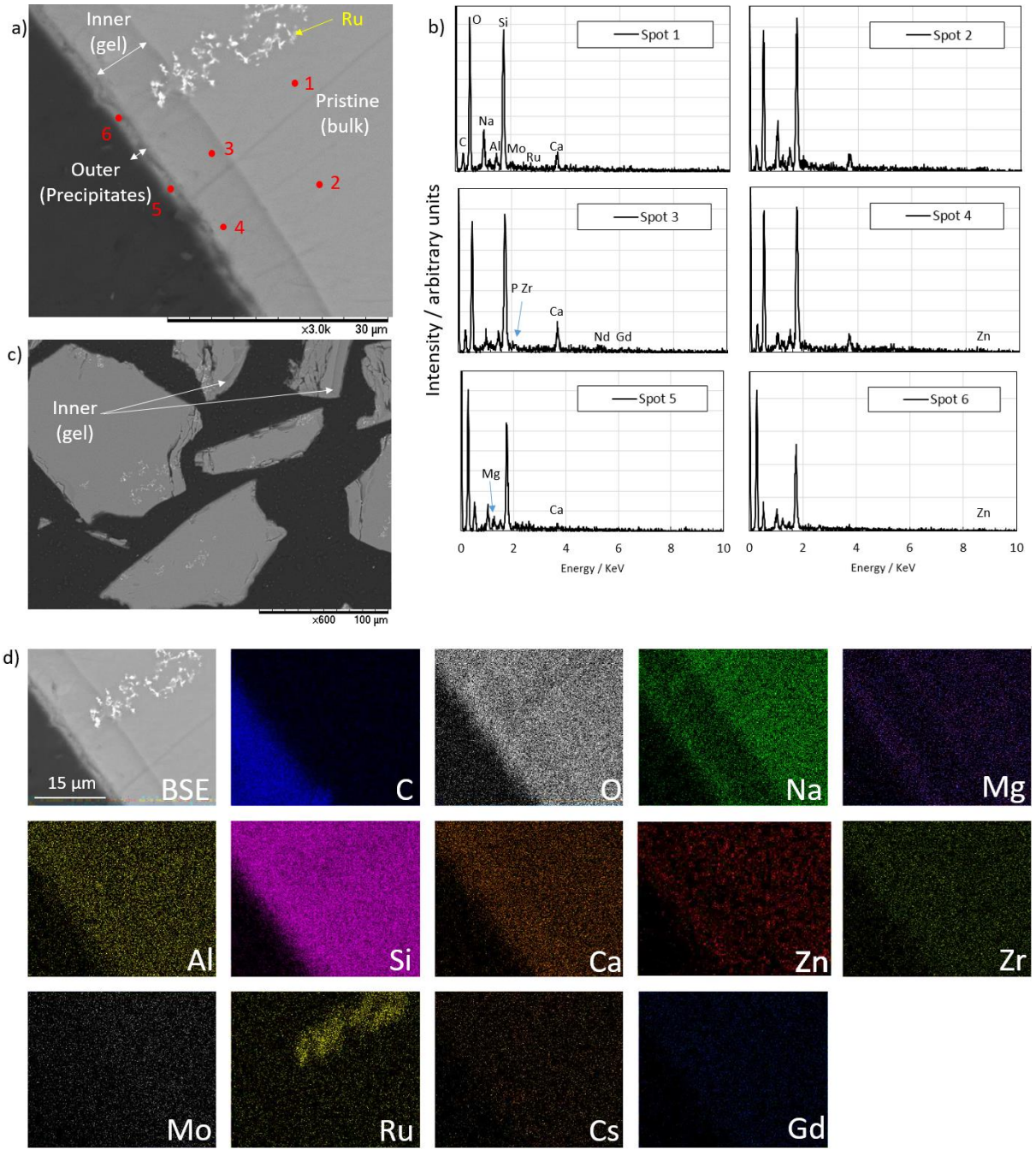

Figure 6.14. SEM and EDS mapping of ZnCa 40:60 MW28 after 112 d PCT-B dissolution in UHQ at 90 °C: a) BSE cross section displaying a clear gel layer; b) EDS counts; c) BSE overview of gel layers and d) EDS mapping.

Table 6.6. Elemental At.% of the EDS spot mapping associated with Figure 6.14 for ZnCa 40:60 MW28 after 112 d PCT-B dissolution in UHQ at 90 °C.

		Element At. %											
Spot #	Layer	Si	Al	Na	Zn	Mg	Zr	Gd	Nd	P	Ru	Ca	Mo
1	Pristine	53.5 ± 2.7	4.8 ± 0.2	23.5 ± 1.2	3.1 ± 0.2	3.1 ± 0.2	0.59 ± 0.03	0.59 ± 0.03	0.79 ± 0.04	1.6 ± 0.1	0.10 ± 0.00	7.6 ± 0.4	0.49 ± 0.02
2	Pristine	50.2 ± 2.5	5.4 ± 0.3	27.1 ± 1.4	5.7 ± 0.3	2.5 ± 0.1	1.1 ± 0.1	0.58 ± 0.03	0.77 ± 0.04	0.44 ± 0.02	-	5.7 ± 0.3	0.44 ± 0.02
3	Inner	63.5 ± 3.2	5.6 ± 0.3	10.8 ± 0.5	1.9 ± 0.1	-	1.5 ± 0.1	1.2 ± 0.01	2.3 ± 0.1	-	-	13.3 ± 0.7	-
4	Inner	66.9 ± 3.3	6.4 ± 0.3	9.2 ± 0.5	3.7 ± 0.2	1.8 ± 0.1	1.7 ± 0.1	0.31 ± 0.02	0.73 ± 0.04	0.79 ± 0.04	-	8.6 ± 0.4	-
5	Outer	70.1 ± 3.5	4.1 ± 0.2	6.8 ± 0.3	4.0 ± 0.2	8.0 ± 0.4	1.4 ± 0.1	0.39 ± 0.02	0.26 ± 0.01	-	0.64 ± 0.03	3.7 ± 0.2	-
6	Outer	61.6 ± 3.1	3.7 ± 0.2	12.6 ± 0.6	10.2 ± 0.5	8.8 ± 0.4	0.29 ± 0.01	-	0.29 ± 0.01	-	0.57 ± 0.03	1.9 ± 0.1	0.52 ± 0.03

ZnCa 0:100 MW28

SEM and XRD observations showed that a thin gel layer formed without the precipitation of any secondary phases (Figs. 6.15-6.17 and Table 6.6). Agglomeration of particles post-dissolution was not observed. The gel layer had an enhanced concentration of Ca and it was depleted in Na when compared to the pristine glass (Table 6.7). The absence of secondary precipitation can be attributed to the absence of Zn, without which, Mg would be most likely to be the dominant element driving secondary clay formation (Curti *et al.* 2006). However, since Si and Mg were observed to be retained within the bulk glass and the gel (Table 6.7 and Fig. 6.16), precipitation of Mg-silicates was not induced (Thien *et al.* 2012).

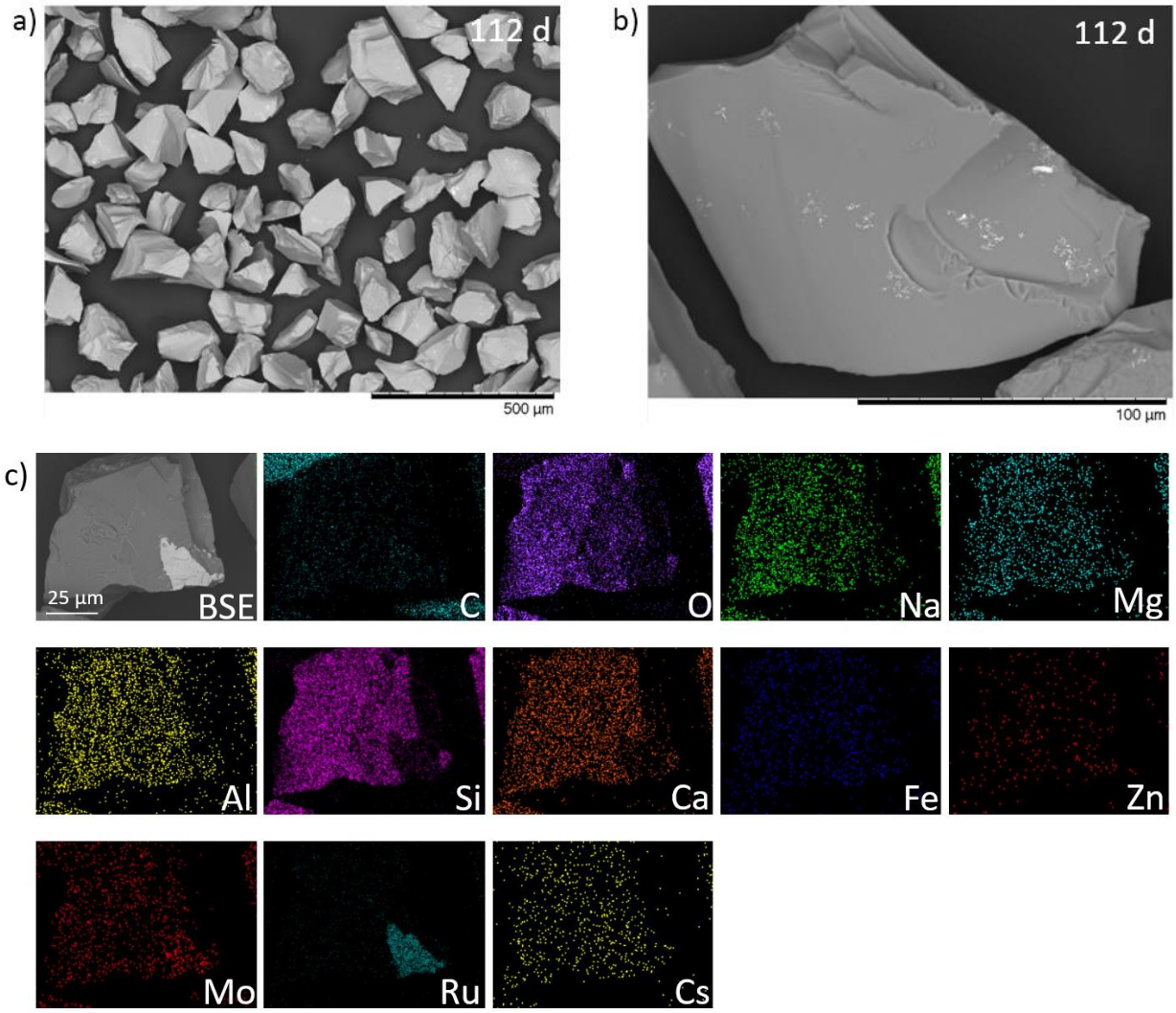

Figure 6.15. a-b) BSE SEM images of ZnCa 0:100 MW28 post 112 d PCT-B dissolution at 90 °C in UHQ. Note the large Ru crystallite inclusion in the pristine glass; c) EDS mapping.

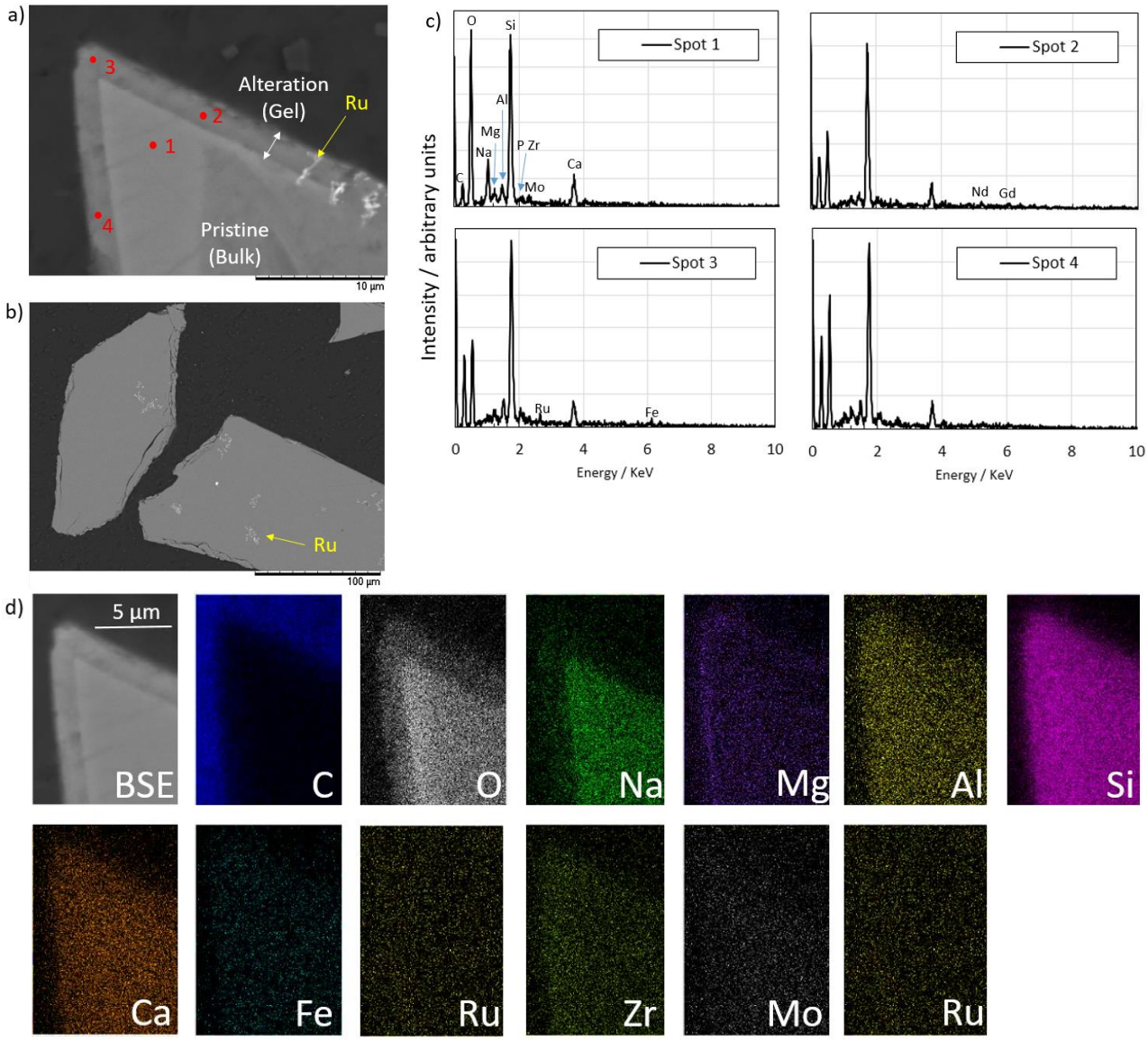

Figure 6.16. SEM and EDS mapping of ZnCa 0:100 MW28 after 112 d PCT-B dissolution in UHQ at 90 °C: a) BSE cross section displaying a gel layer; b) BSE overview, C) EDS counts; and d) EDS mapping.

Table 6.7. Elemental At.% of the EDS spot mapping associated with Figure 6.16 for ZnCa 0:100 MW28 after 112 d PCT-B dissolution in UHQ at 90 °C.

		Element At. %												
Spot #	Layer	Si	Al	Na	Zn	Mg	Zr	Gd	Nd	P	Ru	Fe	Ca	Mo
1	Pristine	53.1 ± 3.4	5.7 ± 0.5	22.9 ± 2.0	-	4.2 ± 0.5	1.1 ± 0.5	0.88 ± 0.49	0.54 ± 0.01	0.54 ± 0.01	0.10 ± 0.01	0.59 ± 0.01	8.3 ± 0.5	1.2 ± 0.5
2	Alteration	70.7 ± 6.7	4.7 ± 2.9	2.3 ± 0.1	0.25 ± 0.1	3.2 ± 0.4	2.8 ± 0.2	1.6 ± 0.4	1.0 ± 0.4	-	0.69 ± 0.14	0.75 ± 0.01	12.0 ± 0.6	0.19 ± 0.01
3	Alteration	68.1 ± 6.4	7.5 ± 1.7	1.5 ± 0.0	0.77 ± 0.01	2.2 ± 0.0	3.0 ± 0.2	1.3 ± 0.1	0.49 ± 0.27	0.98 ± 0.01	0.49 ± 0.00	1.2 ± 0.0	12.0 ± 0.6	0.56 ± 0.01
4	Alteration	66.0 ± 7.8	7.1 ± 1.8	3.8 ± 0.7	0.16 ± 0.01	4.2 ± 0.0	3.1 ± 0.2	0.64 ± 0.6	0.88 ± 0.10	0.48 ± 0.01	1.0 ± 0.0	1.2 ± 0.2	11.1 ± 0.8	0.32 ± 0.01

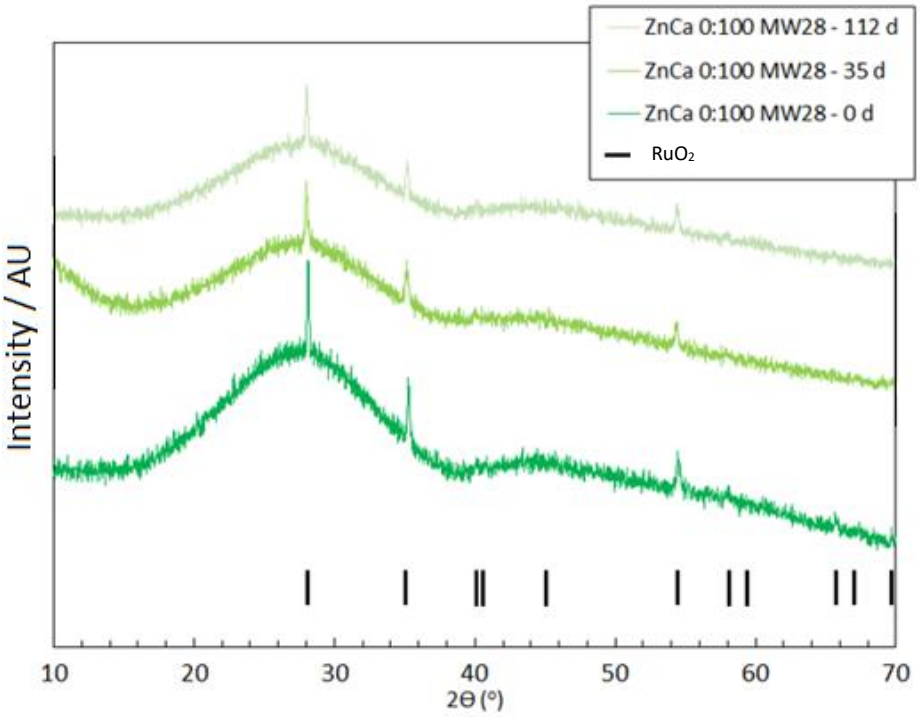

Figure 6.17. XRD temporal evolution of ZnCa 0:100 MW28 particulates post PCT-B dissolution at 90 °C in UHQ.

6.2.2.3 Geochemical modelling

The PHREEQ-C geochemical modelling data for the ZnCa xx:xx MW28 series is displayed in Table 6.8 and Figure 6.18. Phases that were identified to be saturated in solution and, therefore, have the potential to precipitate (indicated by having a saturation index > 1) were composed of a wide variety of phyllosilicates and zeolites.

Table 6.8. Saturated mineral phases identified by PHREEQ-C geochemical modelling for the ZnCa xx:xx MW28 series (75o:25m) and ZnCa MWXX series (50o:50m) subjected to 112 d PCT-B dissolution at 90 °C in UHQ at SA/V = 2,000 m^{-1}. Note the omission of P and Zr containing phases due to the lack of elemental concentration data. Predicted phases limited to the contents of the database (LLNL).

Phases Identified from Lawrence Livermore National Laboratory database				
Phase	Chemical formula	Comments	Associated composition ZnCa XX:XX MW28	Associated composition ZnCa MWXX
Beidellite-Ca	$Ca_{.165}Al_{2.33}Si_{3.67}O_{10}(OH)_2$	Phyllosilicate - Smectite	100:0	
Beidellite-H	$H_{.33}Al_{2.33}Si_{3.67}O_{10}(OH)_2$	Phyllosilicate - Smectite	100:0	
Beidellite-Mg	$Mg_{.165}Al_{2.33}Si_{3.67}O_{10}(OH)2$	Phyllosilicate - Smectite	100:0	
Brucite	$Mg(OH)_2$	Brucite Group	100:0, 40:60 & 0:100	
Ferrite-Ca	$CaFe_2O_4$	-	100:0, 40:60 & 0:100	
Ferrite-Mg	$MgFe_2O_4$	-	100:0, 40:60 & 0:100	
Ferrite-Zn	$ZnFe_2O_4$	-	100:0, 40:60 & 0:100	
Forsterite	Mg_2SiO_4	Nesosilicates	100:0, 40:60 & 0:100	
Grossular	$Ca_3Al_2(SiO_4)_3$	Nesosilicates	40:60 & 0:100	20, 28, 35
Illite	$K_{0.6}Mg_{0.25}Al_{1.8}Al_{0.5}Si_{3.5}O_{10}(OH)_2$	Phyllosilicate - Mica	40:60 & 0:100	20, 28, 35
K-feldspar	$KAlSi_3O_8$	Tectosilicate	40:60 & 0:100	
Kaolinite	$Al_2Si_2O_5(OH)_4$	Kaolinite Subgroup - Kaolinite-Serpentine Group	100:0	
Laumontite	$CaAl_2Si_4O_{12}.4H_2O$	Zeolite	100:0, 40:60 & 0:100	
Margarite	$CaAl_4Si_2O_{10}(OH)_2$	Phyllosilicate - Mica	100:0	
Mesolite	$Na_{.676}Ca_{.657}Al_{1.99}Si_{3.01}O_{10}.2.647H_2O$	Zeolite - Nantrolite subgroup	100:0, 40:60 & 0:100	20, 28, 35
Monticellite	$CaMgSiO_4$	Olivine Group	100:0, 40:60 & 0:100	20, 28, 35
Montmor-Ca	$Ca_{.165}Mg_{.33}Al_{1.67}Si_4O_{10}(OH)_2$	Phyllosilicate - Smectite	100:0, 40:60 & 0:100	
Montmor-K	$K_{.33}Mg_{.33}Al_{1.67}Si_4O_{10}(OH)_2$	Phyllosilicate - Smectite	100:0, 40:60 & 0:100	
Montmor-Na	$Na_{.33}Mg_{.33}Al_{1.67}Si_4O_{10}(OH)_2$	Phyllosilicate - Smectite	100:0, 40:60 & 0:100	
Muscovite	$KAl_3Si_3O_{10}(OH)_2$	Phyllosilicate - Mica	40:60 & 0:100	
Nontronite-Ca	$Ca_{.165}Fe_2Al_{.33}Si_{3.67}H_2O_{12}$	Phyllosilicate - Smectite	100:0, 40:60 & 0:100	
Nontronite-H	$H_{.33}Fe_2Al_{.33}Si_{3.67}H_2O_{12}$	Phyllosilicate - Smectite	100:0, 40:60 & 0:100	
Nontronite-Mg	$Mg_{.165}Fe_2A_{l.33}Si_{3.67}H_2O_{12}$	Phyllosilicate - Smectite	100:0, 40:60 & 0:100	
Nontronite-Na	$Na_{.33}Fe_2Al_{.33}Si_{3.67}H_2O_{12}$	Phyllosilicate - Smectite	100:0, 40:60 & 0:100	
Prehnite	$Ca_2Al_2Si_3O_{10}(OH)_2$	Silicate mineral	40:60 & 0:100	
Saponite-Ca	$Ca_{.165}Mg_3Al_{.33}Si_{3.67}O_{10}(OH)_2$	Phyllosilicate - Smectite	100:0, 40:60 & 0:100	20, 28, 35
Saponite-H	$H_{.33}Mg_3Al_{.33}Si_{3.67}O_{10}(OH)_2$	Phyllosilicate - Smectite	100:0, 40:60 & 0:100	20, 28, 35
Saponite-Mg	$Mg_{3.165}Al_{.33}Si_{3.67}O_{10}(OH)_2$	Phyllosilicate - Smectite	100:0, 40:60 & 0:100	20, 28, 35
Saponite-Na	$Na_{.33}Mg_3Al_{.33}Si_{3.67}O_{10}(OH)_2$	Phyllosilicate - Smectite	100:0, 40:60 & 0:100	20, 28, 35
Scolecite	$CaAl_2Si_3O_{10}.3H_2O$	Zeolite - Nantrolite subgroup	100:0 & 40:60	
Sepiolite	$Mg_4Si_6O_{15}(OH)_2.6H_2O$	Sepiolite group	100:0, 40:60 & 0:100	
Stilbite	$Ca_{1.019}Na_{.136}K_{.006}Al_{2.18}Si_{6.82}O_{18}.7.33H_2O$	Zeolite	0:100	
Talc	$Mg_3Si_4O_{10}(OH)_2$	Pyrophyllite-Talc Group	100:0, 40:60 & 0:100	
Tobermorite-11A	$Ca_5Si_6H_{11}O_{22.5}$	CSH	0:100	
Zn_2SiO_4	Zn_2SiO_4	-	100:0, 40:60 & 0:100[†]	20, 28, 35

* Unidentified in LLNL database

[†]Calculated due to low Zn content in waste calcine

Key phases that were identified by the modelling for all samples, with indirect corresponding experimental evidence (SEM EDS / XRD) were Zn_2SiO_4 and nontronite Ca/H/Mg/Na (phyllosilicate smectite clays). Thermodynamic data for hydrated Zn-bearing silicate phases, for example, sauconite ($Na_{0.3}Zn_3(Si,Al)_4O_{10}(OH)_2{\cdot}nH_2O$), are not available in the database employed in the current study, nor to the best of our knowledge, in other databases available. Other Zn- and Ca-containing phases were identified across all samples due to minor quantities of Zn/Ca in the waste calcine, i.e. Zn/Ca are detected in the ZnCa 0:100/100:0 MW28 samples.

Other phases identified across all samples, for which there is tentative experimental evidence, include the phyllosilicates saponite $Mg_{3.165}Al_{.33}Si_{3.67}O_{10}(OH)_2$, montmorillonite Ca/K/Na ($Ca_{.165}Mg_{33}Al_{1.67}Si_4O_{10}(OH)_2$ / $K_{.33}Mg_{33}Al_{1.67}Si_4O_{10}(OH)_2$ / $Na_{.33}Mg_{33}Al_{1.67}Si_4O_{10}(OH)_2$) and sepiolite ($Mg_4Si_6O_{15}(OH)_2.6H_2O$) (Jantzen *et al*. 2010) and the Ca-containing zeolites scolecite ($CaAl_2Si_3O_{10}.3H_2O$) and laumonite ($CaAl_2Si_4O_{12}.4H_2O$). Phases specific to the Ca-containing glasses only included prehnite (Ca containing inosilicate) ($Ca_2Al_2Si_3O_{10}(OH)_2$), monticellite (Ca-Mg containing of the olivine group) ($CaMgSiO_4$), the micas: muscovite (K-containing) ($KAl_3Si_3O_{10}(OH)_2$) (however, it is doubtful that monticellite and muscovite would form under these hydrothermal experimental conditions, but are listed for completeness) and illite (K and Mg containing) ($K_{0.6}Mg_{0.25}Al_{1.8}Si_{3.5}O_{10}(OH)_2$) - and K-feldspar ($KAlSi_3O_8$). The latter three phases were predicted to be present after 112 d, in agreement with the Ostwald ripening theory described in Section 6.2.2.2 (Dibble & Tiller 1981).

The zeolite phase stilbite ($Ca_{1.019}Na_{.136}K_{.006}Al_{2.18}Si_{6.82}O_{18}{\cdot}7.33H_2O$) was unique to ZnCa 0:100 MW28. In contrast, the zeolite analcime ($Na(Si_2Al)O_6{\cdot}H_2O$), which is a widely reported phase indicative of Stage III glass dissolution (Fournier *et al.* 2014), was calculated to be undersaturated in solution for all samples at all time points, likely due to the pH threshold at which analcime precipitates (> pH 10.5, Ribet & Gin 2004); the pH values from the dissolution experiments in this investigation only exceeded this value in one instance for ZnCa 0:100 MW28 (Fig. 6.5a).

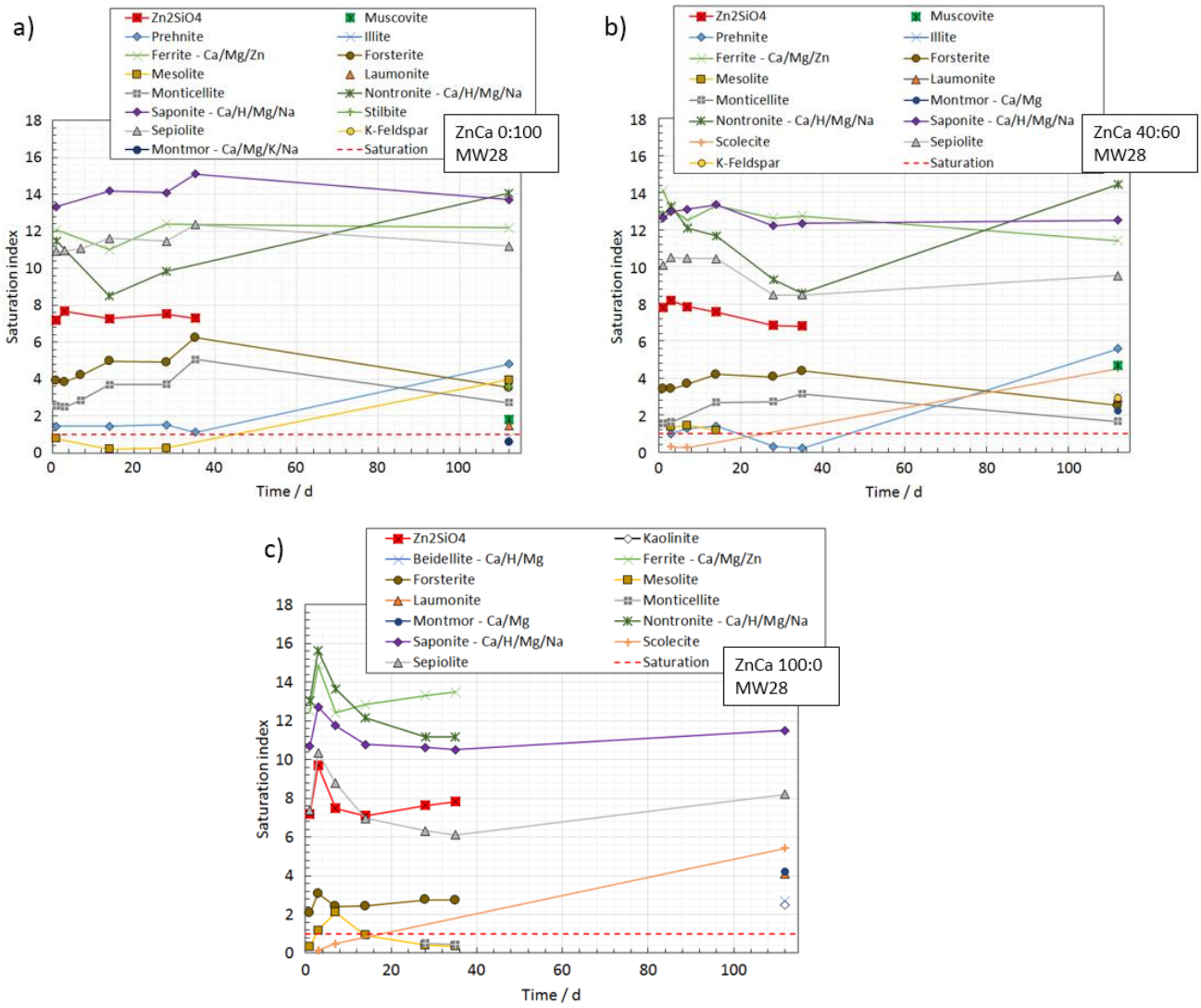

Figure 6.18. PHREEQ-C geochemical modelling from the solution data from the ZnCa xx:xx MW28 112 d PCT-B experiments at 90 °C in UHQ at SA/V = 2,000 m^{-1}.

Nontronite and saponite, tentatively identified experimentally and predicted by geochemical modelling in this study, were reported to form under almost identical dissolution conditions as those utilised here (90 °C, UHQ, 2,000 m^{-1}) on West-Valley borosilicate HLW glass types investigated by Muller *et al.* (2006) in 4,000 d dissolution tests. The authors attributed the observation of rate resumption to the precipitation of zeolite-type phases (particularly phillipsite $(K,Na,Ca_{0.5})_{1\text{-}2}(Si,Al)_8O_{16}.6H_2O)$), but not to nontronite and saponite. Montmorillionite, kaolinite ($Al_2Si_2O_5(OH)_4$) and nontronite have also been observed by Gan *et al.* (2011) in experiments conducted at 150 °C, in groundwater, at SA/V = 6,000 m^{-1}, and after approximately 6,000 d, on a Nd-rich waste loaded glass in an underground repository laboratory in northwest China. Under these conditions 'rate resumption' (Stage III) was hypothesised to be triggered by the additional formation of zeolites. The formation of K-feldspar was observed on SRL 200S glass (90 °C, UHQ, 20,000 m^{-1}, after approximately 4,000 d) (Feng

et al. 1993, Ebert & Tam 1996) and smectite clays, including Na-beidellite were also observed (120 °C, 0.1 M NaOH, at SA/V = 14,000 m^{-1}, after 50 d) on R7T7 (Inagaki *et al.* 2002). Such literature supports the prediction and possible formation of phases identified from the geochemical modelling in this body of work.

The trace elements (including phosphorus and zirconium) were not measured in the ICP-OES concentration analysis, due to concentrations in solution being below the detection limits, therefore they were omitted from the geochemical modelling. However, the presence of phosphorus and zirconium in secondary phases was provided by EDS. Future work, for example utilising micro-focus XRD or Raman techniques could identify such phases. The same is required for Mo phases, which were not available in the database employed in the current study.

6.2.2.4 MCC-1 - ZnCa 40:60 MW28, UHQ, 50 °C (Study B)

The normalised mass loss of all elements over the 540 d MCC-1 test duration from ZnCa 40:60 MW28 (Study B, Table 6.1) are shown in Figure 6.19 (initially introduced in Chapter 5 for a comparison with the corresponding base glasses). Several key stages of dissolution were observed (which are near identical to the Zn-containing base glasses described in Chapter 5 (Sections 5.2.3.4 & 5.3.2.3):

(1) 7-35 d: the NL_i of all elements followed a low rate of dissolution (potentially a residual rate) (Fig. 6.19b). A drop in the pH from 8.2-7.1 was observed, which potentially indicated the formation of secondary phases which consume hydroxyl groups, gradually sustaining a low rate of dissolution over this time period.

(2) 35-95 d: an increase in the NL_i for all elements (to varying degrees), except for Al (which decreased) was observed. However, a drop in ML_{Mo} and NL_{Zn} was observed after 56 & 95 d respectively. The pH approximately stabilised between 7.0-7.4.

(3) 95-540 d: An increase in dissolution rate was observed after 95 d based on $NL_{B, Si, Na, Mo, Mg \& Ca}$. A further, significant, increase in the dissolution rate was observed after 360 d based on the $NL_{B, Si, Na, Mo, \& Ca}$. From 360-540 d, the pH increased from 7.5-9.

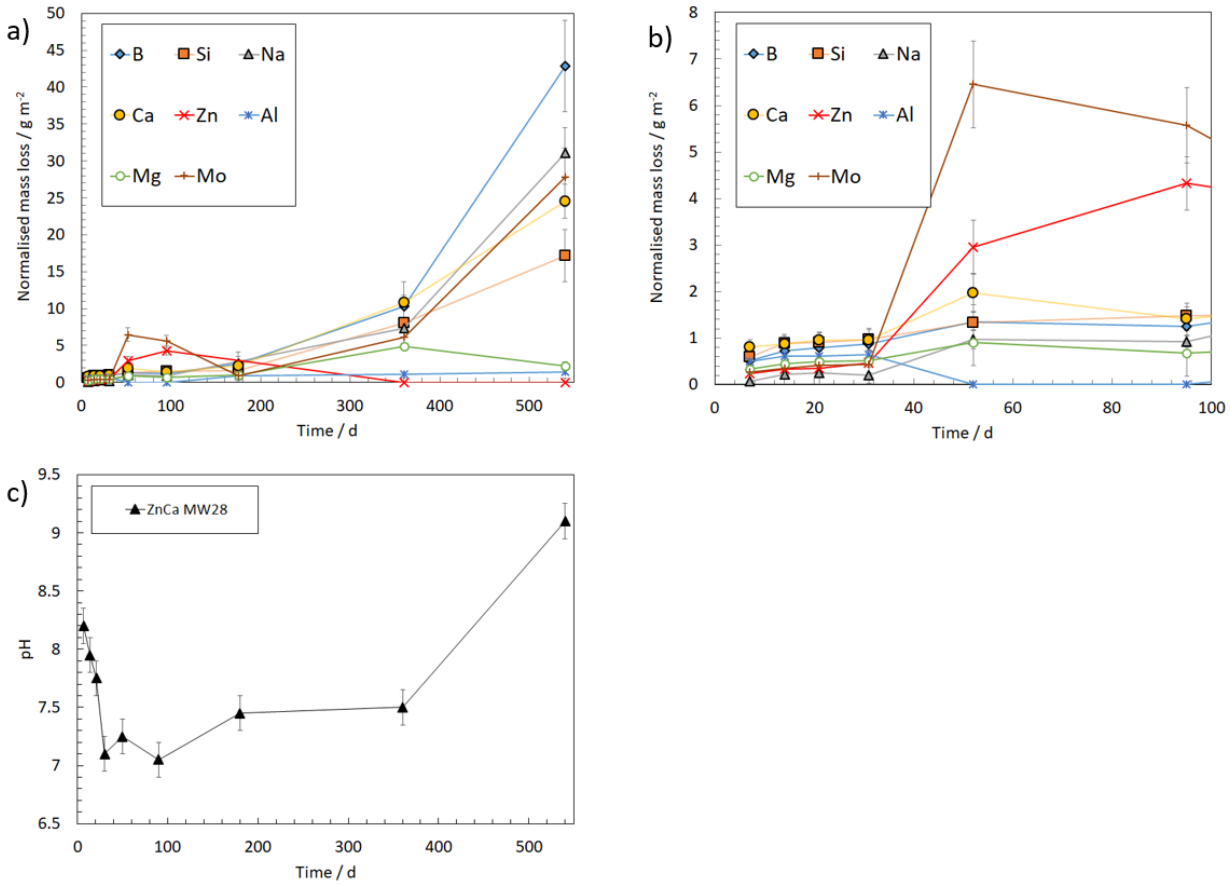

Figure 6.19. a & b) Normalised mass loss of elements from ZnCa 40:60 MW28 after 540 d MCC-1 dissolution in UHQ at 50 °C; c) pH(RT) evolution.

The observation of the rapid increase in the dissolution rate, associated with a decrease in Al concentration and a decrease in pH are in accordance with previously observed behaviour attributed to the classical definition of Stage III 'rate resumption' (Frugier *et al.* 2008, Vienna *et al.* 2013). Although the mechanisms for rate resumption are not yet well understood, it is widely accepted that an increase in dissolution rate occurs when secondary phases (most notably zeolites) form from the major glass network-forming elements (Si, Al) in the gel layer, which nucleate at the surface of the glass, strongly impacting the dissolution kinetics, either by disrupting the passivating properties of the gel layer, or by providing a thermodynamic driving force for silica dissolution (Fournier *et al.* 2014). In the present study on the wasteloaded glass (extending the investigation from the base glasses in Chapter 5), it is clear that rate resumption is linked with Zn, Mg, and Mo concentrations, for example, the decrease in NL_{Zn} (> 95 d) coincides with both the *first* (95 d) and *second* (360 d) rate increases, a decrease in NL_{Mo} also coincides with the first resumption, and a decrease in NL_{Mg} also coincides with the second rate increase. In the following sections the observation and prediction of Zn- and Mg-silicates are discussed, yet no evidence for Mo secondary phases were detected or predicted.

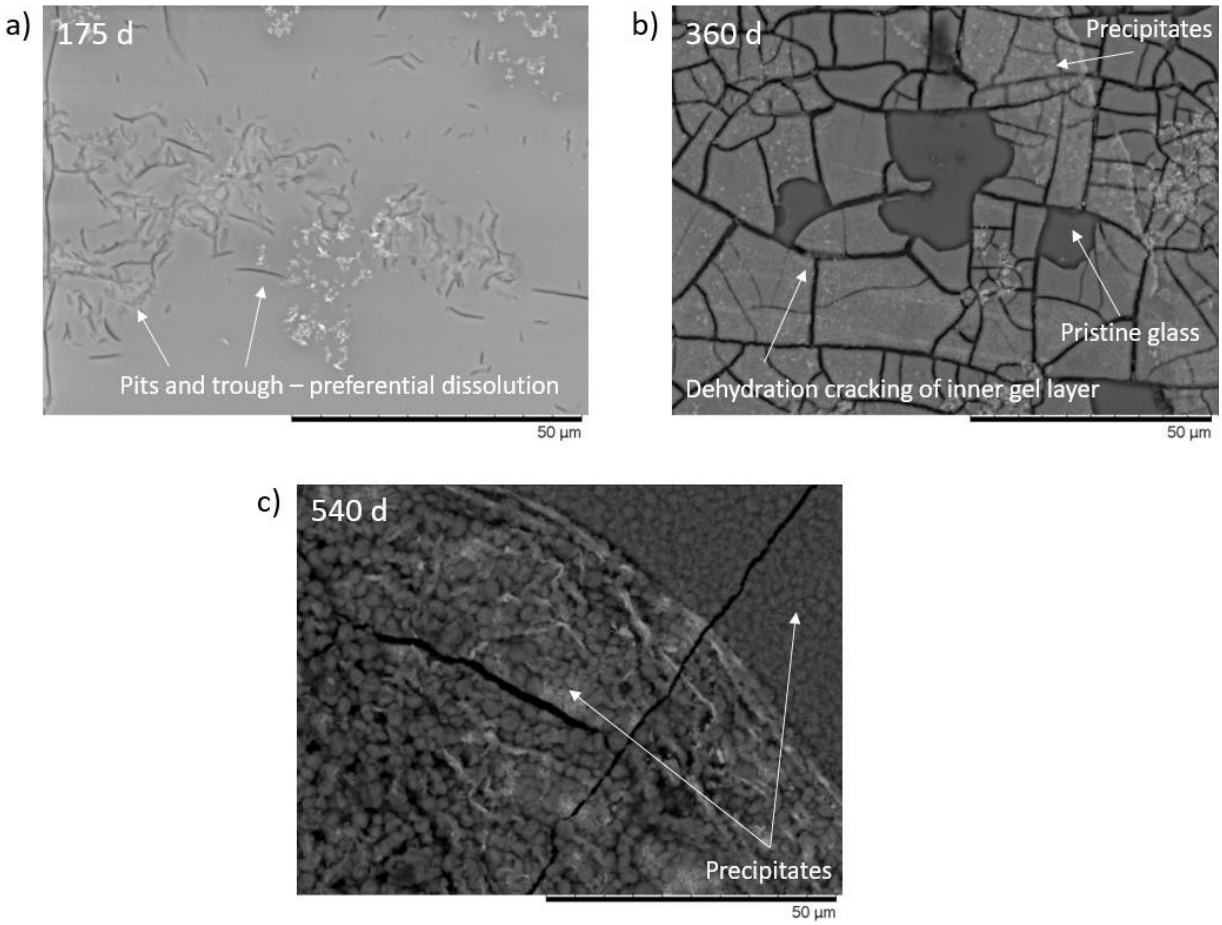

Figure 6.20. BSE-SEM of the top surface of ZnCa 40:60 MW28 monolithic samples after: a) 175 d; b) 360 d; and c) 540 d of dissolution in UHQ at 50 °C, SA/V = 10 m^{-1}.

Figure 6.20 shows the top surface of ZnCa 40:60 MW28 monolithic samples after 175 d (showing pits and troughs near identical to those observed by Kamizono 1985 who studied an MW-type inactive nuclear waste glass), 360 d (displaying secondary precipitates and a dehydrated gel layer) and 540 d (exhibiting clay-like surface morphology (Muller *et al.* 2006)) of dissolution and Figure 6.21 shows the XRD trace after 540 d. Note that the presence of secondary phases were not detected in XRD traces ≤ 360 d. There are clear additional reflections in the XRD pattern when compared with the pristine glass. Due to the broad nature of these peaks, suggesting the nanocrystalline nature of the precipitated phases, precise indexing is not possible (Curti *et al*. 2006, Guittonneau *et al*. 2011, Jolliveet *et al.* 2012). Several suggested phases that match the rough location of these broad reflections include $Zn_2(SiO_4)$ [PDF 85-0453] (potentially willemite – noting that this was absent from the XRD traces post 90 °C PCT-B tests (Fig. 6.12)), based on the peaks at 25.5, 31.6 and 34.0 °2θ, and the phyllosilicate clays - nontronite, sauconite and saponite. Again, these phases are partially consistent with PHREEQ-C geochemical modelling (Table 6.9 and Fig. 6.22).

Aréna *et al.* (2016) suggested that the precipitation of more than one silicate phase could have a multiplying effect on glass dissolution. For example, if the precipitation of Mg-silicate *and* Zn-silicate phases were to occur, the solubility of silica would be different than if only Mg-silicates were to form. Evidence to suggest such a multiplying effect may be based on the *second* observed increase in dissolution rate, which coincided with a reduction in NL_{Mg} from 360 d, and from the PHREEQ-C geochemical modelling, which predicted the formation of Mg-containing phases after 360 & 540 d only, whereas Zn_2SiO_4 was predicted to form throughout the entirety of the experimental duration (Table 6.9 & Fig. 6.22). Speculation may suggest that this second increase in dissolution rate after 360 d may not be observed in a Mg-free glass. Such multiplying (or additive) effects are noted in Chapter 7 of this Thesis.

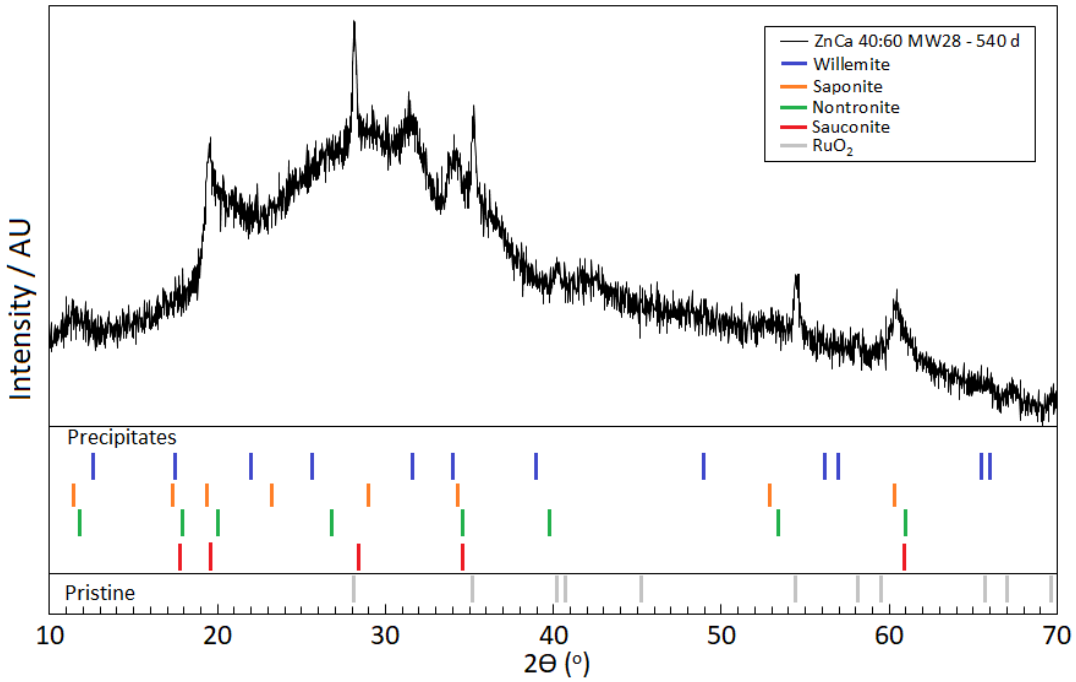

Figure 6.21. XRD trace of ZnCa 40:60 MW28 after 540 d MCC-1 dissolution in UHQ at 50 °C.

Table 6.9. Saturated mineral phases identified by PHREEQ-C geochemical modelling for ZnCa 40:60 MW28 subjected to 540 d MCC-1 dissolution at 50 °C in UHQ at SA/V = 10 m^{-1}. Note the omission of P and Zr containing phases due to the lack of elemental concentration data. Predicted phases limited to the contents of the database (LLNL).

Phases Identified from Lawrence Livermore National Laboratory database		
Phase	Chemical formula	Comments
Beidellite-Ca	$Ca_{.165}Al_{2.33}Si_{3.67}O_{10}(OH)_2$	Phyllosilicate - Smectite
Beidellite-H	$H_{.33}Al_{2.33}Si_{3.67}O_{10}(OH)_2$	Phyllosilicate - Smectite
Beidellite-Mg	$Mg_{.165}Al_{2.33}Si_{3.67}O_{10}(OH)_2$	Phyllosilicate - Smectite
Beidellite-Na	$Na_{.33}Al_{2.33}Si_{3.67}O_{10}(OH)_2$	Phyllosilicate - Smectite
Gibbsite	$Al(OH)_3$	-
Kaolinite	$Al_2Si_2O_5(OH)_4$	Phyllosilicate - Smectite
Laumontite	$CaAl_2Si_4O_{12}.4H_2O$	Zeolite
Mesolite	$Na_{.676}Ca_{.657}Al_{1.99}Si_{3.01}O_{10}.2.647H_2O$	Zeolite
Mordenite	$Ca_{.2895}Na_{.361}Al_{.94}Si_{5.06}O_{12}.3.468H_2O$	Zeolite
Prehnite	$Ca_2Al_2Si_3O_{10}(OH)_2$	-
Quartz	SiO_2	-
Saponite-Ca	$Ca_{.165}Mg_3Al_{.33}Si_{3.67}O_{10}(OH)_2$	Phyllosilicate - Smectite
Saponite-H	$H_{.33}Mg_3Al_{.33}Si_{3.67}O_{10}(OH)_2$	Phyllosilicate - Smectite
Saponite-Mg	$Mg_{3.165}Al_{.33}Si_{3.67}O_{10}(OH)_2$	Phyllosilicate - Smectite
Saponite-Na	$Na_{.33}Mg_3Al_{.33}Si_{3.67}O_{10}(OH)_2$	Phyllosilicate - Smectite
Scolecite	$CaAl_2Si_3O_{10}:3H_2O$	Zeolite
Sepiolite	$Mg_4Si_6O_{15}(OH)_2:6H_2O$	Sepiolite
Zn_2SiO_4	Zn_2SiO_4	Willemite Zn_2SiO_4 (suggested)

* Unidentified in LLNL database

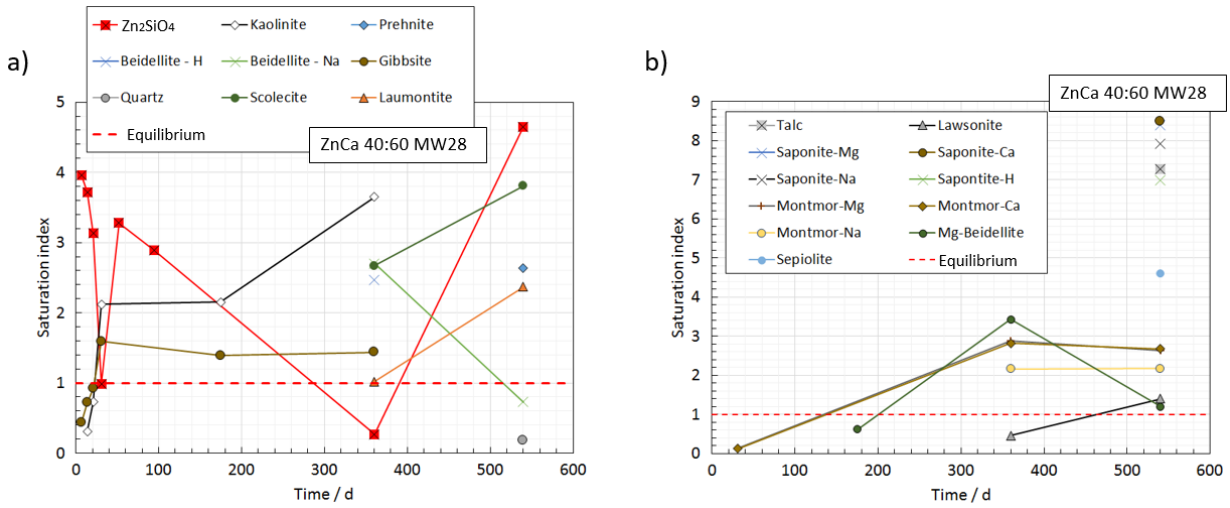

Figure 6.22. PHRREQ-C geochemical modelling and evolution from the solution data from the ZnCa 40:60 MW28 540 d MCC-1 experiments at 50 °C in UHQ at SA/V = 10 m^{-1}: a) phases consistent with base glass investigations in Chapter 5; b) phases unique to waste incorporated version.

Different alteration layer structures and compositions were observed after 360 and 540 d, as shown in Figure 6.23 and Table 6.10. The layers could be divided (working outwards from the pristine glass) into: a deep-inner layer (gel), an inner layer (gel) and an outer layer (precipitates). The inner layers were identified as gel layers (due to their visual nature, composition and lack of precipitated phases) and the outer layer was subsequently identified as secondary precipitates (from XRD Fig. 6.21).

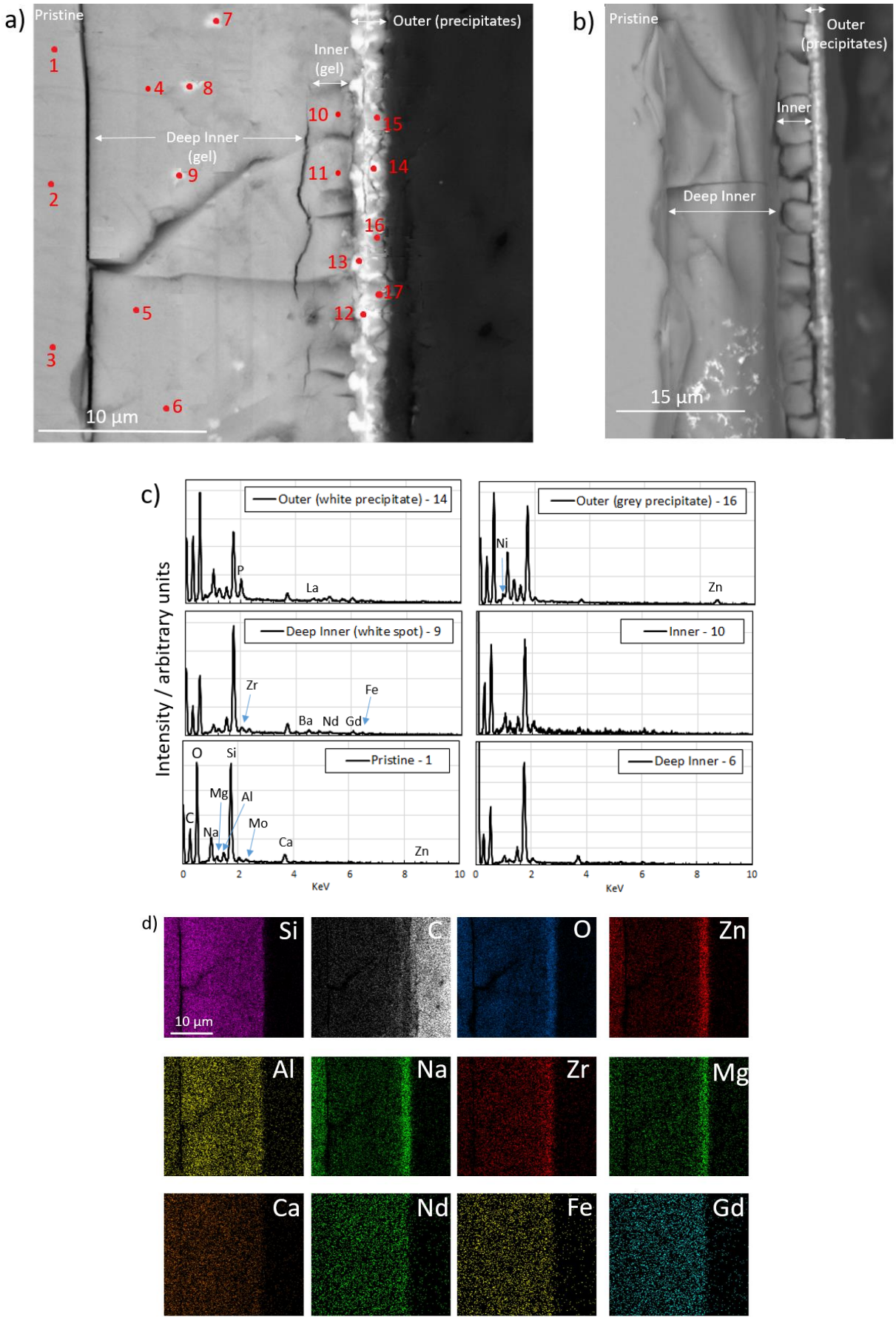

Figure 6.23. SEM and EDS mapping of ZnCa 40:60 MW28 after 540 d MCC-1 dissolution in UHQ at 50 °C: a) BSE cross section displaying EDS spots; b) BSE cross section displaying clear gel layer stratification; c) selected EDS counts and d) EDS mapping.

Table 6.10. Elemental At.% (top) and associated uncertainty (bottom) of the EDS spot mapping associated with Figure 6.23a for ZnCa 40:60 MW28 after 540 d MCC-1 dissolution in UHQ at 50 °C.

Element At. %

Section	Spot #	Si	Al	Na	Zn	Ca	Mg	P	S	K	Fe	Ni	Zr	Mo	Cs	Ba	La	Ce	Nd	Gd
Pristine	1	53.97	5.21	16.06	5.78	7.30	2.76	-	0.41	0.25	2.03	-	1.78	0.57	0.83	-	-	-	1.14	1.68
Pristine	2	56.46	5.44	15.39	5.31	8.52	2.36	-	0.55	0.00	1.65	-	1.55	0.75	-	-	-	-	-	2.04
Pristine	3	54.20	4.52	16.27	5.06	8.23	3.20	-	0.80	-	1.95	-	1.47	-	0.80	-	-	-	0.90	1.51
Deep Inner	4	65.22	9.44	1.00	3.02	9.34	0.57	-	0.36	0.43	3.59	-	2.88	-	-	-	-	-	-	3.78
Deep Inner	5	65.90	9.09	1.24	3.42	8.23	0.65	-	0.19	0.53	3.71	-	2.78	-	-	-	-	-	-	3.88
Deep Inner	6	66.10	9.19	1.05	4.06	7.01	0.71	-	0.79	0.50	3.06	-	2.34	-	0.16	-	-	1.63	-	3.71
Deep Inner (white spot)	7	58.15	8.17	0.71	3.43	7.06	1.09	-	3.94	0.27	4.07	-	2.96	-	-	3.41	-	1.47	1.47	3.47
Deep Inner (white spot)	8	60.60	8.22	1.05	3.84	7.66	0.51	-	3.18	0.26	3.66	-	2.87	-	-	2.92	-	-	1.77	3.05
Deep Inner (white spot)	9	60.70	8.67	1.35	3.48	8.15	0.38	-	2.63	0.10	3.33	-	2.36	-	-	3.11	-	-	1.43	3.96
Inner	10	61.31	5.74	7.27	5.51	5.17	0.01	-	-	-	4.87	-	4.4	-	-	-	-	1.75	1.53	2.43
Inner	11	57.95	7.15	10.93	5.13	4.65	0.73	0.53	-	-	2.95	-	4.23	-	-	-	-	0.75	2.18	2.82
Outer (white precipitate)	12	38.35	7.06	5.24	15.77	4.10	7.28	8.28	0.14	-	2.25	-	-	-	-	-	1.64	-	3.85	4.64
Outer (white precipitate)	13	40.57	7.07	2.49	13.74	5.59	5.05	9.50	0.22	0.13	3.19	-	2.12	-	-	-	-	-	4.96	4.99
Outer (white precipitate)	14	38.52	6.50	2.91	13.67	5.54	4.93	10.12	0.61	0.06	2.88	-	1.76	-	-	-	2.11	-	5.35	4.93
Outer (grey precipitate)	15	43.39	7.56	5.57	20.31	2.26	14.43	2.47	-	-	0.72	2.02	-	-	-	-	-	-	-	1.42
Outer (grey precipitate)	16	44.41	8.14	6.20	18.89	2.06	13.49	1.59	0.36	0.27	1.01	2.30	-	-	-	-	-	-	-	0.74
Outer (grey precipitate)	17	42.87	7.02	3.42	18.66	2.54	11.77	4.40	0.27	0.27	0.83	1.58	-	-	-	-	1.52	-	2.40	2.14

Element At. % (±)

Section	Spot #	Si	Al	Na	Zn	Ca	Mg	P	S	K	Fe	Ni	Zr	Mo	Cs	Ba	La	Ce	Nd	Gd
Pristine	1																			
Pristine	2	1.38	0.48	0.46	0.36	0.64	0.42	-	0.20	0.18	0.20	-	0.16	0.12	0.02	-	-	-	0.17	0.27
Pristine	3																			
Deep Inner	4																			
Deep Inner	5	0.46	0.18	0.13	0.52	1.17	0.07	-	0.31	0.05	0.35	-	0.28	-	-	-	-	-	-	0.08
Deep Inner	6																			
Deep Inner (white spot)	7							-												
Deep Inner (white spot)	8	1.45	0.28	0.32	0.22	0.55	0.38		0.66	0.09	0.37	-	0.33	-	-	0.25	-	-	0.19	0.46
Deep Inner (white spot)	9																			
Inner	10																			
Inner	11	2.38	1.00	2.59	0.27	0.37	0.51	-	-	-	1.36	-	0.12	-	-	-	-	0.71	0.46	0.28
Outer (white precipitate)	12																			
Outer (white precipitate)	13	1.24	0.33	1.48	1.19	0.84	1.32	0.94	0.25	0.04	0.48	-	0.25	-	-	-	0.33	-	0.78	0.19
Outer (white precipitate)	14																			
Outer (grey precipitate)	15																			
Outer (grey precipitate)	16	0.78	0.56	1.46	0.89	0.24	1.35	1.44	0.06	0.01	0.15	0.37	-	-	-	-	-	-	-	0.70
Outer (grey precipitate)	17																			

The *deep inner* gel layer was enriched in Ca and Al compared to the pristine glass and inner gel layer, where Ca is inferred to act as a charge compensator to $[AlO_4]^-$, potentially conferring a region of increased passivity to the gel. Based on knowledge of Ca-rich silica gels, in such a scenario this is likely to have the effect of decreasing pores sizes and densifying the gel, thus limiting the transport of elements and water through the gel layer (Utton *et al.* 2012, Maraghechi *et al.* 2016, Arena *et al.* 2018). The inner gel layer contained significantly less Al and Ca, which may have resulted from the transformation of these elements from the gel to secondary phases, or from loss into solution (Fig 6.23). The inner gel layer was enriched in Na, Zn and Zr compared to deep-inner gel layer, which contained bright spots enriched in Ba and S, which may be unidentified crystalline features in the pristine glass. The secondary precipitates could be separated into two distinct groups: (1) bright regions, which may be a mixture of two or more phases enriched in Si, Zn, Ca, P, Fe, Zr, Nd and Ga; and (2) darker grey regions, rich in Si, Zn and Mg, indirectly consistent with solution data and tentative XRD peak assignment of sauconite and saponite (Fig. 6.21). Images of the top surface of the monoliths post 175, 360 and 540 d are provided in Figure 6.20.

The spatial and temporal evolution of the alteration layer, as a function of depth, is shown in Fig. 6.24. At 360 d, which was the first time point at which the alteration layer was observed, only the inner gel layer (low in Ca and Al, but enriched in Na, Zn and Zr compared to the deep-inner gel layer) and outer layer (enriched in Mg and Zn) comprising secondary precipitates were present. In contrast, at 540 d the *deep inner* layer was observed for the first time, alongside an increase in thickness of the inner and outer precipitate layers. This suggests that during the second rate resumption, that occurred between 360 and 540 d, a significant proportion of Ca and Al were incorporated into the deep inner gel layer.

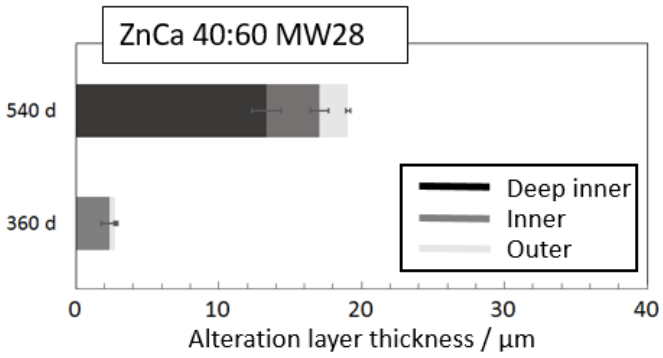

Figure 6.24. Alteration layer thickness evolution of ZnCa 40:60 MW28 after 540 d MCC-1 dissolution in UHQ at 50 °C. Note that pristine glass is represented at < 0 µm.

An increase in the thickness of the outer precipitate layer can be explained by an increase in the precipitation of Zn- and Mg-silicates as suggested by geochemical modelling (Table 6.9 & Fig. 6.22)

and by the potential precipitation of rare earth phosphates appearing at greater reaction progress (Table 6.10 & Fig. 6.23), in agreement with Ostwald ripening described in Section 6.2.2.2. Such an increase in the thickness of the outer precipitate layer coincides with the *second* dissolution rate increase. The increase in the thickness of the deep inner gel layer may be an indirect result of the increase in the outer precipitate layer and rate resumption. As precipitates form it is possible that they weaken the gel by consuming gel elements (Ca and Al) and alteration resumes. In such a scenario, with a rapid increase in dissolution, the gel may lose its passivating influence (or a latency period may exist before the gel restructures sufficiently to confer passivating properties – which, may be elucidated from post 1,000 d sample analysis). The resumption of alteration may lead to a dynamic alteration system, manifesting in complex altered layers, where gel restructuring may be required for Ca to charge compensate Al in the deep inner gel, which may reduce the passivating properties. Note that the NL_{Al} does not increase throughout the *first* and *second* increase in dissolution rate. Note also the concentration and behaviour of Na in both gel layers, and the increase in NL_{Na} with rate resumption: the deep inner gel layer is Na – poor, which means that Ca must be preferentially charge balancing Al in the deep inner gel.

Based on these observations (noting the near constant low dissolution rate for all elements < 35 d prior to the increase in NL_{Zn} (Fig. 5.19), which may represent an early residual rate), it is suggested that the hypothesis implied from the Zn-containing base glasses studied in Chapter 5 (including the two combined mechanisms extensively described in Section 5.3.4.2 – Chapter 5) – that the precipitation of Zn-silicate clays (Fig 5.35) cause *early* Stage III 'rate resumption', which is intrinsic to Zn-containing borosilicate glass compositions containing > 4.7 wt.% ZnO, without the effect of external influences – is applicable for waste loaded ZnCa 40:60 MW28. Noting that the precipitation of Mg-silicates at later time periods (associated with the drop in NL_{Mg} after 360 d) may maintain rate resumption. Further work is required to assess the alteration layer development during this process for the more complex waste loaded glass, however, it is apparent that the formation of Al-containing Zn- and Mg-silicates are linked to the increasing dissolution rates observed. The absence of zeolites in this process (and in Chapter 5), evidenced by the clear lack of zeolite formation in the XRD analysis (Fig. 6.21), SEM imaging (Figs. 6.20 & 6.23), geochemical modelling (Table 6.9, Fig. 6.22) and the mild alkalinity of the system (pH ≤ 9) (Fig. 6.19c), suggests that zeolite formation was not the cause of the rate resumption under these experimental conditions. The CSH phase - tobermorite - (recalling that CSH can cause Stage III rate resumption (Jantzen *et al.* 2013, Fournier 2014)), which was not predicted to form after 540 d from geochemical modelling, was not detected in alteration layers or in the XRD trace, however, later timepoints > 1,000 d may clarify the potential role of CSH on the dissolution.

6.2.2.5 PCT-B - Waste-loading effects on ZnCa MWXX, UHQ, 90 °C (Study C)

The durability of waste loaded (at different waste loadings: 20, 28 & 35 wt.%) VTR-fabricated ZnCa MWXX glasses, based on the NL_B and NR_B values over the course of the 112 d experiment, followed the trend from the most durable to the least durable of: ZnCa MW35 > ZnCa MW28 > ZnCa MW20 (Fig. 6.25 & Table 6.3). Results from MW25 (not containing Zn and Ca in the base glass), obtained from identical test conditions (Harrison 2014) are also shown for a comparison; this clearly shows that MW25 is more durable, based on the residual rate of dissolution, which was met and sustained at a low rate after 21 d (Table 6.3). However, earlier stages of dissolution, < 28 d, showed that the ZnCa MW glasses were more durable (Zhang *et al.* 2015, Cassingham *et al.* 2016) than MW25, which could be explained by the network forming role of Zn and its influence in providing greater resistance to hydrolysis. The decrease in NL_{Mg} (Figs. 6.25g & h) (1-35 d) (consistent with the ZnCa xx:xx MW28 results reported in Section 6.3.3.1 (Fig. 6.4h)) may represent the formation of secondary Mg-precipitates such as Mg-phyllosilicates, which were predicted to form by PHREEQ-C geochemical modelling of these solutions (data not shown). PHREEQ-C results after 112 d returned the same major phases predicted to form from the ZnCa xx:xx MW28 series presented in Figure 6.18 and Table 6.8. It was only possible to detect Zn in solution after 112 d due to the limits of elemental detection in the ICP-OES analysis; < 112 d it may be assumed that leached Zn precipitated as Zn-silicates. Such results suggest, taken collectively alongside a reduction in the NL_{Si} for the ZnCa MW series between 28 – 112 d, that the Stage III 'rate resumption' was potentially observed for ZnCa MW20 and ZnCa MW28 after 28 d, and for ZnCa MW35 after 35 d based on NL_B, again applying the extended definition of Stage III as hypothesied in Chapter 5.

The ZnCa 40:60 MW28 formulation (synthesised at TUoS, using a different ratio of waste calcine, as described in Section 6.2.2.1 and Table 3.3) is overlaid for completeness. This composition was more resistant to dissolution than the almost identical ZnCa MW28 waste composition, suggesting that the ratio of calcine blend has an influence on dissolution rate; in ZnCa 40:60 MW28 (75o:25m calcine) there was a lower quantity of Mg than ZnCa MW28 (50o:50m calcine) – 1.45 wt.% and 2.85 wt.%, respectively, which speculatively limited the quantity of secondary Mg-silicate precipitation, thus suppressing the rate of dissolution. Similarly, ZnCa MW28* is included in Figure 6.25b; these are data taken from an independent study by Harrison & Brown (2018) of ZnCa MW28 glass taken from the same melt as the composition investigated here. Near-identical dissolution behaviour offers good experimental validation for the present study (Fig. 6.25b).

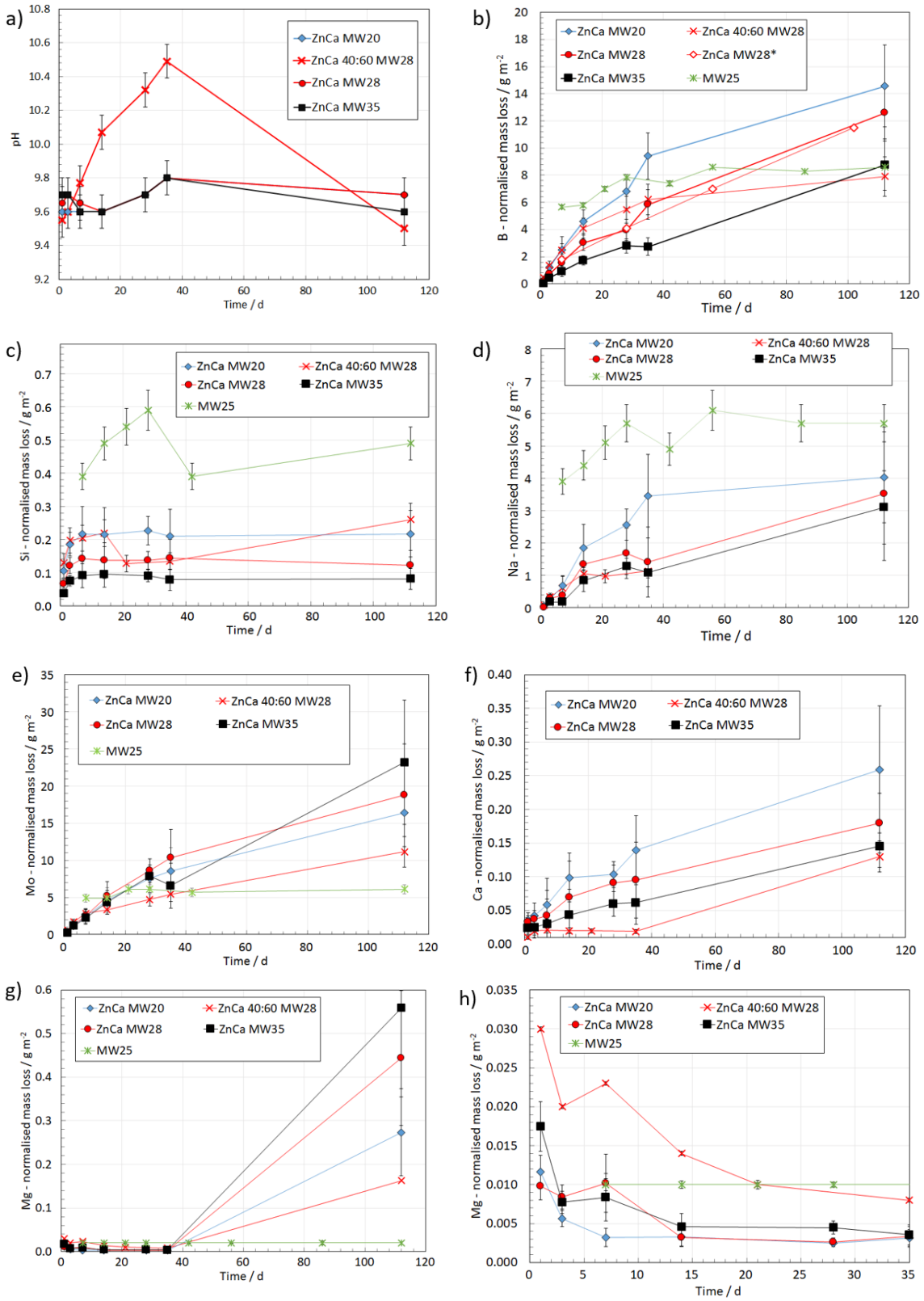

Figure 6.25. (a) pH(RT) measurements of the leachate; (b-h) normalised mass loss of elements for the full range of ZnCa MWXX compositions from the 90 °C, 112 d PCT-B experiments in UHQ and (g) an inset of the normalised mass loss of Mg from 1-35 d. MW25 results provided by Harrison (2014). Note that ZnCa MW28* is taken from an independent study by Harrison & Brown (2018) using identical ZnCa MW28 glass from the same melt. Also, note that the difference between ZnCa 40:60 MW28 and ZnCa MW28 is the waste calcine formulation; 75o:25m and 50o:50m respectively (Table 3.3).

A discrepancy between the pH evolution from the ZnCa MWXX series and ZnCa 40:60 MW28 (overlaid for comparison) was observed (Fig. 6.25a). The ZnCa MWXX pH measurements can be interpreted as maintaining a constant value within instrumental uncertainty throughout the experimental duration. The explanation for the pH evolution for ZnCa 40:60 MW28 was largely inconclusive, based on instrumental uncertainties (Section 6.2.2.1). However, consistency between both data sets is maintained at time periods ≤ 7 d and at 112 d, lending credence to the suggestion that the high pH measurements from 14-35 d for ZnCa 40:60 MW28 may have been incorrect. Despite this, pH evolution is expected based on the complexity of the secondary phases formed throughout the duration of the experiments (Jantzen *et al.* 2010, Fournier *et al.* 2014, Ojovan & Lee 2017), whereby the lower SA/V MCC-1 tests may reveal a more accurate pH evolution compared to the higher SA/V accelerated PCT-B tests which, due to the nature of the PCT-B tests (condensed evolution), may not be sensitive enough to capture a representative pH evolution over limited sampling time points.

EDS analysis and BSE-SEM images revealed the presence of gel layers overlaid with potential clay precipitates and unidentified secondary precipitates (due to the EDS signal been indistinguishable from the surrounding clay layer) on the surface of all particles from all compositions after 35 d, as shown in Figures 6.26-6.28. Since samples from 112 d were unavailable for SEM and XRD analysis, the identification of clays was based on the presence of a similar morphology (‘fuzzy blanket’) to the clays identified by Muller *et al.* (2006) and by a slight Mg-enrichment at the edge of the altered layer in the EDS map (Fig. 6.27g) (potentially indicative of Mg-silicate clays (Curti *et al.* 2006, Maeda *et al.* 2011, Thien *et al.* 2010)), on samples after 35 d leaching.

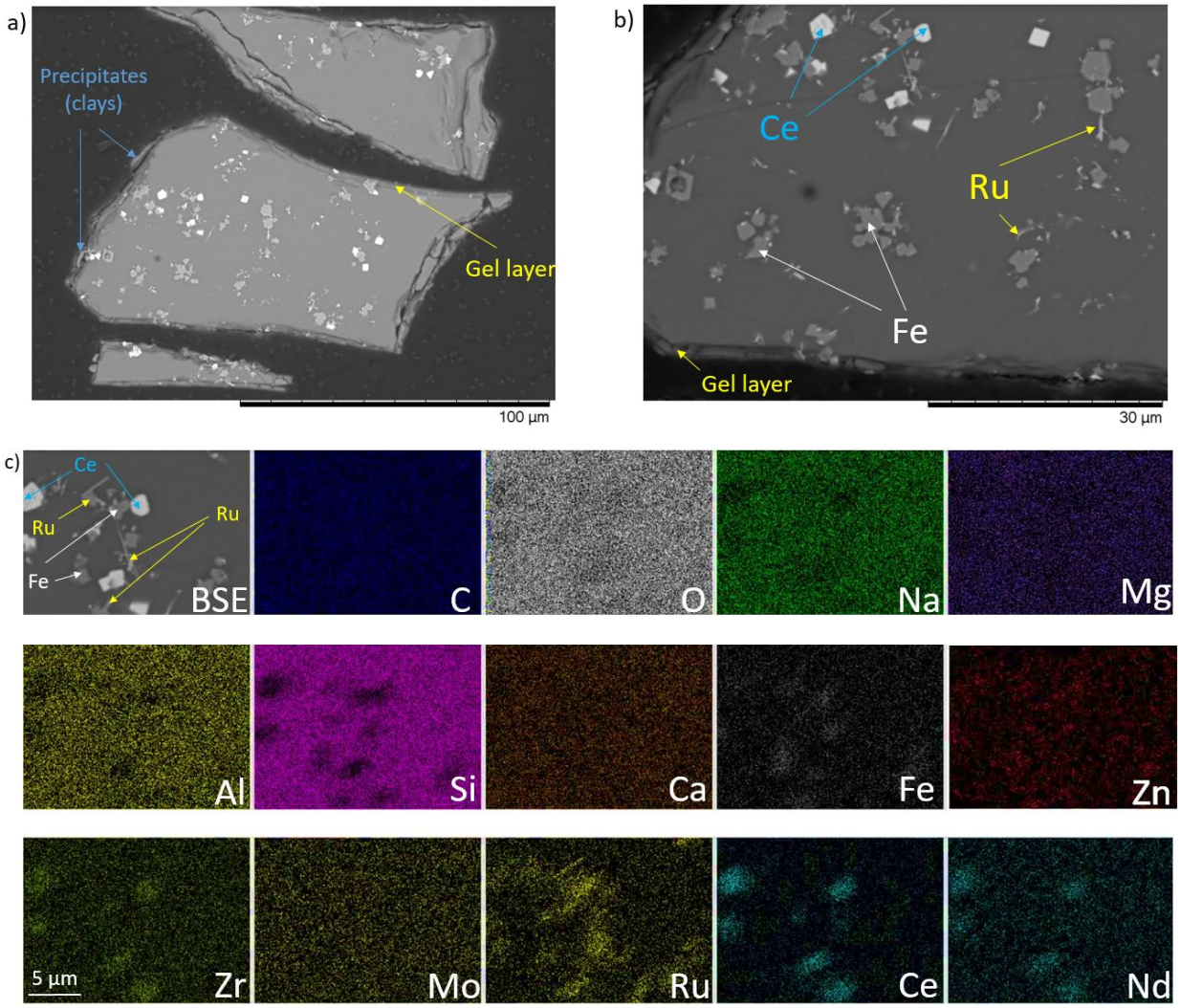

Figure 6.26. SEM and EDS mapping of ZnCa MW35 after 35 d PCT-B dissolution in UHQ at 90 °C: a-b) overview BSE cross section displaying surrounding gel layer, secondary precipitates and expected crystalline inclusions in the pristine glass (Ce, Fe and Ru); c) EDS mapping of the pristine glass.

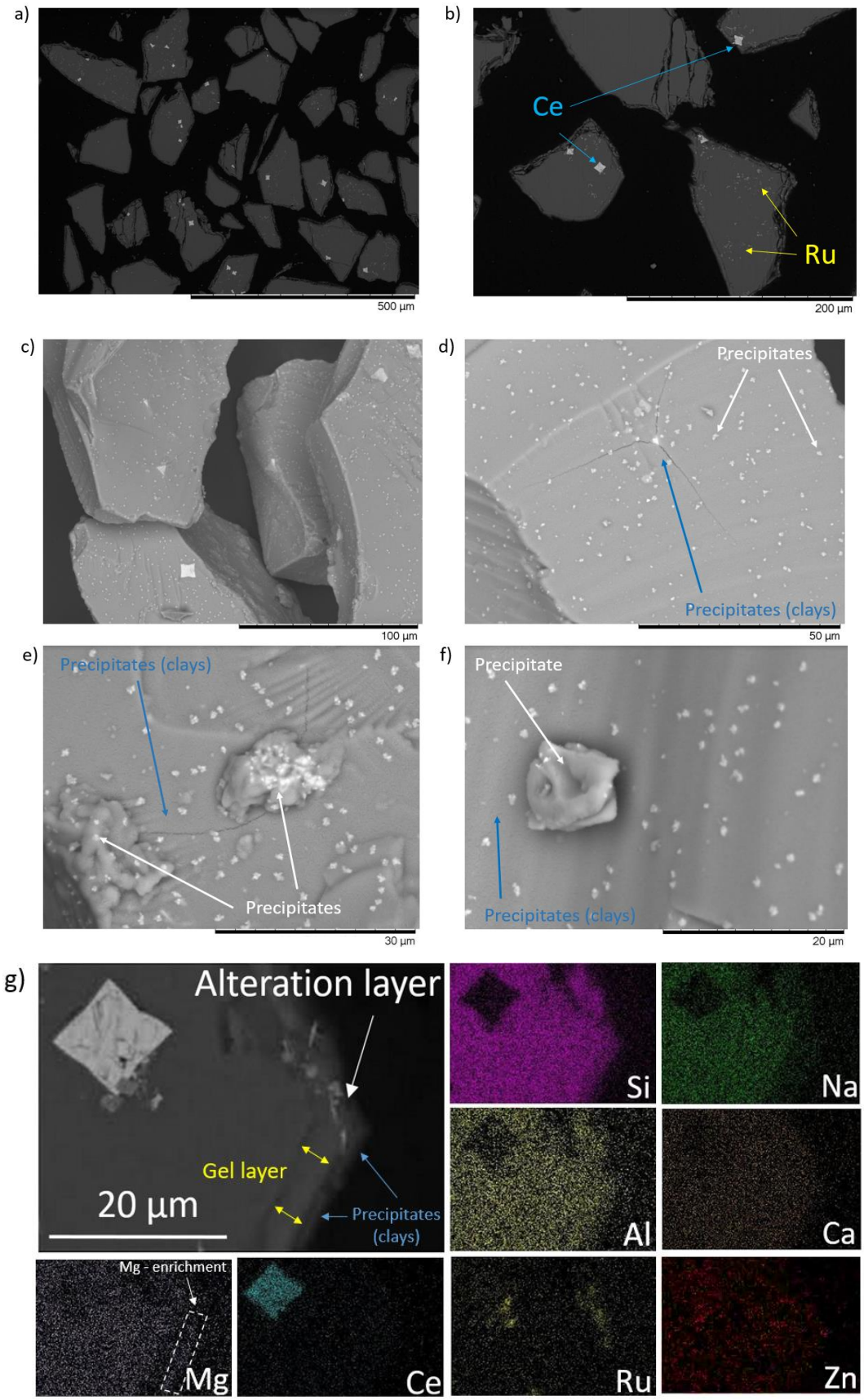

Figure 6.27. SEM and EDS mapping of ZnCa MW28 after 35 d PCT-B dissolution in UHQ at 90 °C: a-b) overview BSE cross section displaying surrounding alteration and crystalline inclusions in the pristine glass (Ce and Ru); c-f) surface features displaying clay layer and unidentified secondary precipitates and g) EDS mapping of a cross-sectioned particle illustrating the gel layer and precipitate clay layer.

Alteration layer thickness (including total gel and secondary precipitates) correlated with the extent of dissolution: the thicker alteration layer correlated with the least durable glass, following along the sequence of ZnCa MW20 (5 ± 3 µm) > ZnCa MW28 (4 ± 1 µm) > ZnCa MW35 (2 ± 1 µm), in accordance with glass dissolution theory (Frugier *et al.* 2008, Vienna *et al.* 2013). Note, as previously mentioned that such alteration layer thickness measurements are loose approximations due to the inherent uncertainty in particle orientation. A study by Brookes *et al.* (2011) suggests that the higher alumina content in glasses with greater waste loading may improve the durability by allowing the passivating gel to form at earlier periods in the dissolution process. Such reasoning may be applicable to this study, however further analysis of the gel layer, for example by TEM/EDS is required to strengthen this hypothesis.

Alteration layer compositions and secondary precipitates were assumed to be similar for all compositions in the ZnCa MWXX series (Fig. 6.27g), which is suggested based on similar glass compositions that only varied in terms of their waste loading. It was difficult to identify the chemical composition of the altered layers and precipitated phases on ZnCa MW35 at the resolution employed on the 35 d altered samples (Figure 6.27 d-f). Future work using micro-focus XRD may confirm the identity of such phases. XRD analysis of the ZnCa MWXX series after 35 d PCT-B tests revealed no evidence for secondary phase precipitation (presumably due to their low abundance) (Fig. 6.29), despite been clearly evident from the SEM analysis (Figs. 6.26 – 6.28).

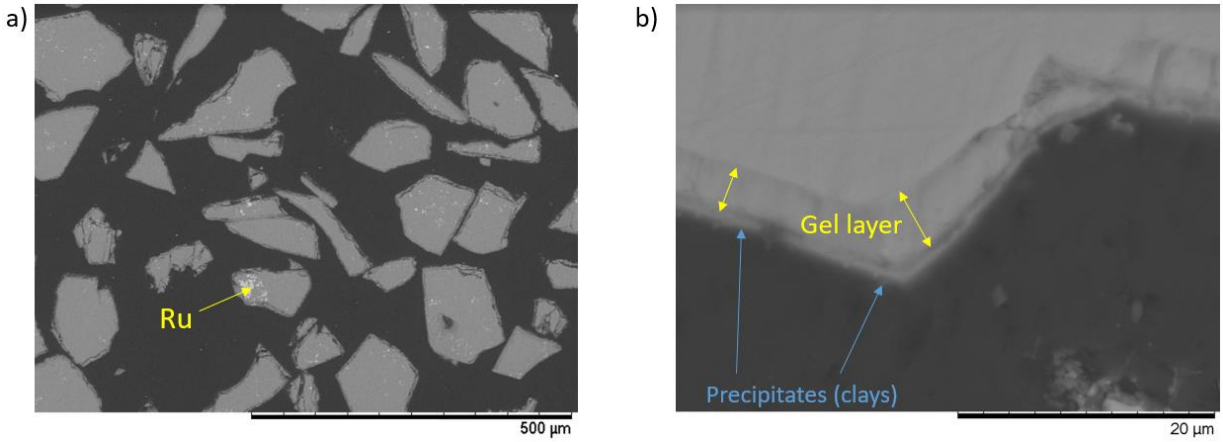

Figure 6.28. SEM of ZnCa MW20 after 35 d PCT-B dissolution in UHQ at 90 °C: a) overview and b) BSE cross section displaying surrounding gel layer and clear smectite clay layer.

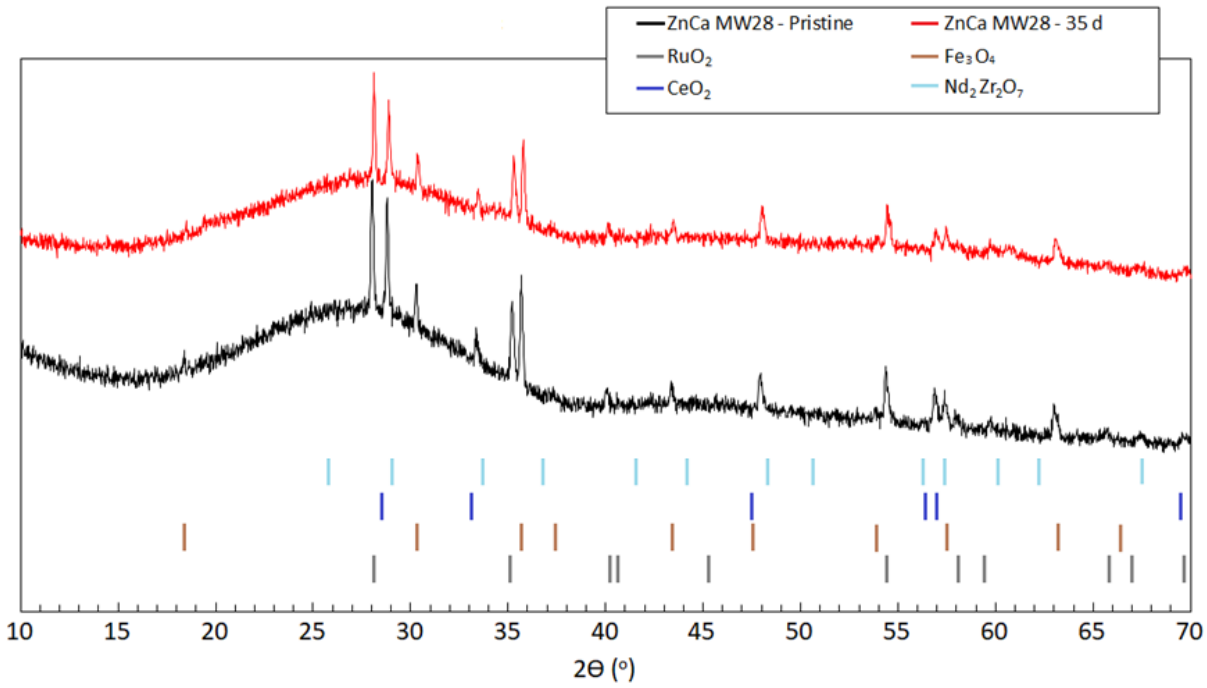

Figure 6.29. XRD traces of ZnCa MW28 pristine (black trace) and post 35 d PCT-B leaching at 90 °C in UHQ water (red trace). Note that significant overlap of the peak positions. Crystalline inclusions are strengthened by EDX measurements (Figs. 6.26-6.27).

6.3 Discussion

6.3.1. Effect of ZnO:CaO ratio in wasteloaded glasses (Study A & B)

Results from the 112 d PCT-B tests (Fig. 6.4 & Table 6.3) clearly indicated that the Ca-rich ZnCa 0:100 MW28 composition exhibited much greater chemical durability by having reached and sustained residual rate (Stage II) dissolution, likely due to the passivating effect of Ca incorporation into the altered gel layer (Chave *et al.* 2011, Corkhill *et al.* 2013, Utton *et al.* 2013, Aréna *et al.* 2018). Such results were consistent with the PCT-B base glass investigations reported in Chapter 5.

The lack of Mg-silicate precipitation after 112 d on the Zn-free ZnCa 0:100 MW28 glass can be attributed to the high chemical durability due to the passivating Ca-rich gel layer. Here, Si is retained in the glass matrix and gel and is thus not released in sufficient quantities to induce the precipitation of Mg-silicates. Thus, a large fraction of Mg is assumed and partially observed to be retained in the altered gel layer playing a charge compensatory role (Table 6.7 and Fig. 6.16) (Thien *et al.* 2012). Note that the concentration of Mg in the gel layer of ZnCa 0:100 MW28 was greater than in the gel layer of ZnCa 40:60 MW28 (Table 6.7 & 6.6 respectively). Mg-silicates are always reported to precipitate in

abundance in dissolution studies of the Ca-free MW25 glass (Curti *et al.* 2006, Brookes *et al.* 2011, Backhouse 2016, Goût *et al.* 2019), whereby the presence of Mg is responsible for the poor chemical resistance of UK HLW waste glass at greater reaction progress due to sustaining a moderately high Stage II residual rate of dissolution (Table 6.3) (Curti *et al.* 2006, Brookes *et al.* 2011, Harrison 2014, Schofield *et al.* 2017). This investigation suggests that the presence of Ca may indirectly reduce the potential for the formation of Mg-silicates, thus inferring greater chemical durability for ZnCa 0:100 MW28 compered to standard MW25.

The chemical durability of ZnCa 100:0 MW28 and ZnCa 40:60 MW28 is thus controlled by the precipitation of Zn-silicates and potentially Mg-silicates. Such an adverse effect could be additive as suggested by the MCC-1 study reported in Section 6.2.2.4 and by Aréna *et al.* (2016), which is to the further detriment of the long-term durability of UK HLW, noting that ZnCa 40:60 MW 28 and ZnCa MW28 contained a combined MgO and ZnO total of 6.17 and 7.22 wt.% respectively.

6.3.2. Effect of wasteloading (Study C)

Clear evidence was provided, which demonstrated that all Zn-containing MW-glass (including various waste loading types) were less durable over longer timescales when compared to standard MW25 (Figs. 6.4a & 6.25b, Table 6.3) due to the aggressive precipitation of Zn- (and Mg-) silicate phases (Gin *et al.* 2013, Aréna *et al.* 2016). An argument can thus be made regarding the exclusion (or limited inclusion) of Zn in the MW base glass formulation. However, this must be reconciled with the beneficial effects of Zn in the melting and processing (Short *et al.* 2008). The beneficial effect of Zn inclusion on Stage I chemical durability is consistent with the base glass studies described in Chapter 5 and is consistent (as well as an extension, in terms of exploring greater reaction progress) to the results of Matlack *et al.* (1998) and Zhang *et al.* (2015), who suggested that ZnCa MW-glass conferred greater durability than MW25 in the short term ≤ 28 d. Note that the compositions studied by Zhang *et al.* (2015) contained waste loading contents of 15 & 20 wt.%.

The effect of increased waste loading on the durability of UK HLW has not been studied extensively in the literature (Brookes *et al.* 2011, Harrison 2014), but it is tentatively suggested that increased waste loads confer greater durability because:

1) Such compositions generally contain less alkali/alkaline earth, therefore less $^{[4]}$B and Q3 Si units are formed, therefore the network should be more connected and more resistant to hydrolysis. Noting that hydrolysis reactions still occur at the interface between the pristine glass and the altered gel layer.
2) A fraction of waste components may act as network intermediates, whereby the transition metals may be playing a network forming role, therefore the network should be more connected and more resistant to hydrolysis.
3) Increased levels of waste loading may induce better melt homogenization, thus negating micro-domain phase separation and the resulting alkali-rich regions, which may be more susceptible to dissolution and act as 'nucleating dissolution sites' as inferred from Chapters 4 & 5. Future work using the SPFT method may elucidate such a suggestion.
4) Increased levels of Al in higher waste loaded glass may improve the chemical durability by allowing the passivating gel layer to form at earlier time periods in the dissolution process (Brookes *et al.* 2011). Future work on simple waste glasses with varying Al incorporation may elucidate this suggestion.

In terms of industrial and disposal considerations, this work identified the ZnCa 0:100 MW28 glass (Zn-free and Ca-rich) to be the most suitable glass in terms of its chemical durability. Such a glass could display similar, if not, better chemical durability with an increased 35 wt.% waste incorporation based on the application of the results from the waste load variation study. Hence, ZnCa 0:100 MW35 glass may be the most suitable glass composition for the eventual incorporation of POCO waste. Future work is needed to validate such a claim, which could trial various Ca-contents, because Ca may, in some cases, have the potential to trigger Stage III 'rate resumption' by inducing the precipitation of CSH phases (Jantzen *et al.* 2010).

6.3.3. Rate Resumption - Stage III

An important area of discussion relates to the justification of the possible attribution of Stage III behaviour, according to the classical definition, to corroding ZnCa MW-type glass. The question arises: is Stage III observed for some Zn-containing glass (Figs. 6.4a, 6.19a & 6.25b), or is such behaviour aggressive runaway residual rate Stage II dissolution? The dissolution plots, particularly from the MCC-1 investigation of ZnCa 40:60 MW28 and the base glass MCC-1 investigations described in Chapter 5, suggest that Stage III has been observed with the hypothesis that the precipitation of Zn-silicate clays

are associated with (and potentially cause) *early* Stage III 'rate resumption', which is intrinsic to Zn-containing borosilicate glass compositions containing > 4.7 wt.% ZnO. Such a hypothesis is likely valid for ZnCa 40:60 MW28, whereby the precipitation of Mg-silicates at later time periods (noting the drop in NL_{Mg} after 360 d (Fig. 6.19a)) may have maintained the rate resumption. However, future work involving Zn- and Mg-clay-seeding experiments may provide some clarity to the suggested hypothesis.

Importantly, the accelerated nature of PCT-B tests conducted on the base glass series (Chapter 5), the ZnCa xx:xx MW28 and the ZnCa MWXX series may have shown potential evidence to *suggest* Stage III 'rate resumption', but may not have been sensitive enough to *confirm* the dissolution trend, such as been indistinguishable from aggressive residual rate (Stage II) within experimental uncertainty (Figs. 6.19a & 6.25b).

6.3.4. Geochemical Models

This work presents new knowledge on the secondary phases that are likely to form from the dissolution of ZnCa MW-type glasses. Such phases were dominated, and empirically evidenced by Mg and Zn-containing smectites (Mg-containing beidellite, nontronite and saponite and Zn-containing sauconite). Such alignment with thermodynamic databases is consistent for the Mg-phases, however, a lack of Zn-bearing phases in the databases hinder modelling predictions. A misalignment of databases and empirical evidence applies to the secondary Zr, P, Mo and rare-earth phases (Figs. 6.10, 6.11 & 6.14). Suggested future work could involve an updating of thermodynamic databases to include phases that contain elements identified (by EDS) in the precipitated phases in this work. Future ZnCa MW formulations incorporating POCO waste streams will contain much greater Mo content (<10.3 wt.% (Harrison 2018)) and waste loadings, which, based on preliminary analysis from this work and the abundant literature (Muller *et al.* 2006, Frugier *et al.* 2008, Jantzen *et al.* 2010 & Fournier *et al.* 2014), may have a greater probability of participating in secondary precipitation and to a hypothesised greater magnitude.

6.4 Conclusion

This investigation highlighted that the dissolution rate of MW-type simulant HLW glasses were increased by the addition of ZnO and CaO compared to standard MW25, demonstrated through PCT-B experiments performed for 112 d at 90 °C in UHQ water. However, greater chemical durability was observed for the Zn-free ZnCa 0:100 MW28 composition compared to MW25 (Study A). The PCT-B results also confirm previous findings for MW25 glasses that increasing the waste-loading in ZnCa MW from 28 to 35 wt.% improves the chemical durability (Study C). The formation of Zn-silicates (particularly the phyllosilicate, sauconite) and potentially Mg-phyllosilicates (saponite/nontronite/beidellite) played a role in driving the dissolution rate to behaviour analogous to Stage III. This was particularly evident from the Stage III 'rate resumption' observed in the MCC-1 test performed for 540 d at 50 °C in UHQ water for ZnCa 40:60 MW28 (Study B), which exhibited similar dissolution behaviour to its base glass counterpart investigated in Chapter 5, thus strengthening the hypothesis that the precipitation of Zn-silicates cause early Stage III 'rate resumption'. Results therefore suggest that Stage III can occur outside the generally accepted bounding experimental conditions of pH values ≥ 10.5 and or temperatures ≥ 90 °C (Gin & Mestre 2001, Ribet *et al.* 2004, Fournier *et al.* 2014) and resultant zeolite and CSH precipitation (Sang *et al.* 1992, Feng *et al.* 1993, Inagaki *et al.* 2002 & 2006) for waste-loaded glass.

Such conclusions are applicable to PCT-B and MCC-1 dissolution tests performed in Teflon vessels, which are permeable to CO_2, which can thus suppress the pH and reaction pathway for *some* glass compositions (Xing and Pegg 1994). It therefore remains inconclusive if such effects are applicable to the ZnCa MW glasses studied here. For a fully descriptive and robust performance assessment (Ewing 2020) of the dissolution behaviour it is recommended to conduct all future experiments under an inert N_2 atmosphere. However, recent investigations show that the reaction pathway under anoxic and oxic conditions, based on the $NL_{B,\ Si\ \&\ Na}$ for similar ZnCa MW waste glass compositions (and MW) are near identical based on 35 d PCT-B tests (40 °C, UHQ) (Fisher & Corkhill 2021) (Appendix 6.5 III).

Results presented in this Chapter demonstrated wasteloaded ZnCa MW glass durability in clean UHQ water dissolution experiments, which enabled the underpinning of the fundamental mechanism. However, evaluation of the durability performance in geological respoitory environments, including the influence of buffer materials, backfill, host rock-type, cannister corrosion products and groundwater solutions will most likely be a fundamental requirement of all safety assessments and is

attempted in Chapters 7 and 8. Until such findings are delivered, any safety assessment will remain incomplete (Mayer 2019).

6.5 Appendix

I - Technical Waste

Technical waste is waste derived from the process that is HLW but not a planned glass product. This basically falls into two categories; 1) the bases of melter crucibles and 2) filters from the pour extract system which are heavily contaminated by Cs (probably as $CsTcO_4$). To date Technical Waste has not been generated, but there is such material which will need to be dealt with in the future. The glass removed from failed melter crucibles will be exported to the vitrification processing site at some future point, which will most likely be loosely filled within a standard container rather than been remelted (Gribble 2018). The container type will probably be standard (neck flange and lid) rather than opening at the shoulder. The bulk density of such container contents will be ~0.5x that of the poured glass containers.

II - ZnCa 40:60 MW28 showing the Ru & Mo phase dispersed throughout the borosilicate glass matrix representative of ZnCa 100:0 MW28 & ZnCa 0:100 MW28

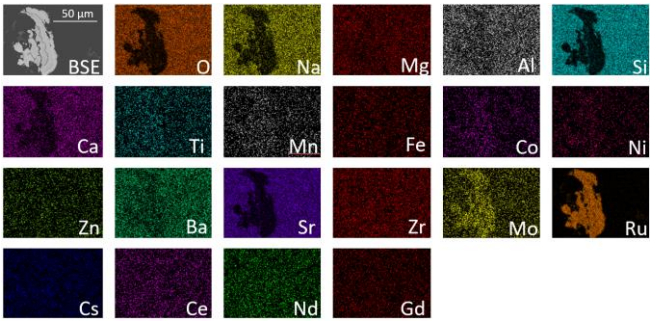

III - Butex CaZn & MW PCT-B (40 °C, UHQ) NL_B data

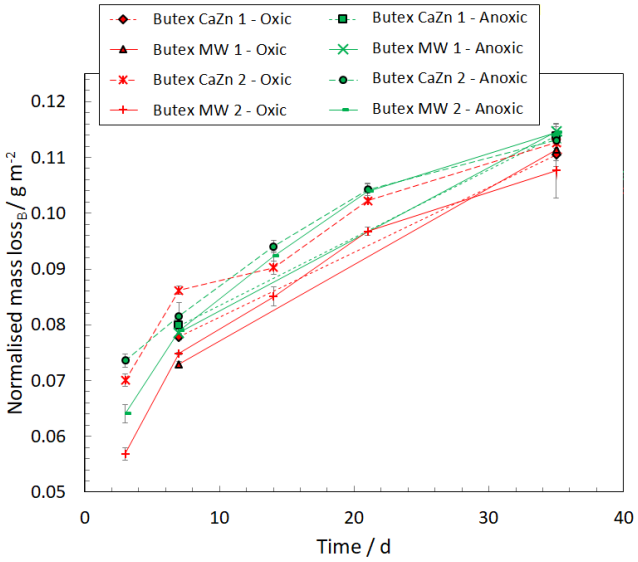

7. The dissolution of simulant waste-loaded ZnO/CaO modified base glass for UK High-Level-Waste in groundwater solutions

Summary

Note to reader – this short chapter is reproduced, in-part from the short communication manuscript published in the Journal of Nuclear Materials:

Adam J. Fisher, Mohammed N. B. Imran, Colleen Mann, Clémence Gausse, Russell J. Hand, Neil C. Hyatt & Claire L. Corkhill. Short Communication: The dissolution of UK simulant vitrified high-level-waste in groundwater solutions. *J. Nucl. Mater*. **538**, 152245 (2020).

This study highlights the fact that different groundwaters (GW) exert a subtle influence on the short-term dissolution rate of ZnCa 40:60 MW28 glass during PCT-B tests compared to dissolution in UHQ water over 35 d at 50 °C, following the trend, from the least to most durable: clay GW > UHQ water > granite GW ≈ saline GW. Rapid Mg-silicate precipitation, enhanced by Mg-containing groundwater (particularly clay GW), as predicted by geochemical modelling of the solutions and tentatively identified by SEM/EDS, was the likely reason for elevated dissolution rates, preventing the formation of a passivating silica gel layer. Additive Mg- and Zn-silicate precipitation is suggested to the further detriment of the chemical durability

7.1 Introduction

This study aims to evaluate the influence of different simulant groundwater solution compositions, compared with initially pure water, on the dissolution rate of ZnCa 40:60 MW28 glass (composition presented in Table 3.3 – Chapter 3) in a short-term accelerated PCT-B leaching experiment, and to identify the role of secondary phases in the dissolution mechanism. There remains uncertainty with regard to the chemical durability of ZnCa-glass, especially under conditions representative of geological disposal, including in groundwater and at expected temperatures. The presence of Mg, as both a glass component and a key constituent of groundwater, is known to trigger the formation of secondary phases, which accelerate glass corrosion (Curti *et al.* 2003 & 2006, Thien *et al.* 2010, Maeda

et al. 2011, Jollivet *et al.* 2012, Fleury *et al.* 2013). Furthermore, similar effects have been observed for glasses incorporating even small quantities of Zn (Gin *et al.* 2013), as demonstrated in Chapter 5. The combined effect of Mg- and Zn- in a vitrified wasteform such as ZnCa MW28 has not been thoroughly investigated, as such, this Chapter aims to advance the field using the PCT-B test at 2,000 m^{-1} (ASTM 2014), conducted at 50 °C in ultra-high-quality (UHQ) water (18.2 MΩ cm) (initial pH(RT) 7.2) and three simulant groundwater solutions (clay, granite and saline (Table 7.1 reproduced from Table 3.8, Chapter 3)).

Table 7.1 Composition of three synthetic solutions representative of generic repository groundwaters (GW) (Vasconcelos *et al.* 2018).

Element	Concentration (mmol L^{-1})		
	Granitic GW (Gascoyne 2002)	Saline GW (Gascoyne 2002)	Clay GW (Vinsot 2008)
Na	2.8	140	55
K	0.1	2.1	1.1
Ca	0.5	19.9	7.5
Mg	0.2	0.4	5.7
Cl	2.1	173	52.5
HCO_3	2.0	2.0	-
SO_4^{2-}	0.1	4.0	15
SiO_2	0.2	-	-
pH(RT)	8.2	7.7	6.5

7.2 Results and Discussion

The measured NL_B (commonly used as an indicator for glass corrosion since boron does not participate in alteration layer formation), showed that dissolution of ZnCa MW28 glass followed the trend, from the least to the most durable after 35 d: clay > UHQ > granite ≈ saline (Fig. 7.1a). The dissolution rates of boron, NR_B, are presented in Table 7.2.

The NL_{Si} (Fig. 7.1b) increased rapidly before slowing; this is typically observed when glass undergoes the 'rate drop' caused by the formation of a passivating silica gel layer before transition into the residual rate (Stage II) of dissolution (Gin *et al.* 2012). However, the NL_B data indicated that there was no rate drop (except for the saline test). Considering that the glass dissolved at a linear rate, approximating an initial rate (Stage I), this behaviour can be attributed to rapid saturation of the solutions with respect to silica, and the almost immediate precipitation of secondary silicate phases,

thus preventing the formation of a passivating silica gel layer and allowing dissolution to proceed at a rapid rate. In previous studies, the drop in NL_{Si} was attributed to the formation of Mg-silicate phases (Maeda *et al.* 2011, Jollivet *et al.* 2012). Indeed, there was a decrease in the NL_{Mg} (Fig. 7.1d) for the clay, UHQ and granite solutions. It seems reasonable to suggest that the formation of secondary Mg-silicate phases may, therefore, drive enhanced glass dissolution, at a relatively rapid rate (similar in magnitude to the 'initial' rate, governed by silicate network hydrolysis), with the source of the Mg from both the solution and the glass (since this behaviour was also observed in UHQ where the only source of Mg was the glass).

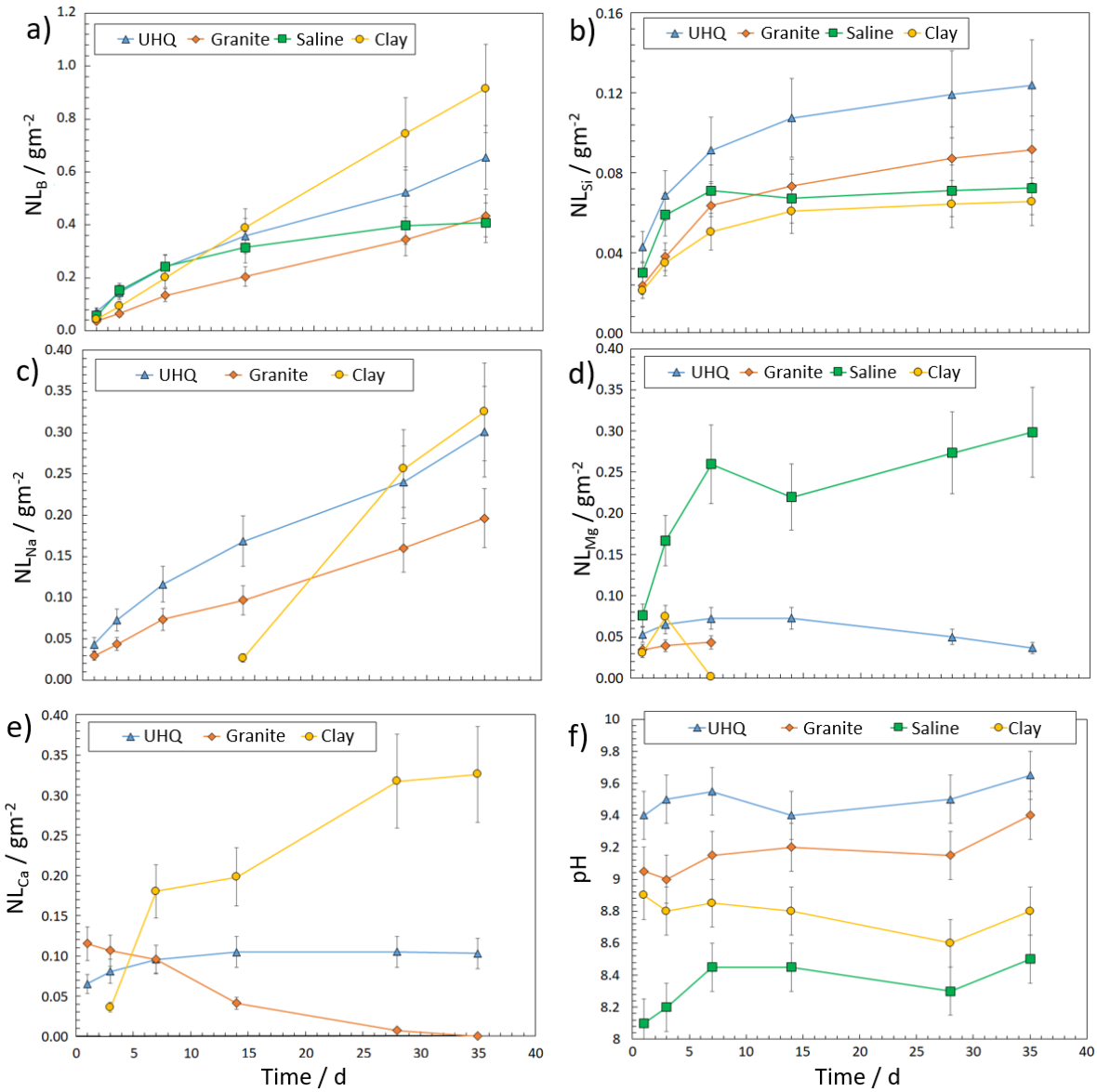

Figure 7.1. (a-e) Normalized mass loss (NL) of elements, *i*, from ZnCa MW28 particles during 35 d PCT-B leaching at 50°C in various groundwater compositions (errors bars were calculated from the sum of uncorrelated random errors); and f) pH(RT) measurements of the leachate ($pH(RT)_{t=0}$: UHQ 7.2, granite 8.2, saline 7.7, clay 6.5).

In contrast, for the saline groundwater, the NR_B was considerably lower, suggesting that the dissolution reaction of the glass in this solution was passivated by the formation of a silica gel layer, as typically observed in borosilicate glass dissolution. This was confirmed by the NL_{Si} data (Fig. 7.1b), which reached a residual rate at ~7 d. It is interesting to note that in this solution, the NL_{Mg} *increased*, rather than decreased. This is discussed further below.

Table 7.2. Normalised dissolution rate of boron (NR_B) calculated between 1 and 35 d for ZnCa 40:60 MW28 using a chi-square fit and between 14 and 35 d for the saline groundwater solution (since this was the linear part of the dissolution reaction).

Solution	B dissolution rate 1 - 35 d (NR_B / g m^{-2} d^{-1})	R^2
Clay	(2.82 ± 0.23) x 10^{-2}	0.999
UHQ	(2.43 ± 0.32) x 10^{-2}	0.882
Granite	(1.54 ± 0.12) x 10^{-2}	0.994
Saline	(1.67 ± 0.14) x 10^{-2}	0.421
Saline 14-35 d	(0.46 ± 0.42) x 10^{-2}	0.947

Analysis of the surface of the glass after 35 d dissolution by SEM / EDS (Fig. 7.2 & 7.3) confirmed the enrichment of Mg (and Al) at the surface of the glass leached in clay groundwater, and a series of precipitates, approximately 2-5 µm in size, with a clay-like morphology (Gin *et al.* 2013, Aréna *et al.* 2018), which were first observed after 28 d of dissolution (Figures. 7.2 & 7.3a-b). X-ray diffraction (Fig. 7.4) analysis of glass dissolved for 35 d in each of the solutions did not reveal distinct crystalline phases (except for halite (NaCl), PDF 02-0818, in the saline groundwater), which is unsurprising given the low quantity of surface precipitates. Crystalline RuO_2 (PDF 21-1172) was observed in the pristine glass and in all glasses after 35 d of leaching; this is an expected feature of the waste glass being studied. It was not possible to observe a silica gel layer on the surface of the glass samples at the resolution employed, with the possible exception of the glass corroded in the saline solution which, after 35 d, appeared to show a 'peeled' dehydrated gel layer with the glass surface underneath (Fig. 7.3d).

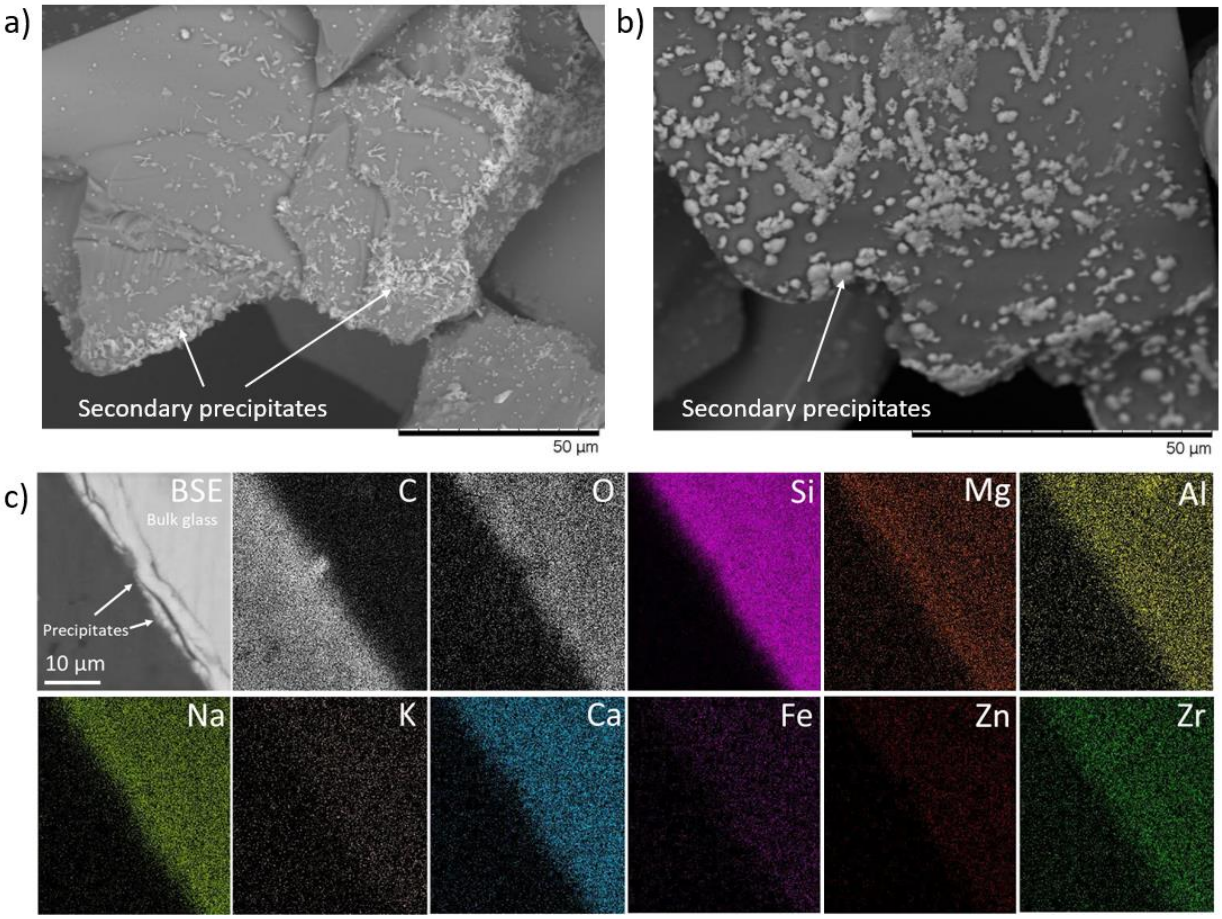

Figure 7.2. (a & b); BSE-SEM images and; (c) elemental mapping from ZnCa 40:60 MW28 after 35 d leaching at 50 °C in clay groundwater.

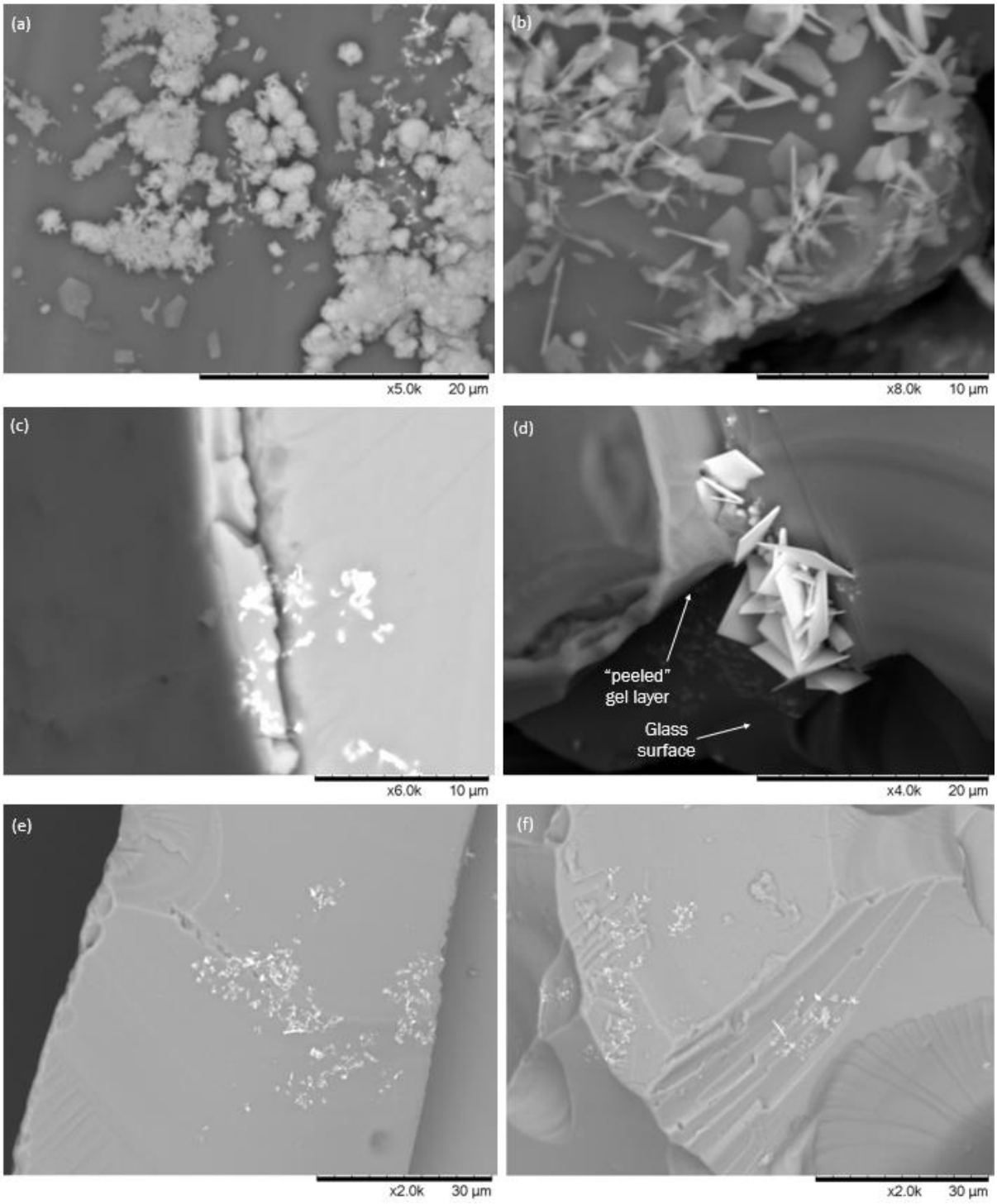

Figure 7.3. BSE-SEM images of ZnCa MW28 glass surface after 35 d of dissolution in groundwater at 50 °C showing (a) and (b) the range of crystalline phases precipitated on the surface of glass dissolved in clay groundwater; (c) the absence of a distinct gel layer at the surface of the glass dissolved in clay groundwater (cross section image); (d) possible evidence for a dehydrated silica gel layer peeled back from the glass surface, in addition to halite crystallites for glass dissolved in saline groundwater; (e) glass surface from the UHQ water and (f) granite tests, which did not show any surface precipitation or gel layers (the bright phases are crystallites of RuO_2).

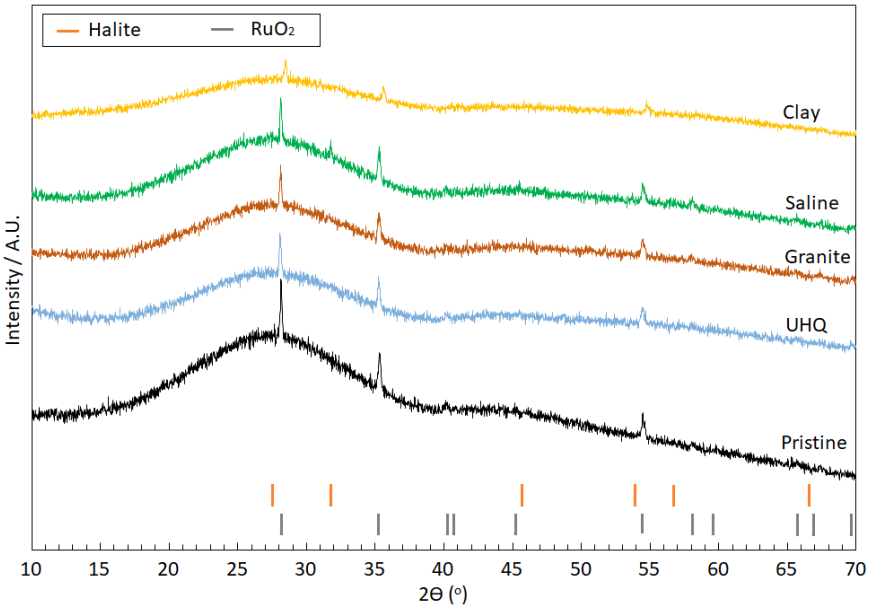

Figure 7.4. XRD traces of ZnCa MW28 particles pre- and post-35 d PCT-B leaching at 50 °C in UHQ and groundwater solutions.

Further indication that there was rapid onset of silica saturation in all solutions, and that Mg-silicate phases may have precipitated, is given by PHREEQ-C geochemical modelling of the solution leachates (Table 7.3 & Figure 7.5). The solutions from all experiments were predicted to be saturated with respect to a number of phyllosilicate phases, rich in Mg, including saponite ($Mg_{3.165}Al_{.33}Si_{3.67}O_{10}(OH)_2$) and sepiolite ($Mg_4Si_6O_{15}(OH)_2{\cdot}6H_2O$). Additionally, they were saturated with respect to a range of Ca-bearing zeolites including mesolite ($Na_2Ca_2(Al_2Si_3O_{10})_3{\cdot}8H_2O$), scolecite ($CaAl_2Si_3O_{10}{\cdot}3H_2O$) and laumonite ($CaAl_2Si_4O_{12}{\cdot}4H_2O$)) at every time point, in accordance with the observed reduction in the NL_{Ca} (Fig. 7.1e), which was particularly evident for the granite and saline groundwaters.

Table 7.3. Chemical formulae for all predicted phases from PHREEQ-C geochemical modelling.

Mineral phase	Chemical formula
Analcime	$NaAlSi_2O_6{\cdot}H_2O$
Beidellite - (Ca,Mg)	$(Ca,Mg)_{0.165}Al_{2.33}Si_{3.67}O_{10}(OH)_2$
Beidellite - Na	$Na_{0.61}Al_{4.7}Si_{7.32}O_{20}(OH)_4$
Clinochlore - 14 Å	$Mg_5Al_2Si_3O_{10}(OH)_8$
Laumonite	$CaAl_2Si_4O_{12}{\cdot}4H_2O$
Lawsonite	$CaAl_2Si_2O_7(OH)_2{\cdot}H_2O$
Mesolite	$Na_{0.676}Ca_{0.657}Al_{1.99}Si_{3.01}O_{10}{\cdot}2.647H_2O$
Saponite - Ca	$Ca_{0.165}Mg_3Al_{0.33}Si_{3.67}O_{10}(OH)_2$
Saponite - H	$H_{0.33}Mg_3Al_{0.33}Si_{3.67}O_{10}(OH)_2$
Saponite - Mg	$Mg_{3.165}Al_{0.33}Si_{3.67}O_{10}(OH)_2$
Saponite - Na	$Na_{0.33}Mg_3Al_{0.33}Si_{3.67}O_{10}(OH)_2$
Scolecite	$CaAl_2Si_3O_{10}{\cdot}3H_2O$
Sepiolite	$Mg_4Si_6O_{15}(OH)_2{\cdot}6H_2O$
Zinc silicate	Zn_2SiO_4

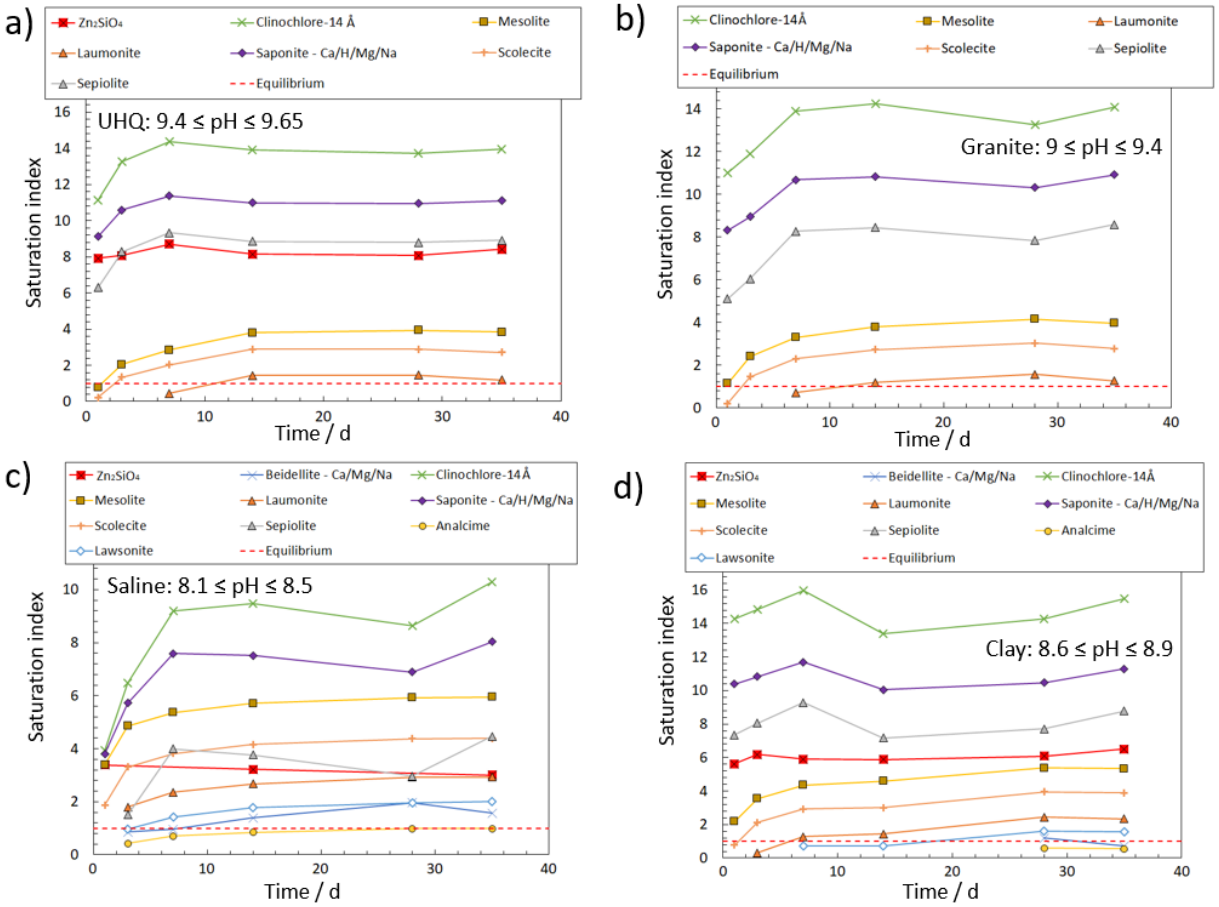

Figure 7.5. PHREEQ-C geochemical modelling of the leachate from from ZnCa 40:60 MW28 post 35 d PCT-B tests at 50 °C in (a) UHQ; (b) granite; (c) saline and; (d) clay groundwater solutions. The pH(RT) range of each data set is provided. Chemical formulae for each phase is provided in Table 7.3.

It is widely understood that Ca can be readily incorporated into silica gel layers, which has the effect of strengthening the gel layer and making it more resistant to dissolution in the short-term (Chave *et al.* 2011, Jollivet *et al.* 2012, Corkhill *et al.* 2013, Utton *et al.* 2013, Schofield *et al.* 2017, Aréna *et al.* 2018, Mann 2018). The only experiment in which a silica gel layer was observed (and inferred from NL_i data) was that performed in the saline solution, which had an initial Ca concentration of 19.9 mmol L^{-1} (Table 7.1). Unlike the other groundwaters, the NL_{Ca} was negative in the saline solution; since NL_i values are calculated by subtracting the concentration of Ca in the blank solution (Eqn. 3.30 – Chapter 3), this indicates that there was significant removal of Ca from the solution, either into the silica gel layer (Fig. 7.3e) or secondary precipitates. Furthermore, in contrast to all of the other solutions, the NL_{Mg} in the saline solution appeared to increase rather than decrease (Fig. 7.1d), suggesting that Mg leached from the glass and remained in solution rather than participating in silica gel charge compensation or secondary precipitate formation. This is in agreement with Aréna *et al.* (2018) who

reported that Ca incorporation into the gel layer of the ISG dissolved in Mg-rich clay groundwater was favoured over Mg incorporation.

Interestingly, the clay groundwater contained significantly more Ca than the UHQ and granite solutions, yet the NL_{Ca} did not decrease, indicating that it was not removed from solution. This highlights the competition for Ca^{2+} and Mg^{2} to form secondary silicate precipitates (Lothenbach *et al.* 2015, Mann 2018), that favour Mg over Ca. This can be attributed to the more negative Gibbs Free Energy of hydration (Haynie 2008) for Mg ($\Delta G_{Hyd}(Mg^{2+})$ -1830 kJ mol^{-1}, compared with ($\Delta G_{Hyd}(Ca^{2+})$ of -1505 kJ mol^{-1} for Ca) (Marcus 1991), which shows that Mg-silicates are thermodynamically more likely to form. Although Ca has a more favourable adsorption constant than Mg ($K_{ads} = 10^{-5.9}$ for Ca compared with $10^{-6.2}$ for Mg) and a higher ligand exchange rate ($K_{ex} = 10^{8.5}$ for Ca and $10^{5.2}$ for Mg), both of which favour the incorporation of Ca within the silica gel layer of corroding glass (Mann 2018, Collin & Fournier 2018), hence, in other words, if Mg ions react with dissolving silica from the glass before a gel layer can form, there can be no Ca-silica gel layer.

The observation that the NL_{Mg} was significantly greater in the saline groundwater compared to all other solutions investigated may also be explained by the lower pH (8.1-8.5) imposed by the saline system (Fig. 7.1f), inhibiting the formation of Mg-silicate phases Aréna *et al.* 2018. This is consistent with the study by Thien *et al.* (2012), who found that the precipitation of saponite ($Ca_{0.25}(Mg,Fe)_3((Si,Al)_4O_{10})(OH)_2{\cdot}nH_2O$), was more efficient at pH 9, while at pH < 9, Mg was partially incorporated into the gel to play a charge compensating role.

Previous studies have shown the propensity for the precipitation of Zn-silicate phases, such as hemimorphite ($Zn_2(SiO_4){\cdot}H_2O$), upon the dissolution of Zn-containing MW glasses (Zhang *et al.* 2015, Cassingham *et al.* 2016). Furthermore, the hydrated zinc silicate phase, zincsilite ($Zn_3Si_4O_{10}(OH)_2{\cdot}4(H_2O)$), was proposed to form upon SON68 dissolution (Debure *et al.* 2019). The Gibbs Free Energy of hydration of Zn^{2+} is more negative than that of Mg^{2+} ($\Delta G_{Hyd}(Zn^{2+})$ is -1955 kJ mol^{-1} and $\Delta G_{Hyd}(Mg^{2+})$ is -1830 kJ mol^{-1}), indicating that if Mg-silicates are capable of forming, then it is highly likely that Zn-silicates will also form, should Zn be dissolved from the glass. In a simple ternary borosilicate glass composition containing Zn, it was hypothesised that the precipitation of Zn-silicate prevents the re-condensation of silica to form a gel layer, sustaining glass dissolution (Gin *et al*. 2013), which agrees well with the behaviour observed in the present study.

In the granite groundwater solution there was no Zn detected, suggesting that Zn was not released to solution (Fig. 7.5). In the UHQ, saline and clay groundwater solutions, however, it was possible to measure Zn in solution but the concentrations were close to the detection limit of the instrument (approx. 0.01 ppm) and, as such, had large errors associated with their values. Despite the absence of evidence for Zn-silicates in SEM/EDS and XRD analyses in this short duration study, geochemical modelling of all solutions showed that Zn_2SiO_4 was predicted to be stable.

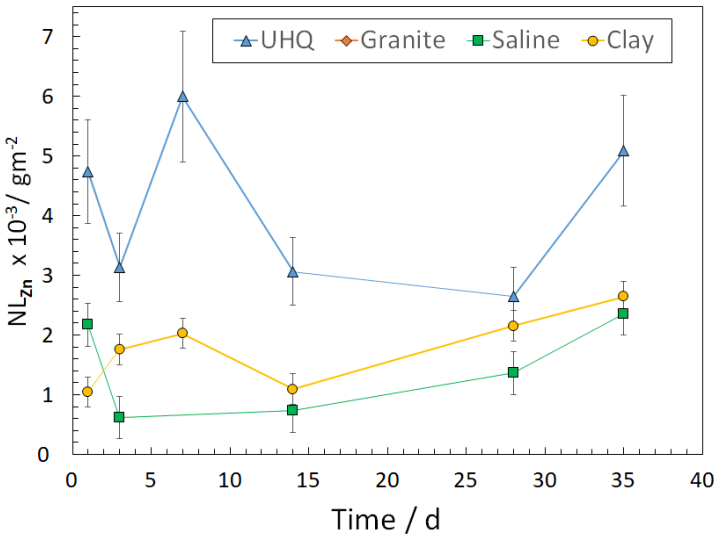

Figure 7.5. Normalised mass loss of Zn (NL_{Zn}) from ZnCa 40:60 MW28 post 35 d PCT-B tests at 50 °C in UHQ, granite, saline and clay groundwater solutions calculated from elemental concentration values (ppm) at the limits of instrument detection.

7.3 Conclusion

This study highlights the fact that different groundwaters exert a subtle influence on the short-term dissolution rate of ZnCa MW28 glass. Rapid onset of silica saturation and Mg-silicate precipitation (Fleury *et al.* 2013), as predicted by geochemical modelling of the solutions and tentatively identified by SEM/EDS, is the postulated reason for elevated dissolution rates, where Mg from both the glass and the solution likely prevents the re-condensation of silica to form a gel layer, sustaining glass dissolution at a rate similar in magnitude to the 'initial' rate. The same solubility limiting phases were predicted to form in all solutions (Table 7.3), therefore, the differences in dissolution rate may be attributed to the kinetics of formation and the quantity of the elements in each solution. The exception is saline groundwater, which may have promoted the formation of a passivating silica gel layer (Fig. 7.3d), did not show a propensity for Mg-silicate formation and had amongst the lowest dissolution rates.

The dissolution behaviour observed here is not well described by any of the accepted dissolution rate definitions: the initial rate is widely defined as the congruent, linear release of elements at the maximum rate controlled by hydrolysis of the silica network (Gin *et al*. 2012); the residual rate occurs once the solution is saturated with respect to silica and glass dissolution is no longer driven by silicate hydrolysis but by diffusion processes (of ions through the silica gel layer) (Gin *et al*. 2012), while the massive precipitation of secondary silicates (almost exclusively zeolite phases) and rapid dissolution of the glass is known as 'rate resumption', which is typically associated with a significant pH increase (Fournier *et al*. 2014). In contrast, in the groundwater solutions of the present study, the ZnCa MW28 glass apparently underwent 'initial rate' dissolution while under conditions of silica saturation, promoted by aggressive precipitation of secondary Mg-phyllosilicate phases, with no change in pH. Seemingly all of the currently defined stages of dissolution occurred simultaneously, thus an alternative definition for such behaviour is required.

As radioactive waste geological disposal programmes mature, and dissolution rates are determined in increasingly complex groundwater solutions, this study serves to highlight the need for further investigation of systems containing divalent cations and their influence on glass dissolution behaviour, particularly in the long-term. This is also important for new glass compositions developed to progress the decommissioning of nuclear facilities, such as the incorporation of Zn in POCO glass compositions (Harrison 2018). In particular, further detailed studies of the role of Mg and Zn-silicate precipitation in glass dissolution, in conjunction with appropriate thermodynamic databases, are required to understand whether Zn-silicate influences glass dissolution by the same mechanism, and to the same magnitude, as Mg-silicate precipitation, and to determine if there is an additive (Aréna *et al.* 2016) or competitive effect when both Mg and Zn are present.

8. High-Level-Waste glass durability: An alternative experimental methodology for geological disposal

Summary

This short Chapter describes a preliminary study that aims to progress the fundamental understanding of UK vitrified HLW dissolution, addressing a further consideration for the safety case for geological disposal: that vitrified HLW may not initially dissolve in water, but in water vapour. The implementation of a hybrid groundwater vapour/solution dissolution methodology – the Cyclic Vapour Static – showed a potential detrimental impact on the dissolution behaviour of ZnCa MW28, which increased the NL_B by an approximate factor of 3.5 compared to standard MCC-1 tests and highlighted the potential for an instant free release fraction of minor active elements from MW25, which may not be observed from conventional dissolution methodologies. The results of this Chapter were presented, in part, in 2019:

Adam J. Fisher, Russell J. Hand, Neil C. Hyatt & Claire L. Corkhill. The corrosion of UK vitrified waste during disposal. The 45th Waste Management Symposia, Phoenix, AZ, USA, **19712** (2019).

8.1 Introduction

The study of HLW glass dissolution has developed over the years to provide data for input to safety assessments for geological disposal (Ojovan & Lee 2014). Despite the abundant literature, a gap still exists relating to realistic geological disposal environments, which is steadily being addressed (Debure *et al.* 2019, Bouakkaz *et al.* 2019, Echave *et al.* 2019, Guo *et al.* 2020). Fully acknowledging the fact that sequential studies (i.e. introducing glass to a series of solutions/conditions in the expected chronological order) are required to develop a robust scientific understanding, their relevance to real disposal conditions and their potential to provide input to modelling is not well constrained and, in the worst case, may not be wholly applicable. The investigation presented in this Chapter aims to elucidate the potential usefulness of sequential methodological studies by demonstrating the

application of a new methodology to the dissolution of vitrified UK HLW simulants. This test, termed the Cyclic Vapour Static (CVS) test (essentially a VHT-MCC-1 hybrid test), applies three experimental stages (A-C) given below (Fig. 8.1), designed to replicate the conditions of glass corroding within a canister in an emplacement tunnel in a GDF. In each stage the experimental parameters specifically investigated in the present work are given in brackets; in this Chapter, results pertaining to Stages A and B will be presented.

1. **Stage A. Groundwater vapour corrosion:** monolithic glass sample is initially subjected to dissolution by groundwater vapour under anoxic conditions (using the ASTM Vapour Hydration Test methodology (ASTM 2009), at 100 °C, 28 d).
2. **Stage B. Aqueous groundwater corrosion:** the same glass sample is subsequently subjected to static ASTM MCC-1 dissolution (ASTM 2014) in groundwater solution and under anoxic conditions. The sample is not dried between steps. Standard MCC-1 tests on glass monoliths not subjected to groundwater vapour treatment are conducted in parallel to compare the methodologies. (The MCC-1 conditions employed in this Chapter are: SA/V = 10 m^{-1}, 50 °C, time points between 3-55 d, granitic groundwater (pH(RT) 8.27, see Table 3.8 - Chapter 3 for composition).
3. **Stage C. Dual aqueous groundwater glass and canister corrosion:** a similar parallel process to Stage B, but the glass is subjected to static dissolution in groundwater with the addition of canister corrosion products – represented by iron particles for time periods of > 720 d (Section 3.3.6).

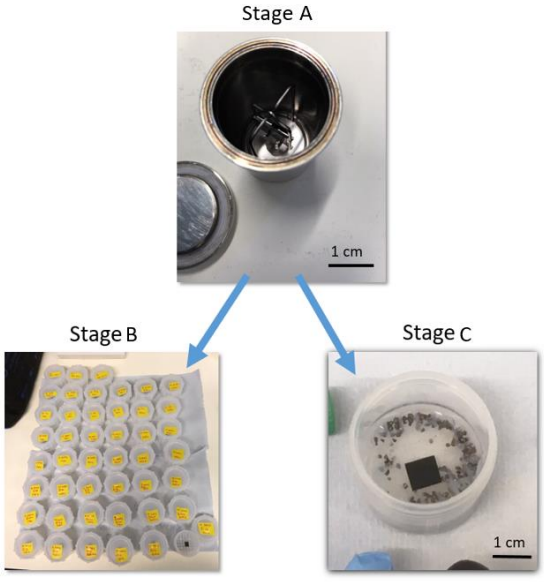

Figure 8.1. The stages of the Cyclic Vapour Static (CVS) methodology.

The rationale for such a CVS methodology is that vitrified HLW in a geological repository may initially come into contact with water vapour before encountering groundwater solution. This is a result of hydrogen gas generation from the corrosion of stainless-steel over-packs under anoxic conditions (Andra 2005), giving rise to void spaces inside and outside the canister that remain open and fill with hydrogen gas, thus preventing a fast saturation of the glass with surrounding groundwater solution (Bouakkaz *et al.* 2019). Such conditions may be expected to last for a period of 10,000 years (Abdelouas 2017 cited this duration, but noted that much further work is required to estimate this time with reduced uncertainty) during which time water vapour could alter a portion of the glass before the volume of hydrogen gas reduces sufficiently for liquid groundwater to contact the glass (Neeway *et al.* 2012). As such, glass corrosion by vapour hydration could dominate for a period of time, leading to the development of high-temperature secondary alteration phases, which have the potential to impact the later groundwater dissolution process. Hence, the *pristine* glass samples used in the wealth of aqueous dissolution literature may not accurately represent the glass surfaces that release elements (including radionuclides) contained in vitrified HLW to the aqueous groundwater, as modelled by safety case assessments.

The CVS methodology can potentially capture, in part, speculated wetting and drying cycles of the HLW glass over the course of its disposal, which may alter the physical properties of altered layers, with possible consequences for further dissolution (particularly important for thermally treated vitrified ILW wastes upon near-surface disposal, where weathering may be a strong factor (Heath *et al.* 2018, Ojovan 2019)). Such a process can be captured by allowing the glass monolith to dry/dehydrate between the stages (A-C) listed above and from imposing periods of dehydration throughout a test duration. However, this Chapter does not explore these considerations. Furthermore, the widely accepted stages of glass dissolution (Fig. 2.1 - Chapter 2), may not be applicable if glass is pre-altered by vapour prior to contact with groundwater and experiences wet and dry periods. The CVS approach for HLW (and ILW) glass corrosion may be more representative of the most realistic scenario and provide a more robust performance assessment.

The proposed CVS methodology is not entirely unique, as static MCC-1 experiments on pre-vapour corroded glass has been reported in the literature (Bates *et al.* 1982, Bates *et al.* 1984, Ait Chaou *et al.* 2010, Bouakkaz *et al.* 2017), which suggest that contact with vapour prior to aqueous media is detrimental to glass durability when compared with non-pre-corroded pristine samples. This has been attributed, in part to the dissolution and instantaneous release of elements from the secondary phases formed in the vapour stage, which raised the pH of the surrounding solution, thus increasing the rate of glass dissolution (Neeway *et al.* 2012). Such literature has focussed on dissolution in UHQ water

vapour and UHQ aqueous solution and, to the best of our knowledge, such experiments have not been reported in groundwater or high pH solutions. Uncertainty surrounds the role and evolution of altered products formed in such experiments (Bouakkaz *et al.* 2017, Lenting *et al.* 2019) and the interaction of these with the corroding glass and solution, thus the long-term stability of vitrified wasteforms, has not been fully evaluated.

By application of the CVS methodology, incorporating a cyclic element and near-field environment (granitic groundwater, canister corrosion product) this Chapter aims to provide new preliminary insight, particularly appropriate for UK HLW. This study reports the initial performance and comparison between ZnCa MW28 and MW25 glass, but without the addition of canister corrosion products. An assessment and determination of the secondary phases formed in the vapour stage was performed prior to the subsequent aqueous stage.

8.2 Results

8.2.1 Stage A - Groundwater Vapour Corrosion

ZnCa MW28

A thin phyllosilicate bed and unidentified zeolites, potentially including pollucite ($(Cs,Na)_2Al_2Si_4O_{12}\cdot 2H_2O$) based on EDS identification of Cs and a similar morphology to pollucite reported by Jing *et al.* (2017), were observed on the surface of ZnCa MW28 monoliths post vapour corrosion at 100 °C for 28 d using granitic groundwater solution (Fig. 8.2). Phyllosilicates entirely covered the surface of the monoliths with, on average, 5-10 individual pollucite precipitates occupying every 3,200 μm^2 (the area of the micrograph displayed in Fig. 8.2a) and one zeolite occupying approximately every 28,800 μm^2. An underlying gel layer was not easily observed, even in cross-section, although a higher magnification SEM might be required to reveal this. The XRD data had weak additional reflections when compared with the pristine glass, but these were not readily identifiable (XRD traces from all stages of the CVS methodology are provided for effective comparisons in Fig. 8.6). It is assumed, based on the results in previous Chapters of this Thesis, that these may be the Zn-containing phyllosilicate clay, sauconite 15-Å.

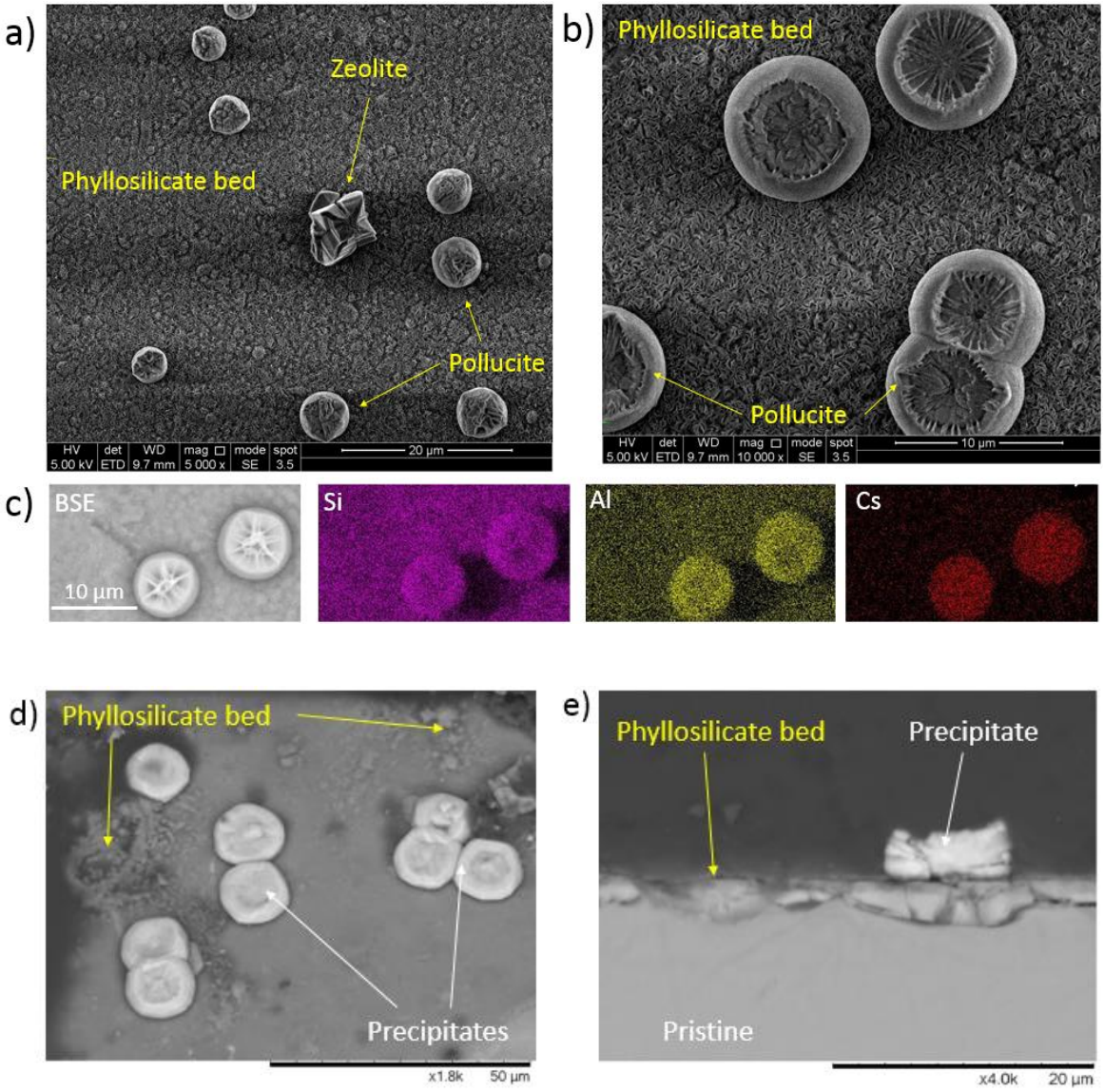

Figure 8.2. Surface and cross-sectional SEM images of ZnCa MW28 monolith post vapour test at 100 °C after 28 d, using granitic groundwater solution; a & b) secondary electron images of the sample topography; c) BSE and EDS of potential pollucite precipitates; d) BSE image of potential pollucite and phyllosilicate bed; e) BSE cross-section of potential pollucite.

MW25

A greater variety of precipitates were observed on the surface of MW25 monoliths than for ZnCa MW28 after the vapour test at 100 °C after 28 d, using granitic groundwater solution (Fig. 8.3). The identification of each precipitate remains somewhat uncertain, owing to the low concentration of each phase, however, EDS indicated that they contained Na, Ru, Mo and rare-earth phosphates, partly consistent with the alkaline-earth molybdate phases observed by Hyatt *et al.* (2004), whom conducted VHT test at 200 °C for 25 d using UHQ vapour on a similar precursor MW25 composition. The observation of a pitted glass surface may imply preferential dissolution of less durable portions of the glass matrix as discussed in Chapters 4 & 5. A gel layer was not observed at the employed SEM resolution. Unlike ZnCa MW28, a phyllosilicate clay layer was not observed, which may indirectly suggest that the presence of Zn heavily promoted the formation of such a clay layer under VHT conditions.

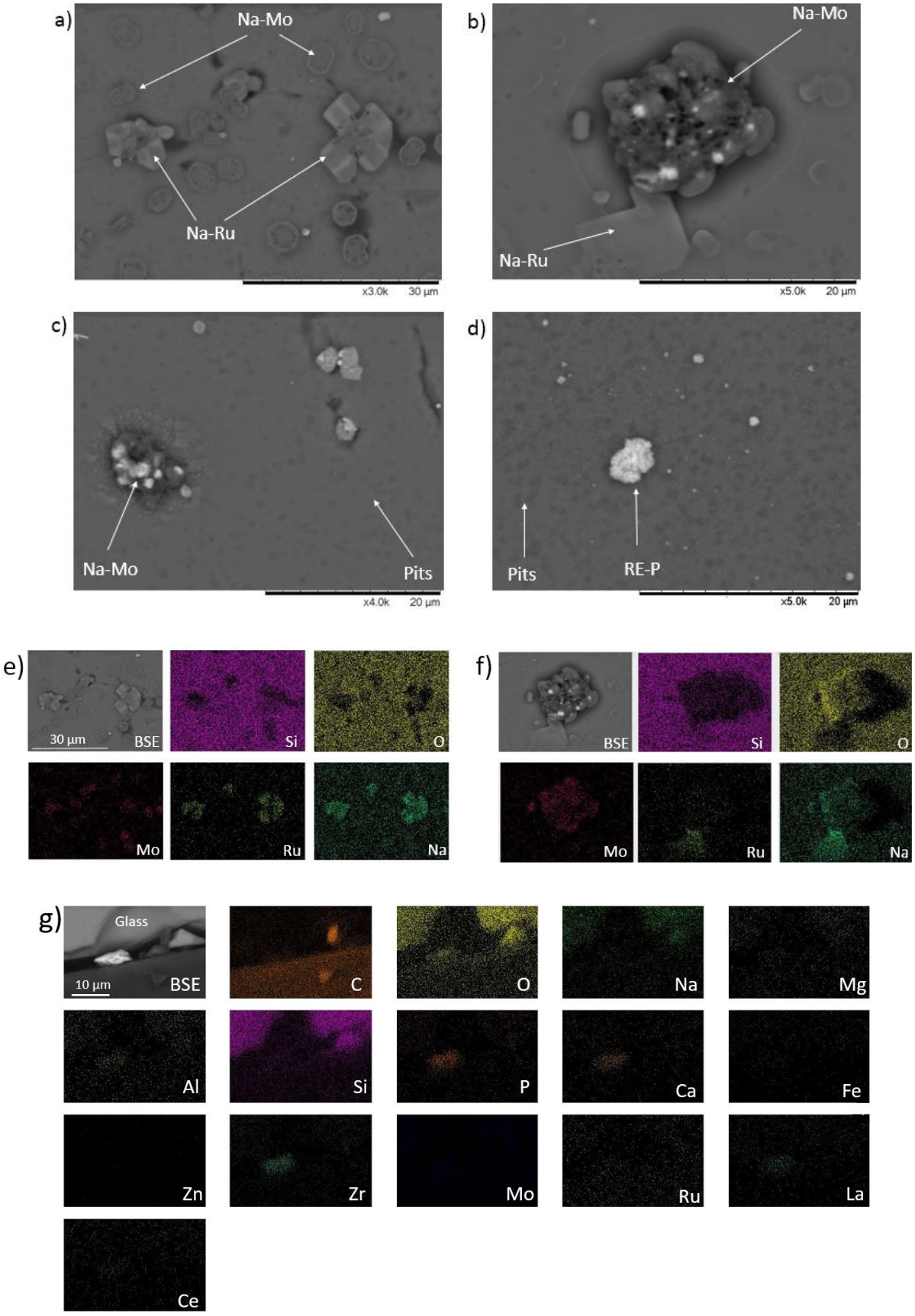

Figure 8.3. Surface of MW25 and cross-sectional SEM images post vapour test at 100 °C after 28 d, using granitic groundwater solution: a-d) BSE of secondary precipitates and pitted glass surface; e & f) EDS of secondary precipitates in (a) & (b); and g) cross-sectional EDS of precipitated potential rare earth phosphate phase (RE-P) (incorporating Ca and Zr).

8.2.2 Stage B. Aqueous Groundwater Corrosion

ZnCa MW28

A comparison of the dissolution behaviour of the pre-vapour corroded (CVS) and non-vapour corroded (standard MCC-1) glass was made after dissolution in aqueous granitic groundwater at 50 °C after 55 d. The normalised mass loss of elements from the CVS monoliths are shown by the red filled symbols in Figure 8.4. The boron normalised mass loss for ZnCa MW28 from the vapour-corroded (CVS) sample was greater than the non-vapour corroded (MCC-1) counterpart at all time points, by an approximate factor of 3.5. A residual rate of dissolution was potentially observed from 7-28 d before the dissolution rate resumed (25-55 d) based on $NL_{B,\ Si,\ Mo\ \&\ Sr}$ from the CVS test (Fig. 8.4 a, b, e & f respectively). Such a rate resumption coincided with a decrease in NL_{Al} (28-55 d). The increasing NL_{Al} behaviour was similar for both CVS and MCC-1 test until 28 d, whereby NL_{Al} decreased for the CVS test and increased for the MCC-1 baseline test. The incorporation of Al into secondary phases may be the most likely explanation for the former (Table 8.1 & Fig. 8.9) and was concurrent with the steadily increasing dissolution rate based on NL_B for the latter. These results suggest that the pre-vapour corrosion stage (captured by the CVS methodology) resulted in elevated dissolution rates during the aqueous dissolution stage compared to the MCC-1 baseline tests. Explanations for such a suggestion are provided in the discussion in Section 8.3.

The slow residual rate of NL_{Zn} (Fig. 8.4h) from the CVS test suggested that Zn was steadily leached into solution between 3-56 d. The hypothesised Zn uptake in secondary silicate phase/s (sauconite clay) during the VHT stage (Fig. 8.2) may have stabilised the Zn release during the MCC-1 stage. However, the Zn released from the residing pristine glass (0-3 d) may have precipitated into Zn-silicates and coalesced with the VHT-formed Zn-silicates. Note the reduction in NL_{Si} (14-38 d), concurrent with the decreasing/invariant NL_{Zn} and lack of Mg detection in solution > 28 d, alongside SEM images and EDS analysis (Figs. 8.8 & 8.9), sugges that secondary silicate phases (Zn- and Mg-phyllosilicate clays) were readily formed. The reduction of NL_{Zn} during the aqueous MCC-1 baseline test (Fig. 8.3h) was concurrent with a decrease in NL_{Si} (> 28 d) (Fig. 8.3b), which suggests the formation of secondary Zn-silicate phases (Aréna *et al.* 2016), in agreement with results in previous Chapters 5 & 6. The NL_{Mg} trend from both CVS and MCC-1 baseline tests was unexpected (Fig 8.4g), whereby any firm quantitative conclusions cannot be justified (based, in part, from ICP-OES difficulties in selecting appropriate emission lines). However, the gradual reduction in NL_{Mg} from 14-55 d for the MCC-1 tests (including the lack of Mg detection in solution from the ZnCa MW28 CVS test) tentatively suggests that

Mg was removed from solution with greater reaction progress, forming Mg-phyllosilicates as evidenced by SEM (Figs. 8.8, 8.9 and Table 8.1) and consistent with the results from Chapter 7.

MW25

There was little variation in the dissolution between the CVS and the MCC-1 baseline counterpart results for MW25. The phases formed during VHT-stage (Fig. 8.3) may not have been detrimental to the overall breakdown of the glass network. However, obtaining the Cs, Ru, P and RE release from IC or ICP-MS may provide evidence to suggest the dissolution and instant release of these elements from such VHT-formed phases, which would be of interest for the safety case for geological disposal. The reduction in the NL_{Mg} from 14-55 d from both the CVS and MCC-1 tests suggested the incorporation of secondary Mg-phyllosilicates, consistent with the results presented in Chapter 7 (Curti *et al.* 2006, Goût *et al.* 2019).

ZnCa MW28 and MW25 comparison

A comparison of the ZnCa MW28 and MW25 CVS tests showed that ZnCa MW28 conferred worse durability based on the NL_B, potentially due to the influence of the VHT-formed phases (most likely Zn-silicates), which is discussed in Section 8.3. A comparison of the ZnCa MW28 and MW25 MCC-1 baseline tests based on the $NL_{B\ \&\ Si}$ indicated that ZnCa MW28 conferred greater durability at earlier dissolution progress (< 55 d, 50 °C), consistent with the work presented in Chapters 5 & 6, which suggested that the greater network polymerisation of Zn-containing glass conferred greater chemical resistance, assuming that the MCC-1 test conditions approximated relatively dilute conditions. It can be also be assumed that > 55 d, MW25 will confer greater durability than ZnCa MW28 based on the PCT-B results presented in Chapter 6. The NL_{Al} was lower for ZnCa MW28 compared to MW25 possibly due to the Al uptake in a secondary phases or early gel layer formation (Fig. 8.9b).

Note that the NL_{Na} from all tests may be an artefact of subtracting the Na background concentration from the initial granitic groundwater solution or from its incorporation into secondary phases, potentially NaCl and/or the phyllosilicate clay, Na-beidellite (in the ZnCa MW28 CVS experiment only) (Fig. 8.6, 8.9 & 8.5 Appendix - I).

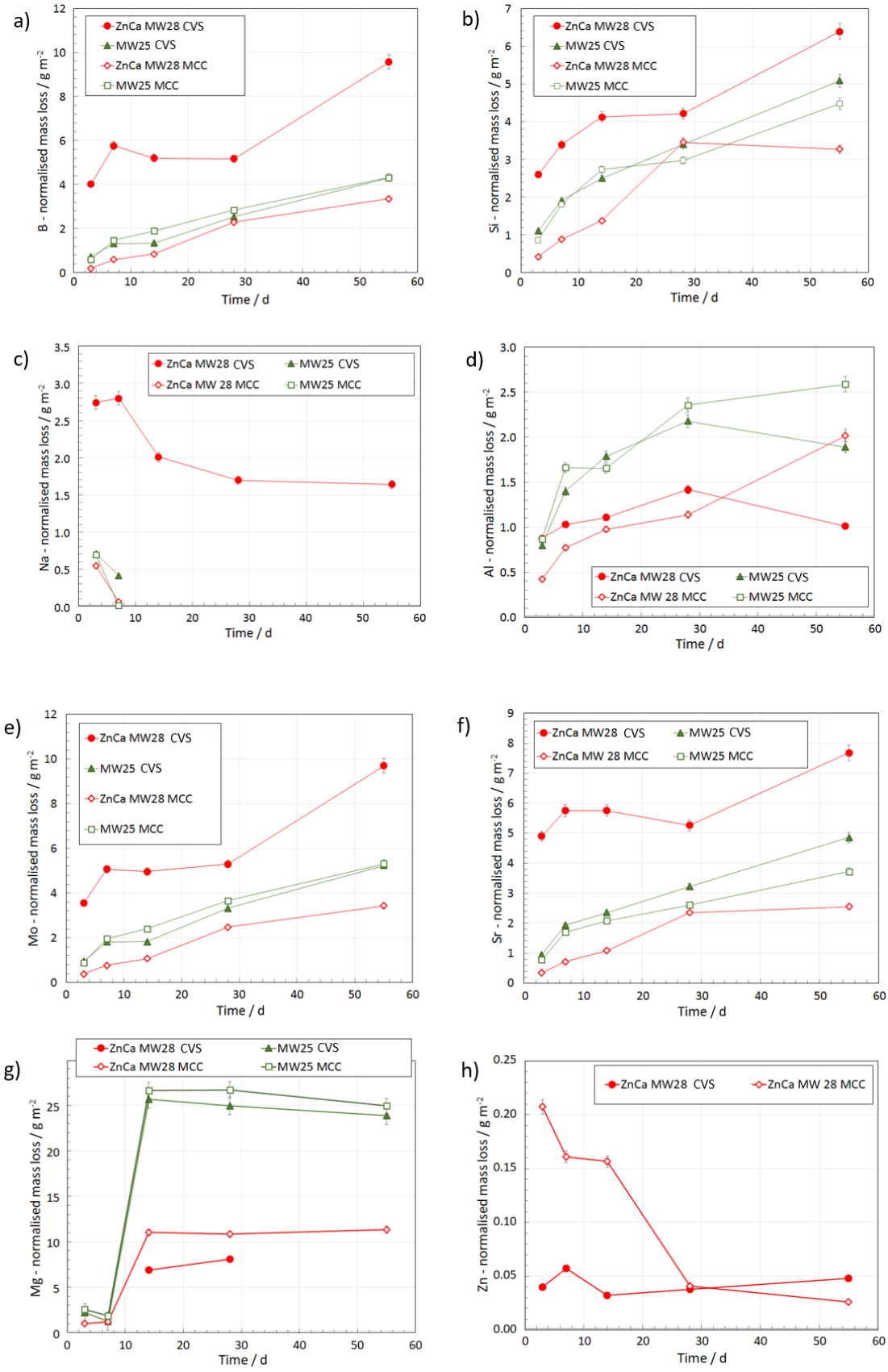

Figure 8.4. A comparison of the normalised mass loss of elements between the CVS and MCC-1 experiments for ZnCa MW28 and MW25. VHT conducted at 100 °C for 28 d with 0.06 ml of granitic groundwater. All MCC-1 conducted at 50 °C for 55 d with granitic groundwater solution under anoxic conditions.

The pH evolution for ZnCa MW28 (CVS and MCC-1) showed a sharp rise (0-3 d) then a decline (3-14 d) before a gradual rise (14 - 55 d). The sharp pH rise (pH 8.25 to 9) coincided with the dissolution of glass from the MCC-1 only test and coincided with the dissolution of the glass and potentially secondary phases, evidenced by the greater pH value after 3 d (pH 9.2) from the CVS test. The subsequent decrease in pH (for both CVS and MCC-1 tests) potentially correlated with the precipitation of secondary phases (Aréna *et al.* 2016), notably Zn-silicates, which subsequently increased the dissolution rate of the glass, leading to the gradual pH rise. Note that residual rate (Stage II) dissolution was not observed from the MCC-1 only tests, hence the pH rise coincides with the increasing dissolution.

The pH evolution for MW25 (CVS and MCC-1) showed a sharp rise (0-7 d), after which MW25 (CVS) followed the same behaviour as ZnCa MW28, which may be due to precipitation of secondary phases (Mg-silicates) (Fig. 8.9), whereas MW25 (MCC-1) maintained a constant average pH value of approximately 9.1 from 7-55 d, corresponding to a gradual residual dissolution rate, whereby secondary precipitates were not observed (Fig. 8.11a).

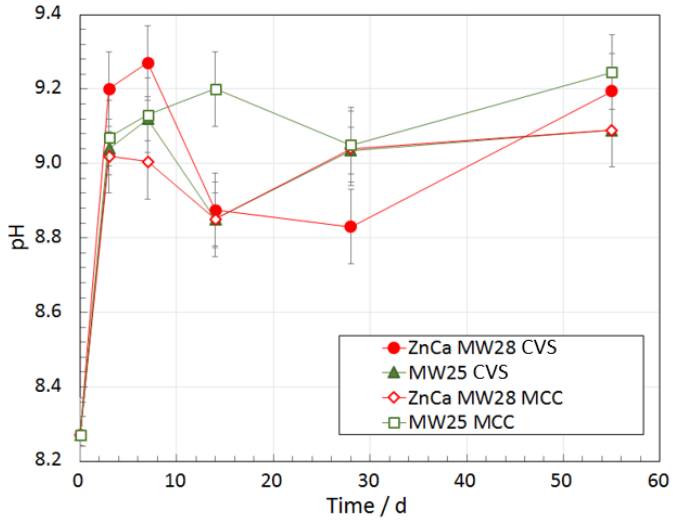

Figure 8.5. A comparison of the pH(RT) evolution between the VHT-MCC-1 hybrid and MCC-1 tests for ZnCa MW28 and MW25.

8.2.3 Secondary Phase Formation

8.2.3.1 XRD

ZnCa MW28

The phyllosilicate clay, sauconite 15-Å ($Na_{0.3}Zn_3(Si,Al)_4O_{10}(OH)_2 \cdot 4H_2O$) [PDF 29-1500] (based on the peaks at 19.57, 34.63 and 60.88 °2Θ) [PDF 29-1500] (Gin *et al.* 2013) and Na-beidellite [PDF 47-0197] (based on the peaks at 20.00, 34.50 and 35.25 °2Θ) were potentially identified on ZnCa MW28 post-VHT and post-CVS tests (Fig. 8.6). Other peaks were from the pristine glass crystalline inclusions as reported in Figure 6.2 (Chapter 6).

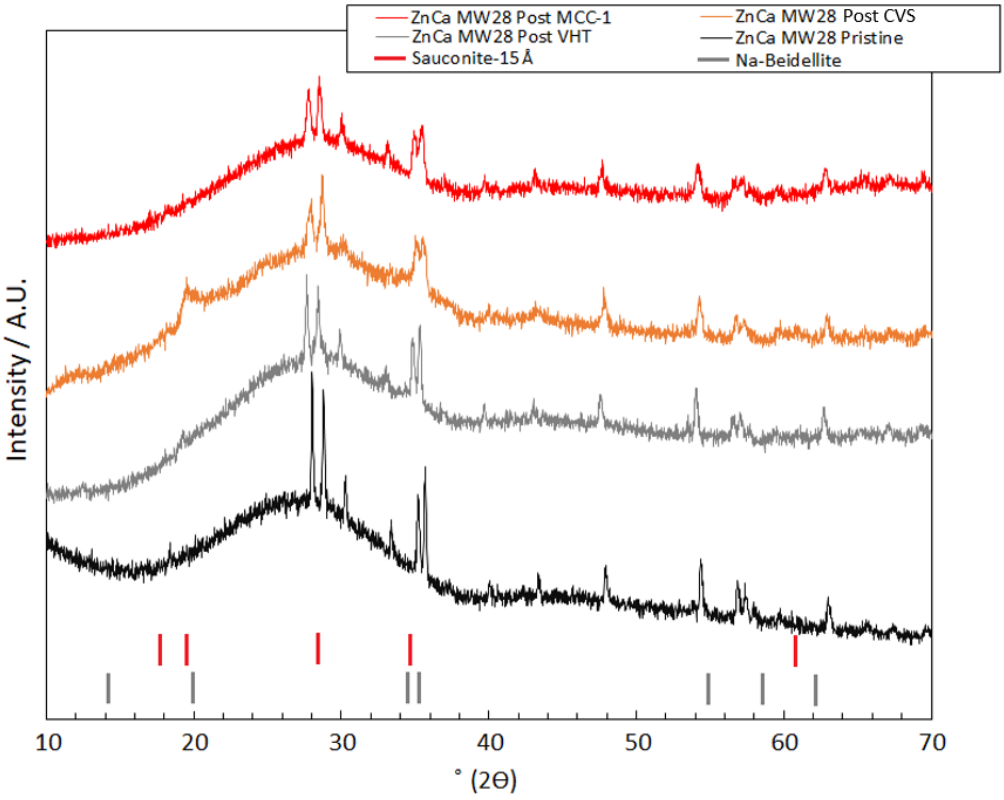

Figure 8.6. A comparison of the XRD traces from the different experimentation methods for ZnCa MW28. Note post-MCC-1 after 55 d at 50 °C and post-CVS after 28 d (100 °C) & 55 d (50 °C) d and post-VHT after 28 d, (100 °C). Peak identification from the pristine glass crystalline inclusions is presented in Fig. 6.2.

MW25

Secondary crystalline phases were not detected on the surface of MW25 as a consequence of either dissolution test. Ruthenium oxide [PDF 21-1172] was observed in the pristine glass, which was an expected feature of the waste glass (Fig. 8.7).

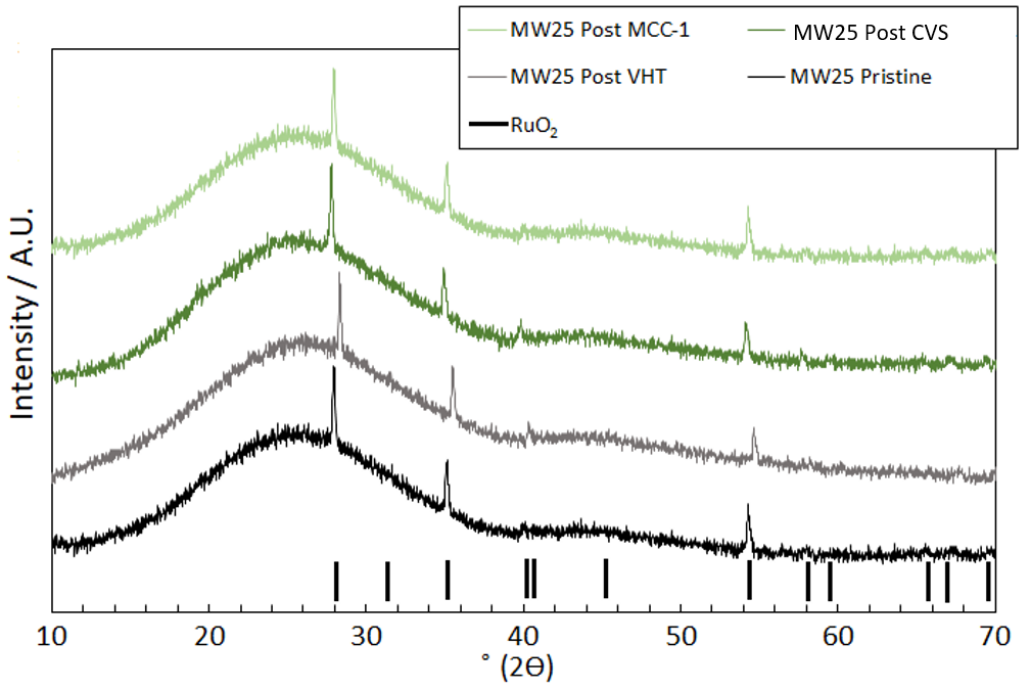

Figure 8.7. A comparison of the XRD traces from the different experimentation methods for MW25. Note post-MCC-1 after 55 d at 50 °C, post-CVS after 28 d (100 °C) & 55 d (50 °C) and post-VHT after 28 d, (100 °C).

8.2.3.2 Surface Characterisation following Stage B

ZnCa MW28

SEM observations post-CVS showed that extensive alteration products formed (Figs. 8.8, 8.9 & 8.5 Appendix - I). The phyllosilicates formed during the VHT phase endured and appeared to increase in quantity throughout 55 d of the MCC-1 stage (compare the increased thickness of the layer from BSE cross sections post-VHT (Fig. 8.1e) with post-CVS (Fig. 8.8c & d)). The Mg content of the glass and from the groundwater solution potentially encouraged the formation of Mg-silicates during the MCC-1 stage, indirectly evidenced from the enhanced concentration of Mg in the secondary products from the EDS analysis (Table 8.1, Fig. 8.7, 8.9 & 8.5 Appendix - I) and suggested from the results of Chapter 7. It is unclear whether the zeolites and pollucite formed during the VHT stage survived the MCC-1

dissolution stage. Evidence of their survival is suggested from cross sectional SEM (Fig. 8.8c), however, topological secondary electron SEM failed to observe these phases, hence, some can be assumed to have dissolved and contributed to the increased normalised mass loss (Bouakkaz *et al.* 2018), either directly (increased NL_{Si}) or indirectly (increased NL_B) (Fig. 8.4a & b).

Secondary precipitates formed during the MCC-1 stage remain unidentified, but are enriched in Zr, Ca, Zn and Mg and may consist of Fe-silicates (noting the 3.15 wt.% Fe content of ZnCa MW28 (Table 3.3)) and rare-earth phosphates (Table 8.1 & Fig. 8.9). A gel layer was not observed beneath the layer of precipitates, which may be expected based on the first appearance of a gel layer after 175-360 d MCC-1 tests in UHQ at the same temperature, but under oxic conditions from the results presented in Chapter 6.

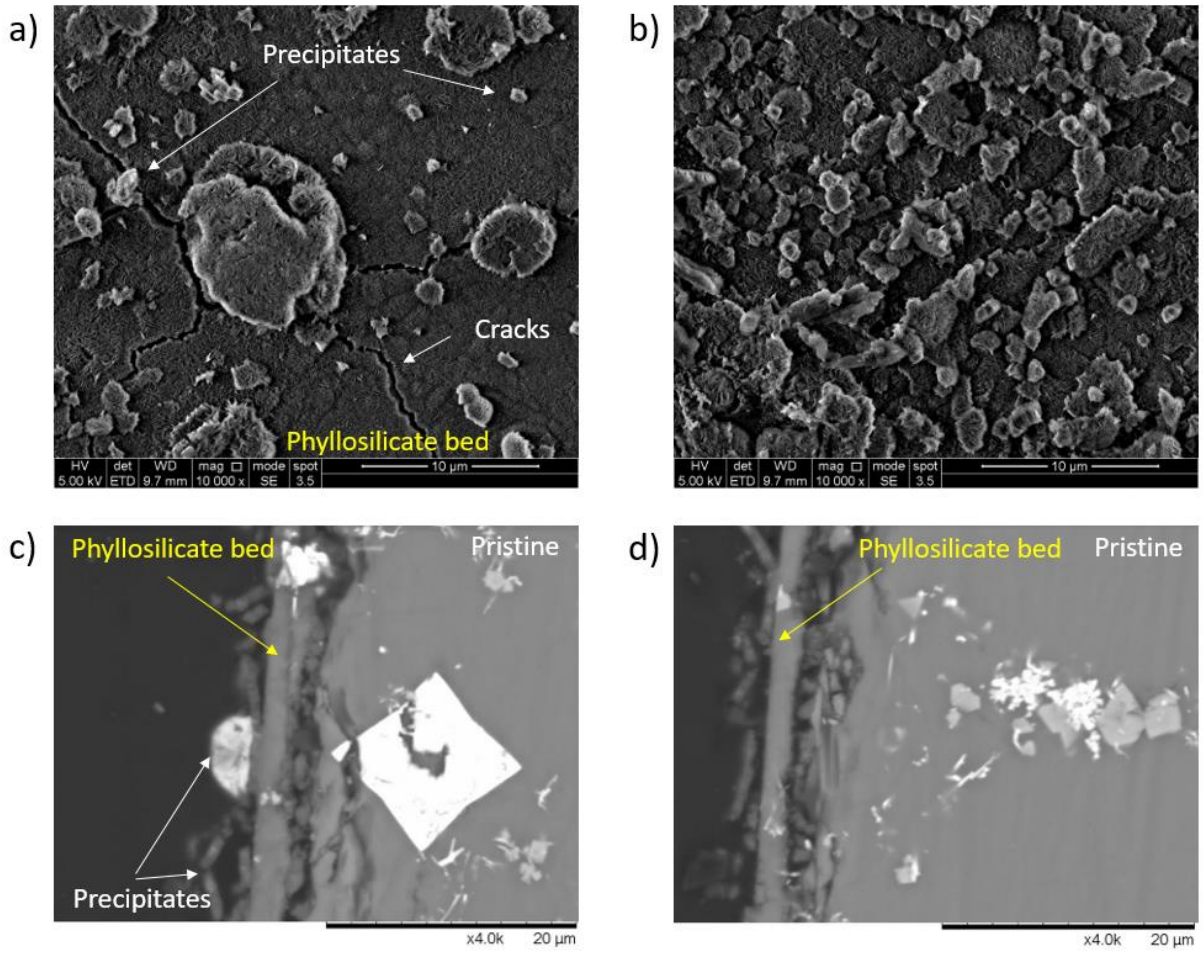

Figure 8.8. Surface of ZnCa MW28 post-CVS at 50 °C after 55 d (MCC-1 stage), using granitic groundwater solution under anoxic conditions.

Table 8.1. EDS spot maps associated with Figure 8.9a from a cross section of ZnCa MW28 post CVS at 50 °C (MCC-1 stage) after 55 d, using granitic groundwater solution under anoxic conditions.

Spot #	Layer	Element At. %													
		Si	Al	Na	Zn	Ca	Mg	Nd	La	P	Ru	Fe	Zr	Mo
1	Precipitate (REP*)	33.1 ± 0.5	13.3 ± 0.2	11.0 ± 0.2	3.0 ± 0.1	4.7 ± 0.1	15.6 ± 0.3	1.9 ± 0.1	0.28 ± 0.01	12.9 ± 0.2	1.6 ± 0.1	-	1.9 ± 0.1	0.63 ± 0.01
2	Precipitate (Ca-rich)	34.6 ± 0.5	13.1 ± 0.2	12.9 ± 0.3	2.6 ± 0.1	13.3 ± 0.2	17.1 ± 0.3	0.86 ± 0.10	0.41 ± 0.01	2.6 ± 0.1	0.74 ± 0.10	1.3 ± 0.1	-	0.42 ± 0.01
3	Precipitate (Zn-rich)	41.2 ± 0.5	16.3 ± 0.2	8.9 ± 0.2	7.2 ± 0.2	3.0 ± 0.1	18.1 ± 0.3	0.88 ± 0.10	0.16 ± 0.01	1.1 ± 0.1	0.39 ± 0.01	-	1.6 ± 0.1	-
4	Precipitate (Mg-rich)	39.9 ± 0.5	16.9 ± 0.3	11.8 ± 0.2	2.2 ± 0.1	5.7 ± 0.1	19.0 ± 0.3	0.13 ± 0.01	0.22 ± 0.01	0.85 ± 0.10	1.2 ± 0.1	1.7 ± 0.1	0.44 ± 0.01	-
5	Altered layer	42.3 ± 0.6	11.5 ± 0.2	14.3 ± 0.3	4.0 ± 0.1	4.9 ± 0.1	13.9 ± 0.2	0.87 ± 0.10	0.02 ± 0.00	0.16 ± 0.01	1.1 ± 0.1	3.2 ± 0.1	2.9 ± 0.1	0.77 ± 0.01
6	Altered layer	41.5 ± 0.7	11.5 ± 0.2	15.4 ± 0.3	4.9 ± 0.2	3.7 ± 0.1	12.6 ± 0.2	1.0 ± 0.1	0.31 ± 0.01	0.89 ± 0.01	0.8 ± 0.1	3.8 ± 0.1	3.2 ± 0.2	0.05 ± 0.00
7	Pristine glass	45.9 ± 0.9	8.8 ± 0.2	24.0 ± 0.4	1.6 ± 0.1	5.8 ± 0.1	5.7 ± 0.1	0.46 ± 0.01	-	-	-	2.2 ± 0.1	1.6 ± 0.1	-
8	Pristine glass	45.5 ± 0.9	8.1 ± 0.2	22.1 ± 0.4	3.7 ± 0.2	7.8 ± 0.1	5.6 ± 0.1	1.1 ± 0.1	0.22 ± 0.01	-	-	2.2 ± 0.1	1.7 ± 0.1	1.3 ± 0.1

REP* = rare earth phosphate

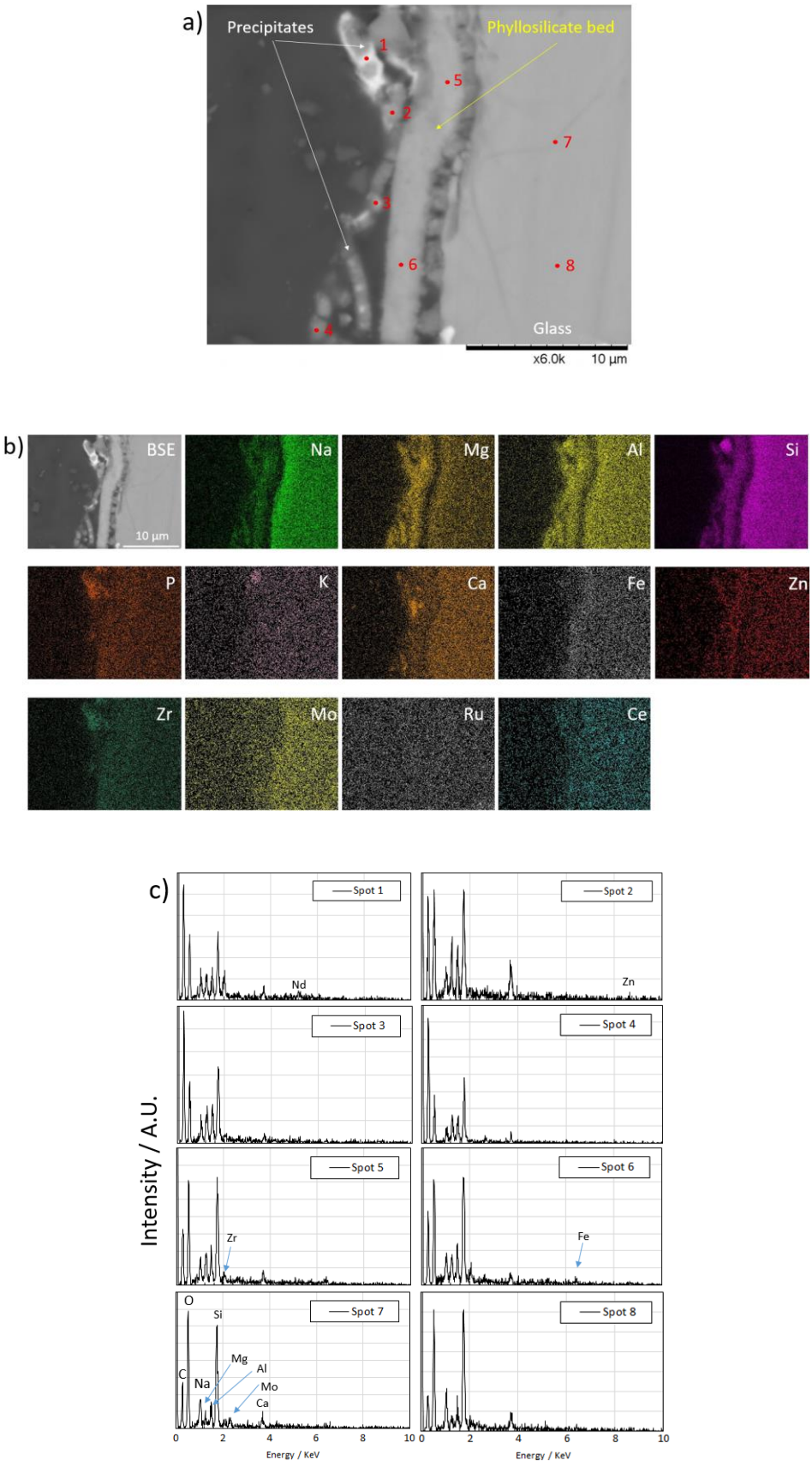

Figure 8.9. SEM of MW28 ZnCa MW28 post-CVS at 50 °C after 55 d (MCC-1 stage), using granitic groundwater solution under anoxic conditions. a) BSE cross section with identified EDS spots; b) associated EDS map and c) EDS counts.

MW25

A thin alteration layer was observed on the surface of MW25 post CVS tests (Fig. 8.10); the elemental composition was unobtainable due to the dominant Si EDS signal. The altered layer may be composed of a hydrated gel and/or secondary clays and precipitates, where the precipitates display similar morphologies to those observed in an MCC-1 study of the French SON68 glass in clayey groundwater solution by Jollivet *et al.* (2012). Pitting was observed beneath the altered layer consistent with similar studies using the MCC-1 methodology on similar waste glass compositions (Jantzen *et al.* 2010) and the ISG (Chinnam *et al.* 2018). Such pits may have developed from those initially formed in the vapour stage. Traces of the phases formed in the VHT stage were particularly absent post MCC-1 stage, which may imply the dissolution and instant elemental release from such phases. Analytical ICP-MS may elucidate such a suggestion. A potential unidentified surviving phase is shown in the SEM cross section in Figure 8.10c, however, such a precipitate was absent from the surface images (Fig. 8.10a & b) despite intensive scans.

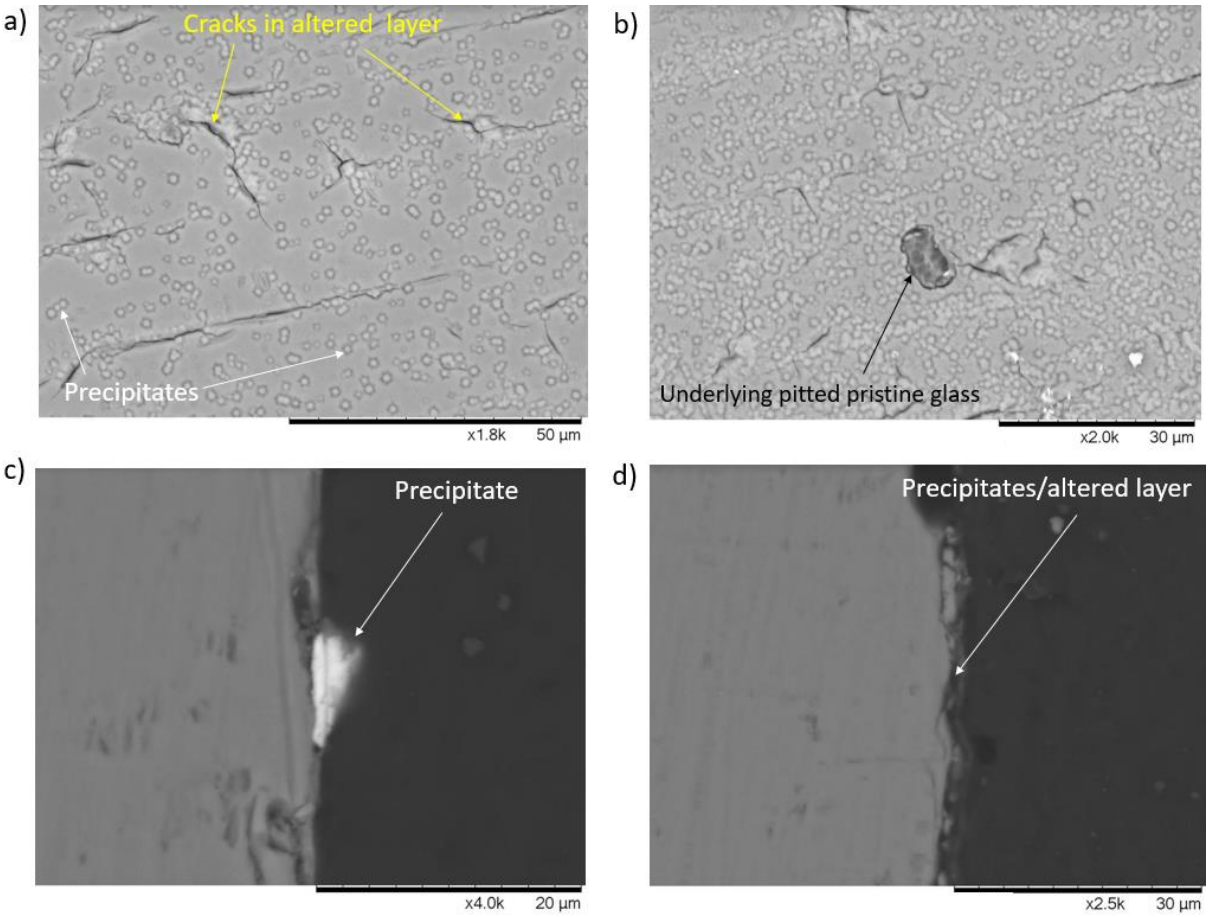

Figure 8.10. SEM of MW25 post-CVS at 50 °C after 55 d (MCC-1 stage), using granitic groundwater solution under anoxic conditions; a-b) BSE surface morphology: c-d) BSE cross section displaying unidentified secondary precipitate and potential thin altered layer respectively.

8.2.3.3 Surface Characterisation following MCC-1 baseline

Early stage corrosion from the 55 d MCC-1 baseline tests did not show any significant alteration, which was to be expected based on the relatively mild dissolution conditions. However, a potential small altered layer can be seen on the surface of ZnCa MW28 from cross sectional analysis, whereby compositional analysis was unobtainable at the SEM resolution employed. Note that in Chapter 6, secondary precipitates were not observed until 175 d in UHQ water under similar test conditions. However, Chapter 7 confirmed that the influence of groundwater had an effect in the early stages of glass dissolution during accelerated PCT-B leaching tests, promoting the rapid formation of secondary phases (particularly Mg-silicates), which may be applicable here.

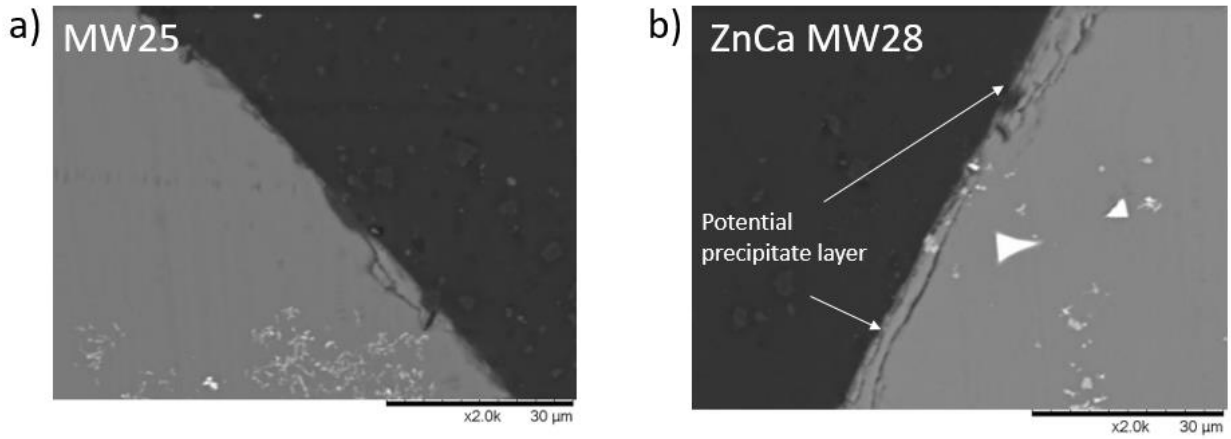

Figure 8.11. BSE cross sections of: a) MW25 and b) ZnCa MW28 post MCC-1 at 50 °C after 55 d, using granitic groundwater solution under anoxic conditions.

8.3 Discussion

Pre-VHT corrosion effect on CVS chemical durability

Implementation of the CVS methodology has shown a definite impact on the dissolution of ZnCa MW28, which increased the NL_B by an approximate factor of 3.5 compared to standard MCC-1 tests. Accounting for such behaviour lies in the pre-altered surface post-VHT corrosion (Fig. 8.2) compared to the pristine 1 µm polished surface of MCC-1 monoliths. Post-VHT samples contained a phyllosilicate bed overlaid with zeolites, which are speculated to have had an effect on the dissolution behaviour, whereby one or more of the following processes may have contributed:

1. The zeolites may have dissolved and raised the pH (Neeway *et al.* 2012), therefore increasing the rate of dissolution, tentatively suggested by the greater leachate pH (Fig. 8.5) compared to standard MCC-1 tests. Note that VHT-MCC-1 hybrid type experiments reported in the literature have always been shown to be less chemically resistant compared to standard MCC-1 tests, due to the dissolution tests conducted in UHQ, which dissolve the zeolites that are less stable at pH < 9.5 (Ribet & Gin, 2004). Results here suggest that in granitic groundwater, the dissolution of secondary phases may not be as drastic as in UHQ water, with some zeolites surviving throughout the MCC-1 stage (Fig. 8.8c). Future work investigating longer time periods and studies conducted in higher alkalinity environments (which may not dissolve the secondary phases, but may trigger further growth) could elucidate such issues and be more relevant to geological disposal conditions.

2. The phyllosilicates formed during the vapour phase may have acted as nucleating seeds for further secondary phase formation during the aqueous phase of the dissolution experiment. The detection of the phyllosilicates formed during the VHT phase endured the MCC-1 stage and increased in quantity over the 55 d MCC-1 stage. Such behaviour may have been enhanced due to Mg incorporation (in the form of Mg-silicates) from groundwater solution, even at low concentrations, as suggested by Chapter 7, although this requires experimental validation. Figure 8.9, Table 8.1 and 8.5 Appendix - I show Mg enhancement in the secondary precipitate layer after 55 d. Additional measurements, made on matured alteration layers at later time points, may help to confirm the hypothesis that seeding occurs. Future work involving artificial clay seeding experiments, analogous to recent zeolite seeding experiments (Fournier *et al.* 2013, Ryan *et al.* 2019, Parruzot *et al.* 2019), may also resolve the hypothesis that rapid and aggressive clay formation may cause Stage III type rate resumption.

3. Substantial gel layers were not formed during the VHT corrosion stage (assumed from the limits of the SEM resolution employed), which may indirectly facilitate the rapid transformation of dissolved glass constituents into secondary precipitates, precluding the formation of gel layers in the MCC-1 stage of the CVS tests (note the omission of gel layers from SEM in Figs. 8.8 & 8.9). Note that the VHT stage was conducted at 100 °C, however, gel layers and secondary phases were observed on similar glass formations in VHT experiments conducted at 200 °C for 25 d (Hyatt *et al.* 2004) and at 200 °C for 30 d (Cassingham *et al.* 2016), which highlights the role of temperature on the formation of alteration products (Neeway *et al.* 2012).

4. The SA/V ratio was assumed to be the same for the pre-VHT corroded and pristine glass samples during the aqueous dissolution phase of the experiment. Figure 8.2 shows surface features, particularly an uneven phyllosilicate bed, which will increase the total sample SA. Therefore, assuming a constant surface area may result in an underestimation of the actual SA in contact with aqueous solution, hence the actual NL_i may be lower than calculate here (Equ. 3.30 - Chapter 3) because the NL_i is proportional to 1/(SA/V). Calculating the actual SA of the corroded sample may prove challenging given the large size of the monolith. Given the uncertainty in SA/V, the results presented here for the VHT corroded samples may, in fact, be quite similar to those from the MCC-1 only tests, suggesting that the dissolution progress is relatively similar despite different mechanisms in operation. From a geological disposal safety case perspective, this could be considered as a positive finding (8.5 Appendix - II). However, this conclusion is limited to short-term (55 d) behaviour, which may not be maintained over extended time periods.

Comparing the ZnCa MW28 CVS hybrid tests to the standard MCC-1 tests; it is clear that different corrosion mechanisms were in operation. Conventional glass dissolution theory (Fig. 2.1) can be applied to MCC-1 tests only, assuming Stage I dissolution (hydrolysis) or a slight transition into stage II with the tenuous observation of secondary precipitates (Fig. 8.11b), based on the 55 d tests. Whereas some form of conventional later stage glass dissolution, impacted by the presence of the pre-formed clays and subsequent potential secondary clay precipitation, may be responsible for the CVS tests, which needs further work to underpin the corrosion mechanisms in operation during the aqueous stage for the pre-VHT corroded samples.

For MW25, no difference in the dissolution behaviour (based on NL_i) between the CVS methodology and MCC-1 tests was observed. During the VHT stage, MW25 formed a variety of unidentified secondary phases rich in Na, Ru, Mo and RE-phosphates (partly consistent with the alkaline-earth molybdates observed by Hyatt *et al.* (2004)), but did not form phyllosilicate clays. Such VHT corrosion progress did not have an effect on the NL_i from the MCC-1 stage. However, it is assumed that the secondary phases formed (Fig. 8.3) may have dissolved during the MCC-1 stage, and the issue of free-release cannot be overlooked and is in need of further investigation. Further analysis using ICP-MS may detect the presence of minor elements (Ru and RE-phosphates) in solution, thus adding clarity to the issue of free release. The potential lack of phyllosilicate clays (it cannot be ruled out that they may be present in small quantities) indirectly supports the findings from ZnCa MW28, which suggest that

the presence of VHT-formed clays effect the MCC-1 dissolution stage by potentially acting as seeds for further clay formation.

Predictions of secondary phase formation from PHREEQ-C are assumed similar to those presented in Tables 6.9 and Fig. 6.27 in Chapter 6 and Fig 7.4 in Chapter 7 for ZnCa MW28. Note that geochemical modelling is limited by the contents of the database. Suggested future work could involve updating databases accordingly in an attempt to account for and to accommodate the unnatural phases that are only expected to form from the corrosion of vitrified nuclear waste. Such work will be a challenging venture, but may be useful to accurately model dissolution behaviour in predicted models over geological time periods.

8.4 Conclusion

Implementation of the CVS methodology showed a potential impact on the dissolution behaviour of ZnCa MW28, which increased the NL_B by an approximate factor of 3.5 compared to standard MCC-1 tests over a 55 d period in granitic groundwater solution at 50 °C. The VHT corrosion stage resulted in a blanket covering of phyllosilicate clays and zeolites, which may have impacted the resulting aqueous MCC-1 stage dissolution behaviour. However, SA/V considerations may have overestimated the dissolution behaviour, which has the positive implication for the disposal safety case, by demonstrating that flexibility in the initial glass state manifests in similar dissolution behaviour. The response of MW25 to both methodologies was near identical, suggesting that the pre-VHT corrosion was not to the detriment of the subsequent aqueous MCC-1 durability. An absence of phyllosilicate clay formation upon MW25 after VHT-corrosion at 100 °C indirectly supports the findings from ZnCa MW28, which suggest that the presence of VHT-formed Zn-phyllosilicate clay effects the aqueous MCC-1 dissolution stage by potentially acting as nucleating seeds. Results from the MW25 and ZnCa MW28 CVS tests demonstrate the potential for free release of minor elements. All conclusions are limited to 55 d early reaction progress, which may not be maintained over extended time periods.

8.5 Appendix

I - CVS ZnCa MW28 SEM

SEM BSE cross section and EDS elemental maps of ZnCa MW28 post CVS at 50 °C after 55 d (MCC-1 stage), using granitic groundwater solution.

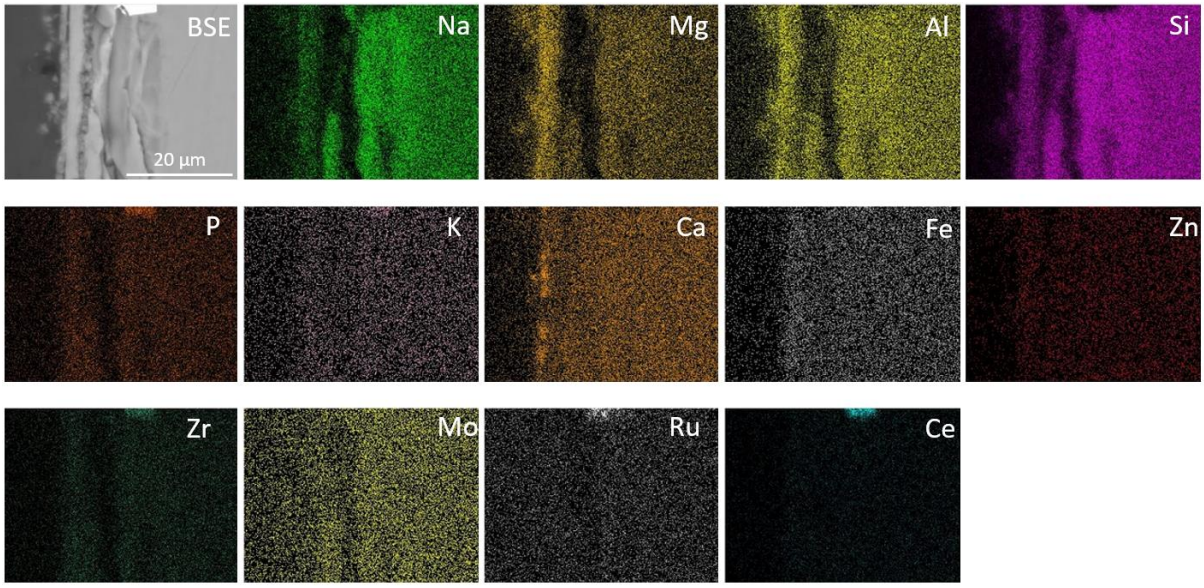

II - Considerations for geological disposal – enhancing the safety case

Work in this chapter was motivated by the potential vapour dissolution period in a GDF for up to 10,000 years (Abdelouas 2017). During this timeframe secondary phases will form. This chapter demonstrated that secondary phases form under VHT tests using granitic groundwater after 28 d at 100 °C for MW25 and ZnCa MW28, which had a potential impact on the dissolution of ZnCa MW28 during the MCC-1 stage, increasing the dissolution by a factor of 3.5, which lay in the identical SA/V assumption. Such a factor may not be a concern from a disposal safety case point of view, noting also that the SA/V assumption illustrates a worst case scenario. If the assumption does not hold true, it has further positive implications for the disposal safety case, by demonstrating that flexibility in the initial glass state manifests in similar dissolution behaviour. However, this conclusion is limited to 55 d tests in conditions that still do not fully replicated expected repository conditions. Future work needs to incorporate high pH solutions (expected from the alkaline plume from the cement backfill from the UK GDF) and the presence of canister corrosion products, whereby the presence of iron has shown to have a detrimental impact on the chemical durability due to formation of Fe-silicates (Burger *et al.*

2013, Echave *et al.* 2019, Debure *et al.* 2019). It should not be overlooked that the precipitation of Zn-, Mg- and Fe-silicates is additive (Aréna *et al.* 2016), and thus detrimental to the chemical durability. Such behaviour needs to be fully understood, especially in the long-term, therefore it is imperative that experiments are conducted in representative geological disposal conditions to evaluate the performance, which the CVS hybrid attempts to capture.

Previous chapters have potentially identified Stage III dissolution due to the precipitation of Zn-silicates from standard MCC-1 tests for ZnCa MW28. Longer term CVS tests will potentially clarify if Stage III-like behaviour occurs, where such comparisons between Stage III-type behaviour from both methodologies (MCC-1 and CVS) may elucidate the suggested Zn-phyllosilicate seeding behaviour, which would be to the greater detriment of ZnCa MW28 chemical durability.

The suggested instant release of elements from secondary phases could potentially be another factor to consider. Such behaviour may not be illustrated from standard aqueous dissolution tests, whereby the elements of concern are immobilised within the glass matrix, but if subjected to a vapour phase, such elements could transform into phases that are less stable to dissolution in aqueous solution. Quantifying the release of the elements: Ru, Mo and RE-phosphates from the phases formed on MW25 and Cs (contained in pollucite) formed on ZnCa MW28 from the CVS tests would attempt to address such a consideration. However, a further question could be asked of the fate of the pollucite zeolite, noting that the canister is expected to last 1,000 years, a large fraction of Cs will have decayed to Ba. What form will pollucite take? Such a consideration can be applied to the whole glass wasteform: are experiments conducted on the appropriate inactive analogue formulations? And if not, what are the consequences? An attempt to reinforce this consideration is presented in the following Chapter.

9. The effect of transmutation of Sr to Zr on the structure-dissolution relationship of simple glasses

Summary

This final Chapter confirms the observations and conclusions arising from Chapter 5 - *Structure-dissolution relationship of simplified High-Level-Waste glass as a function of ZnO:CaO ratio* - which reported a correlation between the network connectivity and initial rate of dissolution (Stage I) and the inverse relationship between the initial and residual rate (Stage II). Whereas Chapter 5 considered the variation of the ZnO/CaO ratio to optimise the ZnCa MW base glass formulation in terms of the long-term chemical durability, this Chapter considers the radioactive decay of the fission product, Sr, to Zr in International Simple Glass-type simple glasses and probes how the structural changes associated with the chemical analogue transmutation of Sr^{2+} to Zr^{4+} effects the chemical durability of the glass. The critical finding was that even very small changes in glass composition simulating this radioactive transmutation had a marked impact on the dissolution behaviour. The implication is that the analogue glass compositions used to study nuclear waste glass corrosion may not be truly representative of those that come into contact with groundwater (or water vapour as alluded to in Chapter 8) in a geological disposal facility, and thus, the resulting dissolution behaviour may not also be representative.

9.1 Introduction

While there is plentiful research in the literature of the effects of structural 'damage' caused to glass by radiation, such as ballistic effects (Delaye *et al.* 2011, Jan *et al.* 2019 and references contained therein) from α-particles and recoiling nuclei, and the resulting impact on chemical durability, there are no published studies that aim to understand how the chemical changes induced by the transmutation of β-emitters influence the structure-dissolution relationship. During disposal timeframes, unstable fission products will β-decay to form new elements. Two such transmutation reactions are particularly important for vitrified HLW:

^{90}Sr ($t_{1/2}$ = 28.79 years) ➔ ^{90}Y ($t_{1/2}$ = 64 hours) ➔ ^{90}Zr

^{137}Cs ($t_{1/2}$ = 30.08 years) ➔ ^{137}Ba

The transmutation of ^{90}Sr to ^{90}Zr is considered in this Chapter. Due to their relatively short half-lives, at the time of groundwater contact in a disposal setting (~1,000 years), a large proportion of transmutation will have occurred. In vitrified HLW, combined quantities of Sr and Cs can reach up to 3 wt. %, especially in cases with increased wasteloading (>35 wt. %) (Harrison *et al.* 2012, Harrison 2014, Schofield *et al.* 2017). When considering radioactive decay and resulting transmutation, modifications to the pristine glass structure and also the altered glass (gel) structure upon dissolution may therefore be significant. Such changes may be related to elemental charge consideration, e.g. Sr^{2+} → Zr^{4+} and Cs^{1+} → Ba^{2+}, and the resulting impact on the local coordination environment of these elements, for example, Sr is likely to play a network modifying role in the glass structure, while Zr is known to be a network former (Farges *et al.* 1991, McKeown *et al.* 1999, Connelly *et al.* 2011). In a transmutation scenario, it is likely that Zr will play the same modifying role as its parent Sr, which may influence the long term chemical durability. Furthermore, there are differences in the relative solubility of transmuted daughter element (Zr) when compared to their parent (Sr). This is likely to have implications for the mechanism by which glass materials dissolve.

This Chapter presents a simulation of the effect of elemental transmutation on glass structure and dissolution by comparing three simplified simulant waste glasses (Table 3.2 – Chapter 3) based on the well-studied International Simple Glass composition, which contains 1.72 mol. % Zr. Compositions representative of three theoretical time points in the radioactive decay of ^{90}Sr to ^{90}Zr were formulated for this investigation. The first composition, called ISGO (International Simple Glass 'Original'), is deemed to represent a glass at the initial time of fabrication, i.e. it contains Sr only (1.72 mol. %) and no Zr. An intermediate timeframe (~ 150 years after fabrication) is represented by a similar glass, but containing equal quantities of Sr (0.85 mol. %) and Zr (0.85 mol. %)); this was called ISGI (International Simple Glass 'Intermediate'). Finally, the International Simple Glass (ISG) is deemed to represent a glass at ~300 years after fabrication and approximately ten ^{90}Sr half-lives and contains Zr (1.72 mol. %) only i.e., no Sr. The ISG is, therefore, within the context of this study, most representative of the expected composition at time of first contact of nuclear waste glass with groundwater in a GDF (vapour contact is neglected in this study). Full glass compositions are reported in Table 3.2 - Chapter 3. The impact of radiation (i.e. β and γ particles) on the structure and dissolution kinetics is not included in this study.

This Chapter follows a similar, but shortened methodology as Chapter 5, which presents structural analysis of each pristine glass composition by ^{11}B and ^{29}Si MAS-NMR and dissolution analysis. Initial

and residual dissolution rates of the ISG-type compositions were obtained by SPFT and PCT-B methodologies. SPFT experiments were performed at pH(RT) 7, 9 and 11 at 40 °C and PCT-B experiments were performed with a SA/V ratio of 2,000 m^{-1} in UHQ for 28 d at 90 °C. Such experimental methodologies and parameters were sufficient to provide insight and clear comparisons between subtle glass compositional changes, induced by simulated radioactive transmutation.

9.2 Results

9.2.1 Structure - ^{11}B and ^{29}Si MAS-NMR

The ^{11}B MAS-NMR spectra revealed subtle changes in the B speciation as a function of glass composition (Fig. 9.1a). No complex spectral deconvolution was performed, due, in part, to the subtleties in the changes in spectra between glass compositions. However, qualitatively, it may be tentatively interpreted that that proportion of BO_3 units, from greatest to smallest, follows the series: ISG (Zr-rich) > ISGI > ISGO (Sr-rich). This trend may be expected if it is assumed that: 1) Sr takes on a charge compensating/network modifying role (based on its chemical similarities with with Ca (Kusumoto *et al.* 2019)), thus creating and charge compensating BO_4 units in the Sr-containing ISGI and ISGO compositions; and 2) it is accepted that Zr takes on a network forming role (Galoisy *et al.* 1999, Ferlat *et al.* 2006, Connelly *et al.* 2011, Lu *et al.* 2018), therefore less BO_4 units are able to form.

The ^{29}Si MAS-NMR spectra also revealed subtle changes in the Si Q_n speciation, with increasing Q4 species following the series ISG > ISGI > ISGO (Fig. 9.1b). Deconvolution was not performed for the same reasons as outlined above for the ^{11}B spectra. This trend may be expected based on the network forming role of Zr (Farges *et al.* 1991, McKeown *et al.* 1999, Connelly *et al.* 2011), thus having a greater polymerising influence on the glass structure as opposed to the assumed network modifying/charge compensating role of Sr. The ISG ^{29}Si MAS-NMR spectrum is consistent with that reported by Gin *et al.* (2015).

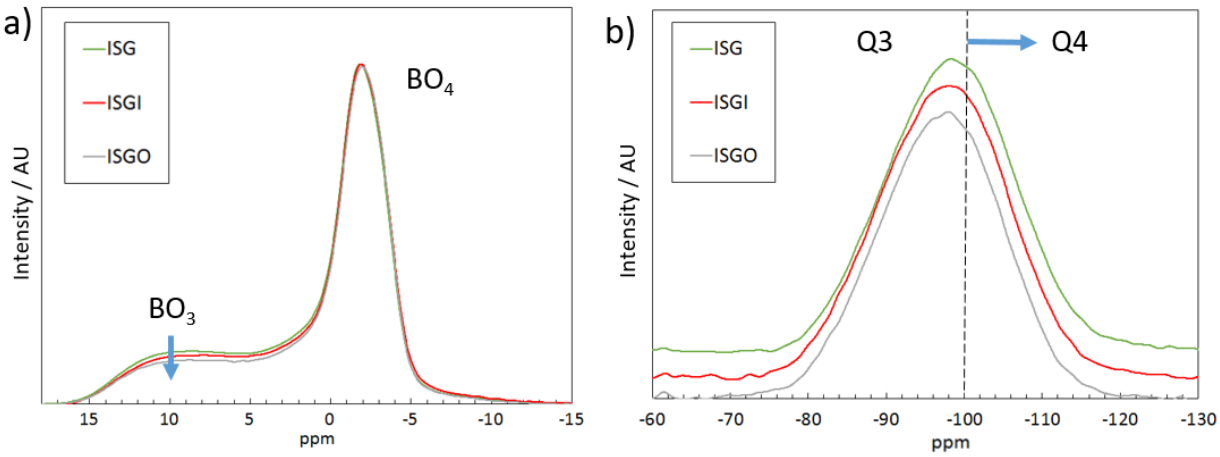

Figure 9.1. MAS-NMR spectra for the ISG, ISGI and ISGO compositions; a) ^{11}B, the arrow indicates the reduction in the BO_3 contribution along the series ISG > ISGI > ISGO; and b) ^{29}Si, the dashed line indicates chemical shift towards greater Si Q_4 speciation (Angeli *et al.* 2012).

9.2.2 Dissolution

9.2.2.1 SPFT

The SPFT experiments were only conducted on the two end member glass compositions (ISGO and ISG). This was due to experimental limitations imposed by the SPFT set-up. All raw data pertaining to the ISG is reported in Chapter 4. Relevant ISG data for comparison is reproduced in this Chapter. Flow-rates ($\log_{10}$([q/S] / m s^{-1}) were selected based on the results from Chapter 4, which were deemed suitable for the attainment of dilute conditions for the ISGO composition.

Determination of steady-state conditions

Using the SPFT methodology, steady-state (SS) conditions were achieved for both glasses, with congruent dissolution observed at pH(RT) 9 and 11 for both glasses and incongruent dissolution at pH(RT) 7, due to the lower solubility of Si at this pH value (Strachan 2017) for ISGO (Fig. 9.2, Table 9.1). Note that during the experiment at pH(RT) 11 (Fig. 9.2c) the input buffer drifted below the desired pH value at approximately 42 d, which resulted in a discontinuous drop in the dissolution rate. Hence, steady-state dissolution was reached at approximately 35 d. Similar issues applied to measurements < 30 d.

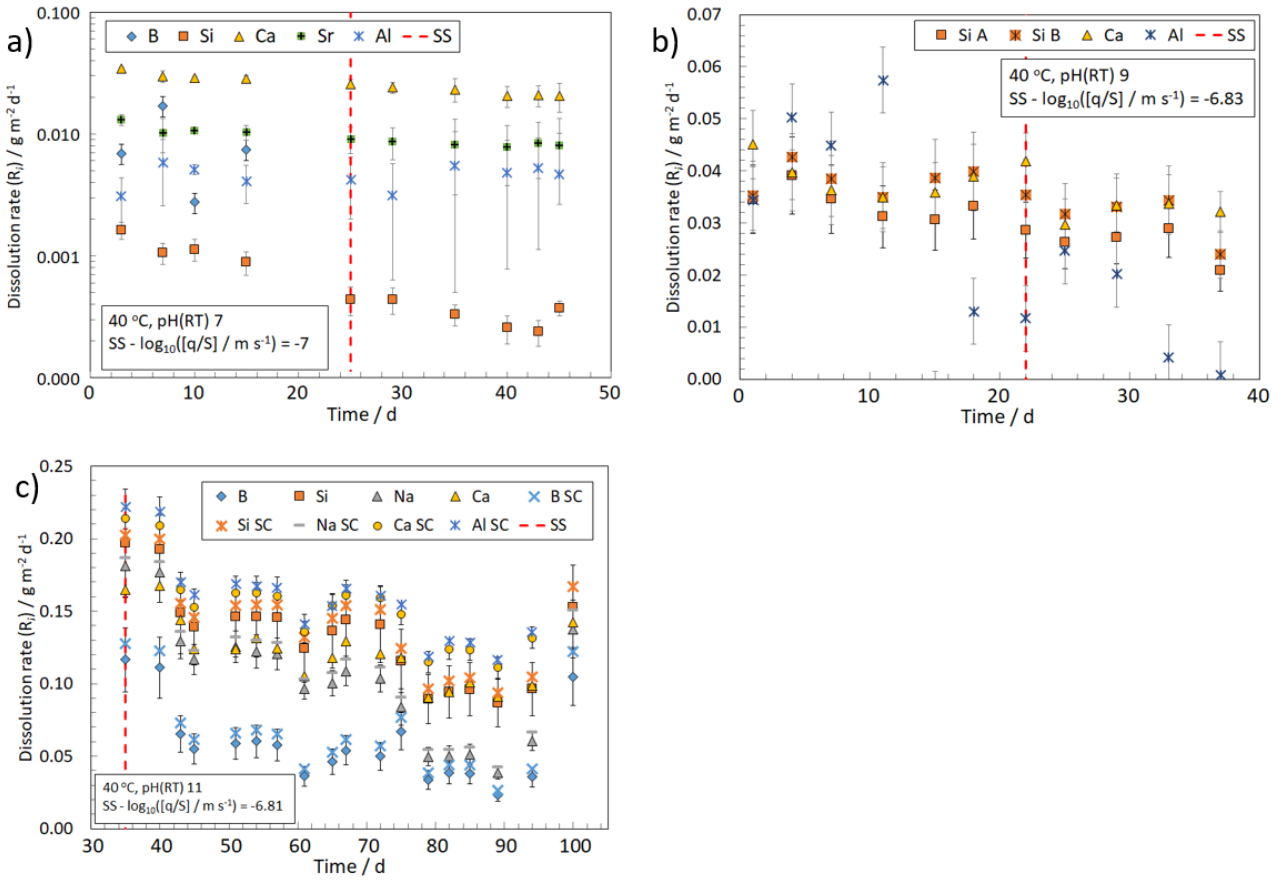

Figure 9.2. The attainment of steady-state (SS) dissolution for ISGO at: a) pH(RT) 7, 40 °C; b) pH(RT) 9, 40 °C (noting that Si data relate to individual vessel data points A & B, as opposed to the average of duplicate samples); and c) pH(RT) 11, 40 °C. SC = shrinking core model applied (McGrail *et al.* 1997).

Table 9.1. Steady-state concentrations (ppm) and dissolution rates (g m^{-2} d^{-1}) from all ISGO experiments. Steady-state ppm values have had background concentrations subtracted where applicable. Note that some values are not reported due to them falling below the elemental detection limit < 0.01 ppm.

Sample	Temp /°C	pH (RT)	Modelled pH(T)	Test duration /d	Time to attain steady-state /d	Initial sample mass /g	Steady-State							Steady-state concentrations/ppm							Steady-state rates / g m^{-2} d^{-1}							
							Average surface area† (S) /10^{-3} m^2	Surface area % of original‡	$\log_{10}[(q/S)$ /m $s^{-1}]$	B	Si	Na	Al	Sr	Ca	B	Si	Na	Al	Sr	Ca
ISGO	40	7	6.57	100	25	0.435	9.20	100	-7	0.03	0.01	-	0.02	0.03	0.09	7.6 ± 1.6 (x10^{-3})	3.5 ± 0.8 (x10^{-3})	-	4.6 ± 0.5 (x10^{-3})	8.4 ± 0.4 (x10^{-3})	2.3 ± 0.4 (x10^{-2})
ISGO	40	9	8.67	35	22	0.290	6.13	100	-6.83	-	0.59	-	-	-	0.09	-	3.1 ± 0.6 (x10^{-2})	-	-	-	3.4 ± 0.6 (x10^{-2})
ISGO	40	11	10.89	100	35	0.290	6.13	98	-6.81	0.47	3.90	0.51	0.54	-	0.58	1.5 ± 0.2 (x10^{-1})	2.0 ± 0.4 (x10^{-1})	1.85 ± 0.2 (x10^{-1})	2.2 ± 0.4 (x10^{-1})	-	2.1 ± 0.4 (x10^{-1})

†On application of the shrinking core model
‡Indicates the need for the application of the shrinking core model if < 100%

The initial dissolution rates (Stage I) for ISGO (based on the Si release) as a function of pH increased by approximately an order of magnitude between pH(RT) 7 and 9 and an order of magnitude between pH(RT) 9 and 11 (Table 9.1). Steady-state dissolution rates for ISGO were assumed to be initial dissolution rates based on the fast flow-rates used log [(q/S) m s^{-1}] > -7, which were consitent with similar rates applied to similar simple glass compostions in the literature (McGrail *et al.* 1997, McGrail *et al.* 2000, Pierce *et al.* 2010, Cassingham *et al.* 2015).

Initial dissolution rates: ISG Vs. ISGO

Faster initial dissolution rates (Stage I) were generally observed for ISGO (Sr-rich) compared to ISG (Zr-rich) based on R_B (similar within experimental uncertainty at pH(RT) = 7) and R_{Si} (Fig. 9.3, Table 9.2). This may be due, in part, to the greater network connectivity of the ISG (greater Q_4 specie contribution as indicated by ^{29}Si MAS-NMR, and hence greater chemical durability compared to ISGO. These results are consistent with those reported in Chapter 5 and by Icenhower *et al.* (2008). At pH(RT) 7 a thin dehydrated altered gel layer was observed on both ISGO (Fig. 9.4) and ISG (Fig. 4.6, Chapter 4), which was more pronounced on ISGO.

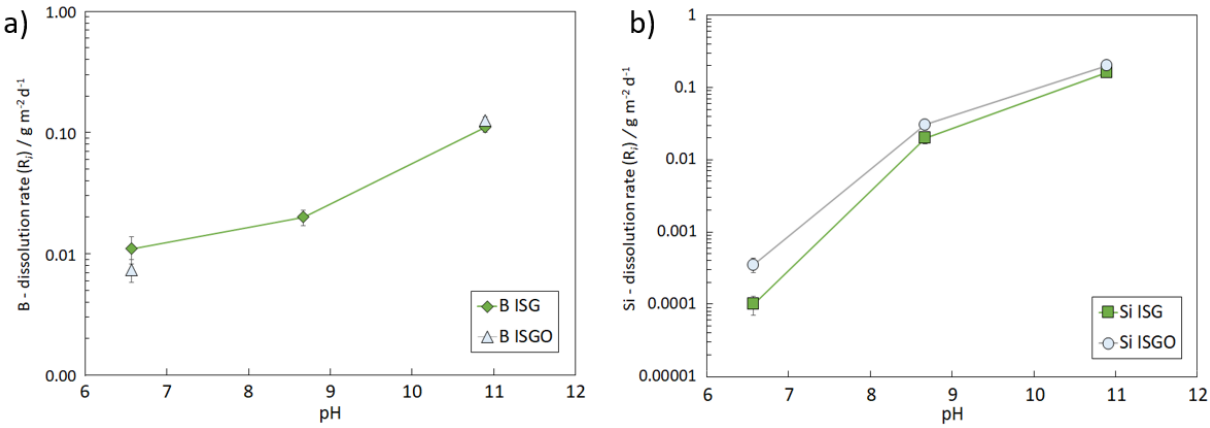

Figure 9.3. ISG and ISGO initial dissolution rates (Stage I) versus pH based on: a) B release and; b) Si release.

Table 9.2. Comparison of ISG and ISGO initial dissolution rates from SPFT experiments.

			Initial Rate (Stage I) (g m^{-2} d^{-1})	
Glass	T / °C	pH(RT)	B	Si
ISG	40	7	1.10 ± 0.28 (x $10^{-2)}$	1.00 ± 0.33 (x 10^{-4})
ISGO	40	7	7.4 ± 1.6 (x $10^{-3)}$	3.5 ± 0.8 (x 10^{-4})
ISG	40	9	2.0 ± 0.3 (x10^{-2})	2.0 ± 0.3 (x10^{-2})
ISGO	40	9	-	3.1 ± 0.5 (x10^{-2})
ISG	40	11	1.10 ± 0.10 (x10^{-1})	1.6 ± 0.2 (x10^{-1})
ISGO	40	11	1.25 ± 0.10 (x10^{-1})	2.0 ± 0.3 (x10^{-1})

Surface features post-SPFT dissolution

Inspection of ISGO particles, post-SPFT tests, revealed the presence of some of the distinct phenomenon observed on the ISG reported in Chapter 4 and on the ZnCa base glasses reported in Chapter 5. The numbers below relate to the features in Figures 9.4-9.6:

1. Glass dehydration cracking
2. Troughs of preferential dissolution along stress lines/intitial surface roughness/cracks on the pristine glass (assumed).
3. Two types of pitted features: a) pitted/pitted trough and b) pitted mechanical (assumed to be intial surface imperfections from mechanical sample preparation (see pristine glass particles Fig. 3.15 in Chapter 3, similar pits were observed on pristine ISGO but images have been omitted for brevity), which developed into dissolution pits.

The fact that the features descibed by 2 were not seen alongside 3a may suggest a temporal evolution. However, this is hypothesied based on the analysis of particles taken from two sets of experiments at 40 °C, at pH(RT) 9 & 11 respectively. Greater insight would be gained from future experiments and the analysis of particles at different time-steps from sacrificial vessels throughout the duration of 100 d SPFT experiments.

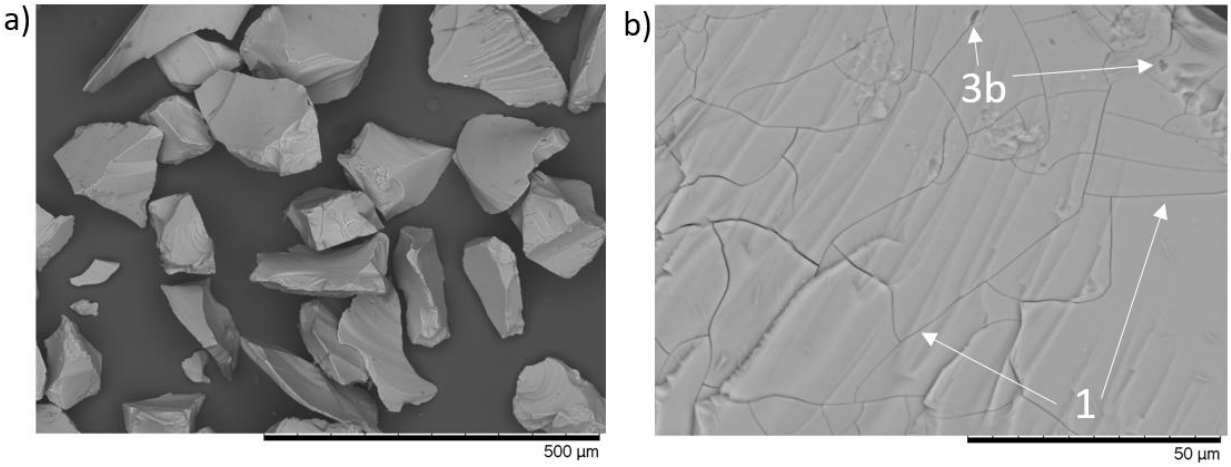

Figure 9.4. ISGO particles post-SPFT at pH(RT) 7, 40 °C after 100 d: a) overview; b) evident altered glass dehydration cracking (1) and mechanical pit formation (3b).

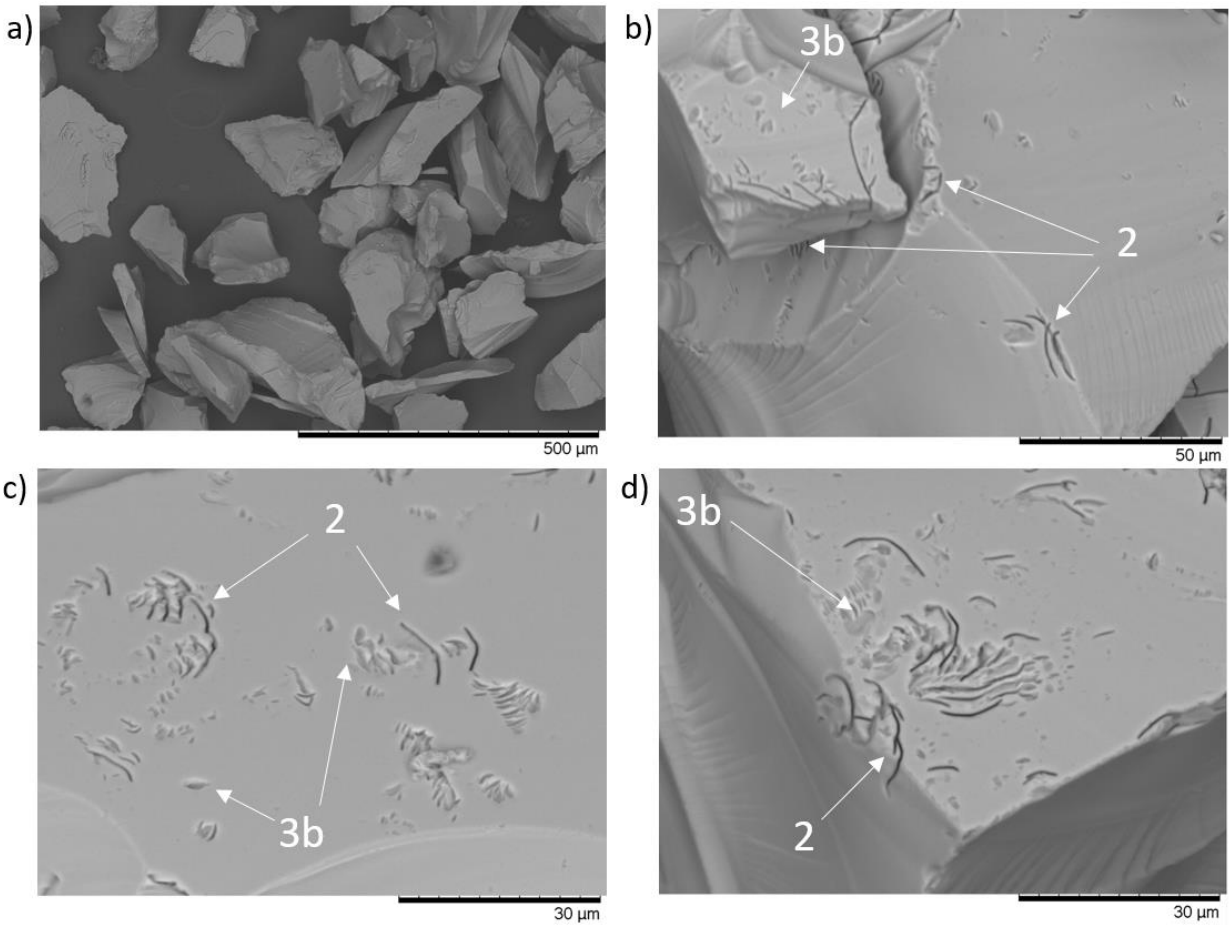

Figure 9.5. ISGO particles post-SPFT at pH(RT) 9, 40 °C after 35 d: a) overview; b, c & d) evident trough (2) and mechanical pit formation (3b).

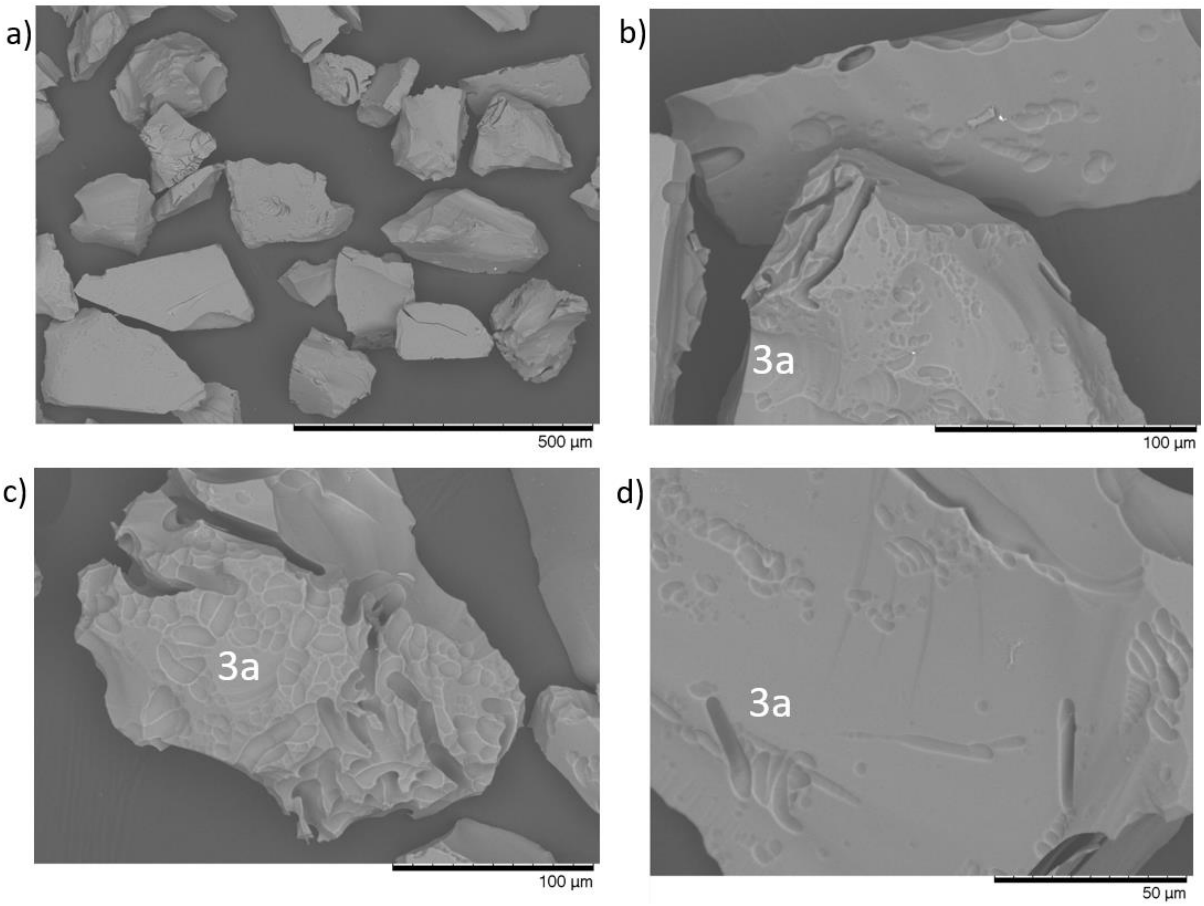

Figure 9.6. ISGO particles post-SPFT at pH(RT) 11, 40 °C after 100 d: a) overview; b, c & d) evident pitted trough features (3a).

9.2.2.2 PCT-B

The normalised mass loss, based on the B release, was approximately two times greater for the ISG (Zr-rich) compared to ISGI and ISGO (Sr-rich) after 28 d (Fig. 9.7a). The normalised mass loss based on the conventional tracers of PCT-B glass dissolution (B, Si and Na) followed the trend (from the most to the least durable) ISGO > ISGI > ISG. The increased chemical resistance of ISGO (compared to ISG) in the residual rate (Stage II) over the period 7-28 d based on NL_B (Table 9.3 & Fig. 9.7) may be due to: 1) the possible passivating effects of Sr in a presumed gel layer, assuming distinct similarities in the behaviour of Sr and Ca based on their same divalent charge; 2) the adverse effects of Zr at greater reaction progress, which inhibits gel structure reorganisation, leading to the retention of pores in the (assumed) gel layer (Sicard *et al.* 2004, Cailleteau *et al.* 2008) and/or ; 3) a combination of the stated effects. The ISG displayed an aggressive residual rate (Stage II) over the period 7-28 d, which was approximately a factor of three faster than ISGI and ISGO based on the B dissolution rate (Table 9.3).

The trend for NL_{Ca} was reversed when compared with the other elements (Fig. 9.7d). This could be attributed to alteration (gel) layer structural competition between Ca and Sr for ISGI and ISGO, which may be explained by greater retention of Sr in the presumed layer, and therefore greater Ca loss. Note that a hydrated altered gel layer is heavily assumed based on the general description of glass dissolution (Frugier *et al.* 2008, Vienna *et al.* 2013), yet the presence such a layer was not directly observed by SEM (cross sectioned particle images not shown for brevity). Speculatively, the larger ionic radius of Sr may be more suited to charge compensate elements (Al, Zr) in the alteration layer rather than the relatively smaller ionic radius of Ca. This reversed trend was also observed in the Al dissolution behaviour (Fig. 9.7f), which suggests that Al was gradually incorporated into the assumed alteration layer for ISGO with increasing reaction progress, whereas Al was potentially incorporated into an alteration layer at early stages for ISG and ISGI. Hence, it is tentatively suggested that Ca has a greater effect at retaining Al in an altered gel layer when compared with Sr (assuming Sr is incorporated in the gel layer). Unfortunately, it was not possible to clearly observe any alteration layer by SEM analysis at the resolution employed; further work using alternative methods (e.g. ToF-SIMS) or performing experiments for longer durations is therefore required.

XRD traces post PCT-B dissolution did not reveal the presence of any secondary phases (Fig. 9.7h). The pH measurements of the leachate were scattered and therefore largely inconclusive, however measurements from all compositions were approximately equal within experimental uncertainty until 14 d, after which the pH readings from the ISG leachate increased, which coincided with the increased NL_i (Fig. 9.7h & g respectively).

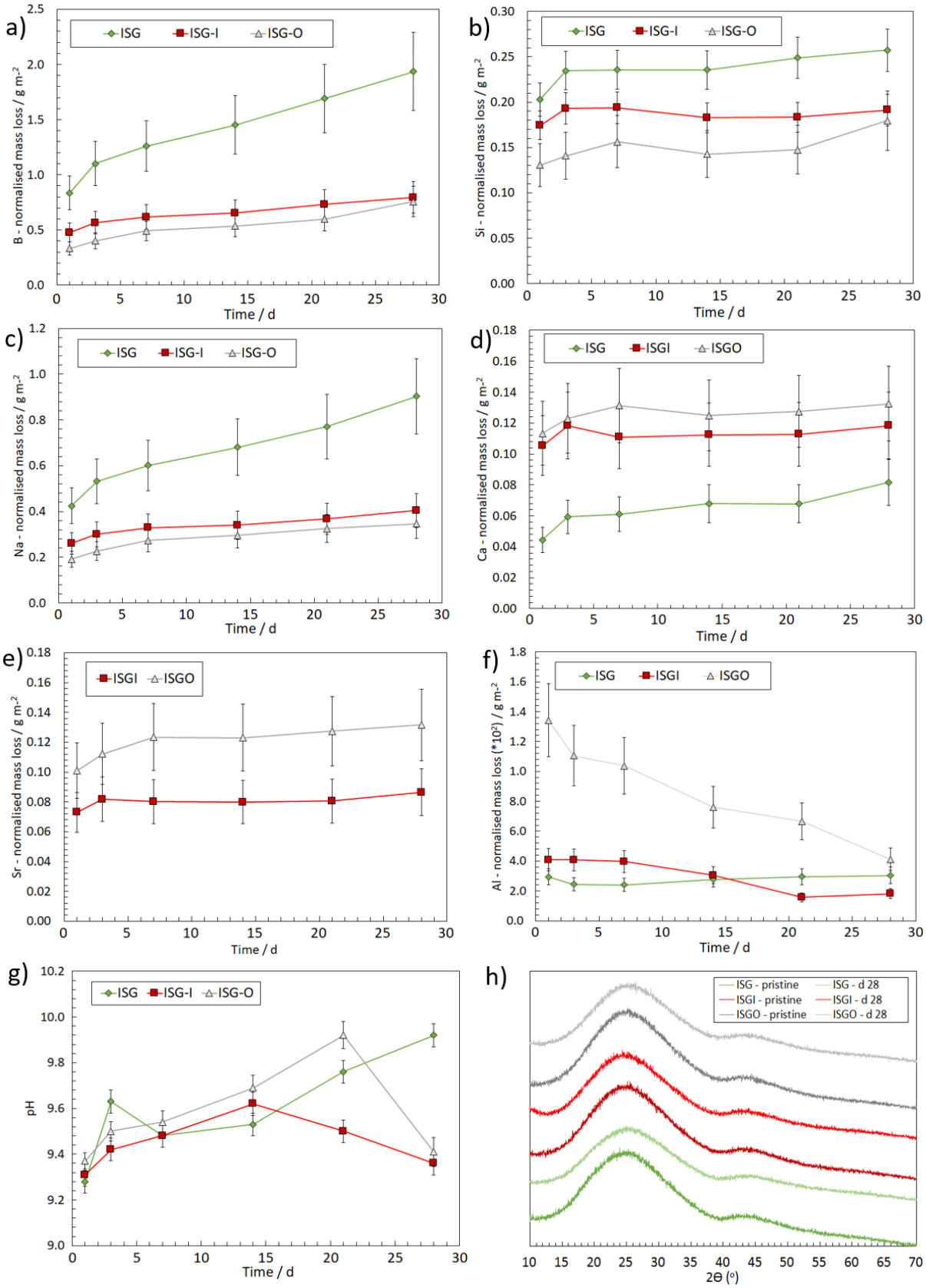

Figure 9.7 a-f) Normalised mass loss of elements; g) leachate pH(RT) measurements and h) XRD traces from the 90 °C, 28 d PCT-B experiments.

Table 9.3. Residual dissolution rates (Stage II) from the 90 °C PCT-B (UHQ) investigations from 7-28 d obtained from a linear regression.

	Residual Rate (Stage II) 7-28 d (g m^{-2} d^{-1})			
Glass	B	R^2	Si	R^2
ISG	$(3.2 \pm 1.8) \times 10^{-2}$	0.998	$(0.57 \pm 2.8) \times 10^{-3}$	0.891
ISGI	$(0.83 \pm 0.82) \times 10^{-2}$	0.974	$(0.14 \pm 2.2) \times 10^{-3}$	0
ISGO	$(1.1 \pm 0.7) \times 10^{-2}$	0.911	$(1.0 \pm 1.9) \times 10^{-3}$	0.377

Surface features post PCT-B dissolution

SEM inspection of whole glass particles from all compositions post 28 d PCT-B dissolution revealed the presence of Ca-containing precipitates (Fig. 9.8), but did not show evidence for a gel layer (cross sectioned particles also failed to detect surface alteration). However, the presence of an hydrated/altered gel layer should not be ruled out (Geisler *et al.* 2019). It was not possible to identify the Ca-containing precipitates by XRD due to their low abundance. Such features were seen in greater abundance along the series ISGO >> ISGI ~ ISG (which correlates with the Ca normalised mass loss from the PCT-B dissolution tests); an estimation (based on a random sample of ten 800 x 800 µm SEM images, similar to Figs. 9.4a, 9.5a and 9.6a) revealed that approximatly 10 % of ISGO and 1 % of ISGI and ISG particles contained such precipitates. The presence of such precipitates could be due to: 1) the transformation of the assumed gel layer into more stable phases during dissolution; 2) the transformation of the gel layer into more stable phases induced by the quenching and drying process post experimentation (Iler 1979, Brinker & Scherer 1990, Geisler *et al.* 2019); 3) the precipitation of elements from solution onto the surface of the glass during dissolution, or quenching and drying.

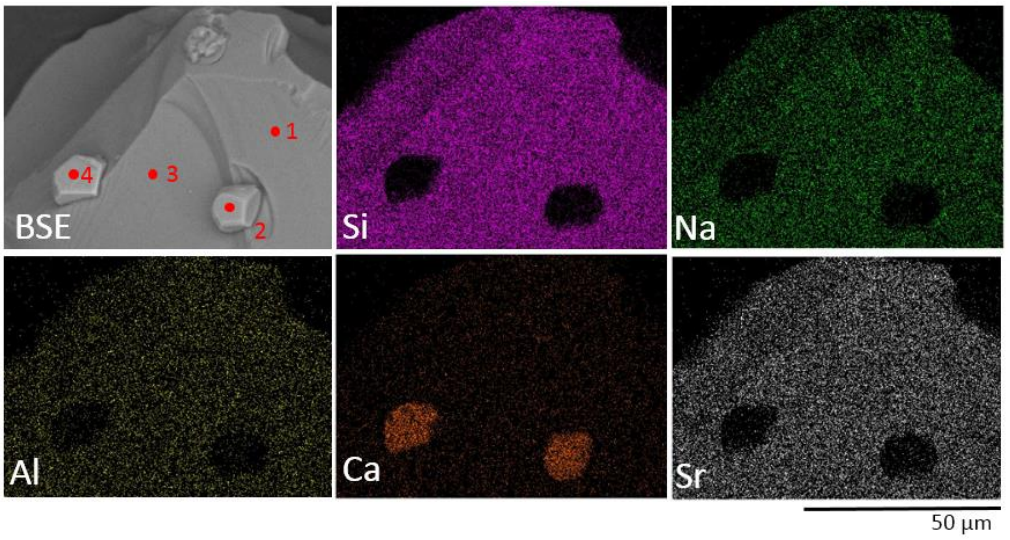

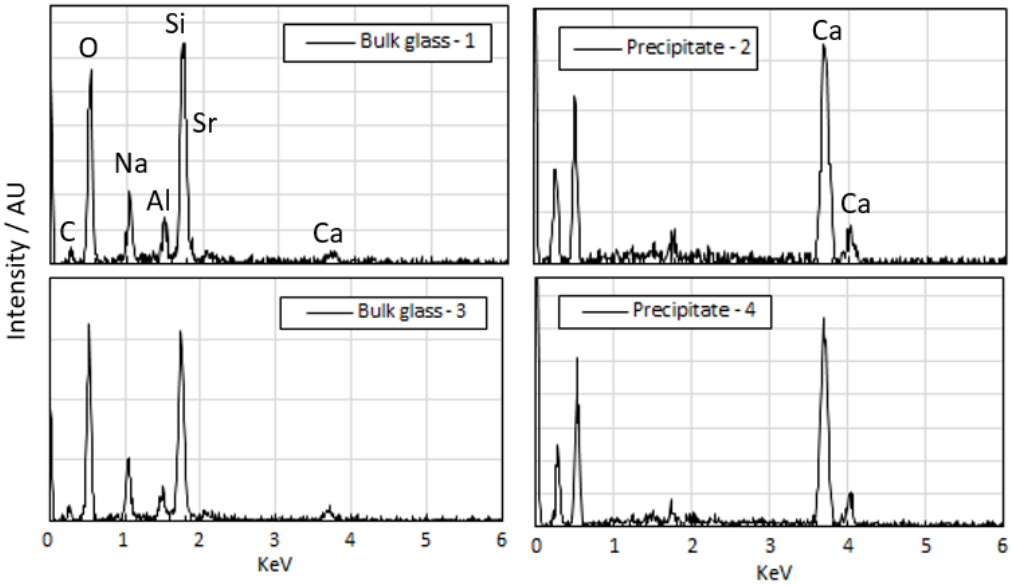

		Element At. %				
Section	Spot #	Si	Al	Na	Ca	Sr
Bulk glass	1	65.5 ± 1.1	9.4 ± 0.2	19.1 ± 0.4	4.8 ± 0.1	1.3 ± 0.1
Precipitate	2	3.9 ± 0.1	2.6 ± 0.1	4.4 ± 0.1	88.5 ± 1.7	0.7 ± 0.1
Bulk glass	3	61.7 ± 1.3	7.6 ± 0.2	23.3 ± 0.1	6.1 ± 0.1	1.3 ± 0.1
Precipitate	4	3.4 ± 0.1	2.6 ± 0.1	3.1 ± 0.1	91.0 ± 1.6	-

Figure 9.8. Ca-rich precipitates on the surface of an ISGO particle post 28 d PCT-B dissolution at 90 °C in UHQ (also representative of ISG and ISGI). EDS analysis and elemental At.% of such features are provided.

9.3 Discussion

Structural analysis of each glass by NMR spectroscopy did not reveal any significant structural changes, but subtle changes may exist, due to the network-modifying role of Sr and network-forming role of Zr. Initial dissolution rates (Stage I) were obtained from SPFT tests, which confirmed the greater durability of the fully transmutated Zr containing ISG, which may be explained by the greater polymerisation and subsequent greater resistance to hydrolysis of the network. However, residual rates suggested the opposite: the fully transmutated Zr containing ISG was the least durable. Such results are consistent with the findings of Chapter 5: that there exists a correlation between δ^{29}Si and initial dissolution rates (Icenhower *et al.* 2008).

The PCT-B results suggest that an aggressive residual rate was observed based on the NL_B and NL_{Na} for the ISG (Fig. 9.7a & c) consistent with Kaspar *et al.* (2019), however a slower residual rate of dissolution was observed based on the NL_{Si}. The faster NL_B, parallel with the slower NL_{Si}, indicates that a passivating Si layer was not formed for the ISG, consistent with Chapter 7 and the studies by Sicard *et al.* (2004) and Cailleteau *et al.* (2008), who showed that the dynamics of protective alteration layer formation are disrupted due to the inclusion of Zr (less soluble than Si), which hinders gel structural reorganisation and the retention of a certain degree of porosity. Such findings interestingly, and paradoxically, show that insoluble elements can lead to a greater degree of corrosion (Cailleteau *et al.* 2008). The formation of a passivating layer is inferred on ISGI and ISGO from the residual rate attainment based on the NL_B, NL_{Na} and NL_{Si}, which may be due, in part, to the passivating effect of Sr in an assumed gel layer. The PCT-B tests also revealed the presence of Ca-rich secondary precipitates on all compositions. If the Ca-rich phases were formed by the transformation of altered glass (gel) into more stable phases during dissolution, this could imply that that Ca-rich precipitates are more readily formed than a gel layer. Such a suggestion is supported by evidence of Ca-rich precipitates on the surface of ZnCa 0:100 glass in Figure 5.24, Chapter 5. However, in-situ Raman experiments/observations of the reaction progress would elucidate such unceartainy (Geisler *et al.* 2019).

An increase in the residual dissolution rate (Stage II) with the addition of Zr to alkali-borosilicate glass was consistent with the literature (Fisher *et al.* 2005 (not the author of this Thesis), Karell *et al.* 2006, Cailleteau *et al.* 2008, Cailleteau *et al.* 2011); in all instances the negative impact on the chemical durability was always observed, irrespective of Zr substitution for network formers, network modifiers and in this study, Sr. In alkali borosilicate glass, Zr exists in 6-coordinated [ZrO_6] network-forming

octahedra (Farges *et al.* 1991, McKeown *et al.* 1999, Connelly *et al.* 2011). However, when Sr decays to Zr in nuclear waste glass, it should be assumed that Zr will play a network modifying role, based on the original role of the parent Sr. Note that Zr in the ISG and ISGI glass has been strongly assumed to be playing a network forming role (Farges *et al.* 1991, McKeown *et al.* 1999, Connelly *et al.* 2011); in transmuted nuclear waste glass it may be suggested to play a network modifying role, thus, making it more susceptible to dissolution. Such a suggestion is particularly important for long-term durability predictions and modelling. Future work, involving molecular dynamic simulations may shed some light on the structural changes imparted on the glass by the radioactive decay/transmutation of Sr to Zr. Determining the structural role of Sr (in pristine nuclear waste glass) and Zr (in transmuted nuclear waste glass) was beyond the scope of this study and is an unresolved question in which further work is required to advance the field.

In UK HLW (particularly MW25 and ZnCa MW28), the content of SrO is < 1 wt. % and the effects of transmutation on the dissolution of the glass may be negligible. However, if the content rises > 1 wt. % due to increased wasteloading (forecast at the Sellafield site (Harrison 2018)), and from higher nuclear fuel burn-up, or advanced vitrified wasteforms, the effect of transmutation on the dissolution of the vitrified product should be considered, alongside the transmutation of Cs → Ba. Thus, further work on the structure-dissolution relationship of Cs_2O (1.07-2.13 wt.% in, and potentially expected in UK HLW (Scales 2011, Brookes *et al.* 2011, Schofield *et al.* 2017, Harrison 2018)) containing glasses in suggested.

Similarities in the behaviour of Sr and Ca in the inferred gel layers in this work has largely been assumed, based on their divalent charge, however no studies have been conducted, to the best of the authors knowledge, in the field of nuclear waste glass corrosion to strengthen this assumption. Similarities and differences have been reported by Fredholm *et al.* (2011) in the field of biological glasses, which suggest that the replacement of Sr for Ca results in glass which is less durable.

This preliminary study, which was essentially a staging point for further investigations, highlights a key indirect point; that almost all dissolution studies in the literature on wasteloaded HLW simulants have proceeded based on initial glass formulations, not based on expected compositions at the time of first groundwater contact in a GDF. Despite the small quantities of transmutation prone fission products in the original glass, this Chapter shows that they do have an impact on the short/medium term dissolution based on the SPFT and PCT-B results. Such results may be strengthened by the further work investigating structure-dissolution relationships of Cs and Ba containing glasses. A question can be therefore posed: are the traditional well-studied HLW nuclear waste glass analogues (SON68,

MW25, ZnCa MW28) truly representative of the glass product in a GDF in > 300 years time? It is well understood, yet under-reported that they are definitely not in terms of the inactive glass analogues dissolving slower than active samples (Gin 2019), but the transmutation of fission products needs to be considered for a fully descriptive performance assessment. Taken collectively, the vitrified nuclear waste corrosion community may be underestimating the chemical durability of vitrified HLW, which should be understood for a comprehensive performance assessment and to inform future modelling and predictions for geological disposal.

9.4 Conclusion

The objective of this Chapter was to account for the compositional effect of the simulated radioactive transmutation of Sr to Zr in ISG-type glasses on the structure-durability relationship across Stages I and II of glass corrosion. Results from structural MAS-NMR analysis and SPFT dissolution tests tentatively suggest that there is a structure-durability relationship – at the initial rate of dissolution, the more polymerised transmutated Zr-rich ISG was more chemically resistant to dissolution than the Sr-rich ISGO. However, the PCT-B dissolution data suggests an inverse relationship between the initial and residual rate (Stage II), whereby the Sr-rich ISGO become more chemically resistant to dissolution after transitioning to the residual rate. This may be due, in part, to the potential passivating effects of Sr on the structure of the assumed gel layer, assuming similar behaviour to Ca, and/or to the detrimental effect of Zr in the assumed gel layer due to its role in retaining a more porous alteration layer. Further work is needed to validate such a claim, yet this preliminary study indirectly raises an issue for the geological disposal of vitrified HLW nuclear waste: that almost all dissolution studies in the literature on wasteloaded HLW simulants have proceeded based on initial glass formulations (incorporating fission products), not based on expected compositions (containing fission daughter products) at the time of first groundwater contact in a GDF, whereby the dissolution behaviour may be not truly representative. Future work investigating the transmutation behaviour of Cs to Ba is suggested to strengthen such a claim, alongside studying the effect of transmutation on more complex simulant HLW compositions.

10. Concluding Remarks and Future Work

The objective of this Thesis was to underpin the impact of ZnO and CaO additions to the alkali-alumina-borosilicate MW HLW glass by assessing the structure-durability relationship of base and simulant waste-loaded glass compositions, which was extended to investigate the dissolution in conditions representative of geological disposal in the UK, incorporating potential groundwater solutions and differing corrosion scenarios. This Thesis has generally demonstrated, irrespective of the dissolution methodology and experimental conditions employed, that the addition of ZnO to base and waste glass compositions (with and without the presence of CaO) lead to Zn-phyllosilicate clay precipitation, which was to the detriment of the longer term chemical durability, facilitating Stage III 'rate resumption'. The addition of CaO (without the presence of ZnO) was found to impart greater resistance to dissolution at greater reaction progress due to the passivating effect that Ca has on the structure of the alteration layer.

In particular:

- Chapter 4 generated new initial dissolution rate data of the International Simple Glass (ISG) in acidic and basic media, alongside obtaining rate law parameters (K_o, η, and E_a) applicable to Transition State Theory.
- Chapter 5 underpinned the fundamentals of dissolution on simple ZnCa MW base glasses, which suggested that changes to the ZnO:CaO ratio produced markedly different behavior in terms of the structure-durability relationship at different stages of dissolution reaction progress. Such structure-dissolution investigations highlighted that glasses that are *initially* durable (i.e. at the initial rate (Stage I)) owing to a greater resistance to hydrolysis due to the greater connectivity of the glass network, such as the more polymerized Zn-rich glasses, *did not translate* to long-term durable glasses due to the precipitation of Zn-phyllosilicates at greater reaction progress causing rate resumption (Stage III).
- Chapter 6 showed that the findings from the simple glasses presented in Chapter 5 were applicable to waste loaded versions of ZnCa MW-type compositions. A ZnO free, but CaO-rich composition conferred the greatest optimal durability. Further work investigating greater time periods of dissolution and in media more relevant to geological disposal conditions is required to further substantiate these results. Further research should also focus on the additive or competing role of Zn- and Mg-phyllosilicate precipitation on the rapid

residual/resumed rates to aid the development of performance models to assess the suitability of the currently adopted ZnCa MW formulation for the vitrification of the UK's HAW.

- Chapters 7 & 8 preliminary explored the dissolution of ZnCa MW28 in conditions more representative of geological disposal, in generic groundwater solutions and in different corrosion scenarios, respectively. These Chapters further highlighted the combined influence of Zn- and Mg-phyllosilicate precipitation on the chemical durability, which resulted in elevated dissolution through a suspected dissolution/re-precipitation mechanism. The Cyclic-Vapour-Static (CVS) methodology showed that ZnCa MW28 was less durable than MW25 and that secondary phases formed during the vapour phase period of dissolution contained inactive fission products, which were likely dissolved during the liquid phase period of dissolution for both compositions. The instantaneous release of such elements – an 'instant release fraction' for vitrified HLW – should be further explored to develop a robust safety case for geological disposal.
- Chapter 9 reflected upon the application of simplified inactive glass samples as an analogue of radionuclide containing HLW undergoing transmutation, with a particular focus on the β-decay of Sr to Zr. Results suggested that small changes in composition, on the order of 2 mol.%, had an effect on the structure-durability relationship (echoing the results presented in Chapter 5), associated with the relative difference in charge of these species (divalent vs tetravalent) and possibly also the solubility. In the example studied here, the overall effect was that the glass durability was overall decreased by the 'transmutation'.

References

Aagaard, P. & Helgeson, H. C. Thermodynamic and kinetic constraints on reaction rates among minerals and aqueous solutions. I. Theoretical Considerations. *Am. J. Sci.* **282**, 237-285 (1982).

Abdelouas, A. Personal communication. 3rd PETRUS-ANNETTE & 11th European Nuclear Education Network, PhD and Early Stage Researchers Conference, Campus of Alameda, Téchnico Lisboa, Portugal, 26th-30th June (2017).

Abraitis, P. K., McGrail, B. P., Trivedi, D. P., Livens, F. R. & Vaughan, D. J. Single-pass-flow-through experiments on a simulated waste glass in alkaline media at 40 °C. 1. Experiments conducted at variable solution flow rate to glass surface area ratio. *J. Nucl. Mater*. **280**, 196-205 (2000).

Abraitis, P. K., McGrail, B. P., Trivedi, D. P., Livens, F. R. & Vaughan, D. J. Single-pass-flow-through experiments on a simulated waste glass in alkaline media at 40 °C. 2. Experiments conducted with buffer solutions containing controlled quantities of Si and Al. *J. Nucl. Mater*. **280**, 206-215 (2000a).

Abraitis *et al.* The kinetics and mechanisms of simulated British Magnox waste glass dissolution as a function of pH, silicic acid activity and time in low temperature aqueous system. *Appl. Geochem.* **15**, 1399-1416 (2000c).

Advocat *et al.* Long-term alteration mechanisms in water for SON68 radioactive borosilicate glass. *J. Nuc. Mat.* **298**, 55-62 (2001).

Advocat *et al.* Commissariat á L' Énergie atomique, Final report for the IAEA co-ordinated research programme (1991-1996) Long-term behaviour of HLW glasses in geological disposal conditions (1997).

Ait Chaou *et al.* The role of pH in the vapour hydration at 175 °C of the French SON68 glass. *Appl. Geochem.* **76**, 22–35 (2017).

Altaner *et al.* Magic-angle spinning nuclear magnetic resonance investigation of phyllosilicates. *Proceedings of the 9th International Clay Conference, Strasbourg, 1989, V. C. Farmer and Y. Tardy (Eds). Sci. Géol.,* **89***,* p. 159-168 (1990).

Anaf, W. Study on the formation of heterogeneous structures in leached layers during the corrosion process of glass. *CeROArt. No. EGG 1.,* http:/journals.openedition.org/ceroart/1531 (2010).

ANDRA, Dossier 2005 Argile, Tome, Phenomenological Evolution of a Geological Repository, in: ANDRA Report C.RP.ADS.04.0025, 1-525 (2005).

Angeli *et al.* Effect of thermally induced structural disorder on the chemical durability of International Simple Glass. *npj Mater. Degrad.* 2:31 (2018). https://doi.org/10.1038/s41529-018-0052-3

Angeli *et al.* Effect of temperature and thermal history on borosilicate glass structure. *Phys. Rev. B.* **054110** (2012).

Apperley *et al. Solid-State NMR: Basic Principles & Practice,* 1st ed. (New York: Momentum Press) (2012).

Aréna *et al.* Impact of Fe, Mg and Ca elements on glass alteration: Interconnected processes. *Geochim. Cosmochim. Acta* **239**, 420-445 (2018).

Aréna *et al.* Impact of Zn, Mg, Ni and Co elements on glass alteration: Additive effects. *J. Nucl. Mater.* **470** 55-67 (2016).

ASTM Standard, Standard practice for measurement of the glass dissolution rate using the single-pass flow-through test method (SPFT). C1662-18, (2018).

ASTM - Standard Test Methods for Determining Chemical Durability of Nuclear, Hazardous and Mixed Waste Glasses and Multiphase Glass Ceramics: The Product Consistency Test (PCT) (ASTM C1285-14). 1-26 (2014). doi:10.1520/C1285-14.2

ASTM - Standard Test Method for Static Leaching of Monolithic Waste Forms for Disposal of Radioactive Waste (ASTM C1220-10). (2014). doi:10.1520/C1220-10.

ASTM Standard, Standard practice for measurement of the glass dissolution rate using the single-pass flow-through test method (SPFT). C1662-10, (2010).

ASTM Standard, Standard test method for measuring waste glass or glass ceramic durability by vapour hydration test. C1663-09, (2009).

Backhouse *et al.* Investigating of the role of Mg and Ca in the structure and durability of aluminoborosilicate glass. *J. Non. Cryst. Solids* **512**, 41-52 (2019).

Backhouse, D. J. A study of the dissolution of nuclear waste glasses in highly alkaline conditions. Thesis submitted to The University of Sheffield, May (2016).

Bailey L. Development of a Generic Safety Narrative fir a UK Geological Disposal Facility. *Min. Mag.,* **79**, [6], 1633-1640 (2015).

Bakel A. J., Ebert W. L., Strachan D. M. and Brwon N. R. Glass dissolution at 20, 40, 70 and 90 °C: Short-term effects of solution chemistry and long-term Na release. 1996 American Ceramics Society Meeting, Indianapolis, Indiana (1996).

Banba *et al.* Chemical analysis of high-level-radioactive waste glass by ICP-AES *Analytical Sciences,* **14**, 389-394 (1998).

Barinov *et al.* Change of structure and properties of vitrified radioactive wastes during long-term storage in an experimental repository. *Atomic Energy.* **105**, [2] (2008).

Barkatt *et al.* Oscillations in the dissolution kinetics of silicate glass in tri-buffered aqueous media. *J. Non-Cryst. Solids* **155**, 141-148 (1993).

Bates *et al.* Hydration aging of nuclear waste glass. *Science.* **218**, 51-54 (1982).

Bates *et al.* The relevance of vapor phase hydration aging to nuclear waste isolation. *Nucl. Chem. Waste Manag.* **5**, 63-73 (1984).

Bauer *et al. Appl. Geochem.* **13**, 619-629 (1998).

Boast, L. Investigation of the thermal treatment of higher activity waste. Thesis submitted to The University of Sheffield, September (2018).

Boksay, Z., Bouquet, G. & Dobos, S. Diffusion processes in surface layers of glass. *Phys. Chem. Gla*. **8**, [4], 140-144 (1967).

Bouakkaz *et al.* Alteration of ^{29}Si-doped SON68 borosilicate nuclear waste glass in the presence of near-field materials. *Appl. Geochem.* **111,** 104436 (2019).

Bouakkaz *et al.* Kinetic study and structural evolution of SON68 nuclear waste glass altered from 35 to 125 °C under unsaturated H_2O and D_2O^{18} vapour conditions. *Corr. Sci.* **134**, 1-16 (2018).

Bouakkaz *et al.* SON68 glass alteration under Si-rich solutions at low temperatures (35-90 °C): kinetics, secondary phases and isotopic exchange studies. *RSC Adv.* **6** 72616-72633 (2016).

Bouna *et al*. Mineralogical and physico-chemical chatacterization of ferruginous beidellite-rich clayfrom Agadir basin (Morocco). *Clay and Clay Minerals.* **60**, [3], 278-290 (2012).

Bourcier W. L., Weed H. C, Nguyen S. N., Nielsen J. K., Morgan L., Newton L. and Knauss K. G. Solution compositional effects on the dissolution kinetics of borosilicate glass. In: *Water-Rock Interaction* (eds. Y. K. Kharaka and A. S. Maest), Proceedings of the 7th International Symposium on Water-Rock Interaction, WRI-7, Park City, Utah, Balkema, pp 81-84 (1992).

Bourcier, W. L., Carroll, S. A. & Phillips, B. L. Constraints on the affinity term for modelling long-term glass dissolution rates. *Mater. Res. Soc. Symp. Proc.* **333**, 507-512 (1994).

Bourcier W.L. Affinity functions for modelling glass dissolution rates. *U.S DOE report UCRL-JC-131186* (1998).

Brady P.V. & House W.A. Surface-controlled dissolution and growth of minerals. Pp 225-306 in: *Physics and Chemistry of Mineral Surfaces* (P.V. Brady, editor). (CRC Press: New York) (1996).

Brawer, S. A. & White, W. B. Raman spectroscopic investigation of the structure of silicate glasses (II). Soda-alkaline earth-alumina ternary and quaternary glasses. *J. Non-Cryst. Solids* **23**, [2] 261-278 (1977).

Brinker, C. J. & Scherer, G. W. Sol-Gel Science: The Physics and Chemistry of Sol-Gel Processing (Academic: San Diego) (1990).

Brookes *et al.* The effect of increased waste loading on the durability of high level waste glass. *MRS Online Proceeding Library Archive, January 2011.* DOI:10.1557/PROC-1265-AA03-05 (2011).

Bruton, C. Mater. Res. Soc. Symp. Proc. **112** 607 (1987).

Bunker *et al. Phys. Chem. Glasses,* **31** [1], 30-40 (1990).

Burger *et al.* Impact of iron on nuclear glass alteration in geological repository conditions: A multiscale approach. *Appl. Geochem.* **31**, 159–170 (2013).

Cailleteau *et al.* Why do certain glasses with a high dissolution rate undergo a low degree of corrosion? *J. Phys. Chem. C.* **115**, 5846-5855 (2011).

Cailleteau *et al.* Insight into silicate-glass corrosion mechanisms. *Nat. Mater.* **7,** 978-983 (2008).

Calestani *et al.* Influence of some oxides on the durability of a borosilicate glass. *J. Non-Cryst. Solids* **84**, 452-462 (1986).

Callas *et al.* The structural properties of cations in Nuclear glasses. *Proc. Mat. Sci.* **7**, 23-31 (2014).

Callas *et al.* Structure-property relationships in multicomponent oxide glasses. *C.R. Chim.* **5**, 831-843 (2002).

Campbell, R. Public Acceptance Aspects of the Storage and Disposal of Higher-Level Radioactive Waste – UK's Experience. Presentation at the Sixth Review Meeting of the Contracting Parties to the Joint Convention on the Safety of Spent Fuel Management and on the Safety of Radioactive Waste Management, Topical Session 29th August 2018, Vienna, Austria (2018).

Cassingham *et al*. The structural role in nuclear waste glasses. *Int. J. App. Gla. Sci*. **2**, [4] 343-353 (2011).

Cassingham, N. J., Corkhill, C. L., Stennett, M. C., Hand, R. J. and Hyatt N. C. Alteration layer formation of Ca- and Zn-oxide bearing alkali borosilicate glasses for immobilisation of UK high level waste: A vapour hydration study. *J. Nucl. Mater*. **479**, 639-646 (2016).

Cassingham *et al.* The initial dissolution rates of simulated UK Magnox-ThORP blend nuclear waste glass as a function of pH, temperature and waste loading. *Miner. Mag.* **79**, 1529 – 1542 (2015).

Caurel, J. Alteration hydrothermale du verre R7T7 cinétiques de dissolution du verre à 150 et à 25O °C, rôle des phases néoformées (De L'Universite de Poitiers) (1990).

Charles, R. J. Static fatigue of glass. *J. Appl. Phys.* **29,** [11] 1549-1553 (1958).

Chave *et al. J. Nucl. Mater.* **362**, 466 (2007).

Chave, T., Frugier, P., Gin, S. & Ayral, A. Glass-water interphase reactivity with calcium rich solutions. *Geochim. Cosmochim. Acta* **75**, 4125-4139 (2011).

Chinnam, R. K., Fossati, P.C.M., W. E. Lee. Degradation of partially immersed glass: A new perspective. *J. Nucl. Mater.* **503,** 56-65 (2018).

Cohen-Tannoudji *et al.* Quantum Mechanics, Volume 2: Angular Momentum, Spin, and Approximation Methods. John Wiley & Sons (2019).

Coles *et al.* Leaching study of PNL 76-68 glass beads using the LLNL continuous-flow method and the PNL modified IAEA method. Final report UCID—1949-REV.1 https://inis.iaea.org/search/search.aspx?orig_q=RN:14743259 (1982).

Collin, M. & Fournier, M. Impact of alkali on the passivation of silicate glass. *npj Mater. Degrad*. 1-10 (doi:10.1038/s41529-018-0036-3 (2018).

Connelly *et al.* Compositional-structure relationship in simplified nuclear waste glasses: 2. the effect of ZrO_2 additions. *J. Am. Ceram. Soc.* **94**, 137-144 (2011).

Corkhill *et al.* Multi-scale investigation of uranium attenuation by arsenic at an abandoned uranium mine, South Terras. *Npj Mater. Deg.* **1,** 19 (2017).

Corkhill, C. L., Fisher, A. J., Strachan, D. M., Hand, R. J. & Hyatt N. C. Corrigendum to "The initial dissolution rates of simulated UK Magnox-ThORP blend nuclear waste glass as a function of pH, temperature and waste loading" [*Miner. Mag.* **79**, 1529 – 1542 (2015)]. *Miner. Mag.* **82**, [4] 939-942 (2018).

Corkhill, C. L., Cassingham, N. J., Heath, P. G. & Hyatt, N. C. Dissolution of UK High-Level Waste Glass Under Simulated Hyperalkaline Conditions of a Colocated Geological Disposal Facility. *Int. J. Appl. Gla. Sci*. **4**, 341-356 (2013).

CoRWM. Committee on Radioactive Waste Management, CoRWM Position Paper: Policy, Legal and Regulatory Issues for a GDF and Associated Radioactive Waste Management Issues, April (2021).

Cormier *et al.* Competition for charge compensation in borosilicate glasses. *Phys. Rev. B.* **61**, 14495-14499 (2000).

Curti *et al.* Glass dissolution parameters: update for Entsorgungsnachweis, Nagra Technical Report NTB 02-21, Nagra, Wettingen, Switzerland (2003).

Curti *et al.* Long-term corrosion of two nuclear waste reference glasses (MW and SON68) : A kinetic and mineral alteration study, *Appl. Geochem.* **21**, 1152-1168 (2006).

Darab *et al.* NMR characterization of simulated Hanford low-activity waste form chemical durability and its use in understanding waste form chemical durability. *Mater. Res. Soc. Sym. Proc.* (eds. D. J. Wronkiewicz and J. H. Lee). Materials Research Society, Boston Ma (1999).

Darab *et al.* Composition-structure relationships in model Hanford low-level waste glasses. *Environmental Issues and Waste Management Technologies. II – Ceramic Transactions. American Ceramic Society,* Westerville, OH, (1997).

De Echave *et al.* Influence of iron on the alteration of the SON68 nuclear glass in the Callovo-Oxfordian groundwater. *Appl. Geochem.* **100**, 268-278 (2019).

Debure *et al.* In situ nuclear-glass corrosion under geological repository conditions, *npj Mater. Degrad.* 3:38 (2019). Doi.org/10.1038/s41529-019-0100-7

Debure *et al.* Mineralogy and thermodynamic properties of magnesium phyllosilicates formed during the alteration of a simplified nuclear glass. *J. Nucl. Mater*. **475**, 255-265 (2016).

DECC, Department of Energy and Climate Change, Implementing Geological Disposal: A Framework for the long-term management of higher activity radioactive waste, URN 14D/235 (2014).

Denmark National Report from The Unity of the Realm, Joint Convention on the Safety of Spent Fuel Management and on the Safety of Radioactive Waste Management 6th Review Meeting (2018).

Delaye *et al.* Molecular dynamics simulation of radiation damage in glasses. *J. Non-Cryst. Solids.* **357** 2763-2768 (2011).

Dell *et al.* ^{11}B NMR studies and structural modelling of Na_2O-B_2O_3-SiO_2 glasses of high soda content. *J. Non-Cryst Solids,* **58**, 1-16 (1983).

Dhara *et al.* A comparative study on the structural aspects of sodium borosilicate glasses and barium borosilicate glasses: Effect of Al_2O_3 addition. *J. Non-Cryst. Sol,* **447**, 283-289 (2016).

Diallo *et al.* Deconvolution method of ^{29}Si MAS NMR spectra applied to homogenous and phase separated lanthanum aluminosilicate glasses. *J. Non-Cryst. Sol,* **503-504**, 352-365 (2019).

Dibble, W. E. & Tiller, W. A. *Clays Clay Miner.* **29**, 323-330 (1981).

Dohmen *et al.* Pattern formation in silicate glass corrosion zones. *Int. J. Appl. Glass. Sci.* **4**, 357-370 (2013).

Donald, I. W. Waste Immobilisation in Glass and Ceramic Based Hosts: Radioactive, Toxic and Hazardous Wastes (Wiley : London) (2010).

Du L.-S. & Stebbins J. F. Network connectivity in aluminoborosilicate glasses: a high-resolution ^{11}B, ^{27}Aland ^{17}O NMR study. *J. Non-Cryst. Solids*, **351**, 3508-3520 (2005).

Duddridge *et al.* Boron and silicon speciation in waste simulant doped borosilicate glasses using multinuclear MAS-NMR. *Glass. Tech.* **44** [2], 85-89 (2003).

Dumas, T. & Petiau, J. EXAFS study of titanium and zinc environments during nucleation in a cordierite glass. *J. Non-Cryst. Solids* **81**, 201-210 (1986).

Dunnett *et al.* Vitrification of high molybdenum waste. *Glass. Tech.: Eur. J. Glass Sci. Tech.* **53** [4], 166-171 (2012).

Dove, P. M. The dissolution kinetics of amorphous silica into sodium chloride solutions: effects of temperature and ionic strength. *Am. J. Sci.* **294,** 665-712 (1994).

Ebert *et al*. Glass Testing Activities at ANL and SRNL: FY11 Progress Report, [FCRDWAST-2011-000404] from Argonne National Laboratory, Argonne, IL (2011).

Ebert W. L. & Tam S. –W. *Mat. Res. Soc. Symp. Proc*. **465**, 149-156 (1996).

Ebert *et al.* Waste Manage. (Oxford) **11**, 205-221 (1991).

El-Damrawi *et al.* ^{11}B, ^{29}Si, ^{27}Al Nuclear magnetic resonance studies of Na_2O-Al_2O_3-B_2O_3-SiO_2 glasses. *Phys. Chem. Glasses,* **34** [2], 52-60 (1993).

Engelhardt G. & Michel D. High-resolution solid-state NMR of silicates and zeolites. Central Institute of Physical Chemistry, Academy of Science of the GDR Berlin, German Democratic Republic & Department of Physics, Karl Marx University, Leipzig, German Democratic Republic. John Wiley & Sons. 148-149 (1987a).

Engelhardt G. & Michel D. High-resolution solid-state NMR of silicates and zeolites. Central Institute of Physical Chemistry, Academy of Science of the GDR Berlin, German Democratic Republic & Department of Physics, Karl Marx University, Leipzig, German Democratic Republic. John Wiley & Sons. 143-146 (1987b).

Engelhardt *et al. Z. Chem.,* **25**, 252, (1985).

Ewing, R.C. Reflections of a scientist labouring in the nuclear waste field. Groundwater. Ground Water. **59** [2], 154-155 (2021). doi: 10.1111/gwat.13058

Ewing *et al.* Geological Disposal of Nuclear Waste: a Primer. *Elements.* **12**, 233-237 (2016).

Eyring H. The activated complex in chemical reactions. *J. Chem. Phy*. **3**, 107-114 (1935).

Falmon, J. Oscillatory silicon and aluminium aqueous concentrations during experimental aluminosilicate weathering. *Geochim. Cosmochim. Acta* **60**, 2901-2907 (1996).

Farges *et al. Geochim. Cosmochim. Acta.* **55**, 1563-1574 (1991).

Fawcett, T. G., Faber, J., Kabbekodu, S., Mcclune, F. & Rafaja, D. PDF-4+, the material identification database. *Microstruct. Anal. Mater. Sci.* 1–3 (2005).

Feng *et al. Nucl. Technol*. **104**, 193-206 (1993).

Feng, X. and Pegg, I. *J. Non-Cryst. Solids*. **175**, 281-293 (1994).

Ferlat *et al.* Evidence for symmetric cationic sites in zirconium-bearing oxide glasses. *Phys. Rev. B.* **73**, 214207 (2006).

Ferrand, K., Liu, S. & Lemmens, K. The Interaction Between Nuclear Waste Glass and Ordinary Portland Cement. *Int. J. Appl. Glas. Sci.* **4**, 328–340 (2013).

Ferrand. K., Abdelouas. A. & Grambow. B. Water diffusion in the simulated French nuclear waste glass SON 68 contacting silica rich solutions: Experiment and modelling. *J. Nucl. Mater.* **355**, 54-67 (2006).

Fisher, A.J., & Corkhill, C.L. Experimental studies to investigate the durability of UK HLW glasses using a new base glass formulation and glasses from POCO operations – RWM.01.008 09308 POCO Glass Durability Studies (2021).

Fisher *et al.* Soda lime zirconia silicate glasses as prospective hosts for zirconia-containing radioactive wastes. *J. Non-Cryst. Solids.* **351**, 623-631 (2005).

Fisher *et al.* The formation of pitted features on the International Simple Glass during dynamic experiments at alkaline pH. *MRS Advances*. **4**, [17-18], 993-999, (2019).

Fleury *et al.* SON68 glass dissolution driven by magnesium silicate precipitation, *J. Nucl. Mater.* **442**, 17-28 (2013).

Fournier *et al.* Glass dissolution rate measurement and calculation revisited. *J. Nucl. Mater,* **476**, 140-154 (2016).

Fournier *et al.* Resumption of nuclear glass alteration: State of the art. *J. Nucl. Mater.* **448**, 348-363 (2014).

Fournier *et al.* Effect of zeolite formation on borosilicate glass dissolution kinetics. *Procedia Earth Planet. Sci.* **7**, 264–267 (2013).

Fredholm *et al.* Influence of strontium for calcium substitution in bioactive glasses on degradation, ion release and apatite formation. *J. R. Soc. Interface.* **9**, 880-889 (2011).

Frugier *et al.* Application of the GRAAL model to leaching experiments with SON68 nuclear glass in initially pure water. *J. Nucl. Mater.* **392**, 552-567 (2009).

Frugier *et al.* SON68 nuclear glass dissolution kinetics: Current state of knowledge and basis of the new GRAAL model. *J. Nucl. Mater*. **380**, 8-21 (2008).

Galoisy *et al.* Evidence for 6-coordinated zirconium in inactive nuclear waste glasses. *J. Am. Ceram. Soc.* **82**, 2219-2224 (1999).

Gan *et al.* Long-term product consistency test of simulated 90-19/Nd HLW glass. *J. Nucl. Mater.* **408**, 102–109 (2011).

Gascoyne, M. Influence of grout and cement on groundwater composition. POSIVA Working Report 2002-07, Posiva Oy (2002).

Geisler *et al.* Real-time in situ observations of reaction and transport phenomena during silicate glass corrosion by fluid-cell Raman spectroscopy. *Nat. Mater.* **18**, 342-348 (2019)

Geisler *et al.* The mechanism of borosilicate glass corrosion revisited. *Geochim. Cosmochim. Acta* **158**, 112-129 (2015).

Geisler *et al.* Aqueous corrosion of borosilicate glass under acidic conditions: a new corrosion mechanism. *J. Non-Cryst. Solids* **356,** 1458-1465 (2010).

Geneste *et al.* Hydrogen-sodium interdiffusion in borosilicate glasses investigated from first principles. *J. Non-Cryst. Solids* **352, [28-29]** 3147-3152 (2006).

Gin, S. Personal communication – Glass Corrosion Workshop, Massachusetts Institute of Technology, Cambridge, MA, USA, 14th-15th June (2019).

Gin *et al.* Simplifying a solution to a complex puzzle. *npJ. Mater. Degrad.* 2:36 (2018).

Gin *et al.* Atom-probe tomography, TEM and ToF-SIMS study of borosilicate glass alteration rim: a multiscale approach to investigating rate-limiting mechanisms. *Geochim. Cosmochim. Acta.* **202**, 57-76 (2017).

Gin, S., Jollivet, P., Fournier, M., Frugier, P. & Charpentier, T. Origin and consequences of silicate glass passivation by surface layers. *Nat. Comms*. doi:10.1038/ncomms7360 (2015).

Gin *et al.* The fate of silicon during glass corrosion under alkaline conditions: A mechanistic study with the international simple glass. *Geochim. Cosmochim. Acta* **151**, 68-85 (2015).

Gin *et al.* An international initiative on long-term behaviour of high-level nuclear waste glass. *Mat. Tod.* **16**, 243-248 (2013).

Gin *et al.* New insight into the residual rate of borosilicate glasses: effect of S/V and glass composition. *Int. J. App. Gla. Sci.* **4**, [4], 371-382 (2013).

Gin. S., Beaudoux. X., Angeli. F., Jégou. C. & Godon. N. Effect of composition on the short-term and long-term dissolution rates of ten borosilicate glasses of increasing complexity from 3 to 30 oxides. *J. Non-Cryst. Solids* **358**, 2559-2570 (2012).

Gin *et al.* Nuclear glass durability: new insight into alteration layer properties. *J. Phys. Chem.* **115,** 18696-18706 (2011).

Gin et al. Role and Properties of the Gel Formed During Nuclear Glass Alteration: Importance of Gel Formation Conditions *J. Nucl. Mater*. **298** [1–2] 1–10 (2001).

Gin, S. & Mestre, J. P. SON 68 nuclear glass alteration kinetics between pH 7 and pH 11.5. *J. Nucl. Mater*. **295**, 83-96 (2001).

Gin. S. Control of R7T7 nuclear glass alteration kinetics under saturation conditions. *Mater. Res. Soc. Symp. Proc.* **412**, 189-196 (1996).

Godon *et al.* SON68 glass alteration enhanced by magnetite. *Procedia Earth and Planetary Science*. **7**, 300-303 (2013).

Goodhew *et al. Electron microscopy and analysis*, 3rd ed. (London: Taylor & Francis) (2001).

Gong *et al.* Analytical electron microscopy study of surface layers formed on the French SON68 nuclear waste glass during vapour hydration at 200 °C. *J. Nucl. Mater.* **254,** 249-265 (1997).

Goswami *et al.* MAS-NMR study of lithium zinc silicate glasses and glass ceramics with various ZnO content. *J. Sol. Sta. Chem.* **181**, 269-275 (2008).

Goût *et al.* Evaluating the temperature dependence of Magnox waste glass dissolution. *J. Non-Cryst. Solids* **518**, 75-84 (2019).

Grambow, B. Geological disposal of radioactive waste in clay. *Elements.* **12**, 239-245 (2016).

Grambow, B. Nuclear waste glass – how durable? *Elements* **2** 357-364, (2006).

Grambow, B. Uhling's Corrosion Handbook, Chapter 24, Corrosion of Glass (2000).

Grambow, B. Nuclear waste glass dissolution: mechanism, model and application. IAEA, JSS-TR-87-02 (1987).

Grambow B. A general rate equation for nuclear waste glass corrosion. *Mater. Res. Soc. Symp. Proc.* **44**, 15-27 (1985).

Grambow, B. & Giffaut, E. Coupling of chemical processes in the near field. Materials Research Society Symposium Proceedings **932**, 55-66 (2006).

Grambow, B. & Müller, R. First-order dissolution rate law and the role of surface layers in glass performance assessment. *J. Nuc. Mater*. **298**, 112-124 (2001).

Greaves G.N. EXAFS and the structure of glass. *J. Non-Cryst. Sol*ids **71**, [1-3] 203-217 (1985).

Gribble, N. Personal communication, Ukraine Project 9038 - Meeting on Storage Facility for Vitrified HLW Concept, IAEA, Vienna, Austria, 9th August (2018).

Guittonneau *et al.* A 25-year laboratory experiment on French SON68 nuclear glass leached in a granitic environment – First investigations. *J. Nuc. Mat*. **408**, 73-89 (2011).

Guo *et al.* Self-accelerated corrosion of nuclear waste forms at material interfaces. *Nat. Mater.* (2020). https://doi.org/10.1038/s41563-019-0579-x

Güven, N. In: Bailey, S. W. (Ed.), Hydrous Phyllosilicates (Exclusive of Micas). Mineralogical Society of America, Washington, D.C. p. 497 (1988).

Hand, R. Personal communication regarding the prediction of initial dissolution rates (2018).

Harder, H. The role of magnesium in the formation of smectite minerals. *Chem. Geol.* **10**, 31-39 (1972).

Harrison, M.T. Experimental studies to investigate the durability of UK HLW glasses using a new base glass formulation and glasses from POCO operations. National Nuclear Laboratory Report RWM.01.008 (2018)

Harrison, M. T. Personal communication – Next Generation Nuclear Winter School, Solihull, UK, 4th-6th January (2018a).

Harrison, M. T. Vitrification of high level waste in the UK. *Pro. Mat. Sci.* **7**, 10-15 (2014).

Harrison M. The effect of composition on short- and long-term durability of UK HLW glass. *Proc. Mat. Sci*, **7**, 186-192 (2014).

Harrison *et al.* The effect on long term aqueous durability of variations in the compositions of UK vitrified HLW product. *Glass Technol.: Eur. J. Glass Sci. Technol. A*, **53**, [5], 211-216 (2012).

Harrison, M.T. & Brown, G.C. Chemical durability of UK vitrified high level waste in Si-saturated solution. *Mat. Let.* **221,** 154-156 (2018).

Haynie, D. (2008). Gibbs free energy – theory. In *Biological Thermodynamics* (pp. 85-133). Cambridge: Cambridge University Press. doi:10.1017/CBO9780511802690.005

Heath *et al.* Immobilisation of prototype fast reactor raffinate in a barium borosilicate glass matrix. *J. Nucl. Mater*. **508**, 203-211 (2018).

Hedin, A. & Olsson, O. Crystalline rock as a repository for Swedish spent nuclear fuel. *Elements*. 12, 247-252 (2016).

Heinonen, J. Addressing the challenges of geological disposal through a step-wise approach. Presentation at The 6th Review Meeting of the Contracting Parties to the Joint Convention on the Safety of Spent Fuel Management and on the Safety of Radioactive Waste Management, Topical Session, Vienna, Austria 26th August (2018).

Hellman *et al.* Nanometer-scale evidence for interfacial dissolution-reprecipitation control of silicate glass corrosion. *Nat. Mater.* **14,** 307-311 (2015).

Hellman *et al.* Unifying natural and laboratory chemical weathering with interfacial dissolution-reprecipitation: a study based on the nanometer-scale chemistry of fluid-silicate interfaces. *Chem. Geol.* **294-295,** 203-216 (2012).

Hench L.L & Clark D.E. Surface properties and performance prediction of alternative waste forms. *Florida Univ., Gainesville* (1986).

Hieftje, G. M., *Introduction – A forward-looking perspective in inductively coupled plasma spectroscopy and its applications.* Second., S. J. Hill, Ed. (Oxford: Blackwell Publishing Ltd) p. 22 (2007).

Holland *et al.* NMR insights into wasteforms for the vitrification of high-level Nuclear waste. *Appl. Magn. Reson.* **32**, 483-497 (2007).

Hopf *et al.* Glass-water interaction: Effect of high-valence cations on glass structure and chemical durability. *Geochim. Cosmochim. Acta* **181**, 54-71 (2016).

House of Commons. Business, Energy and Industrial Strategy Committee, Draft National Policy statement for Geological Disposal Infrastructure. Twelfth Report of Session 2017-19. HC 1092 (2018).

Hyatt *et al.* Vapour phase hydration of blended oxide – Magnox waste glasses. Materials Research Society Symposium Proceedings **807** (2004).

IAEA. International Atomic Energy Agency Nuclear Energy Series, Status and Trends in Spent Fuel and Radioactive Waste Management, No. NW-T1.14, (IAEA: Vienna) (2018).

IAEA. International Atomic Energy Agency Safety Standards, Classification of Radioactive Waste, General Safety Guide, No. GSG-1, (IAEA: Vienna) (2009).

IAEA. International Atomic Energy Agency, Low and Intermediate Level Waste Repositories: Socioeconomic Aspects and Public Involvement (Proc. Workshop Vienna, 2005), IAEA-TECDOC-1553, (IAEA: Vienna) (2007).

IAEA. International Atomic Energy Agency, Management of Waste from the Use of Radioactive Material in Medicine, Industry, Agriculture, Research and Education. IAEA Safety Standards Series No. WS-G-2.7, (IAEA: Vienna) (2005).

IAEA. International Atomic Energy Agency, Scientific and Technical Basis for the Geological Disposal of Radioactive Wastes. Technical Report Series No. 413, (IAEA: Vienna) (2003).

Icenhower J. P. Personal communication regarding the Nature Materials Degradation publication - Daniel Backhouse D.J., Fisher A.J., Neeway J.J, Corkhill C.L., Hyatt N.C., & Hand R.J. *Corrosion of the International Simple Glass (ISG) under acidic to hyperalkaline conditions*. 2:29 (2018). (2018).

Icenhower, J. Question aired and discussed at 12th Pacific Rim Conference on Ceramic and Glass Technology (PACRIM 12), including Glass & Optical Materials Division Meeting (GOMD 2017), Waikoloa Village Hilton, Hawaii, USA, 22nd-26th May (2017).

Icenhower J.P & Steefel C.I. Experimentally determined dissolution kinetics of SON68 glass at 90 ^{o}C over a silica saturation interval: Evidence against a linear rate law. *J. Nucl. Mater*. **439**, 137-147 (2013).

Icenhower *et al.* Experimentally determined dissolution kinetics of Na-rich borosilicate glass at far from equilibrium conditions: Implications for Transition State Theory. *Geochim. Cosmochim. Acta* **72**, 2767-2788 (2008).

Icenhower J.P & Dove P.M. The dissolution kinetics of amorphous silica into sodium chloride solutions: Effects of temperature and ionic strength. *Geochim. Cosmochim. Acta* **64**, [24], 4193-4203 (2000).

Iler, R. K. The Chemistry of Silica: Solubility, Polymerization, Colloid and Surface Properties and Biochemistry of Silica (Wiley: New York) (1979).

Inagaki *et al. J. Nucl. Mater.* **354**, 171-184 (2016).

Inagaki. Y., Kikunaga, T., Idemitsu. K. & Arima. T. Initial dissolution rate of the international simple glass as a function of pH and temperature measured using microchannel flow-through test method. *Int. J. App. Gla. Sci.* **4** [4], 317-327 (2013).

Inagaki *et al.* Mat. Res. Soc. Symp. Proc. **713**, 589-596 (2002).

Iwalewa. T., Qu. T. & Farnan. I. Investigation of the maximum dissolution rates and temperature dependence of a simulated UK nuclear waste glass in circum-neutral media at 40 and 90 ^{o}C in a dynamic system. *Appl. Geochem.* **82**, 177-190 (2017).

Jan *et al.* Molecular dynamics simulation of ballistic effects in simplified nuclear waste glasses. *J. Non-Cryst. Solids.* **505**, 118-201 (2019).

Jantzen *et al.* Radioactive waste conditioning, immobilisation, and encapsulation processes and technologies: Overview and advances, In *Radioactive waste management and contaminated site clean-up: Processes, technologies and international experience,* W.E. Lee, M.I. Ojovan and C.M. Jantzen, Eds. (Cambridge: Woodhead), 171-272 (2013).

Jantzen *et al.* Durable Glass for Thousands of Years. *Int. J. App. Gla. Sci.,* **1** [1]*,* 38-62 (2010).

Janutcha *et al.* Elasticity, hardness, and fracture toughness of sodium aluminoborosilicate glasses. *J. Am. Cer. Soc.* DOI: 10.1111/jace.16304 (2018).

Jégou C., Gin. S., & Larché F. Alteration kinetics of a simplified nuclear glass in an aqueous medium: effects of solution chemistry and of protective gel properties on diminishing the alteration rate. *J. Nucl. Mater.* **280,** [2], 216-229 (2000).

Jegou,C, PhD thesis, Universite des Sciences et Techniques du Languedoc, Montpellier (1998).

Jing *et al.* Hydrothermal synthesis of pollucite, analcime and their solid solutions and analysis of their properties. *J. Nucl. Mater.* **488** 63-69, (2017).

Jollivet *et al.* Effect of clayey groundwater on the dissolution rate of the simulated nuclear waste glass SON68, *J. Nucl. Mater*. **420**, 508-518 (2012).

Jollivet, P., Gin. S., & Schumacher, S. Forward dissolution rate of silicate glasses of nuclear interest in clay-equilibrated groundwaters. *Chem. Geo.* **330-331**, 207-217 (2012).

Kaky *et al.* Structural, thermal, and optical analysis of zinc boro-aluminosilicate glasses containing different alkali and alkaline modifier ions. *J. Non-Cryst. Sol.* **456**, 55-63, (2017).

Kamizono, H. Leaching behaviour of simulated high-level waste glass in groundwater. *J. Nucl. Mater*. **127**, 242-246 (1985).

Karell *et al.* Properties of selected zirconia containing silicate glasses. *Silik*. **50**, 78-82 (2006).

Kaspar *et al.* Invited review: Physical and optical properties of the International Simple Glass. *npJ. Mater. Degrad.* 3:15 (2019).

Kim *et al.* Geological Storage of High Level Waste. *Journal of Civil Engineering*, **15**, [4], 721-737 (2011).

Kirkpatrick, R.J. MAS-NMR spectroscopy of minerals and glasses, in F.C. Hawthorne (Ed.) Reviews in Mineralogy **18**, *Mineral. Soc. America* 341–403 (1988).

Kirkpatrick *et al.* Solid-state Nuclear magnetic resonance spectroscopy of minerals. *Ann. Rev. Earth Planet. Sci.* **13**, 146-148 (1985).

Knauss *et al.* Dissolution kinetics of a simple analogue nuclear waste glass as a function of pH, time and temperature. *MRS Online Proceedings Library*, **176** (1989).

Kullberg *et al*. Formation and crystallization of zinc borosilicate glasses: Influence of the ZnO/B2O3 ratio. *J. Non-Cryst. Solids.* **441**, 79-85 (2016).

Kusumoto *et al.* Magnesium substitution in calcium and strontium fluoro-phospho-aluminosilicate glasses by multinuclear 19F, 31P, 27Al, and 29Si MAS-NMR spectroscopy. *J. Non-Cryst. Solids: X* **1**, 100008, (2019).

Lasaga, A. C. (1981). Transition state theory. Pp 135-168 in: *Kinetics of Geochemical Processes* (A. C. Lasaga and R. J. Kirkpatrick, editors). Reviews in Mineralogy, **8**, Mineralogical Society of America, Washington DC.

Lasaga, A. C. Fundamental approaches in describing mineral dissolution and precipitation rates. *Reviews in Mineralogy, Chemical Weathering Rates of Silicate Minerals, Min. Soc. Am.* **31**, 353-406 (1995).

Laverov *et al.* The Russian strategy of using crystalline rock as a repository for nuclear waste. *Elements*. 12, 253-256 (2016).

Le Grand *et al.* Zinc environment in aluminoborosilicate glasses by Zn K-Edge extended X-ray absorption fine structure spectroscopy. *J. Mater. Res.* **15**, [9], 2015-2019 (2000).

Ledieu *et al.* Leaching of borosilicate glasses. I. Experiments. *J. Non-Cryst. Sol,* **343**, 3-12 (2004).

Lee, P. Personal communication - Washington River Protection Solutions – January (2017).

Lenting *et al.* Towards a unifying mechanistic model for silicate glass corrosion. *npj. Mater. Degrad.* 2:28 (2018).

Leturcq *et al.* Initial and long-term dissolution rates of aluminosilicate glasses enriched with Ti, Zr and Nd. *Chem. Geo,* **160**, 39-62 (1999).

Lothenbach *et al.* Magnesium and calcium silicate hydrates. *Cement Concrete Res,* **77***,* 60-68 (2015).

LLW Repository Ltd. Waste Informed Decommissioning Model and principles. National Waste Programme. NWP/REP/109 July 2020 Issue 2 (2020).

Lu *et al.* Structural role of ZrO_2 and its impact on properties of boroaluminosilicate nuclear waste glass. *npJ. Mater. Degrad.* 2:19 (2018).

Lusvardi *et al.* A combined experimental and computational approach to $(Na_2O)_{1-x}$ CaO $(ZnO)_x$ $2SiO_2$ glasses characterization. *J. Non-Crys. Sol,* **345 & 346**, 710-714 (2004).

Lutze, W. & Ewing, R. C. *Radioactive waste forms for the future*, Lutze, W. and Ewing, R. C. (Ed.), (North-Holland : Amsterdam) 699-740 (1988).

Ma *et al.* A mechanistic model for long-term nuclear waste glass dissolution integrating chemical affinity and interfacial diffusion barrier. *J. Nucl. Mater*. **486**, 70-85 (2017).

Maeda *et al.* Corrosion behaviour of simulated HLW glass in the presence of magnesium ion, *Int. J. Corr*. 796457 (2011).

Mägi *et al. J. Phys. Chem.,* **88**, 1518 (1984).

Magrabi, C., Smith, W., and Larkin, M. J. Development of the glass formulation for the Windscale vitrification plant. Radioactive waste management and the Nuclear Fuel cycle **19**, 85-106 (1987).

Malfait *et al.* Quantitative Raman spectroscopy: High-temperature speciation of potassium silicate melts. *J. Non-Cryst. Sol,* **335**, 4029-4042 (2007).

Mann, C. A study of the dissolution of UK nuclear waste glass in cement waters, Ph.D Thesis, The University of Sheffield (2018).

Mann *et al.* Influence of young cement water on the corrosion of the International Simple Glass. *npj. Mat. Deg.* 3:5 (2019).

Maraghechi *et al.* Effect of calcium on dissolution and precipitation reactions of amorphous silica at high alkalinity. *Cem. Con, Res.* **87**, 1-13 (2016).

Marcus, Y. Thermodynamics of solvation of ions, *J. Chem. Soc. Faraday Trans*, **87**, 2995 – 2999 (1991).

Marsh *et al*. The important role and performance of engineered barriers in a UK geological disposal facility for hisher activity radioactive waste. *Progress in Nuclear Energy.* **137**, 103736 (2021).

Matlack *et al.* High temperature melter tests for vitrification of BNFL high-level Nuclear waste. Scientific Basis for Nuclear Waste Management XXII, Paper 9.55, *Mater. Res. Soc. Proc. Fall Meeting* (1998).

Mayer, S. Deep geologic repository: A roadmap towards implementation and how to know if, what and when more R&D is needed. Presentation at The 43rd Symposium on the Scientific Basis for Nuclear Waste Management, International Atomic Energy, Vienna, Austria, 24th October (2019). Presentation at The 43rd Symposium on the Scientific Basis for Nuclear Waste Management, International Atomic Energy, Vienna, Austria, 23rd October (2019).

McGrail *et al.* Low-activity waste glass studies: FY 2000 summary report. PNNL-13381 (2000).

McGrail, B. P., Ebert, W. L., Bakel, A. J. & Peeler, D. K. Measurement of the kinetic rate law parameters on a Na-Ca-Al borosilicate glass for low activity waste. *J. Nuc. Mat.* **149,** 175-189 (1997).

McGrail, B.P. & Peeler, D.K. Evaluation of the Single-pass Flow-through Test to Support a Low-activity Waste Specification. PNL-10746. Pacific Northwest Laboratory, Richmond, Washington (1995).

McKeown *et al. J. Non-Cryst. Solids* **258**, 98-109 (1999).

McKeown *et al.* Local environment of Zn in zirconium borosilicate glasses determined by X-ray absorption spectroscopy. *J. Non-Cryst. Solids* **261**, 155-162 (2000).

Mendel, J. E. Final report of the defense high-level-waste leaching mechanisms program. *Pacific Northwest National Laboratory* (1984).

Mercado-Depierre, S., Angeli, F., Frizon, F. & Gin, S. Antagonist effects of calcium on borosilicate glass alteration. *J. Nucl. Mater*. **441**, 402-410 (2013).

Meyer, W. IAEA Coordinated research project on ion beam irradiation for high-level-nuclear wasteform development (INWARD) XLIII symposium on the Scientific Basis of Nuclear Waste Management, Vienna (2019).

Meyer, W. Personal communication, International Pre-disposal Network (IPN) Meeting, IAEA, Vienna, Austria (2018).

Michelin *et al.* Effect of iron metal and siderite on the durability of simulated archaeological glassy materials. *Corros. Sci.* **76**, 403-414 (2013).

Möncke *et al.* Phys. On the connectivity of borate tetrahedra in borate and borosilicate glasses. Chem. Glasses: Eur. J. Glass Sci. Technol. B, **56** [5], 203-211 (2015).

Morey, G. W. & Bowen, N. L. The decomposition of glass by water at high temperatures and pressures. *J. Soc. Glass Tech.* **11,** 97-106 (1927).

Mougnaud *et al.* Heavy ion radiation ageing on long-term glass alteration. *J. Nucl. Mater.* **510**, 168-177 (2018).

Mougnaud *et al.* Effect of low dose electron beam irradiation on the alteration layer formed during nuclear glass leaching. *J. Nucl. Mater.* **482**, 53-62 (2016).

Muller *et al.* Characterization of alteration phases on HLW glasses after 15 years of PCT leaching. *Ceramic Transactions*, **176**, 191-199 (2006).

Musić et *al.* Some microstructural Properties of Zinc Borosilicate Glass as a Possible Matrix in the Immobilization of Various Wastes. Croat. Chem. Acta. **92**, [3] (2019) DOI: 10.5562/cca3574

Nagata *et al.* Analytical study of the formation process of hemimorphite – Part 1 – Analysis of the crystallization process by the co-precipitation method. *Zairyo-to-Kankyo (Japan Society of Corrosion Engineering).* **42**, 225-233 (1993).

NDA – Nuclear Decommissioning Authority, 2019 UK Radioactive Waste Inventory, Department for Business, Energy and Industrial Strategy (2019).

Neeway J. J., Rieke P. C., Parruzot B. P., Ryan J. V. & Asmussen R. M.The dissolution behaviour of borosilicate glasses in far-from equilibrium conditions. *Geochim. Cosmochim. Acta.* **226,** 132-148 (2018).

Neeway *et al.* Vapor hydration of SON68 glass from 90 °C to 200 °C: A kinetic study and corrosion products investigation. *J. Non. Cryst. Solids* **358**, 2894-2905 (2012).

Nieto P. & Zanni H. Polymerization of alkaline-calcium-silicate hydrates obtained by interaction between alkali–silica solutions and calcium compounds. A ^{29}Si nuclear magnetic resonance study. *J. Mater. Sci.* **2**, 3419–3425 (1997).

NNL, Research Studentship Agreement Next Generation Nuclear with RWM-NDA, NNL Req 8035978 (UoS ref 142106) between National Nuclear Laboratory and University of Sheffield, 5th November (2014).

Oelkers E.H. General kinetic description of multioxide silicate mineral and glass dissolution. *Geochim. Cosmochim. Acta.* **65** [21], 3707-3719 (2001).

Oelkers E.H. and Gislason S. G. The mechanisms, rates and consequences of basaltic glass dissolution. I. An experimental study of the dissolution rates of basaltic glass as a function of aqueous Al, Si and oxalic acid concentration at 25 °C and pH = 3 and 11. *Geochim. Cosmochim. Acta.* **65** (21), 3671-3681 (2001).

Ohkubo *et al.* Molecular dynamics simulation of water confinement in disordered aluminosilicate subnanopores. *Sci. Rep.* **8**, 3761 (2018).

Ojovan, M. On alteration rate renewal Stage of nuclear waste glass corrosion. Presentation at The 43rd Symposium on the Scientific Basis for Nuclear Waste Management, International Atomic Energy, Vienna, Austria, 24th October (2019). Presentation at The 43rd Symposium on the Scientific Basis for Nuclear Waste Management, International Atomic Energy, Vienna, Austria, 23rd October (2019).

Ojovan M. On alteration layer renewal stage of nuclear waste glass corrosion *MRS Adv*. DOI: https://doi.org/10.1557/adv.2020 .36 (2019).

Ojovan M. Personal communication. International Atomic Energy Agency, Vienna, Austria, September (2018).

Ojovan M. I. & Lee W. E., About U-shaped glass corrosion rate/pH curves for vitreous nuclear wasteforms*. Inn. Corr & Mat. Sci*. **7**, 30-37, (2017).

Ojovan *et al.* Corrosion mechanisms of low level vitrified radioactive waste in a loamy soil. *Mat. Res. Soc. Symp. Proc.* **807**, 139-144 (2004).

Ojovan *et al.* Product consistency test of fully radioactive high-sodium content borosilicate glass K-26. *Mat. Res. Soc. Symp. Proc.* **824**, 1-13 (2004a).

Padovani C., Personal communication with former RWM employee, The 45th Waste Management Conference, Phoenix, Arizona, USA 5-7th March (2019).

Parkinson, B. G., Effect of minor additions on structure and volatilization loss in simulated nuclear borosilicate glasses. *J. Non. Cryst. Solids* **353**, [44-46], 4076-4083 (2007).

Parkinson *et al.* The effect of oxide additions on medium-range order structures in borosilicate glasses. *J. Phys.: Condens. Matter.,* **19**, 415114 (2007).

Parruzot *et al.* Multi-glass investigation of Stage III glass dissolution behaviour from 22 to 90 °C triggered by the addition of zeolite phases. *J. Nucl. Mater*. **523**, 490-501, (2019).

Pascua *et al.* Synthesis of monodisperse Zn-smectite. Appl. Cla. Sci. **48**, 55-59 (2010).

Pearson, C. *Conservation of Marine Archaeological Objects.* (Elsevier: New York) (1988).

Pegg, I. Personal communication – Joint ICTP-IAEA Workshop on Fundamentals of Vitrification and Vitreous Materials for Nuclear Waste Immobilization, ICTP, Trieste, Italy, 6th-10th November (2017).

Petrescu, S., Structural and physio-chemical characterization of some soda lime zinc alumina-silicate glasses. *J. Non. Cryst. Solids* **358**, 3280-3288 (2012).

Peuget *et al.* International Atomic Energy Agency – TechDoc (IN PRESS).

Peuget *et al.* Radiation effects in ISG glass: from structural changes to long-term behaviour. *npJ. Mater. Degrad.* 2:23 (2018).

Peuget *et al.* Effect of alpha radiation on the leaching behaviour of nuclear glass *J. Nucl. Mater.* **362**, 474-479 (2007).

Peuget *et al.* Effects of deposited nuclear and electronic energy on the hardness of R7T7-type containment glass. *J. Nucl. Mater*. **246**, 379-386, (2006).

Pierce *et al.* Experimental determination of the effect of the ratio of B/Al on glass dissolution along the nepheline ($NaAlSiO_4$)-malinkoite ($NaBSiO_4$) join. *Geochim. Cosmochim. Acta*. **74**, 2634-2654 (2010).

Pierce E. M., Rodriguez E. A., Calligan L. J., Shaw W. J. & McGrail B. P. An experimental study of the dissolution rates of simulated aluminoborosilicate waste glasses as a function of pH and temperature under dilute conditions. *Appl. Geochem.* **223**, 2559-2573 (2008).

Pierce et al., Laboratory Testing of Bulk Vitrified Low-Activity Waste Forms to Support the 2005 Integrated Disposal Facility Performance Assessment, [PNNL-15126, Rev. 2] from Pacific Northwest National Laboratory, Richland, WA (2006).

PNNL., Pacific Northwest National Laboratories. A strategy to conduct an analysis of the long-term performance of low-activity waste glass in a shallow subsurface disposal system at Hanford, PNNL-23503 RPT-66309-001 Rev. 0 (2014).

Putnis, A. Sharpened interface. *Nat. Mater.* **14**, 261 (2015).

Putis, A. & Putnis. C.V. (2007) The mechanisms of reequilibration of solids in the presence of a fluid phase. *J. Solid State Chem.* **180,** 1783-1786.

Rajmohan, N., Frugier, P. & Gin, S. Composition effects on synthetic glass alteration mechanisms: Part 1. Experiments. *Chem. Geol.* **279**, 106 (2010).

Ribet *et al.* Compositional Effects on the Long-Term Durability of Nuclear Waste Glasses: A Statistical Approach. *Mat. Res. Soc. Symp. Proc.* **824**, (2004).

Rébiscoul, D., Bruguier, F., Magnin, V. & Gin, S. Impact of soda-lime borosilicate glass composition on water penetration and water structure at the first time of alteration. *J. Non-Cryst. Solids* **358**, 2951–2960 (2012).

Rebiscoul *et al.* Protective properties and dissolution ability of the gel formed during nuclear glass alteration. *J. Nucl. Mater*. **342**, 26-34 (2005).

Rebiscoul *et al.* Morphological evolution of alteration layers formed during nuclear glass alteration: New evidence of a gel as a diffusive barrier *J. Nucl. Mater*. **326**, 9-18 (2004).

Ribet *et al.* Mat. Res. Soc. Symp. Proc. **824**, 309-314 (2004).

Ribet S.& Gin, S. Role of neoformed phases on the mechanics controlling the resumption of SON68 glass alteration in alkaline media. *J. Nucl. Mater.* **324** 152-164, (2004).

Ross, C.S. Sauconite – a clay mineral of the montmorillonite group. *Am. Min.* **31**, [41] 1-424 (1946).

Russ, J. C. *Fundamentals of Energy Dispersive X-Ray Analysis*, 1st ed. (Bodmin: Butterworths & Co Ltd) (1984).

RWM. Geological Disposal – Concept Status Report October 2017, NDA/RWM/155 (2017).

Ryan, J. *pers comm.* Presentation on Stirred Reactor Coupon Analysis at The International Workshop on Long-Term Glass Corrosion. Virtual Zoom Hosted, 1st April (2020).

Ryan *et al.* In-situ monitoring of seeded and unseeded stage III corrosion using Raman spectroscopy. *npJ. Mater. Degrad.* **3**:34 (2019).

Sanders, D. M. & Hench, L. L. Mechanisms of glass corrosion. *J. Am. Cer. Soc*. **56**, [7], 373-377 (1973).

Sang *et al. J. Non. Cryst. Solids* **208** 170 (1996).

Sang *et al.* Dissolution Mechanism of Soda-Lime Silicate Glass and of PNL 76-68 in the Presence of Dissolved Mg *Mater. Res. Soc. Symp. Proc*. **333** 519 (1993).

Sang *et al. Mat. Res. Soc. Symp*. Proc. **294**, 583-589 (1993).

Scales, C. R. Characterisation of simulated vitrified magnox product manufactured on the VTR, National Nuclear Laboratory Report NNL, 10, p. 10929 (2011).

Schalm, O. & Anaf, W. Laminated altered layers in historical glass: density variations of silica nanoparticle random packings as explanations for the observed lamellae. *J. Non-Cryst. Sol,* **442**, 1-16 (2016).

Schaut, R. Scientific Director for Corning Pharmaceutical Technologies – Comment discussed at the Glass Corrosion Workshop, Massachusetts Institute of Technology, Cambridge, MA, USA, 14th-15th June (2019).

Scheetz *et al.* The role of boron in monitoring the leaching of borosilicate glass waste forms. *Mater. Res. Soc. Proc.* **44**, 129 (1984).

Schofield *et al.* Experimental studies of the chemical durability of UK HLW and ILW glasses, Amec report to Radioactive Waste Management (UK), RWM005105, AMEC/103498/04 Issue 1 (2017).

Scholze, H. *Glass - Nature Structure and Properties, 1st ed*., (New York, Berlin, Heidelberg) (1991).

Scottish Government, Scotland's Higher Activity Radioactive Waste Policy, ISBN 978-0-7559-9892-0, January (2011).

Sessegolo *et al.* Effect of surface roughness on medieval-type glass alteration in aqueous medium. *J. Non-Cryst. Sol,* **505**, 260-271 (2019).

Shelby, J.E. *An Introduction to Glass Science and Technology*, (Cambridge: The Royal Society of Chemistry) p 57 (2005).

Sicard *et al.* Study of the kinetics of glass alteration by small-angle X-ray scattering. *J. Phys. Chem. B.* **108**, 7702-7708 (2004).

Short *et al.* Widening the envelope of UK HLW vitrification-experimental studies with high level waste loadings and new product formulations on a full scale non-active vitrification plant, Waste Management Conference, Phoenix, AZ, 24-28th February (2008).

Short *et al.* Devitrified and phase separated material found in simulated high level nuclear waste glasses containing Ca and Zn additions. *Mater. Res. Soc. Proc.* **1107**, 261-267 (2008).

Smedskjaer *et al.* Impact of ZnO on the structure and properties on sodium aluminosilicate glasses: Comparison with alkaline earth oxides. *J. Non-Cryst. Sol.* **381***,* 58-64 (2013).

Soleilhavoup *et al.* Contribution of first-principles calculations to multinuclear NMR analysis of borosilicate glasses. Paper published as part of the Quantum-Chemical Calculations and their applications special issue. *Magn. Res. Chem.* **48**, S159-170 (2010).

Soleimanzade *et al.* Devitrification and phase separation of zinc borosilicate glasses in the presence of MgO, P2O5 and ZrO2. *Int. J. Appl. Gla. Sci*., **5**, [2], 185-192 (2014).

SRNL. Letter report on compositional measurements of common simple glass. Savannah River National Laboratory, SRNL-L3100-2012-00092 (2012).

Stone-Weiss *et al.* Influence of Tris buffer solution chemistry upon dissolution behaviour of silicate-based glasses with varies B_2O_3/Al_2O_3 ratio. International Congress on Glass, Park Plaza Hotel, Boston, USA (2019) presentation (ICG-SIV-073-2019) (2019).

Stechert *et al.* Predicted mechanism for enhanced durability of zinc containing silicate glasses. *J. Am. Ceram. Soc.* **96**, [5] 1450-1455 (2013).

Strachan D. Glass dissolution as a function of pH and its implications for understanding mechanisms and future experiments. *Geochim. Cosmochim. Acta.* **219**, (2017).

Strachan, D. Glass dissolution as a function of pH and its implications on mechanisms and experiments. Report No. PNNL-SA-82068. Pacific Northwest National Laboratory, Richland, WA, USA (2011).

Taylor, P. A Review of Phase Separation in Borosilicate Glasses, With Reference to Nuclear Fuel Waste Immobilization, Whiteshell Nuclear Research Establishment, Atomic Energy of Canada AECL-10173, 22 (1990).

Taylor, P. and Owen, D. G., Liquid Immiscibility in the System Na2O-ZnO-B2O3-SiO2*, J. Am. Ceram. Soc*., **64** 360–367 (1981)

Thermo Fisher Scientific. *iCAP 6000 Series ICP-OES Spectrometer User Guide V3.1*. (2012).

Thien *et al.* The dual effect of magnesium on the long-term alteration rate of AVM nuclear waste glasses, *J. Nucl. Mater.* **427** 297-310 (2012).

Tromans, S. Views aired in witness evidence select committee, Draft National Policy statement for Geological Disposal Infrastructure, House of Commons, Business, Energy and Industrial Strategy Committee, London, UK, 10th July (2018).

Tournié *et al.* Impact of boron complexation by Tris buffer on the initial dissolution rate of borosilicate glasses. *J. Coll. Int. Sci*. **400**, 161-167 (2013).

United Kingdom. The United Kingdom's Sixth National Report on Compliance with the Obligations of the Joint Convention on the Safety of Spent Fuel and Radioactive Waste Management, Department for Business, Energy and Industrial Strategy (BEIS), October 2017 (2018).

United Nations Economic Commission for Europe, Convention on Access to Information, Public Participation in Decision-making and Access to Justice in Environmental Matters. (UNECE: Geneva) (1998).

Utton *et al.* Dissolution of vitrified wastes in a high-pH calcium-rich solution. *J. Nucl. Mater*. **435**, 112–122 (2013).

Van Iseghem *et al.* GLAMOR A critical evaluation of the dissolution mechanisms of high-level waste glasses in conditions of relevance for geological disposal SCK.CEN, CEA, Subatech, PNNL and SRNL, EUR 23097 (2007).

Van Iseghem *et al.* A critical evaluation of the dissolution mechanisms of High-Level-Waste glasses in conditions of relevance for geological disposal (GLAMOR). Final report, EUR 23097, European Commission, Contract FIKW-CT-2001-20140 (2006).

Vanaecker *et al.* Behaviour of Zn-bearing phases in base metal slag from France and Poland: A mineralogical approach for environmental purposes. *J. Geo. Exp.* **136**, 1-13 (2014).

Vance *et al.* The influence of ZnO incorporation on the aqueous leaching characteristics of a borosilicate glass. *J. Nucl. Mater*. **494**, 37-45 (2017).

Vasconcelos *et al.* Leaching of Nirex Reference Vault Backfill cement by clay, granite and saline groundwaters. In: *MRS Advances. Scientific Basis for Nuclear Waste Management XLI*. Cambridge University Press 1175-1180 (2018).

Vernaz, E. & Brueziere. History of nuclear waste glass in France. *Pro. Mat. Sci.* **7**, 3-9 (2014).

Vernaz, E. & Dussossoy, L.J. Current state of knowledge of nuclear waste glass corrosion mechanisms: the case of R7T7 glass. *Appl. Geochem*. **1**, 13-22 (1992).

Verney-Carron *et al.* Archaeological analogues and the future of nuclear waste glass. *J. Nucl. Mater*. **406,** 365-370 (2010).

Vienna *et al.* Impacts of glass composition, pH, and temperature on glass forward dissolution rate. *npj Mater. Degrad.* **2** (22) (2018).

Vienna *et al.* Current understanding and remaining challenges in modelling long-term degradation of borosilicate nuclear waste glasses, *Int. J. Appl. Glass. Sci.* **4** [4], 283-394 (2013).

Vienna *et al.* Hanford immobilized LAW product acceptance testing: tanks and focus area results. PNNL-13744 (2001).

Vinsot *et al.* In situ characterization of the Callovo-Oxfordian pore water composition. *Phys. Chem. Earth*, **33** [1], 75-86 (2008).

Vogels *et al.* Synthesis and characterization of saponite clays. *Am. Min.* **90**, 931-944 (2005).

Von Berlepsch, T. & Haverkamp, B. Salt as a host rock for the geological repository for nuclear waste. *Elements*. **12**, 257-262 (2016).

Wang *et al.* Modifier clustering and avoidance principle in borosilicate glasses: A molecular dynamics study. *J. Chem. Phys.* **150**, 044502 (2019).

Wang *et al.* Nonlinear dynamics and instability of aqueous dissolution of silicate glasses and minerals. *Sci. Rep.* 6:30256; doi: 10.1038/srep30256 (2016).

Warren, B. E. Summary of Work on Atomic Arrangement in Glass. *J. Am. Cer. Soc.*, **24**, 256-261 (1941)

Wellman, D. M., Gunderson. K. M., Icenhower. J. P. & Forrester. S. W. Dissolution kinetics of synthetic and natural meta-autunite minerals, $X^{(n)+}_{(3-n)}[(UO_2)(PO_4)]_2 \bullet xH_2O$, under acidic conditions. *Geo. Geo. Geo*. **8**, [11], 1-16 (2007).

Wellman *et al.* Elemental dissolution study of Pu-bearing borosilicate glasses. *J. Nucl. Mater.* **340**, 149-162 (2005).

Wolery T. J. EQ3NR, A computer code for geochemical aqueous speciation-solubility calculations: theoretical manual, user's guide and related documentation (Version 7.0). UCRL-MA-110662 PT 1, Lawrence Livermore National Laboratory, Livermore, CA (1992).

Wright, A.C., Amorphography and the modelling of amorphous solid structures by geometric transformations, *J. Non-Cryst. Solids* **42**, 6986 (1980).

Wu & Stebbins. Effects of cation field strength on the structure of aluminoborosilicate glasses: High-resolution ^{11}B, ^{27}Al and ^{23}Na MAS NMR. *J. Non-Cryst. Solids* **355**, 556-562, (2009).

Wulff, G. Über die Kristallröntgenogramme, *Physikalische Zeitschrift*. **14,** 217-220 (1913).

Xing, S.B. and Pegg, I.G. Effects of Container Material on PCT Leach Test Results for High-Level Nuclear Waste Glasses, Scientific Basis for Nuclear Waste Management XVII, Eds. R. Van Konynenberg and A. Barkatt, MRS, Pittsburgh, PA, **333**, 557-564 (1994).

Yokoyama *et al.* Synthesis and characterization of Zn-substituted saponite (sauconite). *Clay. Sci.* **13**, 75-80 (2006).

Yu et al. Synthesis of Zn-Saponite using a microwave circulating reflux method under atmospheric pressure. *Minerals.* **10**, 45 (2020).

Zachariasen, W. H., The atomic arrangement in glass*, J. Am. Chem. Soc.*, **54**, 3841-3851 (1932).

Zhang *et al.* Effect of Zn- and Ca-oxide on the structure and chemical durability of simulant alkali borosilicate glasses for immobilisation of UK high level waste. *J. Nucl. Mat.* **462**, 321-328 (2015).

Zhao *et al.* Leaching kinetics of hemimorphite in ammonium chloride solution. *Metals.* **7**, [237], doi:10.3390/met7070237 (2017).

Notes

-